5-5-2017

Equilibrium and Kinetically-Limited Lattice Relaxation of Multilayered and Compositionally-Graded Semiconductor Metamorphic Heterostructures

Tedi Kujofsa
University of Connecticut - Storrs, tedi.kujofsa@gmail.com

Equilibrium and Kinetically-Limited Lattice Relaxation of Multilayered and Compositionally-Graded Semiconductor Metamorphic Heterostructures

Tedi Kujofsa, PhD

University of Connecticut, 2017

Metamorphic buffer layers (MBLs) allow tremendous flexibility in designing novel semiconductor heterostructures for application in various microelectronic and optical devices. However, device fabrication, reliability and performance are limited by lattice relaxation mechanisms and dislocation defects that are associated with the growth of mismatched material systems. Therefore, understanding the extent of strain relaxation and dislocation dynamics in semiconducting heterostructures has important implications in the design of devices which exhibit desired strain and dislocation characteristics. In this dissertation, we present equilibrium and plastic flow models which are applicable to multilayered and compositionally-graded semiconductor heterostructures and have studied both the thermal equilibrium and kinetically-limited lattice relaxation; in our work, we have accounted for the time evolution of kinetically-limited and equilibrium strain relaxation, thermal activation of glide, and misfit-threading dislocation interactions.

First, this dissertation reports the equilibrium lattice relaxation of various semiconductor epitaxial heterostructures including the distributions of the residual strain and misfit dislocation (MD) characteristics. Up until recently, equilibrium modeling has been accomplished by complex numerical energy-minimization schemes, which are non-intuitive, require specialized code, and are computationally intense. In order to address these complexities, we have developed an electric circuit model (ECM) approach for the equilibrium analysis of an epitaxial stack, in which each sublayer may be represented by an analogous circuit configuration. This new approach enables

analysis using widely accessible circuit simulators, and an intuitive understanding of electric circuits may be translated to the relaxation of strained-layer structures. Furthermore, the ECM allows the development of analytical expressions for the strain, misfit dislocation density, critical layer thickness and widths of MD free zones for a continuously-graded layer having an arbitrary compositional profile.

Second, this dissertation describes the development of novel approaches for controlling the lattice relaxation mechanisms and the generation of dislocation defects based on the equilibrium and plastic flow models. Some of these key approaches include dislocation compensation, strain compensation and combinations of temperature- and compositional-grading for controlling the lattice relaxation rates. For each structure type, we studied the requirements on thickness and compositional profile to remove mobile threading dislocations or tailor the strain.

Equilibrium and Kinetically-Limited Lattice Relaxation of Multilayered and Compositionally-Graded Semiconductor Metamorphic Heterostructures

Tedi Kujofsa

B.S., University of Connecticut, 2011

M.S., University of Connecticut, 2015

A Dissertation

Submitted in Partial Fulfillment of the

Requirements for the Degree of

Doctor of Philosophy

at the

University of Connecticut

2017

2017

APPROVAL PAGE

Doctor of Philosophy Dissertation

Equilibrium and Kinetically-Limited Lattice Relaxation of Multilayered and Compositionally-Graded Semiconductor Metamorphic Heterostructures

Presented by

Tedi Kujofsa, B.S., M.S.

.

Major Advisor _____

John E. Ayers

Associate Advisor _____

Rajeev Bansal

Associate Advisor _____

Eric Donkor

Associate Advisor _____

Faquir C. Jain

Associate Advisor _____

David Tonn

University of Connecticut

2017

To my entire family with the outmost gratitude for without their love, support and sacrifices, I could not have accomplished the completion of this work. To my parents, Muhamed and Eridana, please accept this achievement as a symbol for everything you have done to provide me with a better life. To my wife Lorejna, thank you for making my life beautiful and supporting me in every step of the way. And lastly Basti, who unknowingly provided continual company at my feet during my research.

ACKNOWLEDGMENT

The past few years have been the most challenging years in my life, but at the same time the most rewarding ones. The completion of my Ph. D. would not be possible if it weren't for the group of individuals that have provided continual support and encouragement. I am forever indebted to Dr. John E. Ayers, who not only introduced me to the field but has played a vital role in my professional development. The guidance and support that I received from my mentor cannot be put into word. Dr. Ayers, I believe this thesis is not long enough to describe how much I have appreciated our collaboration. You were always there to provide direction and insight but most importantly your boundless optimism and encouragement always provided another view of the world. I am forever grateful to you for shaping my intellectual capabilities and I want you to know that you will always be a part of our family.

A special thank you goes to my advisory committee – Dr. Rajeev Bansal, Dr. Eric Donkor, Dr. Faquir Jain and Dr. David Tonn – for providing me with constructive feedback throughout my graduate career. I have certainly enjoyed taking courses with each one of the advisors and have gained a great deal of knowledge. Professor Tonn, please note that your metamaterials course sparked my inspiration in developing the electrical circuit model. I am grateful to the Electrical Engineering and Physics department for providing continuous funding through teaching, which supported my academic endeavors but also covered some of the daily living costs. I would also like to thank Epitax Engineering for supporting part of this research work.

The journey over these years has not only included completing a Ph. D., but also starting a wonderful life with my wife Lorejna and spending much of my free time building our home in Cambridge, Massachusetts. I would like to thank my beautiful wife, who was always happy and supportive in starting this new chapter together. I recognized that I owe you some vacation/weekend time and promise to do my best in making up for that in the near future. Most importantly, I would like to dedicate this degree to my parents, Muhamed and Eridana for their sacrifices in enabling me to have this kind of life. To my sister Iva, I will always love you and wish you nothing but the best in life. We had a special life us two but always managed to show the world that "a rose could grow out of the concrete". Every kid has a superhero and mine is definitely my father, therefore I want to thank you Muhamed for pushing me towards the field of electrical engineering and for always teaching me that an education can bring out the best in what life has to offer. And lastly, I would like to thank my partner in crime, a puppy named Basti who has been supporting me throughout my graduate career by keeping me company and helping with some of the "formulas".

PREFACE

This dissertation provides a summary of my work in the field of heteroepitaxy which tells something about the state of the field – theory, fabrication principles and characterization – but more specifically our contribution to its understanding. This dissertation includes all of the published papers which I have contributed to in my time as a graduate student pursuing my Ph.D. at the University of Connecticut. While there have been major advances in the field so far, I am confident that the years to come will bring about a revolution and a greater understanding of the relaxation mechanisms and dislocation dynamics and I hope that my work so far may has made some contribution to that understanding. To the future PhDs, researchers and scientists of the field, I wish you great success and my only advice is to never take for granted the explanation of your work in the simplest terms because that is when we start to fully appreciate the novelty and new advances of our field.

PUBLICATION LIST

Books

John E. Ayers, **Tedi Kujofsa,** Paul B. Rago and Johanna. E. Raphael, "Heteroepitaxy of Semiconductors: Theory, Growth and Characterization, Second Edition," CRC Press, Boca Raton, FL, (2016).

Scientific Journal Articles

1. **T. Kujofsa** and J. E. Ayers, "Critical Layer Thickness: Theory and Experiment in the ZnSe/GaAs (001) Material System," Int. J. Hi. Spe. Ele. Syst., (In Press)
2. **T. Kujofsa** and J. E. Ayers "Progression of Strain Relaxation in Linearly-Graded $GaAs_{1-y}P_y$/GaAs (001) Epitaxial Layers Approximated by a Finite Number of Sublayers," Int. J. Hi. Spe. Ele. Syst., (In Press)
3. **T. Kujofsa** and J. E. Ayers, "Strain Compensation in a Semiconducting Device Structure using an Intentionally Mismatched Uniform Buffer Layer" Semicond. Sci. Technol., 31, 1250005 (2016).
4. **T. Kujofsa** and J. E. Ayers, "Electrical Circuit Model for Strained-Layer Epitaxy," Semicond. Sci. Technol., 31, 115014 (2016).
5. **T. Kujofsa,** S. Cheruku, D. Sidoti, S. Xhurxhi, F. Obst, J. P. Correa, B. Bertoli, P. B. Rago, E. N Suarez, F. C. Jain, and J. E. Ayers, "Critical Layer Thickness in II-VI / GaAs Heterostructures and the Role of Finite Experimental Resolution," J. Vac. Sci. Technol. B, 34, 051201 (2016)
6. **T. Kujofsa** and J. E. Ayers, "Dynamics of Kinetically-Limited Strain and Threading Dislocations in Temperature and Compositionally-Graded ZnSSe/GaAs (001) Metamorphic Heterostructures," J. Electron. Mat., 45, 4580 (2016).
7. **T. Kujofsa** and J. E. Ayers, "Equilibrium Lattice Relaxation and Misfit Dislocations in Step-Graded $In_xGa_{1-x}As$/GaAs (001) and $In_xAl_{1-x}As$/GaAs (001) Metamorphic Buffer Layers," J. Electron. Mat., 45, 2831 (2016).
8. **T. Kujofsa**, and J. E. Ayers, "Design of Nonlinear Metamorphic Buffer Layers for Lattice-Mismatched $In_xGa_{1-x}As$/GaAs (001) Semiconductor Devices," J. Vac. Sci. Technol. B., 33, 052206 (2015).
9. **T. Kujofsa** and J. E. Ayers, "Resolution of X-Ray Rocking Curve Measurements Made with Finite Counting Statistics," Int. J. Hi. Spe. Ele. Syst., (24), 1550007 (2015).
10. **T. Kujofsa** and J. E. Ayers, "Equilibrium Lattice Relaxation and Misfit Dislocation in Continuously- and Step-Graded $In_xGa_{1-x}As$/GaAs (001) and $GaAs_{1-y}P_y$/GaAs (001) Metamorphic Buffer Layers," Int. J. Hi. Spe. Ele. Syst., (24), 1520009 (2015).
11. **T. Kujofsa** and J. E. Ayers, "Evolution of Kinetically-Limited Lattice Relaxation and Threading Dislocations in Temperature-Graded ZnSe/GaAs(001) Metamorphic Heterostructures," J. Electron. Mat., 44, 3030 (2015).
12. **T. Kujofsa** and J. E. Ayers, "Lattice Relaxation and Misfit Dislocations in Nonlinearly Graded $In_xGa_{1-x}As$/GaAs (001) and $GaAs_{1-y}P_y$/GaAs (001) Metamorphic Buffer Layers," J. Vac. Sci. Technol. B, (32), 031205 (2014).
13. **T. Kujofsa** and J. E. Ayers, "Threading Dislocations in S-Graded ZnS_ySe_{1-y}/GaAs (001) Metamorphic Buffer Layers," Int. J. Hi. Spe. Ele. Syst., (23), 1420005 (2014).

14. **T. Kujofsa** and J. E. Ayers, “Comparison of Continuously- and Step-Graded ZnS_ySe_{1-y}/GaAs (001) Metamorphic Buffer Layers,” J. Electron. Mat., 43, 2993 (2014).
15. **T. Kujofsa**, A. Antony, S. Xhurxhi, F. Obst, D. Sidoti, B. Bertoli, S. Cheruku, J. P. Correa, P. B. Rago, E. N. Suarez, F. C. Jain, and J. E. Ayers, “Design of S-Graded Buffer Layers for Metamorphic ZnS_ySe_{1-y}/GaAs (001) Heterostructures," J. Electron. Mat., 42, 3408 (2013).
16. **T. Kujofsa** and J. E. Ayers, "Design of Dislocation-Compensated ZnS_ySe_{1-y}/GaAs (001) Heterostructures," J. Electron. Mat., 42, 3034 (2013).
17. **T. Kujofsa**, S. Cheruku, W. Yu, B. Outlaw, S. Xhurxhi, F. Obst, D. Sidoti, B. Bertoli, P. B. Rago, E. N. Suarez, F. C. Jain, and J. E. Ayers, "Relaxation Dynamics and Threading Dislocations in ZnS_ySe_{1-y}/GaAs (001) Heterostructures," J. Electron. Mat., 42, 2764 (2013).
18. **T. Kujofsa**, S. Cheruku, B. Outlaw, S. Xhurxhi, F. Obst, D. Sidoti, B. Bertoli, P. B. Rago, E. N. Suarez, F. C. Jain, and J. E. Ayers, "Plastic Flow and Dislocation Compensation in ZnS_ySe_{1-y}/GaAs (001) Heterostructures," J. Electron. Mat., 41, 2993 (2012).
19. D. Sidoti, S. Xhurxhi, **T. Kujofsa**, S. Cheruku, J. P. Correa, B. Bertoli, P. B. Rago, E. N. Suarez, F. C. Jain, and J. E. Ayers, "Initial Misfit Dislocations in a Graded Heteroepitaxial Layer," J. Appl. Phys., 109, 023510 (2011).
20. S. Xhurxhi, F. Obst, D. Sidoti, B. Bertoli, **T. Kujofsa**, S. Cheruku, J. P. Correa, P. B. Rago, E. N. Suarez, F. C. Jain, and J. E. Ayers “S-Graded Buffer Layers for Lattice-Mismatched Heteroepitaxial Devices,” J. Electron. Mat., 40, 2348 (2011).
21. D. Sidoti, S. Xhurxhi, **T. Kujofsa**, S. Cheruku, J. Reed, B. Bertoli, P. B. Rago, E. N. Suarez, F. C. Jain, and J. E. Ayers, "Critical layer thickness in exponentially-graded heteroepitaxial layers," J. Electron. Mat., 39, 1140 (2010).
22. B. Bertoli, D. Sidoti, S. Xhurxhi, **T. Kujofsa**, S. Cheruku, J. Reed, P. B. Rago, E. N. Suarez, F. C. Jain, and J. E. Ayers, "Equilibrium strain and dislocation density in exponentially graded $Si_{1-x}Ge_x$/Si (001)," J. Appl. Phys., 108, 113525 (2010).

TABLE OF CONTENTS

1. Introduction 1
2. Properties of Semiconductor Materials 7
   2.1. Miller Indices in Cubic Crystals 8
   2.2. Lattice Constants and Thermal Expansion Coefficients 8
   2.3. Hooke's Law for Isotropic Materials 11
      2.3.1. The Elastic Moduli 15
      2.3.2. Biaxial Stresses and Tetragonal Distortion in Cubic Crystals 16
      2.3.3. Strain Energy in Cubic Crystals 17
   2.4. Dislocations 18
      2.4.1. Slip Systems 19
      2.4.2. Line Energy of Dislocations 21
      2.4.3. Forces on Dislocation 22
      2.4.4. Dislocation Motion 24
3. Lattice Mismatch Profile in Metamorphic Buffer Layers 26
4. Equilibrium Model for Lattice Relaxation 30
   4.1. Mathews and Blakeslee Force Balance Model 30
   4.2. Mathews Energy Model 32
   4.3. Generalized Equilibrium Model 34
      4.3.1. Implementation of the Equilibrium Model for Lattice Relaxation 37
   4.4. Kujofsa & Ayers Electrical Circuit Model 41
      4.4.1. Electrical Circuit Model for Equilibrium Strain Relaxation 46
5. Kinetically-Limited Lattice Relaxation and Dislocation Dynamics Model 53
   5.1. Kujofsa et al. Lattice Relaxation Model 54
   5.2. Kujofsa et al. Dislocation Dynamics Model 57
   5.3. Implementation of the Kujofsa et al. Plastic Flow Model 60
6. Distribution of Equilibrium Strain and Dislocations in MBLs 63
   6.1. Compositionally Uniform Metamorphic Layers 63
   6.2. Linearly-Graded Layers Metamorphic Layers 65
      6.2.1. Initial Misfit Dislocations in a Linearly-Graded Heteroepitaxial Layer 65
      6.2.2. Determination of Interfacial MDFZ: Results and Discussion: 73
   6.3. Equilibrium Lattice Relaxation and Misfit Dislocations in Step-Graded InGaAs/GaAs (001) and InAlAs/GaAs (001) MBLs 77
      6.3.1. Strain and Misfit Dislocations in Step-Graded MBLs 80

6.4. Comparison of Equilibrium Lattice Relaxation and Misfit Dislocations in Continuously and Step-Graded InGaAs/GaAs and GaAsP/GaAs Material Systems 89
6.4.1. Comparison of the Residual Strain and Misfit Dislocation Characteristics 92
6.5. Strain and Misfit Dislocation Density in Exponentially-Graded Layers 97
6.5.1. Distribution of the In-Plane Strain and Misfit Dislocation Characteristics 99
6.5.2. Critical Layer Thickness in Exponentially-Graded Heteroepitaxial Layers 109
6.5.3. Force Balance Theory for the Critical Layer Thickness 110
6.5.4. Determination of the Theoretical CLT in Exponentially-Graded Layers 115
6.6. S-Graded Buffer Layers for Lattice-Mismatched Heteroepitaxial Devices 121
6.6.1. Strain and Misfit Dislocation Density in S-Graded MBLs 122
6.6.2. Design of S-Graded Buffer Layers for Metamorphic ZnSySe1-y/GaAs (001) Semiconductor Devices 138
6.7. Semiconductor Heterostructures with a Logarithmically-Graded Lattice Mismatch 153
6.7.1. Design of Nonlinear Metamorphic Buffer Layers for Lattice-Mismatched InGaAs/GaAs (001) Semiconductor Devices 154
6.7.2. Comparison Lattice Relaxation and Misfit Dislocations in Nonlinearly Graded $In_xGa_{1-x}As$/GaAs (001) and $GaAs_{1-y}P_y$/GaAs (001) Metamorphic Buffer Layers 176
6.8. Strain Compensation in a Semiconducting Device Structure using an Intentionally Mismatched Uniform Buffer Layer 186
6.8.1. Experimental use of Strain-Compensated Heterostructures 187
6.8.2. Strain Compensation in the InGaAs/GaAs Material System 192
7. Applications of the Electrical Circuit Model 203
7.1. Electric Circuit Model for Strained-Layer Epitaxy in SiGe/Si 203
7.1.1. Application of Circuit Model to Representative SiGe/Si: Results and Discussion .. 205
7.2. Electric Circuit Model Analogy for Equilibrium Lattice Relaxation in InGaAs/GaAs... 208
7.2.1. Application to the InGaAs/GaAs Material System: Results and Discussion 210
7.3. Progression of Strain Relaxation in Linearly-Graded GaAsP/GaAs (001) Epitaxial Layers Approximated by a Finite Number of Sublayers 226
7.3.1. Progression of Strain Relaxations: Results and Discussion..... 228
7.4. Design of Strain-Compensated Epitaxial Layers Using an Electrical Circuit Model..... 238
7.4.1. Electrical Circuit Analogy for Equilibrium Relaxation 241
7.4.2. Analytical Expressions for Strain Compensation: Results and Discussion 244
8. Plastic Flow Results 258
8.1. Relaxation and Threading Dislocations in the ZnSSe/GaAs Material System 258
8.1.1. Annihilation-Coalescence Models 258

8.1.2. Application of the Kinetic Model to the Relaxation of ZnSe/GaAs Material System 261
8.1.3. Experimental Procedures 262
8.1.4. Kinetically-Limited Strain Relaxation 264
8.2. Critical Layer Thickness and the Role of Finite Experimental Resolution in ZnSe/GaAs (001) Utilizing Matthews and Blakeslee Equilibrium Theory 271
8.2.1. The Role of Finite Experimental Resolution 272
8.2.2. Kinetic Model for Lattice Relaxation 275
8.2.3. Kinetically-Limited Strain Results Based on a Finite Resolution 279
8.3. CLT: Theory and Experiment in the ZnSe/GaAs Material System 288
8.3.1. Various Models for Equilibrium Critical Layer Thickness 290
8.3.2. Results and Discussion 294
8.4. Plastic Flow and Dislocation Compensation in ZnSSe/GaAs (001) Heterostructures 301
8.4.1. Experimental Verification of Dislocation Compensation 301
8.4.2. Modeling of Dislocation Compensation in ZnSSe/GaAs (001) Heterostructures 305
8.4.3. Tolerance in the Design of Dislocated Compensated ZnSSe on GaAs 310
8.4.4. Dislocation Densities in Dislocated Compensated ZnSSe Heterostructures 313
8.5. Comparison of Step- and Linearly-Graded ZnSSe/GaAs (001) MBLs 317
8.5.1. Comparison of Strain Relaxation in Step- and Linearly-Graded ZnSSe Epilayers .. 321
8.6. Threading Dislocations in S-Graded ZnSSe/GaAs (001) MBLs 333
8.6.1. Benefits of Compositionally-Graded Layers 333
8.6.2. Threading Dislocation Characteristics in S-Graded ZnSSe/GaAs (001) MBL 335
8.7. Evolution of Kinetically-Limited Lattice Relaxation and Threading Dislocations in Temperature-Graded ZnSe/GaAs (001) Metamorphic Heterostructures 339
8.7.1. In-Plane Strain and Threading Dislocation Density 341
8.8. The Dynamics of Kinetically-Limited Strain and Threading Dislocations in Temperature and Compositionally-Graded ZnSSe/GaAs (001) Metamorphic Heterostructures 347
8.8.1. Incorporation of Compositional- and Temperature-Grading 348
8.8.2. Epitaxial Structures Under Consideration 350
8.8.3. Strain and Threading Results 351
9. Resolution of X-Ray Rocking Curve Measurements Made with Finite Counting Statistics .. 360
9.1. Resolution of X-Ray Diffraction Measurements of Peak Position and Peak Width in the Presence of Statistical Noise 361
9.1.1. Gaussian Diffraction Profile 361
9.1.2. Lorentzian Diffraction Profile 364
9.2. Strain Resolution from Peak Position and Width 366

10. General Conclusion and Future Refinements 378
11. Appendix 380
11.1. Detailed Derivation of z_1 and z_2 for the NLG-MBL 380
11.2. Determination of z_1 and z_2 for the SG-SAL 389
11.3. Copyright Permissions 397
12. References 398

1. Introduction

The control over the strain and dislocation dynamics in semiconducting device heterostructures has important implications in the design of high electron mobility transistors, light-emitting diodes, and laser diodes, in which the residual strain and dislocation defects affects the device characteristics. The incorporation of metamorphic buffer layers in semiconductor devices has gained great interest because their use relaxes the compositional constraints of pseudomorphic growth, thereby enabling the use of lattice-mismatched materials with a wide range of desirable properties. In addition, the intentional design of metamorphic buffer layers in semiconductor devices provides the flexibility in controlling the in-plane strain and threading dislocations, thereby allowing improved device performance and reliability. Therefore, understanding the strain relaxation and dislocation dynamics mechanisms enables the development of optimized semiconductor designs; in this dissertation, we aim at studying both the thermal equilibrium and kinetically-limited lattice relaxation of MBLs. Here, we present a plastic flow model to study kinetically-limited lattice relaxation and the generation of non-equilibrium defects such threading dislocations (TDs) in various semiconductor heterostructures. Whereas, previously developed models where only applicable to single and compositionally-uniform epitaxial layers, the current model is applicable to multilayered and compositionally-graded heterostructures and can predict non-equilibrium strain relaxation as well as misfit and threading dislocation densities by accounting for the time evolution of kinetically-limited and equilibrium strain relaxation, thermal activation of glide, and misfit-threading dislocation interactions. In addition, we have also developed a generalized equilibrium model for the analysis of semiconductor strained-layer device structures; the equilibrium analysis of these heterostructures is important for the determination of device stability criteria, but also serves as the starting point for kinetically-limited lattice relaxation.

This dissertation is organized in the following way. Chapter 2 gives a brief overview of the properties of semiconductor materials as they are specific to the zinc-blende and diamond structures. In chapter 3, we discuss the lattice mismatch profiles which are utilized within our models in conjunction with variation in thickness to study the distribution of residual strain, misfit dislocation, and non-equilibrium defects such as threading dislocations. Whereas, there have been extensive studies both theoretically and experimentally on the use of uniform-, step- and linearly-graded epitaxial layers, it has been shown recently that the use of non-linear profiles such as S-, exponentially-, sub- and super-linearly-graded may be more beneficial for controlling the strain and dislocation densities in MBLSs. However, their behavior is complex and necessitates the use of generalized equilibrium models to study the relaxation and dislocation behavior.

Chapter 4 discusses the development of the mathematical framework and the implementation of the generalized equilibrium model. Here, we review the well-known case for equilibrium lattice relaxation of a single and compositionally-uniform epitaxial layer developed by Mathews and Blakeslee and the extension to linearly-graded layers provided by Tersoff. The model developed by Tersoff assumes that graded material can relax completely in the presence of misfit dislocations. This is a simplifying assumption which does not strictly hold in either equilibrium or kinetically-limited relaxation. More specifically, there are two key assumptions embedded in this model; first, there is zero strain in the dislocated region and second they neglect the thickness dependence of the line energies for dislocations. Because of these simplifying assumptions, the interfacial misfit dislocation-free zone is not seen and there is zero strain in the dislocated region. Therefore, on the basis of these models, we developed a generalized mathematical framework for equilibrium lattice relaxation which is applicable to multilayered and compositionally-graded epitaxial layers and which does not suffer from any of the previously

mentioned simplifying assumptions. In this chapter, we also provide a computational algorithm for calculation of the equilibrium profile of an arbitrary heterostructure. The computational algorithm for determining the equilibrium profiles is complex and computationally intense and furthermore does not lend itself to an intuitive understanding of the relaxation mechanisms involved. Therefore, to address these complexities, in Chapter 4 we also present an electrical circuit approach for the equilibrium analysis of an epitaxial stack, in which each sublayer may be represented by an analogous configuration involving a current source, a resistor, a voltage source, and an ideal diode. The resulting node voltages in the analogous electric circuit correspond to the equilibrium strains in the original epitaxial structure. The development of this new approach not only provides a new method for analyzing these heterostructures but also enables the intuitive understanding of electric circuits to be translated to the relaxation of strained-layer structures. Furthermore, the electrical circuit model may be extended to continuously-graded epitaxial layers by considering the limit as the individual sublayer thicknesses are diminished to zero and this extension allows the development of analytical expressions for the strain, misfit dislocation density, critical layer thickness and widths of misfit dislocation free zones for a continuously-graded layer having an arbitrary compositional profile.

In Chapter 5, we discuss the development of the mathematical framework and the algorithmic implementation of the kinetically-limited lattice relaxation model. In this model, it is assumed that the dislocation multiplication rate is proportional to the glide velocity, the effective stress, and the defect density; this is based on the model proposed by Dodson and Tsao but includes the time-variation of the equilibrium and kinetically-limited strain and temperature during growth and is therefore applicable to graded materials. In addition, we have accounted for dislocation-dislocation interactions including the following two mechanisms: (i) dislocation compensation

caused from interactions of misfit-threading dislocations at abrupt interfaces; and, (ii) annihilation and coalescence reactions as described by Tachikawa et al. The annihilation-coalescence model is only applicable to thicker layers where the threading dislocation density decreases with thickness. Pseudomorphic layers are known to contain low dislocation density, comparable to the substrate. Therefore, the dislocation density must increase as the critical layer is reached and continue growing until they reach a maximum at some thickness. It is after this point where the annihilation-coalescence model could predict the reduction of dislocation densities with increasing thickness. The annihilation-coalescence models do not provide insight into the processes which are active during the initial build-up of the threading dislocations. Another limitation of the annihilation-coalescence models is that they do not account for interactions between misfit and threading dislocations at mismatched/abrupt interfaces and in compositionally-graded regions. For this reason, they are only applicable to uniform composition layers, though compositionally-graded and multilayered structures are of greater interest for device applications. However, in this work, the developed dislocation dynamics model accurately predicts all stages of lattice relaxation in terms of both the in-plane strain and dislocation behavior.

In Chapters 6 and 7, we present minimum energy results for various semiconductor heterostructures utilizing the compositionally-graded profiles described in Chapter 3. Chapter 6 results are obtained using the ad-hoc minimum energy engine whereas in Chapter 7 we have utilized the electrical circuit model. For each structure type, we studied equilibrium strain and misfit dislocation as a function of the relative grading constant and buffer layer thickness. In addition, we also developed approximate analytical expressions describing the equilibrium in-plane strain and misfit dislocation density characteristics for epitaxial layers employing a particular compositional-grading profile. Though recently, the electrical circuit model has enabled the

development of exact analytical expression for the strain and misfit dislocations in any arbitrary heterostructure. In Chapter 7, we have investigated two particular cases of importance; first, we considered the progression of strain relaxation in linearly-graded GaAsP metamorphic buffer layers as approximated by a finite number of sublayers and its extension to continuously-graded layers when considering the diminishment of the sublayer thickness to zero. Second, we investigated strain compensation is structures comprising of two compositionally-uniform buffer layers. Utilizing the electrical circuit model, we showed that for a given compositionally uniform device layer with fixed mismatch and layer thickness, a buffer layer may be designed (in terms of thickness and mismatch) to tailor the strain in the device layer. Furthermore, we developed exact expressions for the residual strain characteristics of both the buffer and device layer in the general case where the device layer may exhibit partial strain compensation.

In Chapter 8, we applied the plastic flow model to the ZnSSe/GaAs material system and investigated kinetically-limited lattice relaxation and non-equilibrium defects such as threading dislocations by establishing the appropriate semi empirical parameters that enable good agreement between the modeling and experimental results for ZnSSe/GaAs. On the basis of this established model, we have investigated various concepts related to the kinetically-limited lattice relaxation and dislocation generation. Some of the key ideas presented in this chapter are as follow: First, we have studied the apparent critical layer thickness as a function of the experimental resolution in ZnSe/GaAs heterostructures utilizing various models for the equilibrium relaxation. Second, we have studied the dislocation compensation mechanisms which involves the inclusion of intentionally lattice-mismatched interfaces within graded or multilayered structures in order to bend over existing threading dislocations at these mismatched interfaces. We have considered heterostructures involving a compositionally-uniform ZnSSe device layer grown on top of a GaAs

(001) substrate with an intermediate buffer layer of linearly-graded or uniform ZnSSe. For each structure type, we studied the requirements on the thickness and compositional profile in the buffer layer for the elimination of all mobile threading dislocations from the device layer as well as the allowed tolerance in compositional overshoot to achieve structures with low threading dislocation densities. Third, we studied threading dislocation behavior in single epitaxial layers utilizing various compositional-grading profile and show that non-linear grading profiles may provide an additional degree of freedom in controlling the threading dislocation characteristics. Lastly, we studied the evolution of strain relaxation and dislocation dynamics in heterostructures which utilize a temperature-grading scheme in conjunction with linear variation in composition which may be used to allow control over the relaxation process. Furthermore, we show that the thermal budget available for relaxation in these types of structures is controlled by the temperature-grading profile which was made up of combinations of linear ramps and constant-temperature sections. In Chapter 9, we have analyzed the strain resolution of x-ray rocking curve profiles from measurements of the peak position and peak width made with finite counting statistics and show that experimentally determined values are often at variance with one another because they may have incorrectly estimated their experimental resolution. This dissertation concludes in Chapter 10, in which we give a summary on the current status of our work and the future outlook of our research. Here, we briefly discuss improvements to the plastic flow models and our hopes for the development of an electrical circuit model for kinetically-limited lattice relaxation.

2. Properties of Semiconductor Materials

The design of functional and reliable heteroepitaxial semiconductor devices requires control of the lattice relaxation mechanism and generation of crystal defects. The purpose of this chapter is to review the properties of semiconductors including crystallographic properties, elastic properties, surface properties, and defect structures which are applicable to semiconductor materials that have either the diamond or zince-blende (ZB) structure. The diamond and zince-blende structures belong to the cubic class, with a face-centered cubic (FCC) lattice and a basis of two atoms at each lattice point: one at the origin (0, 0, 0) and the other at a point with coordinates ($\frac{1}{4}a$, $\frac{1}{4}a$, $\frac{1}{4}a$), where a is the lattice constant. The structure can be thought of as two interpenetrating FCC sublattices, one displaced from the other by one quarter of the unit cell diagonal where the atoms are tetrahedrally bonded, and each atom in the structure is covalently bonded to four nearest neighbors. The main difference between these two structures is that the diamond structure contains identical sublattices (i.e. Si), whereas in the zince-blende structure there are two compositionally different sublattices (i.e. GaAs). Because of this asymmetry in the zince-blende structures, the heteroepitaxy of such materials leads to interesting phenomena which may include different relaxation rates in various crystal direction due to unequal generation of dislocation; an important example of (001) heteroepitaxy includes the non-equivalence of 60^o dislocations along the $[1\bar{1}0]$ and $[110]$ directions, which are referred to as α and β dislocations, respectively.

2.1. Miller Indices in Cubic Crystals

In cubic crystals, crystal planes and directions are denoted using Miller Indices. The Miller indices for a plane are obtained as follows. The intercepts of the plane with the three orthogonal axes $\boldsymbol{a}$, $\boldsymbol{b}$, and $\boldsymbol{c}$ are determined in terms of the lattice constant a; this yield three integers which may be positive or negative. The three smallest integers having the same ratios as the reciprocals of these intercepts are the Miller indices h, k, and l, and the plane is denoted (hkl). For example, consider the plane intercepting the $\boldsymbol{a}$, $\boldsymbol{b}$, and $\boldsymbol{c}$ axes at ∞,∞,a. The normalized intercepts are $\infty,\infty,1$. Taking the reciprocals, we have $0,0,1$. These are integers so the plane is denoted (001). It is customary to indicate negative indices with an over bar rather than a minus sign. Thus, the plane $(0-11)$ would usually be denoted as $(0\bar{1}1)$. Families of planes having the same symmetry are denoted by curly brackets, such as $\{hkl\}$. Directions in a crystal are denoted by the smallest set of integers that have the same ratios as any vector in the direction. Thus, a direction is denoted $[uvw]$ and a family of directions having the same symmetry is denoted $<uvw>$. The $[uvw]$ direction is perpendicular to the (uvw) plane.

2.2. Lattice Constants and Thermal Expansion Coefficients

In heteroepitaxy, the growth of disparate materials results in differences of the lattice constants between the substrate and epi-material and often, lattice constants increase with temperature above 300 K due to normal thermal expansion. This can be an important effect during the growth of heteroepitaxial material and especially if the substrate and epitaxial material may have different thermal expansion characteristics. The difference in thermal expansion between two material systems may result in the generation of thermal strain during various growth processes.

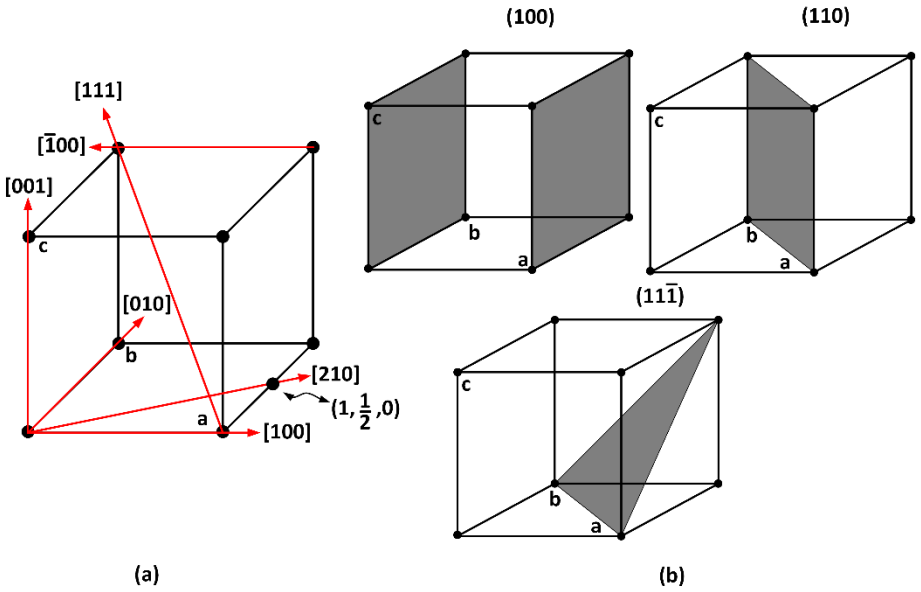

Figure 2.1. Common directions and planes in a cubic crystal system.

The linear thermal coefficient of expansion (TCE) α is defined as

$$\alpha = \frac{1}{a}\frac{\partial a}{\partial T}, \tag{2.1}$$

and has units of K^{-1}. Table 2.1. provides the lattice constants and linear TCEs for some of cubic semiconductor crystals which are used in this work. The thermal coefficient of expansion is itself a function of temperature. Thus, the experimentally obtained thermal expansion characteristics are often fit to a third order polynomial of the form:

$$\frac{\Delta a}{a} = A + BT + CT^2 + DT^3, \tag{2.2}$$

where the fractional change in lattice constant $\Delta a / a$ is with respect to 300K, and T is the absolute temperature in Kelvins. Thus, at a temperature T, the relaxed lattice constant for the crystal is given by

$$a(T) = a(300K)\left[1 + A + BT + CT^2 + DT^3\right]. \tag{2.3}$$

From the polynomial characteristic, the linear coefficient of thermal expansion may be determined as a function of temperature from

$$\alpha = \frac{1}{a}\frac{\partial a}{\partial T} = B + 2CT + 3DT^2 . \qquad \textbf{(2.4)}$$

The constants A, B, C, and D for cubic crystals are provided in Table 2.2.

Table 2.1. Lattice Constants and Thermal Expansion Coefficients for Cubic Semiconductor Crystals.

	$a\,(300K)$ **(Å)**	$\alpha(300K)$ $\left(10^{-6}K^{-1}\right)$
Si	5.43108[1]	2.6
Ge	5.6576[2]	5.7
AlAs	5.660[3]	-
GaP	5.4512[4]	4.7
GaAs	5.65325[5]	5.7
InAs	6.0584[6]	5.19[7]
ZnS	5.4105[8]	7.1
ZnSe	5.6687[9]	7.1

Table 2.2. Temperature Dependence of Thermal Expansion for Cubic Crystals. $\Delta a/a = A + BT + CT^2 + DT^3$**, where T is the absolute temperature.**

	A $\left(10^{-2}\right)$	*B* $\left(10^{-6}K^{-1}\right)$	*C* $\left(10^{-9}K^{-2}\right)$	*D* $\left(10^{-12}K^{-3}\right)$	*Temp. Range*
Si	-0.071	1.887	1.934	-0.4544	(293-1600K)
Ge	-0.1533	4.636	2.169	-0.4562	(293-1200K)
GaP	-0.110	2.611	4.445	-2.023	(293-850K)
GaAs	-0.147	4.239	2.916	-0.936	(200-1000K)
GaAs[10,11,12,13,14]	-0.155	4.411	2.70	-0.667	(293-643K)
ZnS	-0.0863	-3.386	30.18	-29.21	(60-335K)
ZnS[15,16,17]	-0.2173	6.628	2.15	-0.333	(293-820K)
ZnSe10[,18,19,20]	-0.1566	3.044	8.25	-3.33	(293-870K)

The lattice constants and physical parameters of alloyed semiconductors such as binary, ternary, and quaternary alloys are often estimated by linear interpolation (Vegard's Law [21]). For a binary alloy such as Ge_xSi_{1-x}, the lattice constant may be estimated by

$$a(Ge_xSi_{1-x}) = xa_{Ge} + (1-x)a_{Si}, \quad \textbf{(2.5)}$$

where a_{Ge} and a_{Si} are the relaxed lattice constants of Ge and Si, respectively. Ternary alloys can be formed by the mixing of II-VI or III-V semiconductors in which one element is common to both. For example, the relaxed lattice constant of the ternary $In_xGa_{1-x}As$ may be found by

$$a(In_xGa_{1-x}As) = xa_{InAs} + (1-x)a_{GaAs}. \quad \textbf{(2.6)}$$

where a_{InAs} and a_{GaAs} are the relaxed lattice constants of InAs and GaAs, respectively. Often, linear interpolation is not sufficiently accurate to determine the physical parameters and in this case a second-order term must be included through the use of a "bowing parameter." Here, the lattice constant for a ternary with mixing on the cation sites is modified to

$$a(A_xB_{1-x}C) = xa_{AC} + (1-x)a_{BC} - \delta x(1-x), \quad \textbf{(2.7)}$$

where δ is the bowing parameter of the ternary alloy.

2.3. Hooke's Law for Isotropic Materials

Elastic strains in semiconductor crystals are in response to applied deformational forces such as stresses. The growth of mismatched material systems results in physical deformation of the crystal structure. In the analysis below we have adapted the following notation where the strain ε_{ij} corresponds to the response of the strain in the $i-direction$ from a field applied in the $j-direction$.

Hooke's law states that the strain components are linear combinations of the stress components. In an isotropic material, where the physical properties are independent of direction, Hooke's law in compliance form is given by

$$\begin{bmatrix} \varepsilon_{xx} \\ \varepsilon_{yy} \\ \varepsilon_{zz} \\ \varepsilon_{yz} \\ \varepsilon_{zx} \\ \varepsilon_{xy} \end{bmatrix} = \frac{1}{E} \begin{bmatrix} 1 & -\nu & -\nu & 0 & 0 & 0 \\ -\nu & 1 & -\nu & 0 & 0 & 0 \\ -\nu & -\nu & 1 & 0 & 0 & 0 \\ 0 & 0 & 0 & 2+2\nu & 0 & 0 \\ 0 & 0 & 0 & 0 & 2+2\nu & 0 \\ 0 & 0 & 0 & 0 & 0 & 2+2\nu \end{bmatrix} \begin{bmatrix} \sigma_{xx} \\ \sigma_{yy} \\ \sigma_{zz} \\ \sigma_{yz} \\ \sigma_{zx} \\ \sigma_{xy} \end{bmatrix}, \qquad \textbf{(2.8)}$$

where E is the Young's modulus and ν is the Poisson ratio. The stresses may also be written as linear combinations of the strains. In stiffness form, Hooke's law for an isotropic medium is

$$\begin{bmatrix} \sigma_{xx} \\ \sigma_{yy} \\ \sigma_{zz} \\ \sigma_{yz} \\ \sigma_{zx} \\ \sigma_{xy} \end{bmatrix} = \frac{E}{(1+\nu)(1-2\nu)} \begin{bmatrix} 1-\nu & \nu & \nu & 0 & 0 & 0 \\ \nu & 1-\nu & \nu & 0 & 0 & 0 \\ \nu & \nu & 1-\nu & 0 & 0 & 0 \\ 0 & 0 & 0 & \frac{1}{2}-\nu & 0 & 0 \\ 0 & 0 & 0 & 0 & \frac{1}{2}-\nu & 0 \\ 0 & 0 & 0 & 0 & 0 & \frac{1}{2}-\nu \end{bmatrix} \begin{bmatrix} \varepsilon_{xx} \\ \varepsilon_{yy} \\ \varepsilon_{zz} \\ \varepsilon_{yz} \\ \varepsilon_{zx} \\ \varepsilon_{xy} \end{bmatrix}, \qquad \textbf{(2.9)}$$

Cubic crystals are anisotropic in their elastic properties. Nonetheless, it is possible to greatly simplify Hooke's law by considerations of the cubic symmetry. If the x, y, and z axes coincide with the [100], [010], and [001] directions in the cubic crystal, respectively, then Hooke's law in compliance form may be written as

$$\begin{bmatrix} \varepsilon_{xx} \\ \varepsilon_{yy} \\ \varepsilon_{zz} \\ \varepsilon_{yz} \\ \varepsilon_{zx} \\ \varepsilon_{xy} \end{bmatrix} = \begin{bmatrix} S_{11} & S_{12} & S_{12} & 0 & 0 & 0 \\ S_{12} & S_{11} & S_{12} & 0 & 0 & 0 \\ S_{12} & S_{12} & S_{11} & 0 & 0 & 0 \\ 0 & 0 & 0 & S_{44} & 0 & 0 \\ 0 & 0 & 0 & 0 & S_{44} & 0 \\ 0 & 0 & 0 & 0 & 0 & S_{44} \end{bmatrix} \begin{bmatrix} \sigma_{xx} \\ \sigma_{yy} \\ \sigma_{zz} \\ \sigma_{yz} \\ \sigma_{zx} \\ \sigma_{xy} \end{bmatrix}. \qquad \textbf{(2.10)}$$

or

$$\varepsilon = \boldsymbol{S}\sigma. \qquad \textbf{(2.11)}$$

where the S_{ij} are the elastic compliance constants and $\boldsymbol{S}$ is the compliance matrix. Only three independent constants are needed as a consequence of the cubic symmetry.

In stiffness form, Hooke's law for a crystal with cubic symmetry is

$$\begin{bmatrix} \sigma_{xx} \\ \sigma_{yy} \\ \sigma_{zz} \\ \sigma_{yz} \\ \sigma_{zx} \\ \sigma_{xy} \end{bmatrix} = \begin{bmatrix} C_{11} & C_{12} & C_{12} & 0 & 0 & 0 \\ C_{12} & C_{11} & C_{12} & 0 & 0 & 0 \\ C_{12} & C_{12} & C_{11} & 0 & 0 & 0 \\ 0 & 0 & 0 & C_{44} & 0 & 0 \\ 0 & 0 & 0 & 0 & C_{44} & 0 \\ 0 & 0 & 0 & 0 & 0 & C_{44} \end{bmatrix} \begin{bmatrix} \varepsilon_{xx} \\ \varepsilon_{yy} \\ \varepsilon_{zz} \\ \varepsilon_{yz} \\ \varepsilon_{zx} \\ \varepsilon_{xy} \end{bmatrix}. \qquad \textbf{(2.12)}$$

or

$$\sigma = \boldsymbol{C}\varepsilon. \qquad \textbf{(2.13)}$$

where $\boldsymbol{C}$ is the stiffness matrix, and the C_{ij} are the elastic stiffness constants, in units of force per area. Here, too, it is assumed that the x, y, and z axes coincide with the [100], [010], and [001] directions in the cubic crystal. The Poisson ratio and the Young's modulus may also be used in heteroepitaxy if their dependence on the crystal direction is considered. For cubic crystals, the compliance and stiffness constants are related by

$$C_{11} = \frac{S_{11} + S_{12}}{(S_{11} - S_{12})(S_{11} + 2S_{12})}. \quad \textbf{(2.14)}$$

$$C_{12} = \frac{-S_{12}}{(S_{11} - S_{12})(S_{11} + 2S_{12})}. \quad \textbf{(2.15)}$$

$$C_{44} = \frac{1}{S_{44}}. \quad \textbf{(2.16)}$$

$$S_{11} = \frac{C_{11} + C_{12}}{(C_{11} - C_{12})(C_{11} + 2C_{12})}. \quad \textbf{(2.17)}$$

$$S_{12} = \frac{-C_{12}}{(C_{11} - C_{12})(C_{11} + 2C_{12})}. \quad \textbf{(2.18)}$$

and

$$S_{44} = \frac{1}{C_{44}}. \quad \textbf{(2.19)}$$

Table 2.3 provides the elastic stiffness constants C_{ij} for several cubic semiconductor crystals. In this work, we have applied Vegard's Law to determine the elastic stiffness constants in binary, ternary and quaternary alloys.

Table 2.3. Elastic stiffness constants of cubic semiconductor crystals at room temperature, in units of GPa. (1 GPa = 10^{10} dyn/cm^2)

	C_{11}	C_{12}	C_{44}
Si[22]	160.1	57.8	80.0
Ge[23]	124.0	41.3	68.3
AlAs	125	53.4	54.2
GaP[24]	140.50	62.03	70.33
GaAs[25]	118.4	53.7	59.1
InAs[26]	83.29	45.26	39.59
ZnS[27]	104.62	65.33	46.50
ZnSe[28]	87.2(8)	52.4(8)	39.2(4)

2.3.1. The Elastic Moduli

Some elastic properties which are useful in heteroepitaxy are the Young's modulus E, the biaxial modulus Y, the shear modulus G, the Poisson ratio ν, and the biaxial relaxation constant R_B. The Young's modulus is a measure of the stiffness of a material and is defined as the ratio of stress to strain with the assumption of stress in a uniaxial direction:

$$\textbf{Young's Modulus} = E = \left.\frac{stress}{strain}\right|_{uniaxial\,stress} . \qquad \textbf{(2.20)}$$

The biaxial modulus is the ratio of the stress to strain for the biaxial case:

$$\textbf{Biaxial Modulus} = Y = \left.\frac{stress}{strain}\right|_{biaxial\,stress} . \qquad \textbf{(2.21)}$$

The shear modulus is defined as the ratio of the shear stress to shear strain:

$$\textbf{Shear Modulus} = G = \frac{shear\ stress}{shear\ strain} . \qquad \textbf{(2.22)}$$

The Poisson ratio is defined as the ratio of the transverse contraction to the longitudinal extension, for a uniaxial tensile stress in the longitudinal direction:

$$\textbf{Poisson Ratio} = \nu = -\left.\frac{transverse\ strain}{longitudinal\ strain}\right|_{uniaxial\,stress} . \qquad \textbf{(2.23)}$$

The biaxial relaxation constant is analogous to the Poisson ratio, for the case of biaxial stress, so that

$$\textbf{Biaxial Relaxation Constant} = R_B = -\left.\frac{in-plane\ strain}{out-of-plane\ strain}\right|_{biaxial\,stress} . \qquad \textbf{(2.24)}$$

These elastic moduli may be related to the elastic stiffness constants of cubic crystals as follows. For diamond and zinc blende crystals, the shear modulus is

$$G = \frac{(C_{11} - C_{12})}{2}. \tag{2.25}$$

If the growth plane is (001), the Young's modulus is given by

$$E(001) = \frac{(C_{11} + 2C_{12})(C_{11} - C_{12})}{(C_{11} + C_{12})}. \tag{2.26}$$

and the Poisson ratio is

$$\nu(001) = \frac{C_{12}}{C_{11} + C_{12}}. \tag{2.27}$$

The biaxial modulus is given by

$$Y(001) = C_{11} + C_{12} - \frac{2C_{12}^2}{C_{11}} = \frac{E(001)}{1 - \nu(001)}. \tag{2.28}$$

and the biaxial relaxation constant is

$$R_B(001) = \frac{2C_{12}}{C_{11}}. \tag{2.29}$$

2.3.2. Biaxial Stresses and Tetragonal Distortion in Cubic Crystals

Throughout dissertation we have assumed that heteroepitaxial growth exhibits biaxial stress. Using a Cartesian coordinate system, if growth proceeds along the z direction and the growth plane is the x-y plane, then the in-plane stresses applied by the substrate are equal:

$$\sigma_{xx} = \sigma_{yy} = \sigma_{\parallel}, \tag{2.30}$$

whereas, the out-of-plane stress is assumed to be zero:

$$\sigma_{zz} = \sigma_{\perp} = 0. \tag{2.31}$$

Two key assumptions in our work are that shear stresses are negligible and the substrate material is unstrained, because under most circumstances the substrate will be many times thicker (factor of ~100) than the epitaxial layer. In the case of a biaxial stress applied to an (001) cubic crystal,

the unit cell of the epitaxial layer becomes tetragonal with an in-plane lattice constant a and an out-of-plane lattice constant c. In this situation, referred to as *tetragonal distortion*,

$$\varepsilon_{\parallel} = \varepsilon_{xx} = \varepsilon_{yy} = \frac{a - a_0}{a_0} \,. \tag{2.32}$$

and

$$\varepsilon_{\perp} = \frac{c - a_0}{a_0} \,. \tag{2.33}$$

where a_0 is the relaxed (unstrained) lattice constant for the epitaxial layer. The in-plane strain is related to the biaxial stress by,

$$\sigma_{\parallel} = Y\varepsilon_{\parallel} = \left(C_{11} + C_{12} - \frac{2C_{13}^2}{C_{33}} \right) \varepsilon_{\parallel} \,. \tag{2.34}$$

where the constant of proportionality Y is the biaxial modulus. The in-plane and out-of-plane strains are related by the biaxial relaxation constant R_B,

$$\varepsilon_{\perp} = -R_B \varepsilon_{\parallel} = -\frac{2C_{12}}{C_{11}} \varepsilon_{\parallel} \,. \tag{2.35}$$

The strain tensor is therefore

$$\mathrm{E} = \begin{bmatrix} \sigma_{\parallel}/Y & 0 & 0 \\ 0 & \sigma_{\parallel}/Y & 0 \\ 0 & 0 & -\sigma_{\parallel} R_B / Y \end{bmatrix} . \tag{2.36}$$

2.3.3. Strain Energy in Cubic Crystals

The amount of work per unit volume associated with an applied force to produce a deformation on a crystal is given by

$$\delta U = \sigma_{xx}\delta\varepsilon_{xx} + \sigma_{yy}\delta\varepsilon_{yy} + \sigma_{ZZ}\delta\varepsilon_{ZZ} + \sigma_{xy}\delta\varepsilon_{xy} + \sigma_{yz}\delta\varepsilon_{yz} + \sigma_{zx}\delta\varepsilon_{zx} \,. \tag{2.37}$$

The total strain energy may be found by integrating the above expression where

$$U = \frac{C_{11}}{2}\left(\varepsilon_{xx}^2 + \varepsilon_{yy}^2 + \varepsilon_{zz}^2\right) + C_{12}\left(\varepsilon_{xx}\varepsilon_{yy} + \varepsilon_{yy}\varepsilon_{zz} + \varepsilon_{zz}\varepsilon_{xx}\right) + \frac{C_{44}}{2}\left(\varepsilon_{xy}^2 + \varepsilon_{yz}^2 + \varepsilon_{zx}^2\right). \quad \textbf{(2.38)}$$

For a biaxially-strained heteroepitaxial layer, in which the shear terms vanish,

$$U = \frac{C_{11}}{2}\left(2\varepsilon_{\parallel}^2 + \varepsilon_{\perp}^2\right) + C_{12}\left(\varepsilon_{\parallel}^2 + 2\varepsilon_{\parallel}\varepsilon_{\perp}\right) = \varepsilon_{\parallel}^2\left[C_{11} + C_{12} - \frac{2C_{12}^2}{C_{11}}\right] = \varepsilon_{\parallel}^2 Y. \quad \textbf{(2.39)}$$

Therefore, the strain energy per unit area is given by

$$E_{\varepsilon} = Uh = \varepsilon_{\parallel}^2 Yh. \quad \textbf{(2.40)}$$

where $\varepsilon_{\parallel}$ is the in-plane strain, Y is the biaxial modulus, and h is the layer thickness.

2.4. Dislocations

For epitaxial layers which are beyond the critical layer thickness it becomes energetically favorable for the introduction of misfit dislocations to relieve some the mismatch strain. However, threading dislocation emanate through these misfit dislocation ends and generally run through the thickness of the heteroepitaxial layer. An important aspect of epitaxy involves the control of threading dislocations given that they are detrimental to the device performance. Dislocations are linear defects in which cause a disturbance in local interatomic bonding and results in a buildup of local strain. Although dislocation core behavior is quite complex, dislocation may be understood as the combination of the two basic types: screw and edge dislocations. A screw dislocation can be created in a regular crystal lattice by the application of a shear stress parallel to the dislocation line which results in cause the atoms on either side of the shear plane to be displaced by one atomic spacing. An edge dislocation involves the inclusion of an extra half-plane of atoms by the application of a shear stress perpendicular to the dislocation line.

2.4.1. Slip Systems

The geometry of a crystal dislocation is specified by its line vector, Burgers vector, and glide plane. The line vector **l** is a vector in the direction of the line of the dislocation. It need not be a unit vector, and it is usually expressed as a basic lattice translation or combination of lattice translations. The Burgers vector may be determined by consideration of a Burgers circuit. A Burgers circuit is any atom-to-atom path which forms a closed loop around the dislocation core, in a clockwise direction, when looking in the line vector direction. For example, the path MNOPQ shown in Figure 2.2a is a Burgers circuit around an edge dislocation. (The line of the dislocation is into the plane of the page.) Suppose the same sequence of atom-to-atom jumps is made in a perfect crystal as shown in Figure 2.2b. The failure of the Burgers circuit to close upon itself in the perfect crystal shows the presence of the dislocation, and the closure failure is the Burgers vector:

$$\boldsymbol{b} = \overrightarrow{QM} \quad . \tag{2.41}$$

The character of a dislocation can be specified by the angle between the Burgers vector and the line vector. For an edge dislocation such as the one shown in Figure 2.2, the Burgers vector is always perpendicular to the line vector. Therefore, edge dislocations are sometimes referred to as *90^o dislocations*. For a screw dislocation, the line vector and Burgers vector are parallel, resulting in the terminology *0^o dislocation*. Although pure edge and screw dislocations are encountered in real crystals, dislocations of mixed character are far more common and in this work, we have assumed that 60^o misfit dislocations are present in diamond and zinc blende crystals. The 60^o dislocation exhibits an angle of 60^o between the Burgers vector and the line vector. Its nature and core structure can therefore be considered part edge and part screw. The Burgers vector

is conserved for any dislocation passing through a crystal. Although, real dislocations are imperfect, any Burgers circuit enclosing the dislocation will reveal the unique Burgers vector and this process may involve changes in dislocation direction which results in a change in dislocation character along its path. The Burgers vector shows the direction and amount of slip associated with the crystal distortion in response to the applied stress. The slip direction is the same as the Burgers vector and the slip plane is the plane containing the Burgers vector and the line vector. A perfect dislocation may dissociate into two partial dislocations, but the Burgers vector is always conserved in the process. Reactions involving two or more dislocation are possible if the total Burgers vector is always conserved. In this work, we do not distinguish between such reactions but rather considers the net Burgers vector.

The slip planes in a crystal are usually the planes with the highest density of atoms (the close-packed planes) because these have the greatest separation. In diamond and zinc blende semiconductors, the usual glide planes are the {111} planes and the direction of slip usually corresponds to the shortest lattice translation vector. Typically, slip directions (Burgers vectors) in the cubic semiconductors are of the type $\frac{a}{2}\langle 110\rangle$. In a zinc blende semiconductor, 60^o dislocations may be further classified as α and β dislocations according to the chemical make-up of their cores [29,30]. During the early stages of relaxation misfit dislocations are not created in equal numbers along the two $\langle 110\rangle$ directions [31,32], possibly due to differences in mobility between the α and β dislocations. At higher mismatch, the misfit dislocation network becomes much more irregular due to possibility of multiple reactions.

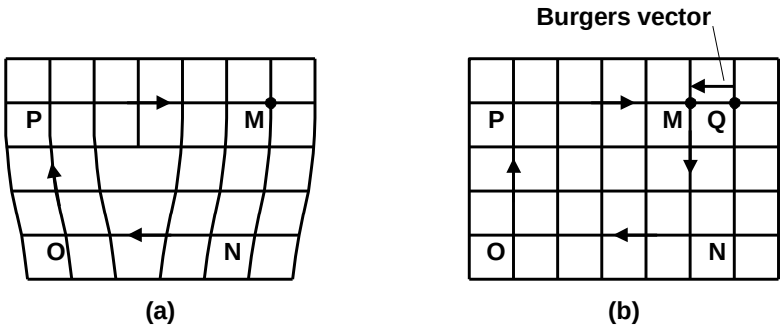

Figure 2.2. The Burgers circuit. (a) The Burgers circuit MNOP starts and ends on the same point M, and encloses a positive edge dislocation with its line into the plane of the paper. (b) In the perfect crystal, the same circuit starting at point M but fails to close, instead ending on the point Q. The closure failure QM is the Burgers vector.

2.4.2. Line Energy of Dislocations

A dislocation line is surrounded by a strain field, which raises the energy of the crystal and interacts with externally applied stresses. The elastic strain energy is also an important contribution to the dislocation line energy, with the balance determined by the inelastic contribution of the dislocation core. Strain field interactions give rise to dislocation motion in stressed crystals, and cause pairs of dislocations to repel or attract.

For a dislocation of mixed character, the strain field is the superposition of the individual strain fields for its edge and screw components. There is no interaction between the two component strain fields, so the line energy is the sum of the screw and edge contributions,

$$E(mixed) = \frac{Gb^2(1-\nu\cos^2\alpha)}{4\pi(1-\nu)}\left[\ln\left(\eta\frac{R}{r_0}\right)\right]. \qquad \textbf{(2.42)}$$

where η is the angle between the Burgers vector and the line vector. Calculation of the total energy per unit length of dislocation requires adding a core energy, which in general will include non-Hookian elastic energies as well as the energy of dangling bonds. Two approaches to including the

core energy are as follows: i) the core energy term may be accounted for by adjusting the cutoff parameter r_0 to some value much less than b, the length of the Burgers vector[33], or ii) a value of b is assigned somewhat arbitrarily to the cutoff parameter r_0, and a "core parameter" is added to the logarithm in Equation 2.42 [34]. In this work, we have adopted a dislocation core parameter of 1, a dislocation core constant of $\eta = e$ and a cutoff parameter $r_0 = b$ resulting in the line energy to be modeled by

$$E(mixed) = \frac{Gb^2\left(1-\nu\cos^2\alpha\right)}{4\pi(1-\nu)}\left[\ln\left(\frac{R}{b}\right)+1\right]. \qquad \textbf{(2.43)}$$

2.4.3. Forces on Dislocation

The dislocations in a crystal will move under the influence of an applied stress. The glide of many dislocations results in slip which is manifested as a successive displacement of many planes of atoms along a slip plane as shown in Figure 2.4a. Figure 2.4a show a misfit dislocation along with its associated threading dislocation and their orientation with respect to the slip plane. The load producing the applied stress therefore does work on the crystal, and the dislocation therefore responds as though it experiences a force equal to the work done divided by the distance moved [35].

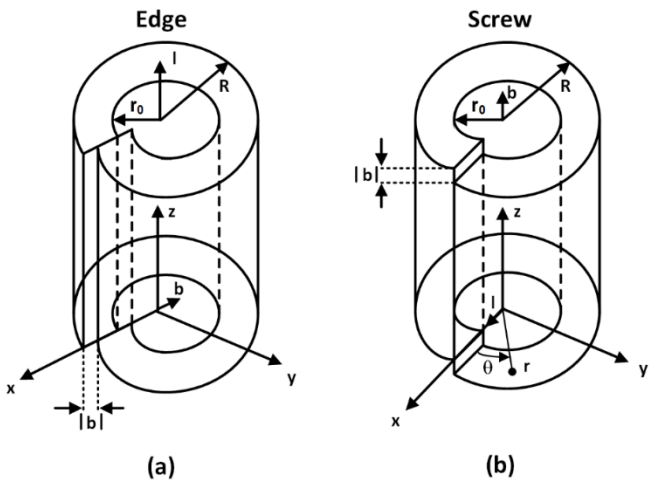

Figure 2.3. Model of (a) edge and (b) screw dislocation for calculation of the strain energy.

The force on a dislocation in a crystal with an arbitrary stress tensor is given by the Peach-Koehler formula [36]:

$$\frac{\mathrm{F}}{L} = (\boldsymbol{\sigma} \cdot \mathbf{b}) \times \mathbf{s}\,. \qquad \textbf{(2.44)}$$

where $\boldsymbol{F}/L$ is the vector force per unit length, $\boldsymbol{b}$ is the Burgers vector, and $\boldsymbol{s}$ is the unit vector in the direction of the line of the vector. In scalar form,

$$F = \tau b\,, \qquad \textbf{(2.45)}$$

where b is the length of the Burgers vector and τ is the shear stress, resolved on the slip plane, in the slip direction. If the stress in the crystal is produced by a tensile force F applied to a cross section of area A, then the stress is $\sigma = F/A$ and the resolved shear stress is

$$\tau = \sigma \cos\phi \cos\lambda\,, \qquad \textbf{(2.46)}$$

where ϕ is the angle between the applied force and the normal to the slip plane, and λ is the angle between the applied force and the slip direction as shown in Figure 2.4a-b. The quantity $\cos\phi\cos\lambda$ is referred to as the Schmid factor [37]. The most common misfit dislocations

generated in zinc blende epilayer are 60° in character and contain a Burgers vector of the type <110>; these vectors lie at 60° to the <110> line directions and 45° to the interfacial plane. Furthermore, because these are considered mixed dislocations, each 60° dislocation contains a screw and edge component (Figure 2.4c). However, only the edge component of the Burgers vectors (the component which lies in the interfacial plane) acts in relaxing the mismatch strain. Therefore, based on the geometry of Figure 2.4a-b, the edge component of the burgers vector is given by

$$b_{\parallel} = b\cos\alpha = b\sqrt{\cos^2\lambda - \cos^2\delta}\,. \qquad \textbf{(2.47)}$$

2.4.4. Dislocation Motion

Dislocations move by glide, climb, or a combination of both. Glide is motion in the direction of the Burgers vector, and is called conservative motion. Climb is motion out of the glide plane (non-conservative motion). Both processes are thermally activated because they involve the breaking of crystal bonds, but climb requires long-range diffusion and is only important at very high temperatures.

In this work, we have assumed that the dislocation glide velocity may be described by a phenomenological relationship[38]

$$v = v_0 \exp\left(-\frac{\tau_0}{\tau}\right)\exp\left(-\frac{U}{kT}\right). \qquad \textbf{(2.48)}$$

where v_0 is a characteristic velocity, τ_0 is a characteristic stress, τ is the resolved shear stress on the glide plane in the slip direction, U is the activation energy for glide, T is the absolute temperature and k is the Boltzmann constant. Over restricted ranges of stress this relationship is commonly approximated by

$$v = B\tau^m \exp\left(-\frac{U}{kT}\right). \qquad \textbf{(2.49)}$$

where m and B are constants.

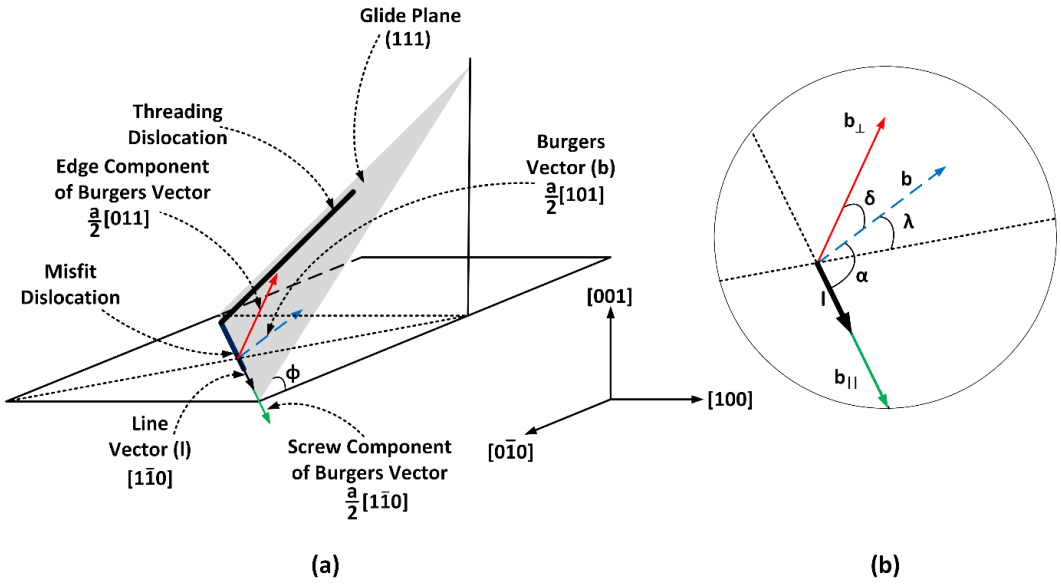

Figure 2.4. (a) Schematic representation of slip in crystalline material. (b) Interfacial misfit and threading dislocation orientation in a slip plane. (c) The geometrical components associated with the Burgers vector. (d) Angles between the Burgers vector and line vector, edge and screw components.

The values reported in the literature are in the range $1 < m < 3$, and here we have assumed that $m = 1$. It should be emphasized that Equations 2.48 and 2.49 are empirical in nature, and that it has been reported that the activation energy U is stress-dependent [39] in SiGe alloys. An alternate model for dislocation glide is the kink model described by Hirth and Lothe [40]. This model is physics-based [41] and assumes that the mechanism of dislocation glide involves the nucleation and propagation of kinks along the dislocations.

3. Lattice Mismatch Profile in Metamorphic Buffer Layers

In this work, we consider multilayered and compositionally-graded buffers with the zinc blende or diamond structure grown on a GaAs or Si substrate with (001) crystal orientation. The lattice mismatch is defined as $f(z) \equiv (a_s - a(z))/a(z)$, where a_s is the relaxed lattice constant of the substrate and $a(z)$ is the relaxed lattice constant of the epitaxial crystal at a distance z from the substrate interface. Here, we have considered various compositional grading profiles, which include uniform- (U), linear- (L), step- (ST), S- (S), sublinear-, and superlinear-grading. In a uniform layer (UL), the lattice mismatch profile at a distance from the interface z is a constant and is given by

$$f_{UL}(z) = C \,, \tag{3.50}$$

where C is a constant. For linearly-graded metamorphic buffer layers (LG-MBL) the lattice mismatch profile at a distance from the interface z is given by

$$f_{LG}(z) = f_0 + C_f z \,, \tag{3.51}$$

where $C_f = (f_h - f_0)/h$ is the grading constant and is determined from the starting and ending lattice mismatch. Above, f_0 refers to the starting lattice mismatch (or composition) at the substrate interface whereas f_h is the value of lattice mismatch at the top of the buffer layer with thickness h. Step-graded metamorphic buffer layers (STG-MBL) layers contain a set of n uniform layers in which there are equal compositional changes from one layer to the next ("linear step grading"). Depending on the profile choice, one may choose to have a lattice matched or lattice-mismatched sublayer near the interface and examples of such profiles are shown on Figure 3.1. The compositional profile of a STG-MBL may resemble that of linearly graded layer if the number of

uniform layers is chosen sufficiently large ($n \to \infty$). Moreover, an increase in n leads to lower compositional changes from one step to the next. The lattice mismatch profile in the S-graded metamorphic buffer layer (SG-MBL) is designed to be a normal cumulative distribution function, given by

$$f_S = \begin{cases} \frac{f_h - f_0}{2}\left[-erf\left(\frac{\mu - z}{\sigma\sqrt{2}}\right) + erf\left(\frac{\mu}{\sigma\sqrt{2}}\right)\right], & z < \mu; \\ \frac{f_h - f_0}{2}, & z = \mu \\ \frac{f_h - f_0}{2}\left[erf\left(\frac{z - \mu}{\sigma\sqrt{2}}\right) + erf\left(\frac{\mu}{\sigma\sqrt{2}}\right)\right], & z > \mu \end{cases}, \quad \textbf{(3.52)}$$

where μ is the "mean parameter" and σ is the "standard deviation parameter". The parameters μ , σ, f_0, f_h, and h can be chosen by the crystal grower to obtain the desired buffer layer characteristics. Sublinear- and superlinear- grading may be achieved by using different functions. In this work, for sublinearly-graded MBL we have used three distinct functions: exponential (EXP), logarithmic (LOG) and power law (PL). A sublinear exponential lattice mismatch profile is given by

$$f_{EXP}(z) = f_0 + (f_\infty - f_0)(1 - e^{-z/\gamma}) \ , \quad \textbf{(3.53)}$$

where f_∞ is the limiting mismatch and γ is the grading length constant. The lattice mismatch profile in the logarithmically-graded metamorphic buffer layer is given by

$$f_{LOG}(z) = f_0 + (f_h - f_0)\left[\ln\left(1 + \frac{z}{h}\right) - \ln(2)\right]^m , \quad \textbf{(3.54)}$$

where m is the power grading coefficient. Compositional grading profiles with a power grading coefficient $m = 1$, the logarithmic-graded-MBL has a convex-up compositional grading profile

(sublinear) while for heterostructures with $m \geq 2$ the concavity of the compositional profile changes sign to concave-down (superlinear). Structures with convex-up compositional grading profile exhibit a small sublinearity coefficient whereby the average lattice mismatch of the structure is approximately equal to that of a linearly-graded buffer layer. The nonlinearity coefficient is defined as $C_S = \bar{x}_{NLG} / \bar{x}_{LG}$ where $\bar{x}_{NLG}$ and $\bar{x}_{LG}$ are the average compositions of the nonlinearly- and linearly- graded MBL respectively. Moreover, power-law grading can be used to obtain sublinear and superlinear compositional profiles whereby the lattice mismatch profile in the power-law-graded metamorphic buffer layer (PLG-MBL) is given by

$$f_{PL}(y) = f_0 + (f_h - f_0)\left(\frac{z}{h}\right)^{\alpha}, \qquad \textbf{(3.55)}$$

resulting in sublinear grading for $\alpha < 1$, superlinear grading for $\alpha > 1$ and linear grading for $\alpha = 1$. Figure 3.1 shows some representative lattice mismatch profiles as a function of distance from the interface characteristics employing various compositional-grading profiles. Throughout this work we will use some particular type of grading profile in conjunction with variolations in thickens to study either equilibrium or kinetically-limited lattice relaxation by observing the distribution of in-plane strain, misfit dislocations and non-equilibrium defects such as the threading dislocations.

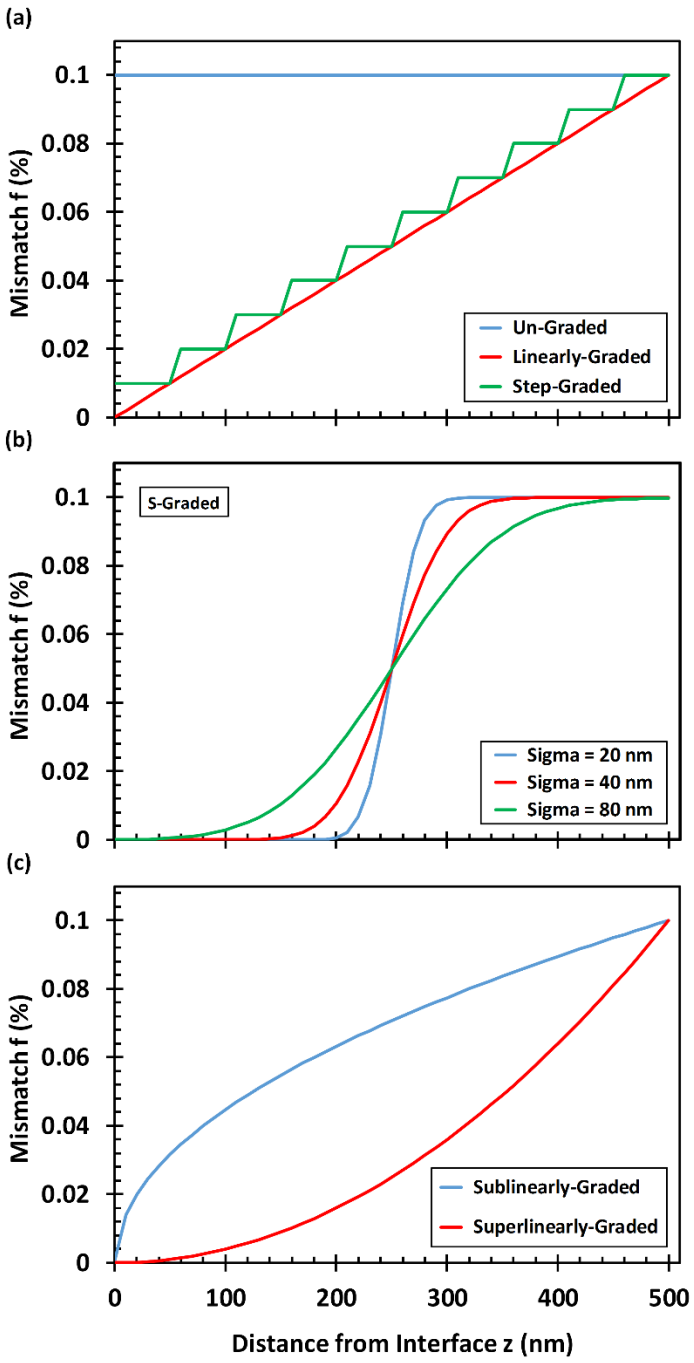

Figure 3.1. Lattice mismatch as a function of the distance from substrate interface for compositionally-graded metamorphic buffer layers employing various grading profiles. (a) The well-known and simple cases of uniform-, step- and linearly-graded, (b) S-graded and (c) nonlinear cases of sub- and super-linearly-graded.

4. Equilibrium Model for Lattice Relaxation

Equilibrium analysis of semiconductor heterostructures is important for the determination of device stability criteria, but also serves as the starting point for the analysis of kinetically-limited relaxation and non-equilibrium defects such as threading dislocations. In the following chapter, we will review the Mathews and Blakeslee equilibrium model for a single epitaxial layer and develop the mathematical framework for its extension to a generalized structure. Up until recently in time, equilibrium modeling of semiconductor strained-layer heterostructures has been accomplished by complex numerical energy-minimization schemes, which are non-intuitive, require specialized code, and are computationally intense. However, recently we have developed, a circuit model which represents a significant breakthrough in the analysis of semiconductor heterostructures, in that it enables equilibrium calculations to be performed by widely-available circuit simulators. In the last sections of this chapter, we show the complete development of the circuit model analogy, including the physical justification for the choice of analogies and also provide improvements to the previously developed equilibrium models.

4.1. Mathews and Blakeslee Force Balance Model

Matthews and Blakeslee [55] developed a force-balance model for the equilibrium strain in a single layer with uniform composition. In it, the equilibrium strain was the value at which the glide force on a grown-in dislocation is equal to the opposing line tension. A preexisting threading dislocation in the substrate replicates in the growing epilayer, and can bend over to create a length of misfit dislocation in the interface once the critical layer thickness is reached. The resolved shear stress acting in the direction of slip is [42]

$$\sigma_{res} = \sigma_{\|} \cos\lambda \cos\phi \,, \tag{4.1}$$

where $\sigma_{\|}$ is the biaxial stress, λ is the angle between the Burgers vector and the line in the interface plane which is perpendicular to the intersection of the glide plane with the interface, and ϕ is the angle between the interface and the normal to the slip plane. The glide force acting on the dislocation is given by

$$F_G = \frac{\sigma_{res} bh}{\cos\phi} = \sigma_{\|} bh \cos\lambda \,, \tag{4.2}$$

where b is the length of the Burgers vector for the threading dislocation and h is the film thickness. Assuming biaxial stress in an isotropic and pseudomorphic semiconductor,

$$\sigma_{\|} = \frac{2G(1+\nu)}{(1-\nu)} \varepsilon_{\|} = \frac{2G(1+\nu)}{(1-\nu)} f \,, \tag{4.3}$$

so that

$$F_G = \frac{2Gbfh(1+\nu)\cos\lambda}{(1-\nu)}, \tag{4.4}$$

where G is the shear modulus and ν is the Poisson ratio. The line tension of the misfit segment of the dislocation is given by

$$F_L = \frac{Gb^2(1-\nu\cos^2\alpha)}{4\pi(1-\nu)}\left[\ln\left(\frac{h}{b}\right)+1\right], \tag{4.5}$$

where α is the angle between the Burgers vector and the line vector for the dislocations. The critical layer thickness h_c, is the value at which the glide forces balances the line tension for the misfit segment of the dislocation and therefore,

$$h_c = \frac{b(1-\nu\cos^2\alpha)}{8\pi|f|(1+\nu)\cos\lambda}\left[\ln\left(\frac{h_c}{b}\right)+1\right]. \tag{4.6}$$

The critical layer thickness is the greatest thickness for which the equilibrium in-plane strain is equal to the lattice mismatch,

$$\varepsilon_{\parallel}(h) = f, \quad h \le h_c \,. \tag{4.7}$$

We can consider the equilibrium strain by rearranging the two equations above in such a way that

$$\varepsilon_{\parallel}(h) = \frac{b(1-\nu\cos^2\alpha)}{8\pi h(1+\nu)\cos\lambda}\left[\ln\left(\frac{h}{b}\right)+1\right]. \tag{4.8}$$

4.2. Mathews Energy Model

It has been shown that an equivalent result may be found by minimizing the sum of the strain energy and the line energy of misfit dislocations [56]. In a partly-relaxed and compositionally uniform epitaxial layer (as shown in Figure 4.1a) which contains misfit dislocations, the in-plane strain ε is given by

$$\varepsilon = f - \frac{f}{|f|}\rho b \sin\alpha \sin\phi, \tag{4.9}$$

where f is the lattice mismatch, $f \equiv (a_s - a_e)/a_e$, a_s and a_e are the relaxed lattice constants of the substrate and epitaxial crystal (cm), respectively, the term $f/|f|$ accounts for the sign of the mismatch, ρ is the linear misfit dislocation density in at the mismatched interface (cm^{-1}), b is the length of the Burgers vector (cm), α is the angle between the Burgers vector and dislocation line vector, and ϕ is the angle between the glide plane and interface. We will define the lattice mismatch of the substrate (layer 0) as $f_0 \equiv 0$ to simplify the mathematical descriptions that will follow. The areal strain energy (erg/cm^2) associated with a partially-relaxed epitaxial layer with thickness h and an in-plane strain ε, is

$$E_\varepsilon = Yh\varepsilon^2, \tag{4.10}$$

where Y is the biaxial modulus (dyn/cm^2), $Y = C_{11} + C_{12} - 2C_{12}^2 / C_{11} = 2G(1+\nu)/(1-\nu)$, G is the shear modulus (dyn/cm^2), C_{11} and C_{12} are the elastic stiffness constants (dyn/cm^2), and ν is the Poisson ratio (unitless). The line energy of dislocations per unit area (erg/cm^2), assuming two orthogonal networks with equal cross-sectional density is

$$E_d = \rho \frac{Gb^2(1-\nu\cos^2\alpha)}{2\pi(1-\nu)}\left[\ln\left(\frac{h}{b}\right)+1\right] = (f-\varepsilon)\frac{f}{|f|}\frac{Gb(1-\nu\cos^2\alpha)}{2\pi(1-\nu)\sin\alpha\sin\phi}\left[\ln\left(\frac{h}{b}\right)+1\right], \tag{4.11}$$

Here, the dislocation energy is determined using a mean-field approach without including dislocation-dislocation interactions, and this is the main approximation used in this work. The equilibrium condition is found by minimizing the sum of the dislocation line energy and the strain energy, $E = E_d + E_\varepsilon$. Differentiating the energy, E, and setting the partial derivative to zero we obtain

$$\frac{\partial E}{\partial \varepsilon} = \frac{\partial(E_\varepsilon + E_d)}{\partial \varepsilon} = 2Yh\varepsilon - \frac{f}{|f|}\frac{Gb(1-\nu\cos^2\theta)}{2\pi(1-\nu)\sin\alpha\sin\phi}\left[\ln\left(\frac{h}{b}\right)+1\right] = 0. \tag{4.12}$$

The solution for equilibrium in-plane strain, accounting for the possibility of pseudomorphic growth, is

$$\varepsilon(h) = \begin{cases} f, & h \le h_c \\ \dfrac{f}{|f|}\dfrac{b(1-\nu\cos^2\alpha)}{8\pi h(1+\nu)\sin\alpha\sin\phi}\left[\ln\left(\dfrac{h}{b}\right)+1\right], & h > h_c \end{cases}, \tag{4.13}$$

where h_c is the critical layer thickness at which it becomes energetically favorable to introduce misfit dislocations. Below h_c, the in-plane strain is equal to the coherency strain (lattice mismatch).

4.3. Generalized Equilibrium Model

If we consider an epitaxial structure involving a stack of three disparate layers as shown in Figure 4.1b, the strain in each layer may be related to the misfit dislocation densities for that layer and those below it. The in-plane strain ε_n in the n^{th} sublayer of a general structure is given by

$$\varepsilon_n = f_n - \frac{f_n - f_{n-1}}{|f_n - f_{n-1}|} \sum_{j=1}^{n} \rho_j b_j \sin\alpha \sin\phi . \qquad \textbf{(4.14)}$$

For the case of three layers illustrated in Figure 4.1b, the in-plane strains are

$$\begin{aligned} \varepsilon_3 &= f_3 - \rho_3 b_3 \sin\alpha \sin\phi - \rho_2 b_2 \sin\alpha \sin\phi - \rho_1 b_1 \sin\alpha \sin\phi \\ \varepsilon_2 &= f_2 - \rho_2 b_2 \sin\alpha \sin\phi - \rho_1 b_1 \sin\alpha \sin\phi \\ \varepsilon_1 &= f_1 - \rho_1 b_1 \sin\alpha \sin\phi \end{aligned} \quad . \qquad \textbf{(4.15)}$$

By rearranging the equations above, the linear misfit dislocation densities for the three mismatched interfaces are given as

$$\begin{aligned} \rho_3 &= \frac{f_3 - f_2}{|f_3 - f_2|} \frac{(f_3 - \varepsilon_3) - (f_2 - \varepsilon_2)}{b_3 \sin\alpha \sin\phi} \\ \rho_2 &= \frac{f_2 - f_1}{|f_2 - f_1|} \frac{(f_2 - \varepsilon_2) - (f_1 - \varepsilon_1)}{b_2 \sin\alpha \sin\phi} \\ \rho_1 &= \frac{f_1 - f_0}{|f_1 - f_0|} \frac{f_1 - \varepsilon_1}{b_1 \sin\alpha \sin\phi} \end{aligned} . \qquad \textbf{(4.16)}$$

The sum of the strain and dislocation line energy per unit area may be found by adding the contributions of the three sublayers:

$$
\begin{aligned}
E &= E_{d,1} + E_{\varepsilon,1} + E_{d,2} + E_{\varepsilon,2} + E_{d,3} + E_{\varepsilon,3} \\
&= \left[\begin{array}{l}
\rho_1 \dfrac{G_1 b_1^2 \left(1-\nu_1 \cos^2\alpha\right)}{2\pi\left(1-\nu_1\right)} \left[\ln\left(\dfrac{h_1+h_2+h_3}{b_1} \right) + 1 \right] + 2Y_1 h_1 \varepsilon_1 \\
+ \rho_2 \dfrac{G_2 b_2^2 \left(1-\nu_2 \cos^2\alpha\right)}{2\pi\left(1-\nu_2\right)} \left[\ln\left(\dfrac{h_2+h_3}{b_2} \right) + 1 \right] + 2Y_2 h_2 \varepsilon_2 \\
+ \rho_3 \dfrac{G_3 b_3^2 \left(1-\nu_3 \cos^2\alpha\right)}{2\pi\left(1-\nu_3\right)} \left[\ln\left(\dfrac{h_3}{b_3} \right) + 1 \right] + 2Y_3 h_3 \varepsilon_3
\end{array} \right].
\end{aligned}
\tag{4.17}
$$

To determine the equilibrium strain of the three-sublayer system shown in Figure 4.1b, we must differentiate the energy with respect to the in-plane strain at each sublayer and set each partial derivative equal to zero:

$$
\begin{aligned}
0 &= \frac{\partial E}{\partial \varepsilon_3} = 2Y_3 h_3 \varepsilon_3 - \frac{f_3 - f_2}{\left| f_3 - f_2 \right|} \frac{G_3 b_3 \left(1-\nu_3 \cos^2\alpha\right)}{2\pi\left(1-\nu_3\right)\sin\alpha \sin\phi} \left[\ln\left(\frac{h_3}{b_3} \right) + 1 \right] \\
0 &= \frac{\partial E}{\partial \varepsilon_2} = 2Y_2 h_2 \varepsilon_2 - \frac{f_2 - f_1}{\left| f_2 - f_1 \right|} \frac{G_2 b_2 \left(1-\nu_2 \cos^2\alpha\right)}{2\pi\left(1-\nu_2\right)\sin\alpha \sin\phi} \left[\ln\left(\frac{h_2+h_3}{b_2} \right) + 1 \right] \\
&\quad + \frac{f_3 - f_2}{\left| f_3 - f_2 \right|} \frac{G_3 b_3 \left(1-\nu_3 \cos^2\alpha\right)}{2\pi\left(1-\nu_3\right)\sin\alpha \sin\phi} \left[\ln\left(\frac{h_3}{b_3} \right) + 1 \right] \\
0 &= \frac{\partial E}{\partial \varepsilon_1} = 2Y_1 h_1 \varepsilon_1 - \frac{f_1 - f_0}{\left| f_1 - f_0 \right|} \frac{G_1 b_1 \left(1-\nu_1 \cos^2\alpha\right)}{2\pi\left(1-\nu_1\right)\sin\alpha \sin\phi} \left[\ln\left(\frac{h_1+h_2+h_3}{b_1} \right) + 1 \right] \\
&\quad + \frac{f_2 - f_1}{\left| f_2 - f_1 \right|} \frac{G_2 b_2 \left(1-\nu_2 \cos^2\alpha\right)}{2\pi\left(1-\nu_2\right)\sin\alpha \sin\phi} \left[\ln\left(\frac{h_2+h_3}{b_2} \right) + 1 \right]
\end{aligned}
\tag{4.18}
$$

Concurrent solution of the three equations above yields the equilibrium in-plane strains ε_1, ε_2, and ε_3. A similar analysis may be extended to any multilayered and compositionally-graded structure with N sublayers (as shown in Figure 4.1c) and in the general case, we consider the sum of the strain and dislocation line energy, $E = \sum_{j=1}^{N} E_{d,j} + E_{\varepsilon,j}$. The equilibrium in-plane strains are found

by setting each partial derivative to zero, $\partial E/\partial \varepsilon_n = 0$ and solving the resulting system of N equations:

$$0 = \frac{\partial E}{\partial \varepsilon_N} = 2Y_N h_N \varepsilon_N - \frac{f_N - f_{N-1}}{|f_N - f_{N-1}|} \frac{G_N b_N \left(1 - \nu_N \cos^2 \alpha\right)}{2\pi(1-\nu_N)\sin\alpha \sin\phi} \left[\ln\left(\frac{h_N}{b_N}\right) + 1 \right], \qquad n = N$$

$$0 = \frac{\partial E}{\partial \varepsilon_n} = \left(\begin{array}{l} 2Y_n h_n \varepsilon_n - \dfrac{f_n - f_{n-1}}{|f_n - f_{n-1}|} \dfrac{G_n b_n \left(1 - \nu_n \cos^2 \alpha\right)}{2\pi(1-\nu_n)\sin\alpha \sin\phi} \left[\ln\left(\sum_{j=n}^{N} \dfrac{h_j}{b_n}\right) + 1 \right] \\ + \dfrac{f_{n+1} - f_n}{|f_{n+1} - f_n|} \dfrac{G_{n+1} b_{n+1} \left(1 - \nu_{n+1} \cos^2 \alpha\right)}{2\pi(1-\nu_{n+1})\sin\alpha \sin\phi} \left[\ln\left(\sum_{j=n+1}^{N} \dfrac{h_j}{b_{n+1}}\right) + 1 \right] \end{array} \right), \quad 1 \le n < N \qquad \textbf{(4.19)}$$

Essentially, the analysis provided above is the basis for the development of the Bertoli et al. [43] model, which utilizes an ad-hoc numerical approach to minimize the sum of the strain energy and dislocation line energy for an arbitrary multilayered heterostructure. The approach is generally applicable, and compositionally-graded layers may be represented by staircase profiles with arbitrary precision.

In an arbitrary compositionally graded and multilayered structure, the equilibrium configuration may be found by minimization of the strain and dislocation energy. In a partly relaxed layer containing misfit dislocations of cross-sectional density $\rho_A(y)$, the strain energy per unit area is

$$E_\varepsilon = \int_0^h Y \varepsilon_{||}^{\,2} dz = \int_0^h Y \left[f(z) + b' \int_0^z \rho_A(\zeta) d\zeta \right]^2 dz \,. \qquad \textbf{(4.20)}$$

where b' is the misfit relieving component of the Burgers vector parallel to the interface, $b' = \pm b \sin\alpha \sin\phi$, Y is the biaxial modulus, $Y = C_{11} + C_{12} - 2C_{12}^2 / C_{11}$, C_{11} and C_{12} are the elastic stiffness constants, and ζ is a variable of integration. The misfit dislocation density ρ is always positive, but b' may be positive or negative, depending on the sign of the mismatch strain (tensile

or compressive) which is being relieved. The line energy of dislocations per unit area, assuming two orthogonal networks with equal cross-sectional density, is

$$E_d = 2\int_0^h F_d(z)\rho_A(z)dz\,. \qquad \textbf{(4.21)}$$

where $F_d(z)$ is the line tension of the dislocation at a distance z from the substrate interface and is given by

$$F_d(z) \approx \frac{G(z)b^2(z)\left[1-\nu(z)\cos^2\alpha\right]}{4\pi(1-\nu(z))}\left[\ln\left(\frac{h-z}{b(z)}\right)+1\right]. \qquad \textbf{(4.22)}$$

where G is the shear modulus, $G=(C_{11}-C_{12})/2$, ν is the Poisson ratio, $\nu = C_{12}/(C_{11}+C_{12})$ for the (001) orientation. The dislocation density ρ is always positive, but b' may be positive or negative, depending on the sign of the mismatch strain which is being relieved. For a uniform mismatched layer, $sign(b') = -sign(f)$. Here, the dislocation energy is determined using a mean-field approach, without including second-order dislocation-dislocation interactions and this is the primary approximation used. In this work, the equilibrium configuration was determined by the semiconductor heterostructure generalized energy minimization (SH-GEM) approach described by Bertoli et al. [43] and modified to a three step look ahead minimizer by Kujofsa & Ayers. The equilibrium configuration may be determined numerically by minimizing $E_d + E_\varepsilon$. Equilibrium modeling serves as the starting point for calculation of kinetically-limited relaxation.

4.3.1. Implementation of the Equilibrium Model for Lattice Relaxation

Bertoli et al. [43] have described a numerical approach for the determination of the equilibrium configuration of strain and misfit dislocations in a generalized semiconductor heterostructure. This approach is based on the minimization of the sum of the dislocation line

energy and strain energy, and represents a generalization of the Tersoff[44] model for linearly-graded structures. In the implementation of the generalized semiconductor heterostructure energy minimization numerical tool by Bertoli et al. [43], a structure with arbitrary compositional profile is approximated by N constant-composition layers, each having a thickness no more than h_{max}. (h_{max} is set to a value corresponding to the desired spatial resolution, typically 5 nm or less.) The lattice constant and elastic constants for the jth layer are $a_e[j]$, $C_{11}[j]$, and $C_{12}[j]$, and these may be estimated using linear interpolation (Vegard's law) for semiconductor alloys such as $Si_{1-x}Ge_x$ or $In_xGa_{1-x}As$. The lattice mismatch strain (with respect to the substrate) in the jth layer is

$$f[j] = \frac{a_s - a_e[j]}{a_e[j]}, \tag{4.23}$$

the biaxial modulus for the jth layer is

$$Y[j] = C_{11}[j] + C_{12}[j] - \frac{2C_{12}^2[j]}{C_{11}[j]}, \tag{4.24}$$

and the Poisson ratio for the jth layer is

$$\nu[j] = \frac{C_{12}[j]}{C_{11}[j] + C_{12}[j]}. \tag{4.25}$$

The strain energy per unit area is found using

$$E_\varepsilon = \sum_{j=1}^{N} \varepsilon^2[j] Y[j] h[j], \tag{4.26}$$

and the dislocation line energy is calculated by

$$E_d = \sum_{j=1}^{N} K[j] \rho[j] h[j], \tag{4.27}$$

where

$$K[j]=\frac{G[j]b^2[j]\{1-\nu[j]\cos^2\alpha\}}{2\pi(1-\nu[j])}\left[\ln\left(\frac{1}{b[j]}\left[\sum_{k=1}^{N}h[k]-\sum_{i=1}^{j}h[i]\right]\right)+1\right]. \quad \textbf{(4.28)}$$

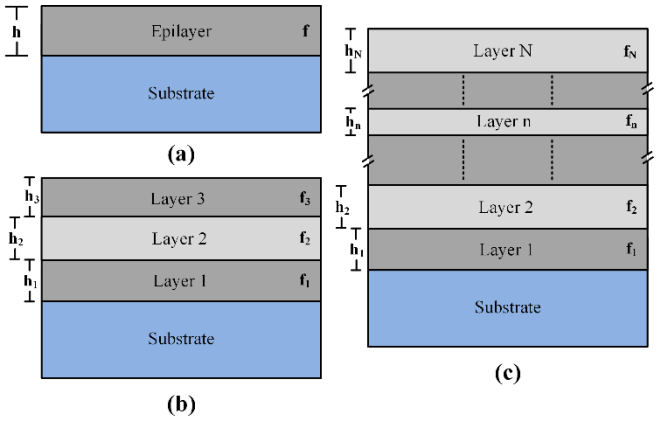

Figure 4.1. Schematic representation of (a) a single compositionally uniform epitaxial layer with lattice mismatch f and thickness h, (b) an epitaxial structure comprised of three compositionally uniform layers with varying thickness and compositional mismatches and (c) a generalized epitaxial structure divided into N sublayers with varying thickness and mismatch.

In general, the compositional profile may include a combination of graded and uniform sublayers. Any sublayer thicker than h_{max} is subdivided. The strain profile is arbitrarily initialized to the pseudomorphic profile: $\varepsilon[j]=f[j]$ for each layer j. The misfit dislocation density is arbitrarily initialized to zero for every layer in the structure.

The basic process of finding the minimum energy configuration is as follows. Starting with the first layer ($j=1$), the dislocation density in each layer j is adjusted up by Δ ($\rho[j]=\rho[j]+\Delta$). Accounting for this adjustment, the modified strain profile is calculated by

$$\varepsilon[n]=f[n]+\sum_{i=1}^{n}h[i]b'[i]\rho[i], \quad \textbf{(4.29)}$$

and the energy per unit area $E^{\uparrow}$ is calculated using

$$E = \sum_{n=1}^{N} \left\{ \varepsilon^2[n] Y[n] h[n] + K[n] \rho[n] h[n] \right\}. \qquad \textbf{(4.30)}$$

Next the dislocation density in layer j is adjusted back to its starting point ($\rho[j] = \rho[j] - \Delta$), the resulting strain profile is calculated and the energy E^{-} is found. Finally, the dislocation density in the first layer is adjusted down by Δ ($\rho[j] = \rho[j] - \Delta$), the revised strain profile is found and the energy $E^{\downarrow}$ is calculated. At this point the values $E^{\uparrow}$, E^{-}, and $E^{\downarrow}$ are compared. The configuration corresponding to the lowest energy is adopted, and the process is repeated with the next layer $j+1$.

Once the dislocation density has been adjusted in each layer of the structure, the adjustment parameter Δ is reduced by a convenient multiplier (less than 1, and typically 0.95) and the process is repeated for each of the layers in the structure. This is continued until Δ has been reduced to a value below the desired dislocation density resolution Δ_{res}. (In the work of Bertoli et al. the value $\Delta_{res} = 50\, cm^{-2}$ was adopted.) The value of Δ is initialized to Δ_{start}, where

$$\Delta_{start} = \frac{1}{Nb'[1] h[1]} \sum_{n=1}^{N} f[n], \qquad \textbf{(4.31)}$$

and the final solution is unaffected by this initial value if it is sufficiently large to allow convergence.

In some work, it was found that the constraint of adjusting the dislocation density in one layer at a time gave rise to non-physical oscillations in the dislocation density profile and to avoid this problem it is necessary to adopt a *look ahead energy minimizer*, which considers two or more layers at a time. In the case for which two layers are adjusted together, nine values of energy need

to be compared: $E^{\uparrow\uparrow}, E^{\uparrow -}$, $E^{\uparrow\downarrow}$, $E^{-\uparrow}$, $E^{--}, E^{-\downarrow}$, $E^{\downarrow\uparrow}, E^{\downarrow -}, E^{\downarrow\downarrow}$. Here $E^{\uparrow\uparrow}$ is the energy corresponding to the case in which the dislocation density has been increased by Δ in both layer j and layer $j+1$; $E^{\uparrow -}$ is the energy corresponding to the case in which the dislocation density has been increased by Δ in layer j but kept unchanged in layer $j+1$; and so on. The configuration with the lowest energy is adopted out of these nine cases, and then the process is repeated with layers $j+1$ and $j+2$. A look ahead energy minimizer could also consider three or more layers at a time. For example, consideration of three layers at a time involves comparing the energies for twenty-seven permutations at each step. This greatly increases the computational time without any apparent improvement in the accuracy of the final solution, so a two-layer look ahead energy minimizer was used in the original work by Bertoli et al. [43]. As a proof of concept Kujofsa and Ayers have developed such an energy minimizer and its use is suited when dealing with complex multilayered and compositionally-graded heterostructures.

4.4. Kujofsa & Ayers Electrical Circuit Model

The design and analysis of semiconductor strained-layer device structures require an understanding of the equilibrium profiles of strain and dislocations associated with mismatched epitaxy. Though it has been shown that the equilibrium configuration for a general semiconductor strained-layer structure may be found numerically by energy minimization using an appropriate partitioning of the structure into sublayers, such an approach is computationally intense and non-intuitive. We have therefore developed a simple electric circuit model approach for the equilibrium analysis of these structures. In it, each sublayer of an epitaxial stack may be represented by an analogous circuit configuration involving an independent current source, a resistor, an independent

voltage source, and an ideal diode. A multilayered structure may be built up by the connection of the appropriate number of these building blocks, and the node voltages in the analogous electric circuit correspond to the equilibrium strains in the original epitaxial structure. This enables analysis using widely accessible circuit simulators, and an intuitive understanding of electric circuits can easily be extended to the relaxation of strained-layer structures. Furthermore, the electrical circuit model may be extended to continuously-graded epitaxial layers by considering the limit as the individual sublayer thicknesses are diminished to zero. In this work, we describe the mathematical foundation of the electrical circuit model, demonstrate its application to several representative structures involving $In_xGa_{1-x}As$ strained layers on GaAs (001) substrates, and develop its extension to continuously-graded layers. This extension allows the development of analytical expressions for the strain, misfit dislocation density, critical layer thickness and widths of misfit dislocation free zones for a continuously-graded layer having an arbitrary compositional profile. It is similar to the transition from circuit theory, using lumped circuit elements, to electromagnetics, using distributed electrical quantities. We show this development using first principles, but in a more general sense, Maxwell's equations of electromagnetics could be applied.

The understanding of the equilibrium lattice relaxation has important implications in the determination of the stability criteria for electronic and optical devices [45,46,47,48,49,50]. Furthermore, the equilibrium configuration serves as the starting point for kinetically-limited lattice relaxation calculations and is critical in determining the effective stress and therefore the driving force for dislocation flow. Several models have been developed for the determination of the equilibrium configuration [34,43,44,51,52,53,54,55,56] and although it has been shown that the equilibrium configuration for a general semiconductor strained-layer structure may be

determined numerically by energy minimization using an appropriate partitioning of the structure into sublayers[51,52,53,54] such an approach uses specialized code, is computationally intense, and does not lend itself to an intuitive understanding necessary for innovative structure design.

To avoid these limitations, and to enable the development of analytical solutions for compositionally-graded heterostructures, we propose the use of an electrical circuit model analogy. Several mechanical-electrical analogs have been developed and used, particularly for the load beam analysis. The most common of these are the so-called "force-current" and "force-voltage" analogs [57,58,59,60,61], but others have been developed as well. It is possible to use any of these to provide a physically correct description of behavior in a mechanical system; however, some are better suited to certain applications. For example, our work relates to the static behavior of a semiconductor heterostructure in equilibrium, and there is no need to include electrical components such as capacitors and inductors, which may be included for transient (time-dependent) modeling.

Among the previously published work on mechanical-electrical analogies, a report of particular interest is that by Olsson and Bath [61], which describes two choices of analogies for application to problems of geophysics. Their second transcriptive system considers electrical current to be analogous to mechanical stress, electrical voltage to be analogous to mechanical strain, and electrical resistance to be analogous to the reciprocal of an elastic modulus. Olsson and Bath point out that an advantage of this transcriptive system is that it facilitates simple electrical analogies, and lends itself to series or parallel connections, which correspond to each other in the mechanical and electrical domains.

The purpose for developing an analogy between one field of physics and another is to take advantage of theoretical framework, which exists in one field but not the other. In a recent short publication [62] we have shown that an arbitrary semiconductor heterostructure, approximated by a stack of uniform composition layers, may be modeled using an electric circuit analogy similar to Olsson and Bath's, in which electrical voltage is considered analogous to mechanical strain. In this model, each sublayer of a general strained-layer device may be represented by an analogous electrical circuit configuration involving an independent current source, a resistor, an independent voltage source, and an ideal diode. A multilayered structure may be built up by the connection of the appropriate number of these basic building blocks, after which the node voltages in the electric circuit correspond to the equilibrium strains in the original epitaxial structure. If any sublayer in the structure is grown coherently on the sublayer below, the difference in strain in these sublayers is given by the lattice mismatch difference. This is modeled by introducing an independent voltage source between the nodes representing the two sublayers, and the resulting strains are analogous to the node voltages, which may be found using supernode theory. The theoretical framework of supernodes exists in electrical circuits but not in mechanical systems, and represents an important motivation for using the electric circuit analogy in this case. Another significant point is that the voltage source, which is related to the coherency state of the sublayer, is connected through an ideal diode, which conducts only in the case of coherent growth. Use of this device in the electric circuit analogy allows a physically correct description of the mechanical behavior, though no such device exists in mechanical systems. This represents a second key motivation for the application of the electric circuit model analogy to a strained semiconductor heterostructure.

In this dissertation, we describe the further development of the mathematical framework for the electrical circuit model approach, starting with a single strained layer and then generalizing to a multilayer structure. We relate the physical quantities in the epitaxial stack to those in an analogous electrical circuit.

Using the circuit model, we demonstrate the equilibrium analysis of a number of $In_xGa_{1-x}As$ / GaAs (001) epitaxial structures, including a single strained layer, three-layer stacks, step-graded layers, linearly-graded layers and S-graded layers. We show that the strain results of the circuit model calculations are in agreement with the theory of Matthews and Blakeslee [55] for the single strained layer. We also develop exact results for the case of a linearly graded layer, whereas previously only an approximate solution had been developed by Tersoff [44]. In the approximate solution of Tersoff, it was assumed that the strain was completely relieved in the region containing dislocations, and that the dislocation line energy was independent of distance from the surface. We have not relied on these simplifying assumptions when applying the circuit model, and therefore provide exact in-plane strain results for the linearly-graded case. Furthermore, we show the extension of the circuit model to any continuously-graded semiconductor layer by taking the limit as the thickness of the individual sublayers approaches zero. This enables the development of analytical expressions for the strain, misfit dislocation density, critical layer thickness and widths of misfit dislocation free zones (MDFZ) in a continuously-graded epitaxial layer having any compositional grading profile, including linear [63], exponential [64], power law, and S-graded [52,65] profiles. The extension from a finite number of sublayers to the continuously-graded case is analogous to the transition from circuit theory, using lumped circuit elements, to electromagnetics, wherein the electrical quantities are distributed. We show this development

based on first principles, but in a more general sense, Maxwell's equations of electromagnetics could be applied to continuously-graded strained layers.

4.4.1. Electrical Circuit Model for Equilibrium Strain Relaxation

The development of an electric circuit model stems from the fact that Equation 4.12 resembles the node voltage expression for the top node of the simple electrical circuit shown in Figure 4.2a:

$$0 = 2Yh\varepsilon - \frac{f}{|f|}\frac{Gb\left(1-\nu\cos^2\theta\right)}{2\pi(1-\nu)\sin\alpha\sin\phi}\left[\ln\left(\frac{h}{b}\right)+1\right] \quad \leftrightarrow \quad \frac{V}{R} - I = 0\,. \tag{4.32}$$

The node voltage is determined from Kirchhoff's current law, which states that the algebraic sum of the currents flowing away from a node must equal zero[*]. In the equation above, the symbol $\leftrightarrow$ implies that quantities or relationships on either side of the arrow are analogous though they generally possess different units. The derivative of the strain energy with respect to the in-plane strain is analogous to the current flowing through the resistor R, $\partial E_\varepsilon / \partial\varepsilon \quad \leftrightarrow \quad I_R$, whereas the change in the dislocation energy with respect to the in-plane strain is analogous to the value of the independent current source I, $\partial E_D / \partial\varepsilon \quad \leftrightarrow \quad I$. Given that the partial derivatives are analogous to electrical currents, comparison of the two forms of Equation 4.32 reveals that the equilibrium strain is analogous to the node voltage[†]:

$$\varepsilon \quad \leftrightarrow \quad V, \tag{4.33}$$

the factor multiplying the strain is analogous to a conductance (reciprocal of resistance):

[*] In this analysis, an electrical current which enters the node is considered negative.
[†] It should be noted that the choice to represent the partial derivatives by analogous current sources is not unique, but was made for convenience. The analogous circuit could be defined differently and still yield the correct results, as long as a consistent set of analogs was used.

$$2Yh \quad \leftrightarrow \quad \frac{1}{R}, \tag{4.34}$$

and the subtracted term is analogous to an independent current source entering the top node of the circuit (see Figure 4.2a):

$$\frac{f}{|f|}\frac{Gb\left(1-\nu\cos^2\theta\right)}{2\pi(1-\nu)\sin\alpha\sin\phi}\left[\ln\left(\frac{h}{b}\right)+1\right] \quad \leftrightarrow \quad I. \tag{4.35}$$

To account for the possibility of pseudomorphic epitaxy, we can include an independent voltage source and an ideal diode in the circuit, which together form a clipping circuit as shown in Figure 4.2b. The ideal diode acts as a switch that is conductive only when an epitaxial layer is coherently-grown. The numerical value of the voltage source V_S is equal to the coherency strain in the layer:

$$f \quad \leftrightarrow \quad V_S. \tag{4.36}$$

To properly account for the sign of the lattice mismatch (tensile or compressive), the ideal diode must always face toward *the true positive terminal* of the independent voltage source (Figure 4.2b illustrates both cases). Therefore, in terms of the electrical circuit model, the two analogous forms of the solution for the node voltage (or the equivalent equilibrium strain) are given as,

$$V=\begin{cases} V_S, & h\le h_c \\ I\cdot R, & h>h_c \end{cases} \quad \leftrightarrow \quad \varepsilon(h)=\begin{cases} f, & h\le h_c \\ \dfrac{f}{|f|}\dfrac{b\left(1-\nu\cos^2\alpha\right)}{8\pi h(1+\nu)\sin\alpha\sin\phi}\left[\ln\left(\dfrac{h}{b}\right)+1\right], & h>h_c \end{cases}. \tag{4.37}$$

We can extend the electrical circuit model described above to the three-layer structure shown in Figure 4.1b. By a similar approach, Equation 4.18 resembles the node voltage expressions for three essential nodes[‡] and therefore we can consider the consecutive stacking of

[‡] An essential node is defined as a node connected to more than two circuit elements. Therefore, the number of essential nodes in the analogous circuit corresponds to the minimum number of equations which must be utilized to solve the circuit.

the electrical circuit given in Figure 4.2b to obtain an equivalent circuit that describes a three-layered heterostructure (Figure 4.2c). The appropriate connections of the electrical circuit block are done in such a way that the separation of two essential nodes consist on one end the combination of the independent voltage source and the ideal diode and in the other end the independent current source. Furthermore, in each building block the resistor shares one of its terminals with the essential node and the other with the ground connection. Thus, in the analogous electrical circuit model, the node voltages for three essential nodes are given by

$$
\begin{aligned}
0 &= 2Y_3 h_3 \varepsilon_3 - \frac{f_3 - f_2}{|f_3 - f_2|} \frac{G_3 b_3 \left(1 - \nu_3 \cos^2 \alpha\right)}{2\pi(1-\nu_3)\sin\alpha \sin\phi} \left[\ln\left(\frac{h_3}{b_3}\right) + 1 \right] \quad &\leftrightarrow \quad \frac{V_3}{R_3} - I_3 = 0 \\
0 &= 2Y_2 h_2 \varepsilon_2 - \frac{f_2 - f_1}{|f_2 - f_1|} \frac{G_2 b_2 \left(1 - \nu_2 \cos^2 \alpha\right)}{2\pi(1-\nu_2)\sin\alpha \sin\phi} \left[\ln\left(\frac{h_2 + h_3}{b_2}\right) + 1 \right] \\
&\quad + \frac{f_3 - f_2}{|f_3 - f_2|} \frac{G_3 b_3 \left(1 - \nu_3 \cos^2 \alpha\right)}{2\pi(1-\nu_3)\sin\alpha \sin\phi} \left[\ln\left(\frac{h_3}{b_3}\right) + 1 \right] \quad &\leftrightarrow \quad \frac{V_2}{R_2} - I_2 + I_3 = 0 . \qquad \textbf{(4.38)} \\
0 &= 2Y_1 h_1 \varepsilon_1 - \frac{f_1 - f_0}{|f_1 - f_0|} \frac{G_1 b_1 \left(1 - \nu_1 \cos^2 \alpha\right)}{2\pi(1-\nu_1)\sin\alpha \sin\phi} \left[\ln\left(\frac{h_1 + h_2 + h_3}{b_1}\right) + 1 \right] \\
&\quad + \frac{f_2 - f_1}{|f_2 - f_1|} \frac{G_2 b_2 \left(1 - \nu_2 \cos^2 \alpha\right)}{2\pi(1-\nu_2)\sin\alpha \sin\phi} \left[\ln\left(\frac{h_2 + h_3}{b_2}\right) + 1 \right] \quad &\leftrightarrow \quad \frac{V_1}{R_1} - I_1 + I_2 = 0
\end{aligned}
$$

It can be shown that the numerical value of the voltage at each node is equivalent to the equilibrium strain of that sublayer, $\varepsilon_1 \leftrightarrow V_1$, $\varepsilon_2 \leftrightarrow V_2$ and $\varepsilon_3 \leftrightarrow V_3$. In the three-layer system, the diode-connected independent voltage sources are determined by the difference in the lattice mismatch of the two adjacent layers where:

$$
\begin{aligned}
V_{S3} &\leftrightarrow f_3 - f_2 \\
V_{S2} &\leftrightarrow f_2 - f_1 . \qquad \textbf{(4.39)} \\
V_{S1} &\leftrightarrow f_1 - f_0
\end{aligned}
$$

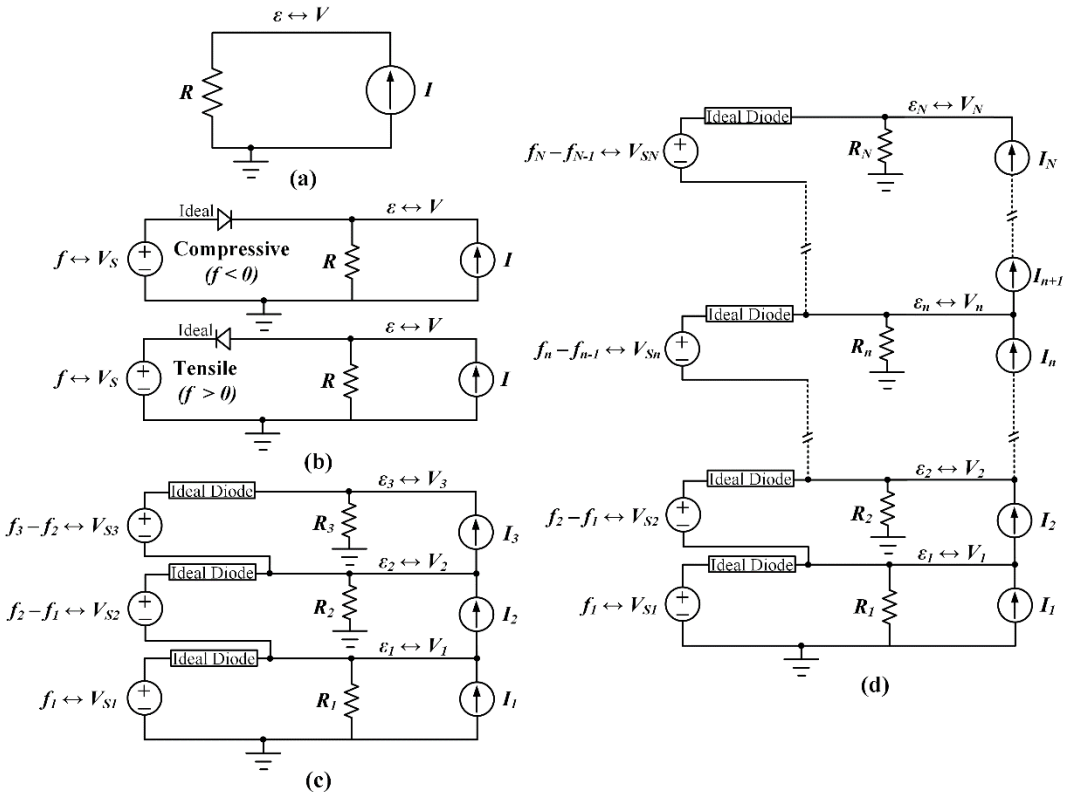

Figure 4.2. (a) A simple resistive circuit comprised of a resistor and independent current source. (a) The equivalent electrical circuit to determine the equilibrium lattice relaxation of (a) a single compositionally uniform epitaxial layer with either compressive and tensile cases, (b) an epitaxial layer consisting of three sublayers with varying compositional mismatch and thickness and (c) an epitaxial layer broken down into N sublayers.

For the case in which all sublayers are coherently grown, the diodes all operate in the forward conduction mode, and therefore the voltage at each essential node is determined by accounting for the sum of all the independent voltage sources up to and including the layer in consideration:

$$\begin{aligned} V_3 &= V_{S3} + V_{S2} + V_{S1} \quad &\leftrightarrow \quad \varepsilon_3 &= f_3 \\ V_2 &= V_{S2} + V_{S1} \quad &\leftrightarrow \quad \varepsilon_2 &= f_2 \\ V_1 &= V_{S1} \quad &\leftrightarrow \quad \varepsilon_1 &= f_1 \end{aligned} . \tag{4.40}$$

Upon the growth of strained material in which misfit dislocation networks are present at each mismatched interface, the diodes are all in the reverse blocking mode (non-conductive), and the

node voltages (layer strains) may be found by solution of the node voltage equations without inclusion of the independent voltage sources:

$$\begin{aligned} V_3 &= R_3 \cdot I_3 \quad &\leftrightarrow \quad \varepsilon_3 \\ V_2 &= R_2 \cdot (I_2 - I_3) \quad &\leftrightarrow \quad \varepsilon_2 \\ V_1 &= R_1 \cdot (I_1 - I_2) \quad &\leftrightarrow \quad \varepsilon_1 \end{aligned} \text{ .} \qquad \textbf{(4.41)}$$

In some cases, a coherent epitaxial layer may be grown on top of a metamorphic buffer. In such a case the coherent interface, free from misfit dislocations, corresponds to a conducting diode in the electrical circuit. The presence of one or more interfaces free from misfit dislocations can be described by the existence of a misfit dislocation free zone. The conduction of the diode results in the connection of an independent voltage source directly between essential nodes, which in circuit theory can be considered to form a supernode[§]. In other words, the presence of a MDFZ may be likened to the formation of a supernode in electrical circuit theory. The existence of the supernode modifies the node voltage equations for the nodes involved, and therefore the resulting node voltages, which will be described in more detail below when considering the general treatment of an arbitrary heterostructure.

In the most general case, where we can consider an arbitrary heterostructure consisting of multiple and/or compositionally-graded epitaxial layers as shown in Figure 4.1c, we can extend the above analysis by dividing the epitaxial layer into N disparate sublayers (Figure 4.2d). The partial derivatives shown in Equation 4.19 are given in terms of their analogous electrical circuit components as

[§] A supernode in electrical circuit theory refers to the case where two essential nodes are separated by an independent voltage source.

$$0 = 2Y_N h_N \varepsilon_N - \frac{f_N - f_{N-1}}{|f_N - f_{N-1}|} \frac{G_N b_N (1-\nu_N \cos^2\alpha)}{2\pi(1-\nu_N)\sin\alpha\sin\phi}\left[\ln\left(\frac{h_N}{b_N}\right)+1\right] \quad \leftrightarrow \quad \frac{V_N}{R_N} - I_N = 0, \qquad n = N$$

$$0 = \begin{pmatrix} 2Y_n h_n \varepsilon_n - \frac{f_n - f_{n-1}}{|f_n - f_{n-1}|} \frac{G_n b_n (1-\nu_n \cos^2\alpha)}{2\pi(1-\nu_n)\sin\alpha\sin\phi}\left[\ln\left(\sum_{j=n}^{N}\frac{h_j}{b_n}\right)+1\right] \\ + \frac{f_{n+1} - f_n}{|f_{n+1} - f_n|} \frac{G_{n+1} b_{n+1} (1-\nu_{n+1} \cos^2\alpha)}{2\pi(1-\nu_{n+1})\sin\alpha\sin\phi}\left[\ln\left(\sum_{j=n+1}^{N}\frac{h_j}{b_{n+1}}\right)+1\right] \end{pmatrix} \quad \leftrightarrow \quad \frac{V_n}{R_n} - I_n + I_{n+1} = 0, \quad 1 \le n < N \tag{4.42}$$

In this extended analogy, the n^{th} sublayer may be modeled by an electrical subcircuit in which:

$$R_n \quad \leftrightarrow \quad \frac{1}{2Y_n h_n}, \quad 1 \le n \le N, \tag{4.43}$$

$$I_n \quad \leftrightarrow \quad \frac{f_n - f_{n-1}}{|f_n - f_{n-1}|} \frac{G_n b_n (1-\nu_n \cos^2\theta)}{2\pi(1-\nu_n)\sin\alpha\sin\phi}\left[\ln\left(\sum_{j=n}^{N}\frac{h_j}{b_n}\right)+1\right], \quad 1 \le n \le N, \tag{4.44}$$

and

$$V_{Sn} \quad \leftrightarrow \quad f_n - f_{n-1}, \quad 1 \le n \le N, \tag{4.45}$$

The ideal diode in each sublayer is always facing the *true positive terminal* of the independent voltage source at that sublayer; when the diode conducts, the independent voltage source is dissipative. In the case in which each sublayer contains misfit dislocations, none of the diodes conduct, and the in-plane strain (node voltage) at the n^{th} sublayer is determined by

$$\varepsilon_n \quad \leftrightarrow \quad V_n = \begin{cases} R_n \cdot (I_n - I_{n+1}), & 1 \le n < N \\ R_n \cdot I_n, & n = N \end{cases}. \tag{4.46}$$

The linear misfit dislocation density at each sublayer may then be determined by

$$\rho_n = \frac{f_n - f_{n-1}}{|f_n - f_{n-1}|} \frac{(f_n - \varepsilon_n) - (f_{n-1} - \varepsilon_{n-1})}{b_n \sin\alpha\sin\phi}, \quad 1 \le n \le N. \tag{4.47}$$

From a fabrication point of view, the growth of mismatched and compositionally-graded epitaxial layers yields metamorphic heterostructures which may contain misfit dislocation free zones. In

this situation, where the epitaxial structure as a whole is incoherent but some of the sublayers are coherently-grown with respect to the ones below, the presence of a misfit dislocation free zone is equivalent to the formation of a supernode in the analogous electrical circuit model. Therefore, the node voltage (or the equivalent in-plane strain) in the bottom layer of the supernode is determined by accounting for the equivalent resistance of all the layers included in the supernode. If the supernode is bounded inclusively by sublayers σ and ω, then the equilibrium strain (node voltage) in the bottom layer of the supernode is given by

$$\varepsilon_\sigma \quad \leftrightarrow \quad V_\sigma = \left[\left(I_\sigma - I_{\omega+1} \right) - \sum_{j=\sigma}^{\omega} \frac{\sum_{i=1}^{j} V_{Si} - \sum_{i=1}^{\sigma} V_{Si}}{R_j} \right] R_{SN}\,, \tag{4.48}$$

where the equivalent parallel resistance of the supernode (R_{SN}) is defined as the equivalent resistance for a series of resistors in parallel, $R_{SN} = R_\sigma \,\|\, ... \,\|\, R_\omega$, and is given by

$$R_{SN} = \left(\sum_{j=\sigma}^{\omega} \frac{1}{R_j} \right)^{-1}. \tag{4.49}$$

The in-plane strain (node voltage) at each sublayer of the *supernode* is then determined by adding the appropriate sum of independent voltage sources to the voltage at the bottom of the supernode. In other words, the node voltage (or the equivalent in-plane strain) of each sublayer of the *supernode* is determined from

$$\varepsilon_i = \varepsilon_\sigma + \sum_{j=\sigma+1}^{i} f_j - f_{j-1} \quad \leftrightarrow \quad V_i = V_\sigma + \sum_{j=\sigma+1}^{i} V_{Sj}, \quad \sigma < i \le \omega\,, \tag{4.50}$$

5. Kinetically-Limited Lattice Relaxation and Dislocation Dynamics Model

The traditional approach to the design of lattice-mismatched electronic and optical devices with minimal defects involved pseudomorphic growth, in which all epitaxial layer thicknesses are kept below the critical layer thickness for defect formation. However, in many cases materials or performance constraints prevent the use of pseudomorphic structures. Metamorphic growth, in which the layers relax by the introduction of misfit dislocations, enables a wider range of layer thicknesses and compositions and has been exploited in a variety of devices. A critical challenge with metamorphic device design involves control of the threading dislocation density, and compositionally-graded buffer layers have been used for this purpose. Understanding the lattice relaxation mechanisms in such devices requires the development of appropriate dislocation dynamics models; several kinetics models have been proposed [66,67,68,69,70,71] which account for thermally activated glide of pre-existing dislocations [66,68], dislocation multiplication [68], dislocation nucleation [70] and impediments to dislocation mobility [71]. Earlier relaxation models were applicable only to uniform composition layers in which misfit dislocations were concentrated at the epilayer-substrate interface [67,68,69,70,71]. Fitzgerald [72,73] extended this work to compositionally-graded Ge_xSi_{1-x}/Si heterostructures by assuming the threading dislocation rapidly reaches a steady-state value during growth of the compositionally-graded layer.

In this chapter, we discuss the development of a generalized model applicable to compositionally-graded and multilayered semiconductor heterostructures. The developed includes dislocation multiplication, annihilation, and coalescence, as well as interactions between threading and misfit dislocations at abrupt interfaces. In the kinetic model, it is assumed that the dislocation multiplication rate is proportional to the velocity of dislocations, effective stress, and the density

of dislocations; this is similar to the model proposed by Dodson and Tsao [68] for uniform layers. The reduction of threading dislocation density is modeled by including the mechanisms of (i) dislocation compensation caused from interactions of misfit-threading dislocations at abrupt interfaces which account for the possibility that threading dislocations can be bent over to produce misfit dislocation segments at abrupt interfaces or even in compositionally-graded material and (ii) annihilation and coalescence reactions as described by Tachikawa and Yamaguchi; these reactions are known to be important in partly-relaxed semiconductor heterostructures and in uniform layers much greater than the critical layer thickness and these phenomena lead to a threading dislocation density which is usually inversely proportional to layer thickness in uniform layers. In addition to reviewing the mathematical framework of the plastic flow model, we also provide the algorithmic implementation.

5.1. Kujofsa et al. Lattice Relaxation Model

The foundation for the dislocation dynamics model used in this work is derived in [66, 74]. This model predicts lattice relaxation and threading dislocation behavior in heteroepitaxial layers of arbitrary thickness and compositional profile. In a general semiconductor heterostructure with lattice mismatch profile $f(z)$, the rate of lattice relaxation at a distance z from the interface is determined by the glide of dislocations in the underlying material, and is given by

$$\frac{d\gamma(z)}{dt} = KBb\sin\alpha\sin\phi\tau_{eff}^2(z)\exp\left(-\frac{U}{kT}\right)\int_0^z\left[\rho_A(\zeta)+\rho_0\right]d\zeta\,. \qquad \textbf{(5.1)}$$

where K and B are constants, b is the length of the Burgers vector, α is the angle between the Burgers vector and line vector, λ is the angle between the Burgers vector and the direction in the interface which is perpendicular to the intersection of the glide plane and the interface, τ_{eff} is the

effective stress, U is the activation energy for dislocation glide, k is the Boltzmann constant, T is the temperature, ρ_A is the areal density of misfit dislocations, ρ_0 is a constant which represents the initial sources of dislocations, and ξ is the variable of integration. The effective stress is the driving force for lattice relaxation; the effective stress at a distance z from the interface is determined by the difference of the actual and equilibrium strain profiles in the material above, given by

$$\tau_{eff}(z) = \left[\frac{2\cos\phi\cos\lambda}{h-z}\right]\int_z^h \left\{\frac{G(1+\nu)\left[\varepsilon_{\|}(\zeta)-\varepsilon_{eq}(\zeta)\right]}{(1-\nu)}\right\}d\zeta . \qquad \textbf{(5.2)}$$

where h is the layer thickness, ψ is the angle between the surface normal and the slip plane, G is the shear modulus, ν is the Poisson ratio, $\varepsilon_{\|}$ is the in-plane strain, and ε_{eq} is the equilibrium in-plane strain. For an arbitrary heteroepitaxial structure, the equilibrium configuration may be determined by minimization of the strain and dislocation energy in the film as described previously. The areal density of misfit dislocations is related to the grading and lattice relaxation by

$$\rho_A(z) = \left(\frac{1}{b\sin\alpha\sin\phi}\right)\left(\frac{d\varepsilon_{\|}(z)}{dz} - \frac{df(z)}{dz}\right). \qquad \textbf{(5.3)}$$

At an abrupt interface, the misfit dislocations are localized in the interface, giving rise to a delta function in the misfit dislocation density profile, but for compositionally graded material the misfit dislocations are distributed throughout the thickness, necessitating the use of the areal misfit dislocation density described here. Assuming that dislocations occur in the form of half-loops, the average length of misfit segments increases at a rate equal to twice the dislocation glide velocity,

$$\frac{dL_{MD}(z)}{dt} = 2B\tau_{eff}(z)\exp\left(-\frac{U}{kT}\right). \quad \textbf{(5.4)}$$

which has been assumed to be linear in the effective stress. In the general case, the dislocation glide velocity may not be linearly depended on the effective stress and may be written as

$$\frac{dL_{MD}(z)}{dt} = 2B\tau_{eff}^{m}(z)\exp\left(-\frac{U}{kT}\right). \quad \textbf{(5.5)}$$

where m describes the power-law dependence of the dislocation glide velocity on the effective stress. The dislocation glide is governed by the balance of the Peach-Kohler and Peierls forces acting on dislocations [75]. This physical behavior is implicit in Equation 5.4 and gives rise to the linear dependence on the effective stress.

If the sample temperature is varied, either during growth or the post-growth cool-down, it is necessary to take into account the thermal strains introduced by the difference in thermal expansion coefficients, according to

$$\varepsilon_{\|}(T) = \varepsilon_{\|}(T_0) + \int_{T_0}^{T}(\alpha_s - \alpha_e)d\tau\,. \quad \textbf{(5.6)}$$

where $\varepsilon_{\|}(T_0)$ and $\varepsilon_{\|}(T)$ are the in-plane strains at temperatures T_0 and T, respectively, and α_s and α_e are the thermal coefficients of linear expansion for the substrate and epitaxial material, respectively. The thermal expansion characteristics in this work were calculated using the second-order polynomial fits to the experimental characteristics for a given material systems and is given below:

$$\alpha = B + 2CT + 3DT^2. \quad \textbf{(5.7)}$$

where T is the absolute temperature in Kelvins. The polynomial coefficients for thermal expansion are summarized in Chapter 2 of this dissertation.

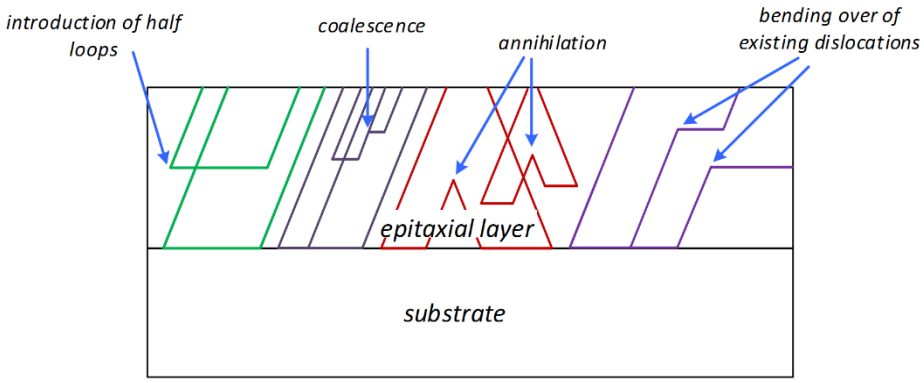

Figure 5.1. Interaction of threading dislocations.

5.2. Kujofsa et al. Dislocation Dynamics Model

The previously described lattice relaxation model is complemented by including two important misfit-threading dislocation interactions which bear on dislocation compensation: (i) the introduction of dislocation half loops [76] and (ii) the bending over of existing threading dislocations at mismatched interfaces [34,77]. When misfit dislocations are created by the introduction of half loops, each misfit dislocation segment of length L_{MD} is associated with two threading segments which intersect the surface, thereby adding to the threading dislocation population. In contrast, the creation of misfit segments by the bending over of grown-in threading dislocations takes away from the number of threading dislocations, because dislocations bent over at an interface can combine in an annihilation reaction or glide to the edge of the sample. This model does not consider attractive or repulsive forces between misfit and threading dislocations and this is the main approximation used in this work. We use the idea of the net Burgers vector content to quantify the assertion that misfit dislocations are formed by either the bending over of threading dislocations or the introduction of new half loops. In addition to misfit dislocation mediated annihilation, there can be second-order coalescence and annihilation reactions involving only threading dislocations as modeled by Tachikawa and Yamaguchi [78] and Romanov et al.

[79]. The basic types of dislocation interactions are shown schematically in Figure 5.1, and the resulting differential equation for the threading dislocation density is

$$\frac{dD(z)}{dz} = \frac{4\rho_A(z)}{L_{MD}(z)sign\int_0^z \rho_A(\zeta)d\zeta} - C_2 D^2(z). \quad \textbf{(5.8)}$$

where $\rho_A(z)$ is the areal density of misfit dislocations, $L_{MD}(z)$ is the average length of misfit dislocation segments and C_2 is a constant. The first term in equation above accounts for the interactions between misfit and threading dislocations. Considering mechanism (i), new misfit dislocations are introduced via half loops if the new misfit dislocations have the same sense (relax the same sign of lattice mismatch) as the underlying misfit segments. The constant 4 accounts for one pair of dislocations in two orthogonal slip systems. This corresponds to the case of $sign(\rho_A(z)) = sign\int_0^z \rho_A(\zeta)d\zeta$ and results in positive $dD(z)/dz$. With respect to mechanism (ii), misfit dislocations are produced by the bending of existing threading dislocations if these misfit dislocations have the opposite sense (relax the opposite sign of mismatch) compared to the underlying misfit segments. This corresponds to $sign(\rho_A(z)) = -sign\int_0^z \rho_A(\zeta)d\zeta$ and results in negative $dD(z)/dz$. The second term accounts for second-order annihilation-coalescence reactions involving threading dislocations. In the implementation of the model, a structure with an arbitrary compositional profile is approximated by a stack of N lamina (sublayers). In order to model the plastic flow in the structures, the N sublayers are considered to be deposited one at a time. After the deposition of a layer of the on-growing structure the numerical tool calculates the overall equilibrium configuration and for each layer in the stack the rate of lattice relaxation is

determined from the glide velocity of the threading dislocation arms and the growth time for the sublayer under consideration.

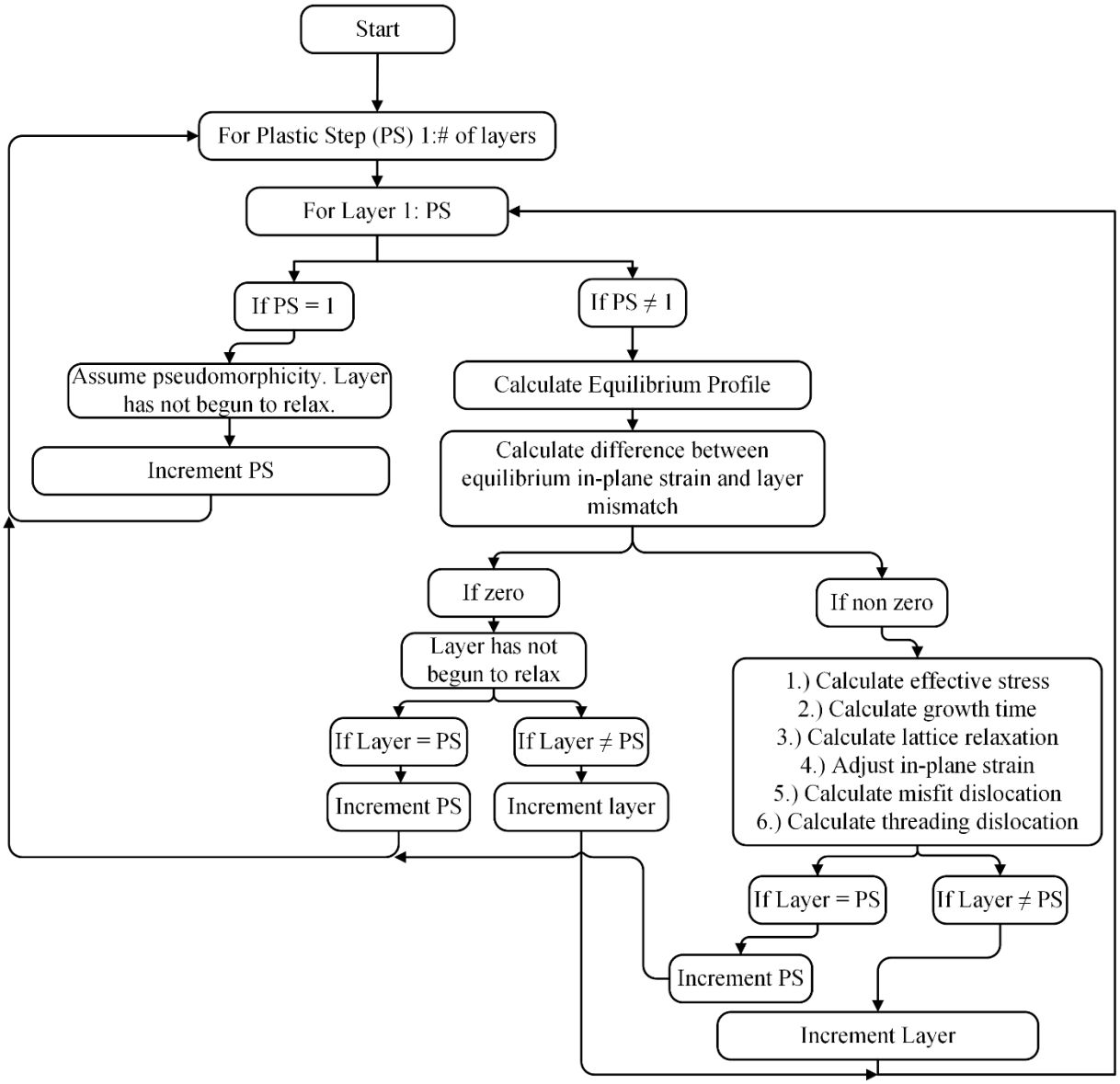

Figure 5.2. Schematic of computational algorithm for the plastic flow model.

5.3. Implementation of the Kujofsa et al. Plastic Flow Model

To implement such a model, the structure is considered to grow in a step-by-step fashion, one sublayer per step. The algorithm for the implementation of the plastic flow model will be described as follows and a schematic of it is shown in Figure 5.2. At step one in the plastic flow modeling process the structure is considered to comprise only the substrate and sublayer one. The layer is assumed to be deposited coherently (pseudomorphically) with its in-plane strain equal to the lattice mismatch: $\varepsilon_{||}[1] = f[1]$. The equilibrium strain is calculated by an energy minimization procedure as described in the previous section. If the equilibrium strain differs from the coherency strain, this results in a non-zero effective stress:

$$\tau_{eff}[1] = \frac{2G(1+\nu)\cos\phi\cos\lambda}{(1-\nu)}\left\{\varepsilon_{||}[1] - \varepsilon_{eq}[1]\right\}. \quad \textbf{(5.9)}$$

Layer one is considered to anneal for a duration equal to its growth time, $t[1] = h[1]/g[1]$, during which the lattice relaxation is

$$\Delta\gamma[1] = sign\left\{\varepsilon_{eq}[1] - \varepsilon_{||}[1]\right\} KBb\sin\alpha\sin\phi\,\tau_{eff}^2[1]\exp\left(-\frac{U}{k_B T[1]}\right)\rho_0 h[1]t[1]. \quad \textbf{(5.10)}$$

The in-plane strain $\varepsilon_{||}[1]$ is replaced by $\varepsilon_{||}[1] + \Delta\gamma[1]$, the areal misfit dislocation density in sublayer one is set to $\rho[1] = \left(\varepsilon_{||}[1] - f[1]\right)h[1]/\left(b\sin\alpha\sin\phi\right)$, and the process proceeds with step two.

At any step m (for which $m > 1$), the m^{th} sublayer is added to the structure and is assumed to be strained in such a way that it is coherent with the $(m-1)^{th}$ layer. The starting value of strain in the m^{th} layer is therefore $\varepsilon_{||}[m] = \varepsilon_{||}[m-1] + f[m] - f[m-1]$. To account for any possible

temperature change at the m^{th} layer, the in-plane strain in each of the layers is adjusted by an amount $\Delta\varepsilon_{Th}[i]$ given by

$$\Delta\varepsilon_{Th}[i] = \int_{T[m-1]}^{T[m]} (\alpha_S - \alpha[i]) dT \,, \qquad \textbf{(5.11)}$$

where $T[m-1]$ and $T[m]$ are the growth temperatures for the $(m-1)^{th}$ and m^{th} sublayers, respectively, α_S is the thermal coefficient of expansion for the substrate, and $\alpha[i]$ is the thermal coefficient of expansion for the i^{th} sublayer. Next the effective stress is found for each of the sublayers; in the n^{th} layer during the m^{th} step of the relaxation process it is

$$\tau_{eff}[n] = \frac{2\cos\phi\cos\lambda}{\sum_{i=n}^{m} h[i]} \sum_{i=n}^{m} \left\{ G[n]h[i](1+\nu[n])(\varepsilon_{\|}[n] - \varepsilon_{eq}[n]) / (1-\nu[n]) \right\}. \qquad \textbf{(5.12)}$$

Using this effective stress profile, the lattice relaxation is calculated for each of the sublayers up to sublayer m. For the n^{th} layer during the m^{th} step of the relaxation process the lattice relaxation is

$$\Delta\gamma[n] = sign\{\varepsilon_{eq}[1] - \varepsilon_{\|}[1]\} KBb \sin\alpha \sin\phi \tau_{eff}^2[n] \exp\left(-\frac{U}{k_B T[n]}\right) t[n] \sum_{i=1}^{n} [(\rho[i] + \rho_0) h[i]]. \qquad \textbf{(5.13)}$$

Once $\Delta\gamma[1]$, $\Delta\gamma[2]$, … $\Delta\gamma[m]$ have been calculated, the strain profile is adjusted by replacing each in-plane strain $\varepsilon_{\|}[n]$ with $\varepsilon_{\|}[n] + \Delta\gamma[n]$. Finally, the misfit dislocation density profile is adjusted according to

$$\rho[i] = \begin{Bmatrix} \dfrac{(\varepsilon_{\|}[i] - f[i])}{bh[i]\sin\alpha\sin\phi}, & i = 1; \\ \dfrac{(\varepsilon_{\|}[i] - \varepsilon_{\|}[i-1] - f[i] - f[i-1])}{bh[i]\sin\alpha\sin\phi} & i \neq 1. \end{Bmatrix}, \qquad \textbf{(5.14)}$$

and the process proceeds to step $m+1$.

A growth rest is modeled as a "sublayer" having an associated time and temperature but zero thickness. (In practice, a layer of negligible thickness is used.) A linear temperature ramp can be treated approximately in the same way, using the approach adopted for the treatment of temperature ramping in diffusion furnaces [80]. If the temperature is ramped from T_1 to T_2 with a ramp time t_{ramp}, the lattice relaxation can be approximated by using an annealing step at T_1 for an effective time t_{eff} given by

$$t_{eff} = \frac{k\left(T_2^2 - T_1^2\right)}{U\left(T_2 - T_1\right)} t_{ramp}, \qquad \textbf{(5.15)}$$

where k is the Boltzmann constant and U is the activation energy for dislocation glide.

6. Distribution of Equilibrium Strain and Dislocations in MBLs

The following chapter investigates equilibrium lattice relaxation in multilayered heterostructures utilizing various compositional-grading profiles. In each subsection, we investigate the distribution the in-plane strain and misfit dislocation densities and develop design criteria for heterostructures which exhibit desired residual strain and dislocation characteristics. The results in the following work are obtained utilizing the numerical minimum energy engine.

6.1. Compositionally Uniform Metamorphic Layers

Matthews and Blakeslee developed an expression for the equilibrium in-plane strain for a single and compositionally uniform layer given by

$$\varepsilon(h)=\begin{cases} f, & h\le h_c \\ \dfrac{f}{|f|}\dfrac{b(1-\nu\cos^2\alpha)}{8\pi h(1+\nu)\sin\alpha\sin\phi}\left[\ln\left(\dfrac{h}{b}\right)+1\right], & h>h_c \end{cases}, \qquad \textbf{(6.1)}$$

where f is the lattice mismatch, $f\equiv(a_s-a_e)/a_e$, a_s and a_e are the relaxed lattice constants of the substrate and epitaxial crystal (cm), respectively, the term $f/|f|$ accounts for the sign of the mismatch, ρ is the linear misfit dislocation density in at the mismatched interface (cm^{-1}), b is the length of the Burgers vector (cm), α is the angle between the Burgers vector and dislocation line vector, ϕ is the angle between the glide plane and interface, Y is the biaxial modulus (dyn/cm^2), $Y=C_{11}+C_{12}-2C_{12}^2/C_{11}=2G(1+\nu)/(1-\nu)$, G is the shear modulus (dyn/cm^2), C_{11} and C_{12} are the elastic stiffness constants (dyn/cm^2), ν is the Poisson ratio (unitless) and h_c is the critical layer thickness at which it becomes energetically favorable to introduce misfit dislocations. The expression above accounts for the possibility of pseudomorphic growth where below the critical

layer thickness, the equilibrium strain is equal to the lattice mismatch. The growth of mismatched epilayers which are beyond the critical layer thickness requires the formation of a misfit dislocation network to relax some portion of the lattice mismatch. In uniform layers, misfit dislocations are introduced at the mismatched interfaces and they can be modeled using the Dirac delta function. Figure 6.1 shows the linear misfit dislocation density as a function of the strain-thickness product for a single InGaAs layer on a GaAs (001) substrate with lattice mismatch as a parameter. Above the CLT, the equilibrium strain is inversely proportional to the epitaxial layer thickness and also exhibits a weak logarithmic dependence as shown in Figure 6.1. In addition, for the same strain-thickness product, an increase in the compositional mismatch between the epitaxial layer and substrate will require the introduction of more misfit dislocations.

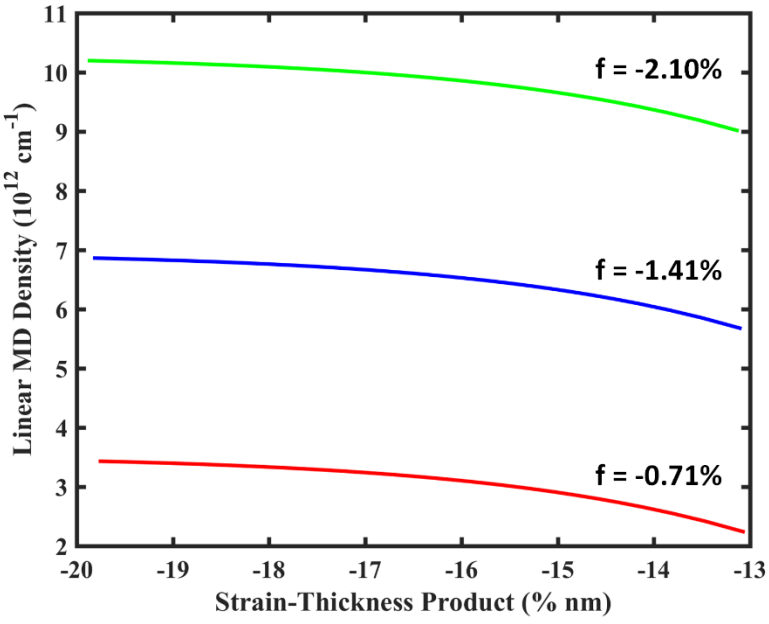

Figure 6.1. Linear misfit dislocation density as a function of the strain-thickness products with lattice mismatch as a parameter for a single and compositionally-uniform InGaAs layer on GaAs (001). The thickness of the epitaxial layer was varied from 50 to 1000 nm in steps of 10 nm.

6.2. Linearly-Graded Layers Metamorphic Layers

The equilibrium configuration in linearly-graded epitaxial layers has been explored in great detail by Tersoff [44], Fitzgerald et al. [72], Dunstan [81] and Romanato et al. [82]. However, these models assume that graded material can relax completely in the presence of misfit dislocations. This is a simplifying assumption which does not strictly hold in either equilibrium or kinetically-limited relaxation. More specifically, there are two key assumptions embedded in these models; first, there is zero strain in the dislocated region and second, they neglect the thickness dependence of the line energies for dislocations. Because of these simplifying assumptions, the interfacial misfit dislocation-free zone is not seen and there is zero strain in the dislocated region. The generalized equilibrium theory and the equivalent electrical circuit models which we have developed do not make such simplifying assumptions, and therefore the residual strain characteristics is slightly different from the previously developed models. In the following sections related to linearly-graded epitaxial layers we will give a treatment on the distribution of strain and misfit dislocations.

6.2.1. Initial Misfit Dislocations in a Linearly-Graded Heteroepitaxial Layer

We show that for a mismatched heteroepitaxial layer with linear compositional grading the first misfit dislocations will be introduced at a finite distance z_c from the substrate interface. This is of practical as well as fundamental importance: it alters the value of the critical layer thickness for lattice relaxation and it moves the misfit dislocations away from the interface, where contaminants and defects may cause dislocation pinning or mobility reduction. We have calculated the position of the initial misfit dislocations z_c for linearly-graded $Si_{1-x}Ge_x$ / Si (001) heteroepitaxial layers with

lattice mismatch given by $f = C_f z$, where C_f is the grading coefficient and z is the distance from the interface. The distance of the first misfit dislocations from the interface z_c decreases with increasing grading coefficient, but can exceed 40 nm in layers with shallow grading ($|C_f| < 12$ cm^{-1}). For the range of grading coefficients investigated, z_c varies from 6% to 11% of the critical layer thickness. Based on the model presented here it is possible to choose the grading coefficient to achieve the desired separation of the misfit dislocations from the substrate interface.

The realization of heterojunction devices such as modulation doped field effect transistors and light-emitting diodes requires heteroepitaxial growth of lattice mismatched materials. Typically, these device structures are implemented on metamorphic (partly relaxed) graded composition buffer layers [44,72,83,84,85,86,87,88,89,90,91,92,93,94,95,96,97,98]. However, the design of these structures requires an understanding of their misfit dislocations and strain relaxation, which can greatly influence device performance.

In previous work we demonstrated that, for exponentially-graded layers of $In_xGa_{1-x}As$ on GaAs (001) substrates, the first misfit dislocations are introduced at a distance z_c from the substrate interface [99]. This is of practical as well as fundamental importance, for this behavior influences the critical layer thickness for the onset of lattice relaxation. Moreover, it is advantageous for misfit dislocations to be located away from the interface, where defects or chemical contamination on the substrate surface can lead to the pinning or reduced mobility of misfit dislocations, which can in turn result in higher threading dislocation densities in devices realized on the graded structure.

Here we calculate the position (distance from the interface z_c) of the first misfit dislocations introduced in a linearly-graded layer of $Si_{1-x}Ge_x$ / Si (001). The approach presented here may be

extended to other material systems or grading profiles. An important conclusion of this work is that the grading profile may be tailored to achieve the desired separation of the misfit dislocations from the substrate interface.

In this work, we considered a linearly-graded layer with the zinc blende or diamond structure and grown on a substrate with (001) crystal orientation. For such a structure, suppose the first two misfit dislocations are introduced at a distance z_c from the interface and along the $[1\,1\,0]$ and $\left[1\,\bar{1}\,0\right]$ directions as illustrated in Figure 6.2. Although we have assumed straight misfit dislocations, the results are equally applicable to bent-over substrate dislocations or half loops gliding from the surface; this is because, as will be shown below, the length of the misfit dislocation cancels out in the analysis. Therefore, there will only be second-order differences between the straight misfit dislocations and the other configurations due to the modification of the dislocation line energy by the interaction of the strain fields associated with the misfit and threading segments. These second-order interactions will be ignored in the present analysis.

The areal misfit dislocation density in either direction can be modeled using a Dirac delta function:

$$\rho(z)=\frac{1}{L}\delta(z-z_C), \qquad \textbf{(6.2)}$$

where L is the length of a side of the (square) substrate.

In general, the in-plane strain in a compositionally-graded layer with a misfit dislocation density $\rho(z)$ is given by

$$\varepsilon_{\parallel}(z)= f(z)+b'\int_0^z \rho(z)dz \qquad \textbf{(6.3)}$$

where $f(z)$ is the lattice mismatch at the distance z from the interface, $f(z) \equiv (a_S - a(z))/a(z)$, where a_S is the relaxed lattice constant of the substrate and $a(z)$ is the relaxed lattice constant of the graded semiconductor at the point z and b' is the misfit relieving component of the Burgers vector parallel to the interface, $b' = \pm b \sin\alpha \sin\phi$, where b is the length of the Burgers vector, α is the angle between the Burgers vector and the line vector, and ϕ is the angle between the glide plane and interface. The sign of b' is such that strain is relieved (opposite to the sign of the lattice mismatch).

In the structure containing only the two orthogonal misfit dislocations the in-plane strain found by integrating Equation 6.3 is

$$\varepsilon_{\parallel}(y) \approx \begin{cases} f(z); & z \le z_{C,} \\ f(z) + \dfrac{b'}{L}; & z > z_{C.} \end{cases}, \qquad \textbf{(6.4)}$$

The strain energy per unit area is

$$E_{\varepsilon} = \int_0^h Y\varepsilon_{\parallel}^{\,2} dz = \int_0^{z_C} Yf^{\,2}(z)dz + \int_{z_C}^h Y\left[f(z) + \frac{b'}{L} \right]^2 dz, \qquad \textbf{(6.5)}$$

where h is the thickness of the layer, Y is the biaxial modulus (dyn/cm^2), $Y = C_{11} + C_{12} - 2C_{12}^2/C_{11} = 2G(1+\nu)/(1-\nu)$, C_{11} and C_{12} are the elastic stiffness constants (dyn/cm^2). The line energy of dislocations per unit area, based on the first two orthogonal misfit dislocations, is

$$E_d = \frac{2}{L}\int_0^h F_d(z)\delta(z - z_C)dz \approx \frac{2F_d(z_C)}{L}, \qquad \textbf{(6.6)}$$

where

$$F_d(z)=\frac{Gb^2\left[1-\nu\cos^2\alpha\right]}{4\pi(1-\nu)}\left[\ln\left(\frac{h-z}{b}\right)+1\right] \qquad \textbf{(6.7)}$$

is the line energy for a straight misfit dislocation located a distance z from the interface, where G is the shear modulus, $G=(C_{11}-C_{12})/2$, and ν is the Poisson ratio, $\nu=C_{12}/(C_{11}+C_{12})$ for the (001) orientation. G, b, and ν are assumed to constant and this is the primary approximation made in these calculations. Therefore

$$E_d=\frac{Gb^2\left[1-\nu\cos^2\alpha\right]}{2L\pi(1-\nu)}\left[\ln\left(\frac{h-z_C}{b}\right)+1\right]. \qquad \textbf{(6.8)}$$

For the case of a linearly-graded layer, the lattice mismatch is given by

$$f(z)=C_f z, \qquad \textbf{(6.9)}$$

where C_f is the grading constant. For this situation, the sum of the strain energy and dislocation line energy is

$$(E_\varepsilon+E_d)=\int_0^{z_C} YC_f^2z^2dz+\int_{y_C}^{h} Y\left[C_f z+\frac{b'}{L}\right]^2dz+\frac{Gb^2\left[1-\nu\cos^2\alpha\right]}{2L\pi(1-\nu)}\left[\ln\left(\frac{h-z_C}{b}\right)+1\right]. \qquad \textbf{(6.10)}$$

To find the equilibrium distance from the interface for the first misfit dislocations we minimize the sum of the strain energy and dislocation line energy with respect to z_C:

$$\begin{aligned}0&=\frac{\partial(E_\varepsilon+E_d)}{\partial z_C}\\ &=\frac{\partial}{\partial z_C}\left\{\int_0^{z_C} YC_f^2z^2dz+\int_{z_C}^{h} Y\left[C_f z+\frac{b'}{L}\right]^2dz+\frac{Gb^2\left[1-\nu\cos^2\alpha\right]}{2\pi L(1-\nu)}\left[\ln\left(\frac{h-z_C}{b}\right)+1\right]\right\} \qquad \textbf{(6.11)}\\ &=\frac{2Yb'C_f z_C}{L}-Y\left(\frac{b'}{L}\right)^2-\frac{Gb^2\left[1-\nu\cos^2\alpha\right]}{2\pi L(h-z_C)(1+\nu)}\end{aligned}$$

Now with $G=Y(1-\nu)/[2(1+\nu)]$ and $b'=-\text{sign}\,(C_f)b\sin\alpha\sin\phi$, we obtain

$$0 = -2z_C + \frac{|b'|}{|C_f|L} + \frac{b(1-\nu)\left[1-\nu\cos^2\alpha\right]}{4\pi|C_f|(h-z_C)(1+\nu)^2\sin\alpha\sin\phi}. \quad \textbf{(6.12)}$$

For the practical case of $L >> h$ this can be simplified to

$$0 = -2z_C + \frac{b(1-\nu)\left[1-\nu\cos^2\alpha\right]}{4\pi|C_f|(h-z_C)(1+\nu)^2\sin\alpha\sin\phi}. \quad \textbf{(6.13)}$$

or

$$z_C^2 - z_C h + \frac{b(1-\nu)\left[1-\nu\cos^2\alpha\right]}{8\pi|C_f|(1+\nu)^2\sin\alpha\sin\phi} = 0. \quad \textbf{(6.14)}$$

Solving this quadratic, and recognizing that the first misfit dislocations appear at $h = h_C$, the critical layer thickness, we obtain

$$z_C = \frac{h_C}{2} - \sqrt{\frac{h_C^2}{4} - \frac{b(1-\nu)\left[1-\nu\cos^2\alpha\right]}{4\pi|C_f|(1+\nu)^2\sin\alpha\sin\phi}}. \quad \textbf{(6.15)}$$

Table 6.1. Material properties used for Si, Ge, and the alloy $Si_{1-x}Ge_x$.

parameter	Si	$Si_{1-x}Ge_x$	Ge
a (nm)	0.543108	0.543108 + x(0.022652)	0.56576
b (nm)	0.384	0.384 + x(0.016)	0.400
C_{11} (GPa)	160.1	160.1 – x(36.1)	124
C_{12} (GPa)	57.8	57.8 – x(16.5)	41.3
α	60°	60°	60°
λ	60°	60°	60°

The critical layer thickness for a linearly-graded layer has been calculated by Fitzgerald et al. [7] using an approach based on energy as

$$h_C^2 = \frac{3b(1-\nu\cos^2\alpha)\left[\ln(h_C/b)+1\right]}{8\pi|C_f|(1+\nu)\cos\lambda} \quad \textbf{(6.16)}$$

and this can be used to solve Equation 6.16. In the model presented above the areal density of misfit dislocations was approximated using a Dirac delta function. However, the strain fields of real dislocations decay with the reciprocal of distance from the core. An accurate calculation of the strain energy in the film should therefore consider a spreading out of the misfit dislocation density over a thickness of up to several times the Burgers vector. To investigate this, we recalculated the position of the first misfit dislocations assuming that the areal misfit dislocation density is a Pi function with width W:

$$\rho(z) = \frac{1}{WL}\Pi\left(\frac{z - z_C}{W}\right); \tag{6.17}$$

that is,

$$\rho(z) = \begin{cases} 0, & z \le (z_C - W/2); \\ \dfrac{1}{WL}, & (z_C - W/2) < z < (z_C + W/2); \text{ and} \\ 0, & z \ge (z_C + W/2). \end{cases} \tag{6.18}$$

Based on the Pi approximation for the misfit dislocation density, the in-plane strain is

$$\varepsilon_{\parallel}(z) = \begin{cases} C_f z, & z \le (z_C - W/2); \\ C_f z + \left(\dfrac{b'}{WL}\right)(z - z_C + W/2), & (z_C - W/2) < z < (z_C + W/2); \text{ and} \\ C_f z + \dfrac{b'}{L}, & z \ge (z_C + W/2). \end{cases} \tag{6.19}$$

The strain energy per unit area is

$$\begin{aligned} E_\varepsilon = {} & Y\int_0^{z_C - W/2} C_f^2 z^2 dz + Y\int_{z_C - W/2}^{z_C + W/2}\left[C_f z + \left(\frac{b'}{WL}\right)(z - z_C + W/2)\right]^2 dz \\ & + Y\int_{z_C + W/2}^{h}\left[C_f z + \frac{b'}{L}\right]^2 dz \end{aligned}. \tag{6.20}$$

The misfit dislocation line energy per unit area is

$$E_d = \frac{2}{WL}\int_{z_C-W/2}^{z_C+W/2} \frac{Gb^2\left[1-\nu\cos^2\alpha\right]}{4\pi(1-\nu)}\left[\ln\left(\frac{h-z}{b}\right)+1\right]dz\,. \qquad \textbf{(6.21)}$$

To find the value of z_C corresponding to minimum energy, we can set $\partial(E_\varepsilon + E_d)/\partial z_C = 0$ as before. Using the fundamental theorem of calculus to differentiate and solving with $L >> h$ we obtain

$$z_C = \frac{b\left[1-\nu\cos^2\alpha\right]}{8\pi W\left|C_f\right|(1+\nu)\sin\alpha\cos\lambda}\ln\left(\frac{h_C - z_C + W/2}{h_C - z_C - W/2}\right). \qquad \textbf{(6.22)}$$

This expression can be used in conjunction with the Fitzgerald model for the critical layer thickness (Equation 6.16) to determine the position of the first misfit dislocations. As will be shown, the choice of W has only a weak effect on the predicted value of z_C.

The value of z_C and the critical layer thickness may also be determined by numerical energy minimization calculations. The equilibrium configuration may be determined numerically by minimizing $E_d + E_\varepsilon$, and the critical layer thickness is the minimum thickness at which it becomes energetically favorable to introduce a misfit dislocation anywhere in the structure. It should be noted that Equations 6.18 - 6.29 are generally applicable to cubic semiconductors and can be solved for any arbitrary compositional profile using the numerical approach developed in reference.

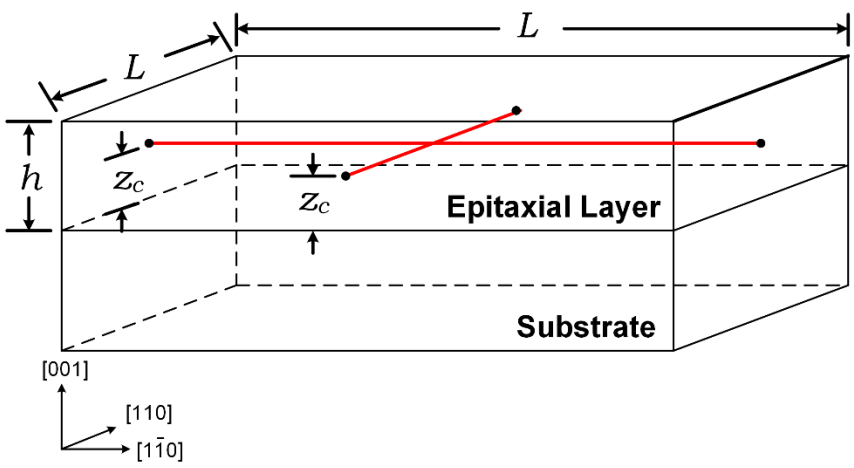

Figure 6.2. Two straight misfit dislocations located at a distance z_C from the interface in a lattice mismatched layer on a (001) diamond or zinc blende substrate. The dislocations are parallel to the $[1\,1\,0]$ and $[1\,\bar{1}\,0]$ crystal directions.

6.2.2. Determination of Interfacial MDFZ: Results and Discussion:

The separation of the first misfit dislocations from the interface z_C was calculated for linearly-graded layers of $Si_{1-x}Ge_x$ on Si (001) substrates using the material parameters given in Table 6.1. Figure 6.3 shows z_C as a function of the grading coefficient C_f. For $Si_{1-x}Ge_x$ / Si (001), $f = -0.04x$ and $C_f = df/dy = -0.04dx/dz$. For example, $|C_f| = 100cm^{-1}$ corresponds to compositional grading of 25% / μm. Here the solid curve was calculated using the Dirac delta approximation for the dislocation density (Equation 6.15) in conjunction with the Fitzgerald et al. expression for the critical layer thickness, (Equation 6.16). The dashed curve was calculated using the Pi approximation (Equation 6.22). The filled squares were determined using numerical energy minimization calculations based on Equations 6.24 – 6.26 and the numerical algorithm described in [19]. The Pi approximation provides an accurate estimate of z_c which is only weakly affected by the choice of W, the width of the Pi function. For the calculation of the results shown in Figure

6.3 it was assumed that $W = 2b$, but changing this value by a factor of two alters the predicted value of z_c by less than $\pm 1\%$. The discrepancy between the energy minimization results and the Pi approximation (~ -20%) comes about because the Fitzgerald model overestimates the critical layer thickness, as will be considered below. Inherent in the Dirac delta approximation is an overestimate of z_c by ~10%. This offsets some of the error associated with the use of the Fitzgerald critical layer thickness and renders the predicted values in between those found using energy minimization and the values obtained with the Pi approximation.

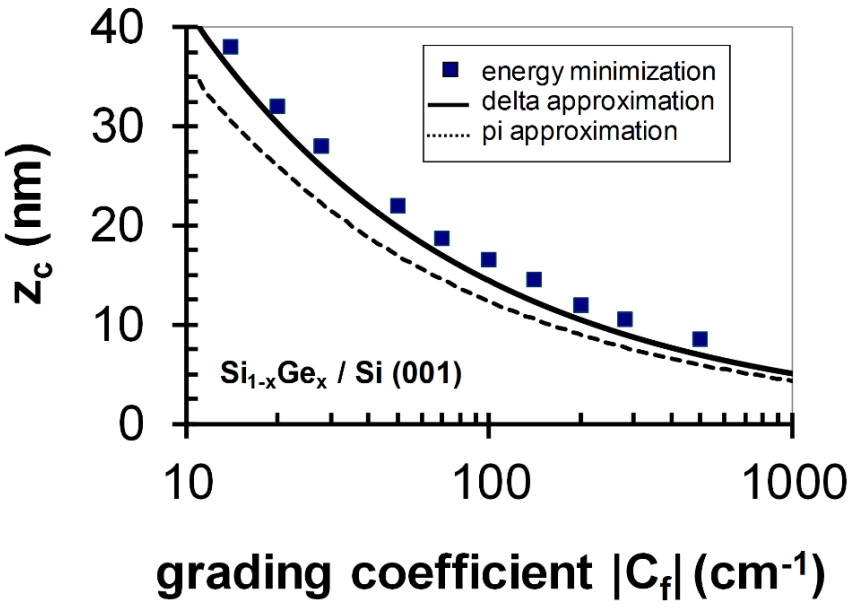

Figure 6.3. The separation of the first misfit dislocations from the interface, z_C, as a function of the grading coefficient C_f for $Si_{1-x}Ge_x$ / Si (001) with linear compositional grading.

Figure 6.4 shows the critical layer thickness for the onset of lattice relaxation as a function of the grading coefficient, for $Si_{1-x}Ge_x$ / Si (001) with linear compositional grading. The solid curve was calculated using the Fitzgerald et al. expression, Equation 6.16, while the solid squares

were determined by numerical energy minimization calculations. Here it can be seen that Equation 6.16 overestimates the critical layer thickness compared to the energy minimization calculations by ~20%.

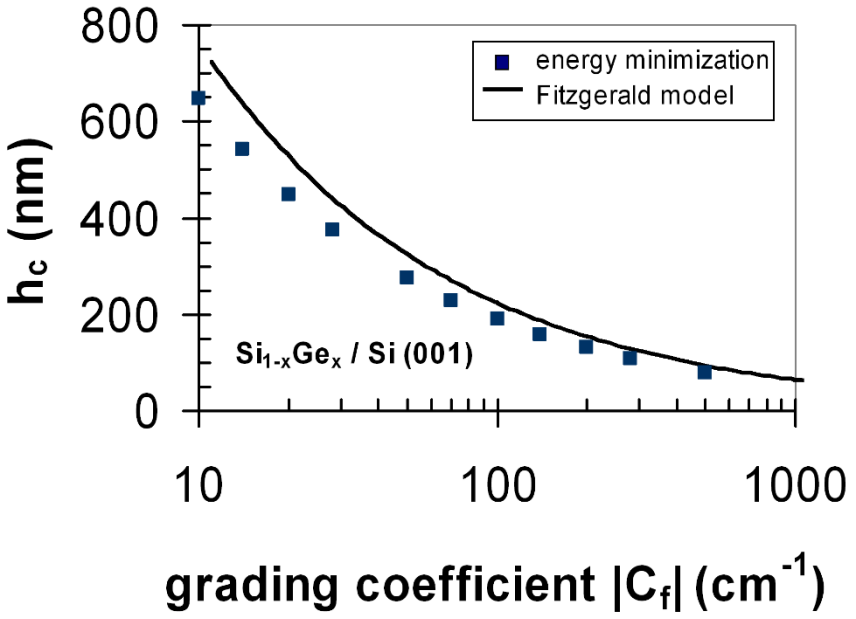

Figure 6.4. The critical layer thickness, h_c, as a function of the grading coefficient C_f for $Si_{1-x}Ge_x$ / Si (001) with linear compositional grading.

Using numerical energy minimization calculations, we can calculate the equilibrium misfit dislocation density profiles in graded layers with different grading coefficients or thicknesses. This is illustrated in Figure 6.5, which shows the equilibrium misfit dislocation density profiles calculated using Equations 6.24 – 6.26 and the method of [19] for $Si_{1-x}Ge_x$ / Si (001) layers with $C_f = 100 cm^{-1}$ and thicknesses of 190 nm, 192 nm, and 194 nm. Here the 190 nm thick layer is just over the critical layer thickness and has misfit dislocations concentrated near $z = z_C = 16nm$. As the layer is made thicker, more misfit dislocations are introduced to relax the strain energy, but

most of these new misfit dislocations are introduced farther away from the interface (that is, at $z > z_C$). Even in much thicker layers, there remains an interfacial region free from misfit dislocations, and this region has a thickness of approximately z_c.

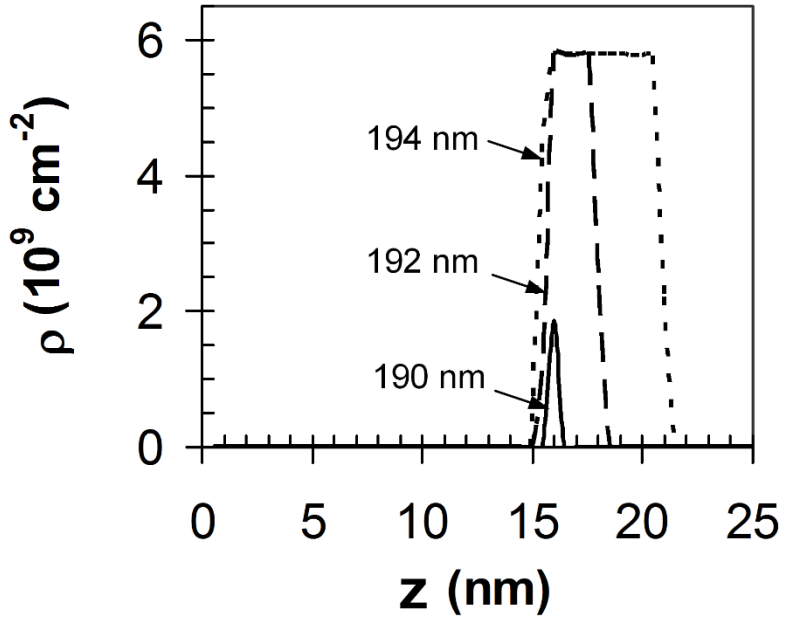

Figure 6.5. Equilibrium misfit dislocation density in $Si_{1-x}Ge_x$ / Si (001) layers with linear compositional grading (grading coefficient $C_f = 100 cm^{-1}$) and thicknesses of 190 nm, 192 nm, and 194 nm. The 190 nm thick layer is just over the critical layer thickness.

These results indicate that it is possible to tailor the grading in the layer to achieve a desired separation between the interface and the misfit dislocations. The relevant design equation, obtained by rearranging Equation 6.12, is

$$\left|C_f\right| = \frac{b(1-\nu)\left[1-\nu\cos^2\alpha\right]}{8\pi\, y_C (h-z_C)(1+\nu)^2 \sin\alpha\cos\lambda}\,. \qquad \textbf{(6.23)}$$

Moreover, this result may be generalized to graded layers with other (nonlinear) grading profiles.

We have calculated the position of the initial misfit dislocations z_c for linearly-graded $Si_{1-x}Ge_x$ / Si (001) heteroepitaxial layers with lattice mismatch given by $f = C_f z$, where C_f is the grading coefficient and z is the distance from the interface. The distance of the first misfit dislocations from the interface z_c decreases with increasing grading coefficient, but can exceed 40 nm in layers with shallow grading (C_f < 12 cm^{-1}). For the range of grading coefficients investigated, z_c varies from 6% to 11% of the critical layer thickness. It is possible to choose the grading coefficient to achieve the desired separation of the misfit dislocations from the substrate interface, and we have developed a design equation for this purpose.

6.3. Equilibrium Lattice Relaxation and Misfit Dislocations in Step-Graded InGaAs/GaAs (001) and InAlAs/GaAs (001) MBLs

The inclusion of metamorphic buffer layers (MBL) in the design of lattice-mismatched semiconductor heterostructures is important in enhancing reliability and performance of optoelectronic and electronic devices through proper control of threading dislocations; threading dislocation can be reduced by allowing the distribution of the misfit dislocations throughout the MBL, rather than concentrating them at the interface where substrate defects and tangling can pin dislocations or otherwise reduce their mobility. Compositionally graded layers have been particularly used for this purpose and in this work, we considered heterostructures involving a step-graded $In_xGa_{1-x}As$ or $In_xAl_{1-x}As$ epitaxial layer on a GaAs (001) substrate. For each structure type, we present minimum energy calculations including (i) the surface and (ii) average in-plane strain and (iii) the misfit dislocation density profile with various grading coefficients (thickness

and indium composition variation). In both types of structures the average in-plane strain and misfit dislocation density profile scale with the average grading coefficient, but $In_xAl_{1-x}As$ structures with a greater average elastic stiffness constants exhibit slightly higher average compressive in-plane strain (absolute valued) which is associated with higher misfit dislocation densities. However, the rate of change in the normalized relaxation percentage per unit thickness of each step with respect to the lattice mismatch of the step is lower in the $In_xAl_{1-x}As$ material system. The difference of the in-plane strain is small (< 3%), however, so that these material systems are virtually interchangeable in terms of their mechanical behavior (< 5.1% change in elastic constants).

Metamorphic or partly-relaxed semiconductor devices are of great interest because their use removes the compositional constraints associated with pseudomorphic design, enabling the use of lattice-mismatched materials with a wide range of desirable properties such as energy gap, low-field mobility, and carrier saturation velocity. The realization of semiconductor heterostructures on lattice-mismatched wafers, such as strain-engineered $In_xGa_{1-x}As$ and $In_xAl_{1-x}As$ on GaAs substrate, has become critical for the fabrication of electronic and optical devices. These applications require growth of metamorphic (partly relaxed) structures with compositionally-graded buffer layers to accommodate the strain associated with the mismatch between the substrate and epilayer. The graded layer allows for the introduction and distribution of misfit dislocations (MDs) away from the substrate interface which results in the reduction of the dislocation-dislocation interactions with substrate associated defects; such interactions may give rise to dislocation pinning and therefore render threading dislocations immobile. Therefore, the enhancement of dislocation mobility from the use of a compositionally graded layer, allows

for devices with reduced threading dislocation densities. In addition, the graded layer has a greater built-in residual strain near the surface which can reduce the density of threading defects by enhancing the glide velocities of dislocations, yielding the longest possible misfit segment parallel to the interface and therefore the least number of threading dislocations emanating from misfit dislocation ends. Although metamorphic growth has been exploited in a variety of devices [44,72,100,101,102,103,104,105,106,107,108], most designs employ a linearly-graded [109,110] or step-graded buffer layer [107,111,112]. Unlike linearly-graded buffer, there has been relatively little modeling work on step graded layers and therefore its relaxation behavior is not well understood but some important aspects regarding their dislocation and strain distributions have been shown experimentally. It is therefore worthwhile to compare the two material systems ($In_xGa_{1-x}As$ and $In_xAl_{1-x}As$) utilizing a step-graded scheme in terms of their equilibrium relaxation behavior. Equilibrium modeling in turn serves as the starting point for the understanding of kinetically-limited relaxation and its results may be helpful in the optimized design of compositionally graded heterostructures.

In this work, we considered $In_xGa_{1-x}As$ and $In_xAl_{1-x}As$ step-graded buffers grown on a GaAs substrate with (001) crystal orientation. Step-graded layers contain a set of n uniform layers in which there are equal compositional changes from one layer to the next ("linear step grading"). For the structures studied here, the grading profile is composed of ten uniform buffer layers where the indium composition in the buffer layer is varied with a uniform step size of $0.1x_h$ to a final surface composition x_h corresponding to a lattice mismatch of f_h. We have investigated

structures with thicknesses of 250, 500 and 1000 nm. The material constants used in this work are summarized in Table 6.2.

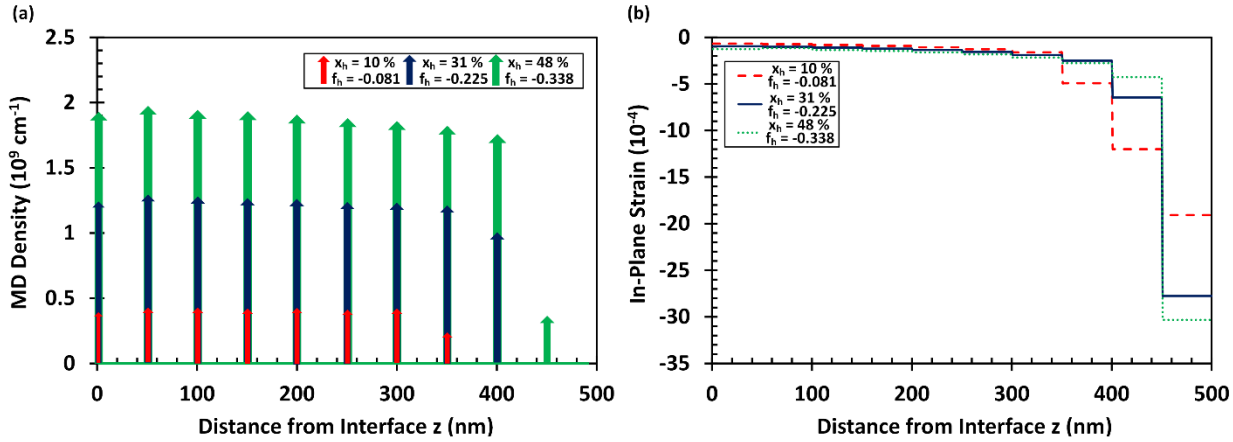

Figure 6.6. (a) Misfit dislocation and (b) in-plane strain as a function of the distance from the interface with various ending compositions for step-graded $In_xGa_{1-x}As$/GaAs and $In_xAl_{1-x}As$/GaAs heterostructures.

Table 6.2. Material Properties for InAs, AlAs, GaAs and the alloys $In_xGa_{1-x}As$ and $In_xAl_{1-x}As$.

	Parameter		
Material	a (nm)	C11 (GPa)	C12 (GPa)
InAs	0.50584	83.3	45.3
AlAs	0.5660	125	53.4
GaAs	0.56534	118.4	53.7
$In_xGa_{1-x}As$	0.56534 + x(0.0405)	118.4 – x(35.1)	53.7 – x(8.4)
$In_xAl_{1-x}As$	0.5660 + x(0.06016)	125 – x(41.7)	53.4 – x(8.1)

6.3.1. Strain and Misfit Dislocations in Step-Graded MBLs

The $In_xGa_{1-x}As$ and $In_xAl_{1-x}As$ structures considered in this work have an ending lattice mismatch ranging from f_h =0.8% to 3.4% and the two material systems were compared using identical indium composition profiles. Figure 6.6a shows the equilibrium misfit dislocation density profiles for 500 nm thick $In_xGa_{1-x}As$ layers on a GaAs (001) substrate with various ending indium

compositions. In uniform layers, misfit dislocations are introduced at the mismatched interfaces and they can be modeled using the linear misfit dislocation density. The structures modeled in Figure 6.6a exhibit at most 10 misfit dislocation regions (Dirac delta functions) which are equivalent with the number of mismatched interfaces. At low mismatch, the absence of peaks indicates that for layers near the surface, the strain energy is sufficient in relaxing the mismatch strain. However, at higher misfit strain, there exists a monotonic increase in the peak misfit dislocation density with increasing ending composition (mismatch) therefore necessitating the introduction of more misfit segments to relax the excess mismatch strain. In step-graded layers the interfacial and surface misfit dislocation free zones are limited by the growth step-size which in this case is one tenth of the buffer layer thickness. Figure 6.6b shows the equilibrium in-plane strain distribution for 500 nm thick $In_xGa_{1-x}As$ on GaAs (001) with various ending compositions. The in-plane strain profile comprises a series of step functions with discontinuities at the mismatched interfaces. Apart from the dislocated interfaces, the equilibrium strain in each sublayer is constant as expected. Correlating the results of Figure 6.6a with b, it can be seen that the misfit dislocations relieve most of the excess strain associated with the compositional mismatch in sublayers near the interface whereas the absence of dislocations near the surface results in higher residual elastic strain; in other words for layers near the substrate interface, the in-plane strain is relatively small and does not change significantly from one layer to the next whereas near the surface, the absence of peaks signify the major role of the strain energy in relaxing the local strain associated with the compositional mismatch. Furthermore, it can be seen from the results of Figure 6.6b, that the lowest mismatch shows the highest in-plane strain in the 8^{th} and 9^{th} steps whereas in the final step the relation is reversed. The following is expected on the basis that at low mismatch,

both the strain and misfit dislocation energy play a major role in relaxing the misfit strain, whereas at higher mismatch, the misfit strain is mainly accommodated by the introduction of misfit dislocation. This phenomenon is also seen results of Figure 6.6a where a low peak intensity or the absence of a MD peak indicates a noticeable contribution of the strain energy in relaxing the misfit strain (Figure 6.6b). In the last step, the relation is reversed because it is energetically unfavorable for misfit dislocation to be introduced at the surface of the epilayer and therefore the misfit strain at the last step is accommodated by the strain energy. Experimental studies have also shown the absence of misfit dislocations [113,114] above the top step interface; in addition, the top step exhibits the maximum residual strain in the step-graded layer and the following holds with the deposition of each successive step [113].

Figure 6.7a compares the average in plane strain for $In_xGa_{1-x}As$ and $In_xAl_{1-x}As$ layers as a function of the average grading coefficient C_f where $C_f = f_h / h$. The results of Figure 6.7a indicate a monotonic increase in the average in-plane strain in structures with a higher grading coefficient and smaller layer thickness. Moreover, structures with $In_xAl_{1-x}As$ as the epi-material exhibit greater average compressive strains (absolute valued) than $In_xGa_{1-x}As$/GaAs (001). However, the curve separation between the two material systems becomes more prominent at higher grading coefficient and in structures with a smaller layer thickness. It is interesting to note that the strain-thickness product $\varepsilon_{\|}h$ for both material systems is approximately ~ 2 nm. Although, there is a slight dependence of the strain-thickness product $\varepsilon_{\|}h$ on the elastic stiffness constants, the associated difference is within ± 0.1 nm. Even though the elastic stiffness constants are

composition dependent, the percent difference ΔC_{11} and ΔC_{12} with respect to the average value of both materials is given by

$$\left|\Delta C_{11}\right| = \left| \frac{C_{11,InAlAs} - C_{11,InGaAs}}{\frac{1}{2}\left(C_{11,InAlAs} + C_{11,InGaAs}\right)} \right| \cdot 100\% = \left\| \left[0.17 - \frac{0.37}{3.17 - x} \right] \right\| \cdot 100\%. \qquad \textbf{(6.24)}$$

and

$$\left|\Delta C_{12}\right| = \left| \frac{C_{12,InAlAs} - C_{12,InGaAs}}{\frac{1}{2}\left(C_{12,InAlAs} + C_{12,InGaAs}\right)} \right| \cdot 100\% = \left\| \left[\frac{0.2}{6.5 - x} - 0.04 \right] \right\| \cdot 100\%. \qquad \textbf{(6.25)}$$

where x is the indium mole fraction. For the structures studied in this work, the percent difference in the material constants ΔC_{11} and ΔC_{12} ranges from 4.3% to 5.1% and 0.8% to 0.9% respectively. The associated variation in the average in plane strain due to the difference in the material constants ranges approximately from $4.3 \cdot 10^{-6}$ to $2.7 \cdot 10^{-5}$ corresponding to a percent difference of the in-plane in the range of 1.8% to 3%. Figure 6.7b compares the surface in-plane strain for $In_xGa_{1-x}As$ and $In_xAl_{1-x}As$ layers as a function of the average grading coefficient C_f. The surface in-plane strain exhibits a two-regime behavior; in regime one, the surface strain is monotonically increasing whereas there exists a combination of ending indium composition and layer thickness (critical grading coefficient) where the surface strain exhibits saturation. This saturated value corresponds to the thickness of the individual steps and is associated with force balance on grown-in dislocations. The presence of dislocation peaks at the last mismatched interface indicates that the introduction of a misfit dislocation affords smaller energy budgets than relaxation via the strain energy. Below the critical grading coefficient, structures with $In_xGa_{1-x}As$

as the epilayer material contain a slightly higher compressive surface in-plane strain (absolute valued).

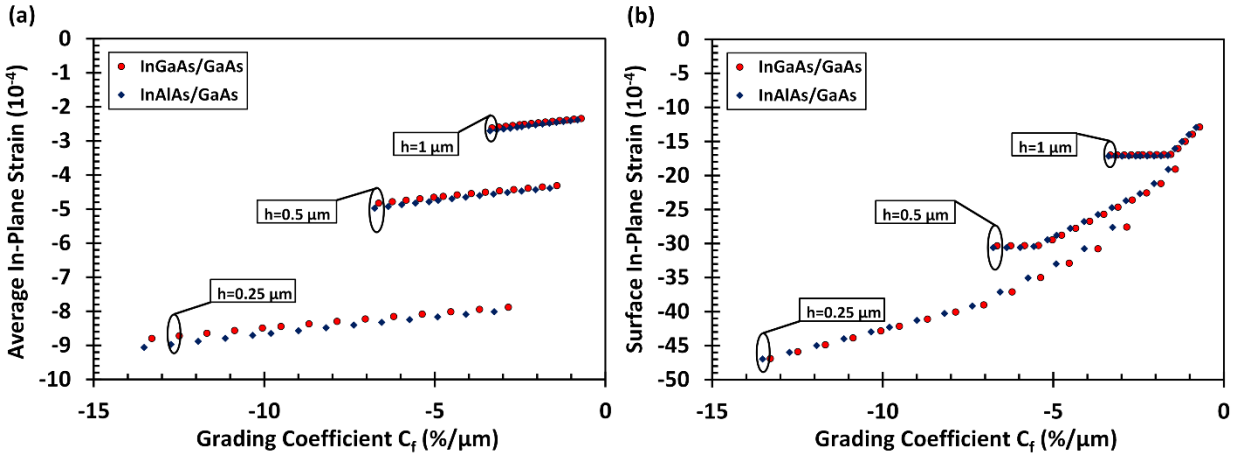

Figure 6.7. (a) Average and (b) surface in-plane strain as a function of the grading coefficient for step-graded $In_xGa_{1-x}As/GaAs$ and $In_xAl_{1-x}As/GaAs$ heterostructures.

Experiments with $In_xAl_{1-x}As$ on GaAs substrates showed that step- and linearly-graded layers exhibited similar values of surface in-plane strain [115] which allows the analysis above to indicate similar properties between the step- and linearly-grading schemes. Furthermore, experimental investigation of step-graded layers involving a large number of steps has showed that the relaxation behavior to approach that of linearly-graded buffers [116]; however, at low step numbers these properties may be somewhat unique to step-graded layers. If we consider the force-balance model on a grown-in dislocation, then, the average residual strain in each step would be the same as that in a uniform layer with the same total thickness. Lynch et al. applied in-situ multibeam optical stress sensor to study the relaxation of $In_xAl_{1-x}As$ on GaAs (001) substrate and showed that the deposition of each successive step gives rise to the relaxation of the underlying layers [117]; moreover, in order to maintain the $\varepsilon_{\parallel} h = \text{constant}$ relationship, the residual strain

must be concentrated in the top layer of the step-graded buffer. The results of Figure 6.7b show that the top of the step-graded buffer is near fully relaxed in relatively thick layers. For step-graded layers with a thickness of $h = 250nm$ and an ending mismatch varying from f_h =0.8% to 3.4%, the percent relaxation in the top step ranged from 60% to 85% respectively. In thicker structures the percent relaxation in the top step is higher; for structures with a thickness of $h = 500nm$, the percent relaxation in the top step ranged from 73% to 91% respectively whereas in structures with a thickness of $h = 1000nm$, the percent relaxation in the top step ranges from 82% to 95%. This behavior has also been shown experimentally in $In_xGa_{1-x}As$ and $In_xAl_{1-x}As$ step-graded buffer layers, however these structures involve the use of a thick device layer on top of the step-graded buffer. Jiang et al. [118] used high resolution x-ray diffraction to study the relaxation of a multilayered structure composed of a 1 μm uniform layer of $In_{0.75}Al_{0.25}As$ layer grown on top of a GaAs substrate with an intermediate 900 nm thick step-graded (9 steps) layer of $In_xAl_{1-x}As$ with an indium composition ranging from 5% to 85%. Analysis of the x-ray rocking curves revealed that the device layer was near fully relaxed (98%) as a consequence of the overshoot design. In contrast, Shang et al. [119] showed 98% relaxation of the device layer in multilayered $In_xAl_{1-x}As$ structures without using overshoot; however, the use of a thick step-graded buffer layer in this work resulted in a high degree of lattice relaxation in the device layer which removes the need for overshoot. Furthermore, Chen et al. [120] demonstrated 96% relaxation of the device layer in $In_xGa_{1-x}As$ multilayered structures.

The results of Figure 6.8 indicate that there is an approximately linear and monotonic increase in the average equilibrium misfit dislocation density as a function of the average grading

coefficient. In addition, an increase in the epilayer thickness yields higher dislocation densities. This behavior is expected on the basis that larger misfit strain requires the introduction of more misfit dislocation to relax the excess stress; moreover, for both material systems, the misfit dislocation introduction occurs at an approximate rate of $5.4 \cdot 10^{8} (\% \cdot cm^{-1})$. Small differences in these two material systems are introduced by the difference in the elastic stiffness constants. Abrahams et al. [121] considered a simple model for step-graded layers and argued that the threading dislocation density would reach a steady-state value which depends on the average grading coefficient. Although, threading dislocations are non-equilibrium defects, it can be argued that since each MD is associated with at most two threading dislocations and if we assume that the average length of misfit segments is fixed, then the steady threading dislocation density (and therefore the misfit dislocation density) at each step is proportional to the grading coefficient.

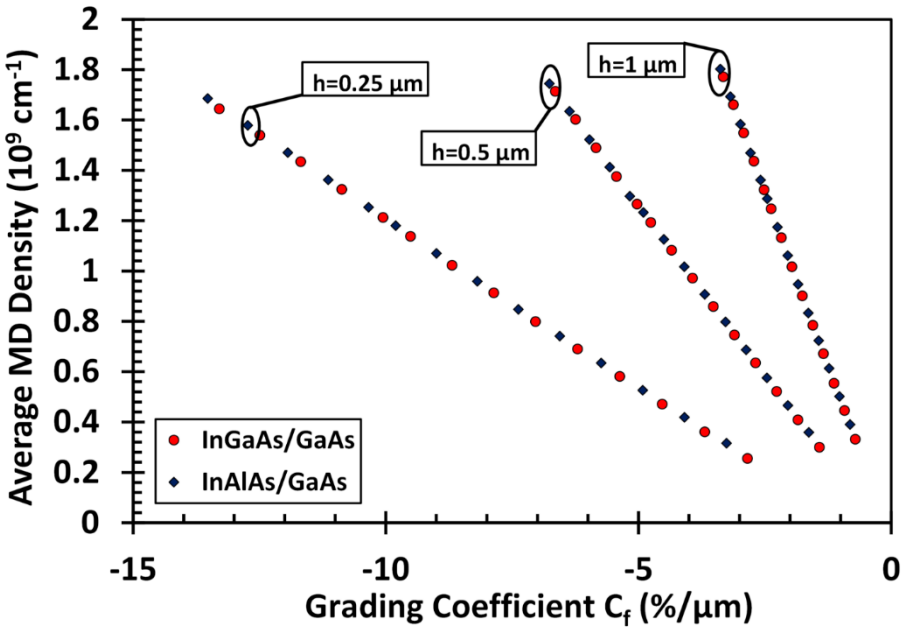

Figure 6.8. Average misfit dislocation density as a function of the grading coefficient for step-graded $In_xGa_{1-x}As/GaAs$ and $In_xAl_{1-x}As/GaAs$ heterostructures.

Figure 6.9 shows the normalized relaxation percentage per unit thickness as a function of the lattice mismatch at each step with the ending lattice mismatch as a parameter for $In_xGa_{1-x}As$ / GaAs (001) and $In_xAl_{1-x}As$ / GaAs (001) heterostructures. We define the normalized relaxation percentage per unit thickness of each step as:

$$| R_N | = \frac{f_N - \varepsilon_{\|,N}}{h_N f_N} \cdot 100\% . \qquad \textbf{(6.26)}$$

where f_N and $\varepsilon_{\|,N}$ are the lattice mismatch and the in-plane strain of the step N respectively and h_N is the thickness of the step. We further define the normalized relaxation rate per unit thickness as the slope of the characteristic shown in Figure 6.9. The results of Figure 6.9 indicate higher normalized relaxation rate per unit thickness in structures with lower buffer layer thickness; this is expected on the basis that for the same ending composition, structures with a lower buffer thickness exhibit a higher grading coefficient and therefore require higher relaxation in accommodating the misfit strain. Structures with lower ending indium composition and therefore mismatch contain higher relaxation rates near the surface and this phenomenon is associated with the absence of misfit dislocations as shown on Figure 6.6a. Moreover, there is an increase in the slope of the characteristic shown in Figure 6.9 near the substrate interface with higher indium composition, however the normalized relaxation rate per unit thickness becomes sluggish with increasing layer thickness. In comparison, for the same lattice mismatch profile, $In_xAl_{1-x}As$/GaAs structures contain slightly higher misfit dislocation density (MDD) and therefore have a lower change in the normalized relaxation percentage from one mismatched interface to the other. Table 6.2 shows that for the heterostructures studied in this work, $In_xAl_{1-x}As$/ GaAs (001) material system exhibits higher elastic stiffness coefficients. Combining the results of Figure 6.7, Figure

6.8 and Figure 6.9, structures with $In_xAl_{1-x}As$ as the epilayer material exhibit higher average misfit dislocation densities and slightly higher average compressive in-plane strain (absolute valued) but contain much lower rate of change in the normalized relaxation percentage per unit thickness of each step observable from the smaller slope values in Figure 6.9.

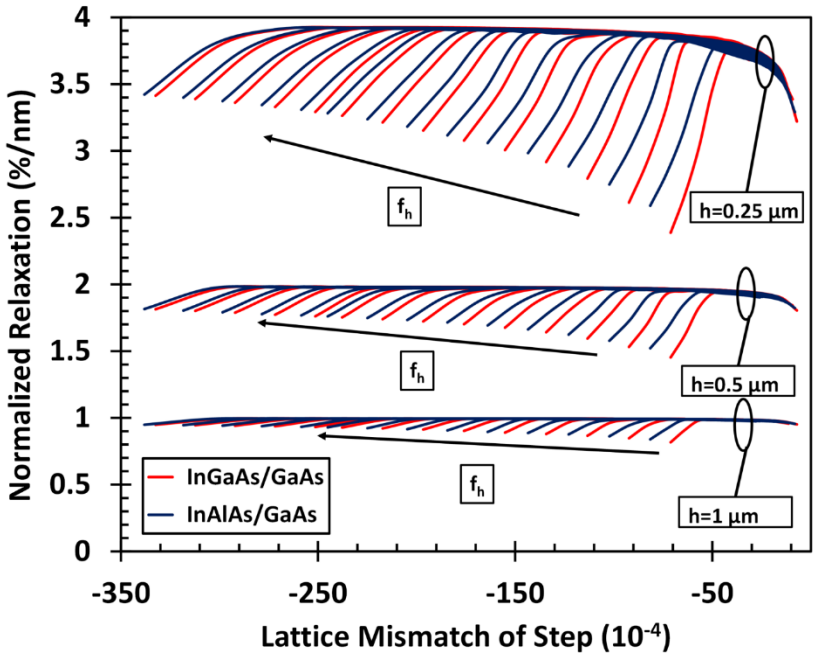

Figure 6.9. Normalized relaxation percentage per unit thickness as a function of the ending lattice mismatch for step-graded $In_xGa_{1-x}As$/GaAs and $In_xAl_{1-x}As$/GaAs heterostructures. Each curve of a particular color represents an ending lattice mismatch value.

We have investigated equilibrium lattice relaxation in metamorphic in $In_xGa_{1-x}As$ / GaAs (001) and $In_xAl_{1-x}As$ / GaAs (001) heterostructures involving step-graded buffer layers. We have explored the equilibrium structure by studying the evolution of the misfit dislocation density and in-plane strain at the mismatched interfaces. The main conclusion to this study is that structures with higher elastic stiffness coefficients such as $In_xAl_{1-x}As$/ GaAs (001) material system exhibit greater average compressive in-plane strain (absolute valued) and misfit dislocations. In addition, the normalized relaxation rate per unit thickness at each step is determined by the misfit dislocation

density at each mismatched interface. Equilibrium calculation are important when considering the kinetically-limited relaxation of step-graded $In_xGa_{1-x}As$ / GaAs (001) and $In_xAl_{1-x}As$ / GaAs (001) structures and understanding the misfit dislocation and in-plane strain distribution has important implications in the device design of semiconductor heterostructures.

Table 6.3. Material Properties for InAs, GaP GaAs and the alloys $In_xGa_{1-x}As$ and $GaAs_{1-y}P_y$.

Parameter	GaP	InAs	$GaAs_{1-y}P_y$	$In_xGa_{1-x}As$	GaAs
a (nm)	0.54505	0.50584	0.56534 - y(0.02029)	0.56534 + x(0.0405)	0.56534
C11 (GPa)	140.5	83.3	118.4 + y(22.1)	118.4 – x(35.1)	118.4
C12 (GPa)	62.03	45.3	53.7 + y(8.33)	53.7 – x(8.4)	53.7

6.4. Comparison of Equilibrium Lattice Relaxation and Misfit Dislocations in Continuously and Step-Graded InGaAs/GaAs and GaAsP/GaAs Material Systems

The inclusion of metamorphic buffer layers (MBL) in the design of lattice-mismatched semiconductor heterostructures is important in enhancing reliability and performance of optical and electronic devices. These metamorphic buffer layers usually employ linear grading of composition, and materials including $In_xGa_{1-x}As$ and $GaAs_{1-y}P_y$ have been used. Non-uniform and continuously graded profiles are beneficial for the design of partially-relaxed buffer layers because they reduce the threading dislocation density by allowing the distribution of the misfit dislocations throughout the metamorphic buffer layer, rather than concentrating them at the interface where substrate defects and tangling can pin dislocations or otherwise reduce their mobility as in the case of uniform compositional growth. In this work, we considered heterostructures involving a linearly-graded (type A) or step-graded (type B) buffer layer grown on a GaAs (001) substrate. For each structure type, we present minimum energy calculations and compare the cases of cation (Group III) and anion (Group V) grading. In addition, we studied the (i) average and surface in-

plane strain and (ii) average misfit dislocation density for heterostructures with various thickness and compositional profile. Moreover, we show that differences in the elastic stiffness constants give rise to significantly different behavior in these two commonly-used buffer layer systems.

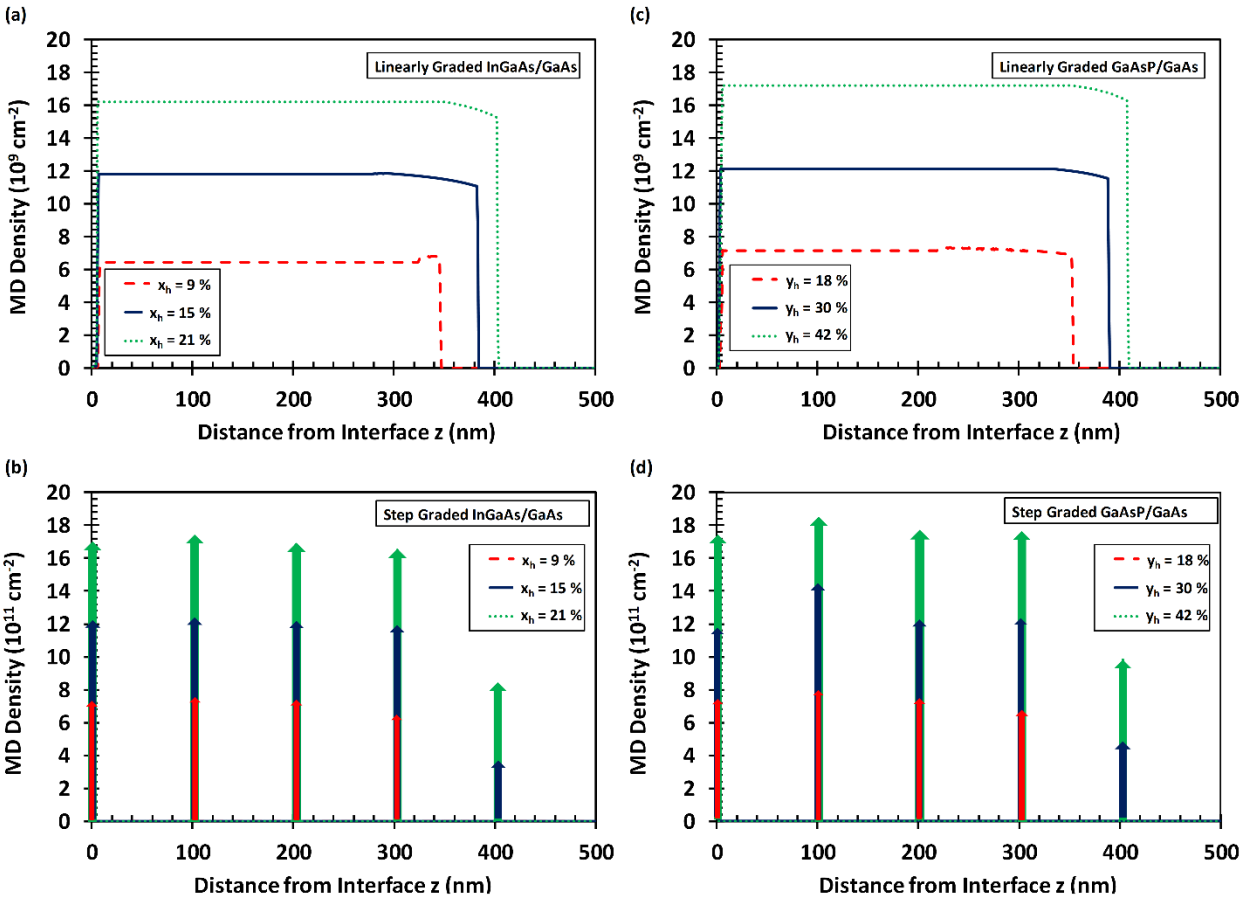

Figure 6.10. Misfit dislocation density as a function of the distance from the interface with various ending compositions for (a) linearly-graded InGaAs/GaAs, (b) step-graded InGaAs/GaAs, (c) linearly-graded GaAsP/GaAs and (d) step-graded GaAsP/GaAs

The use of metamorphic buffer layers (MBLs) has enabled the growth and design of highly lattice-mismatched electronic and optical devices. Metamorphic growth, in which the layers relax by the introduction of misfit dislocations, enables a wider range of layer thicknesses and compositions and has been exploited in a variety of devices [122, 123, 124, 125, 126, 127, 128,

129, 130]. A critical challenge with metamorphic device design involves control of the threading dislocation density, and compositionally-graded buffer layers have been used for this purpose. Most metamorphic device designs employ linearly-graded [131,132,92,133] or step-graded buffer layers [134,135,136]. Depending on the application of the device heterostructure material systems such as $In_xGa_{1-x}As$ [122,123,124] and $GaAs_{1-y}P_y$ [137,138,139,140,16-19] have been used. The use of MBL takes advantage of the enhanced built-in strain fields which allows for higher glide velocities and therefore the longest possible misfit segments. This gives rise to fewer threading dislocations originating from misfit dislocation ends. In addition, the graded layer allows for the introduction and distribution of misfit dislocations away from the substrate interface which results in the reduction of the dislocation interactions with substrate associated defects that may give rise to dislocation pinning and therefore rendering them immobile. It is therefore worthwhile to compare the two material systems utilizing a linearly- or step-graded scheme in terms of their equilibrium relaxation behavior.

In this work, we considered linearly-graded and step-graded buffers with the zinc blende structure grown on a GaAs substrate with (001) crystal orientation. Step-graded layers contain a set of n uniform layers in which there are equal compositional changes from one layer to the next ("linear step grading"). For type A structures, the cation/anion composition in the buffer layer is varied from lattice matched to GaAs at the substrate interface to a composition at thickness h of x_h / y_h corresponding to the same lattice mismatch at the surface of f_h for both material systems. Similarly, for type B structures, the grading profile is composed of five uniform buffer layers, where the cation/anion composition is varied with equal step sizes from lattice mismatched at the

GaAs substrate (first uniform layer) to a composition of x_h / y_h at thickness h (last uniform layer). The composition is varied as such to achieve the same grading coefficient for each grading scheme. In addition, we have investigated structures with a buffer layer thickness of 250, 500 and 750 nm. The material constants used in this work are summarized in Table 6.3.

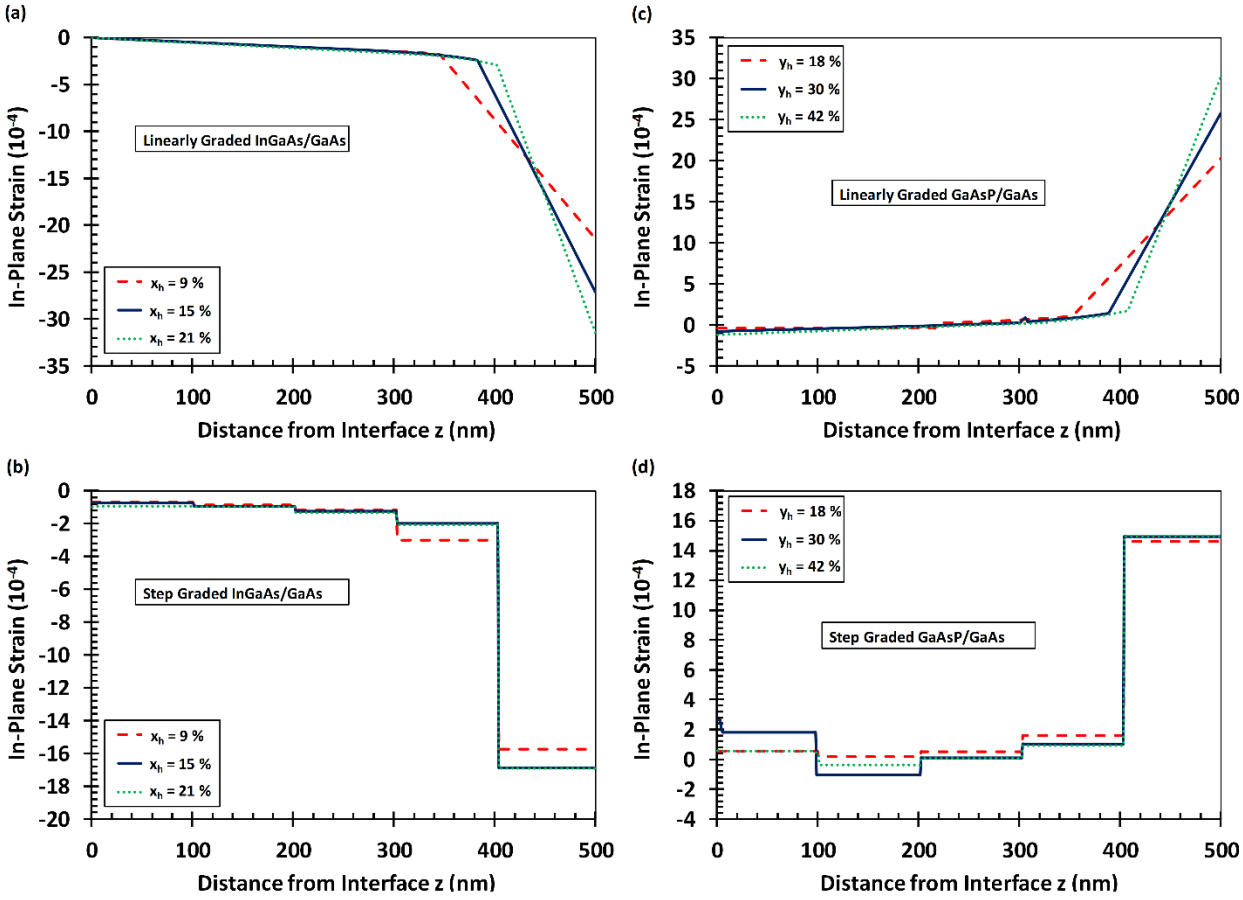

Figure 6.11. In-plane strain as a function of the distance from the interface with various ending compositions for (a) linearly-graded InGaAs/GaAs, (b) step-graded InGaAs/GaAs, (c) linearly-graded GaAsP/GaAs and (d) step-graded GaAsP/GaAs.

6.4.1. Comparison of the Residual Strain and Misfit Dislocation Characteristics

The structures considered in this work have an ending lattice mismatch ranging from f_h =0.21% to 2.2%. Figure 6.10 shows the equilibrium misfit dislocation density profiles for 500 nm

thick $In_xGa_{1-x}As$ and $GaAs_{1-y}P_y$ on GaAs (001) with various ending compositions for type A and type B structures. In linearly graded layers, the misfit dislocations are introduced at a finite distance from the interface and the distribution profile could be modeled using a rectangular function. In addition, there exists a misfit dislocation free zone (MDFZ) near the surface which limits interaction of misfit segments with the device layer which may be grown on top. However, the width of the surface MDFZ diminishes with higher ending composition (mismatch) values.

In uniform layers, misfit dislocations are introduced at the mismatched interfaces and they can be modeled using Dirac delta functions. The results of Figure 6.10b and d exhibit at most 5 MD regions (delta functions) which are equivalent with the number of mismatched interfaces. There exists a monotonic increase in the peak misfit dislocation density with increasing composition (mismatch) therefore necessitating the introduction of more misfit segments to relax the excess mismatch strain. Also, it can be seen that at low mismatch, the top mismatched interface in the step graded layers exhibit a MDFZ indicating that in these structures the strain is responsible for accommodating the lattice strain associated with compositional mismatch.

Figure 6.11 shows the equilibrium in-plane strain distribution for 500 nm thick $In_xGa_{1-x}As$ and $GaAs_{1-y}P_y$ on GaAs (001) with various ending compositions for type A and type B structures. In the dislocated region of a linearly-graded MBL, the introduction of misfit dislocations is just sufficient to relax the strain associated with the lattice mismatch and therefore the in-plane strain is approximately constant. However, beyond the dislocated region, the in-plane strain increases linearly with distance from the interface and is proportional to the lattice mismatch profile.

In type B structures, the in-plane strain is composed of a series of step functions with discontinuities at the mismatched interfaces. Apart from the dislocated interfaces, the equilibrium

strain in each sublayer is constant. Correlating the results of Figure 6.10 with Figure 6.11, it can be seen that the dislocation line energy relieves most of the excess strain associated with the compositional mismatch in sublayers near the interface. Moreover, in step graded layers the absence of dislocation peaks results in higher local unrelieved strain. In comparison to linear composition profiles, step graded layers with the same average mismatch exhibit a lower in-plane strain near the substrate interface and a higher in-plane strain at the surface.

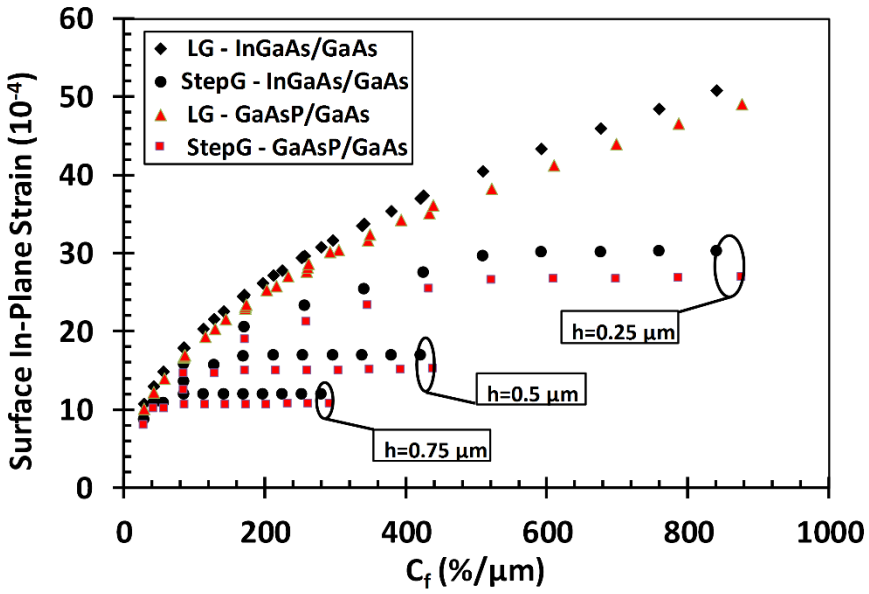

Figure 6.12. Surface in-plane strain as a function of the grading coefficient.

Figure 6.12 compares the surface in-plane strain for between $In_xGa_{1-x}As$ and $GaAs_{1-y}P_y$ layers as a function of the grading coefficient for type A and B structures. The surface in plane strain exhibits an increasing sublinear behavior with greater grading coefficient. The results of Figure 6.12 demonstrate that (i) structures with $In_xGa_{1-x}As$ as the epilayer and (ii) structures with type A grading profile contain a higher surface in-plane strain. However, the curve separation

between the two material systems for both grading profiles becomes more prominent at higher C_f . In addition, differences in the surface in-plane strain between $In_xGa_{1-x}As$ and $GaAs_{1-y}P_y$ are quite pronounced in structures with a higher grading coefficient; this occurs in structures with smaller buffer layer thickness and similar ending lattice mismatch. In type B structures, there are two main characteristics. First, there is a saturation of surface strain with increasing C_f . Second, structures with a lower epilayer thickness exhibit lower strain values.

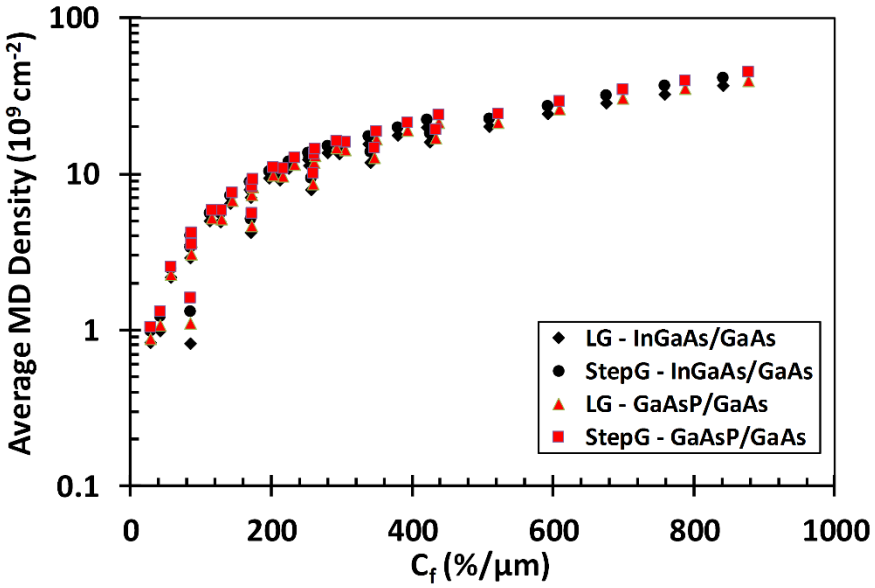

Figure 6.13. Average misfit dislocation density as a function of the grading coefficient.

The results of Figure 6.13 indicate that there is a sublinear and monotonic increase in the average equilibrium misfit dislocation density as a function of the ending mismatch. In addition, apart from slight departures, it can be seen that the average misfit dislocation density does not depend on the type of grading scheme. Figure 6.14a shows that that the in-plane strain increases monotonically in structures with $In_xGa_{1-x}As$ as the epilayer, whereas the in-plane strain decreases

monotonically (Figure 6.14b) in structures utilizing $GaAs_{1-y}P_y$ as the material system. For $In_xGa_{1-x}As/GaAs$, type A and B grading profiles exhibit similar strain values. However, in $GaAs_{1-y}P_y/GaAs$ metamorphic buffer layers, there is a curve separation for type A and B structures which becomes more prominent with increasing C_f.

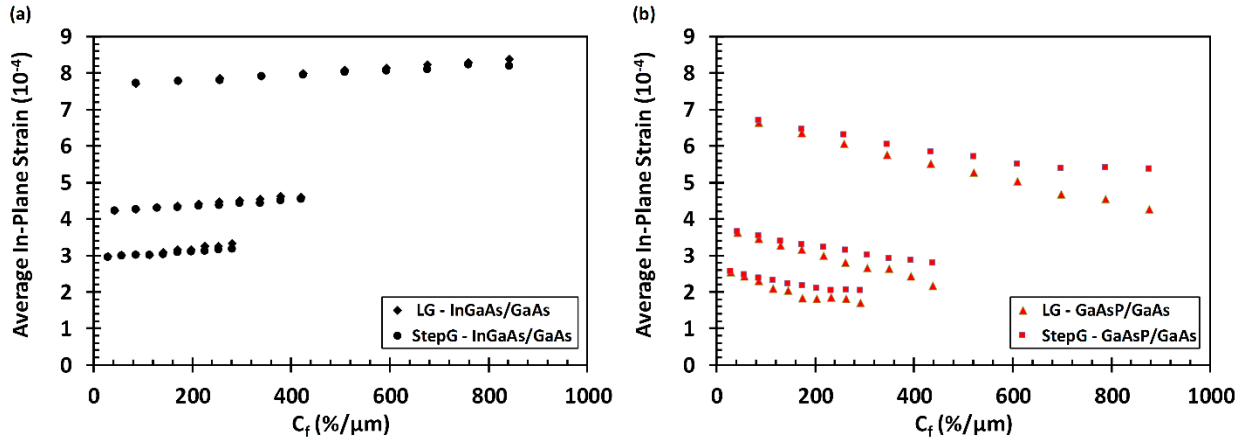

Figure 6.14. Average in-plane strain as a function of the grading coefficient for (a) InGaAs/GaAs and (b) GaAsP/GaAs.

Table 6.3 show that for the heterostructures studied in this work, the $GaAs_{1-y}P_y$ / GaAs (001) material system exhibits higher elastic stiffness coefficients. From an equilibrium point of view, structures with smaller elastic constants exhibit higher relaxation rates. In addition, for a given lattice mismatch, heterostructures with higher stiffness coefficients require a greater misfit dislocation density in relaxing the excess strain. Therefore, it can be seen from the results of Figure 6.12, Figure 6.13 and Figure 6.14 that structures with $GaAs_{1-y}P_y$ as the epilayer material have greater elastic stiffness coefficients which is associated with lower average misfit dislocation densities and lower surface in-plane strain.

We have investigated equilibrium lattice relaxation in metamorphic in $GaAs_{1-y}P_y$ / GaAs (001) and $In_xGa_{1-x}As$ / GaAs (001) heterostructures involving linearly- and step-graded buffer layers. We have explored the equilibrium structure by studying the evolution of the average and surface in-plane strain, average misfit dislocation density and have analyzed how the difference in elastic coefficients effect the equilibrium structure.

6.5. Strain and Misfit Dislocation Density in Exponentially-Graded Layers

We have calculated the equilibrium strain and misfit dislocation density profiles for heteroepitaxial $Si_{1-x}Ge_x$ / Si (001) with convex exponential grading of composition. A graded layer of this type exhibits two regions free from misfit dislocations, one near the interface of thickness z_1 and another near the free surface of thickness $h - z_d$, where h is the layer thickness. The intermediate region contains an exponentially tapered density of misfit dislocations. We report approximate analytical models for the strain and dislocation density profile in exponentially-graded $Si_{1-x}Ge_x$ / Si (001) which may be used to calculate the effective stress and rate of lattice relaxation. The results of this work are readily extended to other semiconductor material systems and may be applied to the design of exponentially-graded buffer layers for metamorphic device structures including transistors and light emitting diodes.

The growth of semiconductor heterostructures on lattice-mismatched substrates, such as strain-engineered $Si_{1-x}Ge_x$ on silicon wafers, has become increasingly important for the realization of a variety of devices including high electron mobility transistors and light-emitting diodes. These applications require the growth of metamorphic (partly relaxed) structures involving compositionally-graded buffer layers. Experimental and modeling studies have focused on

linearly-graded buffer layers, but non-linear grading provides an additional degree of control for the optimization of the dislocation density and residual strain in heteroepitaxial devices.

Design of these structures requires an understanding of their strain relaxation and dislocation dynamics, which can be strongly influenced by kinetic factors. Plastic flow models for kinetically-limited relaxation in uniform $Si_{1-x}Ge_x$ layers on Si (001) substrates have been presented by several workers including 'Matthews, Mader, and Light', 'Dodson and Tsao', and 'Houghton'. Matthews, Mader and Light assumed that the difference between the strain force and line tension on misfit dislocations is balanced by a Peierls force and calculated the strain relaxation as a function of time with the assumption of a constant areal dislocation density. This, amounts to balancing the effective stress with a stress associated with the Peierls force, where the effective stress is given by

$$\tau_{eff} = \frac{2G(1+\nu)}{(1-\nu)}\left[\varepsilon - \varepsilon_{eq}\right], \qquad \textbf{(6.27)}$$

where G is the shear modulus, ν is the Poisson ratio, ε is the in-plane strain in the film, and ε_{eq} is the equilibrium in-plane strain. Then, following the work of Haasen, the dislocation glide velocity was assumed to be thermally activated and a linear function of the effective stress. Based on the work of Alexander and Haasen [18], Dodson and Tsao developed a nonlinear ordinary differential equation for the strain relaxation including a phenomenological model for dislocation multiplication whereby the time rate of increase of the dislocation density is proportional to the square of the effective stress times the dislocation density. In the model of Houghton [16] it was assumed that the dislocation velocities are proportional to τ_{eff}^{m} and thermally activated, where

$1 \le m \le 1.5$, and that the time rate of change of the dislocation density is proportional to τ_{eff}^{n} , where $n \approx 2.5$, times a constant density of sources. A feature common to all the models for relaxation by plastic flow in semiconductor heterostructures is that they involve the use of the effective stress. Application of these models therefore requires knowledge of the equilibrium strain. For a compositionally graded structure this equilibrium strain varies with distance from the interface, and its profile must be known for the determination of the relaxation behavior.

Here we have calculated the equilibrium strain and misfit dislocation density profiles in $Si_{1-x}Ge_x$ / Si (001) heteroepitaxial layers with (001) orientation and exponential grading, by using a numerical method based on the minimization of the strain and dislocation line energy per unit area [19]. We report approximate analytical models for the strain and dislocation density profile in an exponentially-graded layer, and show that these models are in close agreement with detailed minimum energy calculations. Though $Si_{1-x}Ge_x$/Si (001) has been used as a model material system, the results may be readily extended to other materials and serve as the starting point for the design of exponentially-graded buffer layers for metamorphic device structures such as modulation doped field effect transistors and light emitting diodes.

6.5.1. Distribution of the In-Plane Strain and Misfit Dislocation Characteristics

The lattice mismatch in a (convex up) exponentially-graded layer can be written as

$$f(z) = f_{\infty}\left(1 - e^{-z/\gamma}\right), \qquad \textbf{(6.28)}$$

where γ is a length parameter (the "exponential grading constant").

Using the energy minimization approach described previously, the equilibrium misfit dislocation density and in-plane strain profiles were calculated for exponentially-graded layers of

$Si_{1-x}Ge_x$ / Si (001) with compositional profiles given by $x = x_\infty\left[1-\exp\left(-z/\gamma\right)\right]$. The material parameters for $Si_{1-x}Ge_x$ were assumed to be $a = \left(0.543108 + x0.022652\right)nm$, $C_{11} = \left(160.1 - x36.1\right)GPa$, and $C_{12} = \left(57.8 - x16.5\right)GPa$.

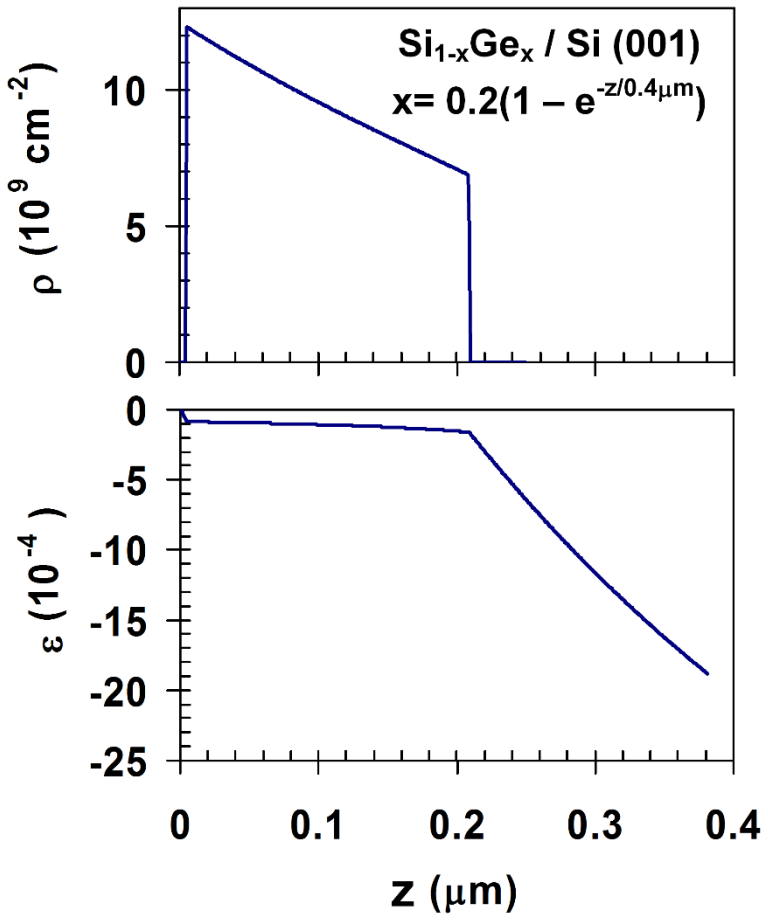

Figure 6.15. Equilibrium misfit dislocation density and strain in a 0.381 μm-thick $Si_{1-x}Ge_x$ / Si (001) layer with convex, exponential compositional grading given by $x = 0.2\left(1-e^{-z/0.4\mu m}\right)$.

Figure 6.15 shows representative results for an exponentially-graded layer of $Si_{1-x}Ge_x$ / Si (001), 0.38 μm-thick, with $x = 0.2\left[1-\exp\left(-z/0.4\mu m\right)\right]$; the limiting value of $x = 0.2$ corresponds to $f_\infty = -0.83\%$. The profiles in Figure 6.15 illustrate several general features of partially-relaxed

exponentially-graded layers (i.e., exponentially-graded layers which are greater than the critical layer thickness). First, there is a dislocation-free region of thickness z_1 near the interface in which the in-plane strain is equal to the lattice mismatch. Second, there is a region of thickness $z_d - z_1$ which contains a tapered misfit dislocation density and a nearly constant in-plane strain. Third, there is a dislocation-free region ($z > z_d$) near the surface which contains an exponential strain profile, with the greatest in-plane strain at the free surface.

The region near the interface ($z < z_1$) is free from misfit dislocations for two reasons. First, the composition is graded from zero and the initial deposit is lattice-matched to the substrate. Introducing misfit dislocations at the interface would therefore increase the strain energy in the film. Second, misfit dislocations have greater line energy if they are located farther from the free surface (closer to the interface).

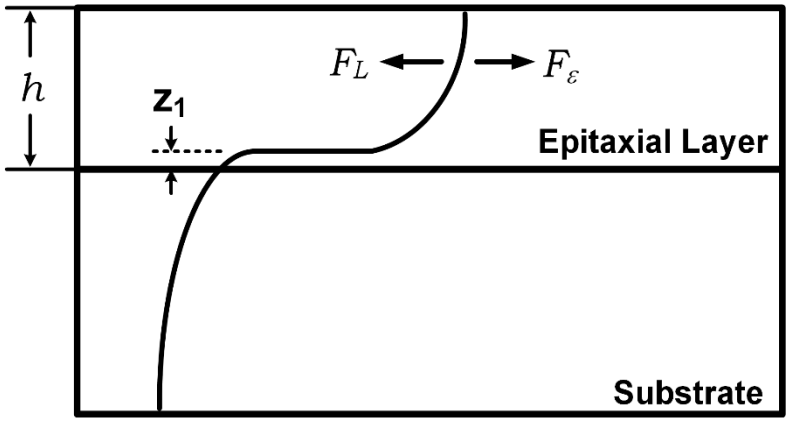

Figure 6.16. Force balance involving a grown-in dislocation which has bent over to produce a length of misfit dislocation near the interface. In equilibrium, the line tension in the misfit segment F_L is equal to the strain force F_ε acting to extend the misfit segment.

In the dislocated region ($z_1 < z < z_d$), the equilibrium strain is approximately constant as noted above. This is governed by a balance of the line tension and strain force on the misfit

dislocations within this region. The strain force acting on a misfit dislocation in this region is approximately constant, and associated with the strain profile in the near-surface dislocation-free region. The line tension varies gradually with distance from the surface (logarithmically) so the balance of the two forces dictates that the strain is a slowly-varying function of distance.

In the near-surface region ($z > z_d$) the strain gradient is equal to the mismatch gradient because of the absence of dislocations: $d\varepsilon_{\|} / dz = df / dz$. AS noted above, the integrated strain in this region is approximately constant and dictated by force balance considerations for misfit dislocations located closest to the free surface (that is, at $z = z_d$).

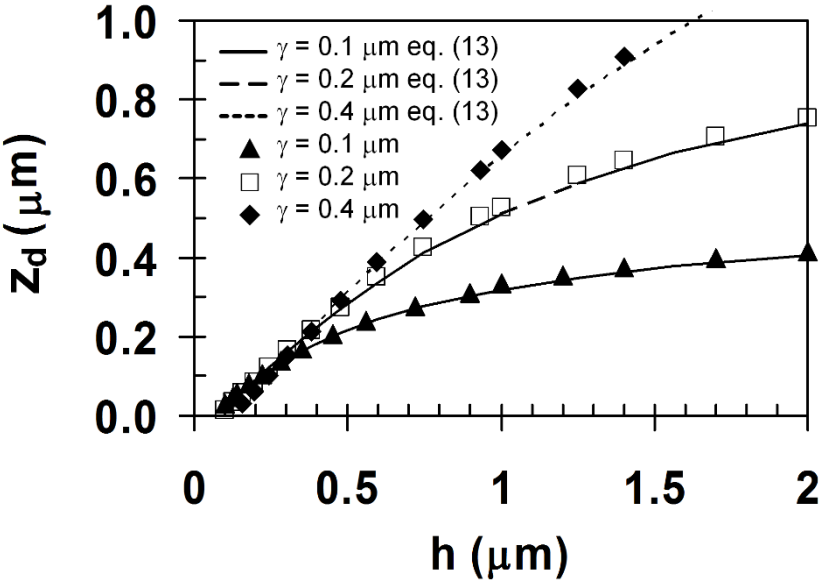

Figure 6.17. Distance from the interface z_d above which there are no misfit dislocations as a function of layer thickness, for convex exponentially graded layers of $Si_{1-x}Ge_x$ / Si (001) with $x = 0.2\left(1 - e^{-z/\gamma}\right)$. The symbols represent results from numerical solutions while the curves were calculated using the approximate model (Equation 6.36).

Based on the general observations above we can develop a quantitative model for the equilibrium misfit dislocation density in a partially-relaxed exponentially-graded layer. In the

dislocated region ($z_1 \le z \le z_d$) the in-plane strain is approximately constant so the misfit dislocation density is just sufficient to relax the strain due to the grading in the layer;

$$\rho = \frac{1}{b'}\left|\frac{df}{dz}\right|, \tag{6.29}$$

where b' is the misfit-relieving component of the Burgers vector in the plane of the interface. Therefore, the misfit dislocation density profile is

$$\rho = \begin{cases} 0, & z < z_1; \\ \left(|f_\infty|/b'\right)e^{-z/\gamma}, & z_1 \le z \le z_d; \text{ and} \\ 0, & z > z_d. \end{cases} \tag{6.30}$$

Consider next the equilibrium in-plane strain. The dislocation-free region near the interface is coherently strained so the in-plane strain is equal to the lattice mismatch:

$$\varepsilon_{\parallel} = f_\infty\left(1-e^{-z/\gamma}\right), \tag{6.31}$$

and the strain at $z = z_1$ (the top of this interfacial dislocation-free layer) is $f_\infty\left(1-e^{-z_1/\gamma}\right)$. For $z_1 \le z \le z_d$ (the dislocated layer) the in-plane strain is approximately constant at $f_\infty\left(1-e^{-z_1/\gamma}\right)$, assuming that the misfit dislocation density is just sufficient to relax the strain due to the compositional grading. For $z > z_d$ there are no misfit dislocations so $d\varepsilon_{\parallel}/dz = df/dz$. Therefore, the equilibrium in-plane strain in an exponentially-graded layer thicker than the critical layer thickness is

$$\varepsilon_{\parallel} = \begin{cases} f_\infty\left(1-e^{-z/\gamma}\right), & z < z_1; \\ f_\infty\left(1-e^{-z_1/\gamma}\right), & z_1 \le z \le z_d; \textit{and} \\ f_\infty\left(1-e^{-z_1/\gamma}+e^{-z_d/\gamma}-e^{-z/\gamma}\right), & z > z_d. \end{cases} \tag{6.32}$$

The model described by Equations 6.31 and 6.33 may be applied to plastic flow calculations and consequently the design of exponential buffer layers if z_1 and z_d are known. To determine the value of z_d we make use of the fact that in equilibrium the average in-plane strain in the graded layer is approximately the same as that in a uniform layer with the same thickness. This can be shown by equating the line tension F_L and strain force F_ε on a single grown-in dislocation located near the interface as shown in Figure 6.16. With the assumption that this grown-in misfit dislocation is located near the interface (that is, $z_1 << h$, where h is the graded layer thickness), the average strain is given by

$$\varepsilon_{\parallel}(ave) = \frac{f_\infty}{|f_\infty|}\frac{b(1-\nu\cos^2\alpha)[\ln(h/b)+1]}{8\pi h(1+\nu)\cos\lambda}. \qquad \textbf{(6.33)}$$

Another expression for the average in-plane strain may be found by integrating (10) and dividing by the total layer thickness:

$$\begin{aligned}\varepsilon_{\parallel}(ave) &= \frac{f_\infty}{h}\left\{\int_0^{z_1}\left(1-e^{-z/\gamma}\right)dz + \int_{z_1}^{z_d}\left(1-e^{-z_1/\lambda}\right) + \int_{z_1}^{z_d}\left(1-e^{-z_1/\gamma}+e^{-z_d/\gamma}-e^{-z/\gamma}\right)dz\right\} \\ &= \frac{f_\infty}{h}\left\{h-\gamma+(\gamma+z_1-h)e^{-z_1/\gamma}+(h-z_d-\gamma)e^{-z_d/\gamma}+\gamma e^{-h/\gamma}\right\}\end{aligned}. \qquad \textbf{(6.34)}$$

By equating (11) and (12) it is possible to determine z_d:

$$z_d = \left\{h-\gamma+(\gamma+z_1-h)e^{-z_1/\gamma}+(h-\gamma)e^{-z_d/\gamma}+\gamma e^{-h/\gamma}-\frac{b(1-\nu\cos^2\alpha)[\ln(h/b)+1]}{8\pi|f_\infty|(1-\nu)\cos\lambda}\right\}e^{z_d/\gamma}. \qquad \textbf{(6.35)}$$

The results of energy minimization calculations show that z_1 increases with the grading parameter γ and decreases exponentially with layer thickness. Here we use a phenomenological model for z_1,

$$z_1 \approx 1.4\sqrt{b\gamma}\, e^{-h/\gamma}, \qquad \textbf{(6.36)}$$

which can be used with (8), (10), and (13) to model the equilibrium strain and misfit dislocation profiles in exponentially-graded layers.

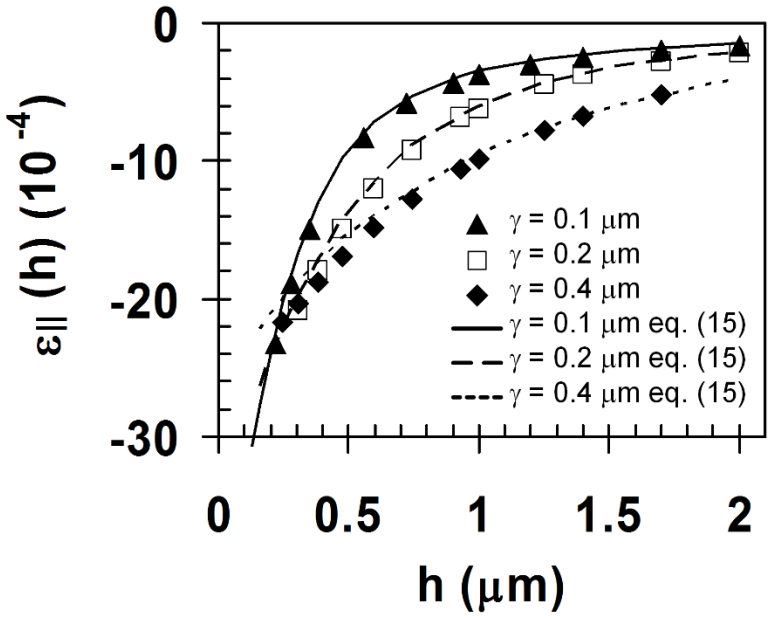

Figure 6.18. In-plane surface strain $\varepsilon_{\parallel}(h_{GL})$ as a function of layer thickness for convex exponentially graded layers of $Si_{1-x}Ge_x$ / Si (001) with $x = 0.2\left(1-e^{-z/\gamma}\right)$. The symbols represent results from numerical solutions while the curves were calculated using the approximate model (Equation 6.38).

Figure 6.17 shows z_d as a function of layer thickness for $Si_{1-x}Ge_x$ / Si (001) with $\gamma = 0.1\,\mu m$, $0.2\,\mu m$, and $0.4\,\mu m$. The points shown by diamonds, squares, and triangles were determined by energy minimization, while the curves were calculated using the model Equation 6.37. Comparison of these results show that Equation 6.37 can be used to predict the distance from the interface above which there are no misfit dislocations with better than $\pm 5\%$ accuracy as long

as the layer thickness is much greater than the critical layer thickness ($h_{GL} > 5h_c$) , where the critical layer thickness for the onset of lattice relaxation is given by

$$h_c = \frac{b\left(1-\nu\cos^2\alpha\right)}{8\pi\left|f_\infty\right|\left(1+\nu\right)}\left[\ln\left(\frac{h_c - z_1}{b}\right)+1\right] + z_1 + \gamma e^{-z_1/\gamma} - \gamma e^{-h_c/\gamma} . \qquad \textbf{(6.37)}$$

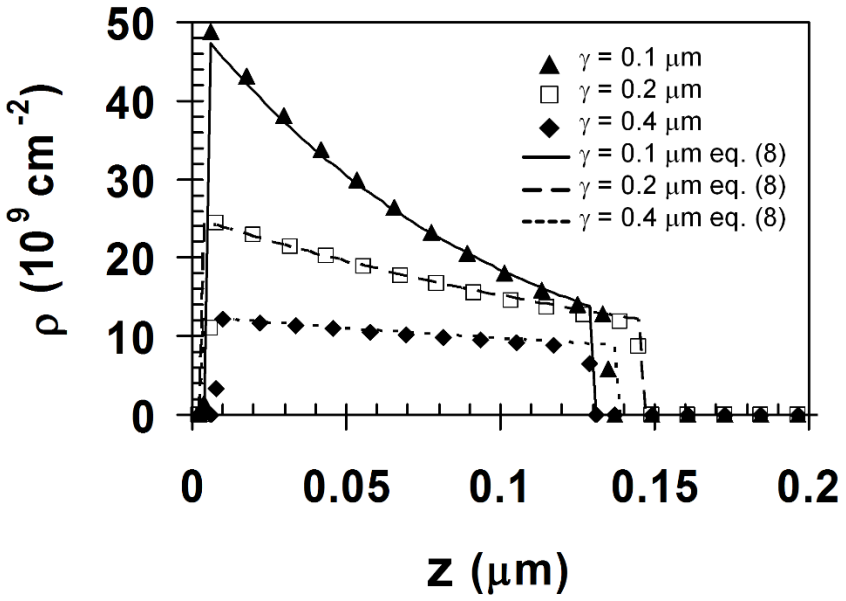

Figure 6.19. Equilibrium misfit dislocation density as a function of distance from the interface for convex exponentially-graded layers of $Si_{1-x}Ge_x$ / Si (001) with $x = 0.2\left(1-e^{-z/\gamma}\right)$. The symbols represent results from numerical solutions while the curves were calculated using the approximate model (Equation 6.30).

Figure 6.18 displays the equilibrium in-plane strain $\varepsilon_{\parallel}(h)$ at the free surface as a function of the layer thickness for exponentially-graded $Si_{1-x}Ge_x$ / Si (001) layers with $x_\infty = 0.2$ and with $\gamma = 0.1\,\mu m$, $0.2\,\mu m$, and $0.4\,\mu m$. Points shown by symbols were determined by numerical energy minimization calculations, while the curves were calculated using the approximate model (Equation 6.39). The accuracy of Equation 6.39 is better than $\pm 5\%$ for layers much thicker than

the critical layer thickness ($h_{GL} > 5h_c$), demonstrating its usefulness for practical device buffer layers.

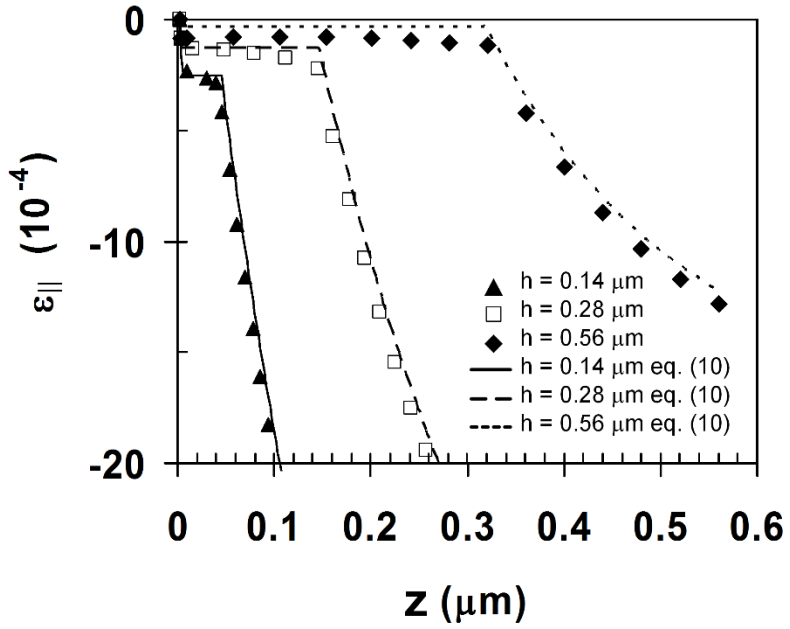

Figure 6.20. Equilibrium in-plane strain as a function of distance from the interface for convex exponentially-graded layers of $Si_{1-x}Ge_x$ / Si (001) with $x = 0.2\left(1 - e^{-z/0.2\mu m}\right)$. The symbols represent results from numerical solutions while the curves were calculated using the approximate model (Equation 6.33).

Figure 6.19 shows the equilibrium misfit dislocation density profiles for exponentially-graded layers of $Si_{1-x}Ge_x$ / Si (001) with a total thickness of $0.28\ \mu m$ and with $\gamma = 0.1\ \mu m$, $0.2\ \mu m$, and $0.4\ \mu m$, and Figure 6.20 shows the equilibrium in-plane strain for exponentially-graded $Si_{1-x}Ge_x$ / Si (001) layers with $\gamma = 0.2\mu m$ and with $h = 0.14\mu m$, $0.28\mu m$, and $0.56\mu m$. The analytical model given in Equation 6.34 predicts the equilibrium in-plane strain with better than $\pm 5\%$ accuracy except in the dislocated region. The main source of error is the use of the phenomenological model (Equation 6.38) for z_1 , and future work could include the development

of a refined z_1 model. Nonetheless, the maximum absolute error in the in-plane strain associated with the use of (Equation 6.34) is 0.7×10^{-4}. For typical graded layers of $Si_{1-x}Ge_x$ with a maximum germanium mole fraction of 0.20 or more, the lattice mismatch will exceed this maximum error in the in-plane strain by an order of magnitude. Therefore, the accuracy of the analytical model will be adequate for use in plastic flow calculations for exponentially-graded $Si_{1-x}Ge_x$ / Si (001) structures, and it will unnecessary to use detailed numerical calculations to find the equilibrium strain and thus the effective stress, for these structures.

We have determined the equilibrium strain and misfit dislocation distributions for $Si_{1-x}Ge_x$ / Si (001) layers with convex exponential grading of their composition using numerical energy minimization calculations. Based on these detailed calculations, we developed simple analytical models to describe the equilibrium behavior for three regions of the exponentially-graded layers: i) a dislocation-free region of thickness z_1 near the interface in which the in-plane strain is equal to the lattice mismatch; ii) a region of thickness $z_d - z_1$ which contains a tapered misfit dislocation density and a nearly constant in-plane strain; and iii) a dislocation-free region ($z > z_d$) near the surface which contains an exponential strain profile, with the maximum in-plane strain at the free surface. The analytical model serves as the starting point for the plastic flow analysis and consequently the design of exponentially-graded buffer layers in metamorphic device structures, for the lattice relaxation and dislocation dynamics in these structures are controlled by the effective stress, which is proportional to the difference between the actual strain and the equilibrium strain which has been modeled here. Moreover, for structures grown at relatively high temperatures, the strain and dislocation density profiles may approach the equilibrium profiles found in this work.

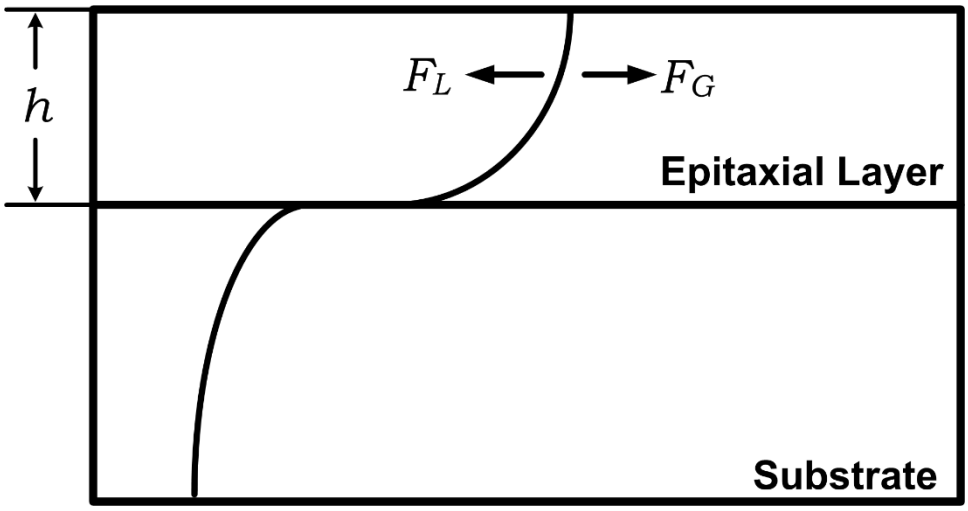

Figure 6.21. Simple force balance model for the critical layer thickness in a graded epitaxial layer. The grown-in dislocation elongates at the interface to create a length of misfit dislocation when the glide force F_G exceeds the line tension F_L.

6.5.2. Critical Layer Thickness in Exponentially-Graded Heteroepitaxial Layers

Exponentially-graded semiconductor layers are of interest for use as buffers in heteroepitaxial devices because of their tapered dislocation density and strain profiles. Here we have calculated the critical layer thickness for the onset of lattice relaxation in exponentially-graded $In_xGa_{1-x}As$ / GaAs (001) heteroepitaxial layers. Upwardly convex grading with $x = x_\infty\left(1-e^{-z/\gamma}\right)$ was considered, where z is the distance from the GaAs interface, γ is a grading length constant, and x_∞ is the limiting mole fraction of In. For these structures, the critical layer thickness was determined by an energy minimization approach and by consideration of force balance on grown-in dislocations. The force balance calculations underestimate the critical layer thickness unless one accounts for the fact that the first misfit dislocations are introduced at a finite distance above the interface. The critical layer thickness determined by energy minimization, or by a detailed force balance model, is approximately $h_c \approx 0.243\mu m\left(\gamma/1\mu m\right)^{0.5}\left(x_\infty/0.1\right)^{-0.54}$.

Although these results were developed for exponentially-graded $In_xGa_{1-x}As$ / GaAs (001), they may be generalized to other material systems for application to the design of exponentially-graded buffer layers in metamorphic device structures such as modulation doped field effect transistors and light emitting diodes.

6.5.3. Force Balance Theory for the Critical Layer Thickness

The realization of heterojunction devices such as modulation doped field effect transistors and light-emitting diodes requires heteroepitaxial growth of lattice mismatched materials. In most cases, materials or performance constraints prevent the use of pseudomorphic structures which are coherently strained to match the in-plane lattice constant of the substrate. The preferred approach therefore involves metamorphic structures which exhibit some degree of lattice relaxation. The design of these structures requires an understanding of their misfit dislocations and strain relaxation, which may strongly influence device performance. Though most experimental work with graded buffer layers has focused on simple linear grading, there is evidence that non-linear grading, grading with overshoot interfaces, reverse grading, or step grading may be beneficial for the reduction of the surface threading dislocation density with minimal buffer thickness. , graded layers with upwardly convex exponential grading are of interest for device buffer layer applications because of the ability to taper the misfit dislocation density and strain with distance from the substrate interface. The design of exponentially-graded device buffer layers requires an understanding of the critical layer thickness and the dislocation dynamics. Here we present calculations of the critical layer thickness in exponentially-graded layers based on force balance as well as energy minimization, and provide an approximate equation for the estimation of the critical layer thickness in exponentially-graded layers. Non-linear profiles of this type may be

realized by the computer control of electronic mass flow controllers during the growth process, for the case of metalorganic vapor phase epitaxy (MOVPE) or gas source molecular beam epitaxy (GSMBE). $In_xGa_{1-x}As$ / GaAs (001) has been used as a model material system but the results may be readily extended to other heteroepitaxial systems.

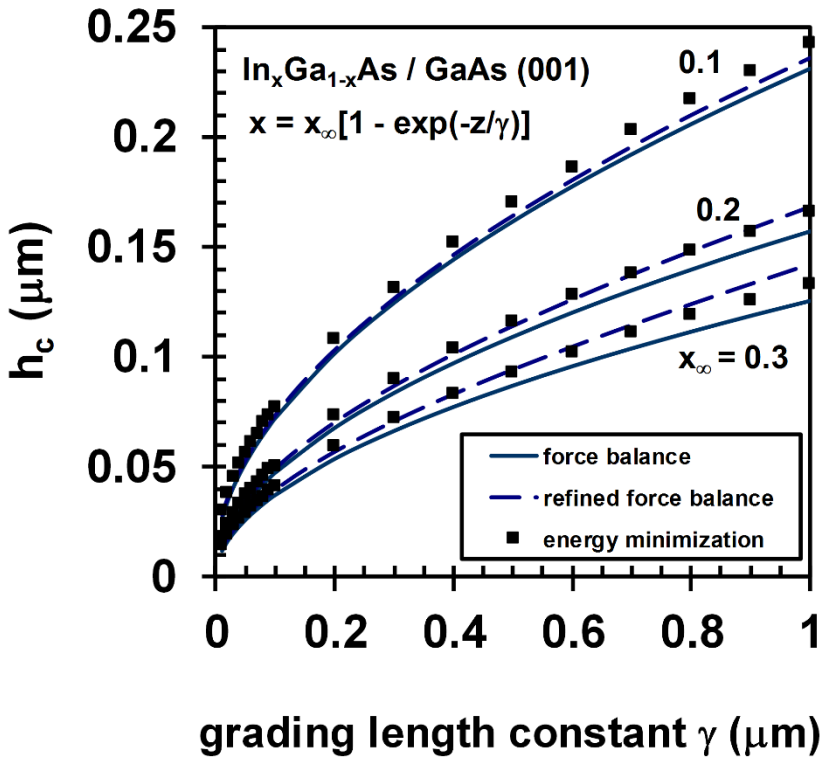

Figure 6.22. Critical layer thickness h_c as a function of the grading length constant with x_∞ as a parameter, for (convex up) exponentially-graded $In_xGa_{1-x}As$/GaAs (001) heteroepitaxial layers as determined by a simple force balance model (Equation 6.43, solid curve), a refined force balance model (Equation 6.51, dashed curves), and energy minimization (Equations 6.45 and 6.47, solid squares).

We can determine the approximate critical layer thickness for such a layer using a simple force balance model as illustrated in Figure 6.21. Following the approach presented by Matthews and Blakeslee for a structure containing uniform strained layers, we assume that a grown-in

dislocation will elongate at the interface to create a length of misfit dislocation once the glide force F_G exceeds the dislocation line tension F_L. The glide force acting on a grown-in dislocation in the coherently-strained layer on a (001) diamond or zinc blende substrate with $\varepsilon_{\|}(z) = f(z)$ is

$$F_G = \frac{2Gb(1+\nu)\cos\lambda}{(1-\nu)}\int_0^h f(z)dz\,, \qquad \textbf{(6.38)}$$

where G is the shear modulus, $G = (C_{11} - C_{12})/2$, in which C_{11} and C_{12} are the elastic stiffness constants, b is the length of the Burgers vector, ν is the Poisson ratio, $\nu = C_{12}/(C_{11} + C_{12})$ for the (001) orientation, and λ is the angle between the Burgers vector and the line in the interface plane which is perpendicular to the intersection of the glide plane with the interface, and h is the layer thickness. For the case of a (convex up) exponentially-graded layer, the glide force is

$$F_G = \frac{2Gb(1+\nu)\cos\lambda}{(1-\nu)}\int_0^h f_\infty\left[1-e^{-z/\gamma}\right]dz = \frac{2Gbf_\infty(1+\nu)\cos\lambda}{(1-\nu)}\left[h+\gamma\left(e^{-z/\gamma}-1\right)\right]. \qquad \textbf{(6.39)}$$

If the grown-in dislocation glides to create a length of misfit dislocation at the substrate interface, the line tension in this misfit segment which opposes the glide is

$$F_L = \frac{Gb^2(1-\nu\cos^2\alpha)\cos\lambda}{4\pi(1-\nu)}\left[\ln\left(\frac{h}{b}\right)+1\right], \qquad \textbf{(6.40)}$$

where α is the angle between the Burgers vector and the line vector for the dislocations. Equating the glide and line tension forces at the critical layer thickness h_c we obtain

$$h_c = \frac{b(1-\nu\cos^2\alpha)\left[\ln(h_c/b)+1\right]}{8\pi|f_\infty|(1+\nu)\cos\lambda} + \gamma\left(1-e^{-h_c/\gamma}\right), \qquad \textbf{(6.41)}$$

which can be solved numerically to determine the approximate critical layer thickness. It is important to point out that Equation 6.43 is based on the assumption that misfit dislocations are first introduced at the substrate interface. Although this is a good assumption for a uniform strained

layer, Equation 6.43 will be subject to some degree of error if the first misfit dislocations are introduced away from the interface. Moreover, the application of Equation 6.43 involves the use of effective values for b and ν, even though these vary with composition in a graded layer.

The critical layer thickness may be determined more accurately by consideration of energy minimization. If the graded layer is sufficiently thick to be partly relaxed, and therefore contains misfit dislocations of cross-sectional density $\rho(z)$, the in-plane strain is relaxed to

$$\varepsilon_{\parallel}(z) = f(z) + b' \int_0^z \rho(z) dy \qquad \textbf{(6.42)}$$

where b' is the misfit relieving component of the Burgers vector parallel to the interface. The strain energy per unit area is

$$E_{\varepsilon} = \int_0^h Y \varepsilon_{\parallel}^{\,2} dz = \int_0^h Y(z) \left[f(z) + b' \int_0^z \rho(\xi) d\xi \right]^2 dz \,, \qquad \textbf{(6.43)}$$

where Y is the biaxial modulus, $Y = C_{11} + C_{12} - 2C_{12}^2 / C_{11}$, and C_{11} and C_{12} are the elastic stiffness constants. The dislocation density ρ is always positive, but b' may be positive or negative, depending on the sign of the mismatch strain which is being relieved. The line energy of dislocations per unit area, assuming two orthogonal networks with equal cross-sectional density, is

$$E_d = 2 \int_0^h F_d(z) \rho(z) dz \,, \qquad \textbf{(6.44)}$$

where

$$F_d(z) \approx \frac{G(z) b^2(z) \left[1 - \nu(z) \cos^2 \alpha \right]}{4\pi (1 - \nu(z))} \left[\ln \left(\frac{h - z}{b(z)} \right) + 1 \right]. \qquad \textbf{(6.45)}$$

Here the dislocation energy is determined using a mean-field approach, without including second-order dislocation-dislocation interactions, and this is the primary approximation used. The equilibrium configuration may be determined numerically by minimizing $E_d + E_\varepsilon$, and the critical layer thickness is the minimum thickness at which it becomes energetically favorable to introduce a misfit dislocation anywhere in the structure. It should be noted that Equation 6.45 – 6.47 are generally applicable to cubic semiconductors and can be solved for any arbitrary compositional profile using the numerical approach developed in reference.

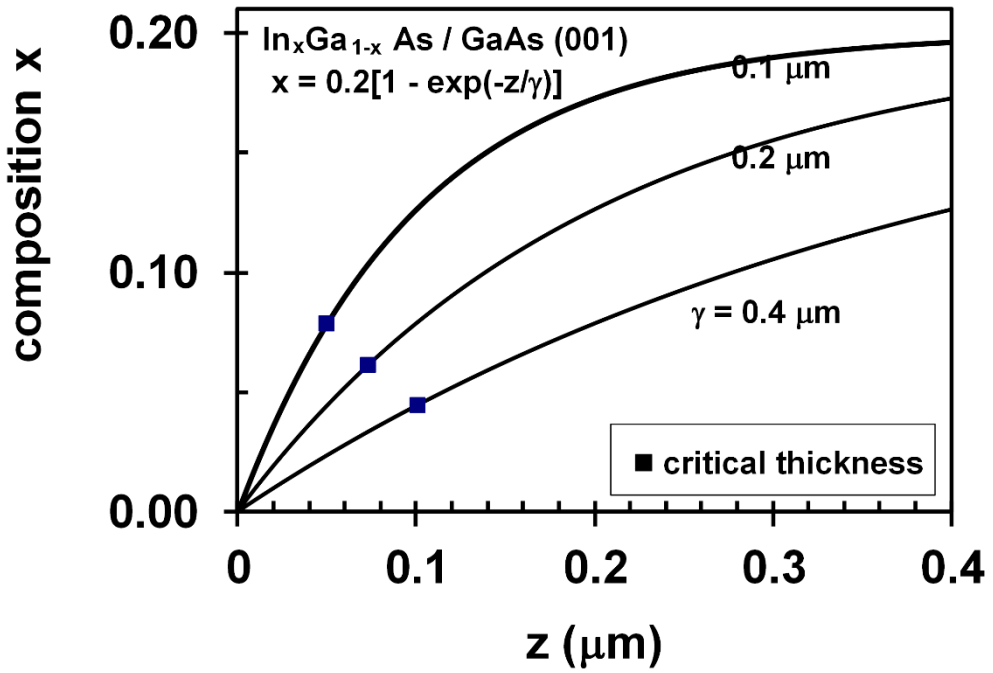

Figure 6.23. Exponential compositional profiles for $In_xGa_{1-x}As$ graded layers with $x = 0.2[1-\exp(-z/\gamma)]$, in which $x_\infty = 0.2$ and $\gamma = 0.1$, 0.2, and 0.4. Also indicated in this figure are the critical layer thicknesses for these three cases.

6.5.4. Determination of the Theoretical CLT in Exponentially-Graded Layers

The critical layer thickness was calculated for (convex up) exponentially-graded layers of $In_xGa_{1-x}As$ on GaAs (001) with $x(z) = x_\infty\left(1 - e^{-z/\gamma}\right)$, where the limiting indium mole fraction x_∞ was set to 0.1, 0.2, and 0.3. The thickness parameter γ was varied from 0.1 μm to 1.0 μm. The assumed material parameters are given in Table 6.4; for energy minimization calculations, linear interpolation was used to estimate the lattice and elastic constants for the ternary alloy $In_xGa_{1-x}As$. In the case of the force balance model, b and ν were estimated for the composition $x_\infty/2$.

Figure 6.22 shows the critical layer thickness as a function of the parameter γ for exponential layers with $x_\infty = 0.1$, 0.2, and 0.3. The critical layer thickness increases monotonically with the thickness parameter γ and decreases with x_∞. Figure 6.23 illustrates exponential profiles in composition $x = 0.2\left[1 - \exp(-z/\gamma)\right]$, with $x_\infty = 0.2$ and with $\gamma = 0.1$, 0.2, and 0.4. Also indicated in this figure are the critical layer thicknesses for these three cases.

It should be noted that the critical layer thicknesses determined here are for thermal equilibrium, and do not take into account kinetic limitations associated with the nucleation, glide, and multiplication of dislocations. For growth on substrates with high crystalline perfection, such as Si, the number of grown-in dislocations is insufficient to give rise to the observed lattice relaxation. Therefore, dislocation nucleation and/or multiplication are important and the measured thickness for observable lattice relaxation may be considerably greater than the equilibrium value. Nonetheless, the equilibrium critical layer thickness is the starting point for development of a kinetic model for lattice relaxation.

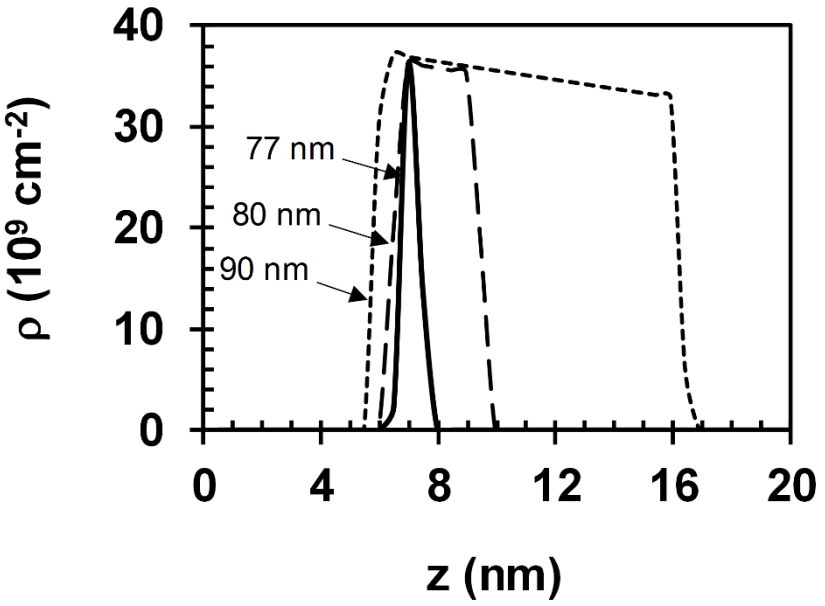

Figure 6.24. Misfit dislocation density as a function of distance from the interface for exponentially-graded $In_xGa_{1-x}As$ layers / GaAs (001) layers of various thicknesses. The indium composition is assumed to have an exponential profile $x = x_\infty\left(1-e^{-z/y}\right)$, where $x_\infty = 0.1$ and $\gamma = 0.1\mu m$. This results in a critical layer thickness $h_c \approx 77nm$.

The simple force balance calculation predicts a smaller value of the critical layer thickness than the energy minimization calculation. As pointed out above, the force balance calculation assumes that the first misfit dislocation is introduced at the interface with the substrate ($z = 0$). If misfit dislocations are instead introduced at a distance z_d from the interface then the glide force acting on the grown-in dislocation is reduced for a given thickness of deposit. It will therefore be necessary to grown a thicker epitaxial layer before the glide force is sufficient to cause the grown-in dislocation to glide and create a length a misfit dislocation; i.e., the critical layer thickness will be increased. To investigate this, we determined the distance from the interface z_d at which misfit dislocations are first introduced using energy minimization calculations.

To perform the energy minimization calculations, we divide the structure into a number of sublayers, each of which is assumed to have uniform strain, dislocation density, and elastic properties. The number of these sublayers may be made arbitrarily large to insure the accuracy of the results. (In this work, the sublayer thickness was set to 0.5 nm. Decreasing the sublayer thickness did not change the results appreciably.) Then, using the procedure described in reference [19], the dislocation densities and strains in the sublayers are varied systematically to find the minimum energy configuration; for this purpose, Equations 6.45 – 6.47 are used to calculate the sum of the strain energy and dislocation line energy.

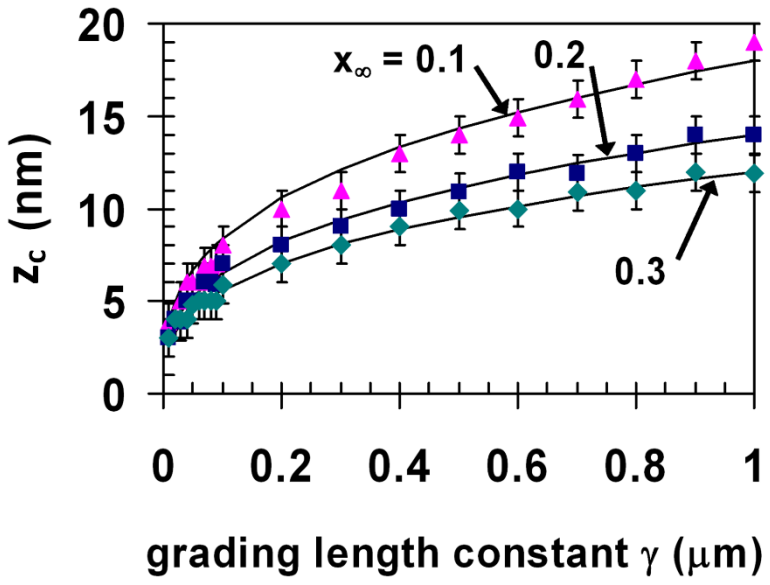

Figure 6.25. Distance from interface where the first misfit dislocations are introduced z_c as a function of the grading constant γ with x_∞ as a parameter, for (convex up) exponentially-graded $In_xGa_{1-x}As/GaAs$ (001) heteroepitaxial layers.

First, we considered exponentially-graded layers with $x_\infty = 0.1$ and $\gamma = 0.1\mu m$. Figure 6.24 shows the equilibrium misfit dislocation density distribution for layers with thicknesses of

77 nm, 80 nm, and 90 nm. Here 77 nm is the minimum thickness for which energy minimization calculations predict the presence of misfit dislocations in the structure, so this is considered to be the critical layer thickness as determined by energy minimization. The first misfit dislocations are introduced at a distance $z_c \approx 7nm$ from the interface. As the film thickness is increased, the width of the dislocated region increases. This is because the misfit dislocation density is limited by the grading in the layer, while the integrated misfit dislocation density must increase as the layer relaxes. Therefore, dislocations are eventually introduced at distances less than z_c from the interface. In consideration of the critical layer thickness, however, we only need to consider the point z_c where dislocations are *first* introduced.

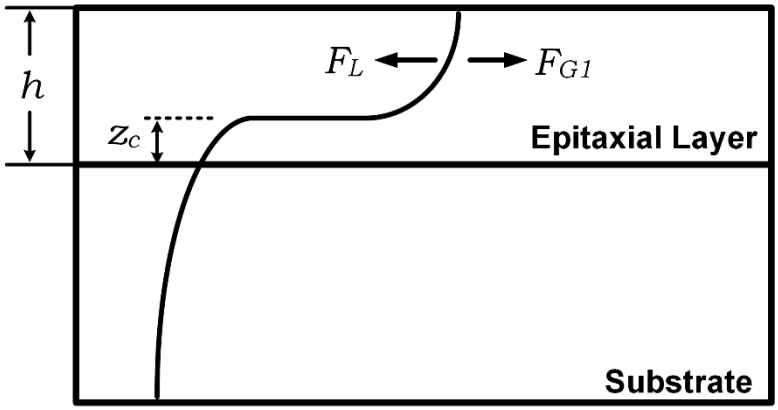

Figure 6.26. Refined force balance model for the critical layer thickness in a graded epitaxial layer. The grown-in dislocation glides to create a length of misfit dislocation at a distance z_c from the interface when the glide force F_{G1} (acting on the section of dislocation above z_c) exceeds the line tension F_L.

There are two reasons for this phenomenon. First, the lattice mismatch strain approaches zero at the interface and the introduction of misfit dislocations in this region would increase the

overall strain energy. Second, misfit dislocations closer to the free surface have reduced line energy.

Figure 6.25 shows z_c as a function of the grading length constant γ with x_∞ as a parameter. The distance from the interface at which misfit dislocations are first introduced increases monotonically with the grading constant and decreases with the limiting indium mole fraction, and may be estimated using the approximation

$$z_c \approx 18nm\left(\frac{\gamma/1\mu m}{x_\infty/0.1}\right)^{0.33}. \quad \textbf{(6.46)}$$

If a grown-in dislocation glides to create a length of misfit dislocation at a distance z_c from the interface as shown in Figure 6.26, the glide force opposing the line tension is

$$F_{G1} = \frac{2Gb(1+\nu)\cos\lambda}{(1-\nu)}\int_{z_c}^{h} f_\infty\left[1-e^{-z/\gamma}\right]dz. \quad \textbf{(6.47)}$$

Also, the line tension in the misfit segment is reduced if this segment is located above the interface:

$$F_L = \frac{Gb^2\left(1-\nu\cos^2\alpha\right)\cos\lambda}{4\pi(1-\nu)}\left[\ln\left(\frac{h-z_c}{b}\right)+1\right]. \quad \textbf{(6.48)}$$

The reduction in the glide force is the more important effect, because of the logarithmic dependence of the line tension on the cutoff parameter $(h-z_c)$. Therefore, the net effect is to reduce the critical layer thickness, as predicted by the energy minimization calculations. Taking this into account we can make a more accurate force balance calculation by Equating 6.47 and 6.48, yielding

$$h_c = \frac{b\left(1-\nu\cos^2\alpha\right)}{8\pi|f_\infty|(1+\nu)}\left[\ln\left(\frac{h_c-z_c}{b}\right)+1\right] + z_c + \gamma e^{-z_c/\gamma} - \gamma e^{-h_c/\gamma}. \quad \textbf{(6.49)}$$

Using the refined force balance model given in Equation 51 and the average values of b and ν,

$$b_{ave} = b_{GaAs} + (b_{InAs} - b_{GaAs})x_{\infty}\left[1 + \frac{\gamma}{h}\left(e^{-h/\gamma} - 1\right)\right] \quad \textbf{(6.50)}$$

and

$$\nu_{ave} = \nu_{GaAs} + (\nu_{InAs} - \nu_{GaAs})x_{\infty}\left[1 + \frac{\gamma}{h}\left(e^{-h/\gamma} - 1\right)\right], \quad \textbf{(6.51)}$$

we calculated the critical layer thickness for comparison to the simple force balance model and the energy minimization calculations as shown in Figure 6.22. This figure shows that the refined force balance model provides better accuracy than the simple force balance model, though the use of invariant values for b and ν introduces some level of error.

For the design of exponentially-graded buffer $In_xGa_{1-x}As$ layers for devices, the critical layer thickness determined by energy minimizations may be conveniently estimated using the approximation

$$h_c \approx 0.243\mu m\left(\frac{\gamma}{1\mu m}\right)^{0.5}\left(\frac{x_{\infty}}{0.1}\right)^{-0.54} \quad \textbf{(6.52)}$$

or may be determined using the refined force balance model (Equation 6.51) with less than 5% error over the range of parameters considered in this study.

In conclusion, the critical layer thickness for the onset of lattice relaxation has been calculated for exponentially-graded $In_xGa_{1-x}As$ / GaAs (001) heteroepitaxial layers. These are equilibrium critical layer thickness values, which do not consider kinetic limitations associated with dislocation nucleation, glide, or multiplication, but which serve as the starting point for kinetic analysis. Upwardly convex grading with $x = x_{\infty}\left(1 - e^{-z/y}\right)$ was considered, where z is the distance from the

GaAs interface. The critical layer thickness was calculated by consideration of energy minimization, by considering the strain energy and the misfit dislocation line energy. In this analysis, the critical layer thickness was considered to be the minimum thickness at which the introduction of misfit dislocations is energetically favorable. Based on the energy minimization criterion, it is found that the first misfit dislocations are introduced at a distance z_c from the substrate interface. If the critical layer thickness is to be determined by force balance on a grown-in dislocation, this phenomenon must be taken into account or the critical layer thickness will be underestimated. The values of the critical layer thickness determined by energy minimization may be estimated by $h_c \approx 0.243\mu m(\gamma/1\mu m)^{0.5}(x_\infty/0.1)^{-0.54}$.

6.6. S-Graded Buffer Layers for Lattice-Mismatched Heteroepitaxial Devices

We have studied the equilibrium strain and misfit dislocation density profiles for "S-graded" buffer layers of $In_xGa_{1-x}As$ on GaAs (001) substrates in which the compositional profile follows a normal cumulative distribution function. We show that the S-graded layer exhibits misfit dislocation free regions near the substrate interface and the free surface (or device interface). The peak misfit dislocation density as well as the thicknesses of the dislocation-free regions may be tailored by the design of the compositional profile; this in turn should enable minimization of the density of electronically active threading dislocations at the top surface. "S-graded" buffer layers may therefore facilitate the achievement of metamorphic device structures with improved performance compared to similar structures having uniform or linearly-graded buffers.

6.6.1. Strain and Misfit Dislocation Density in S-Graded MBLs

The realization of semiconductor heterostructures on lattice-mismatched wafers, such as strain-engineered $Si_{1-x}Ge_x$ on silicon, has become increasingly important for the fabrication of devices including high electron mobility transistors (HEMTs) and light-emitting diodes (LEDs). These applications require growth of metamorphic (partly relaxed) structures with compositionally-graded buffer layers to accommodate the mismatch between the substrate and device material. Experimental and modeling studies have focused on linearly-graded buffers, but non-linear grading provides an additional degree of control for the optimization of the dislocation density and residual strain in fabricated structures.

The dislocations in device structures are primarily half-loops, each comprising a misfit segment and two threading segments. It is desirable to reduce the density of threading dislocations because of their harmful effects on device performance and reliability. Compositionally-graded buffers exhibit three characteristics which promote longer misfit dislocation segments and therefore fewer threading dislocations, as follows. (i) New misfit dislocations are introduced at the top of the growing layer where there are relatively few existing dislocations, and the reduction of the dislocation-dislocation interactions that give rise to pinning or decreased dislocation mobility allow the uninhibited glide of dislocations to form longer misfit segments. (ii) The graded layer exhibits a misfit dislocation free zone (MDFZ) near the surface. This prevents the introduction of new dislocation loops near the surface in the final stages of buffer layer growth, and instead existing misfit dislocations may grow in length by glide. (iii) The graded layer has increased residual strain in its surface misfit dislocation free zone (MDFZ) relative to a uniform buffer, which can promote higher effective stresses and misfit dislocation velocities. We have shown that another

benefit of linear compositional grading is that the initial misfit dislocations form at a finite distance from the substrate interface, which can reduce dislocation pinning or mobility reduction due to defects or chemical contamination at the starting substrate surface. A drawback of the linearly-graded buffer layer is that, upon growth of a device layer upon the top, the misfit dislocation free zone (MDFZ) typically decreases in thickness. In some cases, the MDFZ thickness may vanish – leading to the introduction of new misfit dislocations in the device layer. Exponential grading, in which the lattice mismatch is given by $f = f_0\left[1-\exp(-z/\gamma)\right]$ where z is the distance from the substrate interface and f_0 is the lattice mismatch of the device layer, represents an improvement over the linear case in that the grading constant γ may be chosen to preserve a MDFZ at the top of the buffer. The "S-graded" buffer layer, introduced in this study, represents a further improvement on the concept whereby there are MDFZs of controllable thickness at the bottom and top of the buffer (that is, adjacent to the substrate and device layer interfaces). The lattice mismatch profile in the S-graded layer is assumed to be a normal cumulative distribution function, given by

$$f = \begin{cases} \left(\frac{f_h}{2}\right)\left[-erf\left(\frac{\mu - z}{\sigma\sqrt{2}}\right)+erf\left(\frac{\mu}{\sigma\sqrt{2}}\right)\right], & z < \mu; \\ \left(\frac{f_h}{2}\right), & z = \mu \\ \left(\frac{f_h}{2}\right)\left[erf\left(\frac{z - \mu}{\sigma\sqrt{2}}\right)+erf\left(\frac{\mu}{\sigma\sqrt{2}}\right)\right], & z > \mu \end{cases}, \qquad \textbf{(6.53)}$$

where μ is the "mean parameter" (the distance from the substrate interface where $f = f_h/2$), σ is the "standard deviation parameter," and f_h is the lattice mismatch at the top of the buffer layer with thickness h. The lattice mismatch is defined as $f(z) \equiv \left(a_s - a(z)\right)/a(z)$, where a_s is the

relaxed lattice constant of the substrate and $a(z)$ is the relaxed lattice constant of the epitaxial crystal at a distance z from the substrate interface. The parameters μ , σ, f_h, and h can be chosen by the crystal grower to obtain the desired buffer layer characteristics, and three particular S-graded mismatch profiles are illustrated in Figure 6.27a.

In this work, we present the equilibrium misfit dislocation density and strain profiles for S-graded buffer layers of $In_xGa_{1-x}As$ on GaAs (001) substrates. These results can be used to design S-graded layers for the achievement of desired peak misfit dislocation density or MDFZ thicknesses. The equilibrium strain profiles obtained in this work can be used as the starting point for kinetic calculations, which will enable the determination of the threading dislocation densities in structures grown under non-equilibrium conditions. Though $In_xGa_{1-x}As$/GaAs (001) was used as a model material system, the present results may be readily extended to S-graded metamorphic device structures in other materials as well.

6.6.1.1. Equilibrium Relaxation in the InGaAs/GaAs Material System

It has been assumed that the S-graded buffer lattice matches the substrate (at $z = 0$) as well as the device layer to be grown on top of it (at $z = h$, where h is the thickness of the graded layer). We studied the equilibrium misfit dislocation density and strain profiles in S-graded layers of $In_xGa_{1-x}As$/GaAs (001) with total thickness of 0.5 μm. The standard deviation parameter was varied from 0.005 μm to 0.05 μm. The mean parameter was fixed at one-half the buffer thickness. The material parameters for GaAs were assumed to be $a = 0.56534nm$, $C_{11} = 118.4GPa$, and $C_{12} = 53.7GPa$; the corresponding values for $In_xGa_{1-x}As$ were assumed to be linear functions of the composition: $a = (0.56534 + x0.405)nm$, $C_{11} = (118.4 - x35.1)GPa$, and

$C_{12} = (53.7 - x8.4)GPa$. The starting composition for all layers was set to zero (lattice matched to the GaAs substrate) while the indium mole fraction at the top of the buffer layer was fixed at 0.035, 0.07, or 0.14, corresponding to $f_h \approx -0.25\%$, -0.50%, and -1.00%, respectively. Figure 6.27b and c show the calculated equilibrium misfit dislocation density and in-plane strain profiles, respectively, for 0.5 μm thick S-graded layers of $In_xGa_{1-x}As/GaAs$ (001) with the mismatch profiles of Figure 6.27a. The top indium mole fraction of 3.5% corresponds to a lattice mismatch of -0.25% and the standard deviation parameter values were chosen to be 0.01 μm, 0.02 μm, and 0.04 μm. All samples had a mean parameter of 0.25 μm.

Though the S-graded buffer layers exhibit rather complex behavior, three important general characteristics may be observed in the calculated results. First, there are MDFZs at the bottom of the S-graded layer (adjacent to the substrate interface) and the top of the layer (adjacent to the free surface). We define the edges of these MDFZs as z_1 and z_2; therefore, the thicknesses of the bottom and top MDFZs are z_1 and $h - z_1$, where h is the thickness of the graded layer. Second, there is a dislocated region containing misfit dislocations between the two MDFZs. This dislocated region has a thickness $z_2 - z_1$ and the misfit dislocation density within takes on a profile which is approximately Gaussian in character. Third, there is a nearly uniform in-plane strain in the top MDFZ. The equilibrium strain in this region can be relatively large, and for the cases studied here the calculated in-plane strain is more than twice the equilibrium strain in a 0.5 μm thick uniform layer of $In_{0.035}Ga_{0.965}As$ on GaAs (001). (For such a uniform heteroepitaxial layer the equilibrium in-plane strain is $\varepsilon_{\|} \approx -4 \times 10^{-4}$). These three general characteristics of S-graded layers are discussed physically below.

The existence of the interfacial MDFZ is expected on the basis of energy minimization. There is zero lattice mismatch at $z = 0$ so the introduction of misfit dislocations would increase both the strain energy and dislocation line energy, and misfit dislocations are not expected to form at the interface. There is a finite distance from the interface where the line energy cost of misfit dislocations is balanced by the strain energy they release in the growing film, and this dictates a finite thickness of misfit dislocation free material near the interface. The thickness of this interfacial MDFZ depends on the details of the lattice mismatch profile; that is, f_h, σ, and μ.

The formation of the surface MDFZ may also be understood from the point of view of energy minimization. Although this MDFZ exists in material with significant lattice mismatch, a significant portion of the strain is relaxed by defects in the underlying dislocated zone. Because of this, and because of the proximity to the surface, relatively little strain energy can be released by the introduction of misfit dislocations in this near-surface material. Line energies of misfit dislocations near the surface are not reduced significantly because of the weak logarithmic dependence of the line energy on the distance from the interface. Consequently, there is a finite thickness of material near the surface in which the introduction of misfit segments is not energetically favored. This is analogous to the behavior predicted and observed in linearly-graded layers.

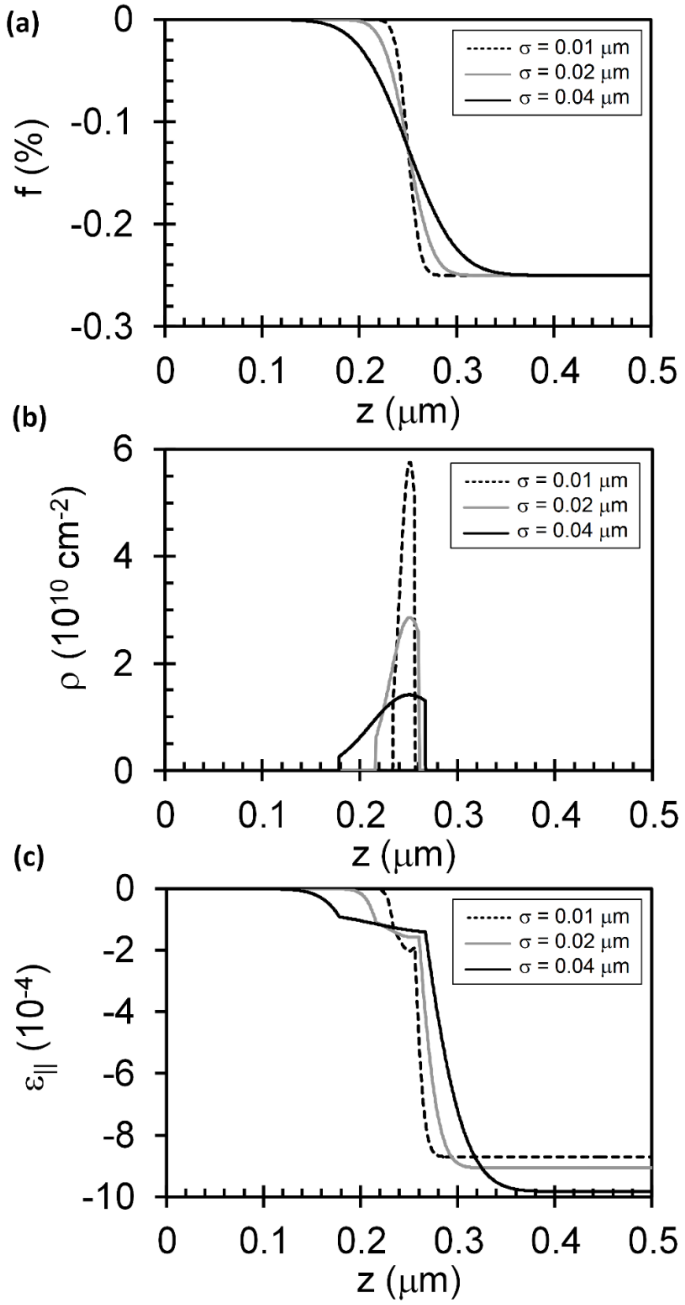

Figure 6.27. Characteristics of 0.5 μm-thick S-graded $In_xGa_{1-x}As$ layers on GaAs (001) substrates with $x_h = 0.035$ (corresponding to $f_h = -0.5\%$) with mean parameter $\mu = 0.25\ \mu m$ and standard deviation parameter values of $\sigma = 0.01\ \mu m$, $0.02\ \mu m$, and $0.04\ \mu m$. (a) Lattice mismatch; (b) misfit dislocation density; and (c) in-plane strain.

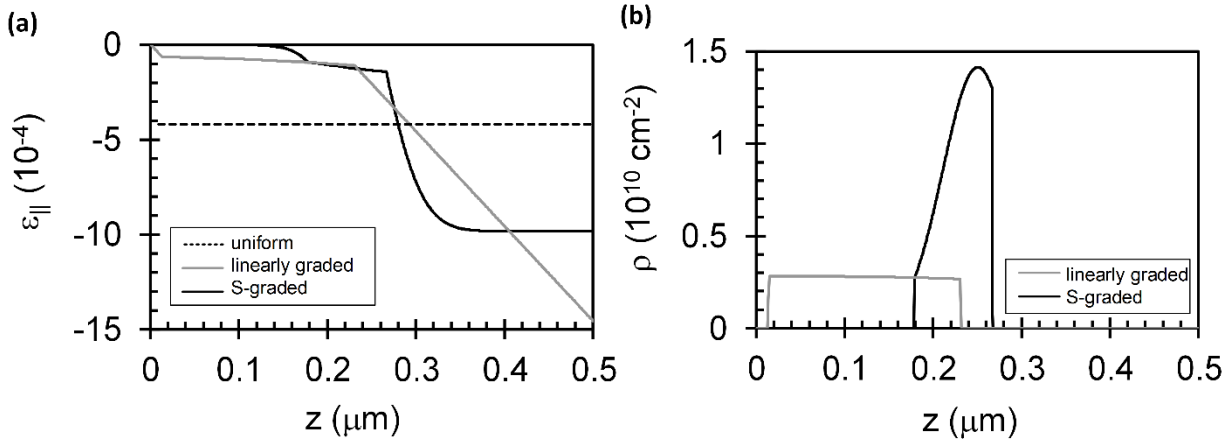

Figure 6.28. Comparison of 0.5 μm-thick $In_xGa_{1-x}As$ layers on GaAs (001) substrates, all with a top composition of $x_h = 0.035$, but with different compositional profiles. (a) In-plane strain profiles for layers with S-grading ($\sigma = 0.04\mu m$), linear grading, and uniform composition. (b) Misfit dislocation density profiles in layers with S-grading and linear grading.

The shape of the misfit defect density profile in the dislocated region is expected if it is assumed that the misfit dislocation density is just sufficient to relax the strain introduced by the compositional grading, as has been found to be the case in linearly-graded layers. If b' is the misfit-relieving component of the Burgers vector, then the areal density of misfit dislocations will be $\rho = |df/dz|/b'$. For the S-grading compositional profile considered here, $|df/dz|$ is Gaussian in character, but the profile is truncated by the existence of the MDFZs as explained above.

Heteroepitaxial layers are not deposited in equilibrium, and tend to exhibit fewer misfit dislocations than predicted by equilibrium models. Nonetheless we can expect S-graded buffer layers to exhibit the general features outlined here, including the two MDFZs sandwiching a dislocated region. These general characteristics of S-graded buffer layers are expected to promote longer misfit segments and improve their performance in threading dislocation reduction as

follows. (i) As in the linearly-graded layer, new misfit dislocations are introduced at the top of the growing material where there are relatively few existing dislocations, and the reduction of the dislocation-dislocation interactions that give rise to pinning or decreased dislocation mobility allow the uninhibited glide of dislocations to form longer misfit segments. Improved performance is expected in the S-graded structure due to the wide interfacial MDFZ and the tapered misfit dislocation density above it. (ii) The misfit dislocation free zone (MDFZ) near the surface prevents the introduction of new dislocation loops near the surface in the final stages of buffer layer growth, and instead existing misfit dislocations are allowed to grow in length by glide. The S-graded buffer can have a thicker surface MDFZ than the linearly-graded layer, which is preserved even after the growth of a top device layer, and which offers improved performance. (iii) A graded layer has increased residual strain in its surface misfit dislocation free zone (MDFZ) relative to a uniform buffer, which can promote higher effective stresses and misfit dislocation velocities. In the S-graded layer, the average strain in the top MDFZ is greater than in the linearly-graded layer, which is expected to improve the threading dislocation reduction performance.

Some of the potential advantages of S-graded layers can be understood quantitatively with the aid of Figure 6.28a and b. Figure 6.28a compares the equilibrium in-plane strain profiles for S-graded (with $\sigma = 0.04\mu m$), linearly-graded, and uniform layers of $In_xGa_{1-x}As$ on GaAs (001), all with thickness 0.5 μm and a top indium composition of $x = 0.035$. Both the linearly-graded and S-graded structures exhibit enhanced surface strain compared to the uniform layer. Although the linearly-graded layer presents the highest strain at its surface, the S-graded case provides a thicker zone of enhanced strain which can provide more benefit in terms of increasing the lengths of misfit dislocations and reducing the threading density. The equilibrium misfit dislocation density profiles

for the S-graded and linearly-graded buffers are compared in Figure 6.28b. Whereas S-grading gives rise to thick MDFZs at the bottom and top of the layer, the linear layer has the undesirable characteristic of a high misfit dislocation density near the substrate interface. The S-graded layer shows a higher peak misfit dislocation density than the linearly-graded film, but this peak misfit dislocation density may be tailored by the choice of the standard deviation parameter.

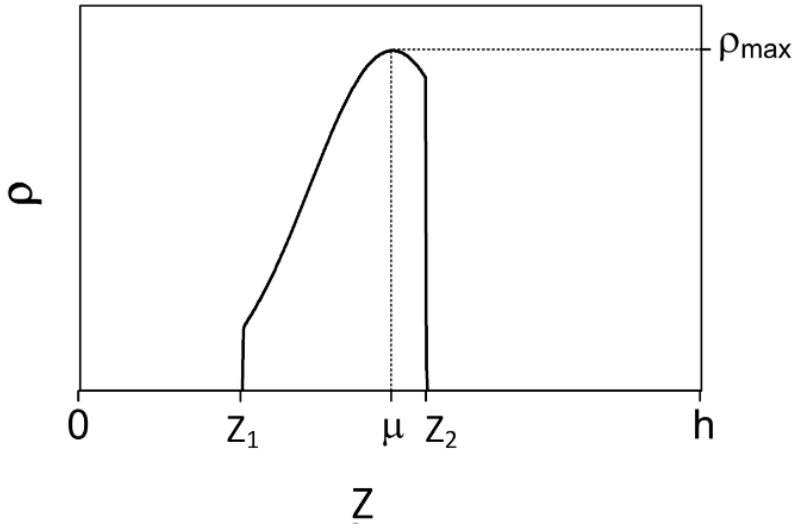

Figure 6.29. Misfit dislocation density profile in an S-graded layer is a truncated Gaussian, with maximum value ρ_{max} occurring at $z = \mu$ and with boundary points z_1 and z_2.

The general behavior of the misfit dislocation density in an S-graded layer, as described above, is reiterated in Figure 6.29. The truncated Gaussian profile reaches a peak dislocation density of ρ_{max} at $z = \mu$. The edges of the MDFZs are at z_1 and z_2; that is, the MDFZ adjacent to the substrate has a thickness equal to z_1 while the MDFZ adjacent to the surface has a thickness of $h - z_2$, where h is the layer thickness.

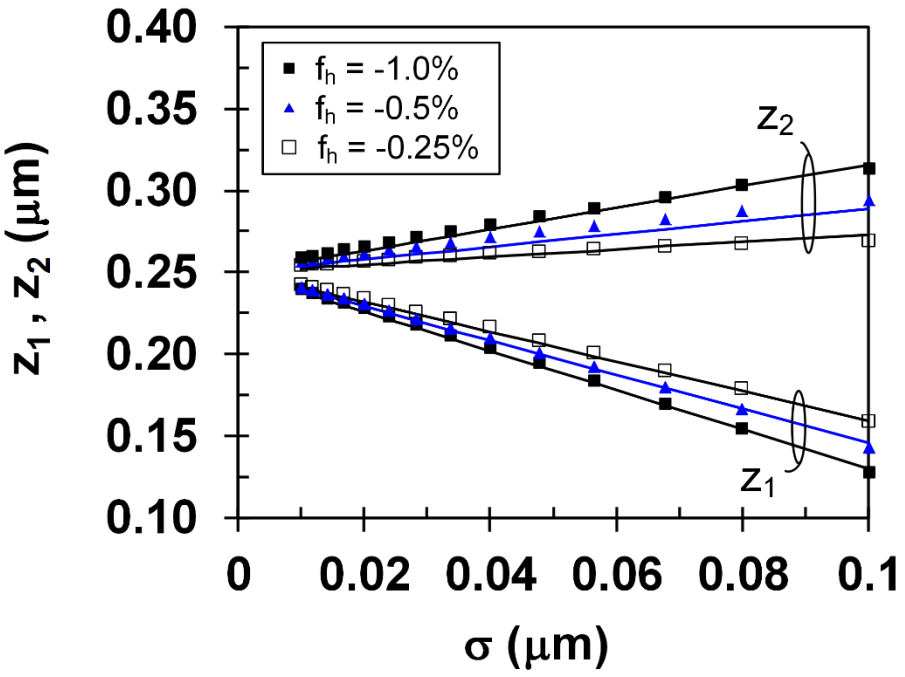

Figure 6.30. Boundary points z_1 and z_2 of the dislocated region for 0.5 μm-thick S-graded $In_xGa_{1-x}As$ layers on GaAs (001) substrates with mean parameter $\mu = 0.25\ \mu m$ and top lattice mismatch $f = -1.00\%$, -0.50%, and -0.25%.

Because of their importance we have studied the widths of the MDFZs in 0.5 μm-thick S-graded layers of $In_xGa_{1-x}As$ / GaAs (001) with top indium composition of 0.035, 0.07, and 0.14, corresponding to $f_h \approx -0.25\%$, -0.50%, and -1.00%, respectively. The standard deviation parameter was varied from 0.005 μm to 0.05 μm. Figure 6.30 shows the values of z_1 and z_2 for these S-graded structures, and it is evident that both vary in approximately linear fashion with the standard deviation parameter σ. We note that z_1 and z_2 may be calculated approximately using the phenomenological models

$$z_1 \approx \mu - \sigma\left(\frac{|f_h|}{f_{01}}\right)^{n_1} \qquad \textbf{(6.54)}$$

and

$$z_2 \approx \mu + \sigma\left(\frac{|f_h|}{f_{02}}\right)^{n_2}, \qquad \textbf{(6.55)}$$

where $f_{01} = 0.0035$, $n_1 = 0.2$, $f_{02} = 0.0150$, $n_2 = 0.75$. The curves in Figure 6.30 were calculated using (6) and (7) for comparison to the points with symbols, which were found by energy minimization calculations. The thickness of the dislocated region, $z_2 - z_1$, is independent of the total thickness as long as $h > 6\sigma$, and scales directly with the standard deviation parameter:

$$z_2 - z_1 \approx \sigma\left[\left(\frac{|f_h|}{f_{01}}\right)^{n_1} + \left(\frac{|f_h|}{f_{02}}\right)^{n_2}\right]. \qquad \textbf{(6.56)}$$

It should be noted that the phenomenological models given in (6) and (7) were developed for S-graded layers of $In_xGa_{1-x}As$ / GaAs (001) by fitting the numerical energy minimization results. In the general case, exact equations for z_1 and z_2 should be derived by minimization of energy, for applicability to other material systems.

Although the detailed behavior of S-graded buffer layers is rather complex, it is possible to develop approximate models for the strain and dislocation density profiles based on reasonable simplifying assumptions, and these quantitative models may be used to design S-graded device structures to take advantage of their desirable properties.

First, we consider the strain profile. In the dislocated region ($z_1 \le z \le z_2$) the in-plane strain is approximately constant so the misfit dislocation density is just sufficient to relax the strain due to the grading in the layer;

$$\rho = \frac{1}{b'}\left|\frac{df}{dz}\right|, \tag{6.57}$$

where b' is the misfit-relieving component of the Burgers vector in the plane of the interface. Therefore, the misfit dislocation density profile is

$$\rho = \begin{cases} 0, & z < z_1; \\ \dfrac{f_h}{b'\sigma\sqrt{2\pi}} \exp\left[\dfrac{-(z-\mu)^2}{\sigma^2/2}\right], & z_1 \le z \le z_2; \text{ and} \\ 0, & z > z_2. \end{cases} \tag{6.58}$$

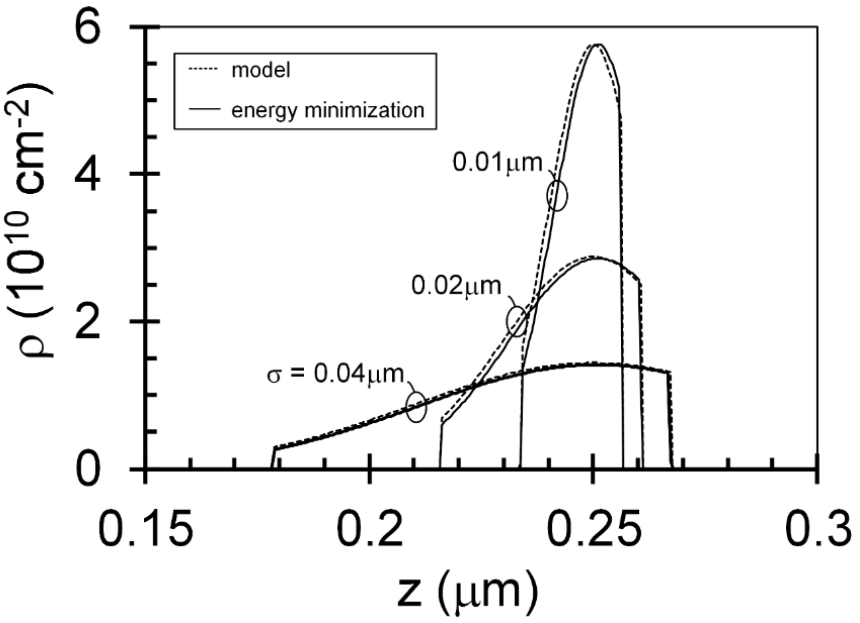

Figure 6.31. Misfit dislocation density profiles for 0.5 μm-thick S-graded $In_xGa_{1-x}As$ layers on GaAs (001) substrates with $x_h = 0.035$ (corresponding to $f_h = -0.5\%$) with mean parameter $\mu = 0.25\ \mu m$ and standard deviation parameter values of $\sigma = 0.01\ \mu m$, $0.02\ \mu m$, and $0.04\ \mu m$. The solid curves were determined by numerical energy minimization calculations and the dashed curves were obtained using the model given in Equation 6.60.

The resulting misfit dislocation density profile is a truncated Gaussian, with the peak misfit dislocation density of

$$\rho_{\max} = \frac{f_h}{b'\sigma\sqrt{2\pi}} \qquad \textbf{(6.59)}$$

occurring at $z = \mu$. The peak misfit dislocation density scales inversely with the standard deviation parameter, so the design of the S-graded layer involves a tradeoff between the width of the dislocated region and the peak dislocation density.

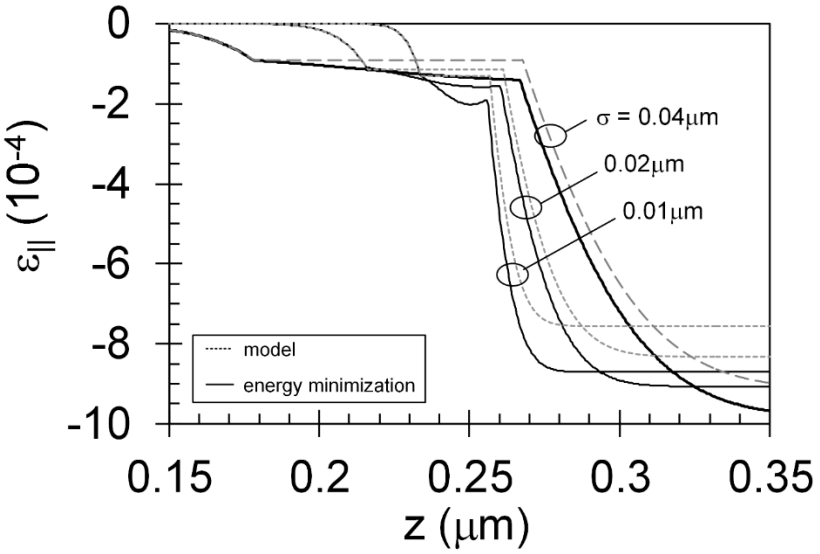

Figure 6.32. In-plane strain profiles for 0.5 μm-thick S-graded $In_xGa_{1-x}As$ layers on GaAs (001) substrates with $x_h = 0.035$ (corresponding to $f_h = -0.5\%$) with mean parameter $\mu = 0.25\ \mu m$ and standard deviation parameter values of $\sigma = 0.01\ \mu m$, $0.02\ \mu m$, and $0.04\ \mu m$. The solid curves were determined by numerical energy minimization calculations and the dashed curves were obtained using the model given in Equation 6.63.

Consider next the equilibrium in-plane strain. The bottom MDFZ ($z \le z_1$) is coherently strained so the in-plane strain is equal to the lattice mismatch:

$$\varepsilon_{\|} = \frac{f_h}{2}\left[-erf\left(\frac{\mu - z}{\sigma\sqrt{2}}\right) + erf\left(\frac{\mu}{\sigma\sqrt{2}}\right)\right]; \qquad z \le z_1 \qquad \textbf{(6.60)}$$

and the strain at $z = z_1$ is $\frac{f_h}{2}\left[-erf\left(\frac{\mu - z_1}{\sigma\sqrt{2}}\right) + erf\left(\frac{\mu}{\sigma\sqrt{2}}\right)\right]$. For $z_1 \le z \le z_2$ (the dislocated layer) the in-plane strain is approximately constant at this value, assuming the misfit dislocation density is just enough to relax the strain associated with the grading. For $z > z_2$ there are no misfit dislocations so $d\varepsilon_{\|} / dz = df / dz$. The equilibrium in-plane strain profile in the partially-relaxed S-graded layer is therefore

$$\varepsilon_{\|} = \begin{cases} \left(\frac{f_h}{2}\right)\left[-erf\left(\frac{\mu - z}{\sigma\sqrt{2}}\right) + erf\left(\frac{\mu}{\sigma\sqrt{2}}\right)\right], & z < z_1; \\ \left(\frac{f_h}{2}\right)\left[-erf\left(\frac{\mu - z_1}{\sigma\sqrt{2}}\right) + erf\left(\frac{\mu}{\sigma\sqrt{2}}\right)\right], & z_1 \le z \le z_2; \text{ and} \\ \left(\frac{f_h}{2}\right)\left[erf\left(\frac{z - \mu}{\sigma\sqrt{2}}\right) - erf\left(\frac{z_2 - \mu}{\sigma\sqrt{2}}\right) - erf\left(\frac{\mu - z_1}{\sigma\sqrt{2}}\right) + erf\left(\frac{\mu}{\sigma\sqrt{2}}\right)\right], & z > z_2. \end{cases} \quad \textbf{(6.61)}$$

The model described by Equations 6.48 and 6.61 may be applied to the design of S-graded structures if expressions for z_1 and z_2 are known. In practice, we may use either analytical expressions for z_1 and z_2, determined by minimizing the sum of the strain and dislocation line energy with respect to each, or simpler, phenomenological expressions for z_1 and z_2 given above. Here we have adopted the latter approach.

In Figure 6.31 we have compared the approximate model (10) to the results of detailed numerical dislocation density calculations, for 0.5 μm-thick S-graded $In_xGa_{1-x}As/GaAs$ (001) layers having $f_h = -0.005$ and $\sigma = 0.01\,\mu m$, $0.02\,\mu m$, and $0.04\,\mu m$. For the cases studied here, the approximate model predicts the misfit dislocation density with better than 5% accuracy, and this indicates that it was reasonable to assume the misfit dislocation density is just sufficient to relieve the strain introduced by the grading.

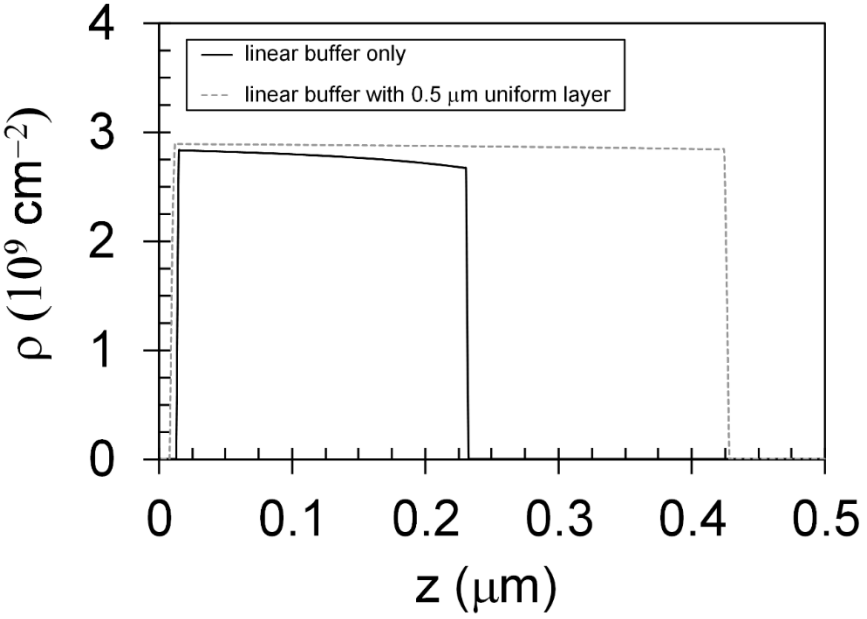

Figure 6.33. Behavior the linearly-graded buffer layer with top loading by a uniform device layer. Misfit dislocation density profiles for 0.5 μm-thick linearly-graded $In_xGa_{1-x}As$ layers on GaAs (001) substrate with $x_h = 0.035$ and no uniform layer on top (solid black curve) and with a 0.5 μm-thick uniform layer on top (dashed gray curve). The composition of the uniform layer is $In_{0.035}Ga_{0.965}As$.

In Figure 6.32 we have compared the approximate model (13) to the detailed numerical strain calculations, for the same set of S-graded layers with $\sigma = 0.01\ \mu m$, $0.02\ \mu m$, and $0.04\ \mu m$. The approximate model underestimates the surface strain somewhat, because of the slight variation in the strain in the dislocated region. All the same the model has sufficient accuracy to make it useful in the design of S-graded buffer layers.

Because the intended application is for device buffer layers, we compared the equilibrium dislocation densities in linearly-graded and S-graded structures, with and without a uniform device layer deposited on top. Figure 6.33 illustrates the misfit dislocation density in a 0.5 μm-thick linearly-graded layer of $In_xGa_{1-x}As$, with the indium mole fraction graded from zero to 3.5%, both

with and without a uniform 0.5 μm-thick layer of $In_{0.035}Ga_{0.965}As$ on top. The addition of the uniform layer (device layer) on top of the buffer increases the width of the dislocated region from 218 nm to 418 nm – approximately doubling the dislocated thickness. The top MDFZ in the buffer layer is nearly eliminated because the increase of the dislocated thickness is mostly in the top MDFZ. The behavior is quite different in the case of the S-graded buffer, shown in Figure 6.34, where a ~ 0.2 μm top MDFZ remains even after the growth of a 0.5 μm uniform top layer. Therefore, the S-graded buffer provides superior performance compared to the linear buffer in terms of maintaining a wide MDFZ adjacent to the device layer.

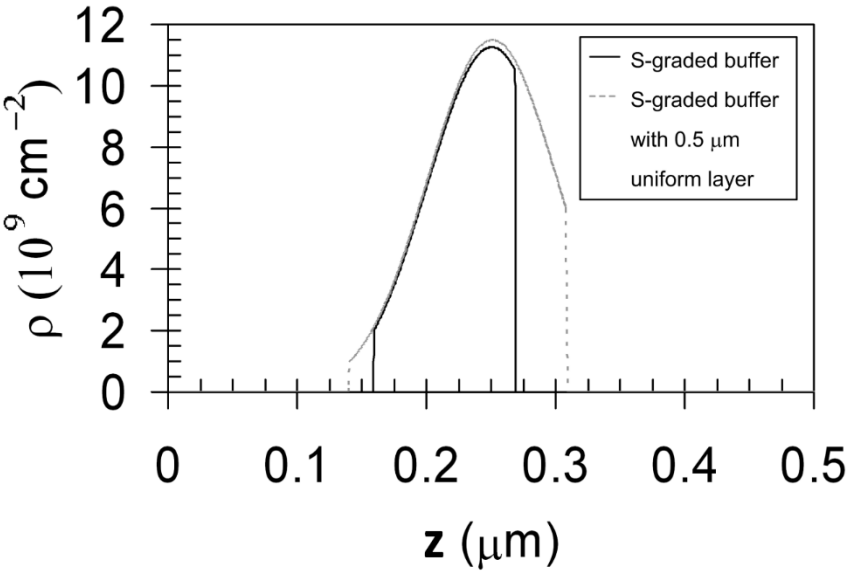

Figure 6.34. Behavior the S-graded buffer layer with top loading by a uniform device layer. Misfit dislocation density profiles for a 0.5 μm-thick S-graded $In_xGa_{1-x}As$ layers on GaAs (001) substrate with $x_h = 0.035$ and no uniform layer on top (solid black curve) and with a 0.5 μm-thick uniform layer on top (gray dashed curve). The composition of the uniform layer is $In_{0.035}Ga_{0.965}As$.

In conclusion, we have studied the equilibrium strain and misfit dislocation density profiles for "S-graded" buffer layers of $In_xGa_{1-x}As$ on GaAs (001) substrates in which the compositional profile follows a normal cumulative distribution function. We show that the S-graded layer exhibits misfit dislocation free regions (MDFZs) near the substrate interface and the free surface (or device interface). The standard deviation parameter may be selected to achieve a particular peak misfit dislocation density, while the mean parameter and total buffer thickness may be designed to achieve the desired MDFZ thicknesses adjacent to the substrate and device layer interfaces. The S-graded buffer layer exhibits two potential advantages compared to the linearly-graded buffer layers often used in metamorphic device layers. First, the ability to design the peak misfit dislocation density and MDFZ thicknesses is expected to enable minimization of the density of electronically active threading dislocations at the top surface, and second, the dislocation density profile in the S-graded layer is less susceptible to loading by the growth of a uniform device layer on top, and avoids the penetration of a dislocated region into the device layer itself.

6.6.2. Design of S-Graded Buffer Layers for Metamorphic ZnSySe1-y/GaAs (001) Semiconductor Devices

We present design equations for error function (or "S-graded") graded buffers for use in accommodating lattice mismatch of heteroepitaxial semiconductor devices. In an S-graded metamorphic buffer layer the composition and lattice mismatch profiles follow a normal cumulative distribution function. Minimum energy calculations suggest that the S-graded profile may be beneficial for the control of defect densities in lattice-mismatched devices because they have several characteristics which enhance the mobility and glide velocities of dislocations, thereby promoting long misfit segments with relatively few threading arms. First, there is a misfit

dislocation free zone (MDFZ) adjacent to the interface which avoids dislocation pinning defects associated with substrate defects. Second, there is another misfit dislocation free zone near the surface, which reduces pinning interactions near the device layer which will be grown on top. Third, there is a large built-in strain in the top MDFZ which enhances the glide of dislocations to sweep out threading arms. In this study, we present approximate design equations for the widths of the misfit dislocation free zones, the built-in strain, and peak misfit dislocation density for the general S-graded semiconductor with diamond or zinc blende crystal structure and (001) orientation, and show that these design equations are in fair agreement with detailed numerical energy minimization calculations for ZnS_ySe_{1-y}/GaAs (001) heterostructures.

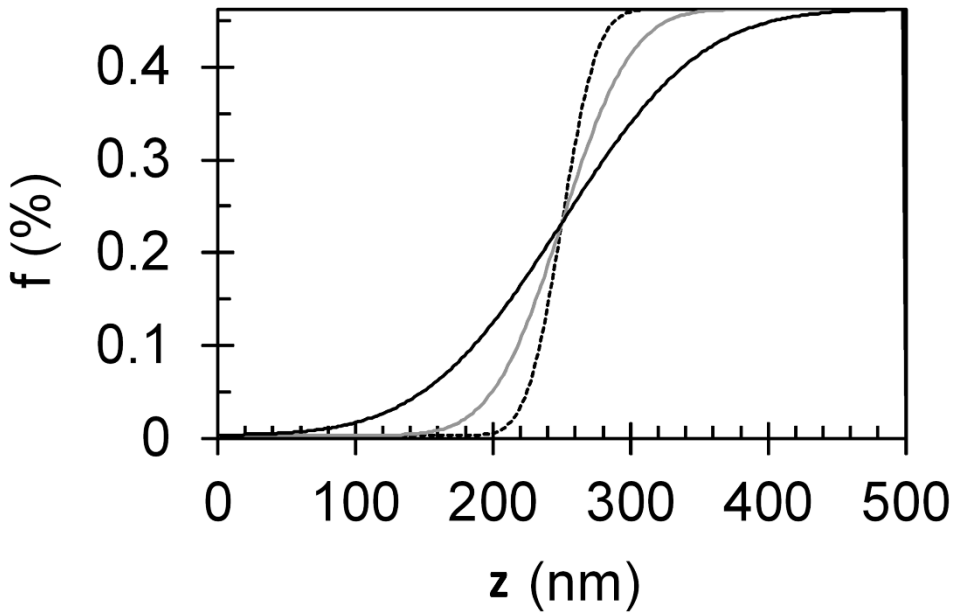

Figure 6.35. Lattice mismatch profiles for 500 nm thick S-graded ZnS_ySe_{1-y} / GaAs (001) layers with $f_h = 0.0046$, $\mu = 250$ nm, and $\sigma = 20$, 40, and 80 nm. The sulfur composition in the S-graded layer is varied from 6% (lattice matched to GaAs) at the interface to 16% at the surface.

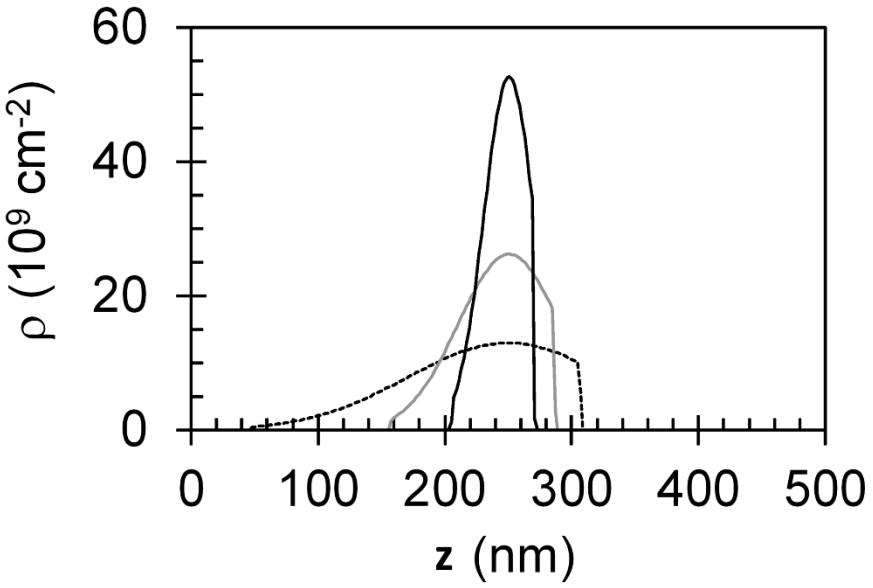

Figure 6.36. Equilibrium misfit dislocation density profiles for 500 nm thick S-graded ZnS_ySe_{1-y} / GaAs (001) layers with $f_h = 0.0046$, $\mu = 250$ nm, and $\sigma = 20$, 40, and 80 nm. The sulfur composition in the S-graded layer is varied from 6% (lattice matched to GaAs) at the interface to 16% at the surface.

The S-graded buffer can have a thicker surface MDFZ than the linearly graded layer, which is preserved even after the growth of a top device layer, and which offers improved performance in terms of increasing the lengths of misfit dislocations and reducing the threading density. This was observed in our previous study and it is possible to develop approximate models for the strain and dislocation density profiles based on reasonable simplifying assumptions and these quantitative models may be used to design S-graded device structures to take advantage of their desirable properties.

Although numerical energy minimization calculations are generally applicable to the analysis of any graded structure which can be approximated by a series of laminae, their use is not well suited to SG-SAL design because of the indirect nature of the approach. In this work, we

present approximate design equations for S-graded strain accommodation layers and demonstrate fair agreement between these design relationships and detailed energy minimization calculations for S-graded ZnS_ySe_{1-y}/GaAs (001) heterostructures. Metamorphic ZnS_ySe_{1-y} buffer layers are of interest for use in ZnCdSSe/ZnMgSSe emitters and modulators for the blue/green portion of the visible spectrum. Control of the threading dislocation density in these devices is critical to their performance and motivates the use of optimized buffer layers for reduced defect density at the buffer surface where the device layers will be deposited. Up to this time, most of the metamorphic buffer layers used in this material system have employed uniform or linearly-graded composition, and little work has been done to explore non-linearly graded buffer layers. In the ZnS_ySe_{1-y} S-graded buffer, the standard deviation parameter may be selected to achieve a peak equilibrium misfit dislocation density, while the mean parameter and total buffer thickness may be designed to achieve the desired MDFZ thicknesses adjacent to the substrate and device layer interfaces. In previous work, phenomenological models were developed for S-graded layers of $In_xGa_{1-x}As$/GaAs (001) by fitting the numerical energy minimization results. Here we show that, in the general case, exact equations for the widths of the edges of the MDFZs can be derived by minimization of energy, and we apply these to the ZnS_ySe_{1-y} system for the sake of specificity.

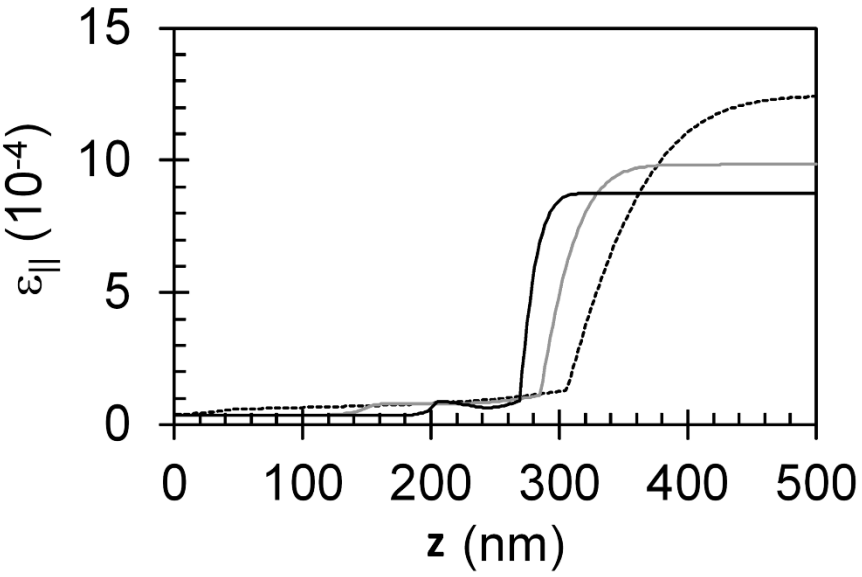

Figure 6.37. Equilibrium in-plane strain for 500 nm thick S-graded ZnS_ySe_{1-y} / GaAs (001) layers with $f_h = 0.0046$, $\mu = 250$ nm, and $\sigma = 20$, 40, and 80 nm. The sulfur composition in the S-graded layer is varied from 6% (lattice matched to GaAs) at the interface to16% at the surface.

6.6.2.1. Equilibrium Strain and Dislocation Density Profiles in the SG-SAL

Three particular S-graded mismatch profiles are illustrated in Figure 6.35 for 500 nm thick ZnS_ySe_{1-y} layers on GaAs (001) with $f_h = 0.0046$, $\mu = 250$ nm, and $\sigma = 20$, 40, and 80 nm. Figure 6.36 illustrates the equilibrium misfit dislocation density profiles for 500 nm thick S-graded ZnS_ySe_{1-y} / GaAs (001) layers with $f_h = 0.0046$, $\mu = 250$ nm, and $\sigma = 20$, 40, and 80 nm. The misfit dislocation density profile is a truncated Gaussian located between two MDFZs which are adjacent to the substrate interface and the free surface. The interfacial MDFZ thickness is 203 nm, 155 nm, and 46 nm for $\sigma = 20$, 40, and 80 nm, respectively. The thickness of the surface MDFZ is 227 nm, 211 nm, and 191 nm for $\sigma = 20$, 40, and 80 nm, respectively.

The misfit dislocation density profile between the two MDFZs has approximately the shape of a truncated Gaussian distribution. This is expected if the density of misfit dislocations is just sufficient to relax the strain introduced by the compositional grading, $\rho = |df/dy|/b'$, where b' is the projection of the misfit-relieving component of the Burgers vector in the interface. This leads to a peak misfit dislocation density which is inversely proportional to the standard deviation parameter, and this is consistent with the results of the minimum energy calculations shown in Figure 6.36, for which the peak misfit dislocation density is 53, 26, and 13 x 10^9 cm^{-2} for $\sigma = 20$, 40, and 80 nm, respectively.

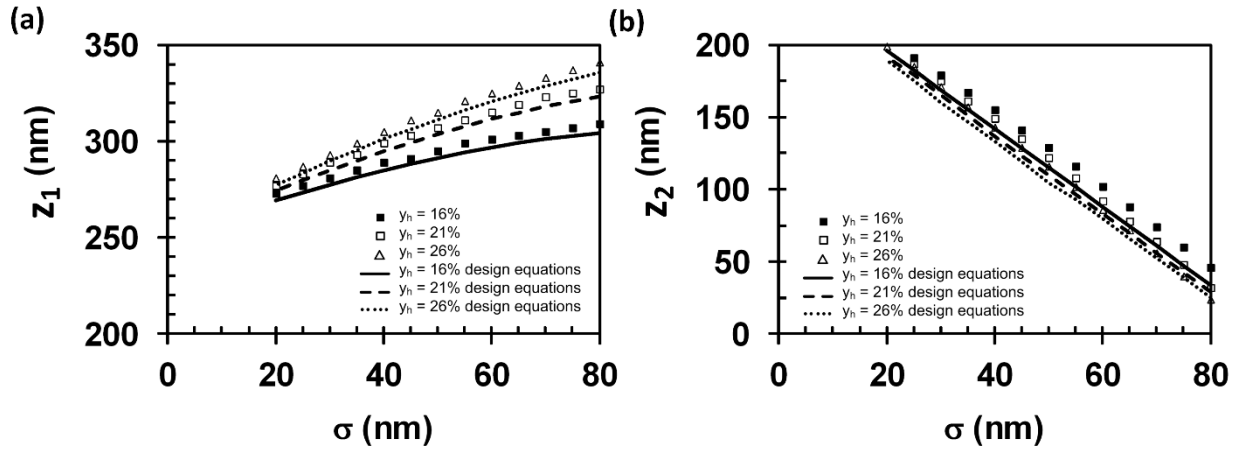

Figure 6.38. (a) Thickness of the interfacial MDFZ, z_1, for 500 nm thick S-graded ZnS_ySe_{1-y} / GaAs (001) layers with μ = 250 nm and a maximum sulfur composition equal to 16%, 21%, and 26%. (b) Distance of the edge of the surface MDFZ from the interface, z_2, for 500 nm thick S-graded ZnS_ySe_{1-y} / GaAs (001) layers with μ = 250 nm and a maximum sulfur composition equal to 16%, 21%, and 26%. The results shown with symbols were found using detailed energy minimization calculations while the solid, dashed, and dotted curves were obtained by the approximate design equations.

Figure 6.37 shows the equilibrium in-plane strain profiles for 500 nm thick S-graded ZnS_ySe_{1-y} / GaAs (001) layers with $y_0 = 0.06$, $y_h = 0.16$, and $\sigma = 20$, 40, and 80 nm. The S-

graded layers exhibit a large built-in strain in the surface MDFZ which can aid in sweeping out threading dislocations prior to the growth of the device structure on top. The in-plane strain is relatively constant in the surface MDFZ with a value of 8.1, 9.3, and 12.7 x 10^{-4} for the cases of $\sigma = 20$, 40, and 80 nm, respectively. These built-in strains are considerably greater than the equilibrium in-plane strain for a uniform layer of $ZnS_{0.16}Se_{0.84}$ on GaAs (001) having the same thickness of 500 nm, which is ~ 4 x 10^{-4}. Therefore, dislocation glide velocities can be several times larger in the surface MDFZ of the SG-SAL compared to a uniform buffer layer of comparable thickness.

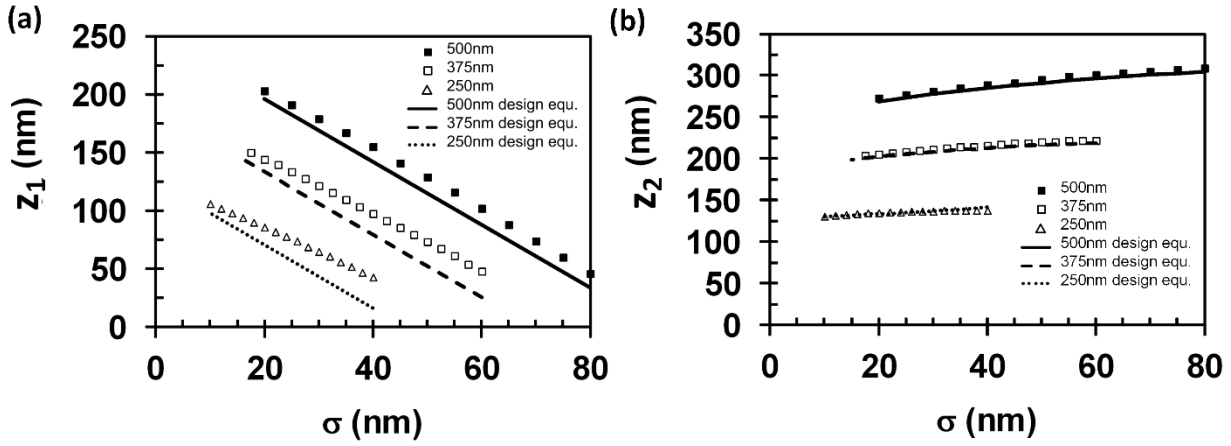

Figure 6.39.(a) Thickness of the interfacial MDFZ, z_1, for S-graded ZnS_ySe_{1-y} / GaAs (001) layers with 16% maximum sulfur composition and thickness of 500 nm, 375 nm, and 250 nm. (b) Distance of the edge of the surface MDFZ from the interface, z_2, for S-graded ZnS_ySe_{1-y} / GaAs (001) layers with 16% maximum sulfur composition and thickness of 500 nm, 375 nm, and 250 nm. The mean parameter μ was set to (250 nm, 187.5 nm, and 125 nm, respectively. The results shown with symbols were found using detailed energy minimization calculations while the solid, dashed, and dotted curves were obtained by the approximate design equations.

The results of Figure 6.36 and Figure 6.37 illustrate that the thicknesses of the MDFZs, the peak misfit dislocation density, and the built-in strain of the top MDFZ may be controlled by the

choice of the lattice mismatch profile for the SG-SAL, that is f_h, σ, and μ. In the following two sections, we present an equilibrium model for the SG-SAL and from this model we develop design equations linking the crystal growth parameters f_h, σ, and μ to the MDFZ thicknesses, the peak misfit dislocation density, and the built-in strain.

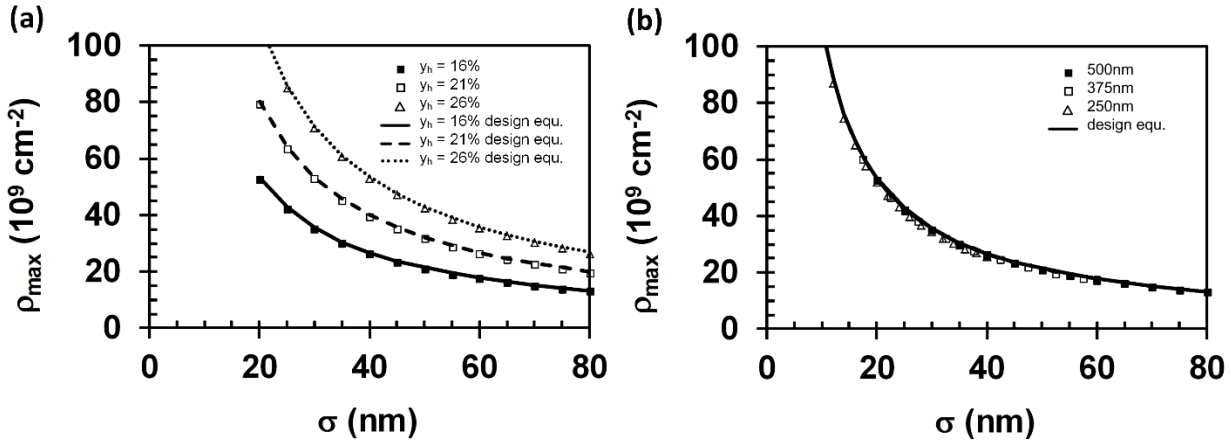

Figure 6.40. (a) Peak misfit dislocation density for 500 nm thick S-graded ZnSySe1-y / GaAs (001) layers with μ = 250 nm and a maximum sulfur composition of 16%, 21%, and 26%. (b) Peak misfit dislocation density for S-graded ZnSySe1-y / GaAs (001) layers with 16% maximum sulfur composition and thickness of 500 nm, 375 nm, and 250 nm. The mean parameter μ was set to 250 nm, 187.5 nm, and 125 nm, respectively. The results shown with symbols were found using detailed energy minimization calculations while the solid, dashed, and dotted curves were obtained by the approximate design equation.

6.6.2.2. Equilibrium Model for the Dislocation Density and Strain profiles in S-Graded Strain Accommodation Layers

In order to develop SG-SAL design equations we summarize approximate models for the equilibrium misfit dislocation density and strain profiles based on the discussion in the previous section and developed as a refinement of the model previously presented in [16]. If the edges of the interfacial and surface MDFZs are located at distances of z_1 and z_2 from the substrate

interface, respectively, and if the misfit dislocation density in the middle region ($z_1 \le z \le z_2$) is just sufficient to relax the strain associated with the compositional grading, then in this region

$$\rho = \frac{1}{b'}\left|\frac{df}{dz}\right|, \qquad \textbf{(6.62)}$$

where b' is the misfit-relieving component of the Burgers vector in the plane of the interface. Therefore, the misfit dislocation density profile is

$$\rho = \begin{cases} 0, & z < z_1; \\ \dfrac{f_h}{b'\sigma\sqrt{2\pi}} \exp\left[\dfrac{-(z-\mu)^2}{2\sigma^2}\right], & z_1 \le z \le z_2; \text{ and} \\ 0, & z > z_2, \end{cases} \qquad \textbf{(6.63)}$$

and the resulting misfit dislocation density profile is a truncated Gaussian.

With the approximate misfit dislocation density given in Equation 6.66 we can find the in-plane strain distribution. The interfacial MDFZ ($z \le z_1$) is coherently strained so the in-plane strain is equal to the lattice mismatch:

$$\varepsilon_{\parallel} = \frac{f_h}{2}\left[-erf\left(\frac{\mu - z}{\sigma\sqrt{2}}\right) + erf\left(\frac{\mu}{\sigma\sqrt{2}}\right)\right]; \qquad z \le z_1 \qquad \textbf{(6.64)}$$

and at the edge of the interfacial MDFZ

$$\varepsilon_{\parallel} = \frac{f_h}{2}\left[-erf\left(\frac{\mu - z_1}{\sigma\sqrt{2}}\right) + erf\left(\frac{\mu}{\sigma\sqrt{2}}\right)\right]; \qquad z = z_1 . \qquad \textbf{(6.65)}$$

In an approximate model, we developed previously in [35], we assumed constant strain in the dislocated region ($z_1 \le z \le z_2$) and the resulting model equations provide fair predictions of the equilibrium strain when compared to the results of detailed numerical calculations. Here we make use of a refined model in which the strain is considered to increase linearly in the dislocated region.

This linear variation, introduced by a factor of (z/z_1), comes about because of the dislocation line energy dependence on distance from the free surface. For $z > z_2$ there are no misfit dislocations so $d\varepsilon_{\|}/dz = df/dz$. Therefore, according to the refined model, the equilibrium strain profile in the S-graded layer is given by

$$\varepsilon_{\|} = \begin{cases} \left(\frac{f_h}{2}\right)\left[-erf\left(\frac{\mu - z}{\sigma\sqrt{2}}\right) + erf\left(\frac{\mu}{\sigma\sqrt{2}}\right)\right], & z < z_1; \\ \left(\frac{f_h}{2}\right)\left[-\frac{z}{z_1}erf\left(\frac{\mu - z_1}{\sigma\sqrt{2}}\right) + \frac{z}{z_1}erf\left(\frac{\mu}{\sigma\sqrt{2}}\right)\right], & z_1 \le z \le z_2; \text{ and} \\ \left(\frac{f_h}{2}\right)\left[erf\left(\frac{z - \mu}{\sigma\sqrt{2}}\right) - erf\left(\frac{z_2 - \mu}{\sigma\sqrt{2}}\right) - \frac{z_2}{z_1}erf\left(\frac{\mu - z_1}{\sigma\sqrt{2}}\right) + \frac{z_2}{z_1}erf\left(\frac{\mu}{\sigma\sqrt{2}}\right)\right], & z > z_2. \end{cases} \quad \textbf{(6.66)}$$

Based on this refined equilibrium model we have developed general design equations for an SG-SAL.

6.6.2.3. Design Equations for S-Graded Strain Accommodation Layers

In the design of an SG-SAL, the most important characteristics to consider are the widths of the MDFZs, the peak misfit dislocation density, and the built-in strain in the surface MDFZ. In this section, we develop design equations for these characteristics based on energy minimization and the model described above.

First, we consider the widths of the MDFZs, with edges located at distances of z_1 and z_2 from the interface. The thickness of the interfacial MDFZ is z_1 and the thickness of the surface MDFZ is $h - z_2$, where h is the total thickness of the strain accommodation layer. Therefore, the problem reduces to one of finding equilibrium values of z_1 and z_2, in other words, those values

which minimize the sum of the strain energy and dislocation line energy per unit area. The dislocation line energy per unit area is

$$\begin{aligned} E_d &= 2\int_{z_1}^{z_2} F_d(z)\rho_A(z)dz \\ &= 2\int_{y_1}^{y_2}\left\{\frac{Gb^2(1-\nu\cos^2\alpha)}{4\pi(1-\nu)}\left[\ln\left(\frac{h-z}{b}\right)+1\right]\right\}\left\{\frac{f_h}{b'\sigma\sqrt{2\pi}}\exp\left[-\frac{(z-\mu)^2}{2\sigma^2}\right]\right\}dz\,, \\ &= \frac{Gbf_h(1-\nu\cos^2\alpha)}{\sigma\sin\alpha\cos\lambda(1-\nu)(2\pi)^{3/2}}\int_{z_1}^{z_2}\left[\ln\left(\frac{h-z}{b}\right)+1\right]\exp\left[-\frac{(z-\mu)^2}{2\sigma^2}\right]dz \end{aligned} \quad \textbf{(6.67)}$$

and the strain energy per unit area is

$$\begin{aligned} E_\varepsilon &= Y\int_0^h \varepsilon_{\|}^2(z)dz \\ &= \frac{Yf_h^2}{4}\int_0^{z_1}\left[-erf\left(\frac{\mu-z}{\sigma\sqrt{2}}\right)+erf\left(\frac{\mu}{\sigma\sqrt{2}}\right)\right]^2 dz + \frac{Yf_h^2}{4}\int_{z_1}^{z_2}\left[-\frac{z}{z_1}erf\left(\frac{\mu-z_1}{\sigma\sqrt{2}}\right)+\frac{z}{z_1}erf\left(\frac{\mu}{\sigma\sqrt{2}}\right)\right]^2 dz \\ &+ \frac{Yf_h^2}{4}\int_{z_2}^{h}\left[erf\left(\frac{z-\mu}{\sigma\sqrt{2}}\right)-erf\left(\frac{z_2-\mu}{\sigma\sqrt{2}}\right)-\frac{z_2}{z_1}erf\left(\frac{\mu-z_1}{\sigma\sqrt{2}}\right)+\frac{z_2}{z_1}erf\left(\frac{\mu}{\sigma\sqrt{2}}\right)\right]^2 dz \end{aligned} \quad \textbf{(6.68)}$$

The equilibrium values of z_1 and z_2 may be found by solving

$$\frac{\partial(E_d+E_\varepsilon)}{\partial z_1}=0 \quad \textbf{(6.69)}$$

and

$$\frac{\partial(E_d+E_\varepsilon)}{\partial z_2}=0\,. \quad \textbf{(6.70)}$$

The solutions to Equation 6.72 and 6.73 are developed in the appendix. For a particular material system, these two equations may be solved to obtain z_1 and z_2 without the need for complex SH-GEM calculations or ad hoc approximations which are specific to a single material system. The approach based on Equations 6.72 and 6.73, though more convenient to apply to design than detailed numerical energy minimization calculations, yields reasonable accuracy for SG-SAL

design. Figure 6.38 a and b show the values of z_1 and z_2 for 500 nm thick S-graded ZnS_ySe_{1-y} / GaAs (001) layers with μ = 250 nm and the maximum sulfur composition equal to 16%, 21%, and 26%. The symbols show results of the detailed energy minimization calculations while the solid, dashed, and dotted curves show results obtained using the approximate design equations. The absolute accuracy of the design equations (~10 nm) appears to be adequate for the design of device structures. An important aspect of such application is that, for given values of f_h, h, and μ there is a maximum value of σ for which there is a finite thickness of the interfacial MDFZ, and this value is ~90 nm for the SG-SAL designs depicted in figure 4a. Larger values of σ cause the interfacial MDFZ to vanish and the presence of interfacial mismatch will cause misfit dislocations to form right at the substrate interface.

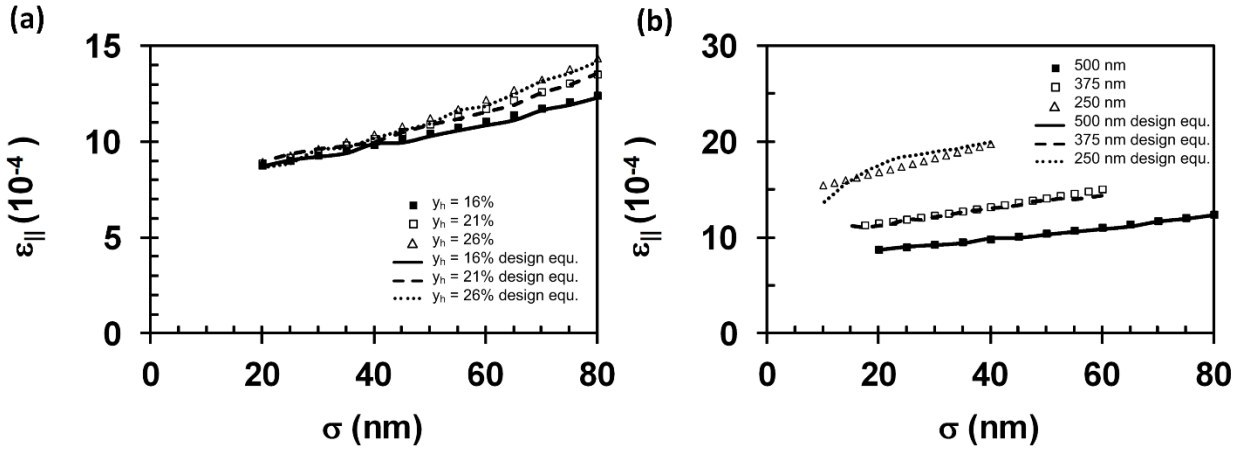

Figure 6.41. (a) Equilibrium surface strain for 500 nm thick S-graded ZnS_ySe_{1-y} / GaAs (001) layers with μ = 250 nm and a maximum sulfur composition of 16%, 21%, and 26%. (b) Equilibrium surface strain for S-graded ZnS_ySe_{1-y} / GaAs (001) layers with 16% maximum sulfur composition and thickness of 500 nm, 375 nm, and 250 nm. The mean parameter μ was set to 250 nm, 187.5 nm, and 125 nm, respectively. The results shown with symbols were found using detailed energy minimization calculations while the solid, dashed, and dotted curves were obtained by the approximate design equation.

Figure 6.39a and b show similar results for S-graded ZnS_ySe_{1-y} / GaAs (001) layers with a maximum sulfur composition equal to 16% but with different layer thicknesses (250 nm, 375 nm, and 500 nm). The mean parameter μ was set to one-half the layer thickness in all three cases. The symbols show results of the detailed energy minimization calculations while the solid, dashed, and dotted curves show results obtained using the approximate design equations. The general conclusions to be drawn are similar to those discussed above with respect to the previous two figures. However, the results of Figure 6.39b demonstrate that the maximum allowable value of ρ_{max} depends strongly on the mean parameter μ (and therefore the available thickness for the expansion of the dislocation region toward the substrate).

To find the peak misfit dislocation density ρ_{max}, we assume that in the dislocated region bounded by z_1 and z_2 the misfit dislocation density is just sufficient to relax the lattice mismatch introduced by the compositional grading. Then

$$\rho_{max} = \frac{f_h}{b'\sigma\sqrt{2\pi}} . \qquad \textbf{(6.71)}$$

This approximate design equation is in excellent agreement with the results of detailed minimum energy calculations for SG-SALs with various sulfur compositions (Figure 6.40a) and various layer thicknesses (Figure 6.40b). In Figure 6.40b there is a single curve associated with the design equation, which neglects the variation of the peak misfit dislocation density with the layer thickness. This second-order effect is associated with the change in the average equilibrium strain with total layer thickness but can be ignored in practical design calculations.

Based on the model described by Equation 6.69, the equilibrium surface strain in the SG-SAL can be found as

$$\varepsilon_{\parallel}(h) = \left(\frac{f_h}{2}\right)\left[erf\left(\frac{h-\mu}{\sigma\sqrt{2}}\right) - erf\left(\frac{z_2-\mu}{\sigma\sqrt{2}}\right) - \frac{z_2}{z_1}erf\left(\frac{\mu-z_1}{\sigma\sqrt{2}}\right) + \frac{z_2}{z_1}erf\left(\frac{\mu}{\sigma\sqrt{2}}\right)\right], \quad \textbf{(6.72)}$$
$$\approx \left(\frac{f_h}{2}\right)\left[1 - erf\left(\frac{z_2-\mu}{\sigma\sqrt{2}}\right)\right]$$

The simplified form of this equation results from the approximations $erf[(h-\mu)/(\sigma\sqrt{2})] \approx 1$, $erf[(\mu - z_1)/(\sigma\sqrt{2})] \approx 1$ and $erf[\mu/(\sigma\sqrt{2})] \approx 1$, with which the surface strain $\varepsilon_{\parallel}$ can be considered approximately independent of z_1. The model Equation 6.75 predicts the surface strain with a useful level of accuracy for SG-SALs with various maximum sulfur composition (Figure 6.41a) and layer thickness (Figure 6.41b). The observed departures between the detailed energy minimization calculations and values found by the design equation are rooted in the slight variation of the strain in the dislocated region, neglected in Equation 6.69, and the small error in the estimation of z_2 using the model equations 6.74 and 6.75. The largest differences are observed in the case of the 250 nm layer, which exhibits the most strain variation in the dislocated region, but the relative accuracy of the design equation is still better than 10%.

Considering the results presented in this section, we propose the following general approach for design of an S-graded strain accommodation layer. The composition and therefore lattice mismatch f_h at the surface of the SG-SAL is dictated by the need to match the average lattice constant in the device structure which will be deposited on top, thereby avoiding the introduction of misfit dislocations in the device. Once this choice has been made the standard deviation parameter σ may be chosen to achieve a desired peak misfit dislocation density by rearrangement of Equation 6.76,

$$\sigma = \frac{f_h}{b'\rho_{\max}\sqrt{2\pi}}. \qquad \textbf{(6.73)}$$

The total thickness of the SG-SAL will include the thicknesses of the interfacial MDFZ, the dislocated region, and the surface MDFZ:

$$h = h_{MDFZ1} + h_D + h_{MDFZ2}, \qquad \textbf{(6.74)}$$

where $h_{MDFZ1} = z_1$, $h_D = z_2 - z_1$, and $h_{MDFZ1} = h - z_2$. In choosing h_{MDFZ2} it should be recognized that the average equilibrium strain in the S-graded layer is approximately the same as in a uniform composition layer having the same thickness, ε_{UL}, as dictated by force balance on grown-in dislocations. The strain in the surface MDFZ of the SG-SAL is therefore larger than ε_{UL} by a factor of approximately h/h_{MDFZ2}. Once desired widths of the MDFZs have been decided, the required total thickness may be estimated with the assumption of $h_D \approx 3\sigma$. Using the resulting estimate for the total thickness, and assuming that the mean parameter is at the center of the dislocated region, $\mu \approx h_{MDFZ1} + 3\sigma/2$, the values of z_1 and z_2 can be found using the design equations from the appendix. Once this preliminary calculation has been made, the final step in SG-SAL design is to adjust h and σ to obtain the desired thicknesses of the MDFZs. The resulting surface strain for the structure may be found using (15). This design process can be readily applied without the need for detailed minimum energy calculations, and because the design equations have been given in terms of the material elastic properties there is no need to invoke ad hoc approximations which apply to a single material system, such as those given in [35] for $In_xGa_{1-x}As/GaAs$ (001).

It should be noted that the design approach described here is based on the equilibrium (minimum energy) of the SG-SAL. The equilibrium configuration is the basis for analyzing the strain and misfit dislocation density profiles in S-graded structures, but because kinetic considerations must be considered to understand the threading dislocation behavior it will be necessary to conduct additional work involving kinetic modeling and experimentation.

We have presented a design methodology and the associated design equations for S-graded strain accommodation layers (SG-SALs) for use in lattice mismatched semiconductor device structures. These design equations are based on a new approximate model for the strain and misfit dislocation density profiles in the SG-SAL, and provides guidance to the crystal grower in choosing the thickness and compositional profile for the achievement of desired SG-SAL properties (the maximum misfit dislocation density and thicknesses of the MDFZs). The design equations developed here can be used without the need for detailed energy minimization calculations and without invoking ad hoc approximations which apply to only a single material system. This work, based entirely on the equilibrium (minimum energy) behavior of the SG-SAL, provides guidance in terms of the misfit dislocation density and strain behavior, but further work will be needed to understand how kinetic considerations impact the threading dislocation densities in SG-SALs.

6.7. Semiconductor Heterostructures with a Logarithmically-Graded Lattice Mismatch

Equilibrium studies of metamorphic (partially relaxed) buffer layers are important in understanding the strain and misfit dislocation density configurations. We present a theoretical study of the equilibrium strain and misfit dislocation density profiles as well as appropriate design equations for nonlinearly-graded (logarithmic) buffers for use in accommodating the lattice

mismatch of heteroepitaxial $In_xGa_{1-x}As/GaAs$ (001) semiconductor devices. Minimum energy calculations show that the nonlinearly-graded profile may be beneficial for the control of defect densities in lattice-mismatched devices because they have several characteristics which enhance the mobility and glide velocities of dislocations, thereby promoting longer misfit segments with relatively few threading arms. This study suggest that the use of nonlinear metamorphic buffer layers are beneficial because they contain (1) a misfit dislocation free zone (MDFZ) adjacent to the interface which avoids dislocation pinning defects associated with substrate defects, (2) a misfit dislocation free zone near the surface, which reduces pinning interactions near the device layer which will be grown on top and (3) a large built-in strain in the top MDFZ which enhances the glide of dislocations to sweep out threading arms. In addition, we show that the use of non-linear compositionally grading may be superior to linearly graded layers depending on the specific application of the heterostructure. Moreover, the use of a nonlinearity coefficient (deviation of the average lattice mismatch) enables comparison of nonlinearly-graded metamorphic buffer layers to traditionally grown linearly-graded heterostructures. We also present approximate design equations for the widths of the misfit dislocation free zones, the built-in strain, and peak misfit dislocation density for the general logarithmically-graded semiconductor with diamond or zinc blende crystal structure and (001) orientation, and show that these design equations are in fair agreement with detailed numerical energy minimization calculations.

6.7.1. Design of Nonlinear Metamorphic Buffer Layers for Lattice-Mismatched InGaAs/GaAs (001) Semiconductor Devices

The realization of semiconductor heterostructures on lattice-mismatched substrates such as light-emitting diodes, high electron mobility transistors (HEMTs), and photo-diodes often requires

the use of metamorphic (partly relaxed) buffer layers. Growth of metamorphic structures on lattice-mismatched substrates requires control of defect densities and strain through device design to improve the performance of electronic and optical devices. A traditional approach to this problem involves a linearly-graded buffer layer [44, 72, 141, 142, 143, 144, 145, 146, 147, 148, 149, 150, 151, 92, 152] to accommodate the mismatch, while recent work suggests that nonlinear grading [153,154] provides additional control of the dislocations and residual strain in devices. In this work, we present equilibrium studies and design equations for nonlinearly-graded metamorphic buffer layers (NLG-MBL) with logarithmic compositional profiles. The use of metamorphic buffer layers can reduce the density of threading defects by enhancing the mobility and glide velocities of dislocations, resulting in the longest possible misfit dislocations parallel to the interface and therefore the least number of threading segments emanating from misfit dislocation ends. This is a consequence of the fact that high-quality substrates do not contain enough grown-in dislocations for the relaxation of the mismatch strain [75155], so new dislocations must be introduced as half loops which glide from the surface. Each half loop has a misfit segment parallel to the interface bounded by two threading segments which lie on a glide plane and intersect the surface. Preferred device designs are those which favor small number of long misfit dislocations. The insertion of a compositionally-graded metamorphic buffer layer can reduce the threading dislocation density compared to the case of abrupt growth on a mismatched substrate by allowing a wider distribution of the misfit dislocations rather than concentrating them at the mismatched interface where substrate defects and tangling can pin dislocations or otherwise reduce their mobility. In addition, the MBL exhibits a misfit dislocation free zone at its surface, which limits dislocation interactions and the surface MDFZ contains a relatively large built-in strain which enhances the sweep rate of

threading dislocations. In contrast to linearly-graded metamorphic buffer layers, nonlinear grading profiles such as exponential [156], S [157.158] and logarithmic may provide three additional benefits. First, there are MDFZs at the bottom of the nonlinearly-graded layer (adjacent to the substrate interface) and the top of the layer (adjacent to the free surface). The interfacial MDFZ can reduce dislocation pinning or mobility reduction due to defects or chemical contamination at the starting substrate surface. Second, the dislocated region can contain a tapered rather than constant misfit dislocation density. Third, there is a larger built-in strain in the top MDFZ which aids in sweeping threading arms and therefore significantly reducing dislocation defects reaching the surface of the buffer layer. Metamorphic devices [159,160,161,162,163,164,165,166,167] such as high electron mobility transistors, heterojunction bipolar transistors, photodiodes, light emitting diodes, laser diodes and solar cells have been fabricated on lattice-mismatched substrates (GaAs, InP, GaSb) by utilizing binary/ternary/quaternary combinations of the AlInGaAsSb material system. Most experimental work has focused on linearly-graded or step-graded buffer layers but none have reported the use of unconventional grading profiles such as described in [156,157,158].

In this work, we used detailed energy minimization calculations [43] for $In_xGa_{1-x}As/GaAs$ (001) heterostructures to show that logarithmically-graded metamorphic buffer layer exhibits the desired advantages. Although numerical energy minimization calculations are generally applicable to any graded structure which can be approximated by a series of laminae, their use is not well suited to design because of the indirect nature of the approach. The ad-hoc energy minimization model used in this work, involves brute force calculations which very time intensive. Furthermore, the model allows one to study the MBL characteristics based on the choice of the thickness and compositional profile. While the brute force energy model allows one to study any general

heterostructure, it is not as straight forward to provide design criteria and/or allow for the tapering of the misfit dislocation profiles, MDFZ and the in-plane strain. Therefore, we present approximate design equations for NLG-MBLs which are relatively simpler to use and allow the crystal grower more flexibility in the choice of thickness and compositional profile. Moreover, we also demonstrate fair agreement between these design relationships and detailed energy minimization calculations for $In_xGa_{1-x}As/GaAs$ (001) heterostructures. These phenomenological models were developed for $In_xGa_{1-x}As$ logarithmically-graded buffer layers by fitting the numerical energy minimization results and in the general case, exact equations of the edges of the MDFZs should be derived by minimization of energy, for applicability to other material systems.

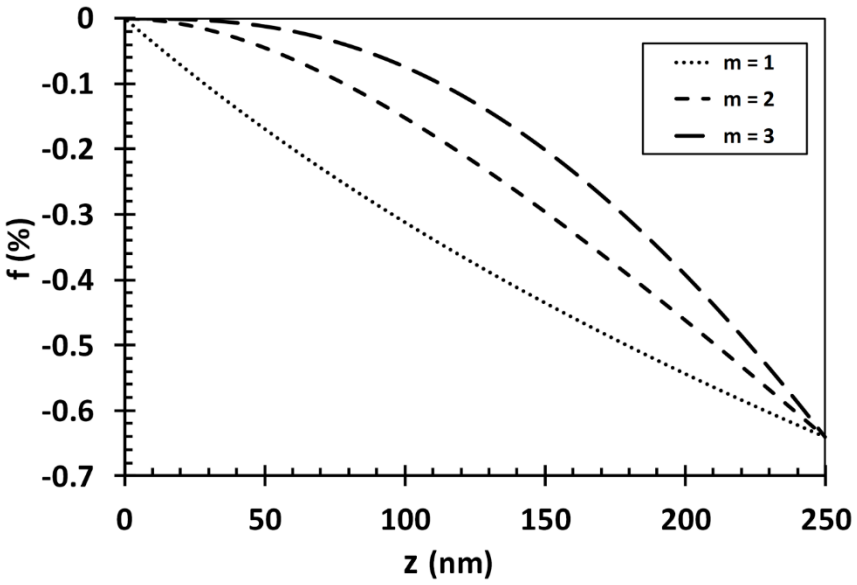

Figure 6.42. Lattice mismatch profiles for 250 nm thick nonlinearly-graded $In_xGa_{1-x}As$/ GaAs (001) layers with $f_h = 0.0046$, and power grading coefficient $m = 1$, 2, and 3. The indium composition in the logarithmically-graded layer is varied from lattice matched to GaAs at the interface to 16% at the surface.

6.7.1.1. Equilibrium Strain and Dislocation Density Profiles in the NLG-MBL

The lattice mismatch profile in the logarithmically-graded metamorphic buffer layer is given by

$$f(z) = f_0 + (f_h - f_0)\left[\ln\left(1+\frac{z}{h}\right) - \ln(2)\right]^m , \qquad \textbf{(6.75)}$$

where f_0 is the lattice mismatch at the substrate-NLG-MBL interface, f_h is the value of lattice mismatch at the top of the NLG-MBL with thickness h, z is the distance from the interface and m is the power grading coefficient. The parameters f_0, f_h, h and m can be chosen by the crystal grower to obtain the desired buffer layer characteristics. In this study, we present a theoretical study of the equilibrium strain and misfit dislocation density profiles for nonlinear logarithmic-graded metamorphic buffer layers of $In_xGa_{1-x}As$ on GaAs (001) substrates. Equilibrium modeling serves as the starting point for kinetic calculations, which enable the analysis of non-equilibrium defects such as threading dislocations. Figure 6.42 illustrates the lattice mismatch profile for 250 nm thick $In_xGa_{1-x}As$ layer on GaAs (001) substrate with $f_0 = 0$, $f_h = 0.0064$, and $m = 1$, 2 and 3. The results of Figure 6.42 show that for power grading coefficient $m = 1$, the NLG-MBL has a convex-up compositional grading profile (sublinear) while for heterostructures with $m \geq 2$ the concavity of the compositional profile changes sign to concave-down (superlinear). Structures with convex-up compositional grading profile exhibit a small sublinearity coefficient whereby the average lattice mismatch of the structure is approximately equal to that of a linearly-graded buffer layer. The nonlinearity coefficient is defined as $C_S = \bar{x}_{NLG} / \bar{x}_{LG}$ where $\bar{x}_{NLG}$ and $\bar{x}_{LG}$ are the average compositions of the nonlinearly- and linearly- graded MBL respectively. The nonlinearity

coefficients (average indium compositions) for the structures of Figure 6.42 are 1.12 (5.03 %), 0.79 (3.55 %), and 0.61 (2.75 %) for $m=1$, 2 and 3 respectively. Whereas linear grading is associated with a constant grading coefficient, the sublinear buffer (with a small nonlinearity coefficient C_S) exhibits a decreasing grading rate with distance from the interface and the superlinear buffer (with a larger nonlinearity coefficient C_S) has an increasing grading rate with distance from the interface.

Figure 6.43a-c (dashed curves) illustrate the equilibrium misfit dislocation density profiles for 250 nm thick logarithmically-graded $In_xGa_{1-x}As$ / GaAs (001) layers with $f_0=0$ and $m=1$ (Figure 6.43 a), 2 (Figure 6.43b) and 3 (Figure 6.43c) for various ending indium composition x_h. The assumed material parameters for GaAs are a = 0.56534 nm, C_{11} = 118.4 GPa and C_{12} = 53.7 GPa. The corresponding values for $In_xGa_{1-x}As$ were assumed to be linear functions of the indium composition: a = (0.56534-0.405x) nm, C_{11} = (118.4 - 35.1x) GPa and C_{12} = (53.7 - 8.4x) GPa. There are two key features in the dislocation density profile for the nonlinear log-graded metamorphic buffer layer. First, there are two misfit dislocation free zones (MDFZ): one adjacent to the substrate interface where the in-plane strain is approximately equal to the lattice mismatch and the other is adjacent to the surface. We have defined the edges of these MDFZs as z_1 and z_2. Second, there is a tapered dislocated region containing misfit dislocations between the two MDFZs ($z_1 < z < z_2$) which contains approximately constant strain and logarithmic-based dislocation profile. The interfacial MDFZ thickness is not as pronounced in sublinear structures where the high grading rate near the interface requires the immediate introduction of misfit dislocations to relax the excess misfit strain. For sublinearly-graded MBL with $m=1$, the interfacial MDFZ thickness

is 15 nm, 6 nm, and 4 nm for $x_h = 2$, 6, and 9 %, respectively. It can be seen that higher mismatch leads to a reduction of the interfacial MDFZ. The existence of this MDFZ is expected on the basis of energy minimization because there is zero lattice mismatch at $z = 0$ and the introduction of misfit dislocations would increase both the strain energy and dislocation line energy. There is a finite distance from the interface where the line energy cost of misfit dislocations is balanced by the strain energy they release in the growing film, and this dictates the extent of the misfit dislocation free material near the interface. The thickness of the surface MDFZ is defined as the distance from the edge of the dislocated region (z_2) to the surface of the epilayer (h); in other words the surface MDFZ is defined as $h - z_2$. For heterostructures with a sublinear grading profile the thickness of the surface MDFZ is 230 nm, 139 nm, and 115 nm for $x_h = 2$, 6, and 9 %, respectively. The surface MDFZ exists in materials with significant lattice mismatch because much of the strain is relaxed by defects in the underlying dislocated region. Due to this, and the proximity to the surface, it is energetically unfavorable to introduce misfit dislocations near the surface of the material. Consequently, line energies of misfit dislocations near the surface are not reduced significantly because of the weak logarithmic dependence of the line energy on the distance from the interface. In contrast, heterostructures with convex-down grading profile (superlinear) where $m \geq 2$, the edge of the MDFZ adjacent to the substrate is located further away from the substrate interface and results in thicker interfacial MDFZ. The interfacial MDFZ thickness for layers with $m = 2$ is 47 nm, 32 nm, and 26 nm for $x_h = 3$, 6, and 9 %, respectively. Furthermore, the effect is more pronounced in heterostructures with $m = 3$ whereby the interfacial MDFZ zone approximately doubles to 75 nm, 63 nm, and 54 nm for $x_h = 4$, 7, and 10 %, respectively.

Structures with a higher power grading coefficient have a relatively low lattice mismatch near the substrate interface and therefore it is energetically unfavorable for the introduction of misfit dislocations earlier in the relaxation process. The drawback of heterostructures with $m \geq 2$ is in the reduction of the surface MDFZ. In heterostructures with $m = 2$, the thickness of the surface MDFZ is 181 nm, 114 nm, and 90 nm for $x_h = 3$, 6, and 9 %, respectively. Similarly, for $m = 3$, the surface MDFZ thickness is 143 nm, 103 nm, and 78 nm for $x_h = 4$, 6, and 9 %, respectively. The reduction of the surface MDFZ becomes apparent in these structures because the grading coefficient in these structures creates a higher lattice mismatch near the surface which cannot be accommodated by the strain energy alone.

The misfit dislocation density profile between the two MDFZs has approximately the shape of a tapered log-based function. This is expected if the density of misfit dislocations is just sufficient to relax the strain introduced by the compositional grading, $\rho = |df / dy| / b'$, where b' is the projection of the misfit-relieving component of the Burgers vector in the interface. The peak misfit dislocation density increases for higher power grading composition if the average composition is maintained constant. With an average composition of $x_{ave} = 2.75$ %, the peak misfit dislocation density is 11.4 x 10^9 cm^{-2}, 12.5 x 10^9 cm^{-2}, and 18.9 x 10^9 cm^{-2} for $m = 1$, 2, and 3, respectively.

Figure 6.44a-c shows the equilibrium in-plane strain profiles (dashed curves) for 250 nm thick NLG-MBL $In_xGa_{1-x}As$ / GaAs (001) layers with $x_h = 3$, 6, and 9 % for $m = 1$, 2 and $x_h = 4$, 7, and 10 % for $m = 3$. There are three main characteristics in the strain profile of a NLG-MBL. First, in the interfacial MDFZ, the in-plane strain is equal to the lattice mismatch. Second, in the

dislocated region, the strain is approximately constant with increasing distance from the interface. Third, in the surface MDFZ, the strain profile is proportional to the lattice mismatch. Although it was assumed that in the dislocated region the dislocation energy is sufficient in relaxing the strain associated with compositional grading, equilibrium modeling shows a small variation of the strain in the dislocated region. In the surface MDFZ, the rate of change of the in-plane strain is higher for increasing power grading coefficient. In addition, the built-in strains in these structures are considerably greater than the equilibrium in-plane strain for a uniform layer of $In_xGa_{1-x}As$ on GaAs (001) having the same thickness and average composition. Therefore, dislocation glide velocities can be several times larger in the surface MDFZ of the NLG-MBL compared to a uniform buffer layer. Furthermore, depending on the device application, the use of nonlinear grading may provide additional benefits in comparison to linearly-graded heterostructures. Although, Dunstan and Bushby [168] showed that interfacial and surface MDFZ are inherent of all compositionally-graded layers, their size depends on the choice of the compositional profile and the thickness of the epilayer. As an example, equilibrium calculations of a 250 nm thick linearly-graded $In_xGa_{1-x}As$ / GaAs (001) layer that is lattice matched at the substrate interface and contains an ending mismatch of $x_h = 6$, yielded an interfacial and surface MDFZ of 7.9 nm and 130 nm respectively. The sublinear grading structure with exact parameters contains a slightly smaller interfacial MDFZ but a larger surface MDFZ. Moreover, the effect is reversed when comparing linear- to super-linear-grading. To illustrate the effect of the MDFZ, Saha et al. [169] experimentally compared the cases of linearly-step-graded and sublinearly-logarithmically-graded InGaAsP-based heterostructures and showed that the use of a sublinear profile results in the improvement of the metamorphic buffer layer quality; in other words, heterostructures with a sublinear compositional profile exhibited less

mosaicity which indicates superior crystal quality. In comparison to linearly-graded MBL, the use of a high grading rate at the initial stages of growth and a low grading rate during the later stages which are characteristics pertinent to sublinearly graded layers produces larger areas free of misfit dislocation (in other words thicker MDFZ) and lower threading dislocation densities. The main role of the MDFZ is to reduce pinning interactions with substrate associated defects (interfacial MDFZ) and enable smooth integration with the device layer (surface MDFZ). Although, the thickness of MDFZ in the structures studied by Saha et al. deviated by less than <20 nm, the resulting full-width-at-half-maximum (FWHM) varied by about ~15% (~150 arcseconds). Therefore, it can be seen that even a slightly thicker surface MDFZ produces a reduction in the threading dislocation density. Furthermore, the low grading rate at the surface of sublinearly graded layers results in regions that exhibit preservation of high built-in strain which is essential to sweeping out threading dislocations. Threading dislocation are detrimental to device performance of many electronic and optical devices and therefore their reduction is essential to the optimization of functionality. Equilibrium studies of structures which contained a nonlinearity coefficient much greater than one, $C_S >> 1$ resulted in the excellent preservation of the surface strain in the top 50 nm; in other words, the in-plane strain in the top 50 nm of the epilayer varied by less than 5%, whereas the strain in linearly graded layers with exact parameters scales proportionally to the lattice mismatch profile and varies greatly in this region. As an example, for a 250 nm thick linearly-graded $In_xGa_{1-x}As$ / GaAs (001) layer that is lattice matched at the substrate interface and contains an ending mismatch of $x_h = 6$, the in-plane strain varies by ~30% in the top 50nm. While the sublinear grading profile is superior to linear grading, the superlinear grading

scheme falls short in containing a thicker MDFZ. However, certain applications require highly strained metamorphic buffer layers and the high grading rate at the surface of the epilayer in superlinearly compositionally graded layers may serve as the better alternative. Although, non-linear grading profiles may be beneficial to taper the dislocation distribution and residual strain, it should also be mentioned that the use of these compositional profiles may provide desired spectral modification of the electrical characteristics as in the case of AlGaAs-based photodetectors [170].

Although the detailed behavior of NLG-MBL is rather complex, it is possible to develop approximate models for the strain and dislocation density which may be used to guide the design of logarithmically-graded device structures to take advantage of their desirable properties. In the following two sections, we present an approximate equilibrium model for the NLG-MBL which can aid the crystal grower during the fabrication of these device heterostructures.

6.7.1.2. Model for the Dislocation Density and Strain Profiles in Logarithmically-Graded Metamorphic Buffer Layers

The equilibrium model used in this work uses a two-step look ahead approach to study the evolution of the equilibrium profile. This model is very calculation intensive and although it can be applied to any heterostructure with arbitrary thickness and compositional profile it is not as straight forward to obtain desired misfit dislocation and in-plane strain distribution profiles. However, the equilibrium minimizer can be used to develop analytical equations that model the misfit dislocations and in-plane strain profiles for any heterostructure with arbitrary thickness and compositional which are much easier to use.

If the edges of the interfacial and surface MDFZs are located at distances of z_1 and z_2 from the substrate interface, respectively, and if the misfit dislocation density in the middle region ($z_1 \le z \le z_2$) is just sufficient to relax the strain associated with the compositional grading, then in this region

$$\rho = \frac{1}{b'}\left|\frac{df}{dz}\right|, \tag{6.76}$$

where b' is the misfit-relieving component of the Burgers vector in the plane of the interface. Therefore, the misfit dislocation density profile is

$$\rho = \begin{cases} 0, & z < z_1; \\ \dfrac{m(f_h - f_0)}{b'(h+z)}\left[\ln^{m-1}\left(1+\dfrac{z}{h}\right) - \ln^m(2)\right], & z_1 \le z \le z_2; \text{ and} \\ 0, & z > z_2, \end{cases} \tag{6.77}$$

With the approximate misfit dislocation density given in Equation 6.80 we can find the in-plane strain distribution. The interfacial MDFZ ($z \le z_1$) is coherently strained so the in-plane strain is equal to the lattice mismatch:

$$\varepsilon_{\parallel} = f_0 + (f_h - f_0)\left[\ln^m\left(1+\frac{z}{h}\right) - \ln^m(2)\right]; \qquad z \le z_1 \tag{6.78}$$

and at the edge of the interfacial MDFZ

$$\varepsilon_{\parallel} = f_0 + (f_h - f_0)\left[\ln^m\left(1+\frac{z_1}{h}\right) - \ln^m(2)\right]; \qquad z = z_1 \tag{6.79}$$

For $z_1 \le z \le z_2$ (the dislocated layer) the in-plane strain is approximately constant at this value, assuming the misfit dislocation density is just enough to relax the strain associated with the

grading. For $z > z_2$ there are no misfit dislocations so $d\varepsilon_{\|} / dz = df / dz$. The equilibrium in-plane strain profile in the partially-relaxed nonlinearly-graded layer is therefore

$$\varepsilon_{\|} = \begin{cases} f_0 + (f_h - f_0)\dfrac{\ln^m\left(1+\dfrac{z}{h}\right)}{\ln^m(2)}, & z < z_1; \\ f_0 + (f_h - f_0)\dfrac{\ln^m\left(1+\dfrac{z_1}{h}\right)}{\ln^m(2)}, & z_1 \le z \le z_2; \text{ and} \\ f_0 + (f_h - f_0)\left[\dfrac{\ln^m\left(1+\dfrac{y}{h}\right)}{\ln^m(2)} + \dfrac{\ln^m\left(1+\dfrac{z_1}{h}\right)}{\ln^m(2)} - \dfrac{\ln^m\left(1+\dfrac{z_2}{h}\right)}{\ln^m(2)}\right], & z > z_2. \end{cases} \quad \textbf{(6.80)}$$

The equilibrium misfit dislocation density (Equation 6.80) and in-plane strain (Equation 6.83) are shown in Figure 6.43a-c and Figure 6.44a-c respectively (solid curves). The model is in good agreement with ad-hoc energy minimizer calculations. The slight variations of the in-plane strain between the energy minimizer (dashed lines) and approximate model (solid lines) could be explained by the fact that the model does not account for strain variations in the dislocated region; In the dislocated region, Equation 6.83 assumes a constant in-plane strain value whereas minimum energy calculations show a gradual decrease of the in-plane strain with increasing distance from the interface. Based on this model we have developed general design equations for an NLG-MBL.

6.7.1.3. Design Equations for Logarithmically-Graded Metamorphic Buffer Layers

In the design of an NLG-MBL, the most important characteristics to consider are the widths of the MDFZs, the misfit dislocation density, and the built-in strain in the surface MDFZ. In this section, we develop design equations for these characteristics based on energy minimization and the model described above. While, the ad-hoc energy model allows for the development and the

confirmation of the analytical model, the design equations are beneficial to the crystal grower because they alloy flexibility in the choice of the thickness and compositional profile to obtain the desired buffer layer characteristics such as the ones described above.

First, we consider the widths of the MDFZs, with edges located at distances of z_1 and z_2 from the interface. The thickness of the interfacial MDFZ is z_1 and the thickness of the surface MDFZ is $h - z_2$, where h is the total thickness of the metamorphic buffer layer. Therefore, the problem reduces to one of finding equilibrium values of z_1 and z_2 - those which minimize the sum of the strain and dislocation line energy per unit area. The dislocation line energy per unit area is

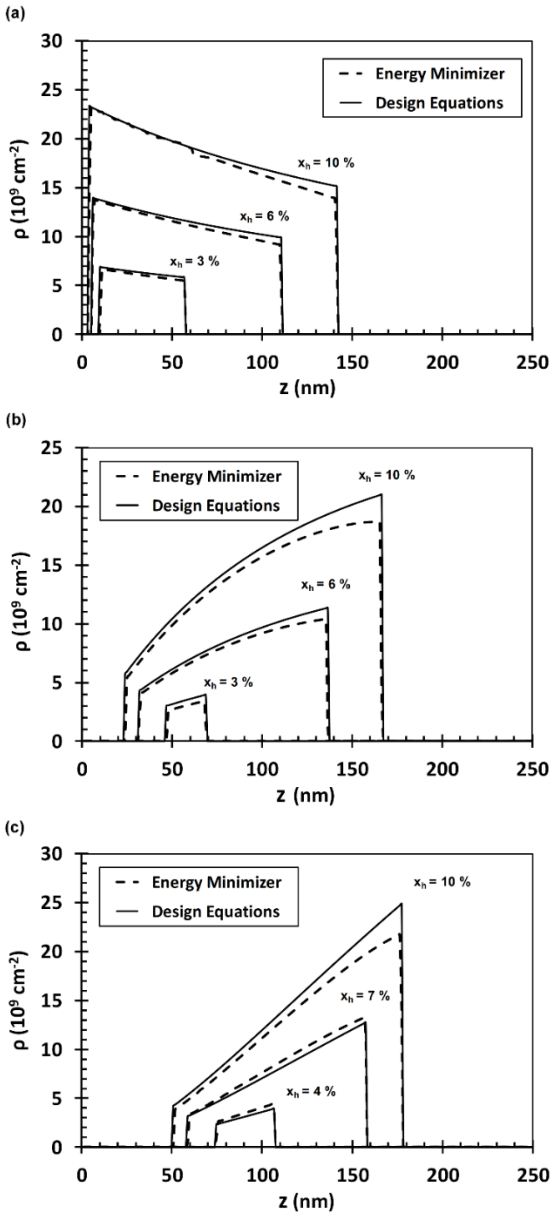

Figure 6.43 Equilibrium misfit dislocation density profiles for 250 nm thick logarithmically-graded $In_xGa_{1-x}As$/ GaAs (001) layers for various ending compositions and power grading coefficient. (a) Structures with a sublinear-grading profile $m=1$ and an ending indium composition at the surface $x_h=3\%$, 6% and 10%. (b) Structures with a superlinear-grading profile $m=2$ and an ending indium composition at the surface $x_h=3\%$, 6% and 10%. (c) Structures with a superlinear-grading profile $m=3$ and an ending indium composition at the surface $x_h=4\%$, 7% and 10%.

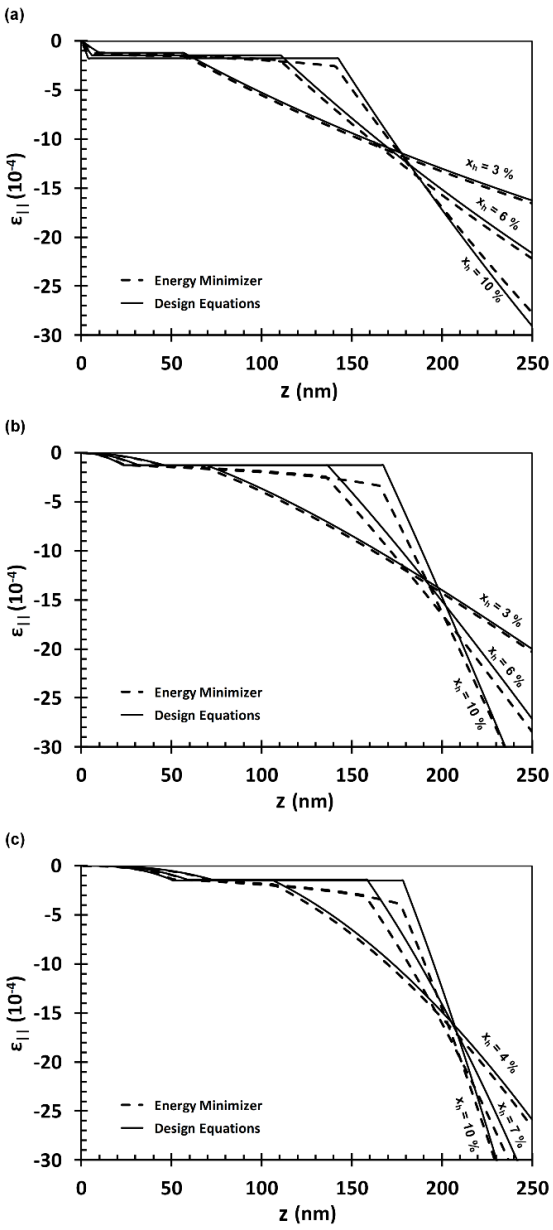

Figure 6.44. Equilibrium in-plane strain for 250 nm thick logarithmically-graded $In_xGa_{1-x}As$/ GaAs (001) layers for various ending compositions and power grading coefficient. (a) Structures with a sublinear-grading profile $m=1$ and an ending indium composition at the surface $x_h=3\%$, 6% and 10%. (b) Structures with a superlinear-grading profile $m=2$ and an ending indium composition at the surface $x_h=3\%$, 6% and 10%. (c) Structures with a superlinear-grading profile $m=3$ and an ending indium composition at the surface $x_h=4\%$, 7% and 10%.

$$E_d = 2\int_{z_1}^{z_2} F_d(z)\rho(z)dz$$

$$= 2\int_{z_1}^{z_2} \left\{ \frac{Gb^2(1-\nu\cos^2\alpha)}{4\pi(1-\nu)} \left[Ln\left(\frac{h-z}{b}\right)+1 \right] \right\} \left\{ \frac{m(f_h-f_0)}{b'(h+z)} \frac{\ln^{m-1}\left(1+\frac{z}{h}\right)}{\ln^m(2)} \right\} dz\,, \qquad \textbf{(6.81)}$$

$$= \frac{Gbm(f_h-f_0)(1-\nu\cos^2\alpha)}{2\pi\sin\alpha\cos\lambda(1-\nu)} \int_{z_1}^{z_2} \left[\ln\left(\frac{h-z}{b}\right)+1 \right] \frac{\ln^{m-1}\left(1+\frac{z}{h}\right)}{(h+z)\ln^m(2)} dz$$

and the strain energy per unit area is

$$E_\varepsilon = Y\int_0^h \varepsilon_{\|}^2(z)dz$$

$$= Y\int_0^{z_1} \left[f_0 + (f_h-f_0)\frac{\ln^m\left(1+\frac{z}{h}\right)}{\ln^m(2)} \right] dz + Y\int_{z_1}^{z_2} \left[f_0 + (f_h-f_0)\frac{\ln^m\left(1+\frac{z_1}{h}\right)}{\ln^m(2)} \right] dz\,. \qquad \textbf{(6.82)}$$

$$+ Y\int_{z_2}^{h} \left[f_0 + (f_h-f_0)\left(\frac{\ln^m\left(1+\frac{z}{h}\right)}{\ln^m(2)} + \frac{\ln^m\left(1+\frac{z_1}{h}\right)}{\ln^m(2)} - \frac{\ln^m\left(1+\frac{z_2}{h}\right)}{\ln^m(2)} \right) \right] dz$$

The equilibrium values of z_1 and z_2 may be found by solving

$$\frac{\partial(E_d+E_\varepsilon)}{\partial z_1} = 0\,, \qquad \textbf{(6.83)}$$

and

$$\frac{\partial(E_d+E_\varepsilon)}{\partial z_2} = 0\,. \qquad \textbf{(6.84)}$$

As shown in the appendix, for a given power grading coefficient, the equilibrium values of z_1 and z_2 satisfy the simultaneous equations

$$0 = \frac{\partial E_d}{\partial z_1} + \frac{\partial I_1}{\partial z_1} + \frac{\partial I_2}{\partial z_1} + \frac{\partial I_3}{\partial z_1}, \tag{6.85}$$

and

$$0 = \frac{\partial E_d}{\partial z_2} + \frac{\partial I_1}{\partial z_2} + \frac{\partial I_2}{\partial z_2} + \frac{\partial I_3}{\partial z_2}. \tag{6.86}$$

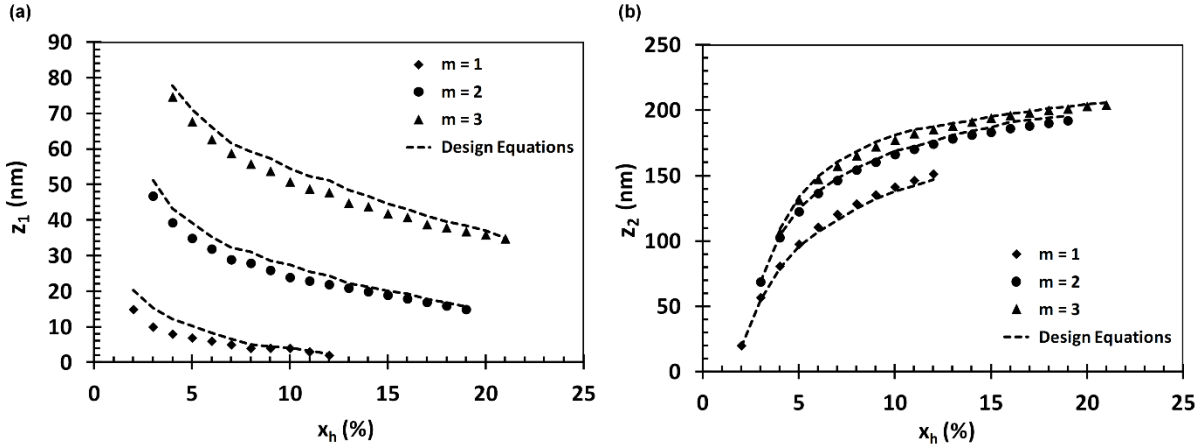

Figure 6.45.(a) Thickness of the interfacial MDFZ, z_1, for 250 nm thick logarithmically-graded $In_xGa_{1-x}As$/ GaAs (001) layers with $f_0 = 0$ for various ending compositions and power grading coefficient. (b) Distance of the edge of the surface MDFZ from the interface, z_2, for 250 nm thick nonlinearly-graded $In_xGa_{1-x}As$/ GaAs (001) layers with $f_0 = 0$ for various ending compositions and power grading coefficient. The results shown with symbols were found using detailed energy minimization calculations while dashed curves were obtained by the approximate design equations.

For a particular material system, these two equations may be solved to obtain z_1 and z_2 without the need for complex SH-GEM calculations or ad hoc approximations which are specific to a single material system. The approach based on Equations 6.84 and 6.85, though far simpler to apply than numerical energy minimization calculations, yields reasonable accuracy for NLG-MBL design. Figure 6.45a-b show the values of z_1 and z_2 respectively for 250 nm thick nonlinear log-graded $In_xGa_{1-x}As$ / GaAs (001) layers with lattice matched condition at the substrate interface and

power grading coefficient $m=1$, 2 and 3. The symbols show results of the detailed energy minimization calculations while the dashed curves show results obtained using the approximate design equations. The approximations inherent in Equations 6.84 and 6.85 have little effect on the calculation of z_2 because there is a relatively high misfit dislocation density adjacent to the surface MDFZ (see Figure 6.43). Therefore, the dislocation line energy per unit area is sensitive to small variations in z_2. The determination of z_1 is more affected by the same approximations because there is a lower misfit dislocation density near the edge of the interfacial MDFZ, reducing the sensitivity of the dislocation energy to the value of z_1. The effect is more pronounced in structures with $m=1$ due to the fact that misfit dislocations are introduced closer to the substrate interface. Nonetheless, the absolute accuracy of the design equations (~10 nm) is adequate for the design of device structures. To find the peak misfit dislocation density ρ_{max}, we assume that in the dislocated region bounded by z_1 and z_2 the misfit dislocation density is just sufficient to relax the lattice mismatch introduced by the compositional grading. However, from the results of Figure 6.43a-c, structures with $m=1$ will contain the maximum misfit dislocation density at $z=z_1$ while structures with $m=2$ at $z=z_2$. Then

$$\rho_{max}=\left\{\begin{array}{l}\dfrac{(f_h-f_0)}{b'(h+z_1)\ln(2)}, \quad m=1; \quad \text{and} \\ \dfrac{m(f_h-f_0)}{b'(h+z_2)}\dfrac{\ln^{m-1}\left(1+\dfrac{z_2}{h}\right)}{\ln^m(2)}, \quad m\geq 2\end{array}\right\}, \qquad \textbf{(6.87)}$$

This approximate design equation is in good agreement with the results of detailed minimum energy calculations for NLG-MBLs with various ending indium compositions and various grading

coefficient $m=1$ (Figure 6.46a), 2 (Figure 6.46b) and 3 (Figure 6.46c). The results of Figure 6.46a-c indicate a monotonic increase in the peak misfit dislocation density as a function of the ending indium composition x_h and demonstrate a strong linear dependence of the peak misfit dislocation density to the surface lattice mismatch. The slight variations arise due to the minor differences in the value of z_1 and z_2 which is a direct result of the approximation that in the dislocated region the introduction of misfit dislocation is sufficient to relax the excess strain. The symbols show results of the detailed energy minimization calculations while the dashed curves show results obtained using the approximate design equations.

Based on the model described by Equation 6.83, the equilibrium surface strain in the NLG-MBL can be found as

$$\varepsilon_{\parallel}(h) = f_0 + (f_h - f_0)\left[1 + \frac{\ln^m\left(1+\frac{z_1}{h}\right)}{\ln^m(2)} - \frac{\ln^m\left(1+\frac{z_2}{h}\right)}{\ln^m(2)}\right], \qquad \textbf{(6.88)}$$

The model Equation 6.91 predicts the surface strain with a useful level of accuracy for logarithmically-graded metamorphic buffer layer with various maximum indium composition as previously indicated in Figure 6.44a-c. The observed departures between the detailed energy minimization calculations and values found by the design equation are rooted in the slight variation of the strain in the dislocated region, neglected in equation 6.83, and the small error in the estimation of z_1 and z_2 using the model equations 6.88 and 6.89.

The largest differences are observed in the case of the structures with $m=2$ and 3 which exhibit the most strain variation in the dislocated region, but the relative accuracy of the design equation is still better than 20%. It should be noted that the design approach described here is based on

the equilibrium (minimum energy) of the NLG-MBL. The equilibrium configuration is the basis for analyzing the strain and misfit dislocation density profiles in nonlinearly-graded structures, but because kinetic considerations must be considered to understand the non-equilibrium threading dislocation behavior it will be necessary to conduct additional work involving kinetic modeling and experimentation. This design process can be readily applied without the need for detailed minimum energy calculations. The design equations given here are applicable to any cubic semiconductor material system. The use of these analytical models enables the crystal grower to taper that misfit dislocation profile, the surface strain and the widths of the MDFZ by appropriately choosing the compositional profile and the parameters f_0, f_h, h and m. While, we have showed that the ad-hoc energy minimizer enables the development and confirmation of these analytical models, their use is relatively much simpler and can be used to study a whole range of heterostructures in a shorter time span.

We have presented equilibrium calculation and design equations for nonlinearly (logarithmic)-graded metamorphic buffer layers for use in lattice mismatched semiconductor device structures. These design equations are based on an approximate model for the strain and misfit dislocation density profiles in the NLG-MBL and are in excellent agreement with minimum energy calculations. The design equations developed here can be used without the need for detailed energy minimization calculations and without invoking ad hoc approximations which apply to only a single material system. This work, based entirely on the equilibrium (minimum energy) behavior of the NLG-MBL, provides guidance in terms of the misfit dislocation density and strain behavior, but further work will be needed to understand how

kinetic considerations impact the threading dislocation densities in nonlinearly-graded metamorphic buffer layer.

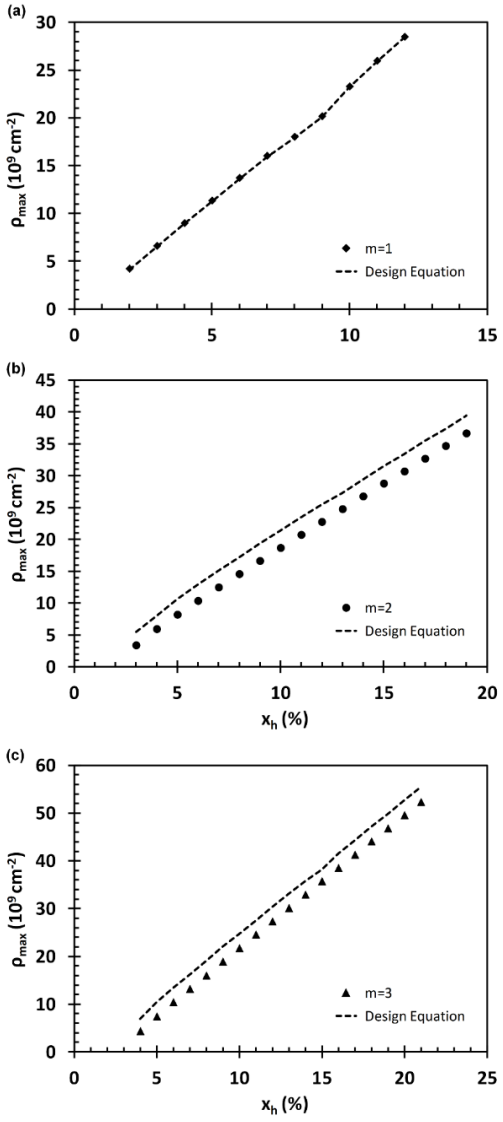

Figure 6.46. Peak misfit dislocation density for 250 nm thick logarthimically-graded $In_xGa_{1-x}As$/ GaAs (001) layers with $f_0 = 0$ for various ending compositions and power grading coefficient. The results shown with symbols were found using detailed energy minimization calculations while dashed curves were obtained by the approximate design equations. (a) Structures with a sublinear-grading profile $m = 1$. (b) Structures with a superlinear-grading profile $m = 2$. (c) Structures with a superlinear-grading profile $m = 3$.

6.7.2. Comparison Lattice Relaxation and Misfit Dislocations in Nonlinearly Graded $In_xGa_{1-x}As/GaAs$ (001) and $GaAs_{1-y}P_y/GaAs$ (001) Metamorphic Buffer Layers

Recent results have shown that nonlinearly-graded buffer layers may be beneficial for the reduction of threading dislocation densities in metamorphic semiconductor devices. In this work, we have studied the equilibrium strain relaxation and misfit dislocation densities in nonlinearly graded (NLG) heterostructures with logarithmic grading, and compare the cases of $In_xGa_{1-x}As/GaAs$ and $GaAs_{1-y}P_y/GaAs$ buffer layers. We show that differences in the elastic stiffness constants give rise to significantly different behavior in these two commonly-used buffer layer systems. Moreover, the width of the dislocated region, the average misfit dislocation density and surface in-plane strain may be related to the nonlinearity coefficient of the grading profile.

In this work, we present modeling results for nonlinearly-graded (logarithmic) $In_xGa_{1-x}As$ and $GaAs_{1-y}P_y$ metamorphic buffer layers grown on GaAs (001) substrates. For each structure, we studied the evolution of the equilibrium lattice relaxation by observing the misfit dislocation and in-plane strain profiles along with the widths of the MDFZ. In addition, to better understand the relaxation process we studied the role of the elastic stiffness coefficients in order to optimize the heterostructures by the inclusion of high surface strain and lower dislocation densities.

In this study, we consider nonlinearly-graded (NLG) buffers with logarithmic-graded composition having the zinc blende structure and grown on a GaAs substrate with (001) crystal orientation. In this study, we present a theoretical study of the equilibrium strain and misfit dislocation density profiles for nonlinear logarithmic-graded metamorphic buffer layers of $In_xGa_{1-x}As$ or $GaAs_{1-y}P_y$ on GaAs (001) substrates. Equilibrium modeling serves as the starting point for

kinetic calculations, which will enable the determination of non-equilibrium defects such as threading dislocations. Figure 6.47 illustrates the lattice mismatch profile for 250 nm thick $In_xGa_{1-x}As$ and $GaAs_{1-y}P_y$ layers on GaAs (001) with $f_0 = 0$, $f_h = 0.0064$, and $m = 1$, and 2. The results of Figure 6.47 show that for power grading coefficient $m = 1$, the NLG-MBL has a convex-up compositional grading (sublinear) profile while for heterostructures with $m = 2$ the concavity of the compositional profile changes sign to convex-down (superlinear). Whereas linear grading is associated with a constant grading coefficient, the sublinear buffer (with a small nonlinearity coefficient m) exhibit a decreasing grading coefficient with distance from the interface the superlinear buffer (with a larger nonlinearity coefficient m) has an increasing grading coefficient with distance from the interface.

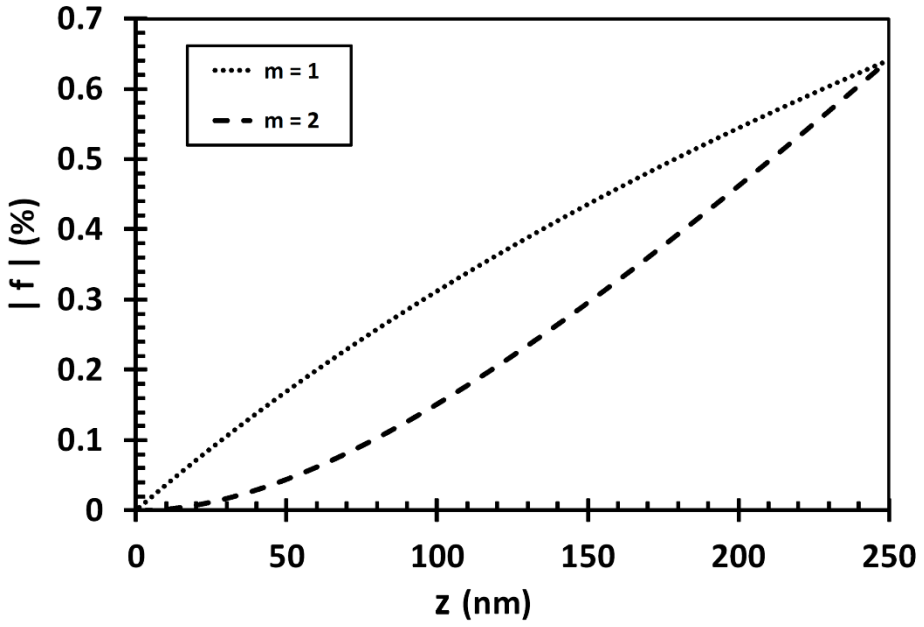

Figure 6.47. Lattice mismatch profiles for 250 nm thick $In_xGa_{1-x}As$ or $GaAs_{1-y}P_y$ layer on GaAs (001) substrate with $f_0 = 0$, $f_h = 0.0064$, and $m = 1$, and 2.

In an arbitrary graded semiconductor layer, the equilibrium strain and misfit dislocation density profiles can be found by minimizing the sum of the strain energy and the dislocation line energy. Mathews [171] used the dislocation line and strain energies to derive the critical layer thickness during the growth of uniformly-graded pseudomorphic structures. Tersoff extended this work by applying it to linearly graded structures. Although the detailed behavior of NLG-MBL is rather complex, it is possible to develop approximate models for the strain and dislocation density which may be used to guide the design of nonlinear log-graded device structures to take advantage of their desirable properties. The following has been described in more detail in the previous section.

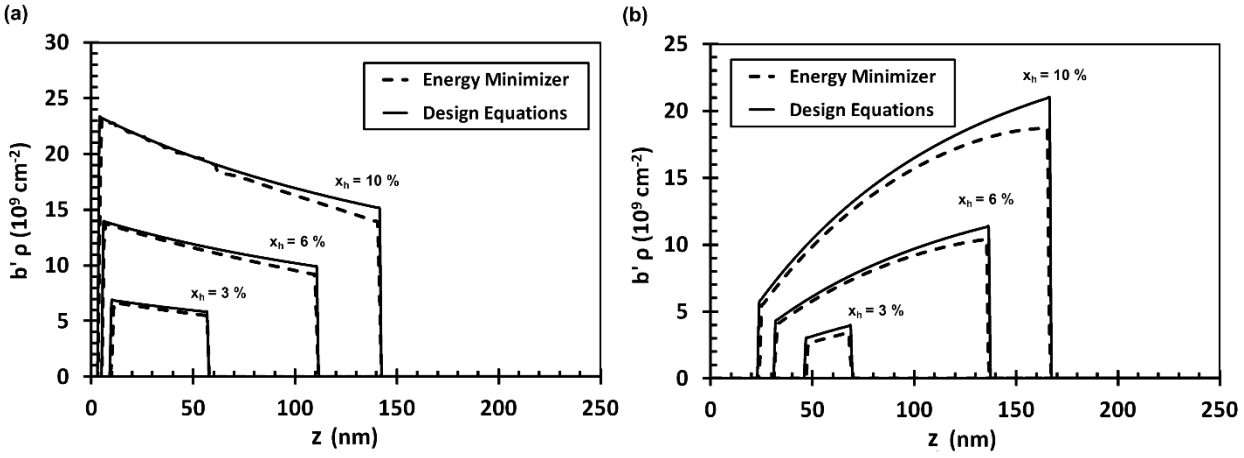

Figure 6.48. Equilibrium misfit dislocation density as a function of the distance from the interface for 250 nm thick nonlinear log-graded $In_xGa_{1-x}As$ / GaAs (001) layers with $f_0 = 0$ and various ending indium composition x_h. The results shown with dashed curves were found using detailed energy minimization calculations while the solid curves were obtained by the approximate design equations. (a) $m = 1$. (b) $m = 2$.

Figure 6.48a-b (dashed curves) illustrate the equilibrium misfit dislocation density profiles for 250 nm thick nonlinear log-graded $In_xGa_{1-x}As$ / GaAs (001) layers with $f_0 = 0$ and $m = 1$ (Fig

2a) and $m = 2$ (Fig. 2b) for various ending indium composition x_h. Figure 6.49a-b show the equilibrium in-plane strain profiles (dashed curves) for 250 nm thick NLG-MBL $In_xGa_{1-x}As$ / GaAs (001) layers with $x_h = 3$, 6, and 9 % for $m = 1$, and 2. The nonlinear log-graded layers exhibit a large built-in strain in the surface MDFZ which can aid in sweeping out threading dislocations prior to the growth of the device structure on top. In the surface MDFZ, the rate of change of the in-plane strain is higher for increasing power grading coefficient. The built-in strains in these structures are considerably greater than the equilibrium in-plane strain for a uniform layer of $In_xGa_{1-x}As$ on GaAs (001) having the same thickness and average composition. Therefore, dislocation glide velocities can be several times larger in the surface MDFZ of the NLG-MBL compared to a uniform buffer layer. In addition, a nonlinear (logarithmic) grading profile exhibits the greatest in-plane strain is at the surface. The equilibrium misfit dislocation density and in-plane strain are shown in Figure 6.48a-b and Figure 6.49a-b respectively (solid curves). The model is in good agreement with ad-hoc energy minimizer calculations. The slight variations of the in-plane strain between the energy minimizer (dashed lines) and approximate model (solid lines) could be explained by the fact that the model assumes that in the dislocated regions the misfit dislocation density is sufficient to completely relax the strain associated with compositional grading. In the dislocated region, Equation 6.83 assumes a constant in-plane strain value whereas minimum energy calculations show a sluggish decrease of the in-plane strain with increasing distance from the interface.

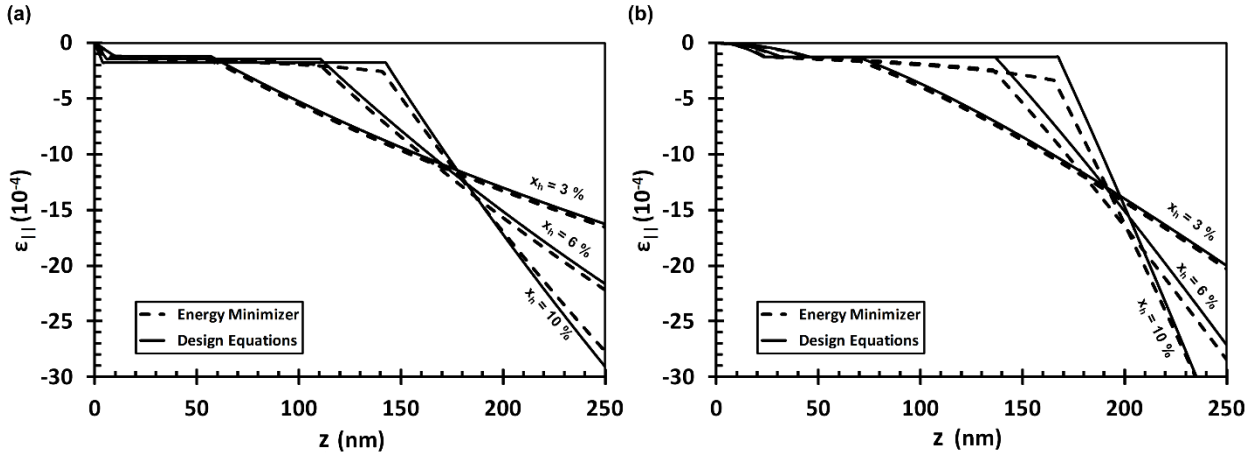

Figure 6.49. Equilibrium in-plane strain as a function of the distance from the interface for 250 nm thick nonlinear log-graded $In_xGa_{1-x}As$ / GaAs (001) layers with $f_0 = 0$ and various ending indium composition x_h. The results shown with dashed curves were found using detailed energy minimization calculations while the solid curves were obtained by the approximate design equations. (a) $m = 1$. (b) $m = 2$.

6.7.2.1. Residual Strain and Dislocation Characteristics in InGaAs and GaAsP on GaAs

In the design of an NLG-MBL, the most important characteristics to consider are the widths of the MDFZs, the misfit dislocation density, and the built-in strain in the surface MDFZ. Moreover, depending in the application of the device heterostructure the choice of the material system may influence the dislocation dynamics of the device. Figure 6.50 illustrates the average equilibrium misfit dislocation density for 250 nm thick nonlinear log-graded $In_xGa_{1-x}As$ or $GaAs_{1-y}P_y$ / GaAs (001) layers as a function of the ending lattice mismatch f_h for sub- and super-linear grading compositional profiles. The results of Figure 6.50 indicate that there is an approximately linear and monotonic increase in the average equilibrium misfit dislocation density as a function of the ending mismatch. In addition, the results of Figure 6.50 show that (i) $GaAs_{1-y}P_y$ contains a

higher misfit dislocation density than $In_xGa_{1-x}As$ and (ii) structures with super-linear grading profiles contain lower misfit dislocation densities.

Figure 6.51 compares the surface in-plane strain for 250 nm thick nonlinear log-graded $In_xGa_{1-x}As$ or $GaAs_{1-y}P_y$ / GaAs (001) layers as a function of the ending lattice mismatch f_h for sub- and super-linear grading compositional profiles. The surface in plane strain exhibits a sublinear behavior with increasing overshoot. The results of Figure 6.51 demonstrate that (i) structures with $In_xGa_{1-x}As$ as the epilayer and (ii) structures with a sub-linear grading profile contain a higher surface in-plane strain. However, the curve separation between the two material systems for both grading profiles becomes more prominent at higher mismatch. Differences in the surface in-plane strain between $In_xGa_{1-x}As$ and $GaAs_{1-y}P_y$ are quite pronounced in structures with a higher ending lattice mismatch.

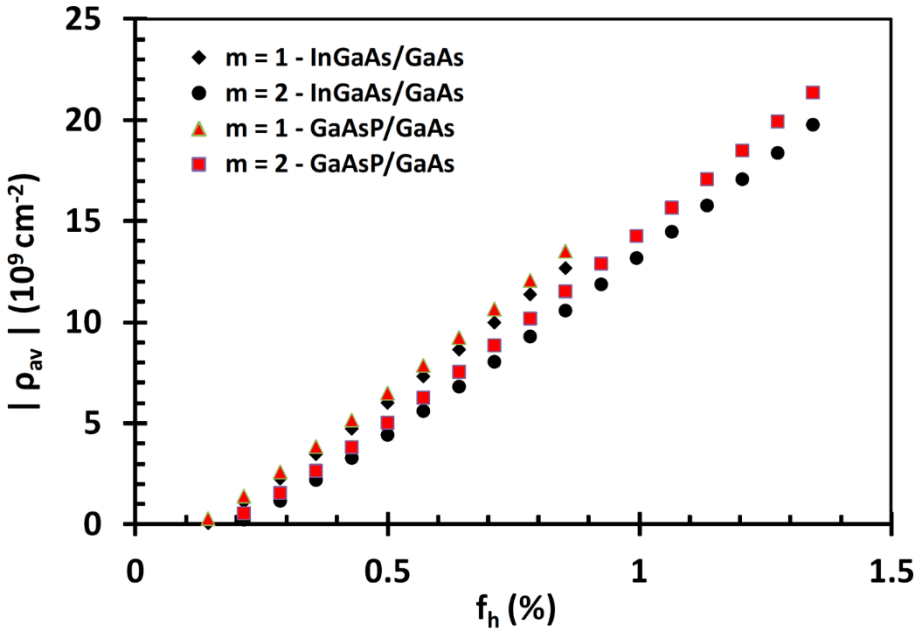

Figure 6.50. (Color Online) Average equilibrium misfit dislocation density for 250 nm thick nonlinear log-graded $In_xGa_{1-x}As$ or $GaAs_{1-y}P_y$ / GaAs (001) layers as a function of the ending lattice mismatch f_h for sub- and super-linear grading compositional profiles.

Figure 6.52a and b show the values of z_1 and z_2 for 250 nm thick nonlinear log-graded $In_xGa_{1-x}As$ or $GaAs_{1-y}P_y$ / GaAs (001) layers as a function of the ending lattice mismatch f_h for sub- and super-linear grading compositional profiles. The interfacial MDFZ (Figure 6.52a) decreases monotonically for increasing lattice mismatch. The existence of this MDFZ is expected on the basis that the introduction of misfit dislocations would increase both the strain energy and dislocation line energy and therefore there is a finite distance from the interface where the line energy cost of misfit dislocations is balanced by the strain energy they release in the growing film, and this dictates the extent of the misfit dislocation free material near the interface. Structures with a super-linear grading profile contain a greater interfacial misfit dislocation free zone. This can be explained by the fact that super-linear grading profile exhibits as sluggish change in the grading

profile near the interface and does not require the introduction of misfit dislocation. In comparison, sub-linearly graded structures contain a sharp increase in the mismatch near the substrate interface and therefore the introduction of misfit dislocations is required to balance the strain energy to the dislocation energy. The results of Figure 6.52b show a sub-linear decrease in the surface MDFZ. Surface MDFZ exists in material with significant lattice mismatch, due to the fact that much of the strain is relaxed by defects in the underlying dislocated zone. Due to this, and the proximity to the surface, relatively little strain energy can be released by the introduction of misfit dislocations in this near-surface material. Line energies of misfit dislocations near the surface are not reduced significantly because of the weak logarithmic dependence of the line energy on the distance from the interface. Consequently, there is a finite thickness of material near the surface in which the introduction of misfit segments is not energetically favored. Furthermore, the results of Figure 6.52 indicate that structures with $In_xGa_{1-x}As$ as the epilayer have a greater interfacial and surface MDFZ.

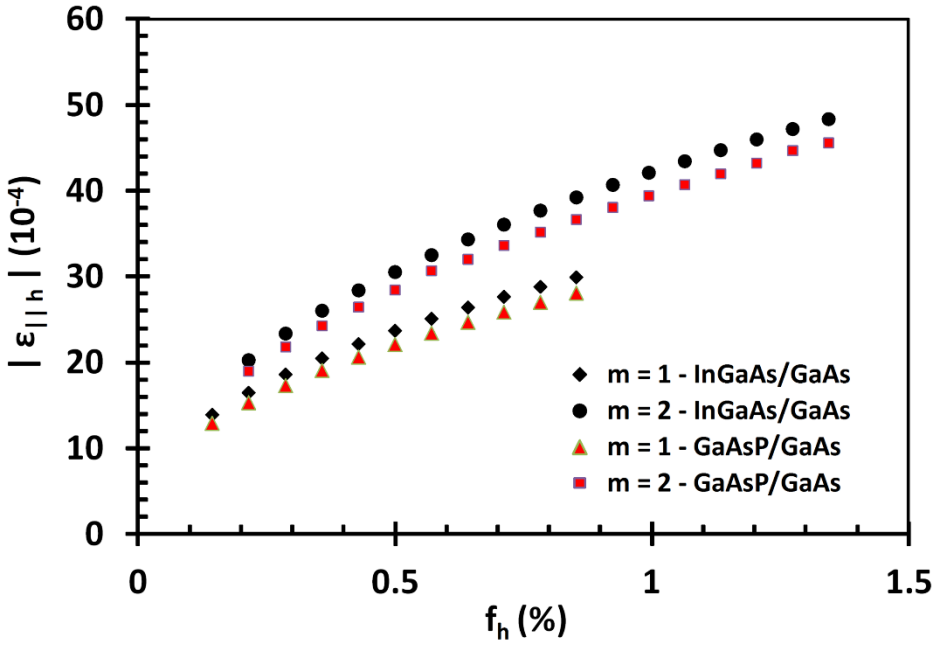

Figure 6.51. (Color Online) Surface in-plane strain for 250 nm thick nonlinear log-graded $In_xGa_{1-x}As$ or $GaAs_{1-y}P_y$ / GaAs (001) layers as a function of the ending lattice mismatch f_h for sub- and super-linear grading compositional profiles.

Table 6.3 shows that for the heterostructures studied in this work, the $GaAs_{1-y}P_y$ / GaAs (001) material system exhibits higher elastic stiffness coefficients. From an equilibrium point of view, structures with larger elastic constants exhibit higher relaxation rates. In addition, for a given lattice mismatch, heterostructures with higher stiffness coefficients require a greater misfit dislocation density in relaxing the excess strain. Therefore, it can be seen from the results of Figure 6.50 and Figure 6.51 that structures with $GaAs_{1-y}P_y$ as the epilayer material have greater elastic stiffness coefficients which is associated with higher average misfit dislocation densities and lower surface in-plane strain. Moreover, $GaAs_{1-y}P_y$/ GaAs (001) heterostructures contain a lower interfacial MDFZ. In cases with a sublinear grading profile, the introduction of defects is insensitive to the lattice mismatch and misfit dislocation are introduced closer to the interface. The

discussion provided here serves as guidance to the crystal grower in choosing the material system and compositional profile for the achievement of desired NLG-MBL properties (the maximum misfit dislocation density and thicknesses of the MDFZs).

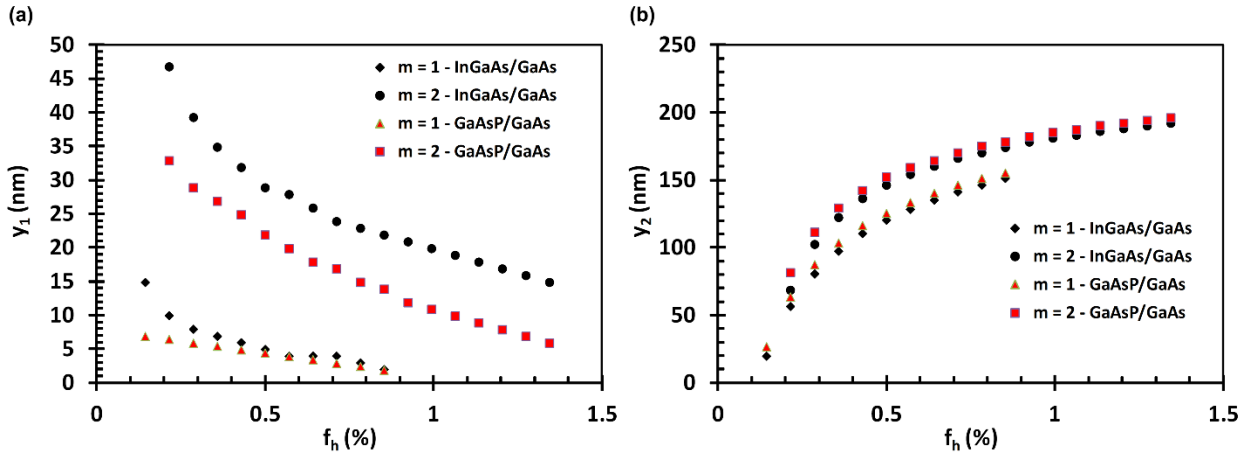

Figure 6.52. (a)Thickness of the interfacial MDFZ, z_1, for 250 nm thick nonlinear log-graded $In_xGa_{1-x}As$ or $GaAs_{1-y}P_y$ / GaAs (001) layers as a function of the ending lattice mismatch f_h for sub- and super-linear grading compositional profiles.(b) Distance of the edge of the surface MDFZ from the interface, z_2, for 250 nm thick nonlinear log-graded $In_xGa_{1-x}As$ or $GaAs_{1-y}P_y$ / GaAs (001) layers as a function of the ending lattice mismatch f_h for sub- and super-linear grading compositional profiles.

We have investigated equilibrium lattice relaxation in metamorphic in $GaAs_{1-y}P_y$ / GaAs (001) and $In_xGa_{1-x}As$ / GaAs (001) heterostructures involving nonlinearly-logarithmic-graded buffer layers. We have explored the equilibrium structure by studying the evolution of the surface in-plane strain, average misfit dislocation density and the widths of the interfacial and surface MDFZ. There are three main conclusions of this study. First, sublinearly-graded layers contain lower average misfit dislocation density, higher surface in-plane strain, interfacial and surface MDFZ. Second, equilibrium calculations predict that material systems with higher elastic stiffness coefficients contain a greater average misfit dislocation density, lower surface in-plane strain,

interfacial and surface MDFZ. Lastly, the use of nonlinearly-grade layers may be beneficial in the device design of metamorphic layers because they provide additional benefits such as high surface strain which may aid in sweeping threading arms and two MDFZ which reduce tangling and pinning interactions.

6.8. Strain Compensation in a Semiconducting Device Structure using an Intentionally Mismatched Uniform Buffer Layer

The extent of strain relaxation in semiconducting device heterostructures has important implications in the design of high electron mobility transistors, light-emitting diodes, and laser diodes, in which the residual strain affects the device characteristics. In this work, we develop the theoretical framework for understanding strain compensation in a semiconductor device layer using a uniform buffer layer which can be intentionally mismatched to the material above. Specifically, we determined the critical condition for complete strain compensation in the device layer by intentionally introducing a compositional mismatch at the device-buffer interface. We present minimum energy calculations and show that for a given device layer with fixed mismatch and layer thickness, the buffer layer may be designed with the appropriate combination of thickness and mismatch such that the device layer will have zero residual strain in equilibrium. Such a structure can be referred to as a completely strain-compensated design. In the more general case, there may be partial strain compensation, and we give a simple physics-based Gaussian-type function describing the residual strain in the device layer. We have applied this general framework to $In_xGa_{1-x}As/GaAs$ (001) heterostructures for the purpose of illustration, but the work is applicable to any diamond or zinc blende (001) heteroepitaxial material system.

6.8.1. Experimental use of Strain-Compensated Heterostructures

The incorporation of metamorphic buffer layers in semiconductor devices has gained great interest because their use relaxes the compositional constraints of pseudomorphic growth, thereby enabling the use of lattice-mismatched materials with a wide range of desirable properties. In addition, the intentional design of metamorphic buffer layers in semiconductor devices provides the flexibility in controlling the in-plane strain and threading dislocations, thereby allowing improved device performance or reliability. In previous work, we have demonstrated the use of a dislocation compensation mechanism in metamorphic structures [172, 66, 173, 174]; here our focus is on strain compensation.

In certain applications such as the design and growth of quantum-dot (QD) based devices including solar cells [175], lasers [176] or photodetectors [177], the use of multilayered metamorphic buffer layers with intentionally mismatched interfaces are beneficial for the enhancement of room temperature QD photoluminescence (PL) [178, 179, 180] and lasing characteristics such as the threshold current density and the PL linewidth [181, 182]. Furthermore, it has also been demonstrated that the use of intentionally mismatched layers results in the control of the in-plane strain [183], improvement of the crystalline quality and/or a reduction of the defect density [178]. More importantly, the incorporation of an intentionally mismatched layer in quantum-dot devices provides improved stability of the QDs during annealing cycles [184].

Although the published experimental work described in References 175-11 and 184 demonstrated an improvement of their QD-based devices by the insertion of intentionally mismatched layers, the focus of these works was on improving the device characteristics rather than the investigation of the detailed underlying physics. Though the physical mechanisms

involved for the stability and functionality of the QD regions are not as clear, the authors demonstrated empirically that the insertion of these intentionally mismatched layers improved the electrical characteristics and crystalline qualities of these devices. The insertion of a GaAsN [180] capping layer above the quantum-dot region yielded device heterostructures with a lower threading dislocation density whereas the insertion of a GaP [175, 184] layer below the quantum-dot region provided a higher degree of symmetry in the self-alignment of QDs.

In recent experimental work, Gocalinska et al. [185] considered InGaAs/GaAs (001) stacked heterostructures consisting of combinations of uniform and parabolically-graded layers. The objective of their work was to understand strain relaxation by adjusting the nominal compositional value and/or thickness of the buffer layer for the purpose of controlling the strain and defect densities in the device layer. In some of the structures they studied, it was apparent that the insertion of intentionally-mismatched buffer layer could control the strain in a top (device) layer. In one such case, the epitaxial stack consisted of two parabolically-graded $In_xGa_{1-x}As$ layers with an intermediate uniform layer of 180 nm $In_{0.1}Ga_{0.9}As$ and a uniform capping layer of 125 nm $In_{0.3}Ga_{0.7}As$. At both interfaces of the compositionally-graded layer the indium composition in the adjacent uniform layer was intentionally designed with undershoot. In this stacked structure, the top layer exhibited a tensile strain (opposite to the compressive lattice mismatch) with approximately ~ 97% strain relaxation and a threading dislocation density less than $< 5 \cdot 10^5$ cm^{-2}. In another such case, Gocalinska et al. considered a uniform layer of 700 nm $In_{0.16}Ga_{0.84}As$ deposited on a parabolically-graded $In_xGa_{1-x}As$ layer with a final indium composition of 33%. The device layer here exhibited tensile strain but there was a lower strain relaxation percentage. In addition, x-ray diffraction rocking curves indicated that although the device layer was grown well

beyond the critical layer thickness, there was no significant formation of a dislocation network (< $5 \cdot 10^5$ cm^{-2}) at the buffer/device interface.

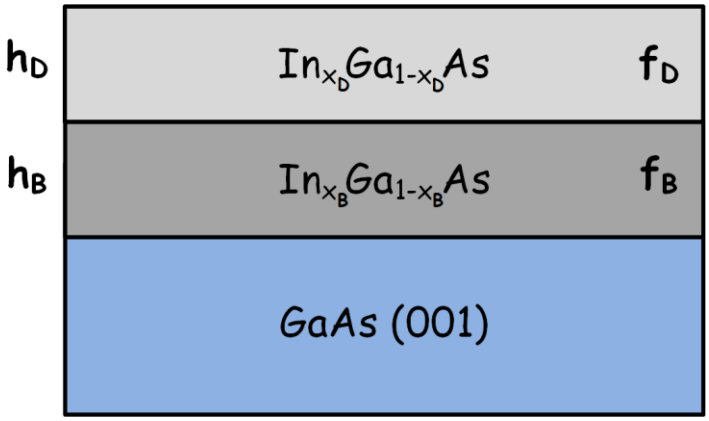

Figure 6.53. Schematic of the $In_xGa_{1-x}As/GaAs$ (001) heterostructures considered in this work.

Though the experimental studies described above are of practical interest, the underlying physical mechanisms are not well understood. We propose that strain compensation – the modification of the strain in a device layer by varying the design of one or more underlying buffer layers – could be the active mechanism. The term "strain-compensation" has been used with various meanings in published literature and specially in reference to the growth of strain-layer-super-lattices where the heteroepitaxy of these structures involves the growth of pseudomorphic and alternating compressive/tensile layers to relatively thick layers such that the final net strain of the structure is fully relaxed. Here however, strain compensation refers to the tailoring of the strain in a device layer by the design of the underlying buffer layer. In this work, the buffer layer has uniform composition, so design of the buffer involves just the thickness and composition. Furthermore, a key requirement for strain compensation involves a compositional mismatch at the buffer/device interface. There is therefore a great need for fundamental studies of strain

compensation in semiconductor device structures, to enable strain-compensated design and improved device characteristics.

In this work, we present a fundamental study of the strain compensation in a uniform device layer grown on a mismatched substrate with an intermediate uniform-composition buffer, and for the purpose of illustration we apply this theoretical framework to $In_xGa_{1-x}As$ / GaAs (001). Our objective was to determine the conditions on the design of the buffer layer such that complete strain compensation could be achieved in a device layer with given composition and thickness. In this work, the device layer was assumed to have uniform composition, but the results are applicable to a device multilayer having the same average composition, if average strain is considered. We present equilibrium (minimum energy) calculations in this work. These are important in their own right, for the determination of stability criteria and the limiting state for annealed devices, but they also serve as the starting point for understanding kinetically-limited strain relaxation, which is driven by the difference between the actual and equilibrium strain. In our work, the fundamental equations for the strain energy and dislocation line energy are essentially the same as those used by Matthews [186], and later by Tersoff [44,187]. However, our work differs significantly from those prior works because Matthews considered a single uniform layer, Tersoff considered a single linearly-graded layer, and our work addresses the case of a uniform device layer deposited on a uniform buffer layer. It should be mentioned that Tersoff provided an analytical expression for the criterion of growing a dislocation-free device layer on top of linearly-graded buffer, however in that work it was assumed that material can relax completely in the presence of misfit dislocations. More importantly, Tersoff's work did not consider the variation of the dislocation line energy with distance from the interface. These are simplifying assumptions which do not hold strictly in either

equilibrium or kinetically-limited relaxation [188] and we have not made this assumption. Kinetically-limited relaxation refers to non-equilibrium strain relaxation where the dislocation generation and glide occur at finite rates depending on growth temperature and conditions. Furthermore, different aspects of strain relaxation in semiconductor heterostructures has been considered in great lengths, whereas the present work is the first of its kind which develops the relationships for partial and/or complete strain-compensation in a device/buffer/substrate heterostructure with compositionally-uniform layers.

In this work, we considered structures comprising a uniform $In_xGa_{1-x}As$ device layer grown on a GaAs (001) substrate with an intermediate uniform $In_xGa_{1-x}As$ buffer layer, which could contain a different composition and thickness. The device layer has thickness h_D and lattice mismatch f_D with respect to the GaAs (001) substrate and the buffer layer has thickness h_B and lattice mismatch f_B as shown in Figure 6.53. We have investigated heterostructures with device and buffer layer thicknesses ranging from 100 nm to 500 nm and indium compositions ranging from 10% to 20%. The corresponding range of lattice mismatch is approximately -0.7% to -1.4%. The material constants used in this work are summarized in Table 6.4.

In the general case, the equilibrium configuration for a mismatched heteroepitaxial device structure may be found by minimizing the energy with respect to strain as described in a previous section.

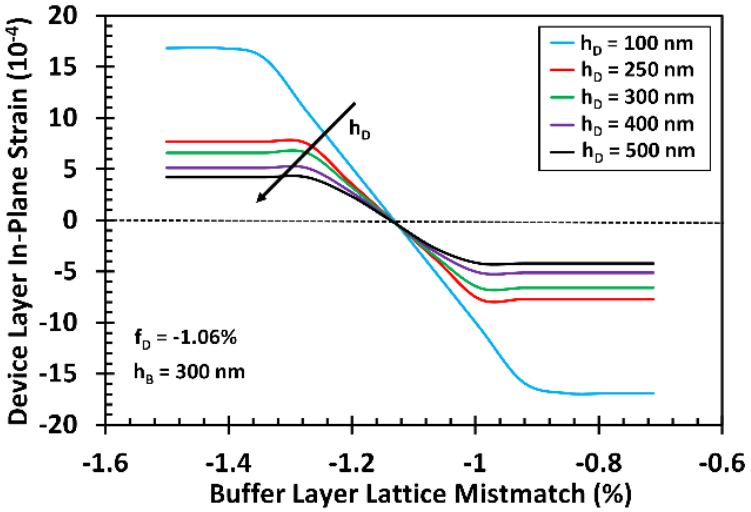

Figure 6.54. Device layer in-plane strain as a function of the buffer layer lattice mismatch for a 300nm thick buffer layer with device layer thickness as a parameter. The indium composition in the device layer is fixed at $x_D = 0.15$ corresponding to a mismatch of $f_D = -1.06\%$. The device layer thickness varies from 100 to 500 nm in steps of 100nm. The direction of the arrow is shown for device layers which exhibit tensile strain, whereas the direction reverses for compressive strain.

Table 6.4. Material Properties for InAs, GaAs and the alloy $In_xGa_{1-x}As$.

	Parameter		
Material	a (nm)	C_{11} (GPa)	C_{12} (GPa)
InAs	0.60584	83.3	45.3
GaAs	0.56534	118.4	53.7
$In_xGa_{1-x}As$	0.56534 + x(0.0405)	118.4 – x(35.1)	53.7 – x(8.4)

6.8.2. Strain Compensation in the InGaAs/GaAs Material System

In the growth of one or more compositionally uniform strained layers, misfit dislocations are introduced at the mismatched interfaces and they can be modeled using Dirac delta functions. For the structures studied here, dislocations may be introduced at the substrate-buffer and buffer-device layer interfaces. For a single uniform layer, the linear density of misfit dislocations

increases monotonically for increasing compositional mismatch due to the necessity for the introduction of more misfit segments to relax the mismatch strain. Apart from the dislocated interfaces, the equilibrium strain in a uniform layer is constant due to the absence of additional misfit dislocations above the interface. This constant strain depends on the lattice mismatch (composition) as well as the thickness. Therefore, a uniform buffer layer serves as a growth platform with adjustable in-plane lattice constant, the value of which depends on the buffer composition and thickness. The buffer layer may therefore be designed in such a way as to achieve complete strain compensation in a device layer to be grown on top.

In this work, we have explored the critical condition for strain compensation (zero strain in the device layer) by varying the compositional mismatch at the buffer layer-device layer interface at given buffer and device layer thicknesses. Figure 6.53 shows a schematic of the heterostructure considered in this work. For a given device layer thickness and composition, we have fixed the buffer layer thickness and have varied the composition of the buffer layer to determine the critical point for zero in-plane strain at the surface of the heterostructure (the strain compensation condition). In other words, for a given device layer thickness and device layer mismatch there exists a combination of the buffer layer thickness and buffer layer mismatch such that the device layer exhibits zero strain.

Figure 6.54 illustrates the device layer in-plane strain as a function of the buffer layer lattice mismatch for a 300 nm thick buffer with device layer thickness as a parameter. The device layer thickness is varied from 100 nm to 500 nm. The fractional indium composition of the device layer shown here is fixed at $x_D = 0.15$ corresponding to a lattice mismatch of $f_D = -1.06\%$. The results of Figure 6.54 show that the in-plane strain in the device layer exhibits a three-regime behavior.

The regimes here refer to specific cases of the absolute value of the compositional mismatch and its effect on the strain state. More specifically, the regimes with constant device layer strain refer to cases where misfit dislocations (MD) are present at the device-buffer interface, however, the sense of the MDs may change depending on the compositional difference whereas the regime with varying strain refers to the case when MDs are absent from the device interface. In the first regime where the absolute lattice mismatch of the buffer layer is much larger than that of the device layer, $|f_B| >> |f_D|$, the in-plane strain in the device layer is constant and exhibits the same sign as the lattice mismatch. In this regime, misfit dislocations at both the substrate and buffer/device interface are of the same sense. In the second regime, the lattice mismatch of the device and buffer layer are comparable to one another and in this region the in-plane strain in the device layer exhibits a sharp transition from compressive to tensile strain. In addition, there is a particular buffer layer lattice mismatch which yields a completely relaxed device layer (perfect strain compensation). Interestingly, in the second regime, there are no misfit dislocations at the device interface even though the device layer thickness is well beyond the critical layer thickness. In the third regime, where the absolute lattice mismatch of the buffer layer is much smaller than that of the device layer, $|f_B| << |f_D|$, the device layer strain is constant with increasing buffer layer mismatch but the layer exhibits tensile strain which is opposite from the lattice mismatch. In contrast to the first regime, misfit dislocations at the substrate and buffer/device interface are of the opposite sense. In the first and third regimes, the large lattice mismatch between the buffer and device layer is accommodated partly by misfit dislocations at the device interface whereas in the second regime, there is an interplay between the in-plane strains of both layers, which is associated with the

absence of misfit dislocations from the device interface. It is interesting to note that for a fixed buffer layer thickness, the critical mismatch for strain compensation is weakly dependent on the device layer thickness. Although the dependence is not clearly evident in Figure 6.54, it will be considered in more detail below. In addition to this dependence in regime two, the device layer thickness determines in part the saturated values of strain in regimes one and three.

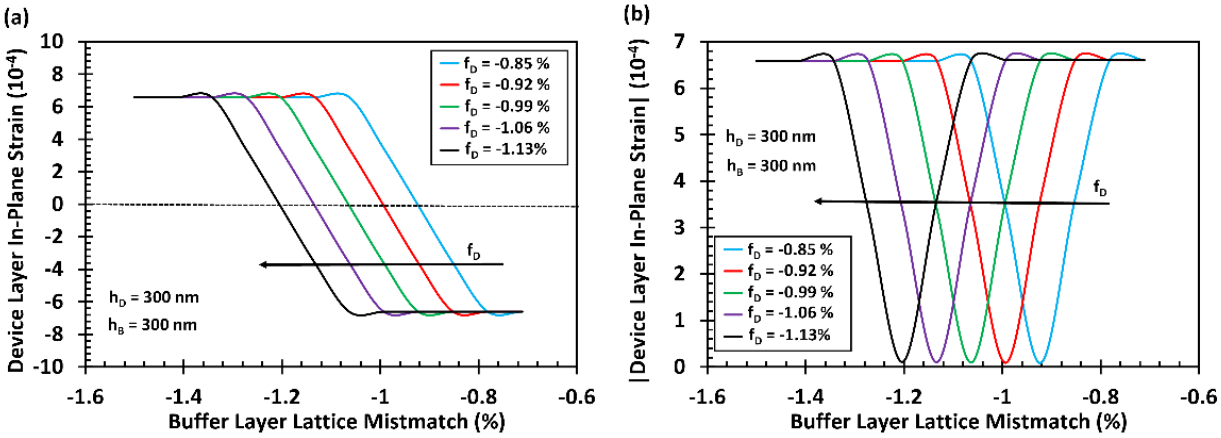

Figure 6.55. Device layer in-plane strain (a) and (b) absolute value as a function of the buffer layer lattice mismatch for a 300nm thick buffer with device layer lattice mismatch as a parameter. The device layer thickness is fixed at 300 nm.

An underlying assumption in some previous work [188,189] is that strain relaxation is an irreversible process. That is, once the threading arms of dislocations begin to glide in one direction it is assumed that they may not glide in the opposite direction, even if the net glide force reverses direction by the growth of additional material. This would be the case if the average threading dislocation density and the average length of the misfit dislocations remained fixed for a layer even after growth of a subsequent layer on top. However, in this work we have not made such an assumption, and we believe that lattice relaxation may be a reversible process. For example, we can consider the case where the average threading dislocation density remains fixed however, the

growth of additional material may reverse the net force acting of the dislocation and therefore the direction of its glide. In such a case, the average length of misfit dislocation may decrease or increase depending on the net force acting on the dislocation and therefore, this would cause a change in the density of misfit dislocations. Therefore, in this work, we are assuming that the net direction of glide for threading arms of dislocations my reverse under the appropriate conditions, as shown previously [190].

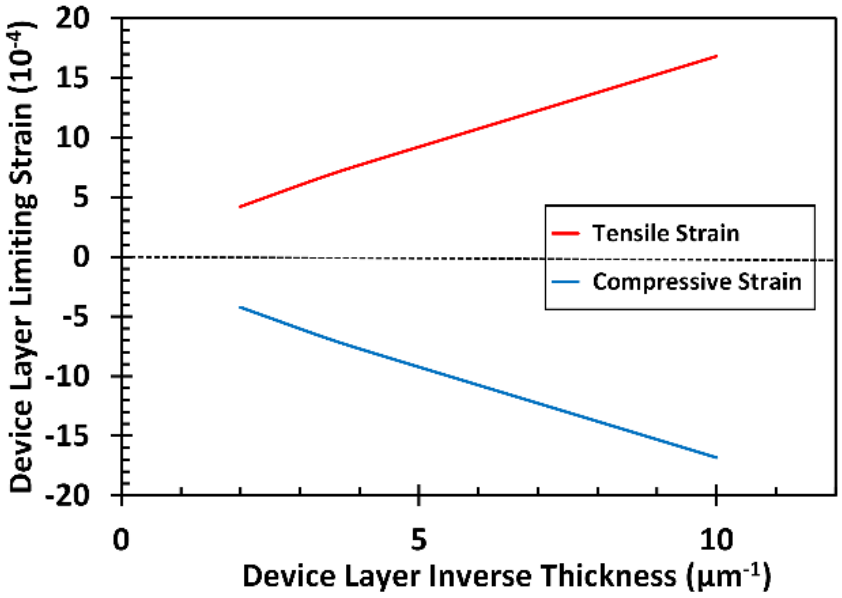

Figure 6.56. Device layer in-plane strain as a function of the device layer reciprocal thickness in the constant strain regimes.

Figure 6.55a shows the device layer in-plane strain as a function of the lattice mismatch of a 300 nm thick buffer layer with device layer lattice mismatch as a parameter. The device layer lattice mismatch f_D here is varied from -0.85% to -1.13% whereas the thickness of the device layer is fixed at 300 nm. The results of Figure 6.55a indicate a behavior similar to that shown in Figure 6.54, but an increase in the device layer indium composition yields a higher critical buffer

layer mismatch for strain compensation (left-shift of the device layer strain versus buffer layer mismatch characteristic). Moreover, observation of the absolute value of the in-plane strain (Figure 6.55b) shows that the tensile and compressive strain in the first and third regimes (constant strain regimes) exhibit symmetrical behavior. In other words, in these regimes, an increase in the lattice mismatch at the buffer-device interface does not alter the device layer in-plane strain and we attribute this behavior to the use of constant thicknesses for the buffer and device layer.

Together, these results show that in the saturation regions (regimes one and three), the device layer in-plane strain is strongly dependent on the device layer thickness. Figure 6.56 shows the device layer in-plane strain as a function of the reciprocal device layer thickness in the regimes of constant strain. The results of Figure 6.56 indicate a monotonic increase (decrease) in the device layer in-plane strain with higher reciprocal thickness in structures exhibiting tensile (compressive) strain. These results are consistent with the Matthews and Blakeslee equilibrium model where the equilibrium strain as a function of layer thickness h for a simple uniform layer of $In_xGa_{1-x}As/GaAs$ (001) is given by

$$\varepsilon_{\parallel}(h)=\begin{cases} f, & h \le h_c; \\ \dfrac{f}{|f|}\dfrac{b\left(1-\nu\cos^2\alpha\right)}{8\pi h(1+\nu)\sin\lambda\sin\phi}\left[\ln\left(\dfrac{h}{b}\right)+1\right], & h > h_c;, \end{cases} \qquad \textbf{(6.89)}$$

where h_c is the critical layer thickness, ν is the Poisson ratio, and α is the angle between the Burgers vector and dislocation line vector. It should be noted that many of the earlier works neglected the logarithmic term in the dislocation line energy which is determined by the cutoff radius in the integral of the strain field surrounding the dislocation. As pointed out by Matthews, the cutoff radius is either the film thickness or one-half the dislocation spacing, whichever is the

smaller quantity. In high-dislocation density material, the latter condition prevails, but the logarithmic-term is still present, and should not generally be considered constant because the dislocation density is not constant. For simplicity, we have defined,

$$C = \frac{Gb\left(1-\nu\cos^2\alpha\right)}{2\pi(1-\nu)\sin\lambda\sin\phi}, \qquad \textbf{(6.90)}$$

In the regions of strain saturation, the device and buffer layers are decoupled by the misfit dislocations at the device layer interface; in these regimes where the lattice mismatch at the device interface is accommodated partly by misfit dislocations, the device layer in-plane strain $\varepsilon_{\|,D}$ saturates at $\pm\varepsilon_{\|,D,SAT}$ where $\varepsilon_{\|,D,SAT}$ is a function of the device layer thickness; specifically the saturated value of the device layer in-plane strain is given by

$$\varepsilon_{\|,D,SAT}\left(h_D\right) = \frac{f_D - f_B}{\left|f_D - f_B\right|}\frac{C_D}{2Y_D h_D}\left[\ln\left(\frac{h_D}{b_D}\right)+1\right], \qquad \textbf{(6.91)}$$

where the subscript D refers to the device layer. In addition, in the saturation regimes, the in-plane strain in the buffer layer is influenced by the strain state of the layer above (that is, by the misfit dislocations at the device interface) and the buffer in-plane strain is given by

$$\varepsilon_{\|,B}\left(h_B\right) = \frac{1}{2Y_B h_B}\left(\frac{f_B}{\left|f_B\right|}C_B\left[\ln\left(\frac{h_B+h_D}{b_B}\right)+1\right] - 2Y_D h_D \varepsilon_{\|,D,SAT}\left(h_D\right)\right). \qquad \textbf{(6.92)}$$

Combining the results of Figure 6.54, Figure 6.55 and Figure 6.56 and Equation 6.95, the in-plane strain of the device layer may be modeled using a simple Gaussian function given by

$$\left|\varepsilon_{\|,D}(h_D)\right| = \left|\varepsilon_{\|,D,SAT}(h_D)\right|\left[1-\exp\left(-\frac{\left(f_B - f_D - f_\Delta\right)^2}{2\sigma^2}\right)\right], \quad \textbf{(6.93)}$$

where f_Δ is the required mismatch for complete strain compensation and σ is the standard deviation parameter. Equation 6.97 includes the dependence of the device layer in-plane strain on the buffer and device layer lattice mismatch as well as the device layer thickness explicitly, but the dependence of the device layer strain on the buffer layer thickness is embodied in the parameters f_Δ and σ. By considering the condition for minimum energy and recognizing that the device layer is coherently strained with respect to the buffer layer in regime two (in other words no misfit dislocations are present at the device interface), it can be shown that the required mismatch for complete strain compensation is given by

$$f_\Delta = \frac{f_B}{|f_B|}\frac{C_B}{2Y_B h_B}\left[\ln\left(\frac{h_B + h_D}{b_B}\right)+1\right]. \quad \textbf{(6.94)}$$

Similarly, the standard deviation parameter can be modeled by

$$\sigma = \frac{C_D}{4\sqrt{2\ln(2)}}\frac{f_D - f_B}{|f_D - f_B|}\left[\ln\left(\frac{h_D}{b_D}\right)+1\right]\frac{Y_B h_B + Y_D h_D}{Y_B h_B Y_D h_D}. \quad \textbf{(6.95)}$$

Figure 6.57 illustrates the device layer in-plane strain as a function of the buffer layer mismatch with buffer layer thickness as a parameter; the buffer layer thickness was varied from 100 nm to 500 nm in steps of 100nm. The fractional indium composition of the device layer shown here is fixed at $x_D = 0.15$ corresponding to a lattice mismatch of $f_D = -1.06\%$ and the device layer thickness is fixed at $h_D = 400nm$. The characteristic of Figure 6.57 shows behavior similar to that in Figure 6.55. The saturation values of the device layer in-plane strain are independent of

the buffer layer thickness at higher mismatch of the buffer-device interface. However, in the second regime, Figure 6.57 shows an increase in the rate of change of the device layer strain with respect to f_B for increasing buffer layer thickness; in other words both f_Δ and the transition width decrease for increasing buffer layer thickness (f_Δ and σ decrease with the buffer layer thickness). This phenomenon can be explained by the fact that the strain in the buffer layer varies with its thickness and therefore the extent of strain relaxation for critical compensation is much lower for thicker buffer layers. In addition, in cases where the device layer is coherently grown on the buffer layer (that is, there are no misfit dislocations at the device interface), the in-plane strain of the buffer layer is controlled in part by the strain-state of the layer on top of it (the device layer). Equation 6.97 indicates that perfect strain compensation is achieved when $f_B - f_D = f_\Delta$. Although not as apparent in the results of Figure 6.55 and Figure 6.56, we can conclude from the results of Equation 6.98, that f_Δ is however weakly dependent on the device layer thickness.

The in-plane strain in the device layer can be analytically modeled by the following Gaussian-based function utilizing Equations 6.95, 6.98 and 6.99 while accounting for both the mismatch and thickness of the device and buffer layers,

$$\left|\varepsilon_{\parallel,D}(h_D)\right| = \left|\frac{f_D - f_B}{|f_D - f_B|}\frac{C_D}{2Y_D h_D}\left[\ln\left(\frac{h_D}{b_D}\right)+1\right]\right| \times$$
$$\left[1-\exp\left(-\frac{\left(f_B - f_D - \frac{f_B}{|f_B|}\frac{C_B}{2Y_B h_B}\left[\ln\left(\frac{h_B+h_D}{b_B}\right)+1\right]\right)^2}{2\cdot\left(\frac{C_D}{4\sqrt{2\ln(2)}}\frac{f_D - f_B}{|f_D - f_B|}\left[\ln\left(\frac{h_D}{b_D}\right)+1\right]\frac{Y_B h_B + Y_D h_D}{Y_B h_B Y_D h_D}\right)^2}\right)\right]. \quad \textbf{(6.96)}$$

Equation 6.100 is in excellent agreement with the detailed numerical results of the equilibrium model. The most important result of Equation 6.100 is that for a given device layer design (f_D and h_D) there exists a combination of f_B and h_B such that the device layer exhibits zero in-plane strain (perfect strain compensation).

In this work, we have presented a fundamental investigation of strain compensation – the modification of the strain in a semiconductor device layer by varying the design of one or more underlying buffer layers – for the case of a uniform device layer grown on a mismatched substrate with an intermediate uniform-composition buffer. For the purpose of illustration, we have applied this work to $In_xGa_{1-x}As$ / GaAs (001) heterostructures. We have explored the equilibrium structure by studying the evolution of the misfit dislocation density and in-plane strain at the mismatched interfaces for the purpose of determining the critical condition for strain compensation in the device layer in terms of the mismatches and thicknesses of the two layers. The main conclusion to this study is that for a given device layer design (thickness and composition), there exist choices of the buffer layer thickness and composition which yield perfect strain compensation in the device layer. In the general case, we show by a physics-based treatment that the device layer in-plane

strain is given by a Gaussian-type function involving the physical properties of the buffer and device layer.

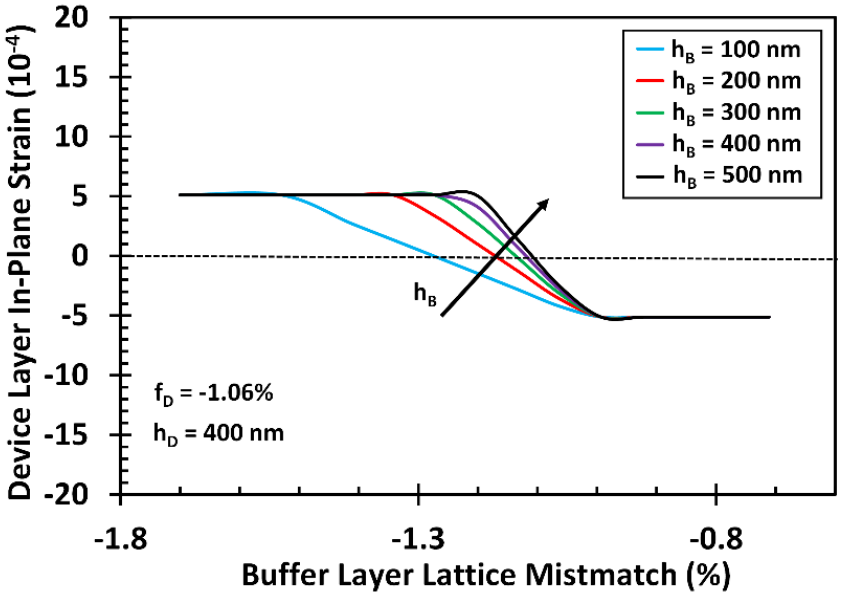

Figure 6.57. Device layer in-plane strain as a function of the buffer layer lattice mismatch with buffer layer thickness as a parameter. The indium composition in the device layer is fixed at $x_D = 0.15$ corresponding to a mismatch of $f_D = -1.06\%$ and the thickness is 400 nm. The buffer layer thickness varies from 100 to 500 nm in steps of 100nm.

7. Applications of the Electrical Circuit Model

In the following chapter, we have briefly described the framework of the electrical circuit model and its application to three simple cases of SiGe epitaxy: a single uniform layer, a step-graded layer, and a linearly-graded layer, approximated as a step-graded structure with many sublayers. In addition, we show the application to continuously-graded structures, wherein the strain is a continuous function of distance from the interface. This enables the development of a closed-form expression for the strain as a function of distance in a continuously-graded layer with any arbitrary compositional profile, including linear, exponential, power-law, or complementary error function profiles. This in turn allows an analytical solution for the critical layer thickness, widths of misfit dislocation free zones, and misfit dislocation density in these graded structures. More importantly, the circuit model allows intuitive understanding of electric circuits to be readily applied to strained-layer semiconductor structures, which represents a significant breakthrough that will revolutionize the design and theoretical treatment of graded buffer layers. Furthermore, we show for the first time that an electrical circuit model analogy for strained-layer epitaxy may be used for the analysis and design of strain-compensated ZnSySe1-y/GaAs (001) heterostructures involving a constant-composition buffer layer and a constant composition device layer. We show that the residual strain in the device layer may be controlled by the choices of composition and thickness in the two layers, and we develop analytical expressions for the strains in the buffer and the device layer.

7.1. Electric Circuit Model for Strained-Layer Epitaxy in SiGe/Si

For the design and analysis of a strained-layer semiconductor device structure, the equilibrium strain profile may be determined numerically by energy minimization but this method

is computationally intense and non-intuitive. Here we present an electric circuit model approach for the equilibrium analysis of an epitaxial stack, in which each sublayer may be represented by an analogous configuration involving a current source, a resistor, a voltage source, and an ideal diode. The resulting node voltages in the analogous electric circuit correspond to the equilibrium strains in the original epitaxial structure. This new approach enables analysis using widely accessible circuit simulators, and an intuitive understanding of electric circuits may be translated to the relaxation of strained-layer structures. In this work, we describe the mathematical foundation of the electrical circuit model and demonstrate its application to epitaxial layers of $Si_{1-x}Ge_x$ grown on a Si (001) substrate.

The design and analysis of semiconductor strained-layer device structures [191,192,193,194,195,196] require an understanding of the equilibrium profiles of strain and dislocations associated with strained epitaxy. The equilibrium profile is important in its own right for the calculation of device stability criteria, but also serves as the entry point for determination of kinetically-limited strain relaxation and concentrations of non-equilibrium defects, such as threading dislocations, which influence device performance and reliability. Although the equilibrium configuration for a general semiconductor strained-layer structure may be determined numerically [43,197,198,199,200], such an approach uses specialized code, is computationally intense, and does not lend itself to an intuitive understanding necessary for innovative structure design. In light of these considerations, we have developed a simple and intuitive electric circuit model approach for the equilibrium analysis of semiconductor strained-layer heterostructures. The use of this electrical circuit model enables analysis using widely-available circuit simulators and provides intuitive design of semiconductor strained-layer structures by analogous association to

electrical characteristics of circuits. In this work, we describe the mathematical framework for the electrical circuit model approach, starting with a single strained layer and then generalizing to a multilayer structure. We relate the physical quantities in the epitaxial stack to those in an analogous electrical circuit. Using the circuit model, we demonstrate the equilibrium analysis of $Si_{1-x}Ge_x$ / Si (001) epitaxial structures, and show that the results of the circuit model calculations are in agreement with the theory of Matthews and Blakeslee [34] for a uniform strained layer, the analysis of Kujofsa and Ayers [199] for a step-graded layer, and the model of Tersoff [44] for a linearly-graded layer.

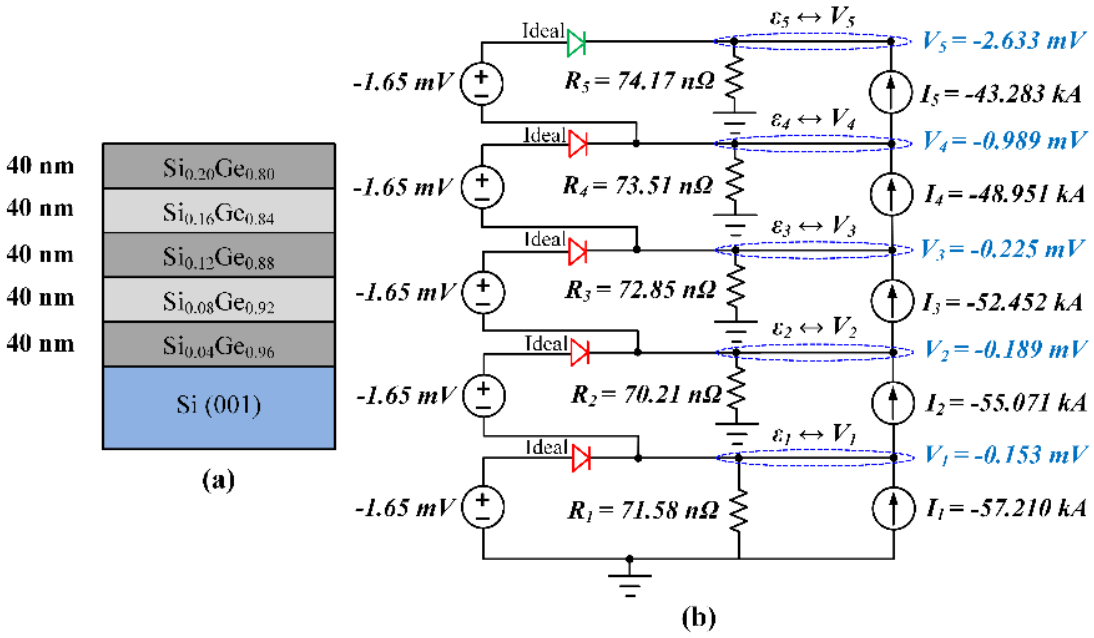

Figure 7.1. (a) Schematic representation of step-graded epitaxial layer with five sublayers and (b) the equivalent electrical circuit.

7.1.1. Application of Circuit Model to Representative SiGe/Si: Results and Discussion

For the purpose of illustration, we have applied the electrical circuit model to the well-known cases of a single $Si_{1-x}Ge_x$ epitaxial layer deposited on Si (001) substrate with (i) uniform

composition, (ii) step- and (iii) linear-grading compositional profile. The material constants used in this work are summarized in Reference 7. For a uniform epitaxial layer with a thickness of 200 nm and a lattice mismatch of $f = -0.8270\%$ (corresponding to 20% germanium mole fraction), the electrical circuit model indicates a residual strain of $\varepsilon = -0.0825\%$ corresponding to a node voltage of $V = -0.825mV$, in agreement with the Matthews and Blakeslee model prediction of $\varepsilon = -0.0825\%$.

Figure 7.1a considers a step-graded $Si_{1-x}Ge_x$ epitaxial layer with five 40 nm thick sublayers in which there are equal compositional changes from one layer to the next. The lattice mismatch is $f_1 = -0.1654\%$, $f_2 = -0.3308\%$, $f_3 = -0.4962\%$, $f_4 = -0.6616\%$, and $f_5 = -0.8270\%$ in the five layers, respectively. Strain relaxation behavior in step-graded layers is similar to that for uniform composition layers, in which the misfit dislocations are concentrated at the mismatched interface and the residual strain is uniform within each sublayer. However, depending on the compositional change the interfacial and surface MDFZ widths may be multiples of the sublayer thickness. For the structure considered here, the generalized equilibrium model predicts residual strains of $\varepsilon_1 = -0.0154\%$, $\varepsilon_2 = -0.0190\%$, $\varepsilon_3 = -0.0257\%$, $\varepsilon_4 = -0.0986\%$, and $\varepsilon_5 = -0.2629\%$ in the five sublayers respectively and this is in excellent agreement with the results of the electrical circuit as can be seen in Figure 7.1b. In addition, the results of Figure 7.1b show that the diodes in the first four essential nodes are non-conductive, indicating the presence of a misfit dislocation network, whereas the conduction of the diode in the fifth essential node indicates a coherently-grown sublayer.

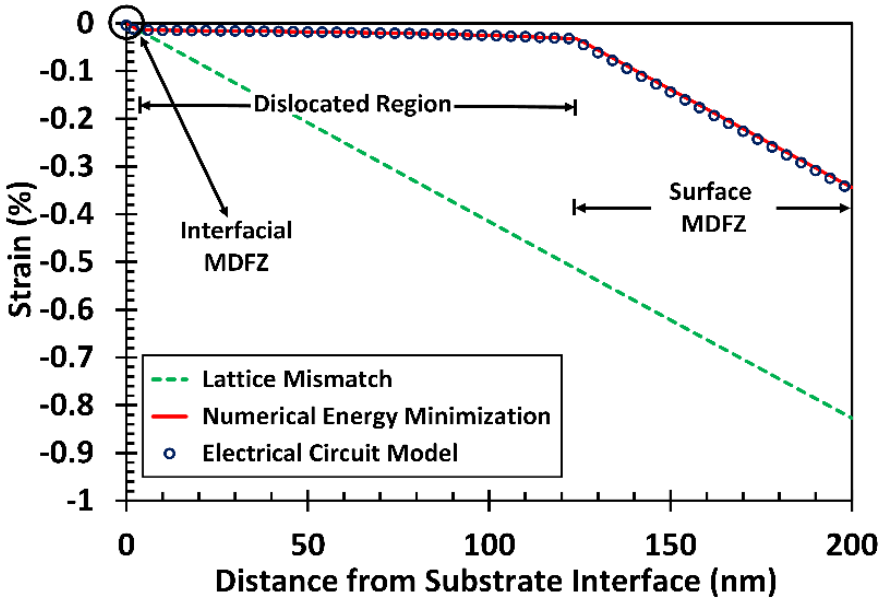

Figure 7.2. Lattice mismatch and in-plane strain as a function of the distance from the interface for a linearly-graded epilayer of SiGe on Si (001) substrate. The in-plane strain is determined using the numerical minimum energy and electrical circuit models.

Figure 7.2 illustrates the lattice mismatch profile and equilibrium strain for a 200 nm thick linearly-graded layer of $Si_{1-x}Ge_x/Si$ (001). Here the dashed line shows the profile of lattice mismatch, which varies linearly from zero (corresponding to zero germanium mole fraction) to $f_h = -0.8270\%$ at the surface (20% germanium). Figure 7.2 also shows the equilibrium strain profile determined by numerical minimum energy calculations (solid line) and the electric circuit model (open circles). These two results are in excellent agreement, and both show the existence of an interfacial misfit dislocation free zone as well as a surface misfit dislocation free zone, as expected on the basis of previous studies [200]. The MDFZs exhibit residual strain profiles with the same slope as the lattice mismatch (proportional to the grading coefficient), and exhibit widths

of 4 nm (at the interface) and 75 nm (at the surface). Between the interfacial and surface MDFZ there is a dislocated region with nearly constant strain.

In conclusion, we have developed an electrical circuit model to study equilibrium lattice relaxation in semiconductor strained-layer heterostructures. In this approach, each sublayer of an epitaxial structure is modeled by an analogous electrical subcircuit utilizing a voltage source, an ideal diode, a resistor and a current source. Multilayered or graded semiconductor structures may be modeled by stacking the appropriate number of these building blocks, after which the numerical values of the node voltages in the circuit correspond to the equilibrium strains in the sublayers of the semiconductor structure. Use of this electric circuit analogy allows the modeling of semiconductor strained-layer structures by readily available circuit simulators, and makes it possible to translate the intuitive understanding of circuits to heteroepitaxial devices.

7.2. Electric Circuit Model Analogy for Equilibrium Lattice Relaxation in InGaAs/GaAs

In the present study, using the circuit model, we demonstrate the equilibrium analysis of a number of $In_xGa_{1-x}As$ / GaAs (001) epitaxial structures, including a single strained layer, three-layer stacks, step-graded layers, linearly-graded layers and S-graded layers. We show that the strain results of the circuit model calculations are in agreement with the theory of Matthews and Blakeslee [55] for the single strained layer. We also develop exact results for the case of a linearly graded layer, whereas previously only an approximate solution had been developed by Tersoff. In the approximate solution of Tersoff, it was assumed that the strain was completely relieved in the region containing dislocations, and that the dislocation line energy was independent of distance from the surface. We have not relied on these simplifying assumptions when applying the circuit model, and therefore provide exact in-plane strain results for the linearly-graded case.

Furthermore, we show the extension of the circuit model to any continuously-graded semiconductor layer by taking the limit as the thickness of the individual sublayers approaches zero. This enables the development of analytical expressions for the strain, misfit dislocation density, critical layer thickness and widths of misfit dislocation free zones (MDFZ) in a continuously-graded epitaxial layer having any compositional grading profile, including linear [201], exponential [202], power law, and S-graded [52,203] profiles. The extension from a finite number of sublayers to the continuously-graded case is analogous to the transition from circuit theory, using lumped circuit elements, to electromagnetics, wherein the electrical quantities are distributed. We show this development based on first principles, but in a more general sense, Maxwell's equations of electromagnetics could be applied to continuously-graded strained layers.

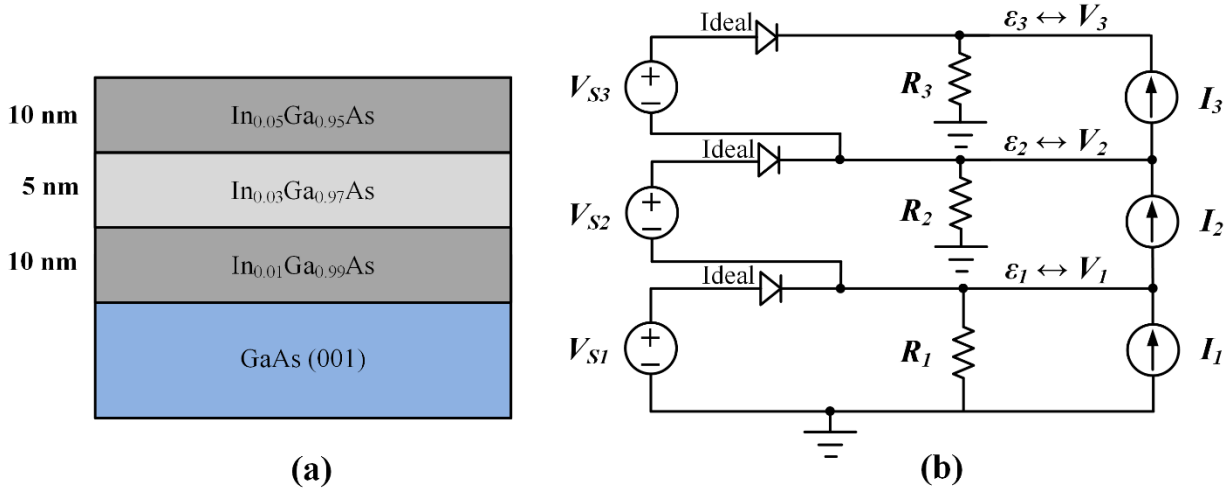

Figure 7.3. (a) Schematic representation of a coherently-grown multilayer heterostructure with three compositionally uniform epitaxial layers consisting of 10 nm $In_{0.05}Ga_{0.95}As$ / 5 nm $In_{0.03}Ga_{0.97}As$ / 10 nm $In_{0.01}Ga_{0.99}As$ on a GaAs (001) substrate. (b) The equivalent electrical circuit for the multilayer heterostructure consisting of the series connection (stacking) of the electrical circuit blocks where the material properties of each sublayer are modeled using the equivalent electrical components (resistor, ideal diode, independent current and independent voltage sources).

7.2.1. Application to the InGaAs/GaAs Material System: Results and Discussion

In applying the electrical circuit model to multilayered heterostructures and comparing its results to the numerical minimum energy calculations we considered the following cases involving the InGaAs/GaAs material system. The physical parameters used in this work are summarized in Table 7.1 The simplest structure is one composed of three pseudomorphic layers in which the whole structure is coherently grown on the substrate. Figure 7.3a shows a multilayered $In_xGa_{1-x}As/GaAs$ (001) heterostructure (Sample A) consisting of three uniform and pseudomorphic layers with indium compositions of $x_1 = 1\%$, $x_2 = 3\%$ and $x_3 = 5\%$, respectively, and thicknesses of $h_1 = 10$ nm, $h_2 = 5$ nm and $h_3 = 10$ nm, respectively. Figure 7.3b illustrates the equivalent electrical circuit model for the entire structure; the numerical values for the electrical components used here are summarized in Table 7.2. Given that the thickness of each layer is below the critical thickness for misfit dislocation formation, the in-plane strain at each sublayer is equal to the coherency strain and therefore its lattice mismatch. In the equivalent electrical circuit model, the ideal diode at each node is conductive and therefore the respective current sources play no role in determining the voltage (i.e. in-plane strain) at each node. Furthermore, the voltage at each node is determined from the sum of all voltage sources up to and including the layer under consideration. The numerical value of the voltage in node one is equal to the lattice mismatch of sublayer one, the voltage at node two is equal to the sum of the voltage sources for sublayers one and two, and the voltage at node three is equal to the sum of all three voltage sources. Therefore, the numerical value of the voltage at each node is equal to the lattice mismatch of that layer as expressed by

$\varepsilon_n = f_n \leftrightarrow V_n = V_{Sn}$. As shown in Table 7.3, the results obtained for Sample A using the circuit model agree with results from the numerical energy minimization approach.

Table 7.1. Material Properties for InAs, GaAs and the alloy $In_xGa_{1-x}As$ [75204] where a is the lattice constant, C_{11} and C_{12} are the elastic stiffness constants and x is the indium mole fraction. Linear interpolation following Vegard's law was used to determine the material properties of the $In_xGa_{1-x}As$ alloy.

	Parameter		
Material	a (nm)	C_{11} (GPa)	C_{12} (GPa)
InAs	0.60584	83.3	45.3
GaAs	0.56534	118.4	53.7
$In_xGa_{1-x}As$	0.56534 + x(0.0405)	118.4 – x(35.1)	53.7 – x(8.4)

The growth of mismatched epilayers which are beyond the critical layer thickness requires the formation of a misfit dislocation network to relax some portion of the lattice mismatch. In uniform layers, misfit dislocations are introduced at the mismatched interfaces and they can be modeled using the Dirac delta function. The heterostructure shown in Figure 7.4a includes three incoherently-grown and mismatched sublayers with lattice mismatch $f_1 = -0.71\%$, $f_2 = -2.1\%$ and $f_3 = -1.06\%$ and thicknesses $h_1 = 75\,\text{nm}$, $h_2 = 100\,\text{nm}$ and $h_3 = 150$ nm. The analogous electrical circuit is shown in Figure 7.4b. The numerical minimum energy results shown in Table 7.3 for Sample B, suggest that all three sublayers are partly relaxed and all interfaces contain misfit dislocation networks. It is interesting to note that sublayers one and two exhibit compressive strain, similar to the lattice mismatch, whereas sublayer three exhibits tensile strain which is opposite to the lattice mismatch; the tensile strain present in the third sublayer suggests that misfit dislocations with Burgers vectors opposite in sense to those at the other two interfaces have been introduced. Standard electrical circuit simulator (SECS) modeling results of the electrical circuit shown in

Figure 7.4b are in excellent agreement with minimum energy calculations. Furthermore, diodes at each node are non-conductive and therefore the node voltage is determined by the sum of the currents flowing through that node and the resistor attached to it. Thus, the voltage (in-plane strain) at each node is given by

$$\begin{aligned} \varepsilon_3 = +0.1035\% \quad &\leftrightarrow \quad V_3 = R_3 \cdot I_3 = +1.035mV \\ \varepsilon_2 = -0.3267\% \quad &\leftrightarrow \quad V_2 = R_2 \cdot (I_2 - I_3) = -3.267mV \\ \varepsilon_1 = -0.0228\% \quad &\leftrightarrow \quad V_1 = R_1 \cdot (I_1 - I_2) = -0.228mV \end{aligned} \qquad \textbf{(7.1)}$$

For the third heterostructure, we considered the important case of a single uniform and incoherently-grown epitaxial layer as shown in Figure 7.5a with a total thickness of $h = 350$ nm and a lattice mismatch of $f = -0.71\%$. For the purpose of illustration and also to provide a stringent test of the electrical circuit model, we divided the epitaxial layer into three sublayers with varying thicknesses ($h_1 = 50$ nm, $h_2 = 200$ nm and $h_3 = 100$ nm), but each sublayer contained the same composition (and therefore the same lattice mismatch with respect to the substrate). The in-plane strain of the heterostructure considered in Figure 7.5a could be easily calculated using the well-known Matthews and Blakeslee's model (Equation 4.8) by considering the total epitaxial thickness. The equilibrium in-plane strain determined for Sample C (Table 7.3) from all three models are in excellent agreement. In addition, SECS modeling of the electrical circuit shown in Figure 7.5c indicates that the ideal diode at sublayer one is non-conductive which suggests the presence of a misfit dislocation network at the substrate interface. However, at the second and third nodes the ideal diodes are conductive; diode conduction at nodes two and three indicates the presence of a misfit dislocation free zone in the epitaxial sublayers two and three and implies that a three-fold supernode will be formed. As a consequence of the supernode formation the current

source at node one (I_1) flows through resistors R_1, R_2 and R_3 arranged in parallel (Figure 7.5c); the voltage at each node is determined from the product of the current source I_1 and the equivalent parallel resistance $R_1 \parallel R_2 \parallel R_3$. Thus, the in-plane strain of each sublayer is given as,

$$\varepsilon_1 = \varepsilon_2 = \varepsilon_3 = -0.0498\% \quad \leftrightarrow \quad V_1 = V_2 = V_3 = \left(\frac{1}{R_1} + \frac{1}{R_2} + \frac{1}{R_3} \right)^{-1} I_1 = -0.498 mV \,. \qquad \textbf{(7.2)}$$

The electrical circuit model could be extended to any arbitrary multilayered heterostructure employing compositional-grading. Figure 7.6a illustrates a step-graded buffer comprising ten uniform layers, each with 10 nm thickness and in which there are equal compositional changes from one layer to the next ("linear step grading"). For the structure studied here, the indium composition is varied from 1% at the sublayer closest to the substrate interface to a final surface indium composition of 10% corresponding to a lattice mismatch of 0.71%; the lattice mismatch profile as a function of the distance from the substrate interface z is shown in Figure 7.6c (dashed line). The corresponding electrical circuit is illustrated in Figure 7.6b. For the case of a step-graded layer consisting of N sublayers, the maximum number of misfit dislocation peaks is equal to the number of mismatched interfaces (10 in the current case). Kujofsa and Ayers [51, 52] have shown that in general, continuously-graded layers contain misfit-dislocation free zones adjacent to the substrate interface and surface, provided that there is zero interfacial mismatch and/or the grading coefficient is sufficiently small. However, in step graded layers, the thicknesses of the interfacial and surface misfit dislocation free zones are constrained to be related to multiples of the step-layer thickness, which in this case is one tenth of the total buffer layer thickness ($h_T = 100\,\text{nm}$) [53]. In $In_xGa_{1-x}As/GaAs$ (001) step-graded layers, the presence of an interfacial MDFZ is evident only

when a very small grading coefficient is used (approximately 2% indium per micron). In addition, for a low ending composition, and therefore ending lattice mismatch, the surface misfit dislocation free zone may extend beyond the top step layer.

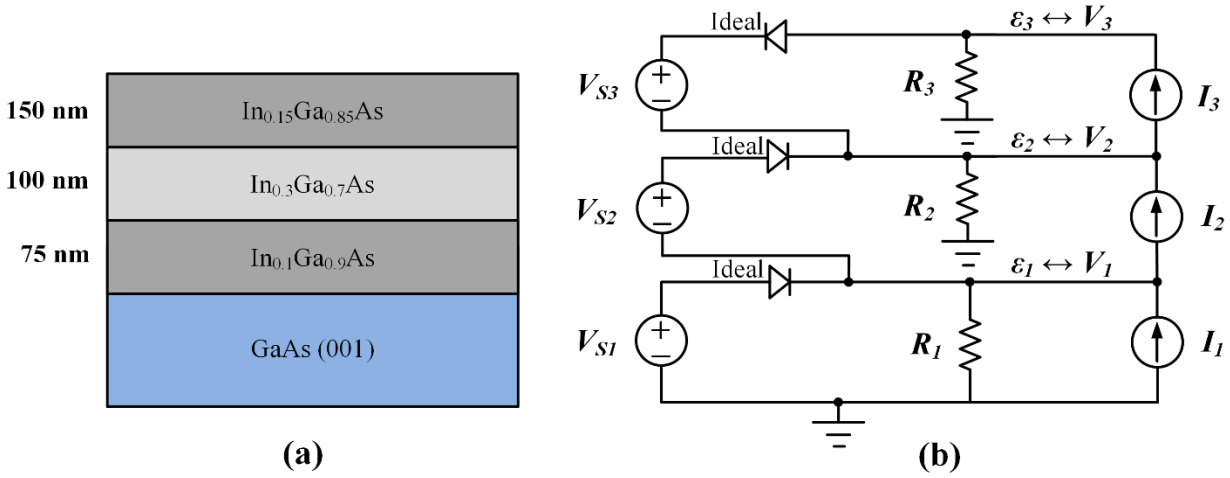

Figure 7.4. (a) Schematic representation of an incoherently-grown multilayer heterostructure with three compositionally uniform epitaxial layers consisting of 150 nm $In_{0.15}Ga_{0.85}As$ / 100 nm $In_{0.3}Ga_{0.7}As$ / 75 nm $In_{0.1}Ga_{0.9}As$ on a GaAs (001) substrate. (b) The equivalent electrical circuit for the multilayer heterostructure consisting of the series connection (stacking) of the electrical circuit blocks where the material properties of each sublayer are modeled using the equivalent electrical components (resistor, ideal diode, independent current and independent voltage sources).

Figure 7.6c depicts the equilibrium in-plane strain distribution determined by numerical minimum energy calculations (solid lines) and the electrical circuit (circle symbols) as a function of the distance from the interface. The in-plane strain profile comprises a series of step functions with discontinuities at the mismatched interfaces. The first five interfaces contain misfit dislocations, which relax most of the mismatch strain and result in small values of the residual strain. The absence of misfit dislocation networks at the top five interfaces results in high built-in

strains. These results from the circuit analysis are in excellent agreement with numerical energy minimization calculations as shown in Figure 7.6c.

Table 7.2. The numerical values of the electrical components for the electrical circuits.

Sample	Resistance (nΩ)	Voltage Source (mV)	Current Source (kA)
A (Figure 7.3b)	$R_1 = 406.6$	$V_{S1} = -0.716$	$I_1 = -28.217$
	$R_2 = 818.9$	$V_{S2} = -1.428$	$I_1 = -25.246$
	$R_3 = 412.4$	$V_{S3} = -1.425$	$I_1 = -22.881$
B (Figure 7.4b)	$R_1 = 55.97$	$V_{S1} = -7.1$	$I_1 = -41.098$
	$R_2 = 45.25$	$V_{S2} = -13.9$	$I_1 = -37.022$
	$R_3 = 28.50$	$V_{S3} = 10.4$	$I_1 = 36.352$
C (Figure 7.5b)	$R_1 = 83.96$	$V_{S1} = -7.1$	$I_1 = -41.494$
	$R_2 = 83.96$	$V_{S2} = 0$	$I_1 = 0$
	$R_3 = 83.96$	$V_{S3} = 0$	$I_1 = 0$
D (Figure 7.6b)	$R_1 = 406.6$	$V_{S1} = -0.716$	$I_1 = -38.385$
	$R_2 = 408.0$	$V_{S2} = -0.715$	$I_2 = -35.144$
	$R_3 = 409.5$	$V_{S3} = -0.714$	$I_3 = -34.388$
	$R_4 = 410.9$	$V_{S4} = -0.713$	$I_4 = -33.550$
	$R_5 = 412.4$	$V_{S5} = -0.712$	$I_5 = -32.605$
	$R_6 = 413.8$	$V_{S6} = -0.711$	$I_6 = -31.513$
	$R_7 = 415.3$	$V_{S7} = -0.710$	$I_7 = -30.206$
	$R_8 = 416.8$	$V_{S8} = -0.709$	$I_8 = -28.560$
	$R_9 = 418.3$	$V_{S9} = -0.708$	$I_9 = -26.292$
	$R_{10} = 419.8$	$V_{S10} = -0.707$	$I_{10} = -22.502$

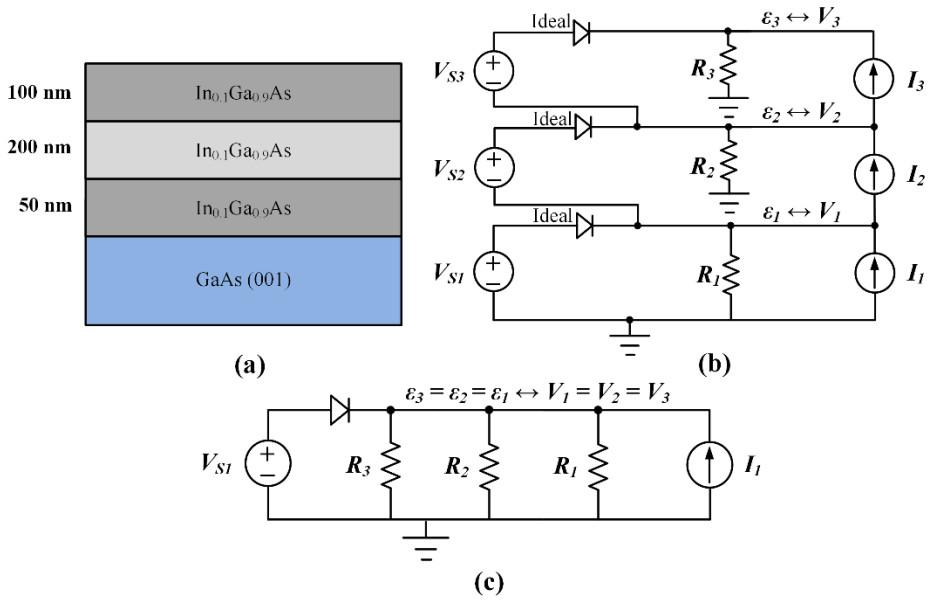

Figure 7.5. (a) Schematic representation of an incoherently-grown multilayer heterostructure with three sublayers where the top two are coherently-grown. Physically the heterostructure can be considered as a single compositionally uniform 350 nm thick $In_{0.1}Ga_{0.9}As$ layer deposited on a GaAs (001) substrate; however for the purpose of illustration it is broken down to 100 nm $In_{0.1}Ga_{0.9}As$ / 200 nm $In_{0.1}Ga_{0.9}As$ / 50 nm $In_{0.1}Ga_{0.9}As$. (b) The equivalent electrical circuit for the multilayer heterostructure consisting of the series connection (stacking) of three electrical circuit blocks where the material properties of each sublayer are modeled using the equivalent electrical components (resistor, ideal diode, independent current and independent voltage sources).

The electrical circuit model could be applied to any heterostructure with an arbitrary number of sublayers. Figure 7.7 illustrates the lattice mismatch profile and equilibrium strain for a linearly-graded layer of $In_xGa_{1-x}As$ grown epitaxially on a GaAs (001) substrate. Here the dashed line shows the profile of lattice mismatch, which varies linearly from zero (corresponding to zero indium mole fraction) to $f_h = -0.71\%$ at the surface (corresponding to 10% indium mole fraction). Figure 7.7 also shows the equilibrium strain profile for the linearly-graded layer, as determined by numerical minimum energy calculations (solid line) and the electric circuit model (open circles). These two results are in excellent agreement, and both show the existence of an interfacial misfit

dislocation free zone as well as a surface misfit dislocation free zone, as expected on the basis of previous studies [7, 9, 10, 54]. The misfit dislocation free zones exhibit residual strain profiles with the same slope as the lattice mismatch, and exhibit widths of 5 nm (at the interface) and 46 nm (at the surface). Between these there is a dislocated region of thickness 49 nm in which the strain is nearly constant.

In our work, the fundamental equations for the strain energy and dislocation line energy are essentially the same as those used by Matthews [56], and later by Tersoff [44]. Although the equilibrium configuration in the linearly-graded epitaxial layer has been explored in great detail by Tersoff, Fitzgerald et al. [72], Dunstan [205] and Romanato et al. [206], these models assume that graded material can relax completely in the presence of misfit dislocations. This is a simplifying assumption which does not strictly hold in either equilibrium or kinetically-limited relaxation. More specifically, there are two key assumptions embedded in these models; first, there is zero strain in the dislocated region and second they neglect the thickness dependence of the line energies for dislocations. Because of these simplifying assumptions, the interfacial misfit dislocation-free zone is not seen and there is zero strain in the dislocated region. Therefore, the in-plane strain characteristic is described by these models as,

$$\varepsilon(z) = \begin{cases} 0 & z \le z_c; \\ C_f (z - z_c) & z_c < z \le h. \end{cases} \qquad \textbf{(7.3)}$$

where z_c is the edge of the dislocated region near the surface and C_f is the grading coefficient.

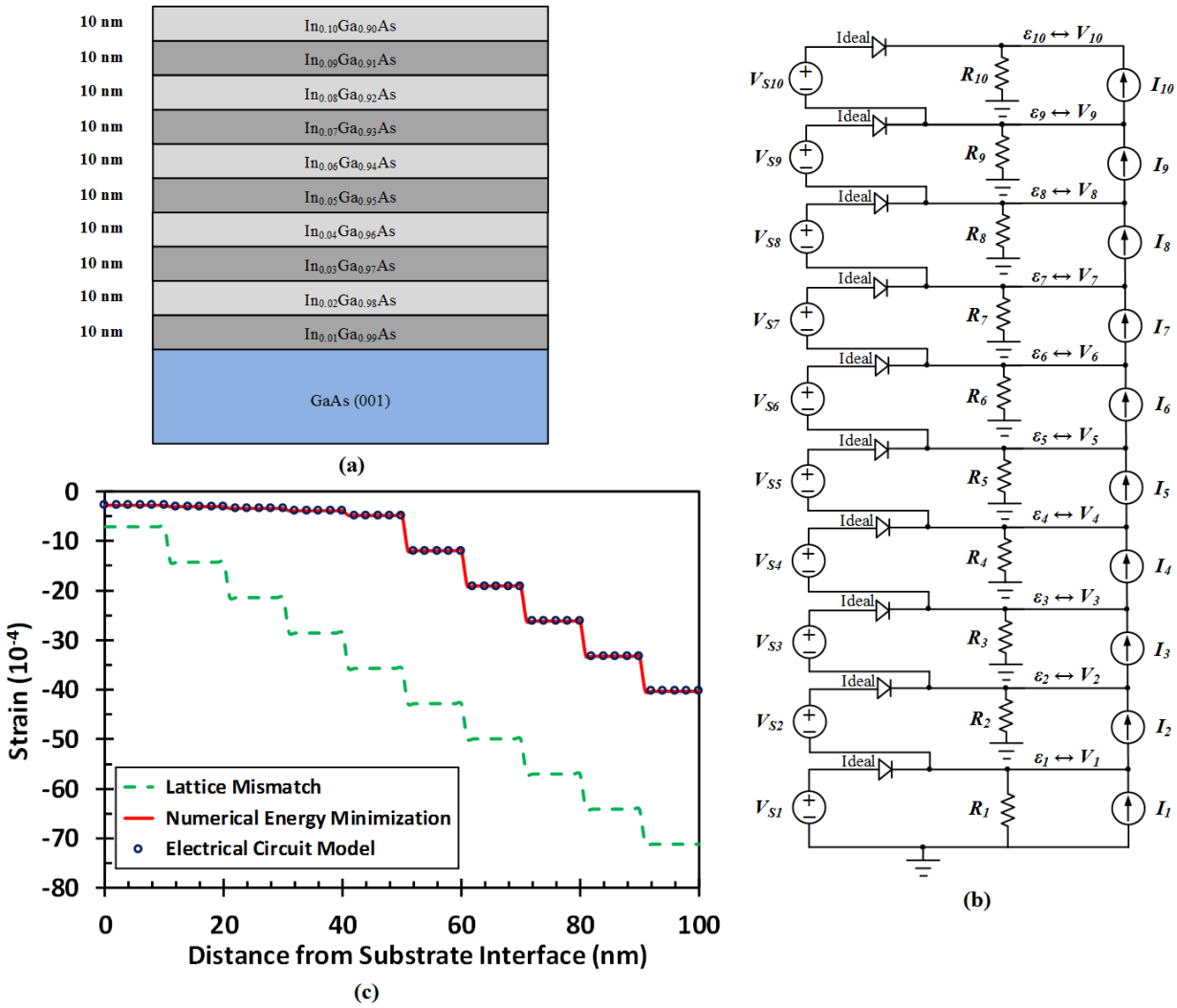

Figure 7.6. (a) Schematic representation of 100 nm thick step-graded $In_{0.1}Ga_{0.9}As$ epitaxial layer with 10 sublayers where the indium composition is varied in steps of 1% starting from 1% at the sublayer nearest the interface and ending at 10% in the sublayer at the surface. (b) The equivalent electrical circuit for the step-graded heterostructure consisting of the series connection (stacking) of 10 electrical circuit blocks where the material properties of each sublayer are modeled using the equivalent electrical components (resistor, ideal diode, independent current and independent voltage sources). (c) Lattice mismatch (dashed) and in-plane strain (solid, circle) as a function of the distance from the interface for the step-graded epilayer. The in-plane strain is determined using the numerical minimum energy (solid line) and electrical circuit (open circles) models.

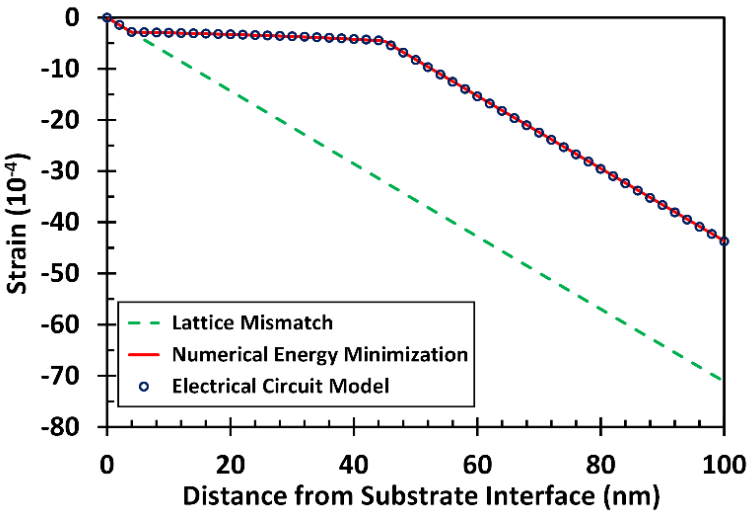

Figure 7.7. Lattice mismatch (dashed) and in-plane strain (solid, circles) as a function of the distance from the interface for a 100 nm thick linearly-graded $In_xGa_{1-x}As$ epitaxial layer where the indium composition is varied linearly from 0 at the substrate interface to 10% at the surface. The in-plane strain is determined using the numerical minimum energy (solid line) and electrical circuit (open circles) models.

The numerical and the equivalent electrical circuit models do not make such simplifying assumptions, and therefore the residual strain characteristics is slightly different from the previously developed models. If the edges of the interfacial and surface MDFZs are located at distances of z_1 and z_2 from the substrate interface as illustrated in Figure 7.7, and therefore the misfit dislocation density is concentrated in the middle region ($z_1 \le z \le z_2$), then the residual strain can be analytically modeled as follows: In the interfacial MDFZ, the absence of misfit dislocations indicates that the residual strain is equal to the lattice mismatch profile and therefore:

$$\varepsilon(z) = C_f z, \quad z \le z_1 . \tag{7.4}$$

In the dislocated region ($z_1 \le z \le z_2$), the residual strain is modeled by the electrical circuit model as

$$\varepsilon_n \quad \leftrightarrow \quad V_n = R_n \cdot \left(I_n - I_{n+1}\right). \tag{7.5}$$

Table 7.3. The in-plane strains of various multilayered heterostructures and comparisons between numerical minimum energy results and the electrical circuit model.

Sample	Numerical Minimum Energy	Electrical Circuit Model
A (Figure 7.3a)	$\varepsilon_3 = -0.3569\%$	$\varepsilon_3 = -0.3569\%$
	$\varepsilon_2 = -0.2144\%$	$\varepsilon_2 = -0.2144\%$
	$\varepsilon_1 = -0.0716\%$	$\varepsilon_1 = -0.0716\%$
B (Figure 7.4a)	$\varepsilon_3 = +0.1035\%$	$\varepsilon_3 = +0.1035\%$
	$\varepsilon_2 = -0.3267\%$	$\varepsilon_2 = -0.3267\%$
	$\varepsilon_1 = -0.0228\%$	$\varepsilon_1 = -0.0228\%$
C (Figure 7.5a)	$\varepsilon_3 = -0.0499\%$	$\varepsilon_3 = -0.0498\%$
	$\varepsilon_2 = -0.0499\%$	$\varepsilon_2 = -0.0498\%$
	$\varepsilon_1 = -0.0499\%$	$\varepsilon_1 = -0.0498\%$

An important application of the electric circuit model analogy is to the case of a continuously-graded layer. This can be considered by approximating the continuously-graded material by a stack of uniform composition sublayers and then taking the limit as the thickness of the individual sublayers approaches zero. This development is similar to the transition from electric circuit theory using lumped circuit elements to electromagnetic theory using distributed electrical quantities. This enables the development of analytical expressions for the strain, misfit dislocation density, critical layer thickness and widths of misfit dislocation free zones in a continuously-graded layer having any arbitrary compositional profile. Previously only the linear [63] and exponential [64] grading cases had been considered theoretically, but the circuit model analogy allows the analysis of any continuously-graded layer, including those with power law, S-graded, or some type of non-linear compositional profiles. This development will be described below.

Using the electric circuit analogy and assuming that the physical constants b, ν, G and Y are slowly varying functions of n, the in-plane strain in the nth sublayer is given by

$$\varepsilon_n = -\frac{1}{2Y_n h_n}\left\{\begin{array}{l}\dfrac{f_n - f_{n-1}}{|f_n - f_{n-1}|}\dfrac{Gb(1-\nu\cos^2\alpha)}{2\pi(1-\nu)\sin\alpha\sin\phi}\left[\ln\left(\displaystyle\sum_{j=n}^{N}\frac{h_j}{b}\right)+1\right] \\ -\dfrac{f_{n+1} - f_n}{|f_{n+1} - f_n|}\dfrac{Gb(1-\nu\cos^2\alpha)}{2\pi(1-\nu)\sin\alpha\sin\phi}\left[\ln\left(\displaystyle\sum_{j=n+1}^{N}\frac{h_j}{b}\right)+1\right]\end{array}\right\}. \qquad \textbf{(7.6)}$$

As a specific example for a monotonic continuously-graded layer $\dfrac{f_n - f_{n-1}}{|f_n - f_{n-1}|} = \dfrac{f_{n+1} - f_n}{|f_{n+1} - f_n|}$. Thus

$$\varepsilon_n = \frac{1}{2Yh_n}\frac{f_{n+1} - f_n}{|f_{n+1} - f_n|}\frac{Gb(1-\nu\cos^2\alpha)}{2\pi(1-\nu)\sin\alpha\sin\phi}\ln\left(\frac{\displaystyle\sum_{j=n}^{N}\frac{h_j}{b}}{\displaystyle\sum_{j=n+1}^{N}\frac{h_j}{b}}\right). \qquad \textbf{(7.7)}$$

The equation above can be simplified to

$$\varepsilon_n = \frac{1}{2Y}\frac{f_{n+1} - f_n}{|f_{n+1} - f_n|}\frac{Gb(1-\nu\cos^2\alpha)}{2\pi(1-\nu)\sin\alpha\sin\phi}\frac{\ln\left(\dfrac{h_n + h - z}{h_n}\right)}{h_n}, \qquad \textbf{(7.8)}$$

where h is the epitaxial layer thickness and z is the distance from the substrate interface to the top of layer n. For simplicity let

$$A = \frac{1}{2Y}\frac{f_{n+1} - f_n}{|f_{n+1} - f_n|}\frac{Gb(1-\nu\cos^2\alpha)}{2\pi(1-\nu)\sin\alpha\sin\phi}. \qquad \textbf{(7.9)}$$

The limiting case of a continuously-graded layer, in which $h_n \to 0$, may be understood using L'Hopital's rule, giving

$$\lim_{h_n \to 0} \{\varepsilon_n\} = \lim_{h_n \to 0} \left\{ \frac{A \dfrac{\partial}{\partial h_n} \left[\ln\left(\dfrac{h_n + h - z}{h_n} \right) \right]}{\dfrac{\partial}{\partial h_n}[h_n]} \right\} = \lim_{h_n \to 0} \left\{ \frac{A}{h_n + h - z} \right\} = \frac{A}{h - z} = \varepsilon(z). \qquad \textbf{(7.10)}$$

Therefore, in the dislocated region of any continuously-graded layer, the in-plane strain will have this dependence on distance from the interface, apart from small compositional variations in b, ν, G and Y. This contrasts with simple models previously developed in which it was assumed that the dislocated region of a graded layer would be unstrained. The characteristic of the above equation describes the residual strain in structures where the misfit dislocation region extends all the way to the substrate interface, however in linearly-graded epitaxial layers, the presence of the interfacial MDFZ leads to the adjustment of the strain profile. In addition, the strain characteristics described here accounts for the variation of the residual strain in the dislocated region. Thus, the in-plane strain in the dislocated region is modeled by

$$\varepsilon(z) = \frac{A}{h - z} - \frac{A}{h} + C_f z_1, \quad z_1 < z \le z_2. \qquad \textbf{(7.11)}$$

The second and third terms in the equation above represent adjustments to account for the strain at the top of the interfacial MDFZ. By a similar analysis, in the surface MDFZ, the absence of misfit dislocations implies that the residual strain is proportional to the lattice mismatch and therefore the strain in this region is given by

$$\varepsilon(z) = C_f (z - z_2) + \frac{A}{h - z_2} - \frac{A}{h} + C_f z_1, \quad z_2 < z \le h. \qquad \textbf{(7.12)}$$

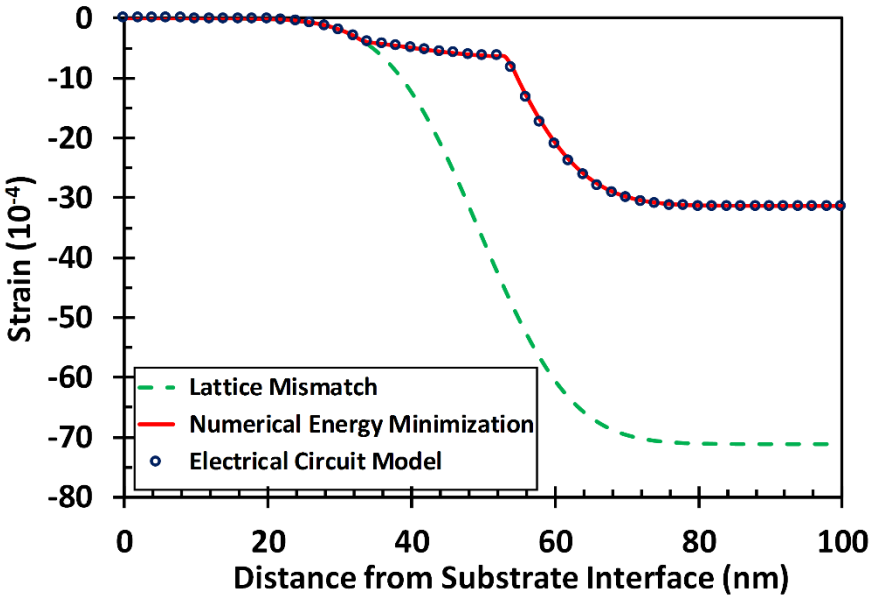

Figure 7.8. Lattice mismatch (dashed) and in-plane strain (solid, circles) as a function of the distance from the interface for a 100 nm thick S-graded epilayer $In_xGa_{1-x}As$ epitaxial layer where the indium composition is varied linearly from 0 at the substrate interface to 10% at the surface. The mean parameter was fixed at half of the epitaxial layer thickness $\mu = 50$ nm, and the standard deviation parameter was $\sigma = 10$ nm. The in-plane strain is determined using the numerical minimum energy (solid line) and electrical circuit (open circles) models.

Therefore, according to this model, the equilibrium strain profile in the linearly-graded layer is given by

$$\varepsilon(z) = \begin{cases} C_f z & z \le z_1; \\ A\dfrac{z}{h(h-z)} + C_f z_1 & z_1 < z \le z_2; \text{and} \\ C_f (z - z_2) + A\dfrac{z_2}{h(h-z_2)} + C_f z_1 & z_2 < z \le h. \end{cases} \tag{7.13}$$

The equation for the surface MDFZ boundary z_2 is given by

$$\int_{z_2}^{h} \varepsilon(z)\, dz = \frac{E_d}{2b'Y} = \int_{z_2}^{h} C_f (z - z_2) + \varepsilon(z_2)\, dz = A\left[\ln\left(\frac{h - z_2}{b}\right) + 1\right]. \tag{7.14}$$

Solving the expression above and recognizing that the width of the surface MDFZ is $W_{MDFZ} = h - z_2$, yields

$$W_{MDFZ} = \sqrt{\frac{2A}{C_f}\left[\ln\left(\frac{W_{MDFZ}}{b}\right)+1\right]+2\frac{Az_2}{h}-C_f z_1}\,. \qquad \textbf{(7.15)}$$

Rearrangement of the equation above results in the surface in-plane strain characteristic to be accurately modeled by

$$\varepsilon_S = \frac{A}{W_{MDFZ}}\ln\left(\frac{W_{MDFZ}}{b}\right)+\frac{A}{h}-C_f z_1\,. \qquad \textbf{(7.16)}$$

The sum of the second and third terms yields a small contribution to the equation since the boundary for the interfacial misfit dislocation free zone z_1 is very small in these structures, however, its value could be found by a similar approach where

$$\int_0^{z_1}\varepsilon(z)\,dz = \frac{E_d}{2b'Y} = \int_0^{z_1} C_f z\,dz = A\left[\ln\left(\frac{h-z_1}{b}\right)+1\right]. \qquad \textbf{(7.17)}$$

Solving, the expression above results in transcendental expression similar to the Matthews and Blakeslee critical layer thickness equation as is applicable to linearly-graded layers,

$$z_1 = \sqrt{\frac{2A}{C_f}\left[\ln\left(\frac{h-z_1}{b}\right)+1\right]}\,. \qquad \textbf{(7.18)}$$

Therefore, Equation 7.16 is modified accordingly to

$$\varepsilon_S = \frac{A}{W_{MDFZ}}\ln\left(\frac{W_{MDFZ}}{b}\right)+\frac{A}{h}-\sqrt{2AC_f\left[\ln\left(\frac{h-z_1}{b}\right)+1\right]}\,. \qquad \textbf{(7.19)}$$

If we make the exact simplifying assumptions as the previous models, the expressions given in Equations 7.15 and 7.19 reduce to the ones provided by Tersoff. The advantage of the electrical circuit model, in addition to providing an intuitive understanding of equilibrium lattice

relaxation by analogy, is that it the development of an analytical model for the strain and dislocation density in any compositionally-graded layer. As a specific example, we consider the nonlinear S-graded epitaxial layer investigated by Kujofsa et al. [52] and Xhurxhi et al. [65]. The lattice mismatch profile in the S-graded metamorphic buffer layer (SG-MBL) is designed to be a normal cumulative distribution function, given by

$$f(z)=\begin{cases}\dfrac{f_h-f_0}{2}\left[-erf\left(\dfrac{\mu-z}{\sigma\sqrt{2}}\right)+erf\left(\dfrac{\mu}{\sigma\sqrt{2}}\right)\right], & z<\mu;\\ \dfrac{f_h-f_0}{2}, & z=\mu\\ \dfrac{f_h-f_0}{2}\left[erf\left(\dfrac{z-\mu}{\sigma\sqrt{2}}\right)+erf\left(\dfrac{\mu}{\sigma\sqrt{2}}\right)\right], & z>\mu\end{cases}, \qquad \textbf{(7.20)}$$

where μ is the "mean parameter," σ is the "standard deviation parameter," f_0 and f_h are the respective values of lattice mismatch at the interface and the surface of the SG-MBL with thickness h. Kujofsa et al. [52] and Xhurxhi et al. [65] developed approximate models for the in-plane strain distribution, however, the residual strain in the dislocated region was modeled to within 10% of the actual value. Figure 7.8 illustrated the lattice mismatch profile for 100 nm thick $In_xGa_{1-x}As$ layer on Ga (001) which varies from zero (corresponding to zero indium mole fraction) at the substrate interface to $f_h=-0.71\%$ at the surface (corresponding to 10% indium mole fraction). The mean parameter was fixed at half of the epitaxial layer thickness $\mu=50$ nm, and the standard deviation parameter was $\sigma=10$ nm. The results of Figure 7.8 show excellent agreement in the residual strain distributions as determined by both the numerical results and the electrical circuit model.

We have developed an electrical circuit model to study equilibrium lattice relaxation in multilayered and compositionally-graded heterostructures. In this approach, each sublayer of an epitaxial structure is modeled by analogy to an electrical subcircuit utilizing an independent voltage source, an ideal diode, a resistor and an independent current source. Multilayered or graded semiconductor structures may be modeled by stacking the appropriate number of these building blocks, after which the numerical values of the node voltages in the circuit correspond to the equilibrium strains in the sublayers of the semiconductor structure. Use of this electric circuit analogy allows the modeling of semiconductor strained-layer structures by readily available circuit simulators, and makes it possible to translate the intuitive understanding of circuits to heteroepitaxial devices. Furthermore, the model may be extended to continuously-graded layers by considering the limit as the individual sublayer thicknesses are diminished to zero. This extension allows the development of analytical expressions for the strain, misfit dislocation density, and critical layer thickness for a continuously-graded layer having an arbitrary profile. It is similar to the transition from circuit theory, using lumped circuit elements, to electromagnetics, using distributed electrical quantities. We show this development using first principles, but in a more general sense, Maxwell's equations of electromagnetics could be applied.

7.3. Progression of Strain Relaxation in Linearly-Graded GaAsP/GaAs (001) Epitaxial Layers Approximated by a Finite Number of Sublayers

We have investigated the residual in-plane strain and width of the surface misfit dislocation free zone in linearly-graded $GaAs_{1-y}P_y$ metamorphic buffer layers as approximated by a finite number of sublayers. For this purpose, we have developed an electric circuit model approach for the equilibrium analysis of these structures, in which each sublayer may be represented by an

analogous configuration involving a current source, a resistor, a voltage source, and an ideal diode. The resulting node voltages in the analogous electric circuit correspond to the equilibrium strains in the original epitaxial structure. Utilizing this new approach, we show that the residual surface strain in linearly-graded epitaxial structures increases monotonically with grading coefficient as well as the number of sublayers, and is strongly dependent on the width of the misfit dislocation free zone, which diminishes with an increasing grading coefficient.

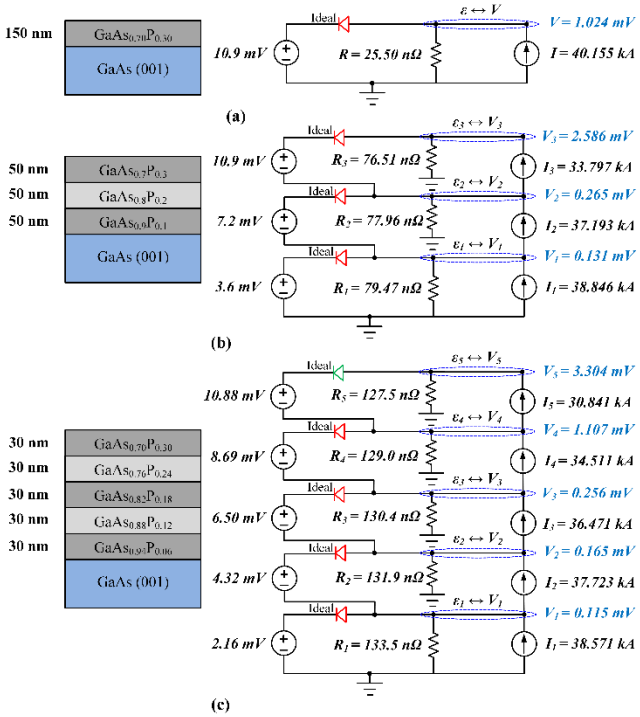

Figure 7.9. Schematic representation of step-graded epitaxial layers and the equivalent electrical circuit with (a) a single, (b) three and (c) five sublayers.

The design of electronic and optical devices [207,208,209] often requires the use of metamorphic buffer layers to accommodate the misfit strain associated with the growth of mismatched materials. Understanding the equilibrium and kinetically-limited lattice relaxation mechanisms as well as the dislocation dynamics has important implications in the optimization of

these device structures for better performance and reliability. Although several models have been established for understanding equilibrium lattice relaxation, such approaches use specialized code, are computationally intense, and furthermore do not lend themselves to an intuitive understanding necessary for innovative structure design. Therefore, in this work we present an analogous electrical circuit model to understand equilibrium lattice relaxation in linearly-graded (LG) GaAsP on GaAs (001) epitaxial layers. Here we have approximated the linearly-graded material by a finite number of sublayers and show the effect of the number of sublayers on the progression of the residual strain characteristics. Furthermore, we have revisited the distribution of the in-plane strain as a function of the distance from the interface and give an improved analytical expression which is a direct product of the electrical circuit model. In the previously developed models, the main assumption was that misfit dislocation density is sufficient to complete relax the lattice mismatch in the dislocated region whereas in this work we account for the small residual strain in the dislocated material. Consequently, the strain profile includes two departures from the model of Tersoff [13], which are a modification of the surface residual strain and a change in the width of the surface misfit dislocation free zone (MDFZ).

Table 7.4. Material Properties for GaP, GaAs and the alloy $GaAs_{1-y}P_y$.

Parameter	GaP	$GaAs_{1-y}P_y$	GaAs
a (nm)	0.54505	0.56534 - y(0.02029)	0.56534
C11 (GPa)	140.5	118.4 + y(22.1)	118.4
C12 (GPa)	62.03	53.7 + y(8.33)	53.7

7.3.1. Progression of Strain Relaxations: Results and Discussion

In this work, we investigated the grading coefficient dependence of the equilibrium strain relaxation by varying the number of sublayers, the ending lattice mismatch or the total thickness

of the epitaxial layer. In this work, we have defined the average grading coefficient as $C_f = f_h / h$ where f_h is the lattice mismatch of the surface and h is the total epilayer thickness. In a linearly-graded layer, the slope of the mismatch versus thickness characteristic is equal to the average grading coefficient. For a step-graded structure, the change in mismatch at each step is $\Delta f = C_f / N$.

Figure 7.9a shows a compositionally uniform, 150 nm thick layer of $GaAs_{0.7}P_{0.3}$ on GaAs (001) and the equivalent electrical circuit. The material parameters used here are summarized in Table 7.4. Using the Matthews and Blakeslee model, the equilibrium in-plane strain is $\varepsilon = 0.1024\%$ and this is equal to the numerical value of the node voltage provided by the equivalent electrical circuit. Whereas the strain is unitless, the node voltage is in Volts (V). Figure 7.9b considers a step-graded $GaAs_{1-y}P_y$ epitaxial layer with three 50 nm thick sublayers in which there are equal compositional changes from one layer to the next. The composition in the top sublayer is fixed at 30% phosphorus. Strain relaxation behavior in a step-graded structure is dictated by the behavior of the individual uniform-composition sublayers, each of which exhibits a concentration of misfit dislocations at the interface and a uniform residual strain in the remaining thickness. Some interfaces may be absent of misfit dislocations, so the width of the surface MDFZ may be an integral multiple of the step thickness. The results of Figure 7.9b show that misfit dislocation networks are present at all interfaces and therefore the width of the surface MDFZ is fixed to that of the top sublayer thickness of 50 nm. However, when increasing the number of sublayers and therefore utilizing a lower compositional change at each interface as shown in Figure 7.9c, it becomes apparent that the width of the surface MDFZ increases. Figure 7.9c shows that

the fifth sublayer is coherent with respect to the one below and therefore the surface MDFZ in this case is twice the sublayer thickness, or 60 nm. Although the average strain is comparable among the three structures illustrated here, the surface strain increases with the average grading coefficient or the number of sublayers.

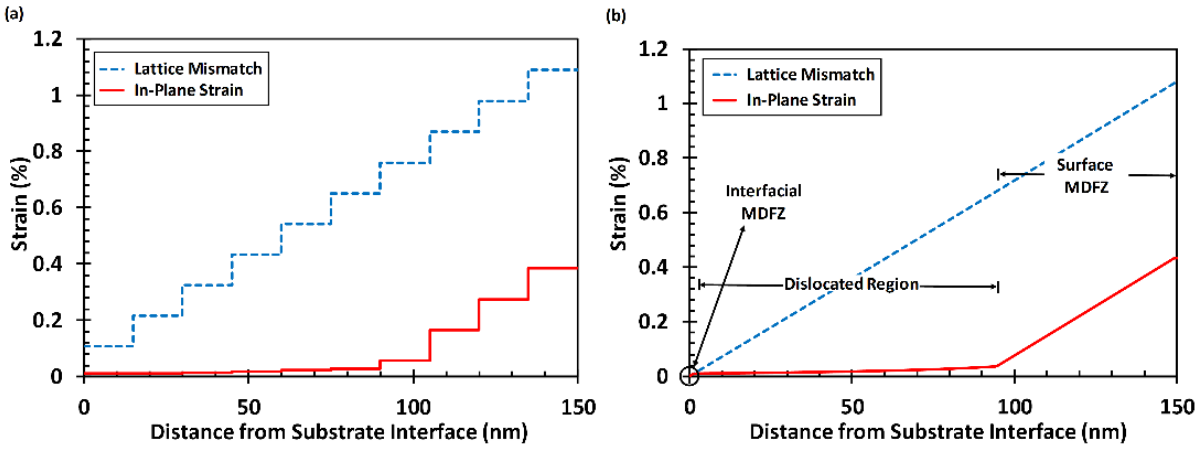

Figure 7.10. Lattice mismatch and in-plane strain as a function of the distance from the interface for a step-graded with 10 sublayers and (b) a linearly-graded epilayer of $GaAs_{0.7}P_{0.3}$ on GaAs (001) substrate.

These characteristic behaviors are more evident in Figure 7.10, which shows the lattice mismatch and in-plane strain as a function of the distance from the interface for a step-graded layer with 10 sublayers as well as a linearly-graded epilayer approximated with 200 sublayers. In both cases, the ending composition is fixed at 30% phosphorus and the total epilayer thickness is 150 nm; however, for the linearly-graded structure, the phosphorus composition at the substrate interface is fixed at zero to match the substrate. The results of Figure 7.10 show a monotonic increase in the surface MDFZ width with the number of sublayers. For the case of linear-grading the surface MDFZ width is 55 nm whereas in the step-graded layer it is constrained to 45 nm (three times the sublayer thickness). In addition, because of the low grading coefficient used in LG

epitaxial layers, the misfit dislocations are introduced at a finite distance from the substrate interface, which results in the formation of an interfacial MDFZ as pointed out in Figure 7.10b. The interfacial MDFZ is shown in the circled region of Figure 7.10b, but is difficult to see with the scale of this figure because its thickness is only a few nanometers. Although increasing the number of sublayers does not result in any noticeable changes in the average residual strain, the results of Figure 7.9 and Figure 7.10 show that the surface in-plane strain changes significantly from 0.102 % for a single layer to 0.434% for 200 sublayers.

The characteristics of Figure 7.11 and Figure 7.12 investigate the effect of the grading coefficient as well as the number of sublayers on the surface strain. Figure 7.11 illustrates that the surface in-plane strain as a function of the number of sublayers (Figure 7.11a) and its reciprocal (Figure 7.11b) with ending lattice mismatch as a parameter for a 150 nm thick $GaAs_{1-y}P_y$ epitaxial layer on GaAs (001). In these structures, the phosphorus composition at the top sublayer is fixed at 30%, 40% and 50% respectively corresponding to an ending lattice mismatch of 1.08%, 1.45% and 1.82%. The structures associated with a particular symbol in both Figure 7.11 and Figure 7.12 contain identical grading coefficients but we can compare them in terms of the number of sublayers. Figure 7.12 displays similar features however, the adjusted parameter is the epitaxial layer thickness; for the structures shown in Figure 7.12, the phosphorus composition at the top sublayer is fixed at 40% and the epitaxial layer thickness is varied to 150, 300 and 600 nm. The characteristics of Figure 7.11 and Figure 7.12 demonstrate a sublinear and monotonically increasing surface in-plane strain with the number of sublayers. More specifically, there is an increase in the residual surface strain when there is a combination of an (i) increase in the ending

lattice mismatch, (ii) a decrease in the total epitaxial layer thickness and (iii) an increase in the total number of sublayers.

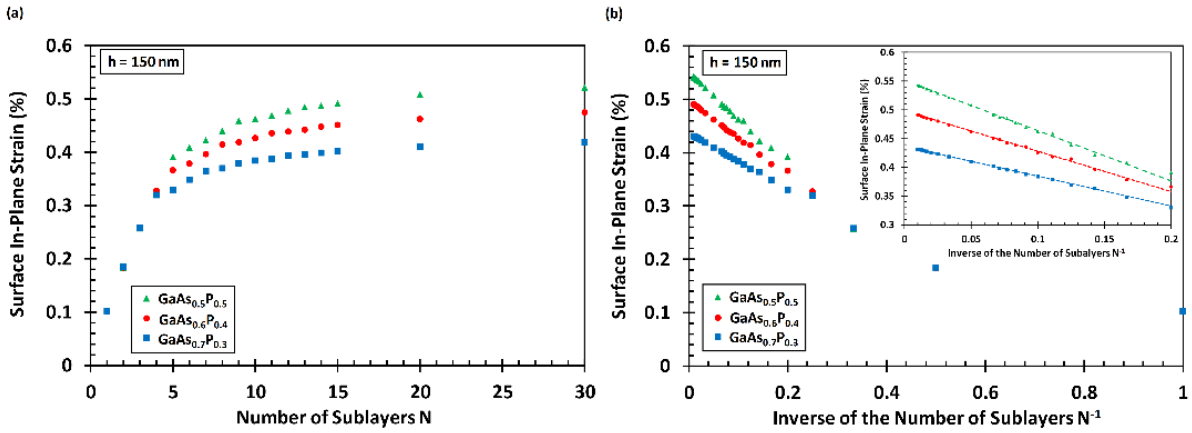

Figure 7.11. Surface in plane strain as a function of (a) the number of sublayers and (b) its reciprocal for a linearly-graded layer approximated with a finite number of sublayers and the ending lattice mismatch as a parameter. The epitaxial layer thickness in these structures is fixed at 150 nm. The inset of part (b) shows a subset of the data shown on Figure b which are associated with a higher number of sublayers. The axis labels for the inset figure are the same as those of Figure b.

The slight departures from smoothness (especially in the region where N ranges from 8 to 16 sublayers) of the surface in-plane strain observed in Figure 7.11 and Figure 7.12 could be explained with the aid of Figure 7.13. Previously, we mentioned that in step-graded layers the width of the surface MDFZ is a multiple of the sublayer number and therefore the actual width is determined from the product of the number of coherent interfaces near the surface and the width of each sublayer. Figure 7.13 shows the width of the surface MDFZ (left vertical axis) and the number of coherent interfaces (right vertical axis) as a function of the number of sublayers for a 150 nm thick $GaAs_{0.7}P_{0.3}$ on a GaAs (001) substrate. Due to the approximation of the linear-grading scheme with a finite number of sublayers, although there is an increase in the number of sublayers,

at a small number of sublayers (N<20), there is a non-monotonic variation of the width of the surface MDFZ. In addition, the results of Figure 7.13 show that there are structures in which the number of coherent interfaces remains the same when increasing the number of sublayers slightly as is the case for N = 4 → 6, 7 → 9, 10 → 12 and 13 → 14. Even though the residual strain increases with the number of sublayers, for small number of sublayers the competing mechanisms of the surface MDFZ width and the incoherent substrate lead observed departures in the smoothness of residual strain characteristic.

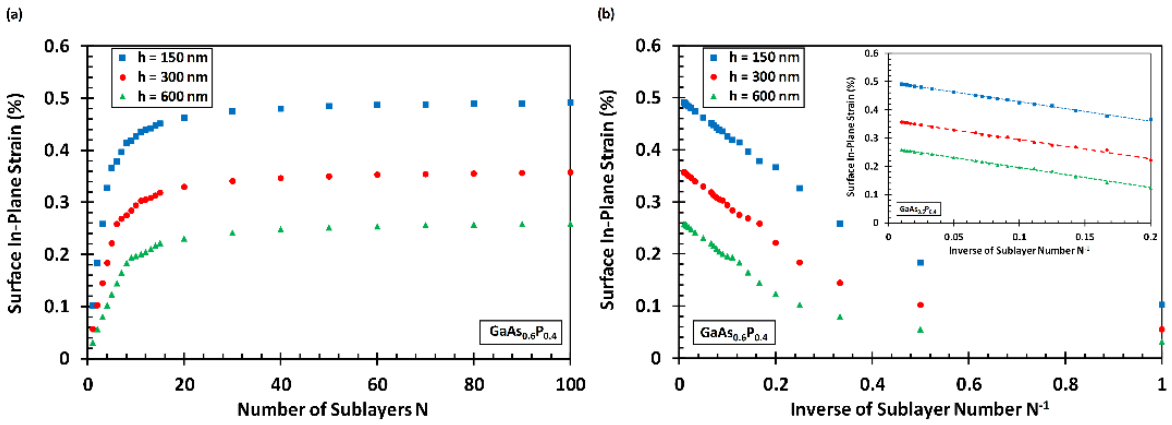

Figure 7.12. Surface in plane strain as a function of (a) the number of sublayers and (b) its reciprocal for a linearly-graded layer approximated with a finite number of sublayers and the epitaxial layer thickness as a parameter. The phosphorus composition at the top sublayer is fixed at 40 corresponding to a lattice mismatch of 1.45%. The inset of part (b) shows a subset of the data shown on Figure b which are associated with a higher number of sublayers. The axis labels for the inset figure are the same as those of Figure b.

In the limiting case, we can consider a linearly-graded epitaxial layer with a large number of sublayers, and the characteristics shown above become more apparent. Figure 7.14a shows the width of the surface misfit dislocation free zone and the surface in plane strain as a function of average grading coefficient. The width of the surface MDFZ decreases sublinearly and monotonically with increasing grading coefficient and this is expected on the basis that higher

mismatch requires the introduction of more misfit dislocations which leads to the extension of the dislocations close to the surface and therefore in the diminishment of the surface MDFZ. It is interesting to note that the results of Figure 7.14b demonstrate that surface in-plane strain is strongly dependent on the width of the surface MDFZ. The novelty of the electrical circuit model is that it enables a complete understanding of the strain profile in linearly-graded structures. Although, Tersoff [44] and Fitzgerald et al. [72] have developed models for the distribution of the in-plane strain as a function of the distance from the substrate interface, these models were approximate because they neglected the interfacial MDFZ as well as the finite in-plane strain in the dislocated region.

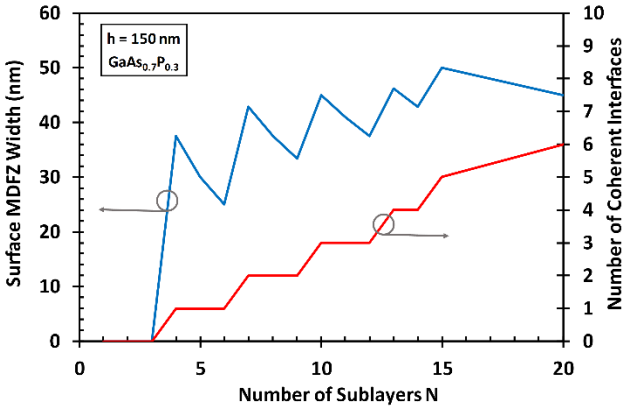

Figure 7.13. (a) Surface MDFZ width and (b) number of coherent interfaces near the surface as a function of the number of sublayers for a 150 nm thick $GaAs_{0.7}P_{0.3}$/GaAs (001).

If the edges of the interfacial and surface MDFZs are located at distances of z_1 and z_2 from the substrate interface, and therefore the misfit dislocation density is concentrated in the middle region ($z_1 \le z \le z_2$), then the residual strain can be analytically modeled as follows: In the

interfacial MDFZ, the absence of misfit dislocations indicates that the residual strain is equal to the lattice mismatch profile and therefore:

$$\varepsilon(z) = C_f z, \quad z \le z_1 . \tag{7.21}$$

In the dislocated region ($z_1 \le z \le z_2$), the residual strain is modeled by the electrical circuit model as

$$\varepsilon_n \quad \leftrightarrow \quad V_n = R_n \cdot (I_n - I_{n+1}) = \frac{(I_n - I_{n+1})}{2Y_n h_n} . \tag{7.22}$$

If we consider the limiting case where $h_n \to 0$, then it can be shown that

$$\lim_{h_n \to 0} \{\varepsilon_n\} = \varepsilon(z) = \frac{A}{h - z}, \quad 0 \le z \le z_1, \tag{7.23}$$

where

$$A = -\frac{f'(z)}{|f'(z)|} \frac{b(1 - \nu \cos^2 \alpha)}{8\pi(1+\nu)\sin\alpha \sin\phi} . \tag{7.24}$$

where $f'(z)$ is the first order derivative of the lattice mismatch profile. The characteristic of Equation 7.23 describes the residual strain in structures where the misfit dislocation region extends all the way to the substrate interface, however in linearly-graded epitaxial layers, the presence of the interfacial MDFZ leads to the adjustment of the strain profile. In this case, the residual strain in the dislocated region is modeled by

$$\varepsilon(z) = \frac{A}{h - z} - \frac{A}{h} + C_f z_1, \quad z_1 < z \le z_2 . \tag{7.25}$$

The second and third terms in the equation above represents adjustments to account for the strain at the top of the interfacial MDFZ. By a similar analysis, in the surface MDFZ, the absence of

misfit dislocations implies that the residual strain is proportional to the lattice mismatch and therefore the strain in this region is given by

$$\varepsilon(z) = C_f(z - z_2) + \frac{A}{h - z_2} - \frac{A}{h} + C_f z_1, \quad z_2 < z \le h. \tag{7.26}$$

Therefore, according to the above model, the equilibrium strain profile in the linearly-graded layer is given by

$$\varepsilon(z) = \begin{cases} C_f z & z \le z_1; \\ A\dfrac{z}{h(h-z)} + C_f z_1 & z_1 < z \le z_2; \text{and} \\ C_f(z - z_2) + A\dfrac{z_2}{h(h - z_2)} + C_f z_1 & z_2 < z \le h. \end{cases} \tag{7.27}$$

The condition for the surface MDFZ boundary z_2 is given by

$$\int_{z_2}^{h} \varepsilon(z) dz = \frac{E_d}{2b'Y} \quad \leftrightarrow \quad \int_{z_2}^{h} \left(C_f(z - z_2) + \varepsilon(z_2)\right) dz = A\left[\ln\left(\frac{h - z_2}{b}\right) + 1\right]. \tag{7.28}$$

Solving the expression above and recognizing that the width of the surface MDFZ is $W_{MDFZ} = h - z_2$, yields the surface in-plane strain characteristic shown in Figure 7.14b to be accurately modeled by

$$\varepsilon_S = \frac{A}{W_{MDFZ}} \ln\left(\frac{W_{MDFZ}}{b}\right) + \frac{A}{h} - C_f z_1. \tag{7.29}$$

The sum of the second and third terms yields a small contribution to the equation since the boundary for the interfacial misfit dislocation free zone z_1 is very small in these structures, however, its value could be found by a similar approach where

$$\int_0^{z_1} \varepsilon(z)dz = \frac{E_d}{2b'Y} \quad \leftrightarrow \quad \int_0^{z_1} (C_f z)dz = A\left[\ln\left(\frac{h-z_1}{b}\right)+1\right]. \tag{7.30}$$

Solving, the expression above results in transcendental expression similar to the Matthews and Blakeslee critical layer thickness equation,

$$z_1 = \sqrt{\frac{2A}{C_f}\left[\ln\left(\frac{h-z_1}{b}\right)+1\right]}. \tag{7.31}$$

Therefore, Equation 7.29 is modified accordingly to

$$\varepsilon_S = \frac{A}{W_{MDFZ}}\ln\left(\frac{W_{MDFZ}}{b}\right)+\frac{A}{h}-\sqrt{2AC_f\left[\ln\left(\frac{h-z_1}{b}\right)+1\right]}. \tag{7.32}$$

We have investigated equilibrium lattice relaxation in metamorphic in $GaAs_{1-y}P_y$ / GaAs (001) heterostructures involving linear grading in composition by utilizing an analogous electrical circuit model. We have approximated the linear grading scheme using a finite number of sublayers and have explored its effect on the surface strain and the width of the misfit dislocation free zone. There are two key conclusions to this study: first, the surface in-plane strain increases with greater grading coefficient and second, the value of the surface strain is strongly dependent on the width of the surface MDFZ which diminishes at higher mismatch.

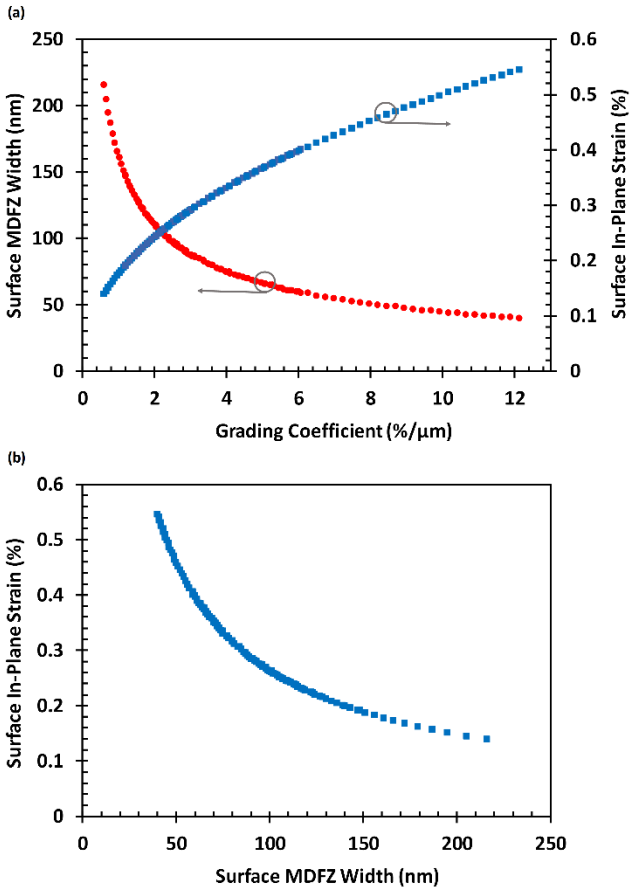

Figure 7.14. (a) Surface MDFZ width and the in-plane strain as a function of the grading coefficient for GaAsP/GaAs (001). (b) Surface in-plane strain as a function of the surface MDFZ width.

7.4. Design of Strain-Compensated Epitaxial Layers Using an Electrical Circuit Model

The design of heterostructures that exhibit desired strain characteristics is critical for the realization of semiconductor devices with improved performance and reliability. The control of strain and dislocation dynamics require an understanding of the relaxation processes associated with mismatched epitaxy, and the starting point for this analysis is the equilibrium strain profile, because the difference between the actual strain and the equilibrium value determines the driving force for dislocation glide and relaxation. Previously, we developed an electrical circuit model

approach for the equilibrium analysis of semiconductor heterostructures, in which an epitaxial layer may be represented by a stack of subcircuits, each of which involves an independent current source, a resistor, an independent voltage source, and an ideal diode. In this work, we have applied the electrical circuit model to study the strain compensation mechanism and show that for a given compositionally uniform device layer with fixed mismatch and layer thickness, a buffer layer may be designed (in terms of thickness and mismatch) to tailor the strain in the device layer. A special case is that in which the device layer will exhibit zero residual strain in equilibrium (complete strain compensation). In addition, the application of the electrical circuit analogy enables the determination of exact expressions for the residual strain characteristics of both the buffer and device layer in the general case where the device layer may exhibit partial strain compensation. On the basis of this framework, it is possible to develop design equations for the tailoring of the strain in a device layer grown on a uniform composition buffer.

The understanding of the equilibrium lattice relaxation has important implications in the determination of the stability criteria for electronic and optical devices [210,211,212,213] in addition to serving as the starting point for kinetically-limited lattice relaxation [66,214,215,216,217]. Although the design of semiconductor heterostructures may involve the incorporation of various approaches to control the relaxation processes or dislocation generation, in this work we have focused on strain compensation. The strain compensation mechanism has been employed in the design of various electrical and optical devices, however, it has gathered special interest in the fabrication of quantum dot based devices [218,219] where the use of intentionally mismatched interfaces has enhanced the electrical/optical characteristics [220,221] in addition to improving the crystalline quality and the reduction of defect density [222].

Previously, we studied the strain compensation mechanism in the $In_xGa_{1-x}As/GaAs$ material system involving the growth of two compositionally uniform layers and developed an approximate Gaussian-based model to describe the device layer in-plane strain [223]. Although, the term "strain-compensation" has been used with various meanings in published literature and especially in reference to the growth of strain-layer-super-lattices, in our work we have defined strain compensation as the tailoring of the strain in a device layer by the design of the underlying buffer layer.

In the general case, the design of the buffer layer for the purpose of strain compensation involves adjustments in thickness and compositional-grading profile; though, in our work the buffer layer has uniform composition, so design of the buffer involves modifying only the thickness and composition. In previous work, we studied strain compensation in the $In_xGa_{1-x}As/GaAs$ material system [223] using an ad-hoc numerical minimum energy approach [43], whereas in the present work, we applied a recently developed electrical circuit analogy for equilibrium lattice relaxation [224] and have investigated strain compensation in the $ZnS_ySe_{1-y}/GaAs$ (001) material system. The electrical circuit model (ECM) is developed based on the generalized equilibrium theory of Matthews [225] and considers an epitaxial layer to be analogously modeled by an equivalent circuit configuration involving an independent current source, a resistor, an independent voltage source, and an ideal diode. Multilayered structures may be modeled by stacking the appropriate number of these building blocks, after which the numerical values of the node voltages in the circuit correspond to the equilibrium strains in the sublayers of the semiconductor structure. The development of the electrical circuit analogy enables the modeling of semiconductor heterostructures by readily available circuit simulators in which the

intuitive understanding of electrical circuits may be easily extended to the equilibrium lattice relaxation of these structures. Furthermore, the electrical circuit analogy allows the derivation of exact expressions for the residual strain and dislocation density characteristics in each of the sublayers of the epitaxial stack. Therefore, in this work we have applied the circuit approach to understand the relaxation process of the two-layered ZnS_ySe_{1-y}/GaAs (001) structure and have developed exact expressions for the equilibrium in-plane strain of each layer. In addition, we provide a comparison of the residual strain characteristics for the device layer using the previously developed Gaussian-based model [223] and exact expressions determined from the circuit model.

7.4.1. Electrical Circuit Analogy for Equilibrium Relaxation

In the present work, we have applied the previously developed electrical circuit model to study the strain compensation mechanism in structures comprising a uniform ZnS_ySe_{1-y} device layer grown on a GaAs (001) substrate with an intermediate uniform ZnS_ySe_{1-y} buffer layer, which could contain a different composition and thickness. The device layer has thickness h_D and lattice mismatch f_D with respect to the GaAs (001) substrate and the buffer layer has thickness h_B and lattice mismatch f_B as shown in Figure 7.15. The theoretical framework for the electrical circuit model is described in more detail in Reference [224], however, we will briefly summarize it below as it specifically applies to a two-layer structure. The electric circuit model approach for the equilibrium analysis of epitaxial heterostructures is based on the generalized equilibrium theory where each sublayer of an epitaxial stack may be represented by an analogous circuit configuration involving an independent current source, a resistor, an independent voltage source, and an ideal diode. A multilayered structure may be built up by the connection of the appropriate number of

these building blocks, and the node voltages in the analogous electric circuit correspond to the equilibrium strains in the original epitaxial structure. For the structure considered in Figure 7.15a, the equivalent circuit model involves the stacking of two building blocks. The equilibrium profile of an arbitrary heterostructures could be determined by minimizing the sum of the strain and dislocation energies.

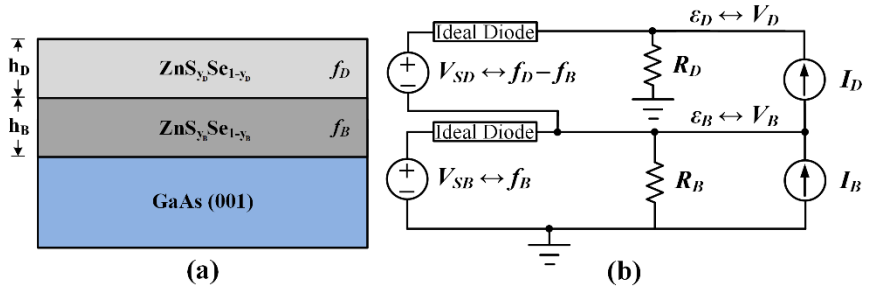

Figure 7.15. (a) A ZnS_ySe_{1-y}/GaAs(001) heterostructure involving two compositionally uniform layers and (b) the equivalent electrical circuit.

If we consider an epitaxial structure involving a stack of two disparate layers as shown in Figure 7.15a, the strain in each layer may be related to the misfit dislocation densities for that layer and those below it. In this case, the in-plane strains are

$$\begin{aligned}\varepsilon_D &= f_D - \rho_D b_D \sin\alpha\sin\phi - \rho_B b_B \sin\alpha\sin\phi \\ \varepsilon_B &= f_B - \rho_B b_B \sin\alpha\sin\phi\end{aligned}. \qquad \textbf{(7.33)}$$

By rearranging the equations above and accounting for the sign of mismatch at each interface, the linear misfit dislocation densities for the mismatched interfaces are given as

$$\begin{aligned}\rho_D &= \frac{f_D - f_B}{|f_D - f_B|}\frac{(f_D - \varepsilon_D) - (f_B - \varepsilon_B)}{b_D \sin\alpha\sin\phi} \\ \rho_B &= \frac{f_B}{|f_B|}\frac{f_B - \varepsilon_B}{b_B \sin\alpha\sin\phi}\end{aligned}. \qquad \textbf{(7.34)}$$

The sum of the strain and dislocation line energy per unit area may be found by adding the contributions of both sublayers:

$$\begin{aligned} E &= E_{d,B} + E_{\varepsilon,B} + E_{d,D} + E_{\varepsilon,D} \\ &= \left[\begin{array}{l} \rho_B \dfrac{G_B b_B^2 \left(1-\nu_B \cos^2\alpha\right)}{2\pi\left(1-\nu_B\right)} \left[\ln\left(\dfrac{h_B + h_D}{b_B} \right) + 1 \right] + 2Y_B h_B \varepsilon_B \\ + \rho_D \dfrac{G_D b_D^2 \left(1-\nu_D \cos^2\alpha\right)}{2\pi\left(1-\nu_D\right)} \left[\ln\left(\dfrac{h_D}{b_D} \right) + 1 \right] + 2Y_D h_D \varepsilon_D \end{array} \right]. \end{aligned} \tag{7.35}$$

To determine the equilibrium strain of this structure, we must differentiate the energy with respect to the in-plane strain for each sublayer and set each partial derivative equal to zero:

$$\begin{aligned} 0 &= \frac{\partial E}{\partial \varepsilon_D} = 2Y_D h_D \varepsilon_D - \frac{f_D - f_B}{\left| f_D - f_B \right|} \frac{G_D b_D \left(1-\nu_D \cos^2\alpha\right)}{2\pi\left(1-\nu_D\right)\sin\alpha \sin\phi} \left[\ln\left(\frac{h_D}{b_D} \right) + 1 \right] \\ 0 &= \frac{\partial E}{\partial \varepsilon_B} = 2Y_B h_B \varepsilon_B - \frac{f_B}{\left| f_B \right|} \frac{G_B b_B \left(1-\nu_B \cos^2\alpha\right)}{2\pi\left(1-\nu_B\right)\sin\alpha \sin\phi} \left[\ln\left(\frac{h_B + h_D}{b_B} \right) + 1 \right] \\ &\quad + \frac{f_D - f_B}{\left| f_D - f_B \right|} \frac{G_D b_D \left(1-\nu_D \cos^2\alpha\right)}{2\pi\left(1-\nu_D\right)\sin\alpha \sin\phi} \left[\ln\left(\frac{h_D}{b_D} \right) + 1 \right] \end{aligned} . \tag{7.36}$$

Concurrent solution of the equations above yields the equilibrium in-plain strains ε_B and ε_D. For the heterostructure of Figure 7.15a, in the analogous electrical circuit model, the node voltages for two essential nodes are given by

$$\begin{aligned} 0 &= \frac{\partial E}{\partial \varepsilon_D} = 2Y_D h_D \varepsilon_D - \frac{f_D - f_B}{\left| f_D - f_B \right|} \frac{G_D b_D \left(1-\nu_D \cos^2\alpha\right)}{2\pi\left(1-\nu_D\right)\sin\alpha \sin\phi} \left[\ln\left(\frac{h_D}{b_D} \right) + 1 \right] \quad \leftrightarrow \quad \frac{V_D}{R_D} - I_D = 0 \\ 0 &= \frac{\partial E}{\partial \varepsilon_B} = 2Y_B h_B \varepsilon_B - \frac{f_B}{\left| f_B \right|} \frac{G_B b_B \left(1-\nu_B \cos^2\alpha\right)}{2\pi\left(1-\nu_B\right)\sin\alpha \sin\phi} \left[\ln\left(\frac{h_B + h_D}{b_B} \right) + 1 \right] \\ &\quad + \frac{f_D - f_B}{\left| f_D - f_B \right|} \frac{G_D b_D \left(1-\nu_D \cos^2\alpha\right)}{2\pi\left(1-\nu_D\right)\sin\alpha \sin\phi} \left[\ln\left(\frac{h_D}{b_D} \right) + 1 \right] \quad \leftrightarrow \quad \frac{V_B}{R_B} - I_B + I_D = 0 \end{aligned} \tag{7.37}$$

It can be shown that the numerical value of the voltage at each node is equivalent to the equilibrium strain of that sublayer $\varepsilon_D \leftrightarrow V_D$, and $\varepsilon_B \leftrightarrow V_B$. In Figure 7.15b, the diode-connected independent voltage sources are determined by

$$\begin{aligned} V_{SD} &\leftrightarrow f_D - f_B \\ V_{SB} &\leftrightarrow f_B \end{aligned}. \tag{7.38}$$

Furthermore, each sublayer in the epitaxial stack may be modeled by an electrical subcircuit in which:

$$\begin{aligned} R_D &\leftrightarrow \frac{1}{2Y_D h_D} \\ R_B &\leftrightarrow \frac{1}{2Y_B h_B} \end{aligned}, \tag{7.39}$$

and

$$\begin{aligned} I_D &\leftrightarrow \frac{f_D - f_B}{|f_D - f_B|} \frac{G_D b_D \left(1 - \nu_D \cos^2 \alpha\right)}{2\pi(1-\nu_D)\sin\alpha \sin\phi} \left[\ln\left(\frac{h_D}{b_D}\right) + 1 \right] \\ I_B &\leftrightarrow \frac{f_B}{|f_B|} \frac{G_B b_B \left(1 - \nu_B \cos^2 \alpha\right)}{2\pi(1-\nu_B)\sin\alpha \sin\phi} \left[\ln\left(\frac{h_B + h_D}{b_B}\right) + 1 \right] \end{aligned}. \tag{7.40}$$

7.4.2. Analytical Expressions for Strain Compensation: Results and Discussion

Strain relaxation of compositionally-uniform epitaxial layers involves the introduction of misfit dislocations at mismatched interfaces which can be modeled using Dirac delta functions. For the structures studied here, dislocations may be introduced at the substrate-buffer and buffer-device layer interfaces as is necessary to accommodate the lattice mismatch at those interfaces. For a single compositionally uniform layer, the linear density of misfit dislocations increases monotonically for increasing compositional mismatch and apart from the dislocated interface, the equilibrium strain is constant due to the absence of additional misfit dislocations above the

interface. The extent of strain relaxation depends on both the lattice mismatch and thickness of the epitaxial layer. Therefore, in this case the buffer layer serves as a growth platform with adjustable in-plane lattice constant, the value of which depends on the buffer composition and thickness. The buffer layer may therefore be designed in such a way as to achieve complete strain compensation in a device layer to be grown on top.

In this work, we have utilized the electrical circuit model to explore the strain compensation mechanism by varying the compositional mismatch at the buffer layer-device layer interface at given buffer and device layer thicknesses. Although a characteristic feature of this work involves the determination of the critical condition for strain compensation (zero strain in the device layer), the application of the electrical circuit model enables the development of design criteria for partial strain compensation (and therefore design of the equilibrium device layer residual strain). To study the strain compensation mechanism we have applied the following analysis: for a given device layer thickness h_D and composition f_D, we have fixed the buffer layer thickness h_B and have varied the composition of the buffer layer f_B to determine the critical point for zero in-plane strain at the surface of the heterostructure (the strain compensation condition). We have investigated heterostructures with device and buffer layer thicknesses ranging from 100 nm to 500 nm and sulfur compositions ranging from 0% to 30%, which correspond to lattice mismatch values of -0.27% to 1.11%.

Figure 7.16 explores the four-dimensional space of the device layer in-plane strain as a function of the buffer layer lattice mismatch with either device layer thickness (Figure 7.16a), device layer lattice mismatch (Figure 7.16b) or buffer layer thickness (Figure 7.16c) as a

parameter. The characteristics of Figure 7.16 show that for a given structure with fixed h_B, f_D and h_D, the device layer strain exhibits a three-regime behavior with respect to f_B (see Figure 7.16d). In the regimes with constant device layer strain, misfit dislocations (MD) are present at both interfaces, but the sense of the MDs may be different depending on the compositional difference at the buffer-device interface. In the regime with varying in-plane device layer strain, MDs are absent from the device interface. Although there may be cases where misfit dislocations are absent from both interfaces, in this work we have chosen buffer layer thicknesses which are beyond h_c and therefore MDs are always present at the substrate-buffer interface.

In the constant strain regimes, the significant difference in the absolute lattice mismatch at the buffer-device interface requires the partial relaxation through the introduction of misfit dislocations. In the constant strain region where $|f_B| >> |f_D|$ (region I), the in-plane strain is of the same sign as the lattice mismatch which indicates the presence of misfit dislocations of the same sense whereas, when $|f_B| << |f_D|$ (region III), there is a reversal in the sign of the in-plane strain with respect to mismatch. In the strain-varying regime (region II), the in-plane strain characteristic in the device layer exhibits a sharp transition from compressive to tensile strain which coincides with partial strain compensation. In this region, there exists a combination of compositional mismatch at the buffer-device interface and buffer thickness such that the device layer is completely relaxed (perfect strain compensation). Although the buffer and device layer thicknesses are well beyond their individual critical layer thicknesses if grown directly on a GaAs substrate, the lattice mismatch at the device interface is accommodated elastically within both layers without necessitating the introduction of misfit dislocations at the buffer-device layer interface. In the

following sections, a key focus will be to understand the strain relaxation and compensation behavior of these heterostructures through the application of the electrical circuit model. Furthermore, we will justify the strain behavior and the limits of strain compensation by using the electrical circuit analogy.

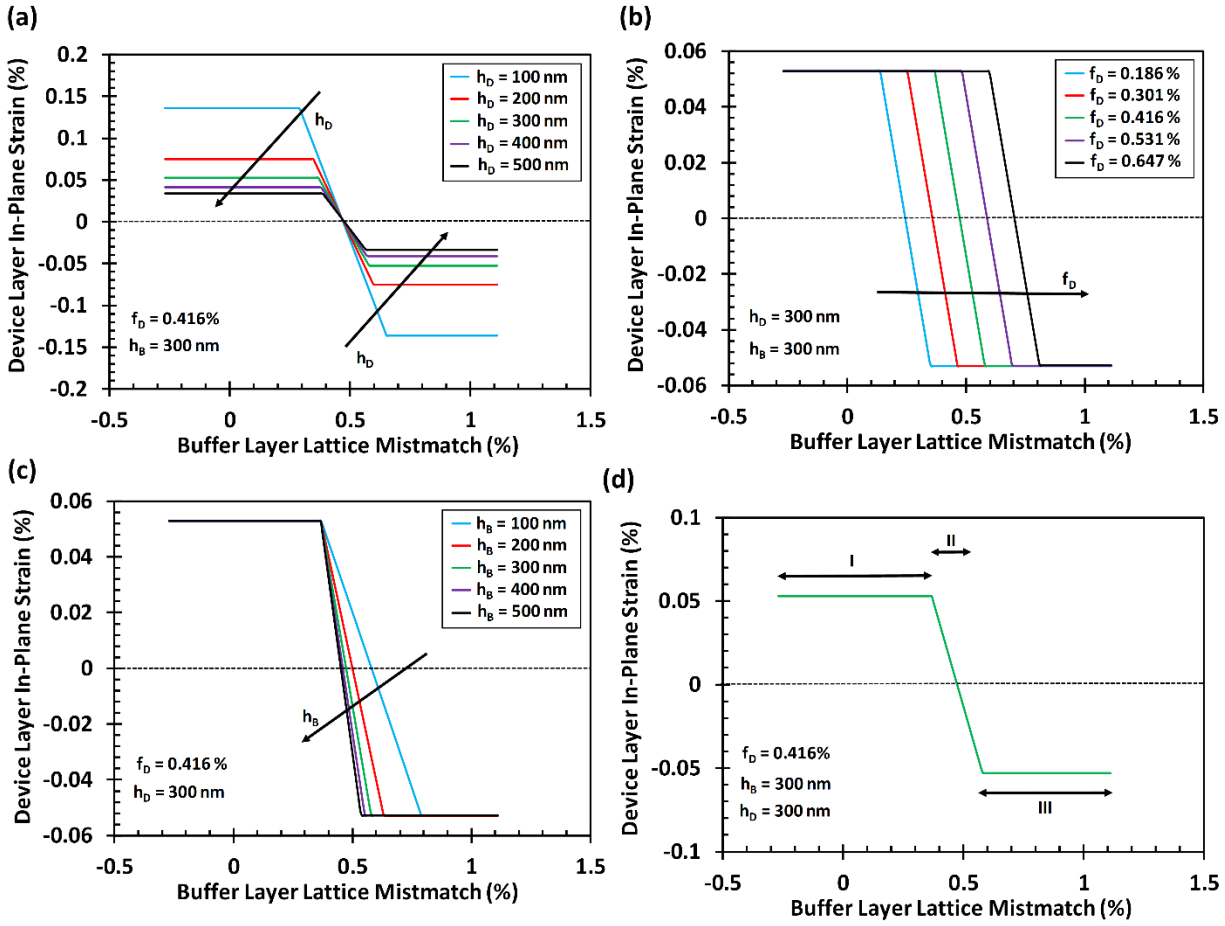

Figure 7.16. Device layer in-plane strain as a function of buffer layer lattice mismatch with (a) device layer thickness, (b) device layer mismatch and (c) buffer layer thickness as parameters. In each case, the remaining parameters were fixed: (a) device layer mismatch is 0.416% and 300 nm thick buffer layer, (b) 300 nm thick buffer layer and 300 nm thick device layer and (c) device layer mismatch is 0.416% and 300 nm thick device layer. The direction of the arrow indicates an increasing value of the parameter. (d) A sample device layer strain characteristics depicting the three distinct regimes.

The results of Figure 7.16a indicate that for a fixed device layer mismatch and buffer layer thickness, an increase in the device layer thickness h_D results in (i) a reduction of the liming strain value in the constant strain regime, (ii) a diminishment of the width of the strain varying regime and (iii) a decrease of the slope in the strain varying regime. Whereas there is a strong dependence of the device layer in-plane strain on h_D, there are weaker variations with increasing f_D and h_B. Figure 7.16b shows that for a fixed h_D and h_B, an increase in the device layer sulfur composition produces a left-shift of the device layer strain versus buffer layer mismatch characteristic which in turn results in a higher value of the critical buffer layer mismatch for complete strain compensation. Furthermore, the results of Figure 7.16c illustrate that for structures with fixed h_D and f_D an increase in the buffer layer thickness results in the (i) diminishment of width of strain varying regime and (ii) a shift of the critical buffer layer mismatch for complete strain compensation. It is interesting to note that for a fixed device layer thickness, observation of the absolute value of the in-plane strain (Figure 7.16) in the constant strain regimes exhibits symmetrical behavior and variations in either f_B, f_D or h_B, and the limiting value of strain is independent of these three parameters, depending only on h_D. The results of Figure 7.17 show that the limiting strain in the device layer varies in approximate inverse relationship with the device layer thickness. The sublinear behavior is due to the logarithmic dependence of the dislocation line energy.

The application of the circuit model to study the strain compensation mechanism in structures involving compositionally uniform layers allows the intuitive understanding of electric circuits to be readily applied to the relaxation of semiconductor heterostructures. Therefore, in the

following sections we will apply the ECM to understand the device layer strain characteristics in the constant strain and strain-varying regimes.

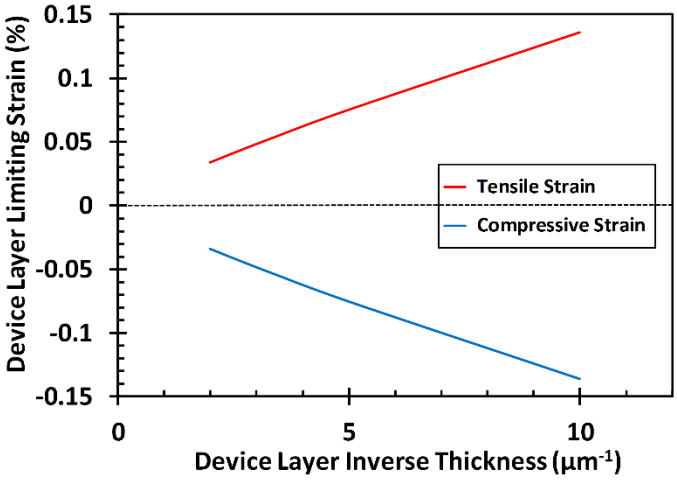

Figure 7.17. Device layer in-plane strain as a function of the device layer reciprocal thickness in the constant strain regimes.

In the constant strain regime (regions I and III), the device and buffer layers are decoupled by the presence of misfit dislocations at the device layer interface. The presence of MDs in a physical structure corresponds to a non-conduction mode for the ideal diode (Figure 7.18) in the analogous electrical circuit. Therefore, the limiting node voltage for the device layer in regions I and III may be determined from the simplified electric circuit shown in Figure 7.18b where

$$V_D = R_D I_D . \qquad \textbf{(7.41)}$$

In terms of the physical model, the limiting value of the device layer strain for a given set of parameters f_B, f_D , h_B and h_D can be translated as

$$\varepsilon_D = \frac{1}{2Y_D h_D}\left\{\frac{f_D - f_B}{|f_D - f_B|}\frac{G_D b_D\left(1-\nu_D\cos^2\alpha\right)}{2\pi(1-\nu_D)\sin\alpha\sin\phi}\left[\ln\left(\frac{h_D}{b_D}\right)+1\right]\right\}$$
$$= \frac{f_D - f_B}{|f_D - f_B|}\frac{b_D\left(1-\nu_D\cos^2\alpha\right)}{8\pi h_D(1+\nu_D)\sin\alpha\sin\phi}\left[\ln\left(\frac{h_D}{b_D}\right)+1\right]. \quad \textbf{(7.42)}$$

It can be seen from the equation above that the limiting device layer in-plane strain is independent of the buffer layer thickness at higher compositional mismatch between the buffer layer and device layer. In the strain varying regime (region II), the absence of MDs at the device layer interface demonstrates the coherent state of the device layer which in terms of the electrical circuit results in conduction of the top ideal diode shown in Figure 7.19a. The conduction of the ideal diode leads to the formation of a supernode where two essential nodes are separated by an independent voltage source. In addition, the formation of this supernode results in the modification of the node voltage at the bottom of the supernode (the buffer layer in this case). Therefore, in region II, the node voltage of the device layer is determined from the simplified circuit of Figure 7.19b by

$$V_D = V_B + V_{SD}, \quad \textbf{(7.43)}$$

whereas the node voltage of the buffer layer (or in other words the node voltage at the bottom of the supernode) is modified accordingly as

$$V_B = \frac{R_B}{R_B + R_D}\left(I_B R_D - V_{SD}\right). \quad \textbf{(7.44)}$$

Equations 7.41, 7.43 and 7.44 enable the determination of the criteria for compete strain relaxation as well as the extent of partial strain compensation in cases which do not satisfy these criteria. The condition for critical strain compensation occurs when the device layer exhibits zero strain ($\varepsilon_D = 0$) which is equivalent to the node voltage at the device layer equaling zero ($V_D = 0$). Therefore

$$V_D = \frac{R_B}{R_B + R_D}\left(I_B R_D - V_{SD}\right) + V_{SD} = 0\,. \tag{7.45}$$

Solving the equation above results in

$$V_{SD} = -I_B R_B\,. \tag{7.46}$$

In terms of the physical model the above expression is translated to the required compositional mismatch between the device and buffer layer for critical strain compensation (f_Δ)

$$f_\Delta \equiv f_D - f_B = -\frac{f_B}{|f_B|}\frac{b_B\left(1-\nu_B\cos^2\alpha\right)}{8\pi h_B\left(1-\nu_B\right)\sin\alpha\sin\phi}\left[\ln\left(\frac{h_B+h_D}{b_B}\right)+1\right], \tag{7.47}$$

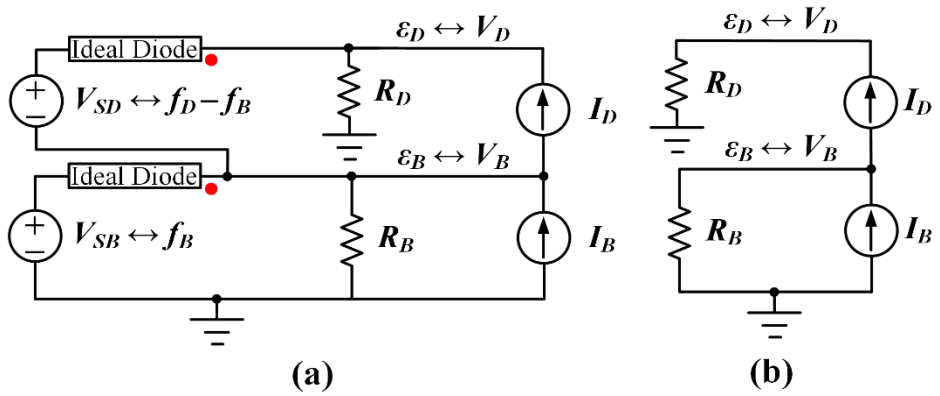

Figure 7.18. (a) Electrical circuit for the analogous case of the constant strain regime and (b) the simplified circuit accounting for the non-conducting mode of the diodes.

In addition, we can determine the condition for which the strain transitions from the constant strain regime (either region I or III) to the strain varying regime (region II). From the electrical circuit point of view this transition occurs when Equations 7.41 and 7.43 are equal. Thus,

$$V_{SD} = I_D\left(R_D + R_B\right) - I_B R\,. \tag{7.48}$$

In the physical model, the required compositional mismatch between the device and buffer layer for the transition between the strain varying regime to constant strain regime (f_σ) is given by

$$f_\sigma \equiv f_D - f_B = \begin{Bmatrix} \dfrac{f_D - f_B}{|f_D - f_B|} \dfrac{G_D b_D (1-\nu_D \cos^2\alpha)}{8\pi (Y_D h_D + Y_B h_B)(1+\nu_D)\sin\alpha \sin\phi} \left[\ln\left(\dfrac{h_D}{b_D}\right) + 1 \right] - \\ \dfrac{f_B}{|f_B|} \dfrac{b_B (1-\nu_B \cos^2\alpha)}{8\pi h_B (1+\nu_B)\sin\alpha \sin\phi} \left[\ln\left(\dfrac{h_B + h_D}{b_B}\right) + 1 \right] \end{Bmatrix}, \quad \textbf{(7.49)}$$

An important result from the development of the electrical circuit model and its application to study the strain compensation mechanism is that it enables the determination of the in-plane strain characteristics for the buffer layer as well. Figure 7.20 compares the buffer and device layer in-plane strain as a function of the buffer layer lattice mismatch for a 300 nm thick buffer and 300 nm thick device layer. The fractional sulfur composition of the device layer shown here is fixed at $y_D = 0.15$ corresponding to a lattice mismatch of $f_D = 0.416\%$. The strain characteristics exhibit similar features for both the buffer and device layer. Although the buffer layer exhibits similar three-regime behavior with exact transitions from the constant strain to strain varying regions, the residual strain of the buffer layer is always the same sign as the lattice mismatch. In region I and III of the strain characteristic, both interfaces are decoupled by the presence of misfit dislocations. Therefore, the node voltage for the buffer layer (Figure 7.18b) is given by

$$V_B = R_B (I_B - I_D). \quad \textbf{(7.50)}$$

In the equivalent physical model, the in-plane strain characteristic in regions I and III is described by

$$\varepsilon_B = \frac{f_B}{|f_B|} \frac{b_B (1-\nu_B \cos^2\alpha)}{8\pi h_B (1+\nu_B)\sin\alpha \sin\phi} \left[\ln\left(\frac{h_B + h_D}{b_B}\right) + 1 \right] - \frac{f_D - f_B}{|f_D - f_B|} \frac{G_D b_D (1-\nu_D \cos^2\alpha)}{4\pi Y_B h_B (1-\nu_D)\sin\alpha \sin\phi} \left[\ln\left(\frac{h_D}{b_D}\right) + 1 \right]. \quad \textbf{(7.51)}$$

The expression above indicates that in the constant strain regime, the extent of strain relaxation of the buffer layer is dependent on the parameters of the device layer. The strain characteristic of the buffer layer is inversely proportional to its thickness; however, it exhibits a weak logarithmic dependence on the total thickness of the structure. In the strain varying regime, we showed that the absence of MDs and therefore the formation of the supernode in the analogous electrical circuit results in the modification of the bottom node of the supernode which in this case is the one representing the buffer layer. Using Equation 7.44, the buffer layer in-plane strain can be modeled as

$$\varepsilon_B = \frac{Y_D h_D}{Y_D h_D + Y_B h_B}\left(\frac{f_B}{|f_B|}\frac{G_B b_B\left(1-\nu_B\cos^2\alpha\right)}{8\pi Y_D h_D(1+\nu_B)\sin\alpha\sin\phi}\left[\ln\left(\frac{h_B+h_D}{b_B}\right)+1\right]-\left(f_D-f_B\right)\right). \quad \textbf{(7.52)}$$

and the device layer strain in the strain varying regime is determined from

$$\varepsilon_D = \frac{f_B}{|f_B|}\frac{G_B b_B\left(1-\nu_B\cos^2\alpha\right)}{8\pi\left(Y_D h_D + Y_B h_B\right)(1+\nu_B)\sin\alpha\sin\phi}\left[\ln\left(\frac{h_B+h_D}{b_B}\right)+1\right]+\left(f_D-f_B\right)\left[1-\frac{Y_D h_D}{Y_D h_D + Y_B h_B}\right]. \quad \textbf{(7.53)}$$

Therefore, the in-plane strain of the device and buffer layer can be analytically modeled by the following piecewise equations:

$$\varepsilon_D = \begin{cases} \dfrac{f_D-f_B}{|f_D-f_B|}\dfrac{b_D\left(1-\nu_D\cos^2\alpha\right)}{8\pi h_D(1+\nu_D)\sin\alpha\sin\phi}\left[\ln\left(\dfrac{h_D}{b_D}\right)+1\right]; & |f_D-f_B|>f_\sigma \\ \dfrac{f_B}{|f_B|}\dfrac{G_B b_B\left(1-\nu_B\cos^2\alpha\right)}{8\pi\left(Y_D h_D+Y_B h_B\right)(1+\nu_B)\sin\alpha\sin\phi}\left[\ln\left(\dfrac{h_B+h_D}{b_B}\right)+1\right] & |f_D-f_B|\le f_\sigma \\ +\left(f_D-f_B\right)\left[1-\dfrac{Y_D h_D}{Y_D h_D+Y_B h_B}\right]; & \end{cases}, \quad \textbf{(7.54)}$$

and

$$\varepsilon_B = \begin{cases} \dfrac{f_B}{|f_B|}\dfrac{b_B(1-\nu_B\cos^2\alpha)}{8\pi h_B(1+\nu_B)\sin\alpha\sin\phi}\left[\ln\left(\dfrac{h_B+h_D}{b_B}\right)+1\right] & \\ -\dfrac{f_D-f_B}{|f_D-f_B|}\dfrac{G_D b_D(1-\nu_D\cos^2\alpha)}{4\pi Y_B h_B(1-\nu_D)\sin\alpha\sin\phi}\left[\ln\left(\dfrac{h_D}{b_D}\right)+1\right]; & |f_D-f_B|>f_\sigma \\ \dfrac{Y_D h_D}{Y_D h_D+Y_B h_B}\left(\dfrac{f_B}{|f_B|}\dfrac{G_B b_B(1-\nu_B\cos^2\alpha)}{8\pi Y_D h_D(1+\nu_B)\sin\alpha\sin\phi}\left[\ln\left(\dfrac{h_B+h_D}{b_B}\right)+1\right]\right); & |f_D-f_B|\le f_\sigma \\ -(f_D-f_B) & \end{cases}, \quad \textbf{(7.55)}$$

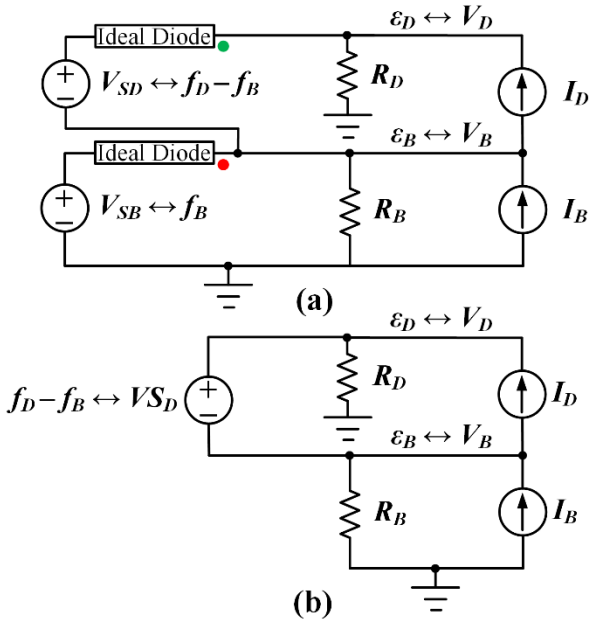

Figure 7.19. (a) Electrical circuit for the analogous case of the strain varying regime and (b) the simplified circuit accounting for the conduction mode of the ideal diode in the top node.

Figure 7.21 compares the device layer in-plane strain as a function of the buffer layer lattice mismatch for a two-layered ZnS_ySe_{1-y}/GaAs structure, where the residual strain characteristic is determined using the exact expression (Equation 7.54) and the approximate Gaussian-based model (Equation 32) developed in our previous work [223]. The structure considered here consists of a 300 nm thick buffer and 300 nm thick device layer of uniform composition. The results of Figure 7.21 show excellent agreement in the residual strain characteristics determined using the two

methods. However, the Gaussian based model is only an approximation which leads to slight departures near the regions of (i) complete strain compensation and (ii) transition between the strain-varying to constant-strain regimes.

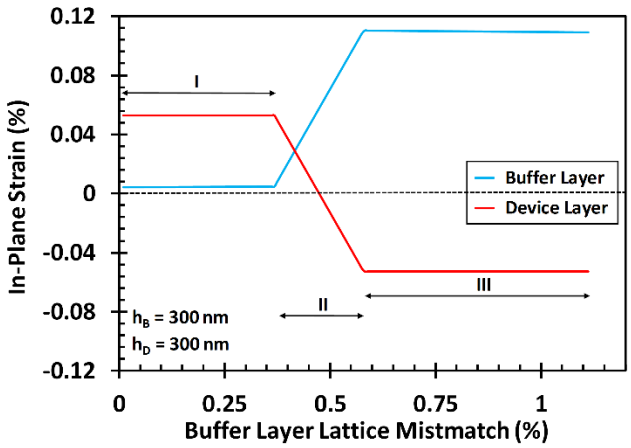

Figure 7.20. Comparison of the buffer and device layer strain characteristics as a function of the buffer layer mismatch for a 300 nm thick buffer and 300 nm thick device layer. Regions I and III represent the constant strain regime whereas region II indicates the strain varying regime.

The application of the electrical circuit model to study the strain compensation mechanism enables the development of exact expressions for modeling the strain characteristics of both the buffer layer and device layer. Therefore, the heterostructure may be designed in such a way that both the device and buffer layer exhibit the desired strain characteristic. As an example, this work could be applied to the design of strained-relaxed MOSFET devices where it is desirable that the channel (similar to the device layer in this work) is highly strained in order to enhance the mobility of the carriers whereas the buffer layer is partly relaxed. Therefore, from a fabrication point of view, the application of the electrical circuit model enables the crystal grower to design devices

with desired strain characteristics based on the appropriate choices of mismatch and thickness for each epitaxial layer.

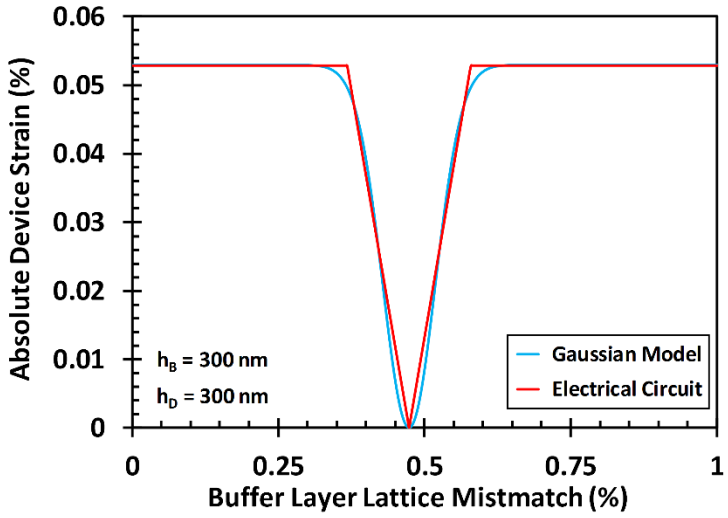

Figure 7.21. Comparison of the device layer strain characteristics as a function of the buffer layer mismatch for a two-layered structure where the strain characteristics are determined from the electrical circuit model and the approximate Gaussian-based model. The thicknesses of the buffer and device layer are each 300 nm and the device layer lattice mismatch is $f_D = 0.416\%$**.**

In this work, we have applied the previously developed electrical circuit model to investigate the mechanism of strain compensation – the modification of the strain in a semiconductor device layer by varying the design of one or more underlying buffer layers – for the case of a uniform device layer grown on a mismatched substrate with an intermediate uniform-composition buffer. In a previous work, we utilized ad-hoc minimum energy calculations to study strain compensation in the $In_xGa_{1-x}As$ / GaAs (001) material system and developed an approximate Gaussian-type model to describe the in-plane strain characteristics in the device layer. Here, the application of the electrical circuit model to study the strain compensation mechanism in the ZnS_ySe_{1-y}/GaAs(001) material system enables the development of exact expressions for the

residual strain characteristics in both the buffer and device layer. The main conclusion to this study is that for a given device layer design (thickness and composition), there exist choices of the buffer layer thickness and composition which result in the device layer exhibiting desired in-plane strain characteristics. In turn, the development of exact expressions to model strain characteristics allow flexibility in the choices of material parameters such that either partial or complete strain compensation may be achieved in these structures.

8. Plastic Flow Results

8.1. Relaxation and Threading Dislocations in the ZnSSe/GaAs Material System

The design of metamorphic semiconductor devices requires a predictive model for strains and threading dislocation densities. Previous work enabled modeling of threading dislocations (TD) in uniform layers but not in device structures with arbitrary compositional grading. In this work, we present a kinetic model for lattice relaxation which includes the misfit-threading dislocation interactions, which have not been considered in previous annihilation-coalescence models. Inclusion of these dislocation interactions makes the kinetic model applicable to compositionally-graded structures, and we have applied it to ZnSe/GaAs (001) and ZnS_ySe_{1-y}/GaAs (001) heterostructures. The results of the kinetic model are consistent with the observed threading dislocation behavior in ZnSe/GaAs (001) uniform layers, and for graded ZnS_ySe_{1-y}/GaAs (001) heterostructures the kinetic model predicts that the threading dislocation density may be reduced by the inclusion of graded buffer layers employing compositional overshoot. This "dislocation compensation" effect is consistent with high-resolution x-ray diffraction experimental results for graded ZnS_ySe_{1-y}/GaAs (001) structures grown by photo assisted metalorganic vapor phase epitaxy.

8.1.1. Annihilation-Coalescence Models

The design of lattice-mismatched semiconductor device structures requires a predictive model for strains and threading dislocation densities, which are important in determining device performance and reliability. Previous work enabled modeling of single heterostructures but not compositionally-graded structures of the types used in mesomorphic transistors and light-emitting diodes. In this work, we present a kinetic model for lattice relaxation in semiconductor

heterostructures which accounts for misfit-threading dislocation interactions and therefore can be applied to partially-relaxed device structures employing compositional grading and mismatched interfaces.

For uniform composition heteroepitaxial layers on mismatched substrates, it is often observed that the threading dislocation density is inversely proportional to the layer thickness, for layers which are much greater than the critical layer thickness and therefore nearly relaxed at the growth temperature [75]. This behavior has been reported for ZnSe/GaAs [226,227], InAs/GaAs [228], GaAs/InP [228], InAs/InP [228], and GaAs/Si [229]. Tachikawa and Yamaguchi [78] devised a semi-empirical model for the threading dislocation density in a uniform, nearly relaxed heteroepitaxial layer which was based on annihilation and coalescence of threading dislocations. The differential equation governing the threading dislocation density D was assumed to be

$$\frac{dD}{dz} = -C_1 D - C_2 D^2 \text{,} \qquad \textbf{(8.1)}$$

where the first and second terms represent first- and second-order threading dislocation reactions, z is the distance from the substrate interface, and C_1 and C_2 are constants. The solution of this equation gives the surface threading dislocation density as a function of total epilayer thickness,

$$D = \frac{D_0}{\left(1 + D_0 C_2 / C_1\right)\exp\left(C_1 h\right) - C_2 / C_1} \text{,} \qquad \textbf{(8.2)}$$

where C_1, C_2, and D_0 may be determined empirically. Though many heteroepitaxial material systems exhibit approximately $D \propto 1/h$ behavior, and can be modeled using similar values of C_1 and C_2, the value of D_0 varies greatly from one material system to another and must be found empirically for the application of Equation 8.2. Romanov et al. [79] extended the annihilation-

coalescence model to selective area growth and argued that the first-order term is associated with glide to sidewalls in patterned or cracked films. They showed that if the first-order term is neglected the solution for the threading dislocation density is

$$D = \frac{D_0}{1 + D_0 C_2 (h - h_0)}, \qquad \textbf{(8.3)}$$

where h_0 is the thickness at which the initial misfit dislocations are introduced. One limitation of the annihilation-coalescence models is that they only apply to layers grown well beyond the critical layer thickness for which the threading dislocation density decreases with thickness. However, pseudomorphic layers are known to contain low dislocation densities, comparable to the substrate. The dislocation density must therefore increase after the critical layer thickness has been exceeded, reach a maximum at some thickness, and then decrease. The annihilation-coalescence models do not provide insight into the processes which are active during the initial build-up of the threading dislocations.

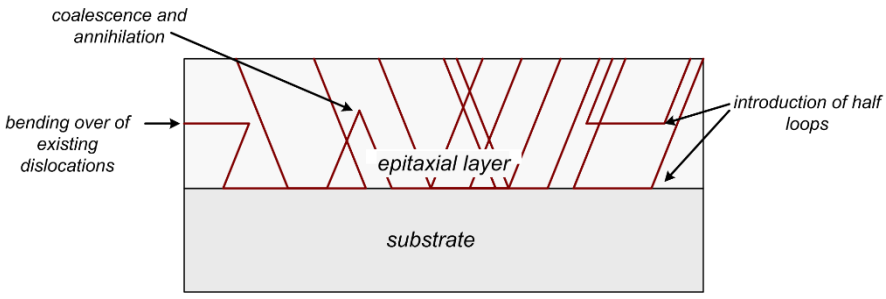

Figure 8.1. Interactions between misfit and threading dislocations in a lattice mismatched structure.

Another limitation of the annihilation-coalescence models is that they only apply to uniform composition layers. This is because they do not account for interactions between misfit

and threading dislocations at mismatched interfaces and in compositionally-graded regions, and this renders them inapplicable to most heteroepitaxial semiconductor devices.

To address these two limitations, we have developed a kinetic model for the lattice relaxation and threading dislocation behavior in heteroepitaxial layers of arbitrary thickness and compositional profile. This model includes empirical parameters, similar to the annihilation-coalescence models, but these empirical parameters may be determined by relatively simple experiments. Inclusion of misfit-threading dislocation interactions in our model enables its use with graded and multilayer structures which are of great importance to metamorphic device design (see Figure 8.1).

8.1.2. Application of the Kinetic Model to the Relaxation of ZnSe/GaAs Material System

For the application of this kinetic model to a particular material system it is necessary to know the values of the constants U, K, and B. The activation energy for the glide of dislocations in ZnSe/GaAs (001) was assumed to be U = 0.6 eV, based on experiments with bulk ZnSe reported by Yonenaga et al. [230]. The activation energy of glide may be different in epitaxial materials due to several factors including dissociation of dislocations into partials. In our work, use of an incorrect value of U may introduce some uncertainty between experimental and modeling results for ZnSe, for which 40% of the total thickness was grown at 595^{o}C and the remaining 60% of the total thickness was grown at 360^{o}C. In thinner samples, the 595^{o}C growth will be pseudomorphic so most of the relaxation will occur at 360^{o}C. But in thicker layers, we expect a greater contribution to the lattice relaxation at 595^{o}C. If the assumed activation energy is low (high), then the 360^{o}C relaxation will be overestimated (underestimated) compared to the relaxation at 595^{o}C. In either case, we assume that negligible relaxation occurs during cool-down, due to the rapid decrease in

temperature and the thermally-activated nature of glide. We conducted a set of experiments involving ZnSe/GaAs (001) single heterostructures to estimate the values of B and K, as will be described below.

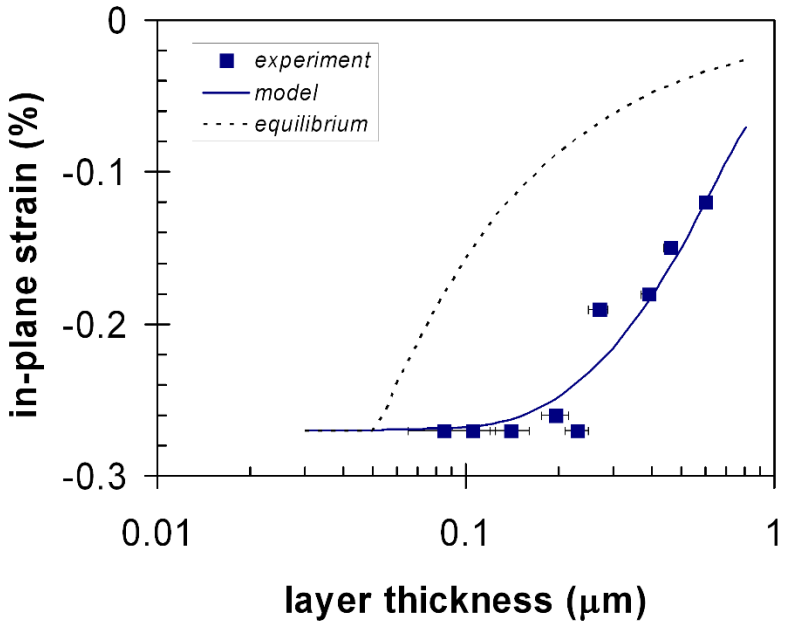

Figure 8.2. Room temperature in-plane strain versus thickness for ZnSe/GaAs (001) single heterostructures grown by the two-step photo assisted MOVPE process.

8.1.3. Experimental Procedures

In this work, we investigated ZnS_ySe_{1-y}/GaAs (001) heterostructures grown by photo assisted metalorganic vapor phase epitaxy (MOVPE) using the sources dimethyl zinc (DMZn), dimethyl selenium (DMSe), and diethyl sulfur (DES). All heterostructures were grown on GaAs (001) substrates. Prior to epitaxy, substrates were cleaned sequentially in boiling trichloroethylene, acetone, and methanol. After a deionized water rinse, the wafers were etched in Caro's etch with a composition of 10:1:1 H_2SO_4:$H_2O_2H_2O$ for 3 min at 60°C. Next the wafers were rinsed again in deionized water and given a 1 min treatment in 1:1 HCl:H_2O to remove the native oxide. Following

this, the substrates were rinsed in deionized water and isopropanol, blown off in filtered nitrogen, and loaded into the epitaxial reactor. Prior to growth, a 2 min deoxidation step was carried out at 595^{o}C at 250 torr with 14 slm hydrogen. Growth was carried out at 250 torr with 14 slm flow of hydrogen carrier gas and with 350 rpm susceptor rotation in an EMCORE vertical, resistance heated reactor. Photoirradiation was provided by an Oriel Hg lamp through a quartz window in the top of the reaction chamber. The structural properties of the heteroepitaxial structures were investigated using high-resolution x-ray diffraction (HRXRD) with a Bartels-type diffractometer employed a four-bounce Ge 022 monochromator and Cu Kα_1 radiation. The in-plane and out-of-plane strains, and compositions in ZnS_ySe_{1-y} layers, were found using 004 and 044 rocking curves measured at opposing azimuths by application of the general approach described by Zhang et al. [231]. The relaxed lattice constants for GaAs [9], ZnSe, and ZnS [232] were assumed to be 0.56534 nm, 0.56687 nm, and 0.54105 nm, respectively. The Poisson ratio was assumed to be 0.38 for ZnSe [233].

Common methods for determination of dislocation densities in mismatched heterostructures include crystallographic etching (etch pit density), x-ray diffraction, cross-sectional and plain-view transmission electron microscopy (TEM). Etch pit density is suited to material systems with low dislocation densities whereby the spatial distribution of dislocations is such that it reduces the encroachment of neighboring pits. Characterization using TEM is suited to metamorphic buffer layers with high dislocation densities, but TEM measurements explore a relatively small sample volume and are susceptible to local fluctuations in the dislocation density. X-ray characterization affords additional benefits by providing an absolute accuracy of approximately a factor of two over a relatively larger sample area (~ 1 mm^2). Therefore, in this

work the dislocation densities in the ZnSe single heterostructures and uniform ZnS_ySe_{1-y} layers on graded buffers were estimated from the 004 rocking curves using the method described by Ayers [234].

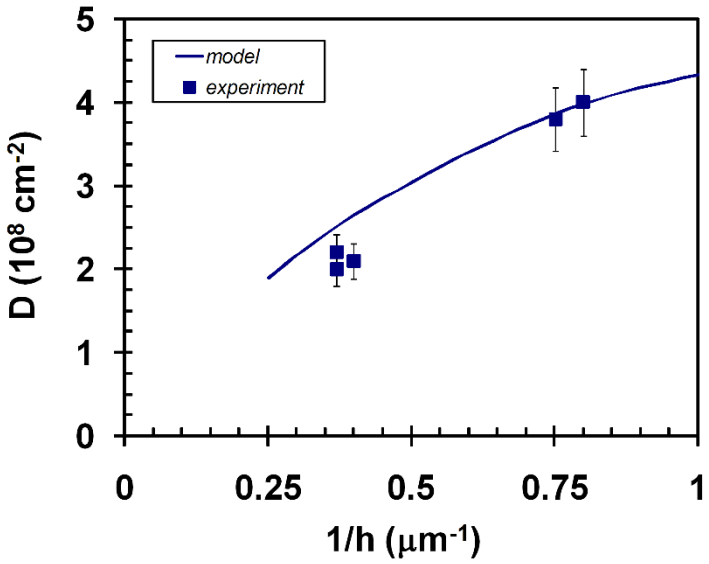

Figure 8.3. Dislocation density versus reciprocal of thickness for ZnSe/GaAs (001) single heterostructures grown by the two-step photo assisted MOVPE process.

8.1.4. Kinetically-Limited Strain Relaxation

In order to characterize the parameters B and K, we first grew a series of ZnSe/GaAs (001) single heterostructures with different thicknesses by the two-step photo assisted MOVPE process, in which 40% of the total thickness was grown at 595°C with 58 mW/cm^2 UV irradiation from an Oriel Hg lamp and the remaining 60% of the total thickness was grown at 360°C with 39 mW/cm^2 irradiation. The source mole fractions were X_{DMZn} = 2 x 10^{-4} and X_{DMSe} = 4 x 10^{-4} and the selenium source flow was started one minute before the zinc source. The in-plane strains were determined by high-resolution x-ray diffraction at room temperature, and the results are shown in

Figure 8.2 by the filled squares. Using the kinetic model for relaxation, the strain versus thickness characteristic is best fit using $BK = 2\times10^{-17} cm^4 dyn^{-2} s^1$ as shown in Figure 8.2 by the solid curve. It should be noted that the strain relaxation occurs much more gradually than predicted by the Matthews and Blakeslee equilibrium theory [77], shown by the dashed curve. The results of Figure 8.2 illustrate that there is some underestimation of the relaxation in thinner samples which are slightly greater than the critical layer thickness, suggesting that the actual activation energy may be slightly lower than the assumed value. Because the strain relaxation is governed by the BK product and U, a second experiment is necessary to find the individual parameters B and K. It would also be possible to design a set of experiments to determine a more accurate value of U in epitaxial ZnSe. This would be somewhat complicated in the case of photo assisted MOVPE, which necessitates two-step buffer deposition, but experiments can be designed such that the high-temperature buffer layer is kept below the critical layer thickness so no relaxation occurs during its growth and therefore the relaxation may be confined to essentially the remaining growth temperature. This could be attempted in future research but for this work we relied on published value of U. The thermal expansion coefficients are summarized in Table 8.1.

To estimate the value of B, we determined the threading dislocation densities in thick, nearly-relaxed ZnSe/GaAs (001) single heterostructures from the same set described above (Figure 8.3) by considering the glide of TDs on {111} type planes. This glide is governed by the excess stress which depends on the line tension in the misfit segments of dislocations. Using our kinetic model for the threading dislocation density, we obtained a best fit to the experimental results using the value $B \approx 5\times10^{-12} cm^3 dyn^{-1} s^{-1}$.

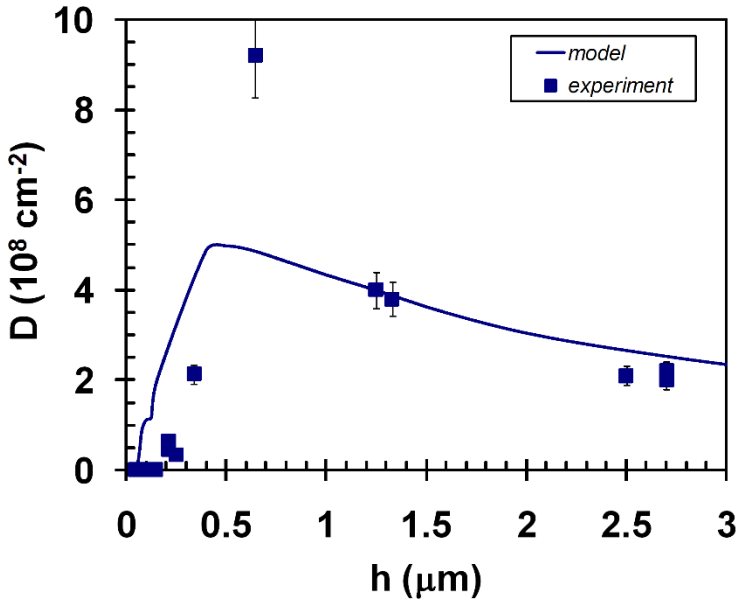

Figure 8.4. Dislocation density versus thickness for ZnSe/GaAs (001) single heterostructures grown by the two-step photo assisted MOVPE process.

Table 8.1. Second-order polynomial coefficients for thermal expansion coefficients in GaAs [235], ZnSe [235], and ZnS [15,236,237,238,239,240] associated with a third-order polynomial fit to Δa/a characteristics.

Crystal	B (10^{-6} K^{-1})	C (10^{-9} K^{-2})	D (10^{-12} K^{-3})
GaAs	4.239	2.916	-0.936
ZnSe	4.419	5.309	-2.158
ZnS	6.628	2.15	-0.333

Using the values of B and K determined above, we applied the kinetic model to calculate the threading dislocation densities in ZnSe/GaAs (001) single heterostructures grown by the two-step process over a wide range of thicknesses, down to and including pseudomorphic layers. The experimental and modeling results are compared in Figure 8.4. It can be seen that the kinetic model predicts a build-up and decay of the threading dislocation density as the layer thickness is increased. Though there are quantitative differences between the modeling and experimental

results for thinner layers, the qualitative behavior suggests that the initial build-up of the dislocation density can be explained by misfit-threading dislocation interactions.

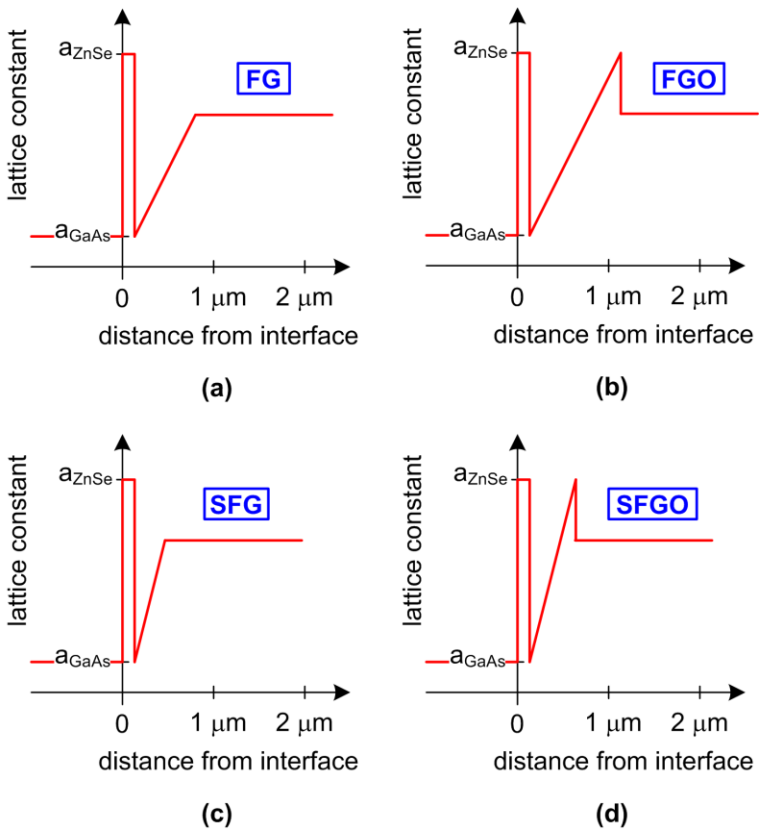

Figure 8.5. Graded ZnS_ySe_{1-y}/ZnSe/GaAs (001) heterostructures investigated in this study.

To further test the kinetic model, we applied it to several graded ZnS_ySe_{1-y}/ZnSe/GaAs (001) heterostructures. Each of these structures comprised a ZnSe buffer, a graded ZnS_ySe_{1-y} layer, and a uniform composition ZnS_ySe_{1-y} layer on top. Each heterostructure had a 135 nm ZnSe buffer layer grown by the two-step procedure described above. The graded ZnS_ySe_{1-y} layer was grown at 360°C with 39 mW/cm^2 photoirradiation. The zinc and selenium source flows were fixed (X_{DMZn} = 2 x 10^{-4} and X_{DMSe} = 4 x 10^{-4}), and the sulfur source flow was varied to control the sulfur content

of the growing layer. The range of the DES mole fraction was $0 \leq X_{DES} \leq 1.5 \times 10^{-4}$, corresponding to $0 \leq y \leq 0.06$. In the forward graded (FG) sample, the sulfur composition was graded from 6% to 2% with a grading rate of -0.05% sulfur/min (-6.4% μ m^{-1}). In the forward graded with overshoot (FGO) sample, the sulfur composition was graded from 6% to 0 with the same grading rate. In the "steeply forward graded" (SFG) sample the sulfur composition was graded from 6% to 2% with a grading rate of - 0.1% sulfur/min (-12.8% μ m^{-1}), and in the "steeply forward graded with overshoot" (SFGO) sample the composition was graded from 6% to 0% with a grading rate of - 0.1% sulfur/min (-12.8% μ m^{-1}). Each structure had a uniform top layer of ZnS_ySe_{1-y}, grown at 360ºC with 39 mW/cm^2 photoirradiation with $X_{DMZn} = 2 \times 10^{-4}$, $X_{DMSe} = 4 \times 10^{-4}$, and $X_{DES} = 0.5 \times 10^{-4}$ for 45 min, resulting in a nominal sulfur composition of 2%. The ZnS_ySe_{1-y}/ZnSe/GaAs (001) structures studied are illustrated in Figure 8.5.

Experimentally, we found that the use of compositional overshoot at the ZnS_ySe_{1-y} graded layer / ZnS_ySe_{1-y} uniform layer interface resulted in a significantly lower surface threading dislocation density compared to a similar structure without overshoot. The FGO structure exhibited a threading dislocation density of 2×10^8 cm^{-2} compared to 5×10^8 cm^{-2} for the FG structure, and the SFGO sample exhibited a dislocation density of 2×10^8 cm^{-2} compared to 4×10^8 cm^{-2} for the SFG structure. More importantly, because the samples being compared had the same grading coefficients and the total thickness of the FGO sample is only slightly greater (~ 10%) than that of the FG sample, these factors cannot explain the ~ 60% reduction in the surface dislocation density.

Table 8.2. Experimental and modeling results for ZnS_ySe_{1-y}/GaAs (001) heterostructures with the forward graded (FG), forward graded with overshoot (FGO), steep forward graded (SFG), and steep forward graded with overshoot (SFGO) structures described in the text.

	Threading Dislocation Density (10^8 cm^{-2})			
Structure	*FG*	*FGO*	*SFG*	*SFGO*
Experiment	*5*	*2*	*4*	*2*
Model $B = 5\times10^{-12} cm^3 dyn^{-1} s^{-1}$	*2.2*	*2.0*	*2.5*	*2.2*
Model $B = 1\times10^{-12} cm^3 dyn^{-1} s^{-1}$	*4.2*	*2.7*	*4.8*	*3.8*

The one significant difference between the samples - the design of interface - could not be expected to alter annihilation and coalescence processes in the graded or uniform layers. Therefore, the reduction is attributed to the bending over of threading dislocations at the overshoot interface in order to create misfit dislocation density line length which also indicates an enhancement of the annihilation and coalescence mechanisms at the interface itself. To examine this further, we applied the kinetic model to the graded ZnS_ySe_{1-y} samples with the FG, FGO, SFG, and SFGO designs, and the results are summarized in Table 8.2. The model correctly predicts that the inclusion of an overshoot interface reduces the threading dislocation density at the surface, but there are significant quantitative differences between the experimental and model results. The value $B \approx 5\times10^{-12} cm^3 dyn^{-1} s^{-1}$ was determined from a best fit to the date for ZnSe and was applied to ZnS_ySe_{1-y} heterostructures with the assumptions that B is independent of the both the sulfur content and the dislocation density. The second value of B ($B \approx 1\times10^{-12} cm^3 dyn^{-1} s^{-1}$) was applied ZnS_ySe_{1-y} with the same assumptions as in the case of ZnSe/GaAs (001) single heterostructures to get within a factor of two accuracy in the dislocation compensation associated with overshoot interfaces. This value is not intended to be a best fit of ZnS_ySe_{1-y} but it illustrates that the value of B is very different in these samples compared to ZnSe heterostructures considered previously. We

considered two possible explanations for this difference. i) It is possible that the value of B is different for ZnS_ySe_{1-y} compared to ZnSe. However, our samples contained relatively dilute concentrations of sulfur and it seems unlikely that the composition changes alone could explain a factor of five change in B. ii) It is possible that the effective value of B varies with the dislocation density, because of threading dislocation interactions which could retard the dislocation mobility and glide velocities. Explanation (ii) cannot be ruled out at the present time, and warrants further investigation by using a refined model which takes into account the dependence of B on the dislocation density. This might also be the reason for the quantitative differences between model and experimental results for layers of ZnSe less than 500 nm thick. It is possible that the model underestimates the growth of misfit dislocation segments in the thinner layers, and this could be the case if the dislocations have greater mobility in the thinner layers compared to the thicker layers. It is known that dislocation interactions in highly-defected layers can lead to reduced mobility or even pinning of dislocations. Future refinements of this kinetic model might take into account a dislocation mobility which depends on (i) the dislocation density and (ii) the second order effect of dissociation of dislocations into partials which may affect somewhat the line tension in the misfit segments of dislocations.

In conclusion, in this work we have developed a dislocation dynamics model which accounts for misfit-threading dislocation interactions as well as annihilation and coalescence, and which is therefore applicable to device structures with arbitrary compositional profiles. The kinetic model provides a qualitative prediction of the build-up and decay of the dislocation density with thickness in single heterostructures, and it also predicts dislocation compensation by overshoot

interfaces in graded heterostructures. A future refinement of the model could include a dislocation density dependence of the dislocation mobility.

8.2. Critical Layer Thickness and the Role of Finite Experimental Resolution in ZnSe/GaAs (001) Utilizing Matthews and Blakeslee Equilibrium Theory

The critical layer thickness h_c for the onset of lattice relaxation has important implications for the design of pseudomorphic and metamorphic II-VI device structures on lattice-mismatched substrates. Several theoretical models have been developed for the critical layer thickness, including the well-known force-balance model of Matthews and Blakeslee. Experimentally-measured critical layer thicknesses in ZnSe/GaAs (001) heterostructures are often at variance with one another as well as the Matthews and Blakeslee model. By assuming that the lattice relaxation is a fixed fraction of the equilibrium relaxation (constant γ / γ_{eq}), Fritz [Appl. Phys. Lett., 51, 1080 (1987)] has shown that the measured h_c may be much larger than the equilibrium value when using a finite experimental resolution. However, the assumption of constant fractional relaxation is not applicable to any heterostructure exhibiting kinetically-limited lattice relaxation. In order to reconcile the conflicting results for II-VI materials, we applied a general dislocation flow model to determine the apparent critical layer thickness as a function of the experimental resolution for ZnSe/GaAs (001) heterostructures. We show that the Matthews and Blakeslee model is consistent with several measured values of h_c once the kinetically-limited relaxation and finite experimental strain resolution are taken into account.

8.2.1. The Role of Finite Experimental Resolution

The critical layer thickness h_c for the introduction of misfit dislocations is important to the design of pseudomorphic and metamorphic II-VI device structures on mismatched substrates. Several models have been proposed for the critical layer thickness [34,241,242,243,244,245] however, the most commonly used and well-known model is that of Matthews and Blakeslee [241] which is based on equating the line tension and glide force acting on a grown-in dislocation. It is important to note that we have considered only experimental results for continuous layers of ZnSe/GaAs (001), for which the Matthews and Blakeslee model is applicable. Other theoretical models have been developed for three-dimensional deposits, or island growth, but these will not be considered further here. The equilibrium strain in an epitaxial layer of thickness h is given by

$$\varepsilon_{eq}(h) = \begin{cases} f, & h \le h_c; \\ \dfrac{f}{|f|}\dfrac{b(1-\nu\cos^2\alpha)}{8\pi h(1+\nu)\cos\lambda}\left[\ln\left(\dfrac{h}{b}\right)+1\right], & h > h_c; \end{cases} \qquad \textbf{(8.4)}$$

where b is the length of the Burgers vector, ν is the Poisson ratio, α is the angle between the Burgers vector and dislocation line vector, f is the lattice mismatch, and λ is the angle between the Burgers vector and the direction in the interface which is perpendicular to the intersection of the glide plane and the interface. The critical layer thickness is the greatest thickness for which $\varepsilon_{eq}(h) = f$. Using the room temperature (20 °C) lattice mismatch of ZnSe, $f = -0.270\%$, the equilibrium critical layer thickness of ZnSe/GaAs (001) is 44 nm assuming $\alpha = 60^\circ$, $\lambda = 60^\circ$ and $\nu = 0.38$. In contrast, experimentally measured values of the critical layer thickness for epitaxially-grown ZnSe/GaAs (001) range from 50 nm to 225 nm

[246,247,248,249,250,251,252,253], or up to five times the equilibrium value at room temperature. Measurements of the critical layer thickness for ZnSe/GaAs (001) show variations based on the growth method, temperature and method of characterization (i.e., experimental resolution). In addition, the nature of the dislocations also impacts the resolution and in this work, we are assuming 60° dislocations gliding on (111) planes.

In the ZnSe/GaAs (001) material system, the lattice mismatch and therefore the critical layer thickness vary with growth temperature owing to the difference in thermal expansion coefficients. In the temperature range from 20 ºC to 600 ºC, the coefficient of thermal expansion α_{CTE} varies from 6.975 x 10^{-6} K^{-1} to 8.754 x 10^{-6} K^{-1} for ZnSe and from 5.707 x 10^{-6} K^{-1} to 7.190 x 10^{-6} K^{-1} for GaAs as shown in Table 8.3 [254]. The characteristics provided in Table 8.3 represent second-order polynomial fits to the available experimental data, which are given by

$$\alpha_{CTE}(T) = B + 2CT + 3DT^2 \qquad \textbf{(8.5)}$$

where T is the absolute temperature in Kelvins. The polynomial coefficients for the substrate and the epilayer are collected in Table 8.3.

Table 8.3. Second-order polynomial coefficients for thermal expansion coefficients in ZnSe and GaAs [254], as determined from the third-order polynomial fits to the $\Delta a / a$ expansion characteristics.

	B (10^{-6} K^{-1})	C (10^{-9} K^{-2})	D (10^{-12} K^{-3})
ZnSe	4.419	5.309	-2.158
GaAs	4.239	2.916	-0.936

The lattice mismatch in ZnSe/GaAs (001) at a growth temperature T_G is given by

$$f(T_G) = f(T_0) + \int_{T_0}^{T_G} \left(\alpha_{CTE,GaAs} - \alpha_{CTE,ZnSe}\right) dT \,, \qquad \textbf{(8.6)}$$

where T_0 is the reference temperature, usually assumed to be room temperature. The lattice mismatch in the ZnSe/GaAs (001) system therefore varies from -0.270% at 20 ^{o}C to -0.364% at 600 ^{o}C. The increase in the absolute value of mismatch causes a reduction in the critical layer thickness from the often-quoted room-temperature value, so this cannot explain the differences between the measured and equilibrium critical layer thickness values. At a growth temperature of 600 ^{o}C, the equilibrium critical layer thickness for ZnSe/GaAs (001) is ~ 31 nm.

The lattice constant for ZnSe, and therefore its lattice mismatch with respect to GaAs, could vary by several parts per million due to variations in stoichiometry. However, we have neglected such variations in this work because (i) they are small compared to the absolute mismatch and (ii) they are small in comparison to the temperature variation of the mismatch [255].

For the $Si_{1-x}Ge_x$/Si (001) and $In_xGa_{1-x}As$/GaAs (001) material systems Fritz [256] has argued that the differences between experimentally measured (apparent) critical layer thicknesses and equilibrium values stem from kinetically-limited relaxation combined with finite experimental resolution. By assuming that the lattice relaxation is a fixed fraction of the equilibrium relaxation ($\gamma / \gamma_{eq} = \mathrm{Q}$), Fritz showed that the measured critical layer thickness h_c^* may be much larger than the equilibrium value when using finite experimental resolution R, according to $f - R/Q = \varepsilon_{eq}\left(h_c^*\right)$. The resolution refers to the strain sensitivity of the measurement, and is unitless. However, experimental results for heteroepitaxial II-VI materials such as ZnS_ySe_{1-y}/GaAs [257] and ZnSe/GaAs [246,258] show that the lattice relaxation is not a fixed fraction of the

equilibrium relaxation, and this is expected to be the case for any material exhibiting kinetically-limited relaxation. If we remove the assumption of constant γ / γ_{eq}, the relationship between the resolution R and the apparent critical layer thickness h_c^* is

$$R = f - \varepsilon_{\parallel}\left(h_c^*\right). \quad \textbf{(8.7)}$$

Stated differently, the apparent critical layer thickness h_c^* is the minimum thickness at which the lattice relaxation can be detected using an experimental resolution R. By applying a kinetic model for lattice relaxation by dislocation flow in ZnSe/GaAs (001) heterostructures we can determine the strain relaxation versus thickness and therefore find the apparent critical layer thickness as a function of experimental resolution by applying Equation 8.7.

8.2.2. Kinetic Model for Lattice Relaxation

Previously, we reported a kinetic model for lattice relaxation by dislocation flow similar to the one proposed by Dodson and Tsao [68]. In order to simplify the analysis, Dodson and Tsao approximated the strain relaxation as occurring with a fixed thickness equal to the final film thickness during an annealing step of duration equal to the growth time. Therefore, the layer thickness and equilibrium strain point were considered fixed during the strain relaxation. Although use of these approximations is reasonable for thick, uniform layers grown at constant temperature, it is necessary to use a different approach for layers close to the critical layer thickness.

In this work, we consider the time dependence of the film thickness - and therefore equilibrium strain - in the growing film. We also take into account thermal strain, which is typically introduced during the cool-down to room temperature but which can also be introduced during growth if the growth temperature is varied. In order to do this, we use the generalized

effective stress, which varies with time as the layer is grown and which can account for changes in composition as well as temperature during growth. The driving force for relaxation is the effective stress acting on threading segments of dislocations; the effective stress at a distance z from the substrate interface is determined by the difference between the actual and equilibrium strain profiles in the material above and is given by

$$\tau_{eff}(z) = \left[\frac{2\cos\phi\cos\lambda}{h-z}\right]\int_z^h \left\{\frac{G(1+\nu)\left[\varepsilon_{\parallel}(\zeta)-\varepsilon_{eq}(\zeta)\right]}{(1-\nu)}\right\}d\zeta, \qquad \textbf{(8.8)}$$

where z is the distance from the substrate interface, ϕ is the angle between the surface normal and the slip plane, G is the shear modulus, $\varepsilon_{\parallel}$ is the actual in-plane strain, and ζ is a variable of integration. The equilibrium strain profile for an arbitrary heteroepitaxial structure may be determined by minimizing the sum of the strain energy and dislocation energy as described by Bertoli et al. [43]. In the model of Haasen [259], the glide of a 60° dislocation in a diamond or zinc blende crystal can be described as the diffusion of a nanocrack with atomic dimensions under the influence of a Peierls-Nabarro force. This leads to a semiempirical relation for the velocity V of misfit dislocation extension given by

$$V = A\tau_{eff}\exp\left(-\frac{U}{k_B T}\right), \qquad \textbf{(8.9)}$$

where U is the activation energy for diffusion of the dislocation core, k_B is the Boltzmann constant, T is the temperature, and A is a constant. In this work, we have assumed that the velocity of misfit dislocations is linear in the effective stress. The rate of lattice relaxation at a

distance z from the substrate interface is determined by the glide of dislocations in the material below:

$$\frac{d\gamma(z)}{dt} = AKb\sin\alpha\sin\phi\,\tau_{eff}^2(z)\exp\left(-\frac{U}{k_B T}\right)\int_0^z [\rho_A(\zeta)+\rho_0]d\zeta\,, \qquad \textbf{(8.10)}$$

where K is a constant, ρ_0 accounts for initial sources of misfit dislocations, and $\rho_A(z)$ is the areal density of misfit dislocations in the graded material,

$$\rho_A(z) = \left(\frac{1}{b\sin\alpha\sin\phi}\right)\left(\frac{d\varepsilon_{\|}(z)}{dz} - \frac{df(z)}{dz}\right), \qquad \textbf{(8.11)}$$

in which $f(z)$ is the lattice mismatch strain as defined in Reference [260].

During growth of any mismatched heterostructure, changes in temperature during growth introduce thermal strain. If there is a change in temperature from T_1 to T_2, made rapidly enough so that insignificant lattice relaxation occurs during the temperature change, the in-plane strain is modified by the thermal strain according to

$$\varepsilon_{\|}(T_2) = \varepsilon_{\|}(T_1) + \int_{T_1}^{T_2} (\alpha_{CTE,GaAs} - \alpha_{CTE,ZnSe})dT\,. \qquad \textbf{(8.12)}$$

In practice, a temperature ramp can be subdivided into a series of small steps to account for finite strain relaxation during temperature changes.

By using Equations 8.8 through 8.12 we can find the room temperature strain, and therefore lattice relaxation, as a function of thickness, and thereby determine the apparent critical layer thickness as a function of experimental resolution by using Equation 8.4. In order to do this, we divide the layer into a number of sublayers having uniform thickness, and we consider the growing structure to be built up one sublayer at a time. After the growth of each sublayer the equilibrium

strain is calculated by energy minimization, the effective stress is calculated, and then the lattice relaxation is found by assuming that the sublayer is annealed at its growth temperature for its time of growth. These sublayers may be reduced in thickness (to a few monolayers) to obtain the desired accuracy; in this work, the sublayer thickness was fixed at 1 nm. When using this approach for the case of a uniform composition layer, the misfit dislocations are confined to the interface (first sublayer). Also, both the actual in-plane strain and the equilibrium in-plane strain are constant throughout the thickness (equal for all sublayers at any given point in the growth).

By subdividing the layer in this way, we can account for the fact that the thickness and equilibrium strain are changing during the growth. Therefore, the driving force for relaxation is changing during growth even if the temperature is held constant. Temperature changes, associated with two-step growth or cooling after growth, alter the strain and lattice mismatch due to the differential thermal expansion. Inclusion of these effects provides a more accurate calculation of the residual strain than the approximate Dodson and Tsao model [68], which provides an estimate of the lattice relaxation based on the annealing of a fully-grown, constant thickness layer for a time equal to the growth time, without including temperature changes or the evolution of the equilibrium strain.

Using the kinetic model for relaxation and methods described in Reference 66, 260, the strain versus thickness characteristic for ZnSe/GaAs (001) was fit very accurately using the model parameters $AK = 2.3 \cdot 10^{-17} cm^4 dyn^{-2} s$, $U = 0.6 eV$, and $\rho_0 = 1.0 \cdot 10^4 cm^{-2}$. The basis for the model, as described above, is the Matthews and Blakeslee theory for the critical layer thickness, and the Mathews and Blakeslee equilibrium strain, which was used to compute the effective stress, and therefore the driving force for lattice relaxation.

In this work, the previously-developed model was applied in order to answer the question of whether the Matthews and Blakeslee model is consistent with reported measurements of the critical layer thickness for ZnSe/GaAs (001). We did not modify the previously-developed model, nor did we use any fitting or adjustable parameters. To answer the question at hand, we applied the kinetic model for lattice relaxation in order to predict the room-temperature residual strain in ZnSe/GaAs (001) as a function of thickness for given growth temperature conditions. Then, through use of Equation 8.4, we calculated and plotted the apparent critical layer thickness as a function of experimental resolution for each of these growth temperature conditions. Each measured value of the critical layer thickness was then plotted on the same graph according to the strain resolution of the particular measurement, using error bars to indicate the range of the experimental resolution in each case. In such an analysis, if the experimental points fall upon the calculated curves, when accounting for the error bars, then we may conclude that the Matthews and Blakeslee model for the critical layer thickness is consistent with the measurements.

8.2.3. Kinetically-Limited Strain Results Based on a Finite Resolution

Figure 8.6 shows the calculated in-plane strain as a function of thickness for ZnSe/GaAs (001) grown under different temperature conditions: 300 ^{o}C, 330 ^{o}C, 360 ^{o}C, 480 ^{o}C, 595 ^{o}C, and two-step growth, for which 40% of the thickness is grown at 595^{o}C and then the remaining 60% of the thickness is grown at 360 ^{o}C. Pseudomorphic layers all exhibit an in-plane strain of -0.27% at room temperature, even though the growth-temperature strain varies with T_G, because this variation is offset during cooling. For metamorphic (partly relaxed) layers, on the other hand, the growth-temperature strain is important in determining the rate of relaxation and this relaxation is not offset during cool-down. ZnSe layers grown at higher temperatures exhibit a much more rapid

decrease in the residual strain with thickness compared to those grown at lower temperatures. Because of this, measurement of the same apparent critical thickness will require much better experimental resolution with a growth temperature of 300 ^{o}C compared to the case of 595 ^{o}C. As expected, the relaxation characteristic for two-step growth is intermediate between the characteristics for single-temperature growth at 360 ^{o}C and 595 ^{o}C. For very thin layers, however, the curve for two-step growth almost coincides with the 360 ^{o}C curve, because for these layers the critical layer thickness is not exceeded until after 40% of the thickness is grown and no apparent relaxation occurs at the initial temperature. The results of Figure 8.6 indicate that the growth temperature has important implications in the final strain state; one key result here is that structures with a higher thermal budget exhibit much higher relaxation rates and therefore lower values of the in-plane strain. As an example, a structure grown at 595 °C exhibits near complete relaxation (> 95%) at a thickness of ~300 nm whereas for a growth temperature of 480 °C, > 95% relaxation does not occur until a thickness of ~700 nm. At lower temperatures, the structures studied here exhibit extremely sluggish relaxation rates and the curve separation between the growth temperatures of 300 °C, 330 °C and 360 °C does not become apparent until a thickness of ~500 nm is reached. Furthermore, even at a thickness of ~1000 nm structures grown at relatively low temperatures (< 360 °C) exhibit less than 20% strain relaxation.

From the results of Figure 8.6, we created a plot of apparent critical layer thickness versus experimental resolution for each of the growth temperature conditions investigated, as follows. For each thickness and temperature condition, we found the extent of lattice relaxation observed at room temperature utilizing the kinetically-limited lattice relaxation model. An experimental method with a strain resolution equal to or less than (i.e., better than) this value would be able to

detect the onset of lattice relaxation. Thus, for the temperature of interest we may plot this thickness as the apparent critical layer thickness with a resolution equal to the expected lattice relaxation from Figure 8.6. This yields a plot of apparent critical layer thickness as a function of experimental resolution, with growth temperature as a parameter, and this is given in Figure 8.7.

The experimental values for the apparent critical layer thickness are 97 nm (O'Donnell et al. [249] for molecular beam epitaxy (MBE) at 330 ^{o}C using x-ray topography), 140 nm (Zhang et al. [246] for two-step metallo-organic vapor phase epitaxy (MOVPE) growth using the x-ray full-width-at-half-maximum (FWHM) method), 150 nm (Petruzzello et al. [248] for 360 ^{o}C growth by MBE using the x-ray diffraction strain method), 210 nm (Zhang et al. [246] for two-step MOVPE growth using the x-ray strain method), and 225 nm (Reisinger et al. [247] for MBE growth at 300 ^{o}C using the x-ray diffraction strain method).

Table 8.4.Summary of measured apparent critical layer thicknesses for ZnSe/GaAs (001) along with the estimated resolution values.

Reference	h_c^* (nm)	Characterization Method	Estimated Resolution	Growth Method
O'Donnell et al. [249]	97	X-ray topography	$1.0 \times 10^{-6} < R < 4.0 \times 10^{-6}$	MBE, 330^{o}C
Zhang et al. [246]	140	X-ray FWHM	$4.4 \times 10^{-6} < R < 1.4 \times 10^{-5}$	MOVPE, two-step
Petruzzello et al. [248]	150	X-ray strain	$5.9 \times 10^{-6} < R < 1.9 \times 10^{-5}$	MBE, 360^{o}C
Zhang et al. [246]	210	X-ray strain	$2.4 \times 10^{-5} < R < 7.5 \times 10^{-5}$	MOVPE, two-step
Reisinger et al. [247]	225	X-ray strain	$3.9 \times 10^{-6} < R < 1.2 \times 10^{-5}$	MBE, 300^{o}C

In order to plot the experimental values on Figure 8.7, and to compare them to the values expected from Equation 8.4, we estimated the experimental resolution for the three techniques. In order to do this, we assumed least-squares fitting of the diffraction peak to a Gaussian profile shape, which is the common approach applied in experimental work. For the x-ray diffraction

strain method (XSM), using a symmetric reflection such as the 004 from an (001) heterostructure, the resolution with respect to the in-plane strain is [75,246]

$$R_{XSM} = \left(\frac{2\nu}{1-\nu}\right)\left(\frac{0.9\lambda_x C_P}{h_c^* \sin\theta_B}\right), \quad \textbf{(8.13)}$$

where λ_x is the x-ray wavelength and θ_B is the Bragg angle. The parameter C_P describes the uncertainty in the Bragg peak position for the epitaxial layer peak as a fraction of the epitaxial layer full width at half maximum; its value depends on the x-ray counting statistics as described in the appendix, and is given by

$$C_P = \frac{1}{2}\sqrt{-\frac{1}{\ln(2)}\ln\left(1-\frac{1}{SNR}\right)}, \quad \textbf{(8.14)}$$

where SNR is the signal-to-noise ratio for the x-ray measurement, assuming a Gaussian diffraction profile. The emission and detection of x-rays are random processes and as a consequence the signal-to-noise ratio improves with the effective number of x-ray counts detected and is given by

$$SNR = \sqrt{N_{eff}}, \quad \textbf{(8.15)}$$

where N_{eff} is the effective number of x-ray photons detected. Most x-ray measurements involve the use of oversampling (measurement of m points within the angular range $\Delta\theta$) in conjunction with curve-fitting. If the number of counts per point is N and the oversampling is by a factor of m the resulting effective number of counts is $N_{eff} = mN$. Combining three of the equation above, we find the resolution of the x-ray strain method to be

$$R_{XSM} = \left(\frac{\nu}{1-\nu}\right)\left(\frac{0.9\lambda_x}{h_c^* \sin\theta_B}\right)\sqrt{-\frac{1}{\ln(2)}\ln\left(1-\frac{1}{\sqrt{N_{eff}}}\right)}, \quad \textbf{(8.16)}$$

For the x-ray diffraction FWHM method (XFM), the resolution with respect to the in-plane strain is given by [246]

$$R_{XFM} = \frac{0.15\lambda_x \sqrt{C_w}}{h_c^* \cos\theta_B \sqrt{n_d}}, \qquad \textbf{(8.17)}$$

where n_d is the number of threading dislocations associated with each misfit dislocation. The assumption of $n_d = 2$ corresponds to dislocation half loops whereas the assumption $n_d = 1$ corresponds to the substrate associated dislocations. Here we assume $n_d = 2$, corresponding to dislocation half loops. In ZnSe on GaAs which is substantially relaxed, the threading dislocation density is on the order of ~1x10^8 cm^{-2} whereas the substrate dislocation density is ~1x10^5 cm^{-2}. Therefore 99.8% of the misfit dislocations have two threading arms while only 0.2% have a single threading arm, and it is appropriate to assume $n_d = 2$. The value of C_w represents the fractional uncertainty in the Bragg peak width as described in the appendix, and is given by

$$C_w = \frac{1}{SNR \cdot \ln(2)}. \qquad \textbf{(8.18)}$$

Combining Equations 8.15, 8.17, and 8.18, and assuming $n_d = 2$, we obtain the resolution of the x-ray FWHM method as

$$R_{XFM} = \frac{0.15\lambda_x}{h_c^* \cos\theta_B N_{eff}^{1/4} \sqrt{2\ln(2)}}. \qquad \textbf{(8.19)}$$

In the x-ray topography method (XTM), it is possible to observe a single misfit dislocation. If the area observed in the topography is $l \times l$, then the minimum detectable linear misfit dislocation density is l^{-1} and the resolution with respect to the in-plane strain is

$$R_{XTM} = \frac{b \sin\alpha \sin\phi}{l}. \qquad \textbf{(8.20)}$$

Here we assumed 50 μm < l < 200 μm to estimate the experimental resolution for the x-ray topography measurement.

Using the calculations described above, we estimated the expected range of experimental strain resolution for each of the experimental measurements. For all x-ray diffraction measurements, we estimated the effective number of counts by assuming ten times oversampling with curve fitting; therefore, the typical peak number of counts (intensity multiplied by count time) was multiplied by ten to obtain the effective number of counts. For Zhang et al. [246] using the x-ray strain method and a Bartels diffractometer with a sealed Cu x-ray tube and an effective number of counts between 2.0 x 10^4 and 2.0 x 10^6, the strain resolution is estimated to be between 2.4 x 10^{-5} and 7.5 x 10^{-5}. For Zhang et al. [246] using the x-ray FWHM method with the same diffractometer and an effective count between 2.0 x 10^4 and 2.0 x 10^6 the expected resolution is between 4.4 x 10^{-6} and 1.4 x 10^{-5}. For Petruzzello et al. [248] using the x-ray strain method with a biaxial diffractometer and a rotating Cu anode x-ray tube, the expected resolution is between 5.9 x 10^{-6} and 1.9 x 10^{-5} for an effective number of counts between 2.0 x 10^7 and 2.0 x 10^9. For Reisinger et al. [247] using a Bartels type diffractometer with a rotating Cu anode source and an effective number of counts between 2.0 x 10^7 and 2.0 x 10^9, the expected resolution is between 3.9 x 10^{-6} and 1.2 x 10^{-5}. For O'Donnell et al. [249] using the x-ray topography method, with 50 μm < l < 200 μm the expected resolution is between 1.0 x 10^{-6} and 4.0 x 10^{-6}. These estimates are summarized in Table 8.4. Although, other measurements of the critical layer thickness [250,251,252,253] for ZnSe/GaAs (001) also show variations based on the growth temperature

and method of measurement, insufficient information was given in these references for the estimation of the experimental resolution, so they cannot be compared against the curves of Figure 8.7.

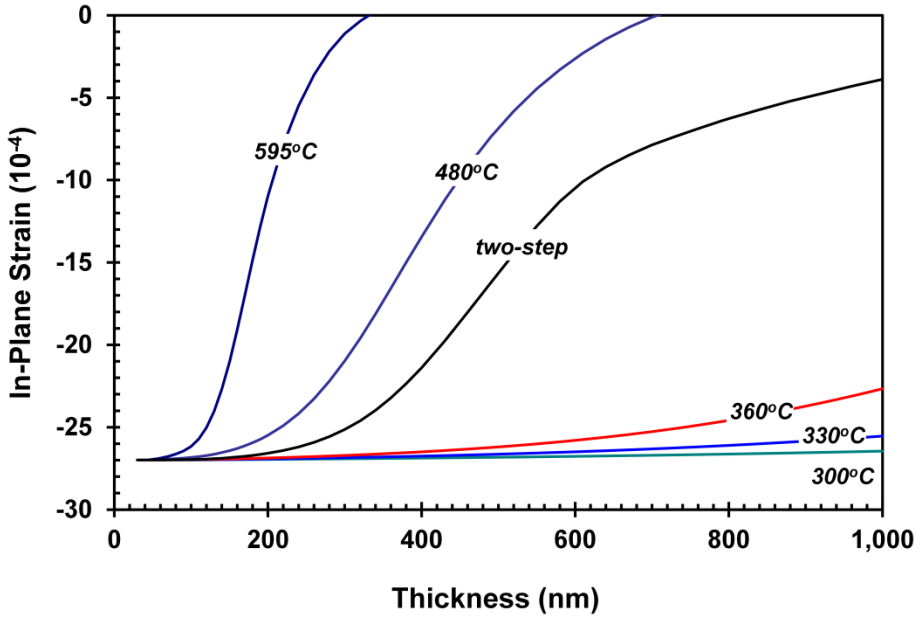

Figure 8.6. (Color Online) Calculated in-plane strain at room temperature as a function of thickness for ZnSe/GaAs (001) grown under different temperature conditions.

To answer the question of whether the Matthews and Blakeslee theory is consistent with the measured critical layer thicknesses, we plotted the experimentally determined values of critical layer thickness on Figure 8.7, using the resolution of the experiment as the horizontal coordinate, and using error bars to display the range of the experimental strain resolution. The placement of the experimental point is determined by the geometrical mean $\overline{R}$ of the range of the experimental strain resolution:

$$\overline{R} = \sqrt{R_{\min} R_{\max}}\,, \qquad \textbf{(8.21)}$$

where R_{min} and R_{max} are the limiting resolutions determined from the appropriate effective counts. Then, if the Matthews and Blakeslee theory is consistent with the measurements, the experimental points should overlap with the corresponding temperature curve, once the error bars are taken into account.

In Figure 8.7, the measurement of O'Donnell et al. falls upon the 330°C curve when accounting for the error bars, the measurements of Zhang et al. fall upon the curve generated for two-step growth, the measurement of Reisinger et al. falls upon the 300°C curve and the measurement of Petruzzello et al. falls upon the 360°C curve. Therefore, the Matthews and Blakeslee model is consistent with all of these measured values of critical layer thickness when finite experimental resolution is taken into account. Furthermore, an important result of Figure 8.7 is that for the same experimental resolution and x-ray counting statistics, an increase in the growth temperature would lead to a lower determined h_c^*.

It is important to note that we have not considered the uncertainty in film thickness due to growth rate variations or experimental error in the thickness characterization. If we had considered such thickness uncertainties, they would introduce vertical error bars. Then each data point would be plotted as a rectangle rather than a horizontal line segment. However, to the extent that the horizontal line segments intersect the theoretical curves, the rectangular boxes would also intersect the theoretical curves, since each rectangular box includes the associated horizontal line segment as a cross section. Therefore, if we were to account for error bars associated with thickness variations, our finding would remain unchanged, and we would conclude that the Matthews and Blakeslee model is consistent with the experimental data.

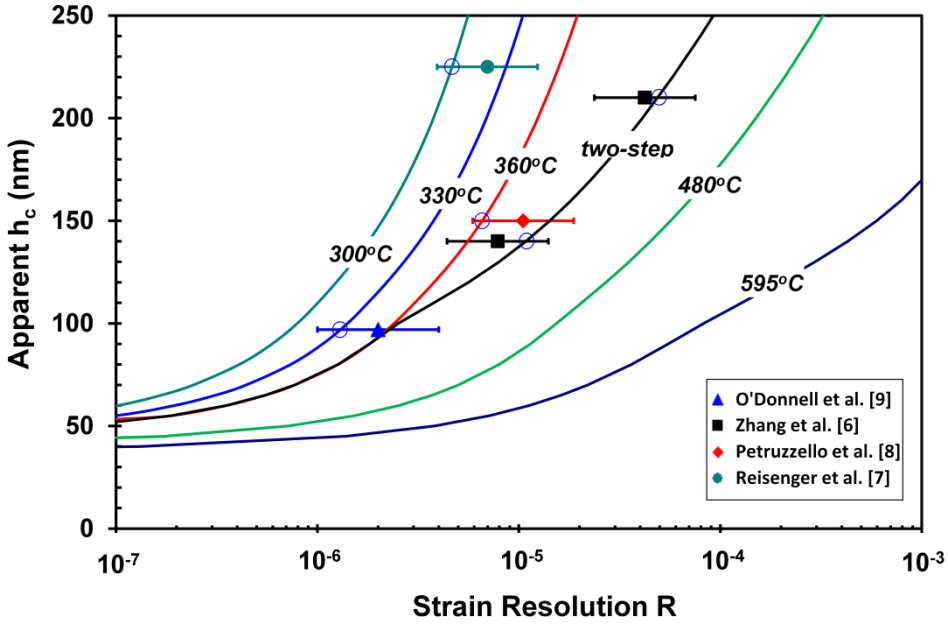

Figure 8.7. (Color Online) Apparent critical layer thickness for ZnSe/GaAs (001) as a function of the experimental resolution for different temperature conditions. The symbols represent experimental measurements and the horizontal error bars show the range of the estimated resolution. Each open circle indicates the intersection of the experimental point with the appropriate temperature curve.

Finally, it should be made clear that this analysis, though it shows the Matthews and Blakeslee model for the critical layer thickness is consistent with the experimental data for ZnSe/GaAs (001) once kinetically-limited lattice relaxation and finite experimental strain resolution is taken into account, does not enable us to reject other models for the critical layer thickness in continuous epitaxial layers, nor does it allow a comparison of different models for the critical layer thickness. Such a comparison, though beyond the scope of the present work, will be considered in a forthcoming publication.

Using a kinetic model for dislocation flow we have calculated the kinetically-limited lattice relaxation as a function of layer thickness for ZnSe/GaAs (001) layers grown under six different

temperature conditions: 300 ºC, 330 ºC, 360 ºC, 480 ºC, 595 ºC, and two-step growth, for which 40% of the thickness is grown at 595 ºC after which the remaining 60% of the thickness is grown at 360ºC. On the basis of these lattice relaxation results, we have determined the apparent critical layer thickness as a function of the experimental resolution for each of these temperature conditions using a new model described by $R = f - \varepsilon_{\parallel}\left(h_c^*\right)$; that is, we have found the minimum thickness at which there will be detectable lattice relaxation using a given resolution. An analysis of reported experimental critical layer thicknesses for ZnSe/GaAs (001) using estimates of the experimental resolution reveals that the Matthews and Blakeslee critical layer thickness theory is consistent with the measured values of Reisinger et al., Petruzzello et al., O'Donnell et al., and Zhang et al. once the kinetically-limited relaxation and finite experimental strain resolution are taken into account. In addition, the variations in the experimentally determined critical layer thickness depend on the growth method, temperature and the counting statistics employed for the characterization measurement.

8.3. CLT: Theory and Experiment in the ZnSe/GaAs Material System

The critical layer thickness (CLT) determines the criteria for dislocation formation and the onset of lattice relaxation. Although several theoretical models have been developed for the critical layer thickness, experimentally-measured CLTs in ZnSe/GaAs (001) heterostructures are often at variance with one another as well as with established theories. In a previous work [T. Kujofsa et al., J. Vac. Sci. Technol. B, 34, 051201 (2016)], we showed that the experimentally measured CLT may be much larger than the equilibrium value when using finite experimental resolution. In this work, we apply a general dislocation flow model to determine the apparent critical layer thickness

as a function of the experimental resolution for ZnSe/GaAs (001) heterostructures. More importantly, we compare the results utilizing different equilibrium theories and therefore varying driving forces for the lattice relaxation in order to determine which established models are consistent with several measured values of CLT for ZnSe/GaAs (001) once kinetically-limited relaxation and finite experimental strain resolution are taken into account.

Table 8.5. Summary of the critical layer thickness models.

Model	Critical Layer Thickness
Matthews and Blakeslee [241]	$h_c = \frac{b\left(1-\nu\cos^2\alpha\right)}{8\pi\lvert f\rvert(1+\nu)\cos\lambda}\left[\ln\left(\frac{h_c}{b}\right)+1\right]$
van der Merwe [242]	$h_c = \frac{a_e(1-2\nu)}{4\pi\lvert f\rvert(1-\nu)^2}\left[\ln(\lvert f\rvert)+\ln\left(\frac{2\pi}{e(1-\nu)}\right)\right]$
People and Bean [243]	$h_c = \frac{(1+\nu)b^2}{16\pi\sqrt{2}f^2(1-\nu)a_e}\ln\left(\frac{h_c}{b}\right)$
Fischer et al. [244]	$h_c = \frac{b\cos\lambda}{4\lvert f\rvert(1+\nu)}\left[1+\frac{\left(1-\nu\cos^2\alpha\right)}{4\pi(1+\nu)\cos^2\lambda}\ln\left(\frac{h_c}{b}\right)\right]$
Freund [245]	$h_c = \frac{b(1-\nu)\sin\alpha\tan\alpha}{8\pi\lvert f\rvert(1+\nu)\cos\lambda}\ln\left(\frac{h_c}{b}\right) + \frac{b\cos\alpha}{8\pi\lvert f\rvert(1+\nu)\cos\lambda}\left[\ln\left(\frac{h_c}{b}\right)-\frac{\cos 2\lambda}{2}-\frac{1-2\nu}{4(1-\nu)}\right]$

b is the length of the Burgers vector, ν is the Poisson ratio, α is the angle between the Burgers vector and dislocation line vector, f is the lattice mismatch, λ is the angle between the Burgers vector and the direction in the interface which is perpendicular to the intersection of the glide plane and the interface and a_e is the lattice constant of the epilayer. In this work, we have assumed a room temperature (20 ºC) lattice mismatch of ZnSe, $f = -0.270\%$, $\alpha, \lambda = 60^\circ$, and $\nu = 0.38$.

8.3.1. Various Models for Equilibrium Critical Layer Thickness

Understanding the critical layer thickness (CLT or h_c) for the introduction of misfit dislocations has important implications in the design and functionality of metamorphic devices. Although several models have been proposed for the critical layer thickness [34,245,244,243,242], the most commonly used and well-known model is that of Matthews and Blakeslee [241]. The critical layer thickness is the greatest thickness for which the equilibrium in-plane strain is equal to the lattice mismatch,

$$\varepsilon_{eq}(h) = f, \quad h \le h_c \,. \tag{8.22}$$

In a previous work [261], we investigated the apparent critical layer thickness and the role of finite experimental resolution in the ZnSe/GaAs material system by considering the model of Matthews and Blakeslee (MB) for the equilibrium strain and the model of Kujofsa et al. [215] for the kinetically-limited strain. For epitaxially-grown ZnSe/GaAs (001), experimentally measured values of the critical layer thickness range from 50 nm to 225 nm [246,247,248,249,250,251,252,253] and these measurements show variations based on the growth method, temperature and characterization technique (i.e., experimental resolution). Although, in the ZnSe/GaAs (001) material system, the lattice mismatch and therefore the critical layer thickness vary with growth temperature owing to the difference in thermal expansion coefficients, such variation of the h_c from the often-quoted room-temperature value cannot explain the differences between the measured and equilibrium critical layer thickness values. Fritz [256] has argued that the differences between experimentally measured (apparent) critical layer thicknesses and equilibrium values stem from kinetically-limited relaxation combined with finite experimental

resolution. In his work relating to SiGe and InGaAs, Fritz assumed that the lattice relaxation is a fixed fraction of the equilibrium relaxation ($\gamma / \gamma_{eq} = \mathrm{Q}$), and showed that the measured critical layer thickness h_c^* may be much larger than the equilibrium value when using finite experimental resolution R, according to

$$f - R/Q = \varepsilon_{eq}\left(h_c^*\right). \quad \textbf{(8.23)}$$

Because kinetically-limited lattice relaxation is never a fixed fraction of the equilibrium strain, in our previous work [261], we considered the relationship between the resolution R and the apparent critical layer thickness h_c^* as

$$R = f - \varepsilon_{\parallel}\left(h_c^*\right). \quad \textbf{(8.24)}$$

Utilizing the kinetic-model described in Reference 66, we determined the apparent critical layer thickness h_c^* at which the lattice relaxation can be detected using an experimental resolution R. A key result from that work was the finding that the Matthews and Blakeslee model is consistent with reported measurements of the critical layer thickness for ZnSe/GaAs (001). In this work, we use a similar approach to determine whether the experimental results are consistent with the models of van der Merwe (vdM) [242], People and Bean (PB) [243], Fischer at al. (Fis) [244] and Freund (Fre) [245]. For a more detailed description of this work, we refer the reader to Reference 261. However, we will briefly summarize the procedure of this work below. We applied the kinetic model for lattice relaxation in order to predict the room-temperature residual strain in ZnSe/GaAs (001) as a function of thickness for given growth temperature conditions. Then, through use of Equation 8.4, we calculated and plotted the apparent critical layer thickness as a function of

experimental resolution for each of these growth temperature conditions (300 ^{o}C, 330 ^{o}C, 360 ^{o}C, 480 ^{o}C, 595 ^{o}C, and two-step growth where 40% of the thickness is grown at 595^{o}C and then the remaining 60% of the thickness is grown at 360 ^{o}C). Each measured value of the critical layer thickness was then plotted on the same graph according to the strain resolution of the particular measurement, using error bars to indicate the range of the experimental resolution in each case. The resolution range for each of the experimental points was determined by taking into account the effect of the counting statistics involved with determination of x-ray rocking curve peak position and width (for x-ray measurements). A more detailed description of this work could be found in Reference 173. In such an analysis, if the experimental points fall upon the calculated curves, when accounting for the error bars, then we may conclude that the critical layer thickness Models for the Critical Layer Thickness and Equilibrium Strain

Although many theoretical models have been developed for three-dimensional deposits, or island growth, these will not be considered here and our main focus will be only on experimental results for continuous layers of ZnSe/GaAs (001), for which the Matthews and Blakeslee, van der Merwe, People and Bean, Fischer at al. and Freund models are applicable. The critical layer thickness expressions for all of the models considered here are summarized in

Figure 8.8 compares the critical layer thickness as a function of the lattice mismatch for the various models considered here. Although all models show a monotonically decreasing CLT with increasing mismatch, there are wide departures amongst them. For the range of lattice mismatch investigated here, the Matthews and Blakeslee model yields the lowest critical layer thickness and therefore in the below analysis we will consider its results when differentiating with the other models; it should also be mentioned that there is no particular bias towards the Matthews

and Blakeslee's model and its choice is made out of pure convenience. The van der Merwe characteristic is similar to the Matthews and Blakeslee curve and for the mismatch range considered in this work this model shows less than 15% difference in the prediction of the CLT compared to Matthews and Blakeslee. Although the Fischer et al. and Freund models exhibit similar expressions to the Matthews and Blakeslee model, they yield values which are higher by 25 to 50%. It should be mentioned that at low mismatch values (<0.1%), the CLT characteristics for these two models overlap one another. However, at higher mismatch, the Freund model approaches the van der Merwe curve. The People and Bean critical layer thickness model was attractive in earlier work because it predicted fair agreement with experimental results for SiGe; however, in low mismatched material systems it greatly overestimates the critical layer thickness. In ZnSe/GaAs, for example, the People and Bean model predicts a critical layer thickness of ~15 μm which is orders of magnitude higher than experimentally-determined values.

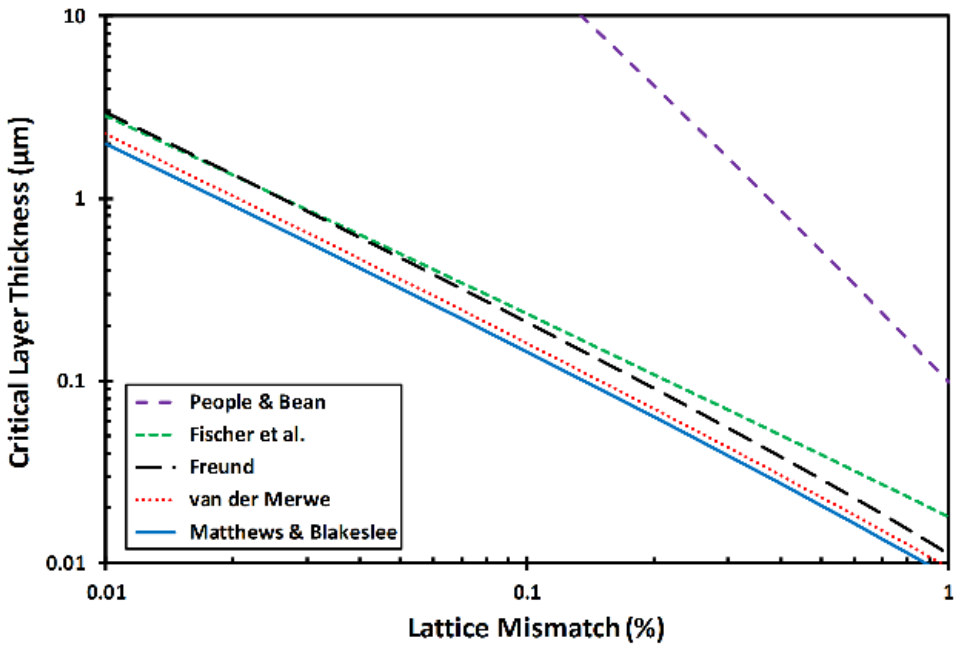

Figure 8.8. Critical layer thickness as a function of the lattice mismatch for the models of Matthews and Blakeslee, van der Merwe, Freund, Fischer et al., and People and Bean.

In order to utilize the Kujofsa et al. plastic flow model for the determination of the strain-relaxation characteristics, the expressions of Table 8.5 must be rearranged in terms of the equilibrium in-plane strain. It should be noted that a key assumption here is that at the critical layer thickness, the equilibrium strain is equal to the lattice mismatch. Table 8.6 shows the equilibrium in-plane strain expressions for the various models. As a consequence of the results shown in Figure 8.8, it is expected that the equilibrium in-plane strain characteristics will be different amongst these models which in turn will affect the kinetically-limited lattice relaxation.

8.3.2. Results and Discussion

Figure 8.9a, c, e, and g illustrate the calculated in-plane strain for the various models investigated here as a function of thickness for ZnSe/GaAs (001) grown under different temperature conditions: 300 ºC, 330 ºC, 360 ºC, 480 ºC, 595 ºC, and two-step growth, for which

40% of the thickness is grown at 595^{o}C and then the remaining 60% of the thickness is grown at 360 ^{o}C. For the heterostructures considered here, the kinetically-limited in-plane strain characteristic exhibits a four-regime relaxation behavior (pseudomorphic, sluggish, rapid and saturation). The visibility of the four regimes is strongly controlled by the available thermal budget for relaxation and such phenomena have been shown in temperature-graded ZnSe/GaAs [262] and ZnS_ySe_{1-y}/GaAs [263] heterostructures. More importantly, ZnSe layers grown at higher temperatures exhibit a much more rapid decrease in the residual strain with thickness compared to those grown at lower temperatures. In addition, at relatively low temperature <360 ^{o}C, due to the sluggish relaxation, a noticeable reduction in the residual strain does not become apparent until a thickness of ~500 nm. Because of this, measurement of the same apparent critical thickness will require much better experimental resolution with a growth temperature of 300 ^{o}C compared to the case of 595 ^{o}C. Not shown in Figure 8.9 are the results from the consideration of the People and Bean model; because the critical layer thickness utilizing this particular model in ZnSe/GaAs (001) is ~15 μm, all the heterostructures considered here are below the critical thickness for dislocation formation and therefore according to the People and Bean model they are all predicted to be pseudomorphic layers which exhibit an in-plane strain of -0.27% at room temperature.

Although the characteristic behavior of the residual strain is similar for the models of the Matthews and Blakeslee, van der Merwe, Fischer at al. and Freund, the numerical value of the strain differs at a given growth temperature and thickness. This variance in the residual strain stems from the difference in the equilibrium strain expressions given in Table 8.6. A key assumption of the plastic flow model is that the effective stress, which is the driving force of the lattice relaxation, is proportional to the difference of the actual and equilibrium strain. Therefore, a lower equilibrium

strain will lead to a higher effective stress which in turn results in rapid relaxation rates and lower residual strain values. In comparison, for a given growth temperature and thickness the residual strain is lowest when considering the Mathews and Blakeslee model and highest utilizing the People and Bean model ($\varepsilon_{MB} < \varepsilon_{vdM} < \varepsilon_{Fre} < \varepsilon_{Fis} < \varepsilon_{PB}$).

Table 8.6. Summary of the equilibrium in-plane strain for various models.

Model	Critical Layer Thickness
Matthews and Blakeslee [241]	$\varepsilon_{eq}(h) = \frac{f}{\lvert f \rvert} \frac{b(1-\nu\cos^2\alpha)}{8\pi h(1+\nu)\cos\lambda}\left[\ln\left(\frac{h}{b}\right)+1\right]$
van der Merwe [242]	$\varepsilon_{eq}(h) = \frac{f}{\lvert f \rvert} \frac{a_e(1-2\nu)}{4\pi h(1-\nu)^2}\left[\ln\left(\lvert\varepsilon_{eq}(h)\rvert\right)+\ln\left(\frac{2\pi}{e(1-\nu)}\right)\right]$
People and Bean [243]	$\varepsilon_{eq}(h) = \frac{f}{\lvert f \rvert}\sqrt{\frac{(1+\nu)b^2}{16\pi\sqrt{2}h(1-\nu)a_e}\ln\left(\frac{h}{b}\right)}$
Fischer et al. [244]	$\varepsilon_{eq}(h) = \frac{f}{\lvert f \rvert} \frac{b\cos\lambda}{4h(1+\nu)}\left[1+\frac{(1-\nu\cos^2\alpha)}{4\pi(1+\nu)\cos^2\lambda}\ln\left(\frac{h}{b}\right)\right]$
Freund [245]	$\varepsilon_{eq}(h) = \frac{f}{\lvert f \rvert}\left(\begin{array}{l}\frac{b(1-\nu)\sin\alpha\tan\alpha}{8\pi h(1+\nu)\cos\lambda}\ln\left(\frac{h}{b}\right) \\ +\frac{b\cos\alpha}{8\pi h(1+\nu)\cos\lambda}\left[\ln\left(\frac{h}{b}\right)-\frac{\cos 2\lambda}{2}-\frac{1-2\nu}{4(1-\nu)}\right]\end{array}\right)$

The term $f/\lvert f \rvert$ accounts for the sign of the lattice mismatch and the equilibrium in-plane strain.

From the results of Figure 8.9a, c, e, and g, we created a plot of apparent critical layer thickness versus experimental resolution for each of the growth temperature conditions investigated, as follows. For each thickness and temperature condition, we found the extent of

lattice relaxation observed at room temperature utilizing the kinetically-limited lattice relaxation model. An experimental method with a strain resolution equal to or less than (i.e., better than) this value would be able to detect the onset of lattice relaxation. Thus, for the temperature of interest we may plot this thickness as the apparent critical layer thickness with a resolution equal to the expected lattice relaxation from Figure 8.9a, c, e, and g. This yields a plot of apparent critical layer thickness as a function of experimental resolution, with growth temperature as a parameter, and this is given in Figure 8.9b, d, f, and h for all the various equilibrium models considered in this work. An important general finding from these plots is that, for the case of fixed resolution (for example, as determined by the counting statistics), an increase in the growth temperature is expected to lead to a lower determined h_c^*.

The experimental values for the apparent critical layer thickness considered here are 97 nm (O'Donnell et al. [249] for molecular beam epitaxy (MBE) at 330 ^{o}C using x-ray topography), 140 nm (Zhang et al. [246] for two-step metalorganic vapor phase epitaxy (MOVPE) growth using the x-ray full-width-at-half-maximum (FWHM) method), 150 nm (Petruzzello et al. [248] for 360 ^{o}C growth by MBE using the x-ray diffraction strain method), 210 nm (Zhang et al. [246] for two-step MOVPE growth using the x-ray strain method), and 225 nm (Reisinger et al. [247] for MBE growth at 300 ^{o}C using the x-ray diffraction strain method). For Zhang et al. [246], using the x-ray strain method, the strain resolution is estimated to be between 2.4 x 10^{-5} and 7.5 x 10^{-5}. For Zhang et al. [246] using the x-ray full-width-at-half-maximum method, the expected resolution is between 4.4 x 10^{-6} and 1.4 x 10^{-5}. For Petruzzello et al. [248], the expected resolution is between 5.9 x 10^{-6} and 1.9 x 10^{-5} for an effective number of counts between 2.0 x 10^{7} and 2.0 x 10^{9}. For Reisinger et al. [247], the expected resolution is between 3.9 x 10^{-6} and 1.2 x 10^{-5}. For O'Donnell et al. [249],

the expected resolution is between 1.0 x 10^{-6} and 4.0 x 10^{-6}. For a complete description of the determination of the experimental resolution, we refer the reader to Reference 261. The placement of the experimental point is determined by the geometrical mean $\overline{R}$ of the range of the experimental strain resolution:

$$\overline{R} = \sqrt{R_{\min} R_{\max}}\ , \qquad \textbf{(8.25)}$$

where $R_{\min}$ and $R_{\max}$ are the limiting resolutions determined from the appropriate effective counts. It is now possible to compare the five models for the critical layer thickness on the basis of Figure 8.9 b, d, f, h. Figure 8.9f shows that the van der Merwe [242] model is consistent with all of the experimental data considered in this study and therefore appears to provide the most accurate description of the critical layer thickness and equilibrium strain, at least in the case of ZnSe/GaAs (001), from among the five models considered. The Matthews and Blakeslee [34] model is consistent with four out the five experimental data, but overestimates the critical layer thickness in the case of the Zhang et al. measurement based on the FHWM method. It should be noted at this point that we have not considered the uncertainty in film thickness due to growth rate variations or experimental error in the thickness characterization. If we had considered such thickness uncertainties, they would introduce vertical error bars. Then each data point would be plotted as a rectangle rather than a horizontal line segment. For the Zhang et al. data point based on the FWHM method, a thickness error of only 7% would cause this point to coincide with the Matthews and Blakeslee model. Considering this, we note that the Matthews and Blakeslee model provides a description which is nearly as accurate as the van der Merwe model, and may be applied to ZnSe/GaAs (001) for most practical purposes. On the other hand, the model of Freund [245] is

consistent with only two of the experimental data points, and thickness tolerances of $\pm$ 15% would have to be considered in order for this model to coincide with the experimental data. The model of Fischer et al. [244] is not consistent with any of the experimental data points, and thickness tolerances of $\pm$ 30% would need to be introduced to account for the observed differences. Therefore, we conclude that that these two models provide a less accurate description of the critical layer thickness and the equilibrium strain, compared to the van der Merwe and Matthews and Blakeslee models, in the case of ZnSe/GaAs (001).

Using a kinetic model for dislocation flow we have calculated the kinetically-limited lattice relaxation as a function of layer thickness for ZnSe/GaAs (001) layers grown under various temperature conditions. The effective stress, which is the driving force for lattice relaxation has been determined by considering various equilibrium models which include the Matthews and Blakeslee, van der Merwe, People and Bean, Freund and Fischer et al. On the basis of these lattice relaxation results, we have determined the apparent critical layer thickness as a function of the experimental resolution for each of these temperature conditions and CLT theories using a new model described by $R = f - \varepsilon_{\parallel}\left(h_c^*\right)$; that is, we have found the minimum thickness at which there will be detectable lattice relaxation using a given resolution. On the basis of this analysis, we conclude that the van der Merwe [242] and Matthews and Blakeslee [34] models are preferred for use in the ZnSe/GaAs (001) system. The models of Freund [245] and Fischer et al. [244] appear to provide less accurate descriptions of the critical layer thickness and equilibrium stain for ZnSe/GaAs (001). Finally, the People and Bean model greatly overestimates the critical layer thickness for this material system.

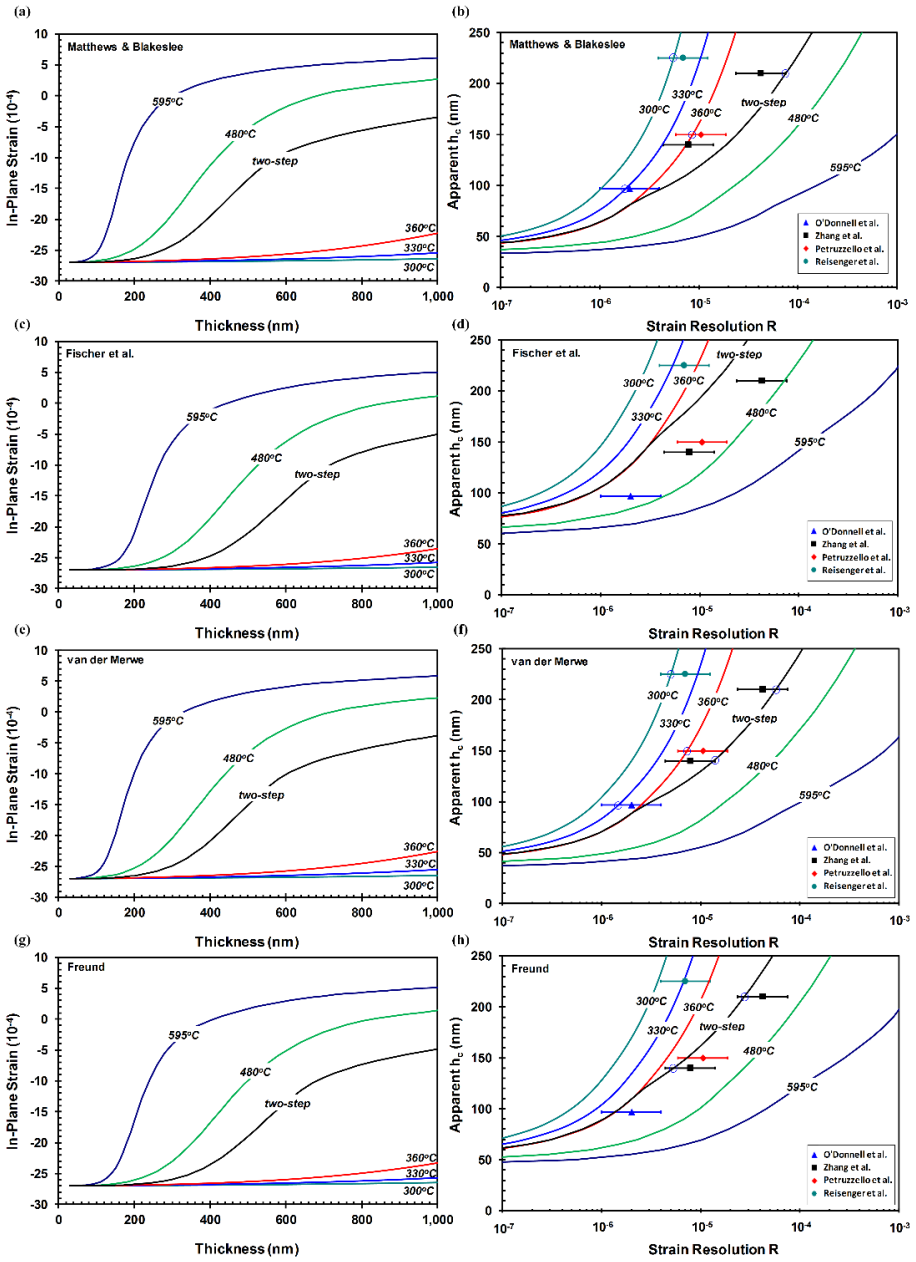

Figure 8.9. (a, c, e, g) Calculated in-plane strain at room temperature as a function of thickness for ZnSe/GaAs (001) grown under different temperature conditions. (b, d, f, h) Apparent critical layer thickness for ZnSe/GaAs (001) as a function of the experimental resolution for different temperature conditions. The symbols represent experimental measurements and the horizontal error bars show the range of the estimated resolution. Each open circle indicates the intersection of the experimental point with the appropriate temperature curve.

8.4. Plastic Flow and Dislocation Compensation in ZnSSe/GaAs (001) Heterostructures

An important goal of lattice-mismatched semiconductor device design is the control of the threading dislocation densities, which are of particular importance for optoelectronic devices such as photodetectors and light-emitting diodes; the basis for this field of research is an understanding of the dislocation dynamics in mismatched heteroepitaxial structures. Previously we developed a plastic flow model for lattice relaxation and applied it to ZnSe/GaAs (001) heterostructures. In this work, we have extended this work to ZnS_ySe_{1-y}/GaAs (001) structures, including misfit-threading dislocation interactions to account for the variation of the threading dislocation in compositionally-graded material. On the basis of this model, we demonstrate that the dislocation compensation mechanism, whereby threading dislocations can be removed by insertion of a mismatched interface in a graded structure, can be explained by the bending over of threading dislocations associated with misfit segments of one sense by misfit dislocations having the opposite sense.

8.4.1. Experimental Verification of Dislocation Compensation

Design of lattice-mismatched semiconductor devices for enhanced reliability or performance requires control of the strain and threading dislocation densities, and several strain and defect engineering approaches have been proposed. In previous work, we discovered that a dislocation compensation mechanism is active in compositionally-graded semiconductor heterostructures involving abrupt interfaces [264]. This finding was made during a study of overshoot graded ZnS_ySe_{1-y}/GaAs (001) structures for the purpose of controlling strain relaxation. This experimental work involved the growth of ZnS_ySe_{1-y} on GaAs (001) substrates by photo assisted metalorganic vapor phase epitaxy (MOVPE). Each of the test structures comprised a ZnSe buffer, a graded ZnS_ySe_{1-y} layer, and a uniform composition ZnS_ySe_{1-y} layer on top. Each

heterostructure had a 135 nm ZnSe buffer layer grown by a two-step photo assisted MOVPE process, in which 40% of the total thickness was grown at 595^{o}C with 58 mW/cm^2 UV irradiation from an Oriel Hg lamp and the remaining 60% of the total thickness was grown at 360^{o}C with 39 mW/cm^2 irradiation. The source mole fractions were X_{DMZn} = 2 x 10^{-4} and X_{DMSe} = 4 x 10^{-4}. The graded ZnS_ySe_{1-y} layer was grown at 360^{o}C with 39 mW/cm^2 photo irradiation. The zinc and selenium source flows were fixed (X_{DMZn} = 2 x 10^{-4} and X_{DMSe} = 4 x 10^{-4}), and the sulfur source flow was varied to control the sulfur content of the growing layer. The range of the DES mole fraction was $0 \leq X_{DES} \leq 1.5 \times 10^{-4}$, corresponding to $0 \leq y \leq 0.06$. In the forward graded (FG) sample, the sulfur composition was graded from 6% to 2% with a grading rate of -0.05% sulfur/min (-6.4% μm^{-1}). In the forward graded with overshoot (FGO) sample, the sulfur composition was graded from 6% to 0 with the same grading rate. In the "steeply forward graded" (SFG) sample the sulfur composition was graded from 6% to 2% with a grading rate of - 0.1% sulfur/min (-12.8% μm^{-1}), and in the "steeply forward graded with overshoot" (FGO) sample the composition was graded from 6% to 0% with a grading rate of - 0.1% sulfur/min (-12.8% μm^{-1}). Each structure had a uniform top layer of ZnS_ySe_{1-y}, grown at 360^{o}C with 39 mW/cm^2 photo irradiation with X_{DMZn} = 2 x 10^{-4}, X_{DMSe} = 4 x 10^{-4}, and X_{DES} = 0.5 x 10^{-4} for 45 min, resulting in a sulfur composition of approximately 2%. The threading dislocation densities in the top uniform layers were determined by high-resolution x-ray diffraction and are given in Table 8.2. The remarkable result was that 2-3 x 10^8 cm^{-2} threading dislocations were removed by the insertion of an overshoot interface between the graded layer and the top uniform layer. (At the overshoot interface the composition of the graded layer was made to intentionally overshoot the composition of the uniform layer on top.) We hypothesized that the mechanism of this dislocation compensation was the bending of

threading dislocations at the mismatched (overshoot) interface to create misfit dislocation line length, and to better understand this mechanism we developed a plastic flow model for lattice relaxation which incorporates dislocation multiplication, annihilation and coalescence as well as threading-misfit dislocation interactions. The development of this model will be described in the following two sections.

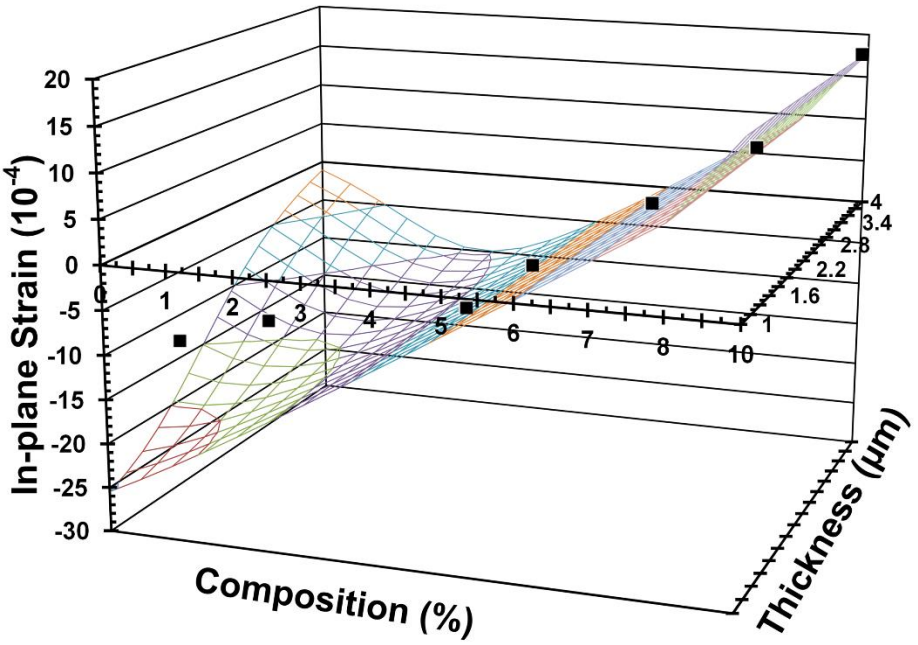

Figure 8.10. Room-temperature in-plane strain for $ZnSe_ySe_{1-y}$/ZnSe/GaAs (001) heterostructures grown at 360 ºC with a 135 nm ZnSe buffer with sulfur composition and layer thickness.

The annihilation-coalescence model is only applicable to thicker layers where the threading dislocation density decreases with thickness. Pseudomorphic layers are known to contain low dislocation density, comparable to the substrate. Therefore, the dislocation density must increase as the critical layer is reached reach a maximum at some thickness. It is after this point where the annihilation-coalescence model could predict the reduction of dislocation densities with increasing

thickness. The annihilation-coalescence models do not provide insight into the processes which are active during the initial build-up of the threading dislocations. Another limitation of the annihilation-coalescence models is that they do not account for interactions between misfit and threading dislocations at mismatched/abrupt interfaces and in compositionally graded regions. For this reason, they are only applicable to uniform composition layers, though compositionally-graded and multilayered structures are of greater interest for device applications.

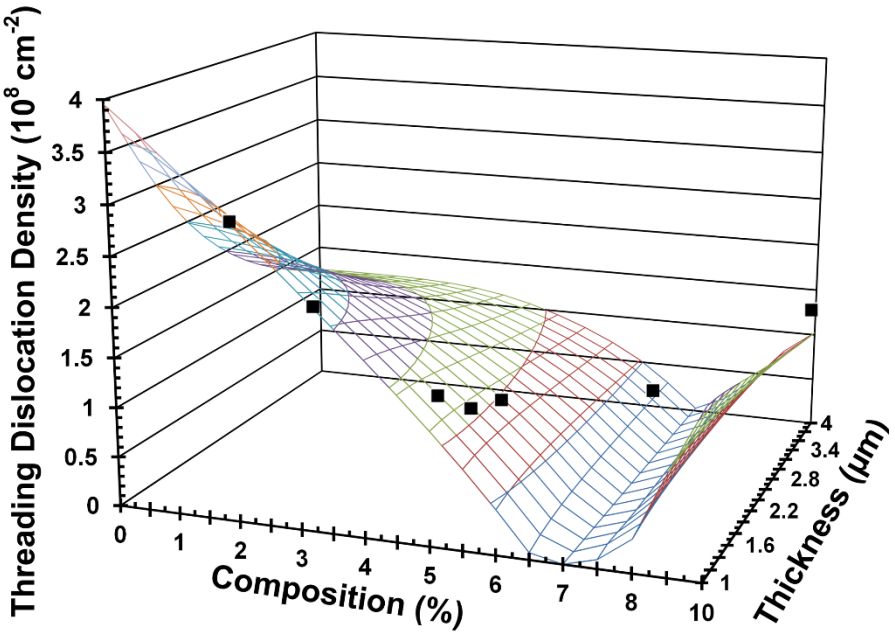

Figure 8.11. Threading dislocation densities for $ZnSe_ySe_{1-y}$/ZnSe/GaAs (001) heterostructures grown at 360 ºC with a 135 nm ZnSe buffer with sulfur composition and layer thickness.

To address these two limitations, we have utilized the dislocation dynamics model explained on Page 57. In this work, we adopt the value C_2 = 1.8 x 10-5 cm as given by Tachikawa and Yamaguchi for GaAs/Si (001), based on the finding that ZnSe/GaAs (001) and GaAs/Si (001)

heteroepitaxial layers exhibit approximately the same thickness dependence of the threading dislocation density [226].

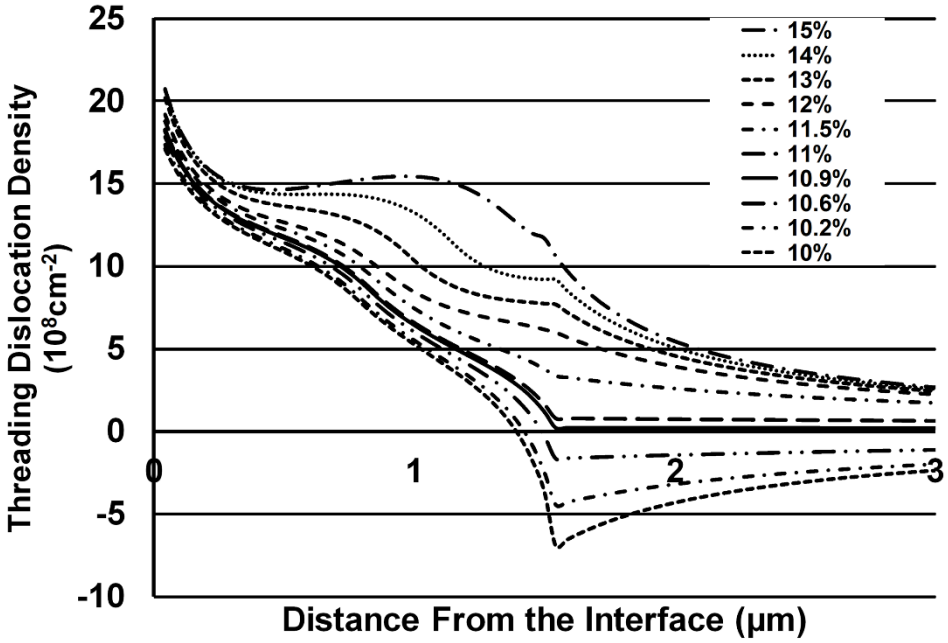

Figure 8.12. Threading dislocation density as a function of distance from the interface for U-ZnS_ySe_{1-y}/G-ZnS_ySe_{1-y}/GaAs (001) structures with an assumed growth temperature of 360°C. The G-ZnS_ySe_{1-y} layer was 1.5 μm thick and its sulfur composition varied from 10% to 15%. The U-ZnS_ySe_{1-y} layer had a fixed thickness of 1.5 μm but its composition was varied as indicated in the legend.

8.4.2. Modeling of Dislocation Compensation in ZnSSe/GaAs (001) Heterostructures

In order to characterize the parameters B and K, we first grew a series of ZnSe/GaAs (001) single heterostructures with different thicknesses by the two-step photo assisted MOVPE process described above. The in-plane strains were determined by high-resolution x-ray diffraction at room temperature, and the results are shown in Figure 8.2 by the filled squares. Using the kinetic model for relaxation, the strain versus thickness characteristic is best fit using $BK = 10^{-16} cm^4 dyn^{-2} s^1$ as shown in Figure 8.2 by the solid curve. It should be noted that the strain

relaxation occurs much more gradually than predicted by the Matthews and Blakeslee equilibrium theory [34], shown by the dashed curve. To estimate the value of B, we determined the threading dislocation densities in thick, nearly-relaxed ZnSe/GaAs (001) single heterostructures from the same set described above (Figure 8.3). Using our kinetic model for the threading dislocation density, we obtained a best fit to the experimental results using the value $B \approx 0.8 \times 10^{-12} cm^3 dyn^{-1} s^{-1}$.

Using the estimated the values of the material constants B and K for ZnSe, we compared the results of the plastic flow model to experimentally-determined strains and threading dislocation densities in ZnS_ySe_{1-y} heterostructures grown at 360°C. We grew a set of ~2 μm thick layers of ZnS_ySe_{1-y} with various sulfur concentrations on 135 nm ZnSe buffers at 360°C. Figure 8.10 compares the room-temperature in-plane strain values measured by high-resolution x-ray diffraction to the results of the plastic flow model using $BK = 10^{-16} cm^4 dyn^{-2} s^1$. In this figure, the in-plane axes correspond to sulfur composition and layer thickness while the vertical axis corresponds to the in-plane strain. The modeling results show that layers with zero sulfur composition (ZnSe) will exhibit a transition from compressive to tensile strain as the thickness is increased; this is expected on the basis of the differential thermal expansion and is observed experimentally in this material system. In contrast, layers with 10% sulfur content are expected to contain tensile strain for the entire range of thicknesses because both the lattice mismatch strain and thermal strain are tensile. For a constant thickness of 2 μm, the model results predict a transition from compressive to tensile strain as the sulfur content is increased. The experimentally-measured strain values are very close to this cross section of the characteristic, with small

departures observed in the two samples with the lowest sulfur concentrations. However, the thicknesses of these samples were estimated from the expected growth rate for the experimental conditions, and it can be seen from the figure that a 20% error in the thickness could account for the observed differences. We also compared the experimental threading dislocation densities for this set of samples to those found using the plastic flow model as shown in Figure 8.11. Even though the lattice matching composition is ~6% sulfur at room temperature, the minimum threading dislocation densities are expected with slightly greater sulfur content (~7%) due to the larger thermal expansion coefficient of ZnS_ySe_{1-y} compared to GaAs. The threading dislocation density rises steeply for compositions less or greater than this, with higher densities expected in thinner layers as in the ZnSe characteristic. As seen in Figure 8.11, the model results are in good agreement with the experimentally observed threading dislocation densities over the range of composition studied. In general, the material constants for ZnS and the ternary alloys may differ from those for ZnSe, but our work here was limited to relatively dilute sulfur concentrations so we expect the values to be similar to those for ZnSe.

Having established estimates for the material constants B and BK applicable to ZnSe and dilute ZnS_ySe_{1-y} alloys we investigated the behavior of hypothetical graded structures including overshoot or undershoot. In a single overshoot structure, a linearly-graded buffer layer (G-ZnS_ySe_{1-y}) is grown on the substrate followed by a uniform device layer (U-ZnS_ySe_{1-y}), resulting in the U-ZnS_ySe_{1-y}/G-ZnS_ySe_{1-y}/GaAs (001) heterostructure. The composition in the linearly-graded layer is varied from y_0 at the substrate interface to y_{hGL} at the uniform layer interface. The composition in the uniform layer is y_{UL}. The thicknesses of the graded and uniform layers are h_{GL} and h_{UL}, respectively, and the total thickness of the epitaxial material is $h=h_{GL}+h_{UL}$. If the sulfur

concentration at the interface is greater than 6%, misfit dislocations will be introduced to relax tensile strain in the material, and we will refer to these misfit dislocations as having *negative sense*. If the composition at the top of the graded layer is made to overshoot that of the uniform layer ($y_{hGL} > y_{UL}$), then misfit dislocations of *positive sense* will be introduced at the U-ZnS_ySe_{1-y}/G-ZnS_ySe_{1-y} interface. These can be introduced by the bending of threading dislocations associated with the negative sense misfit dislocations below, rather than the creation of new half loops, so the threading dislocation density can be reduced. If, however, too much overshoot is introduced, all of the existing mobile dislocations will be bent at the interface *and additional misfits will be introduced by the production of half loops.* Therefore, for a given graded layer thickness, there is a particular overshoot $y_{hGL} - y_{UL}$ which will exactly eliminate all mobile threading dislocations from the uniform device layer. Stated differently, for a given overshoot $y_{hGL} - y_{UL}$, there is a particular graded layer thickness h_{GL} which will allow the elimination of all mobile threading dislocations from the uniform device layer. The condition for complete removal of the mobile threading dislocations is

$$0 = \int_0^h \left[\frac{4\rho_A(z)}{L_{MD}(z)\,sign\int_0^y \rho_A(\zeta)d\zeta} - C_2 D^2(z) \right] dz \,. \qquad \textbf{(8.26)}$$

To investigate this dislocation compensation mechanism, we modeled the threading dislocation behavior in 1.5 μm U-ZnS_ySe_{1-y} / 1.5 μm G-ZnS_ySe_{1-y} /GaAs (001) structures. In the graded layer the sulfur composition was increased linearly from 10% at the substrate interface to 15% at the uniform layer interface. The composition of the top layer was varied, and the growth temperature was assumed to be 360°C. Figure 8.12 shows the threading dislocation density profiles for

structures with ten different U-ZnS_ySe_{1-y} compositions ranging from 10% to 15% as given in the legend. Structures with high sulfur content in the uniform layer exhibit high threading dislocation densities in both the graded the uniform layers, and the density decreases monotonically with distance in the uniform layer. In these samples, the misfit dislocations have negative sense at both interfaces so no compensation is expected. For structures with lower sulfur concentration in the uniform layer, the high dislocation density in the graded layer is overcompensated by misfit dislocations of positive sense at the U-ZnS_ySe_{1-y}/G-ZnS_ySe_{1-y} interface, leading to similar numbers of threading dislocations in the uniform layer. However, at a uniform layer composition of ~10.9% there is almost perfect compensation of the graded layer threading dislocations by the misfit dislocations having positive sense at the interface. In principle, it should be possible to remove all mobile threading dislocations by the dislocation compensation mechanism through control of the mismatch at an abrupt interface.

We have developed a plastic flow model for the strain relaxation and dislocation dynamics in ZnS_ySe_{1-y} / GaAs (001) heterostructures. This model includes misfit-threading dislocation interactions as well as dislocation multiplication, annihilation and coalescence, and provides a qualitative understanding of the dislocation compensation mechanism whereby grown-in threading dislocations of a compositionally-graded heterostructure may be bent over at an intentionally mismatched interface. Additionally, modeling and experimental studies should make it possible to design dislocation compensated device structures in which essentially all mobile dislocations can be removed by this mechanism.

8.4.3. Tolerance in the Design of Dislocated Compensated ZnSSe on GaAs

The understanding of lattice relaxation and dislocation dynamics in lattice-mismatched semiconductors have made it possible to design device structures utilizing the dislocation compensation mechanism for reduced defects, improved performance, and enhanced reliability. We have developed a dislocation dynamics model accounting for misfit-threading interactions and have applied it by studying strain relaxation in ZnSe/GaAs (001) and ZnS_ySe_{1-y} /GaAs (001) heterostructures [215]. Dislocation compensation involves the inclusion of intentionally lattice-mismatched interfaces within graded or multilayered structures in order to bend over existing threading dislocations at these mismatched interfaces. We have investigated the design of dislocation compensated ZnS_ySe_{1-y}/GaAs (001) heterostructures with an emphasis on overshoot grading and have considered the sulfur mole fraction tolerances applicable to such structures. We have considered heterostructures involving a constant composition ZnS_ySe_{1-y} device layer grown on top of a GaAs (001) substrate with an intermediate buffer layer of linearly-graded or uniform ZnS_ySe_{1-y}. For each structure type, we studied the requirements on the thickness and compositional profile in the buffer layer for the elimination of all mobile threading dislocations from the device layer as well as the allowed tolerance in compositional overshoot to achieve structures with low threading dislocation densities.

Design of dislocation-compensated semiconductor heterostructures device requires a dislocation model which accounts for (i) time evolution of kinetically-limited strain relaxation, (ii) thermal activation of glide and (iii) misfit-threading dislocation interactions. Several kinetic models have been proposed by Matthews, Mader, and Light [67], Dodson and Tsao [68], Houghton [69], Sasaki et al. [70], and Horbaschk et al. [71] where they account for thermally activated glide

of pre-existing dislocations [66], dislocation multiplication, nucleation and impediment of dislocation mobility. Earlier relaxation models were applicable only to uniform epitaxially grown layers where misfit dislocations were concentrated at the epilayer-substrate interface until Fitzgerald [72,73] studied plastic flow in compositionally-graded Ge_xSi_{1-x}/Si heterostructures. The model of Fitzgerald et al. assumed that there are no impediments to dislocation mobility, whereby the threading dislocation rapidly reaches a steady-state value during growth of the compositionally-graded layer. Kujofsa and Ayers have developed a generalized model applicable to compositionally-graded and multilayered semiconductor heterostructures by extending the Dodson and Tsao model so that it may include abrupt interfaces as well as compositional grading, linear or otherwise, with the inclusion of dislocation multiplication, annihilation and coalescence, and interactions involving threading and misfit dislocations at abrupt interfaces. This model was extended to account for reduction in threading dislocation density by including mechanisms of (i) dislocation compensation caused from interactions of misfit-threading dislocations at abrupt interfaces and (ii) annihilation and coalescence reactions as described by Tachikawa and Yamaguchi [78]. Dislocation annihilation and coalescence reactions are known to be important in partly-relaxed semiconductor heterostructures and in uniform mismatched layers much greater than the critical layer thickness. These phenomena lead to a threading dislocation density which is usually inversely proportional to layer thickness in uniform layers [75] and such behavior has been reported for ZnSe/GaAs [226, 227], InAs/GaAs [228], InAs/InP [229] and GaAs/Si [78]. During the growth of an arbitrary metamorphic (partially relaxed) semiconductor heterostructure, the threading dislocation density is a non-monotonic function of thickness. Pseudomorphic layers are known to contain low dislocation densities, comparable to their substrates, but the dislocation

density will build up after the critical layer thickness is reached by dislocation nucleation, multiplication, or some combination of the two. In a single heterostructure, absent of grading, the threading dislocation density builds up to a maximum and then decreases with thickness as a consequence of coalescence and annihilation. In a multilayered or graded structure the behavior is more complex, because threading dislocations can be bent over to produce misfit dislocation line length at abrupt interfaces or even in compositionally-graded material.

In previous work, we discovered that a dislocation compensation mechanism is active in compositionally-graded ZnS_ySe_{1-y}/GaAs (001) heterostructures involving abrupt interfaces [265] grown by photoassisted metalorganic vapor phase epitaxy (MOVPE). We found that by the insertion of an overshoot interface between the graded layer and the top uniform layer, where the graded layer composition was made to overshoot that of the top uniform layer, the dislocation density could be greatly reduced at the surface of the structure. We hypothesized that threading dislocations associated with misfit dislocation of one sense were being bent over at the mismatched interface from introduction of misfit dislocations of the opposite sense. Molina et al. [266] and Sacedon el at. [267] utilized linearly graded buffer layers of InGaAs to grow dislocation-free device layers. Arimoto et al. [268] extended this work to SiGe buffer layers and concluded that twining is reduced from the use mismatched interfaces. To better understand this mechanism, we studied the role of the buffer layer thickness and compositional tolerance for the heterostructures outlined in Figure 8.13 For practical device fabrication an important issue involves the allowed tolerance in the compositional overshoot to achieve structures with desired mobile threading dislocation densities.

8.4.4. Dislocation Densities in Dislocated Compensated ZnSSe Heterostructures

To investigate this dislocation compensation mechanism and the tolerances in sulfur mole fraction we modeled the threading dislocation behavior of the two heterostructures outlined in Figure 8.13a-b. The assumed growth temperature was 360°C. To obtain better understanding of the dislocation compensation mechanisms and the role of sulfur tolerances for practical growth conditions, we found the required overshoot and buffer layer thickness that will remove all the mobile threading dislocations for a given device layer thickness and sulfur mole fraction. For practical growth conditions, it is important to know the tolerances in sulfur mole fraction which would allow the reduction of threading dislocation density to $3 \cdot 10^6$, 10^7 and $3 \cdot 10^7$ cm^{-2} respectively.

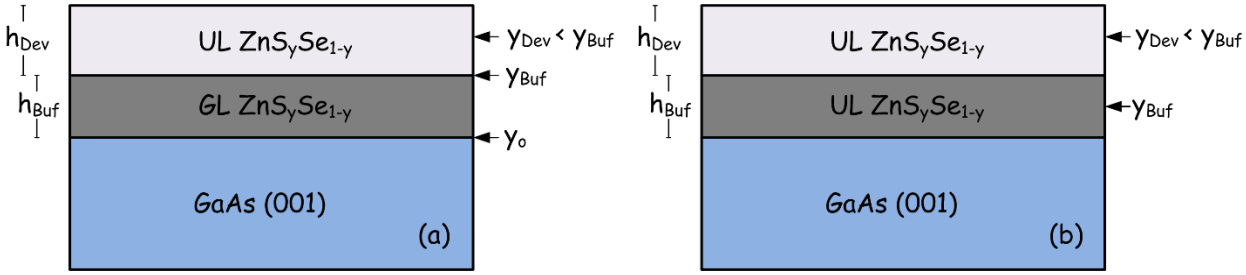

Figure 8.13. (a) Dislocation compensated heterostructure with graded buffer. Uniform layer of ZnS_ySe_{1-y} on a linearly graded layer of ZnS_ySe_{1-y} deposited on a GaAs (001) substrate. y_0 and y_{Buf} refer to the starting and ending sulfur composition for the linearly graded buffer while y_{Dev} refers to the sulfur concentration of the uniform device layer. h_{Buf} and h_{Dev} are the thicknesses of the buffer and device layer respectively. (b) Dislocation compensated heterostructure with uniform buffer. Uniform layer of ZnS_ySe_{1-y} on a uniformly graded layer of ZnS_ySe_{1-y} deposited on a GaAs (001) substrate. y_{Buf} refer to sulfur composition for the uniformly graded buffer while y_{Dev} refers to the sulfur concentration of the device layer. h_{Buf} and h_{Dev} are the thicknesses of the buffer and device layer respectively.

By considering the dislocation dynamics we modeled the behavior of a wide range of overshoot graded structures. The goal of this work is to be able to guide the design of

semiconductor device heterostructures with significantly reduced defect densities. The composition of the linearly graded buffer layer is varied from y_0 at the substrate interface to y_{Buf} at the uniform layer interface. The composition in the uniform layer is y_{Dev}. The thicknesses of the buffer and device layer are h_{Buf} and h_{Dev} respectively and the total thickness is $h = h_{Buf} + h_{Dev}$. For a sulfur mole fraction greater than 6% at the substrate-buffer interface, misfit dislocations of *negative sense* will be introduced to relax the tensile material above. If the composition of the buffer layer is made to overshoot that of the device layer ($y_{Buf} > y_{Dev}$), then misfit dislocations of *positive sense* will be introduced to bend over threading dislocations associated with negative sense misfit dislocations. It should be noted that if too much overshoot is introduced, all of the existing mobile dislocations will be bent at the buffer-device interface and additional half loops will be introduced. The results of Figure 8.14, Figure 8.15 and Figure 8.16 show that for a given buffer layer thickness there is an amount of compositional overshoot at the device-buffer interface which allows the optimum dislocation compensation. Also, for a given compositional overshoot, there is a particular buffer layer thickness for optimum dislocation compensation. For practical device fabrication, an important issue involves the allowed tolerance in the compositional overshoot. The results of our study indicate that it should be possible to achieve fewer than 10^6 cm^{-2} mobile threading dislocations in practical devices using conventional control of the sulfur mole fraction. Figure 8.14, Figure 8.15 and Figure 8.16 also show the contours of sulfur composition which allow reduction of the mobile threading dislocation density to $3 \cdot 10^6$ cm^{-2}, $1 \cdot 10^7$ cm^{-2}, and $3 \cdot 10^7$ cm^{-2}, respectively. The horizontal separation of the contour bands associated with a particular dislocation density reveal the corresponding compositional tolerance, which is of practical

importance for the manufacture of dislocation compensated device structures. The compositional tolerance diminishes with the target dislocation density, so that the achievement of 10^6 cm^{-2} or fewer mobile defects will require relatively precise compositional control in the types of structures investigated here.

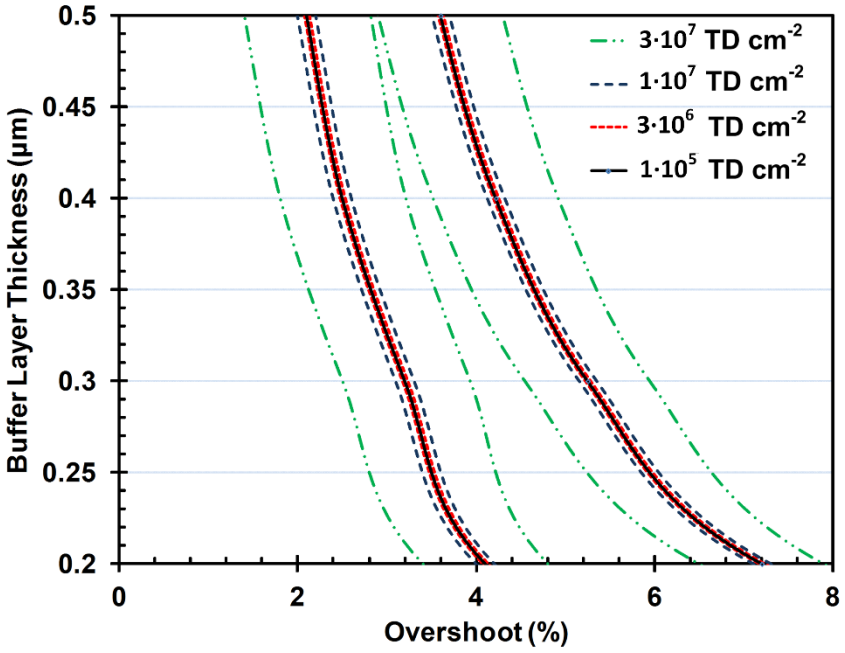

Figure 8.14. Contour plot of sulfur composition for the achievement of various mobile threading dislocation densities using (a) a linearly graded ZnS_ySe_{1-y} buffer and (b) an uniformly-graded ZnS_ySe_{1-y} buffer with a device layer thickness of 0.25 µm and a sulfur concentration of 8%. The starting sulfur composition of the buffer layer was fixed at 8%.

Figure 8.14 compares the contour plots for the linearly graded (Figure 8.14a) and the uniformly graded (Figure 8.14b) buffer. The heterostructures modeled here have a device layer thickness of 0.25 µm and a sulfur mole fraction of 8%. The starting sulfur composition for the linearly graded layer was fixed at 8%. The buffer layer thickness decreases rapidly and monotonically for increasing overshoot amount. In contrast to uniformly graded buffers, for a given buffer layer thickness the linearly graded buffer requires a higher overshoot to bend over

threading dislocations. However, when comparing the average compositions of the buffer layers (Figure 8.17), it becomes clear that graded buffers require a lower average overshoot to bend over the threading dislocation. Linearly graded buffers allow for the distribution of misfit dislocations throughout the layer and allow for the longest possible misfit dislocation length. Moreover, the threading dislocation density is reduced significantly from enhancement of glide motion. Figure 8.15 shows the contour profile for structures which are similar to those of Figure 8.14 but have a device layer thickness of 0.5 μm. The buffer layer thickness decreases monotonically with increasing overshoot but in contrast to Figure 8.14, a more sluggish decrease becomes apparent. As we mentioned previously there are two competing mechanisms which reduce threading dislocations – (i) bending over of dislocations and (ii) annihilation and coalescence. For a fixed buffer layer thickness, as we increase the device layer thickness annihilation and coalescence reactions reduce dislocation density thus requiring a smaller amount of overshoot to bend over the remaining mobile threading dislocations. Structures with higher sulfur concentration display rapid relaxation rates which lead to contraction of the horizontal separation of the contour lines. This behavior becomes more apparent as we increase the sulfur mole fraction of the device layer (y_{Dev} = 10%) as shown in Figure 8.16. The horizontal separation of the contour lines diminishes almost completely. In contrast to Figure 8.14 and Figure 8.15, there is a sluggish decrease in buffer layer thickness with increasing overshoot. Moreover, these structures have high dislocation densities at the buffer-device interface thus requiring a higher overshoot to bend over mobile threading

We have investigated dislocation compensation mechanism in intentionally lattice-mismatch ZnS_ySe_{1-y} / GaAs (001) heterostructures involving linearly-graded or uniformly-graded intermediate buffer layers. We have extended this work to study the compositional tolerance which

would aid in the device design of dislocation-compensated heterostructures. The results of our study indicate that it should be possible to achieve fewer than 10^6 cm^{-2} mobile threading dislocations in practical devices using conventional control of the sulfur mole fraction. Because of the importance of compositional control in dislocation compensated devices, the approach could benefit from in-situ characterization methods or novel techniques for compositional control during growth.

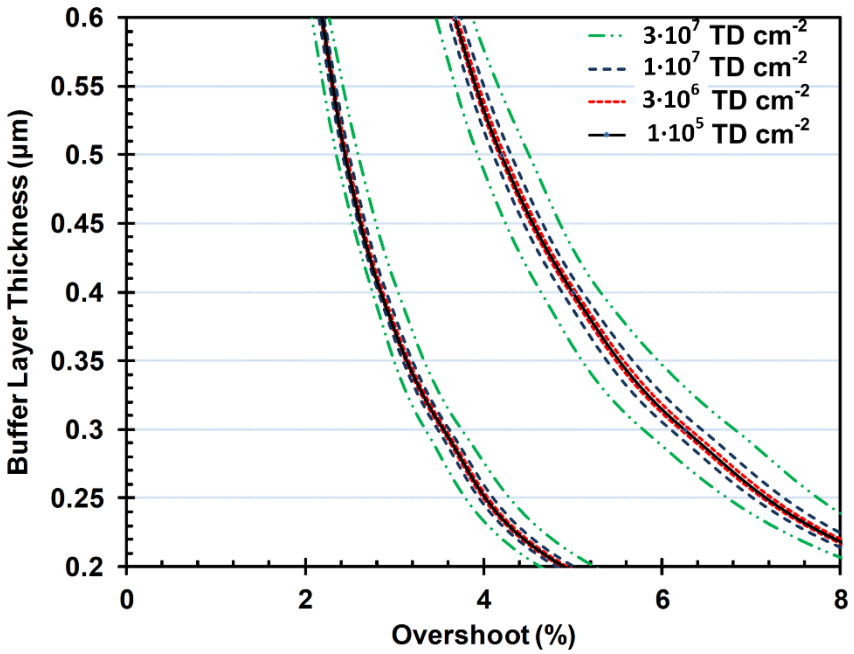

Figure 8.15. Contour plot of sulfur composition for the achievement of various mobile threading dislocation densities using (a) a linearly graded ZnS_ySe_{1-y} buffer and (b) an uniformly-graded ZnS_ySe_{1-y} buffer with a device layer thickness of 0.5 µm and a sulfur concentration of 8%. The starting sulfur composition of the buffer layer was fixed at 8%.

8.5. Comparison of Step- and Linearly-Graded ZnSSe/GaAs (001) MBLs

Design of metamorphic buffer layers (MBLs) for semiconductor devices with reduced defect densities requires control of lattice relaxation and dislocation dynamics. Graded layers are beneficial for the design of these buffers because they reduce the threading dislocation density by

(i) allowing the distribution of the misfit dislocations throughout the buffer layer therefore reducing pinning interactions and (ii) enhancing mobility from the high built-in surface strain which helps sweep out threading arms. In this work, we considered heterostructures involving a linearly-graded (type A) or step-graded (type B) buffer grown on a GaAs (001) substrate. For each structure type, we studied the equilibrium configuration and the kinetically-limited lattice relaxation and non-equilibrium threading dislocations by utilizing a dislocation dynamics model. In this work, we have also considered heterostructures involving a constant composition ZnS_ySe_{1-y} device layer grown on top of a GaAs (001) substrate with an intermediate buffer layer of linearly-graded (type C) or step-graded (type D) ZnS_ySe_{1-y}. For each structure type, we studied the requirements on the thickness and compositional profile in the buffer layer for the elimination of all mobile threading dislocations from the device layer by the dislocation compensation mechanism.

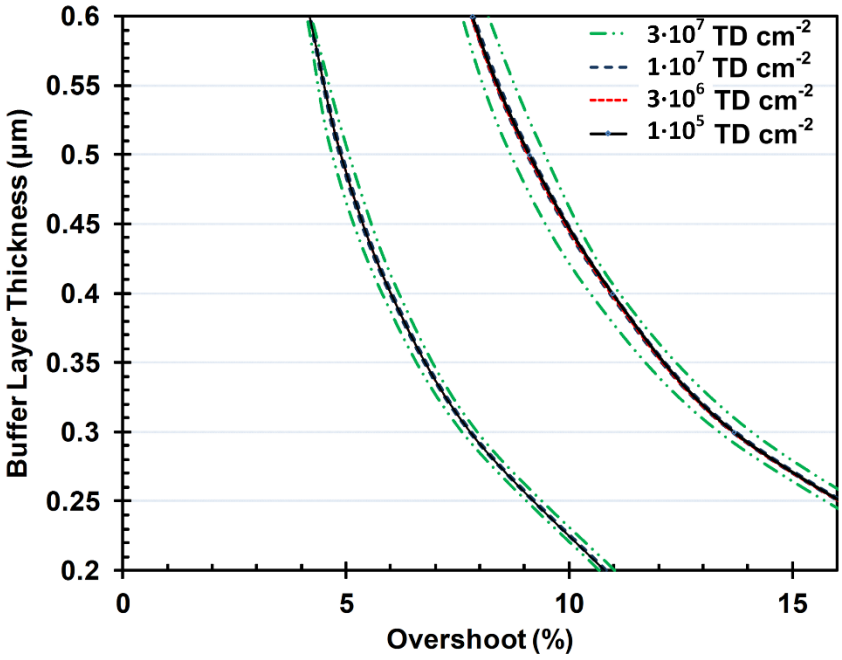

Figure 8.16. Contour plot of sulfur composition for the achievement of various mobile threading dislocation densities using (a) a linearly graded ZnS_ySe_{1-y} buffer and (b) an uniformly-graded ZnS_ySe_{1-y} buffer with a device layer thickness of 0.5 µm and a sulfur concentration of 10%. The starting sulfur composition of the buffer layer was fixed at 8%.

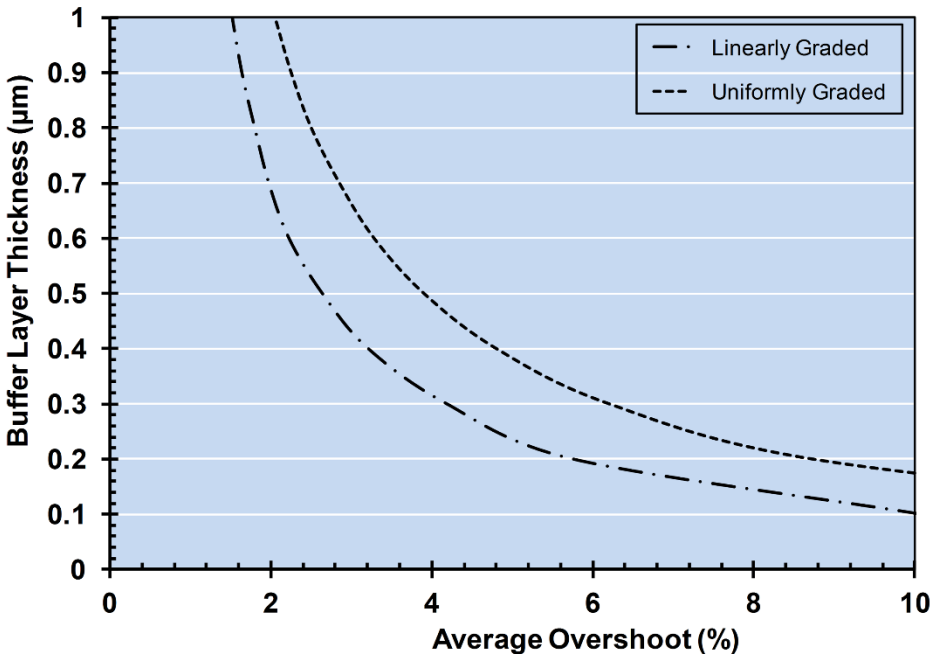

Figure 8.17. Comparison of the average compositional overshoot between linearly- and uniformly- graded buffer layers. The average composition for the linearly- and uniformly-graded buffers are $(y_{Buf} + y_0)/2$ and y_{Buf} respectively.

The traditional approach to the design of lattice-mismatched electronic and optical devices with minimal defects involved pseudomorphic growth, in which all epitaxial layer thicknesses are kept below the critical layer thickness for defect formation. However, in many cases materials or performance constraints prevent the use of pseudomorphic structures. Metamorphic growth, in which the layers relax by the introduction of misfit dislocations, enables a wider range of layer thicknesses and compositions and has been exploited in a variety of devices. A critical challenge with metamorphic device design involves control of the threading dislocation density, and compositionally-graded buffer layers have been used for this purpose. Most metamorphic device designs employ linearly-graded or step-graded buffer layers and it is therefore worthwhile to compare these approaches in terms of their equilibrium and dynamic relaxation behavior. Recently

we reported the mechanism of dislocation compensation, which we define as the removal of threading dislocations associated with one sense of misfit dislocation by bending them over to create misfit dislocations of the opposite sense. We can arbitrarily assign positive and negative sense to dislocations which relax compressive and tensile strain, respectively. Qualitatively, a compressive (tensile) interface can be used for dislocation compensation in a structure with a tensile (compressive) buffer. Therefore, metamorphic buffer layers may be designed to utilize this dislocation compensation mechanism for achieving structures with low threading densities, such as the linearly-graded and step-graded structures investigated here.

In this work, we have considered heterostructures involving a linearly-graded (type A) or a step-graded (type B) ZnS_ySe_{1-y} device layer grown on top of a GaAs (001) substrate. For each structure, we studied the equilibrium and kinetically-limited relaxation and non-equilibrium threading dislocations. In addition, to better understand the dislocation compensation we studied the role of the buffer layer thickness and compositional overshoot in two types of structures: type C involved a uniform composition layer on top of a linearly-graded buffer while type D involved a uniform composition layer grown on a step-graded buffer. For each structure type, we studied the requirements on the thickness and compositional profile in the buffer layer to optimize the removal of mobile threading dislocations from the top uniform layer (device layer).

8.5.1. Comparison of Strain Relaxation in Step- and Linearly-Graded ZnSSe Epilayers

The structures considered in this work have an ending sulfur composition ranging from $y_h = 10\%$ to 20% which correspond to lattice mismatch values varying from $f_h = 0.186\%$ to 0.65%. In linearly graded layers, the misfit dislocations are introduced at a finite distance from the interface and the distribution profile could be modeled using a rectangular function. In addition, there exists

a misfit dislocation free zone (MDFZ) near the surface which limits interaction of misfit segments with the device layer which may be grown on top. However, the width of the surface MDFZ diminishes with higher ending composition (mismatch) values. In step-graded layers, misfit dislocations are introduced at the mismatched interfaces and can be modeled using Dirac delta functions. Type B structures exhibit at most $(n-1)$ MD delta functions, corresponding to the number of mismatched interfaces. There exists a monotonic increase in the peak misfit dislocation density with increasing composition (mismatch) therefore necessitating the introduction of more misfit segments to relax the excess mismatch strain. For type B structures with $n=5$ a higher composition (mismatch) leads to an increase in the number of MD delta functions as well as their peak intensity. The addition of mismatched interfaces ($n=10$) yields a higher population of delta functions but with a lower average peak intensity. In a step graded layer, the surface MDFZ usually has a thickness equal to the step size, but in some cases, it is possible for the thickness of this MDFZ to be an integral multiple of the step size, where the integer is greater than one. It should be noted that the step-graded structure always has a higher average grading coefficient than the linearly-graded layer of similar thickness, because it terminates with a finite thickness, uniform composition layer. We have also included a lattice-matched layer at the bottom of the step-graded buffer, which also increases the average grading coefficient for the lattice-mismatched part of the buffer. Therefore, although the compositional profiles for type A and B structures yield different average grading coefficients, our intent was to tailor the compositional profile in such a way as to induce an interfacial MDFZ similar to the case of the linearly-graded layer (type A), and this is a potential advantage of including a lattice-matched layer. Moreover, the grading profile used in this work allows type A and B structures to contain equal average, initial and ending mismatch.

Compared to structures in which the first step is lattice-mismatched, this alters the average grading coefficient over the remaining layers by up to 20%. However, we have verified by calculations that qualitatively similar results are obtained using either a lattice-matched first step or a lattice-mismatched first step. Therefore, the conclusions drawn from these results hold for either type of step grading scheme. Here the step-graded structures tend to exhibit thicker interfacial MDFZs, which may be beneficial in reducing pinning interactions with substrate defects. In contrast, the linearly graded layers tend to contain thicker surface MDFZs for the same average lattice mismatch, which is beneficial for sweeping threading arms from the structure.

In the dislocated region of a linearly-graded MBL, the introduction of misfit dislocations is just sufficient to relax the strain associated with the compositional grading and therefore the in-plane strain is approximately constant. Beyond the dislocated region, the in-plane strain increases linearly with distance from the interface. In type B structures, the in-plane strain is composed of a series of step functions with discontinuities at the mismatched interfaces. The equilibrium strain in each sublayer of the step-graded buffer is constant. Correlating the discussion of the misfit dislocation density and the in-plane strain, it can be seen that misfit dislocations relieve most of the strain associated with the compositional mismatch in sublayers near the interface. In comparison to linear composition profiles, step graded layers with the same average mismatch exhibit a lower in-plane strain near the substrate interface and a higher in-plane strain at the surface, a phenomenon which has also been shown experimentally [44]. For the structures studied in this work, step graded layers exhibit a thicker interfacial misfit dislocation free zone (MDFZ) imposed by the step size, and the first step is lattice-matched, resulting in minimal strain. The

surface MDFZ, also imposed by the step size, is thinner than in a linearly-graded layer of equal average composition, and this contributes to a larger average strain in this region.

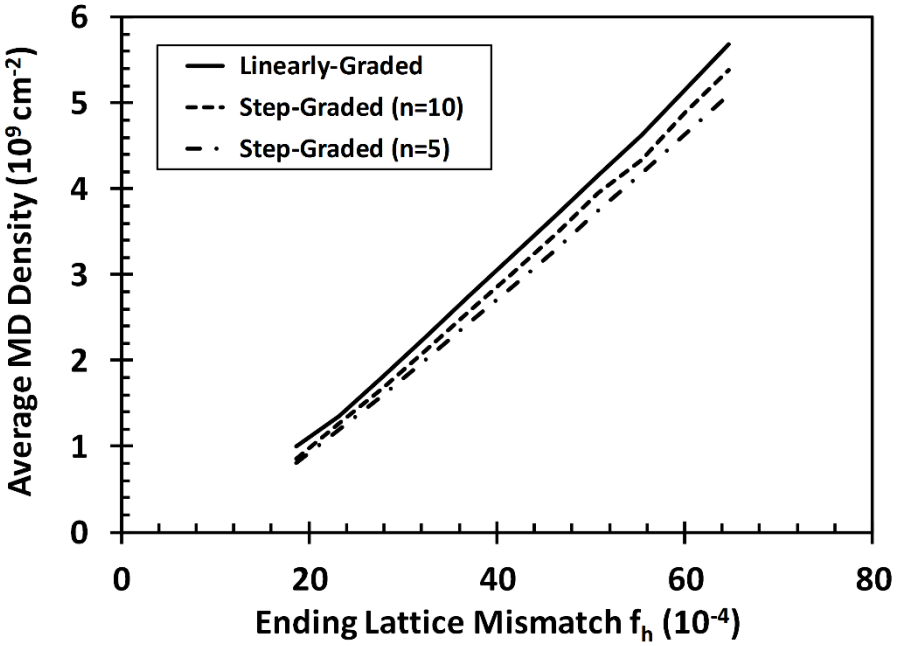

Figure 8.18. Average equilibrium misfit dislocation density as a function of the ending lattice mismatch f_h for 500 nm thick ZnS_ySe_{1-y} / GaAs (001) layers with a linearly-graded (type A) or step-graded (type B) compositional profile.

Figure 8.18 compares the average equilibrium misfit dislocation density for 500 nm thick ZnS_ySe_{1-y}/GaAs (001) layers with various ending lattice mismatch (sulfur compositions) for type A and type B structures. At higher sulfur composition (and therefore mismatch), more misfit dislocations are introduced to relax the strain energy therefore increasing the average density. For a given thickness and compositional profile, the linearly-graded layer contains a higher total dislocation density compared to a step-graded layer. However, increasing the step number in step-graded layers yields an average misfit density which approaches that of linearly graded structures.

These results indicate that it is possible to achieve a structure with behavior similar to a linearly-graded buffer by increasing the number of steps.

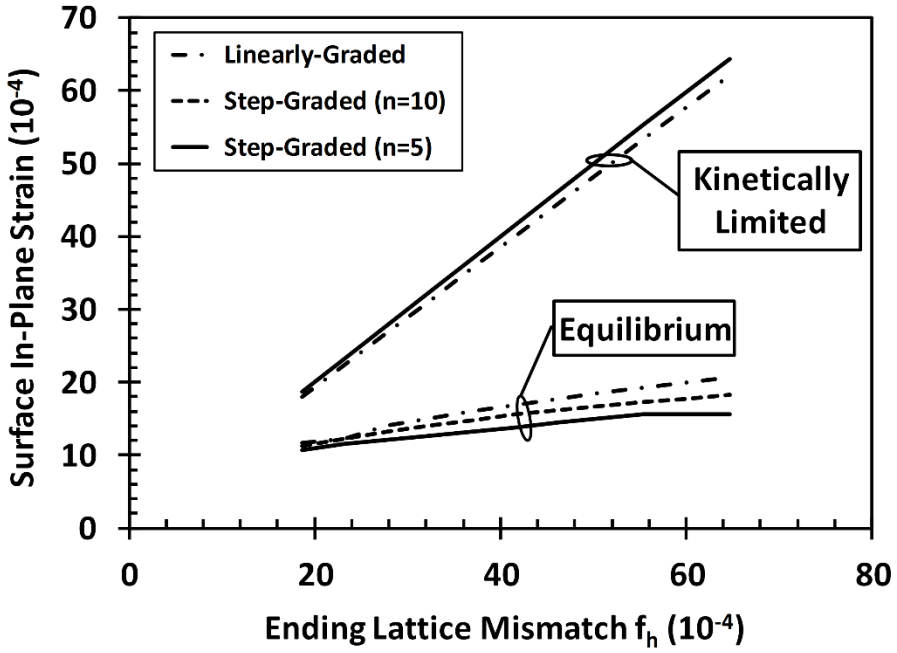

Figure 8.19. Equilibrium and kinetically-limited surface in-plane strain as a function of the ending lattice mismatch f_h for 500 nm thick ZnS_ySe_{1-y} / GaAs (001) layers with a linearly-graded (type A) or step-graded (type B) compositional profile. The starting sulfur composition of the buffer layer was fixed at $y_0 = 6\%$ ($f_0 = 0$).

Figure 8.19 shows the equilibrium and kinetically-limited surface in-plane strain for 500 nm thick ZnS_ySe_{1-y}/GaAs (001) with various ending lattice mismatch (sulfur compositions) for type A and type B structures. The kinetically-limited (or non-equilibrium) strain approaches the equilibrium strain profile if the relaxation is allowed to proceed at a sufficiently high temperature for a sufficiently long time. On the other hand, the kinetically limited strain profile will be approximately equal to the lattice mismatch profile if lattice relaxation is so inhibited by a low temperature or a short time that negligible relaxation can take place. In general, though, the kinetically-limited strain profile will be somewhere between the lattice mismatch profile and the

equilibrium strain profile as shown here. The results of Figure 8.19 demonstrate a monotonic increase in the surface strain and suggest a higher surface in-plane strain for kinetically-limited relaxation. In equilibrium, linearly-graded layers contain a higher surface in-plane strain than step-graded layers whereas kinetically-limited relaxation can result in higher surface in-plane strain for step-graded structures compared to linear grading. This result demonstrates that it is necessary to consider dislocation dynamics for the comparison of these structures. Moreover, in step-graded MBLs, the equilibrium surface strain is greater in structures with a greater number of mismatched interfaces while kinetically-limited calculations predict the opposite effect. In addition, it can be seen that increasing (decreasing) the number of steps yields equilibrium (kinetically-limited) strain values comparable to linearly-graded structures. At higher sulfur composition (and therefore mismatch) Figure 8.19 shows a saturation of the equilibrium strain for type B structures with $n = 5$. Based on the discussion of the distribution of misfit dislocations in step graded layers, a greater lattice mismatch (sulfur composition) is associated with stronger delta functions at the mismatched interface so that a larger fraction of the mismatch is relaxed by the inclusion of these interfacial MDs. The kinetically-limited strain displays similar behavior as the lattice mismatch profile of each structure due to the nature of distribution of dislocations. The relaxation rate at any point above the interface is calculated from the glide of the misfit dislocations below. The surface MDFZ in type B structures is limited by the step size whereas linearly-graded layers exhibit a thicker surface misfit dislocation free zone. In both types of structures studied here, the absence of misfit dislocations near the surface limits the lattice relaxation rate and therefore near the surface the kinetically-limited strain exhibits the same shape as the lattice mismatch profile, though with an offset introduced by the significant lattice relaxation in the underlying material. Step-graded layers

exhibit a high degree of relaxation at the mismatched interfaces indicated by rapid changes in the strain and the inclusion of misfit dislocations. In linearly-graded structures, the lattice mismatch profile increases gradually and the relaxation rate is approximately linear to lattice mismatch profile.

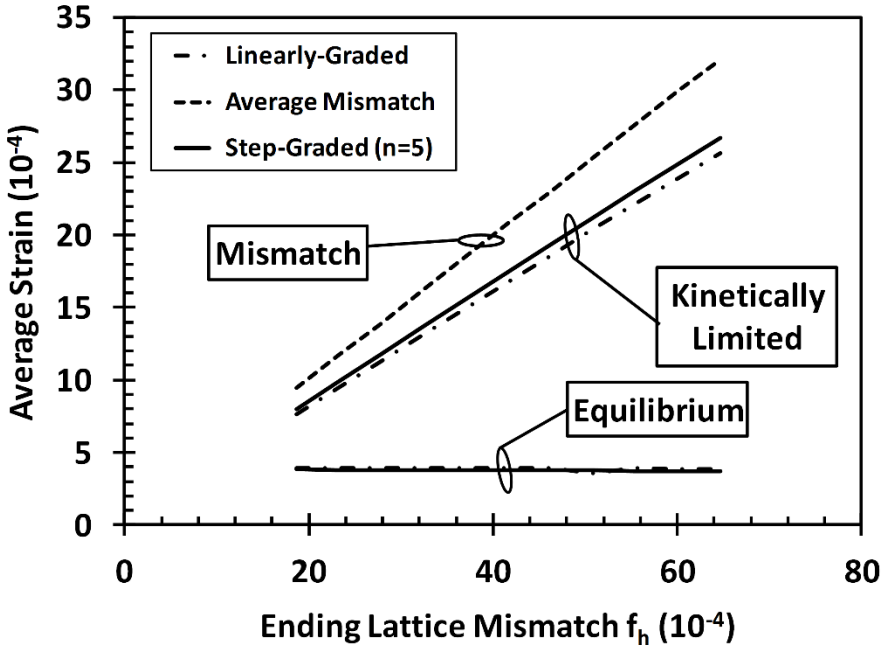

Figure 8.20. Comparison of the average kinetically-limited and equilibrium in-plane strain and average lattice mismatch as a function of the ending lattice mismatch for 500 nm thick ZnS_ySe_{1-y} / GaAs (001) layers with a linearly-graded (type A) or step-graded (type B) compositional profile. The sulfur composition in the buffer layer is varied from $y_0 = 6\%$ (lattice matched to GaAs) at the interface to $f_h = 0.001864$ ($y_h = 15\%$) at the surface.

Despite differences in the thicknesses of the misfit dislocation free zones and the surface strain, the linearly-graded and step-graded structures with equal average lattice mismatch also show nearly the same average in-plane strain are shown in Figure 8.20. The average strain is

intermediate between the average lattice mismatch and the average equilibrium strain as expected, and could approach the equilibrium value if growth was conducted at a higher temperature or a slower rate.

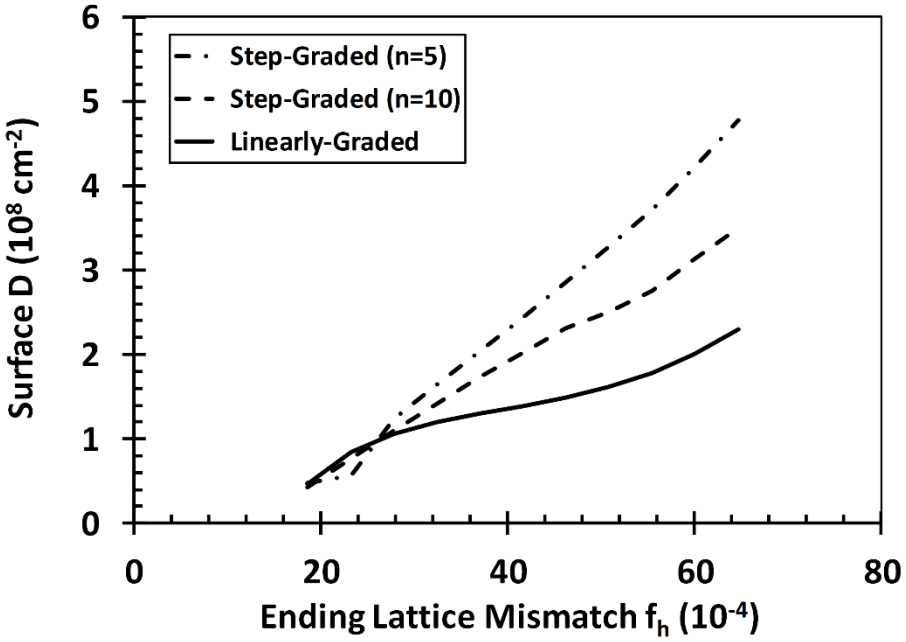

Figure 8.21. Surface threading dislocation density as a function of the ending lattice mismatch f_h for 500 nm thick ZnS_ySe_{1-y} / GaAs (001) layers with a linearly-graded (type A) or step-graded (type B) compositional profile. The starting sulfur composition of the buffer layer was fixed at $y_0 = 6\%$ ($f_0 = 0$).

Figure 8.21 shows the surface threading dislocation density as a function of the ending composition for 500 nm thick ZnS_ySe_{1-y}/GaAs (001) layers. For low values of f_h (y_h), type A and B behave similarly, however at high ending sulfur compositions linearly graded (type A) structures exhibit a significantly lower threading dislocations density. The wider distribution of misfit dislocation density in heterostructures with a linearly-graded composition profile enables the reduction in threading dislocations by enhancing dislocation-dislocation interactions. In

contrast, the surface threading dislocation for type B (step-graded) structures is proportional to the ending lattice mismatch. This effect may be more pronounced in experimentally-grown structures because step graded layers confine dislocations at the mismatched interfaces which can easily render them immobile by pinning and tangling interactions. However, step-graded MBLs with a greater number of steps yield lower threading densities. Linearly-graded MBL contain a greater misfit dislocation free zone which may be a major contributing factor to lower threading dislocation densities by preserving a higher surface strain and a greater sweep rate of dislocations.

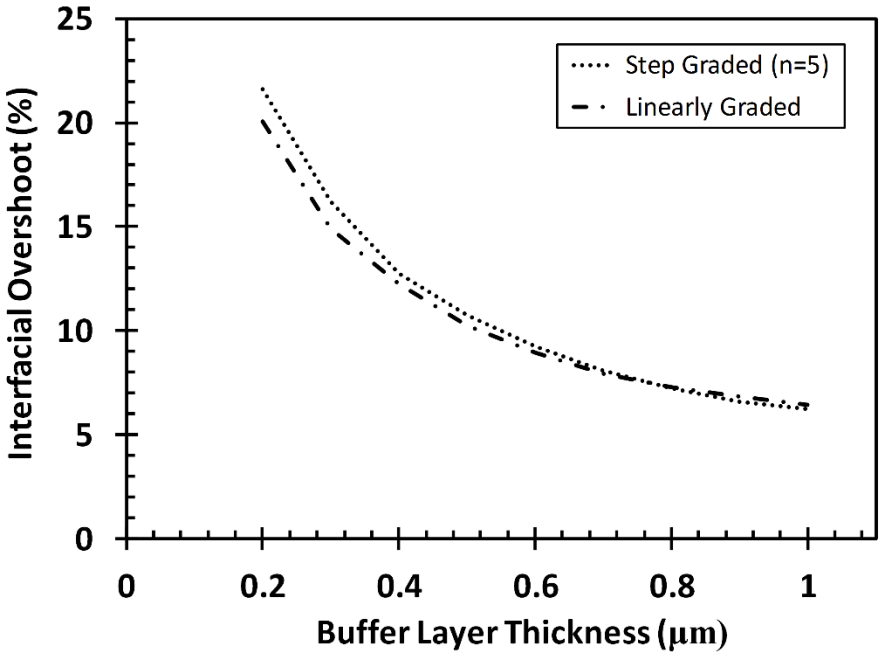

Figure 8.22.The required buffer layer thickness and compositional overshoot for the removal of all mobile threading dislocations using a linearly graded ZnS_ySe_{1-y} buffer (type C structure) and a step-graded ZnS_ySe_{1-y} buffer (type D structure) with a device layer thickness of 0.5 μm and a sulfur concentration of 10%. The starting sulfur composition of the buffer layer was fixed at $y_0 = 6\%$ ($f_0 = 0$).

The results of Figure 8.22 show that for a given buffer layer thickness there is an amount of compositional overshoot at the device-buffer interface which allows the optimum dislocation

compensation (minimum threading dislocation density). Also, for a given compositional overshoot, there is a particular buffer layer thickness for optimum dislocation compensation. Figure 8.22 compares the critical condition for complete dislocation compensation (removal of all mobile TD) for the type C (linearly-graded buffer) and the type D structures (step-graded buffer with n=5). The results shown in Figure 8.22 were obtained by numerical methods – with the assumption that all dislocations are mobile - and allow one to choose the amount of overshoot which will give minimum dislocation density at a given buffer thickness. In practical structures, it may be impossible to remove all threading dislocations because some dislocations could be sessile; however, the main focus of this work is to show that in principle we can remove all mobile threading dislocations by adjusting the overshoot or buffer thickness. Since GaAs (001) substrates have typical dislocation densities of ~ 10^4 cm^{-2}, we have sought to identify combinations of buffer thickness and overshoot which enable a surface dislocation density on the order of 10^4 cm^{-2}. The heterostructures modeled here have a uniform (device) layer with 0.5 μm thickness and a sulfur mole fraction of 10%. The starting sulfur composition in type C structures was fixed at $y_0 = 6\%$ ($f_0 = 0$). The optimum buffer layer thickness decreases rapidly and monotonically for increasing overshoot amount. The behavior is similar for both types of structures, with notable differences only observed in thinner buffer layers. These small differences could be due to the generally thicker MDFZs in the linearly-graded structures. In a practical sense, it is possible to use the same design rules for dislocation compensation using step-graded or linearly-graded buffers. It should also be noted that even in an optimal structure, for which the surface threading dislocation density is zero, there will exist non-zero strain. The strain profile is controlled by the density of misfit dislocation

segments, and not their threading arms. The results of this work could help guide the design of metamorphic ZnS_ySe_{1-y} buffer layers for use in II-VI devices on GaAs substrates by either utilizing step- or linearly- graded MBL. Threading defects are crucial to the performance of these devices and motivates the use of optimized buffer layers to control lattice relaxation and threading dislocations.

We have investigated equilibrium and kinetically-limited lattice relaxation in metamorphic ZnS_ySe_{1-y} / GaAs (001) heterostructures involving linearly-graded or step-graded buffer layers. In addition, we have explored the dislocation compensation mechanism in intentionally lattice-mismatch ZnS_ySe_{1-y} / GaAs (001) heterostructures by studying the requirement on the buffer layer thickness and compositional overshoot to remove all mobile threading dislocations from a uniform layer grown on top of a graded buffer. There are four main conclusions of this study. First, step-graded layers with a finite number of steps may be designed to approximate the behavior of linearly-graded buffers. Second, equilibrium calculations predict a greater surface strain and larger average misfit dislocation density in linearly-graded buffers compared to the step-graded case. Third, kinetically-limited lattice relaxation calculations indicate that metamorphic buffer layers utilizing a step-graded compositional profile contain higher surface in-plane strain and greater surface threading dislocation densities than linearly-graded structures. Fourth, for a given overshoot in a heterostructure involving a uniform layer on top of a graded buffer there is an optimum buffer thickness which minimizes the threading dislocation density by the dislocation compensation mechanism.

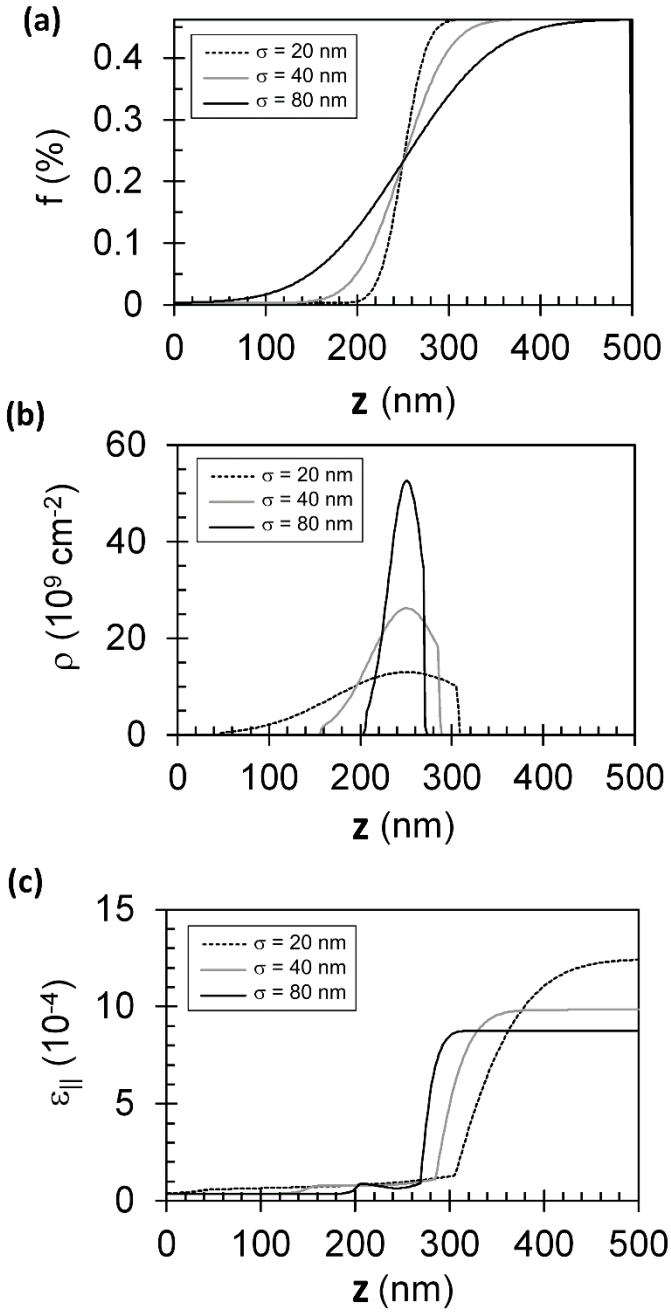

Figure 8.23. (a) Lattice mismatch, (b) equilibrium misfit dislocation and (c) in-plane strain profiles for 500 nm thick S-graded ZnS_ySe_{1-y} / GaAs (001) layers with $f_h = 0.0046$, $\mu = 250$ nm, and $\sigma = 20$, 40, and 80 nm. The sulfur composition in the S-graded layer is varied from 6% (lattice matched to GaAs) at the interface to 16% at the surface.

8.6. Threading Dislocations in S-Graded ZnSSe/GaAs (001) MBLs

Metamorphic semiconductor devices are commonly fabricated with linearly-graded buffer layers, but equilibrium modeling studies suggest that S-graded buffers, following a normal cumulative distribution function, may enable lower threading defect densities. The present work involves a study of threading dislocation density behavior in S-graded ZnS_xSe_{1-x} buffer layers for metamorphic devices on mismatched GaAs (001) substrates using a kinetic model for lattice relaxation and misfit-threading dislocation interactions. The results indicate that optimization of an S-graded buffer layer to minimize the surface threading dislocation density requires adjustment of the standard deviation parameter and cannot be achieved by varying the buffer thickness alone. Furthermore, it is possible to tailor the design of the S-graded buffer layer in such a way that the density of mobile threading dislocations at the surface vanishes. Nonetheless, the threading dislocation behavior in these heterostructures is quite complex, and a full understanding of their behavior will require further experimental and modeling studies.

8.6.1. Benefits of Compositionally-Graded Layers

Compositionally-graded buffer layers have gained great interest for the design of metamorphic devices, which enable a wider range of composition and therefore desirable properties such as energy gap, low-field mobility, and carrier saturation velocity. Metamorphic devices which have been fabricated on lattice-mismatched substrates include InGaAs/InAlAs HEMTs on GaAs [3], InGaAs/InAlAs heterojunction bipolar transistors (HBTs) on GaAs [4], InGaAs/InP HEMTs and HBTs on GaAs [5], InAlAs photodiodes on GaAs [6], InAsSb/AlInAsSb light-emitting diodes (LEDs) on GaSb [7], AlInGaAsSb laser diodes on GaSb [8], InGaAs/InAlGaAs laser diodes on GaAs [9], InGaAsSb/InAlAs quantum cascade laser structures

on GaAs [10], and InAlAs solar cells on GaAs [11]. Most work has focused on linearly-graded buffer layers [2-8, 12-30], while there have been several reports of the use of step-graded buffer layers [12, 31-34] or buffer layers with continuous, but non-linear grading of composition [11, 35-37]. Tersoff's work [12] on equilibrium modeling shows that linearly-graded buffer layers have several characteristics which can be helpful in the control of threading dislocation densities: first, misfit dislocations are distributed throughout the graded layer instead of being concentrated at the interface, where pinning can reduce dislocation mobility; second, there is a misfit dislocation free zone (MDFZ) at the top of the buffer layer; and third, there is a large built-in strain in the MDFZ which helps sweep out threading arms of defects. These characteristics help reduce the device threading dislocation density by enhancing the mobility and glide velocities of dislocations, resulting in the longest possible misfit dislocations parallel to the interface and therefore the least number of threading segments emanating from misfit dislocation ends [12]. Xhurxhi et al. [2] showed that an S-graded compositional profile has characteristics which might provide improved performance compared to linear grading: there is a MDFZ adjacent to the substrate interface which can further diminish pinning reactions or interactions with substrate defects; the MDFZ at the surface is maintained even after a device layer is grown on top, in contrast to the case with some linearly-graded buffers; and the built-in strain in the top MDFZ is generally larger than in a linearly-graded buffer with the same thickness and total amount of compositional change. Kujofsa et al. [37] explored these aspects of S-graded buffer layers and developed design rules based on their equilibrium behavior. Here we consider the kinetically-limited relaxation and dislocation dynamics in S-graded buffer layers and study the threading dislocation behavior. We show that the surface threading dislocation density of the S-graded layer exhibits complex behavior,

depending on the layer thickness, standard deviation parameter, and the overall lattice mismatch. In the following sections, we first review the equilibrium model and the kinetic model, and then threading dislocation density results for ZnS_xSe_{1-x} S-graded buffer layers deposited on GaAs (001) substrates.

The lattice mismatch profile (Figure 8.23a) in the S-graded metamorphic buffer layer (SG-MBL) is designed to be a normal cumulative distribution function, given by

$$f = \begin{cases} \frac{f_h}{2}\left[-erf\left(\frac{\mu - z}{\sigma\sqrt{2}}\right) + erf\left(\frac{\mu}{\sigma\sqrt{2}}\right)\right], & z < \mu; \\ \frac{f_h}{2}, & z = \mu \\ \frac{f_h}{2}\left[erf\left(\frac{z - \mu}{\sigma\sqrt{2}}\right) + erf\left(\frac{\mu}{\sigma\sqrt{2}}\right)\right], & z > \mu \end{cases}, \quad \textbf{(8.27)}$$

where μ is the "mean parameter," σ is the "standard deviation parameter," and f_h is the value of lattice mismatch at the top of the SG-MBL with thickness h. The equilibrium misfit dislocation density profile (see Figure 8.23b) is a truncated Gaussian located between two MDFZs which are adjacent to the substrate interface and the free surface, whereas the equilibrium strain profile is shown in Figure 8.23c. The results of Figure 8.23c indicate that S-graded layers exhibit a large built-in strain in the surface MDFZ which can aid in sweeping out threading dislocations prior to the growth of the device structure on top.

8.6.2. Threading Dislocation Characteristics in S-Graded ZnSSe/GaAs (001) MBL

For the structures considered in this work, the assumed growth temperature was 360°C and the mean parameter μ was fixed at half the buffer layer thickness. Figure 8.24 shows the surface threading dislocation (D_S) density for a 300 nm ZnS_ySe_{1-y} layer deposited on a GaAs (001)

substrate as a function of the standard deviation parameter and for growth with varying ending sulfur composition of the S-graded epilayer: y_h = 10%, 16% and 21%. For each case of the top composition, the surface threading dislocation density reaches a maximum and then decreases. These results indicate that use of a fixed buffer layer thickness does not afford the necessary flexibility to achieve low surface threading dislocation density. For a given value of y_h dictated by the device requirements it will be necessary to tailor h and σ in order to control the surface dislocation density.

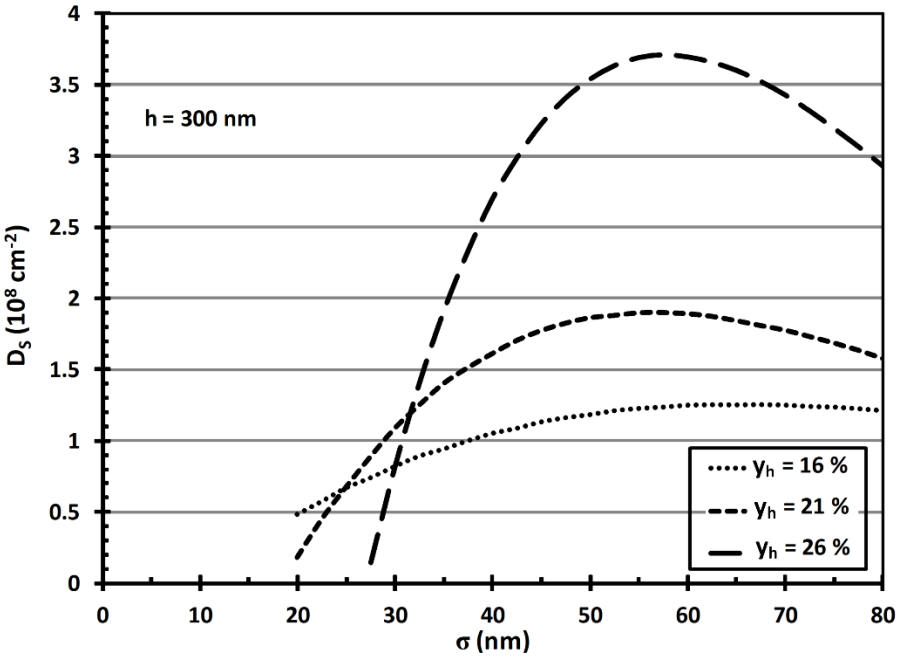

Figure 8.24. Surface threading dislocation for 300 nm thick S-graded ZnS_ySe_{1-y} / GaAs (001) layers as a function of the standard deviation parameter. The maximum sulfur composition (y_h) was equal to 10%, 16%, and 21%, respectively.

Figure 8.25 shows the surface dislocation density as a function of the buffer layer thickness, with σ as a parameter. Each type of buffer exhibits three regimes of threading dislocation behavior. In regime one, dislocations with positive Burgers vector are introduced to relax

compressive mismatch. This occurs as a result of the mismatch in the thermal expansion coefficients between ZnS_ySe_{1-y} and GaAs, which renders compressive strain in material with 6% sulfur at the growth temperature. In regime two, the sulfur composition is sufficient to produce tensile strain, so that dislocations with negative Burgers vector are introduced. The value of $sign(b)*D$ becomes less positive and may even change sign. A change of sign is especially interesting because the density of mobile dislocations may vanish at the buffer layer surface.

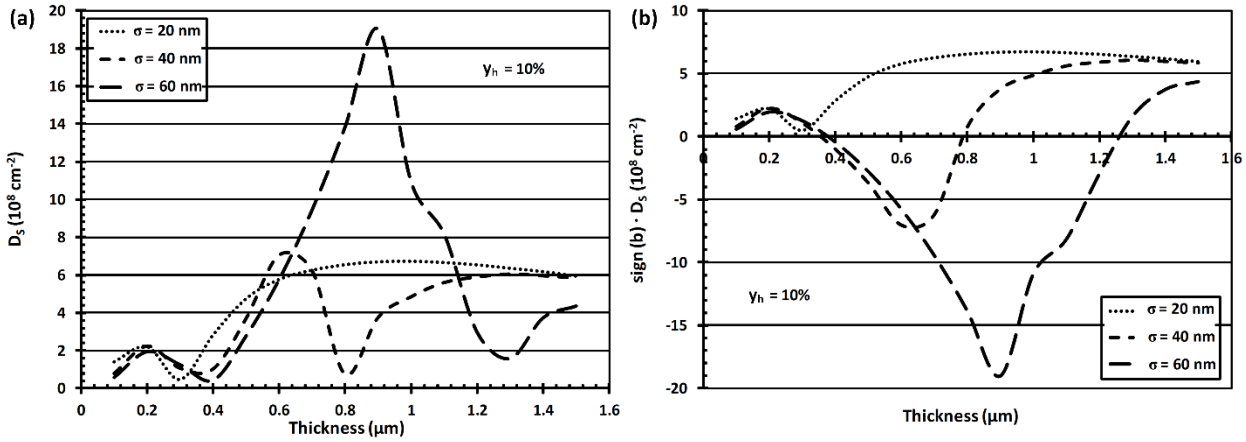

Figure 8.25. (a) Thickness dependence of the surface threading dislocation for an S-graded ZnS_ySe_{1-y} / GaAs (001) layers with a maximum sulfur composition (y_h) equal to 10% with varying standard deviation parameter of 20 nm, 40 nm and 60 nm. (b) sign(b)*D as a function of layer thickness.

In regime three, because of the thermal mismatch, compressive strain requires the introduction of dislocations with positive Burgers vector. The value of $sign(b)*D$ will become more positive, and there can be a second zero crossing, which can be employed to achieve a surface density of zero mobile dislocations. Figure 4a shows the actual surface threading dislocation densities, which are always positive, and illustrates the full complexity of the behavior. It is clear that careful design should enable low surface dislocation densities for improved performance of

metamorphic devices, but more work will be necessary to elucidate the details of this complicated behavior.

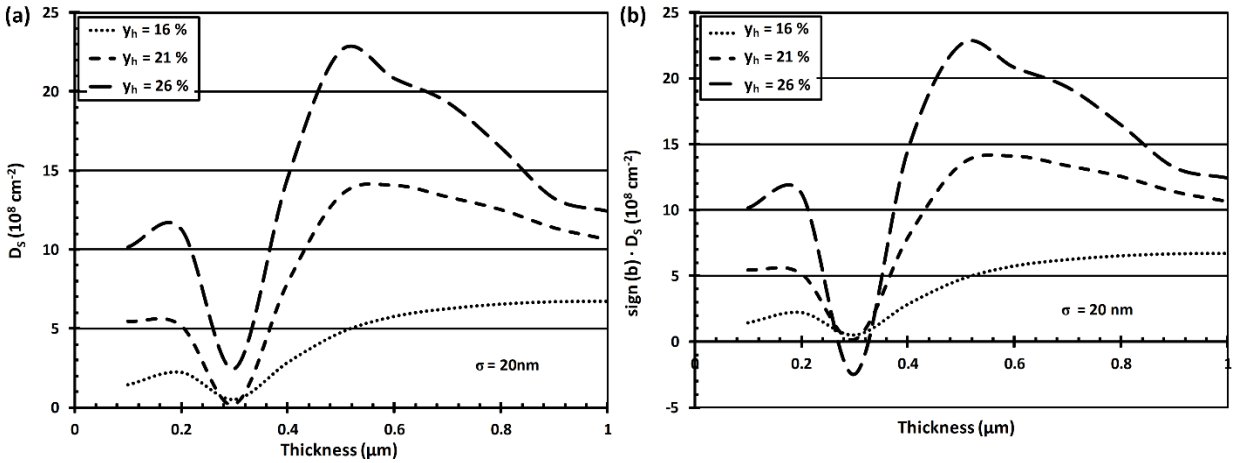

Figure 8.26. (a) Thickness dependence of the surface threading dislocation for an S-graded ZnS_ySe_{1-y} / GaAs (001) layers with σ = 20 nm and varying maximum sulfur composition (y_h) equal to 10%, 13% and 16%. (b) sign(b)*D as a function of layer thickness.

Figure 8.26 shows the surface dislocation density as a function of the buffer layer thickness, with x_h as a parameter. The results of Figure 8.26 further illustrate the 3-regime behavior of the surface threading dislocation density as seen in Figure 8.25, although the effect of relaxing tensile strain is not as pronounced. A common characteristic of the heterostructures studied here is that although the ending sulfur mole composition varies from 10% to 16%, an S-graded buffer layer with a thickness of ~ 300nm can exhibit a low surface threading dislocation density. In regime one, a higher density of dislocations is needed to relax the compressive strain for an increase in the ending sulfur mole fraction. In thicker heterostructures, introduction of dislocation over-compensates the relaxing strain which result in surface threading dislocations associated with a negative $sign(b)$. Furthermore, with increasing thickness, there is a reversal in the $sign(b)$ corresponding yet again to dislocations associated with compressive strain. These heterostructures

can be optimized for lower surface threading dislocation by controlling the standard deviation parameter.

8.7. Evolution of Kinetically-Limited Lattice Relaxation and Threading Dislocations in Temperature-Graded ZnSe/GaAs (001) Metamorphic Heterostructures

We have investigated the evolution of strain and threading dislocation density in metamorphic temperature-graded ZnSe buffer layers. Mismatched semiconductor heterostructures may be designed to take advantage of temperature grading to allow control over the relaxation process. To study temperature grading, we have applied a plastic flow model which predicts non-equilibrium strain relaxation as well as misfit and threading dislocation densities by accounting for the time evolution of kinetically-limited and equilibrium strain relaxation, thermal activation of glide, and misfit-threading dislocation interactions. We considered ZnSe/GaAs (001) heterostructures comprising of a convex-down (type A), linear (type B) and convex-up (type C) temperature grading profile. The thermal budget available for relaxation in these types of structures is controlled by the temperature-grading profile which consists of combinations of linear ramp-down and/or constant temperature growth; the temperature is varied from T_0 (400-600ºC) at the substrate interface to T_F=300ºC at the surface. We show that structures with a higher thermal budget exhibit a greater extent of relaxation (lower strains). At lower thicknesses, the dislocation density is dominated by the extent of relaxation whereas at greater thicknesses it is controlled by annihilation and coalescence mechanisms.

Metamorphic buffer layers allow tremendous flexibility in designing novel semiconductor heterostructures for application in various microelectronic and optical devices. However, device fabrication, reliability and performance are limited by dislocation defects associated with the

growth of mismatched materials such as ZnSe on GaAs substrates. A critical challenge with metamorphic device design involves control of the threading dislocation density, and compositionally-graded buffer layers have been used for this purpose. In the case of uniform layers such as ZnSe/GaAs (001), misfit dislocations are concentrated at the substrate interface and the threading dislocation density may be controlled either by promoting longer misfit dislocations or growing thick layers such that annihilation and coalescence reactions can reduce the threading density. There have been several reports on the use of low temperature growth to minimize surface roughness [269,270,271,272] and optimize the growth condition [273,274,275] which yielded device structures with relatively low threading dislocations. However, in this work, we use temperature grading to control the lattice relaxation rate for the purpose of enhancing the glide of dislocations. To understand the lattice relaxation mechanism in ZnSe/GaAs material system, we have applied a general kinetic model which predicts non-equilibrium strain, misfit and threading dislocation densities. The kinetic model assumes that the dislocation multiplication rate is proportional to the glide velocity of dislocations, the effective stress, and the dislocation density; this is based on the model proposed by Dodson and Tsao but accounts for the time-variation of relaxation dynamics during growth. In addition, we have accounted for dislocation-dislocation interactions by including the mechanisms of (i) dislocation compensation caused from interactions of misfit-threading dislocations at abrupt interfaces and (ii) annihilation and coalescence reactions as described by Tachikawa and Yamaguchi. In this work, we have studied the evolution of kinetically-limited in-plane strain and threading dislocation densities in temperature-graded ZnSe/GaAs (001) metamorphic buffer layers using three different types of temperature profiles.

In addition, we have investigated the effect of the available thermal budget on the relaxation mechanism.

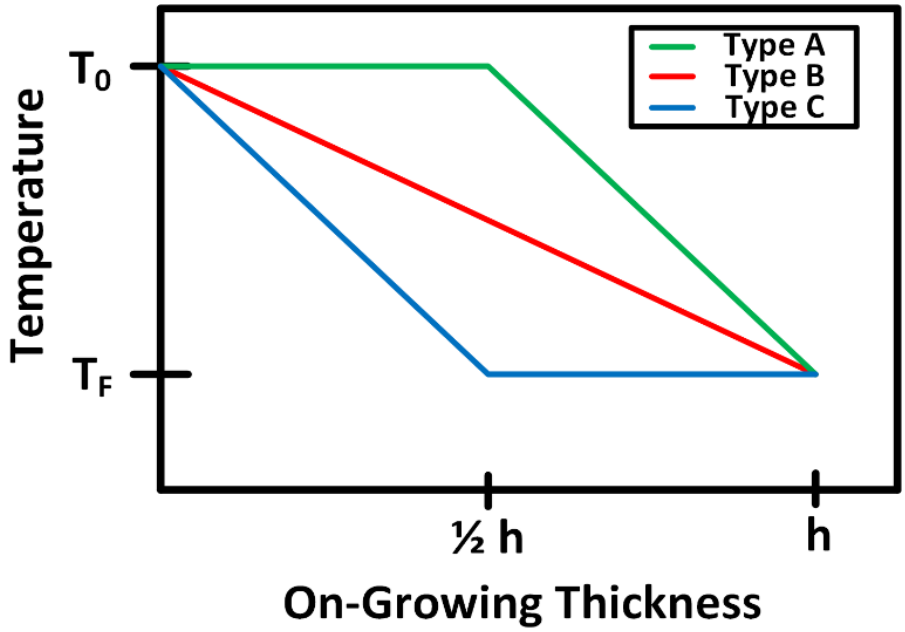

Figure 8.27. Temperature as a function of grown thickness for type A, B and C structures. T_0 and T_F correspond to the temperature at the substrate interface and surface (h) respectively.

8.7.1. In-Plane Strain and Threading Dislocation Density

The structures considered in this work explore the in-plane strain and threading dislocation dependence on epilayer thickness for structures with three types of temperature grading profiles. Figure 8.27 illustrates the growth temperature as a function of the on-growing thickness for each type of temperature grading profile; type A structures consist of a convex down temperature profile where half of the epilayer thickness is grown at constant temperature T_0 and in the remaining structural growth, the temperature is linearly decreased from T_0 to a final temperature T_F = 300ºC at the surface. In type B structures, the temperature is varied linearly from T_0 to T_F = 300ºC as the

growth of the epilayer proceeds. Type C structures consist of a convex up temperature profile where in the first half of the epilayer thickness the temperature is linearly decreased from T_0 at the substrate interface to a final temperature T_F = 300ºC and the remaining growth is carried out at a constant temperature T_F = 300ºC. From a thermodynamics point of view, for a given thickness the available thermal budget during growth is highest in type A and lowest in type C structures. In addition, an increase in the thickness of the epilayer yields a higher thermal budget.

Figure 8.28. compares the average in-plane strain, misfit and equilibrium strain as a function of the on-growing epilayer thickness at an initial temperature T_0 = 400ºC for type A (Figure 8.28a), B (Figure 8.28b) and C (Figure 8.28c) structures. The results of Figure 8.28a-c indicate that the lattice relaxation process in ZnSe/GaAs (001) heterostructures occurs via a three regime (sluggish, rapid, saturation) behavior. In addition, kinetically-limited strain relaxation occurs much more gradually than predicted by the equilibrium theory. Moreover, the choice of the temperature-grading profile and therefore the available thermal budget for lattice relaxation may enhance or reduce the relaxation rate which would obscure the visibility of the three-regime behavior. More importantly, a minimum thermal budget is required to ensure nearly-complete lattice relaxation in these structures. It can be seen from Figure 8.28c that even for a 2 μm thick epilayer, a convex-up temperature profile may yield sluggish relaxation rates and therefore strain values comparable to the lattice mismatch (misfit strain) whereas the strain relaxation in structures with a convex down temperature profile at the given thickness approaches the equilibrium in-plane strain value. Figure 8.29 illustrates the average in-plane strain as a function of the epilayer thickness with initial temperature as a parameter for type A (Figure 8.29a), B (Figure 8.29b) and C (Figure 8.29c) structures. For the structures modeled here, the initial temperature ranges from 400 ºC to 600ºC in steps of 50ºC and the final temperature is fixed at T_F =

300ºC. The results of Figure 8.29a-c indicate a monotonic decrease in the average in-plane strain with greater epilayer thicknesses. However, as predicted by the results of Figure 8.28, convex down temperature grading profile greatly enhances the strain relaxation process at higher initial temperatures which yields fully relaxed structures at relatively low thicknesses. For example, at an initial temperature $T_0 = 600$ºC, convex-down temperature-grading profile yields 95% strain relaxation at a thickness $h \sim 0.7$ μm whereas for type B and C structures, 95% relaxation occurs at $h \sim 1.3$ μm and $h \sim 2.5$ μm respectively. In cases of constant temperature growth, at around 400ºC, growth of ZnSe layers will exhibit a transition from compressive to tensile strain as the thickness is increased; this is expected on the basis of the differential thermal expansion and has been observed experimentally in this material system [276].

It can be seen from the results of Figure 8.29a-c, that at elevated temperatures, the strain transitions from compressive to tensile with increasing thickness. This effect is more pronounced in structures with a higher thermal budget in which the transition occurs at relatively lower thicknesses whereas in type C structures, the transition does not occur below thicknesses of $h = 2$ μm.

Figure 8.30a-c show the average threading dislocation density as a function of the epilayer thickness with initial temperature as a parameter for type A (Figure 8.30a), B (Figure 8.30b) and C (Figure 8.30c) structures. The kinetic model predicts a two regime behavior for the evolution of the threading dislocation density. First, there exists an initial build-up of the threading dislocations associated with layers which are beyond the critical layer thickness but still in the early stage of introducing misfit dislocations to relax the misfit strain. Second, as the epilayer thickness is further increased, the threading dislocation density falls off approximately with the reciprocal of

thickness. At relatively low thickness, structures with lower thermal budget and therefore greater residual strain contain a slower build-up of dislocations which leads to lower threading dislocation densities. In addition, increasing the thermal budget in these structures leads to a decrease in the inflection point; in other words, higher relaxation rates cause a rapid build-up of dislocations and therefore a diminishment of the region with increasing threading dislocations. However, at higher thicknesses, second order reactions dominate threading dislocations and therefore a reciprocal of thickness dependence is prominent among all types of structures. Moreover, at greater thicknesses, the threading dislocation is comparable among type A, B, and C structures. Also, in type A and B structures there exists a thickness where beyond it the threading dislocation is entirely dominated by second order reactions and it can be seen by the overlapping of the curves within the figure.

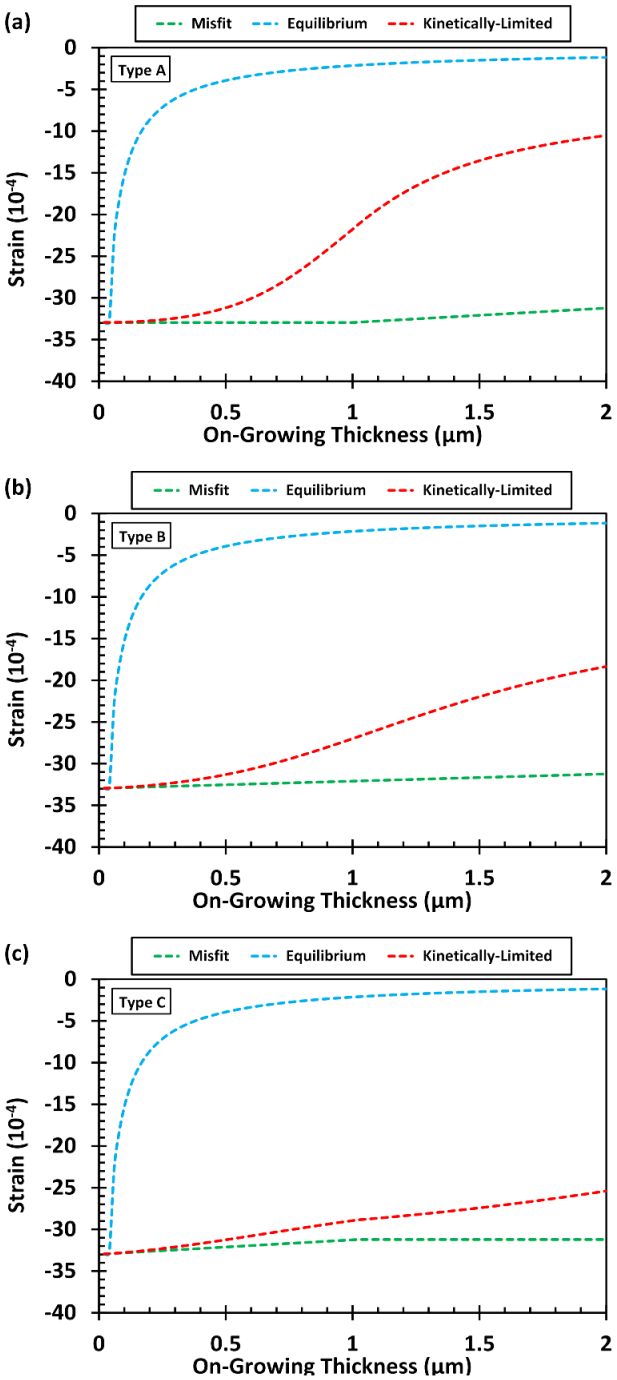

Figure 8.28. The evolution of strain (kinetically-limited, misfit and equilibrium) as a function of the grown thickness for type (a) A, (b) B and (c) C structures. The initial T_0 and final T_F temperatures in these structures are 400 ºC and 300ºC respectively.

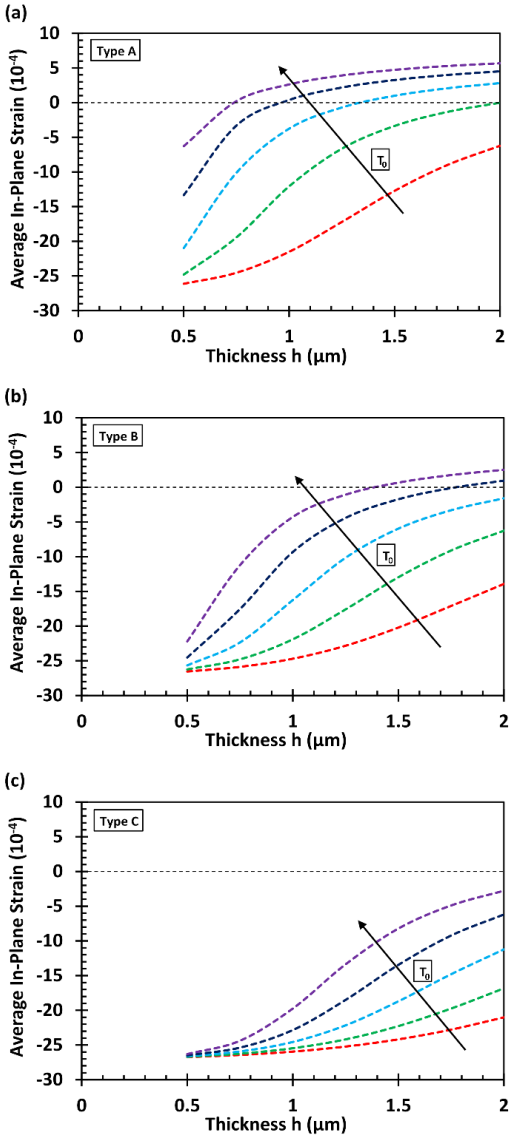

Figure 8.29. Average kinetically-limited in-plane strain as a function of the final epilayer thickness h with initial temperature as a parameter for type (a) A, (b) B and (c) C structures. The initial temperature T_0 is varied from 400-600ºC in steps of 50 ºC and final T_F temperatures is fixed 300ºC.

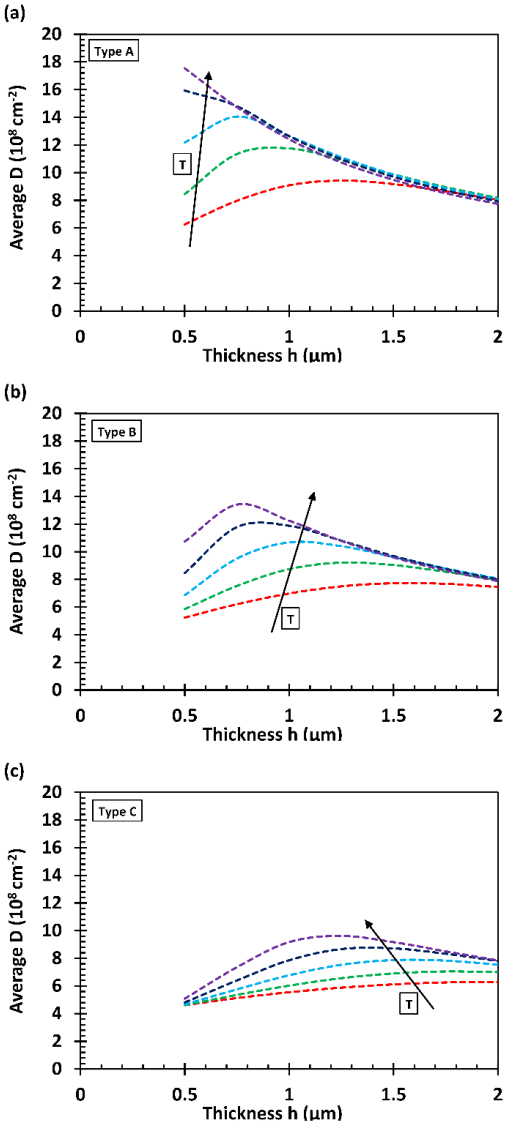

Figure 8.30. Average threading dislocation density as a function of the final epilayer thickness h with initial temperature as a parameter for type (a) A, (b) B and (c) C structures. The initial temperature T_0 is varied from 400-600ºC in steps of 50 ºC and final T_F temperatures is fixed 300ºC.

We have investigated the evolution of strain and threading defects in ZnSe/GaAs (001) heterostructures involving temperature-graded buffer layers. There are two main conclusions of this study. First, structures with a greater thermal budget exhibit a greater extent of relaxation and therefore lower in-plane strain values. Second, at relatively low thicknesses, the threading dislocation density is higher in structures with a greater thermal budget whereas in thicker layers second order reactions dominate the dislocation behavior. A further improvement of this work could include temperature-grading in conjunction with compositional-grading to control the strain and defect behavior in intentionally mismatched heterostructures.

8.8. The Dynamics of Kinetically-Limited Strain and Threading Dislocations in Temperature and Compositionally-Graded ZnSSe/GaAs (001) Metamorphic Heterostructures

We have investigated the evolution of strain and threading dislocation density in metamorphic compositionally- and temperature-graded ZnS_ySe_{1-y} buffer layers. Linear variation in composition in conjunction with temperature grading may be used to allow control over the relaxation process. Previously, we reported the development of general kinetic model by dislocation flow, which accounted for the time evolution of the strain relaxation in semiconductor structures under kinetically-limited conditions, including interactions of threading and misfit defects. In this work, we studied ZnS_ySe_{1-y}/GaAs (001) heterostructures with linear compositional grading and employing a convex-upward (type A), linear (type B) and convex-downward (type C) temperature grading profile. The thermal budget available for relaxation in these types of structures is controlled by the temperature-grading profile which was made up of combinations of linear ramps and constant-temperature sections. In all cases, the temperature was varied from T_0 (400-600 ºC) at the substrate interface to T_F = 300 ºC at the surface. We also investigated the effect

of varying the compositional gradient in the range from 0.18 to 1.6 %/μm. Structures with a higher average temperature (greater thermal budget) and/or higher grading coefficient exhibit a greater extent of relaxation and therefore reduced residual strain. Furthermore, controlling the extent of strain relaxation enables optimization of the dislocation densities in these heterostructures.

8.8.1. Incorporation of Compositional- and Temperature-Grading

The design of highly functional and reliable microelectronic and optical devices requires the use of metamorphic buffer layers (MBLs) for the purpose of accommodating the misfit strain associated with the growth of lattice mismatched materials. However, metamorphic growth generates dislocation defects which are detrimental to the device performance and therefore novel approaches are required to control the extent of strain relaxation and dislocation generation.

Metamorphic device heterostructures employ a wide range of compositional-profiles, which include linearly-graded [44,72,92], step-graded [277,278], or non-linear and continuously-graded buffer layers [279,280,281,282]. The main benefit of compositionally-graded epitaxial layers is that they allow for the distribution of misfit dislocations throughout the graded-layer which in turn reduces any dislocation pinning interactions with substrate associated defects or the material that may be grown on top of the MBL. In addition, the use of a compositionally-graded layer promotes the growth of the misfit dislocation length which in turn results in a lower density of threading dislocations emanating from the misfit segments. A consequential benefit of compositionally-graded MBL is that the surface misfit dislocation free zone provides a high built-in strain which could aid in sweeping threading dislocation arms. In addition, several studies have shown that reduced-temperature growth can decrease the surface roughness [269,270,271,272] and material quality [273,274,275], yielding devices with improved threading dislocation density.

In a previous work [283], we reported the use of a temperature-grading scheme and studied lattice relaxation and threading dislocations in uniform layers of ZnSe grown on GaAs (001). In the growth of a compositionally uniform layer, all misfit dislocations are located at the interface, and the only means for reducing the threading density are the promotion of longer misfit segments or growth of relatively thick layers, in order to enhance annihilation and coalescence reactions between defects. In the previous work with uniform layers, we showed that by employing a temperature-grading scheme and therefore controlling the available thermal budget for relaxation we could optimize the relaxation process as well as the dislocation density by enhancing the thermally activated glide. However, the mismatch constraints imposed by the ZnSe/GaAs material system enabled us to use compositionally-graded ZnSSe/GaAs (001) buffer layers in conjunction with temperature grading to allow more flexibility in the design of mismatched heterostructures.

Here, we have applied a generalized kinetic model for strain relaxation and dislocation dynamics to investigate the combined effect of temperature- and compositional-grading on the lattice relaxation mechanism in ZnSSe/GaAs heterostructures. In this model, it is assumed that the dislocation multiplication rate is proportional to the glide velocity, the effective stress, and the defect density; this is based on the model proposed by Dodson and Tsao but includes the time-variation of the equilibrium strain and temperature during growth and is therefore applicable to graded materials. In addition, we have accounted for dislocation-dislocation interactions including the following two mechanisms: (i) dislocation compensation caused from interactions of misfit-threading dislocations at abrupt interfaces; and, (ii) annihilation and coalescence reactions as described by Tachikawa et al. [78]. Here, we have extended the previous work [283] by utilizing three different temperature-grading profiles in conjunction with a linear variation in composition to study the evolution of kinetically-limited lattice relaxation and threading dislocation behavior.

In addition, we have examined the combined effect of the available thermal budget and the grading constant to the lattice relaxation process.

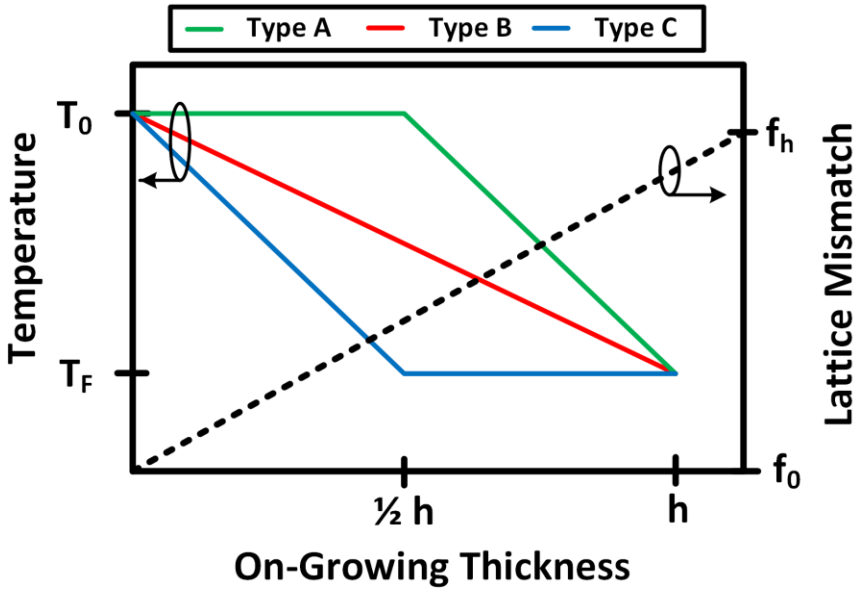

Figure 8.31. Temperature (left axis) as a function of grown thickness for type A, B and C structures. T_0 and T_F correspond to the temperature at the substrate interface and surface (h) respectively. Lattice mismatch profile (right axis) as a function of grown thickness. f_0 and f_h correspond to the lattice mismatch at the substrate interface and surface respectively.

8.8.2. Epitaxial Structures Under Consideration

In this work, we have considered heterostructures involving a linearly-graded ZnS_ySe_{1-y} layer grown on top of a GaAs (001) substrate. For linearly-graded metamorphic buffer layers the lattice mismatch profile at a distance from the substrate interface z is given by

$$f(z) = C_f z \,, \qquad \textbf{(8.28)}$$

where C_f is the grading constant. The equilibrium configuration may be determined numerically by minimizing the sum of the strain and dislocation energy using a similar approach as described by Bertoli et al. [24]. Equilibrium calculations serves as the starting point for the determination of

kinetically-limited lattice relaxation. The foundation for the kinetically-limited lattice relaxation and dislocation dynamics model along with the material/model parameters used in this work are explained in more detail in References 66, and 284 respectively. The kinetic model predicts lattice relaxation and dislocation behavior in (001) arbitrary heteroepitaxial layers which may incorporate graded and multilayered structures. The main assumptions of the model are that at a distance z from the substrate interface, (i) the lattice relaxation rate is governed by the glide of all the misfit dislocations concentrated below and (ii) the glide of the dislocations is governed by the glide force acting on the threading arms of dislocations concentrated above. Furthermore, we have developed a dislocation dynamics model to study threading and misfit dislocation behavior. We have included two important misfit-threading dislocation interactions, which consist of (i) the introduction of dislocation half loops [76]; and, (ii) the bending over of existing threading dislocations at mismatched interfaces [77]. In addition, there can be second-order coalescence and annihilation reactions involving threading dislocations as modeled by Romanov et al. [79] and Tachikawa et al. [78].

8.8.3. Strain and Threading Results

In this work, we have considered heterostructures, which utilize a combination of temperature-grading and a linear variation in composition for the purpose of exploring the dependence of the in-plane strain and threading dislocations. Figure 8.31 shows the growth temperature versus the accumulated thickness for each type of temperature-grading profile. Sample type A (convex-upward profile) involves constant-temperature growth followed by a linear ramp from T_0 to T_F. Sample type B incorporates only a linear ramp from T_0 to T_F. Sample type C (convex-downward profile) incorporates a linear ramp from T_0 to T_F followed by constant-temperature growth. Furthermore, the lattice mismatch profile for the structures considered in this

work employ a linear compositional grading scheme (as shown in Figure 8.31) whereby the epilayer is graded from lattice matched (where y_0 is the sulfur mole fraction) at the substrate interface ($y_0 = 6\%$, $f_0 = 0\%$) to an ending mismatch (y_h, f_h). Here, we have considered structures with an epilayer thickness of 1 μm and ending sulfur mole fraction y_h ranging from 10% to 40% which corresponds to a lattice mismatch 0.18% to 1.58% respectively. In terms of thermodynamics, at a given grading constant the available thermal budget during growth is highest in structures utilizing a convex-upward temperature profile (type A) whereas it is lowest in convex-downward temperature-grading (type C). In the simplest sense, the thermal budget could refer to the average temperature multiplied by the growth time. However, many processes – including the glide of dislocations – are thermally activated, so that it becomes more appropriate to consider the mean value of $\exp(-U/k_BT)$. In the cases studied for this work, samples with higher average temperature also had a higher average value of $\exp(-U/k_BT)$, and these can be referred to as having a greater thermal budget than samples having a lower average temperature and also a lower average value of the exponent.

Figure 8.32 contrasts the evolution of the average in-plane strain, lattice mismatch, and equilibrium strain for the three types of samples, with an initial growth temperature of 400ºC. The structures considered here have a 40% sulfur ending composition corresponding to a lattice mismatch of 1.58%. Whereas equilibrium model shows a rapid relaxation process especially in the early stages of growth, kinetically-limited lattice relaxation in ZnS_ySe_{1-y} epitaxial layers predicts a much more gradual behavior which exhibits four distinct regimes (pseudomorphic, sluggish, rapid, saturation). Although, the onset of lattice relaxation in equilibrium is approximately ~180 nm, depending on the choice of the temperature profile, it is apparent that the onset of kinetically-

limited lattice relaxation could range from 400 nm to 500 nm. The results also indicate that the design of the temperature grading profile and therefore the available thermal budget for lattice relaxation may alter the relaxation kinetics in such a way that four-regime behavior is no longer clearly visible. The results of Figure 8.32a-c show that sluggish lattice relaxation regime is more evident in structures with a lower thermal budget (type C) whereas in type A structures, higher thermally activated glide velocities yield a faster process for lattice relaxation. Regardless of the temperature-grading profile, a minimum thermal budget is required to ensure the onset of lattice relaxation. Furthermore, there also exists a critical thermal budget for the attainment of near-complete relaxation. As an example, the use of a convex-downward temperature grading profile could result in sluggish relaxation rates which yield structures with an in-plane strain value comparable to the lattice mismatch (about ~50% average relaxation in this case) even for a 1 μm thick epitaxial layer. However, the strain relaxation in structures with a convex-upwards temperature profile at the given thickness approaches the equilibrium in-plane strain with a nearly-complete value of 85% average relaxation.

Figure 8.33 provides the average in-plane strain as a function of the compositional grading coefficient with initial growth temperature as a parameter for type A (Figure 8.33a), B (Figure 8.33b) and C (Figure 8.33c) structures. For the cases considered here, the starting growth temperature was in the range from 400 ºC to 600 ºC with 50 ºC steps. The ending temperature was fixed at T_F = 300 ºC. In addition, the grading constant ranges from 0.18 to 1.58 %/μm. The results of Figure 8.33a-c are similar in character to those of Figure 8.32. The results of Figure 8.33a-c indicate that a critical grading constant is required to enable the onset of lattice relaxation. The critical grading constant depends strongly of the available thermal budget and therefore the temperature grading profile along with its initial and ending conditions. The average in-plane strain

exhibits a two-regime behavior. In the first regime, the average in-plane strain increases monotonically with increasing grading constant, whereas in the second regime, the average in-plane strain decreases with increasing grading constant. The first regime corresponds to the initial stages (pseudomorphic and sluggish) of lattice relaxation, while the second regime is correlated with the later stages of lattice relaxation (rapid and saturation). The results of Figures 3a-c indicate that a higher thermal budget results in faster onset of lattice relaxation. For type A structures, the critical grading constant is approximately 0.5 %/μm whereas for type B and C structures the critical grading constant is 0.6 %/μm and 1 %/μm respectively. Furthermore, increasing the initial growth temperature in these structures, results in a lower grading constant for the commencement of lattice relaxation. In addition, the use of a higher thermal budget results in the diminishment of the region with approximately constant strain, evident by the faster transition of increasing strain to decreasing strain regimes as a function of increasing grading constant. The use of convex-upwards temperature grading profile provides a greater thermal budget and therefore enhances the strain relaxation process which results in near-complete relaxed structures at relatively low grading constant. For example, at an initial temperature T_0 = 600 ºC, type A temperature-grading profile yields 85% strain relaxation at a grading constant $C_f \sim 1$ %/μm whereas for type B and C structures, 95% relaxation occurs at $C_f \sim 1.2$ %/μm and $C_f \sim 1.9$ %/μm, respectively. It should also be noted, that the use of a lower thermal budget results in the diminishment of the curve separation. As an example, for type C structures with a grading constant of 1.58 %/μm, changing the initial temperature from 400 ºC to 600 ºC results in ~10% difference in the average strain value.

Figure 8.34a-c display the variation of the surface strain relaxation (in percent) with the lattice mismatch gradient, with initial temperature as a parameter for the three types of structures. The results of Figure 8.34a-c reinforce three key details discussed in the previous paragraph; First,

the surface strain relaxation percentage is monotonically increasing with higher grading constant. Second, for a given grading constant structures with a higher thermal budget (i.e. type A structures or higher initial growth temperature) exhibit higher relaxation percentage of the surface strain. Third, the surface relaxation percentage saturates at about ~80% for the structures studied here. From a fabrication point of view, the surface strain is important in the device design of multilayered heterostructures because it allows the flexibility of controlling the strain at the top of the buffer layer. The results of Figure 8.33 and Figure 8.34 show that for a given grading constant, the surface and average strain can be tightly controlled by optimizing the temperature-grading profile. Furthermore, the results of Figure 8.34 indicate that for a given temperature profile, it may be possible to control the onset of lattice relaxation (and therefore the surface strain), the rate at which strain relaxation occurs for increasing grading constant, and the maximum relaxation percentage attainable. Moreover, for the sake of comparison, we have also calculated the strain relaxation in otherwise samples grown at a constant temperature of 300 ºC and 600 ºC respectively. For the heterostructures studied in this work, the growths at a constant temperature of 300 ºC and 600 ºC individually yield the lower and upper bounds of the lattice relaxation. A key result of Figure 8.34, was that structures with the greatest thermal budget will exhibit the highest relaxation percentage. Therefore, we can conclude that structures grown at a constant temperature of 600 ºC will exhibit the highest relaxation percentage (lowest surface in-plane strain value) whereas structures grown at a constant 300 ºC will exhibit the lowest relaxation percentage (highest surface in-plane strain).

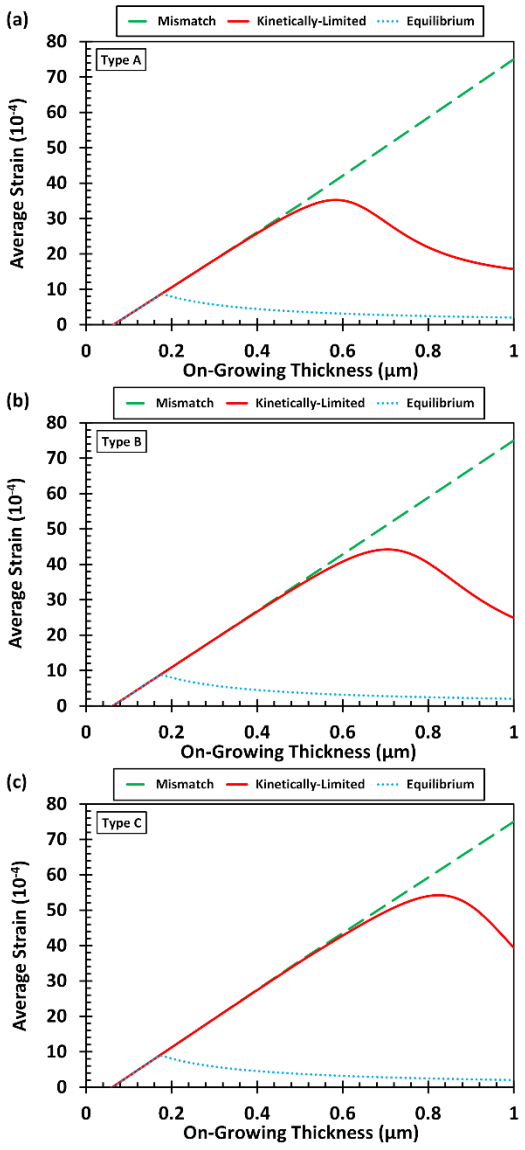

Figure 8.32. The evolution of average strain (kinetically-limited, mismatch and equilibrium) as a function of the on-growing thickness for type (a) A, (b) B and (c) C structures. The initial T_0 and final T_F temperatures in these structures are 400 °C and 300 °C respectively. The ending sulfur composition is fixed at 40% (f_h =1.58%).

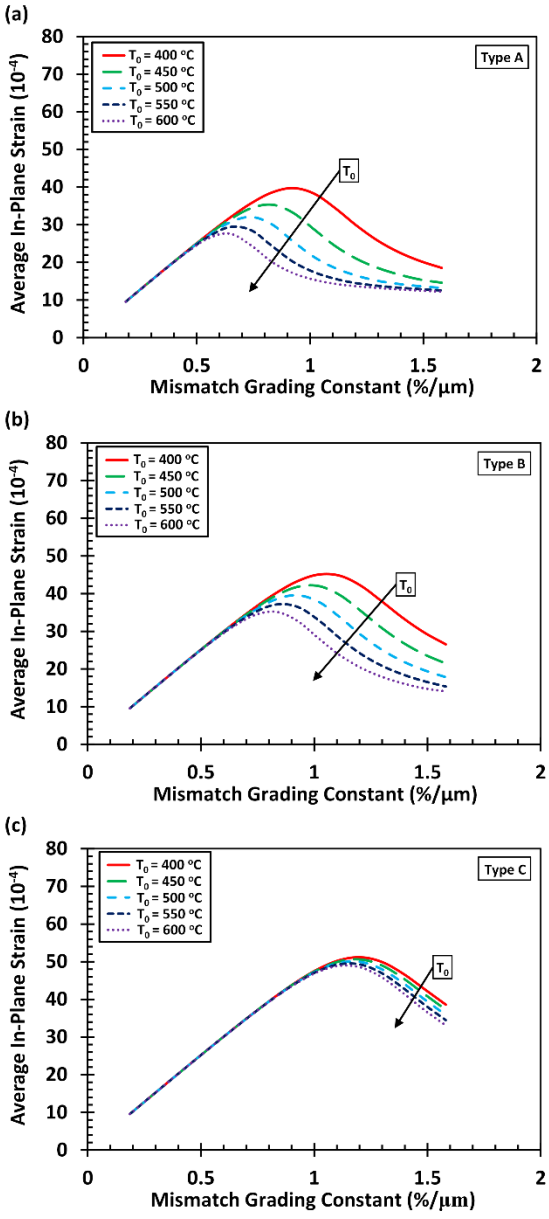

Figure 8.33. Average kinetically-limited in-plane strain as a function of the grading constant C_f with initial temperature as a parameter for type (a) A, (b) B and (c) C structures. The initial temperature T_0 is varied from 400-600 °C in steps of 50 °C and final T_F temperature is fixed 300 °C.

For example, in a heterostructure with a grading coefficient of 1.205 %/μm the use of a type A temperature grading profile with T_0 = 600 ºC and T_F =300 ºC resulted in a surface strain relaxation of 61.2% whereas structures with type B and C yielded 54.5% and 18.9% respectively. Furthermore, structures grown at a constant temperature of 300 ºC and 600 ºC exhibited a surface relaxation percentage of 12.55% and 73.11% respectively. In the specific case of ZnSSe, it is desirable to use a low ending growth temperature in order to optimize the optical properties of the material. Therefore, temperature grading allows us the flexibility of adjusting the strain relaxation and in-plane strain while keeping the ending growth temperature fixed. Also, in a more general sense, temperature grading is of interest because in principle it could allow the depth grading of the average misfit dislocation length, thereby controlling the threading dislocation behavior.

Figure 8.35a-c show the surface threading density versus layer thickness with starting growth temperature as a parameter for type A (Figure 8.35a), B (Figure 8.35b) and C (Figure 8.35c) structures. The dislocation behavior in the structures studied here is slightly more complex in comparison to kinetically-limited in-plane strain, however, the results of Figure 8.35 indicate a monotonically increasing dislocation density with increasing grading constant. Each type of buffer structure exhibits three regimes of threading dislocation behavior. In the first regime, there exists an initial and sluggish build-up of the threading dislocations associated with layers which are in the early stages of lattice relaxation. At relatively low grading coefficient, the dislocation density for a given type of structure is independent of the initial temperature condition. Based on the results of Figure 8.32, structures which exhibit low relaxation rates and therefore a higher in-plane strain are more favorable at sweeping out threading arms. The second regime corresponds to a rapid

relaxation phase whereby threading dislocation are introduced at a more rapid rate to relax the excess mismatch strain. Furthermore, structures with a higher initial growth temperature contain a greater density of surface dislocations. However, in structures with a lower thermal budget, we see a diminishment in the curve separation and therefore a temperature independence of dislocation density. In addition, at greater grading constants, the surface threading dislocation density is comparable among the three structure types. Also, in these structures there exists a grading constant where beyond it the threading dislocation is lower in structures with a higher thermal budget. This phenomenon can be explained by the fact that a higher thermal budget leads to structures with a higher density of dislocations, which can enable a greater reduction in the dislocation density due to thermally activated glide. However, it should be noted that the surface strain contained in these structures plays an important role in the control of threading dislocations.

We have investigated the evolution of kinetically-limited lattice relaxation by dislocation generation in ZnS_ySe_{1-y}/GaAs (001) heterostructures involving a combination of compositionally- and temperature-graded buffer layers. The results lead to two main findings. First, structures grown at a higher average temperature (with greater thermal budget) or with a steeper compositional gradient show a greater extent of relaxation and reduced residual in-plane strain. Second, structures with a higher in-plane strain contain a lower threading dislocation density, however, at higher grading constant it may be possible to tailor the temperature profile such that relatively low threading dislocations may be attainable. An extension of this work could include structures which exhibit a variation in the thickness of the epilayer.

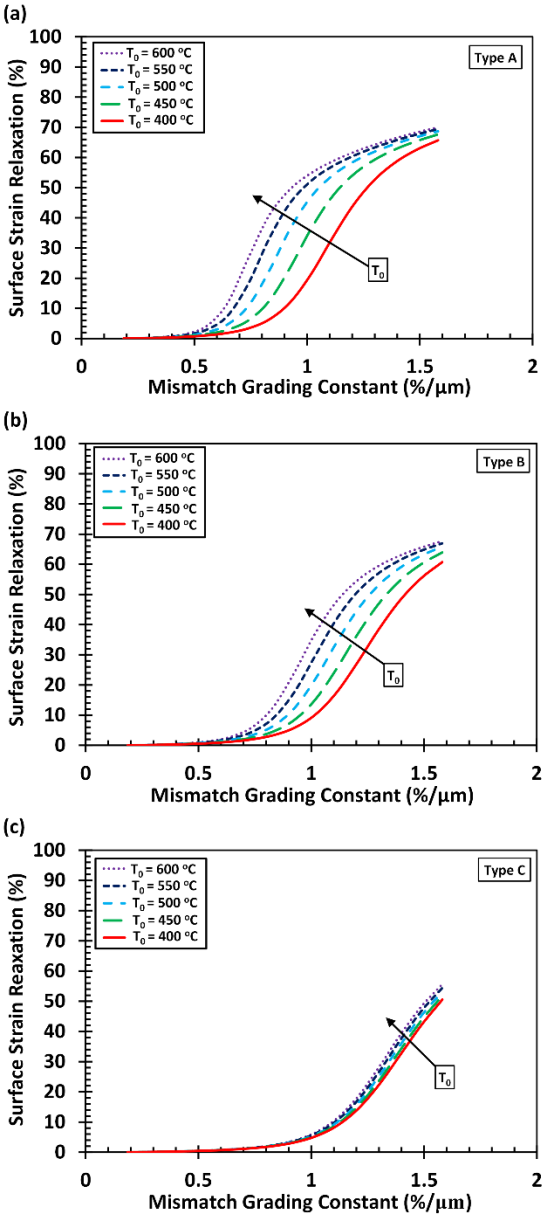

Figure 8.34. Surface strain percent relaxation as a function of the grading constant C_f with initial temperature as a parameter for type (a) A, (b) B and (c) C structures. The initial temperature T_0 is varied from 400-600 °C in steps of 50 °C and final T_F temperature is fixed 300 °C.

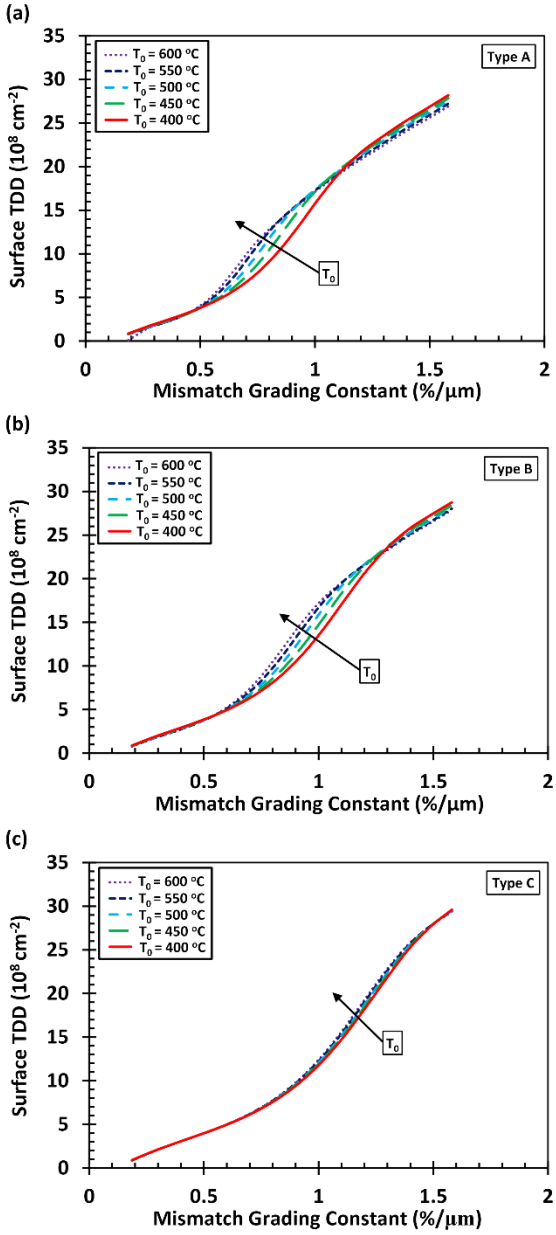

Figure 8.35. Surface threading dislocation density as a function of the grading constant C_f with initial temperature as a parameter for type (a) A, (b) B and (c) C structures. The initial temperature T_0 is

varied from 400-600 ºC in steps of 50 ºC
and final T_F temperature is fixed 300 ºC.

9. Resolution of X-Ray Rocking Curve Measurements Made with Finite Counting Statistics

In this section, we have analyzed the strain resolution of x-ray rocking curve profiles from measurements of the peak position and peak width made with finite counting statistics. In this work, we have considered x-ray rocking curves which may be Gaussian or Lorentzian in character and have analyzed the influence of the effective number of counts, full-width-at-half-maximum (FWHM) and the Bragg angle on the resolution. Often experimental resolution values are estimated on the order of 10^{-5} whereas this work predicts more sensitive values (10^{-9}) with smaller FWHM and larger effective counts and Bragg angles.

X-ray rocking curve measurements are commonly employed to characterize the residual strain and lattice relaxation in metamorphic semiconductor device structures. Therefore, it is important to understand the resolution limits of the technique, especially when studying the initial onset of relaxation at the pseudomorphic / metamorphic boundary. Often researchers estimate the resolution of x-ray measurements as a single number (on the order of 10^{-5}) without giving physical justification. Fewster's summary [285] on x-ray diffraction techniques fails to mention how the counting statistics and conditions of measurements affect the outcome of the experimental results. The Zhang et al. [286] experimental work on the determination of the critical layer thickness involved using x-ray rocking curve strain analysis and also the rocking curve full width at half maximum method; in either case, they concluded that the precision depended on several factors and in their derivation of the resolution they approximated the counting statistics with a constant. Here, we show that the resolution of an x-ray diffraction measurement depends not only on the

width and shape of the diffraction peak being measured but also the counting statistics employed for its measurement. For this reason, the peak number of counts (count rate times count time) should always be provided with any x-ray measurement.

9.1. Resolution of X-Ray Diffraction Measurements of Peak Position and Peak Width in the Presence of Statistical Noise

Diffraction profiles from metamorphic epitaxial layers may usually be approximated by Gaussian or Lorentzian profiles, apart from the tails of the distribution [75,287,288]. In this analysis, we consider Gaussian and Lorentzian diffraction profiles and we analyze the uncertainty in measuring the peak position and peak width in the presence of noise associated with finite counting statistics.

9.1.1. Gaussian Diffraction Profile

First, we consider a normalized Gaussian profile given by

$$I_G(\theta) = \exp\left\{-\left(\frac{\theta-\theta_0}{\sqrt{2}\sigma}\right)^2\right\}. \qquad \textbf{(9.1.)}$$

where θ_0 is the center of the Gaussian peak and σ is the standard deviation parameter. If we suppose that a noise signal $\eta(\theta)$ of amplitude n is added, where n<<1, the resulting signal plus noise is given by

$$I_G(\theta) = Exp\left\{-\left(\frac{\theta-\theta_0}{\sqrt{2}\sigma}\right)^2\right\} + \eta(\theta). \qquad \textbf{(9.2.)}$$

In the presence of this noise, the apparent peak position may shift in either direction by an amount $\Delta\theta$ as a consequence of the added noise, where

$$1-n = Exp\left\{-\left(\frac{\Delta\theta}{\sqrt{2}\sigma}\right)^2\right\}. \quad \textbf{(9.3.)}$$

Solving, the uncertainty in the peak position is

$$\Delta\theta = \sigma\sqrt{-2\ln(1-n)}. \quad \textbf{(9.4.)}$$

For a Gaussian peak the standard deviation σ and the full-width-at-half-maximum β are related by

$$\sigma = \frac{\beta}{2\sqrt{2\ln(2)}}, \quad \textbf{(9.5.)}$$

so that

$$\Delta\theta = \frac{\beta}{2}\sqrt{-\frac{\ln(1-n)}{\ln(2)}}. \quad \textbf{(9.6.)}$$

For a normalized Gaussian profile with noise amplitude n, the signal-to-noise ratio [289] is given as

$$SNR = \frac{1}{n}, \quad \textbf{(9.7.)}$$

so

$$\Delta\theta = \frac{\beta}{2}\sqrt{-\frac{1}{\ln(2)}\ln\left(1-\frac{1}{SNR}\right)}. \quad \textbf{(9.8.)}$$

Therefore, the uncertainty in the measured peak position is proportional to the peak width,

$$\Delta\theta = C_P\beta, \quad \textbf{(9.9.)}$$

with constant of proportionality

$$C_P = \frac{1}{2}\sqrt{-\frac{1}{\ln(2)}\ln\left(1-\frac{1}{SNR}\right)}. \qquad \textbf{(9.10.)}$$

The emission and detection of x-rays is a random process which is governed by Poisson statistics [289]. For a large number of counts, the Poisson distribution becomes approximately Gaussian with a standard deviation equal to $\sqrt{N_{Eff}}$, where N_{Eff} is the number of x-ray photons detected [289,290]. For application to thin films in order to determine the critical layer thickness, in-plane strain, misfit dislocations and threading dislocations, we estimate the typical range of total counts (intensity in counts per second times the count time in seconds) depending on the type of experimental setup (rotating or fixed anode). In most practical experiments, curve fitting is used in conjunction with an excess of measured points. If there are m points measured within the range of uncertainty for the peak position or peak width, then the effective number of counts is increased to $N_{Eff} = mN$. Following the usual assumption that the noise amplitude is equal to the standard deviation [289], the signal-to-noise ratio is

$$SNR = \frac{N_{Eff}}{\sqrt{N_{Eff}}} = \sqrt{N_{Eff}}\,. \qquad \textbf{(9.11.)}$$

Therefore, in terms of the effective counts, Equation 9.10 is modified to

$$C_P = \frac{1}{2\sqrt{\ln(2)}}\sqrt{-\ln\left(1-\frac{1}{\sqrt{N_{Eff}}}\right)}. \qquad \textbf{(9.12.)}$$

The additive noise also introduces an error in the measurement of the peak width. For a normalized Gaussian profile the maximum displacement of the half-intensity point, which is the error in the half width at half maximum (HWHM) is

$$\frac{\Delta\beta}{2} = n\left|\left(\left.\frac{dI_G}{d\theta}\right|_{\theta=\theta_0+\beta/2}\right)^{-1}\right|, \qquad \textbf{(9.13.)}$$

where $\Delta\beta$ is the error in the measurement of the full width at half maximum β. Differentiating the Gaussian profile, we obtain

$$\frac{dI_G}{d\theta} = -\frac{1}{\sigma^2}(\theta-\theta_0)\exp\left\{-\left(\frac{\theta-\theta_0}{\sqrt{2}\sigma}\right)^2\right\}, \qquad \textbf{(9.14.)}$$

so that

$$\Delta\beta = \frac{n\beta}{\ln(2)} = \frac{\beta}{SNR\cdot\ln(2)}. \qquad \textbf{(9.15.)}$$

The uncertainty in the peak width is proportional to the peak width,

$$\Delta\beta = C_w\beta, \qquad \textbf{(9.16.)}$$

with a constant of proportionality

$$C_w = \frac{1}{SNR\cdot\ln(2)} = \frac{1}{\sqrt{N_{Eff}}\cdot\ln(2)}. \qquad \textbf{(9.17.)}$$

9.1.2. Lorentzian Diffraction Profile.

Although uniform composition metamorphic layers often exhibit diffraction profiles which closely resemble Gaussian profiles [288], x-ray profiles from high quality substrate crystals or pseudomorphic epitaxial layers are sometimes more Lorentzian in character [287]. It is therefore of interest to consider a normalized Lorentzian profile given by

$$I_L(\theta) = \frac{\left(\frac{\beta}{2}\right)^2}{(\theta-\theta_0)^2 + \left(\frac{\beta}{2}\right)^2}, \qquad \textbf{(9.18.)}$$

where θ_0 is the center of the Lorentzian peak and β is the FWHM. Similar to the Gaussian analysis, if a noise signal $\eta(\theta)$ of amplitude n is added, where n << 1, the resultant profile is

$$I_L(\theta) = \frac{\left(\frac{\beta}{2}\right)^2}{(\theta-\theta_0)^2 + \left(\frac{\beta}{2}\right)^2} + \eta(\theta). \qquad \textbf{(9.19.)}$$

The added noise may shift the apparent peak position by an amount $\Delta\theta$, where

$$1-n = \frac{\left(\frac{\beta}{2}\right)^2}{\Delta\theta^2 + \left(\frac{\beta}{2}\right)^2}. \qquad \textbf{(9.20.)}$$

Solving, we obtain

$$\Delta\theta = \frac{\beta}{2}\sqrt{\frac{n}{1-n}}. \qquad \textbf{(9.21.)}$$

Similar to the Gaussian case, the uncertainty in the peak position is proportional to the peak width,

$$\Delta\theta = C_P\beta, \qquad \textbf{(9.22.)}$$

where the constant of proportionality is

$$C_P = \frac{1}{2}\sqrt{\frac{1}{SNR-1}} = \frac{1}{2}\sqrt{\frac{1}{\sqrt{N_{Eff}}-1}}. \qquad \textbf{(9.23.)}$$

The introduction of noise also affects the determination of the peak width similar to the case of the Gaussian profile. For a normalized Lorentzian profile the maximum displacement of the half-intensity point, which is the error in the half width at half maximum (HWHM) is

$$\frac{\Delta\beta}{2} = n\left|\left(\left.\frac{dI_L}{d\theta}\right|_{\theta=\theta_0+\beta/2}\right)^{-1}\right|. \qquad \textbf{(9.24.)}$$

Differentiating the Lorentzian profile, we obtain

$$\frac{dI_L}{d\theta} = \frac{2(\theta-\theta_0)\left(\frac{\beta}{2}\right)^2}{\left((\theta-\theta_0)^2+\left(\frac{\beta}{2}\right)^2\right)^2}, \qquad \textbf{(9.25.)}$$

so that

$$\Delta\beta = 2n\beta = \frac{2\beta}{SNR}. \qquad \textbf{(9.26.)}$$

The uncertainty in the peak width is proportional to the peak width,

$$\Delta\beta = C_w\beta, \qquad \textbf{(9.27.)}$$

with a constant of proportionality

$$C_w = \frac{2}{SNR} = \frac{2}{\sqrt{N_{Eff}}}. \qquad \textbf{(9.28.)}$$

9.2. Strain Resolution from Peak Position and Width

The center and the FWHM of a Gaussian or Lorentzian peak may be determined precisely in the absence of noise regardless of the peak FWHM. However, x-ray emission and detection are random processes subject to noise and this introduces errors in the measurement of both the peak position and FWHM. Moreover, both of these errors are directly proportional to the width of the peak as shown above. The sensitivity of the x-ray diffraction method with respect to peak position measurements is limited by the uncertainty in the peak separation, and may be analyzed by differentiating the Bragg law [290],

$$2d\sin(\theta_B) = n\lambda, \tag{9.29.}$$

where d is the interplanar spacing, θ_B is the Bragg angle, n is the order of reflection and λ is the x-ray wavelength. The differentiation of the Bragg law with respect to θ_B yields [290]

$$\frac{\Delta d}{d} = -\Delta\theta_B \cot(\theta_B). \tag{9.30.}$$

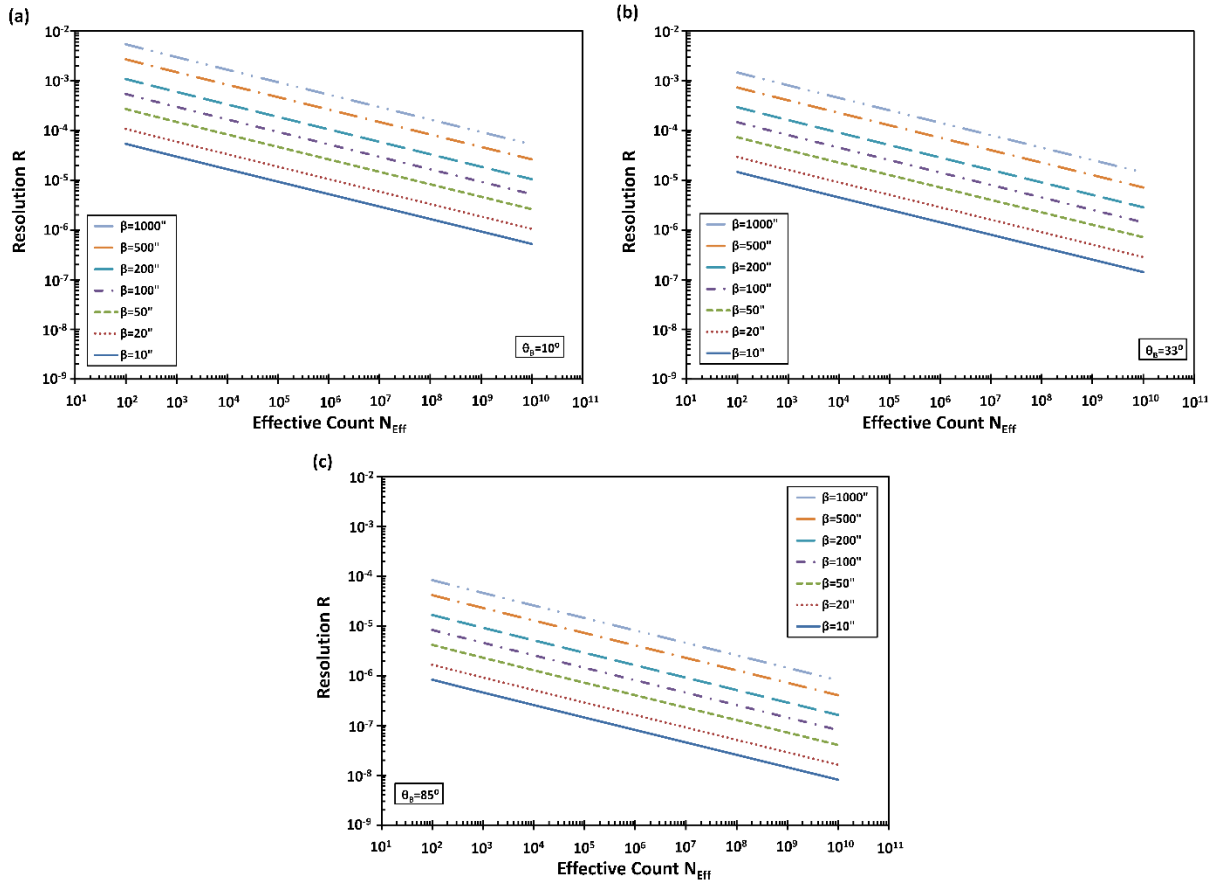

Figure 9.1. Resolution of x-ray diffraction from measurements of a Gaussian peak position as a function of the effective count for various full-width-at-half-maximums at Bragg angles of a) 10°, b) 33° and c) 85°.

If the lattice is tetragonally distorted and a symmetric reflection is considered, the resolution is equal to the amount of strain (change in interplanar spacing) which corresponds to the minimum peak shift that may be detected:

$$\mathrm{R}_{\mathrm{P}}^{\mathrm{G,L}} = \frac{2\nu}{1-\nu}\left|\frac{\Delta d}{d}\right| = \frac{2\nu}{1-\nu}\mathrm{C}_{\mathrm{P}}^{\mathrm{G,L}}\beta\cot(\theta_B)\,. \qquad \textbf{(9.31.)}$$

where ν is the Poisson ratio and $\mathrm{C}_{\mathrm{P}}^{\mathrm{G}}$ and $\mathrm{C}_{\mathrm{P}}^{\mathrm{L}}$ are the Gaussian and Lorentzian constant of proportionality respectively. Measurements of the peak width are commonly used to determine defect densities by determining the FWHM and the broadening of the rocking curve width due to the presence of dislocations. For this work, we have assumed that the minimum detectable broadening β_{min} corresponds to the uncertainty in the broadening $\Delta\beta$ or in other words $\beta_{min} = \Delta\beta$. Assuming that the rocking curve broadening is dominated by the angular mosaic spread rather than the d-spacing mosaic spread, then the minimum broadening is related to the minimum detectable threading dislocation D_{min} by

$$\beta_{\mathrm{min}}^2 = 4.36b^2\mathrm{D}_{\mathrm{min}}^2\,, \qquad \textbf{(9.32.)}$$

where b is the length of the Burgers vector [291,292].

If we assume two orthogonal misfit dislocation (MD) arrays with the same average misfit dislocation length L and that each misfit dislocation has x threading dislocations D associated with it, then the misfit dislocation density ρ_{MD} is given as

$$\rho_{MD} = \frac{DL}{2x}\,. \qquad \textbf{(9.33.)}$$

The value of x can be 0 if both ends of the misfit dislocations terminate at the sides of the bottom of the substrate, 1 corresponding to the bending over of a substrate threading dislocation or 2 corresponding to a half loop introduced at the surface of the epilayer. The average misfit dislocation length L may be estimated by

$$L = \sqrt{\frac{2x}{D}} \,. \qquad \textbf{(9.34.)}$$

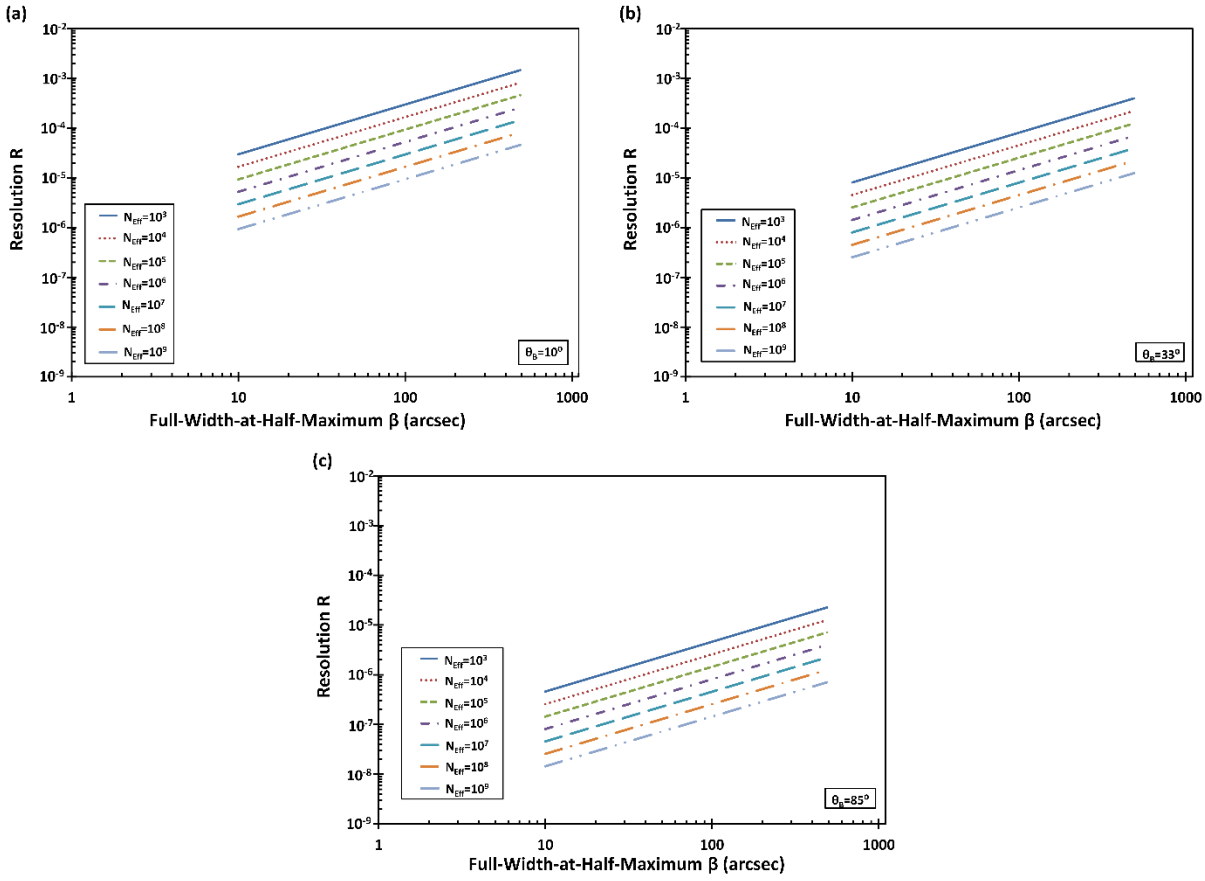

Figure 9.2. Resolution of x-ray diffraction from measurements of a Gaussian peak position as a function of the full-width-at-half-maximum for various effective counts at different Bragg of a) 10º, b) 33º and c) 85º.

Therefore, the sensitivity (resolution) from peak width measurements in the presence of defects is

$$\begin{aligned} \mathrm{R}_{\mathrm{W}}^{\mathrm{G,L}} &= \rho_{MD} b \cos(\alpha)\cos(\phi) \\ &= \frac{1}{\sqrt{4.36x}} \mathrm{C}_{\mathrm{W}}^{\mathrm{G,L}} \beta \cos(\alpha)\cos(\phi) \end{aligned}, \qquad \textbf{(9.35.)}$$

where α is the angle between the Burgers and line vector, ϕ is the angle between the interface and normal to the slip plane and C_W^G and C_W^L are the Gaussian and Lorentzian constant of proportionality respectively.

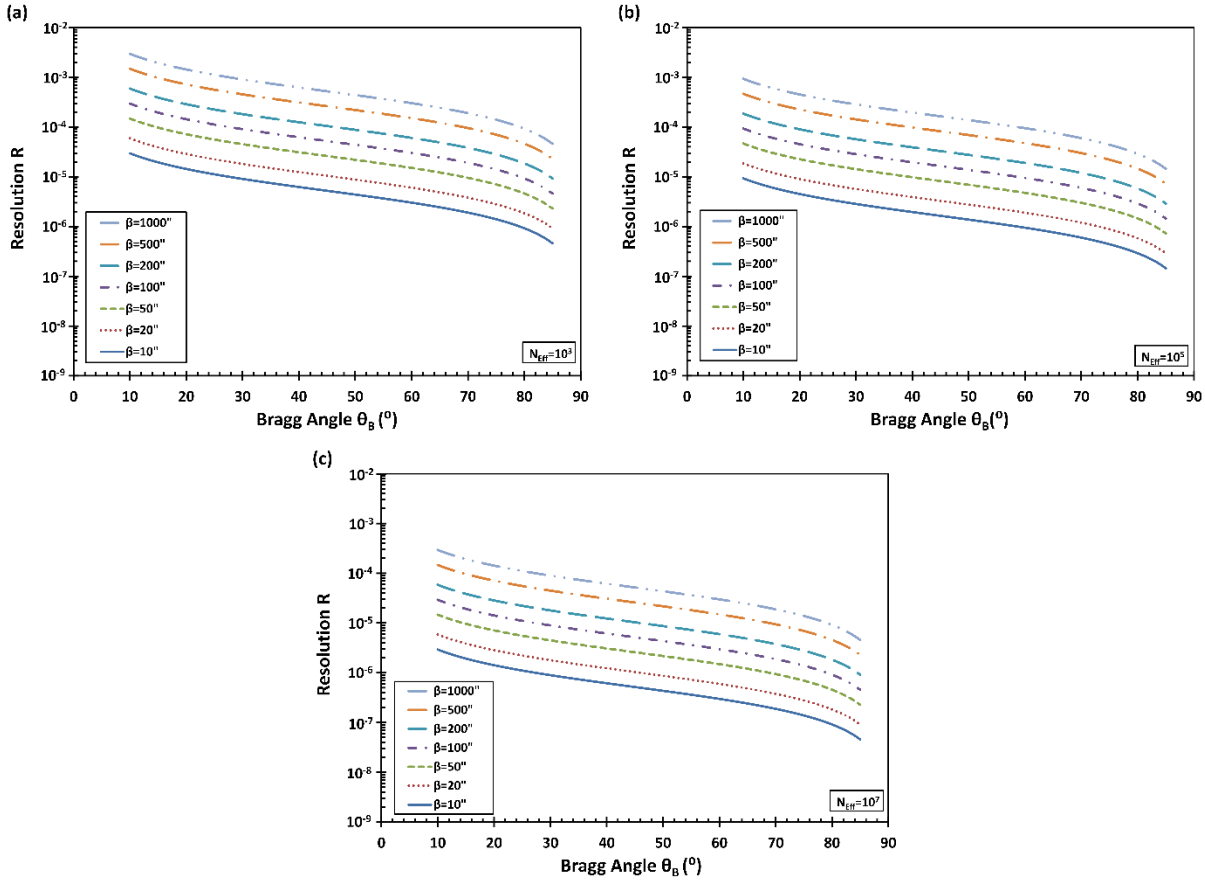

Figure 9.3. Resolution of x-ray diffraction from measurements of a Gaussian peak position as a function of the Bragg angle for various full-width-at-half maximums at effective counts of a) 10^3, b) 10^5 and 10^7.

Figure 9.1 through Figure 9.8 illustrate the resolution (R) of x-ray diffraction from measurements of the peak position and peak width for a Gaussian (Figure 9.1 - Figure 9.3, Figure

9.7) and Lorentzian (Figure 9.4 - Figure 9.6, Figure 9.8) distribution profile in presence of statistical noise. The sensitivity of the x-ray diffraction method from peak position measurements may be calculated by determining the uncertainty in the peak separation. Figure 9.1 through Figure 9.6 explore the three-dimensional space of resolution as a function of the effective count (N_{Eff}), full-width-at-half maximum (FWHM) and Bragg angle (θ_B). In addition, the resolution of x-ray diffraction profiles which may be Gaussian or Lorentzian in character are calculated and shown as functions of the effective count (Figure 9.1 and Figure 9.4 respectively), full-width-at-half-maximum (Figure 9.2 and Figure 9.5) and Bragg angle (Figure 9.3 and Figure 9.6) respectively. For these calculations, we have used Equation 9.31 and assumed a Poisson ratio $\nu=1/3$. Here, we have explored ranges of the effective count, FWHM and Bragg angle spanning 10^2 - 10^{10} counts, 10`` - 1000`` and 10˚ - 85˚ respectively.

For both types of diffraction profiles, the results of Figure 9.1 through Figure 9.6 demonstrate that the resolution is directly proportional to the full-width-at-half- maximum, varies with the Bragg angle and decreases monotonically with the effective number of counts. In contrast, the x-ray profiles which are Lorentzian in character give rise to higher (sensitive) resolution values for similar conditions of N_{Eff}, FWHM and θ_B. In addition, the results of Figure 9.1 through Figure 9.6 show that there is a strong (weak) dependence of the resolution on the effective count (FWHM). For the cases studied here, the three-dimensional resolution space of x-ray diffraction measurements indicates that possible resolution values are in the order of 10^{-2} – 10^{-9}. Sensitive resolution values may be achieved with higher effective count, FHWM and Bragg angle.

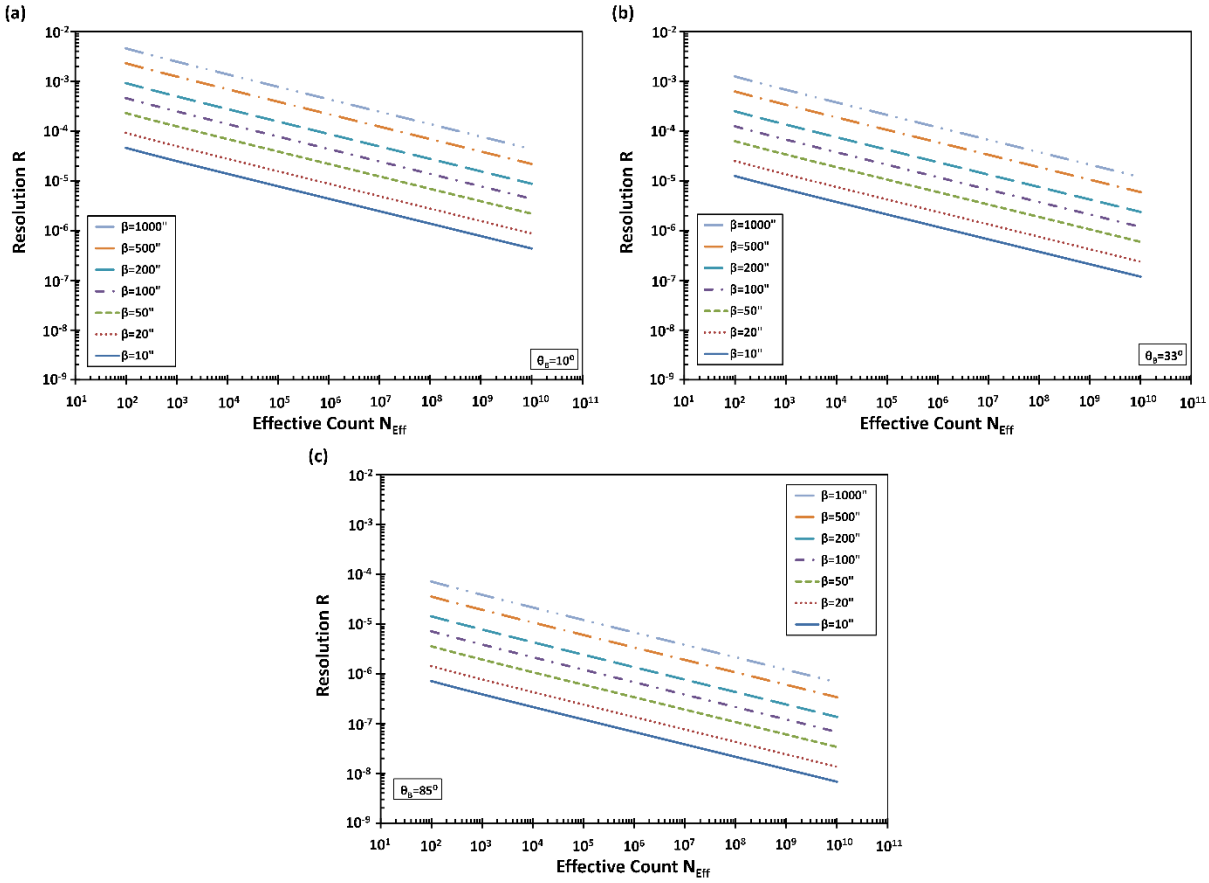

Figure 9.4. Resolution of x-ray diffraction from measurements of a Lorentzian peak position as a function of the effective count for various full-width-at-half-maximums at Bragg angles of a) 10º, b) 33º and c) 85º.

Measurements of the uncertainty in the peak width is commonly used to detect defect densities by determining the FWHM and the broadening of the rocking curve width due to the presence of dislocations. Using Equation 9.35, we have calculated the strain resolution of x-ray diffraction profiles from measurements of the peak width. In this part of the work, we have assumed that each misfit dislocation has two threading dislocations (x=2) associated with it and the angles associated with the slip plane are α, ϕ = 60º. Figure 9.7 and Figure 9.8 explore the resolution from measurements of the peak width for x-ray diffraction profiles which have a

Gaussian or Lorentzian distribution profile. The conditions (effective count and FWHM) explored here are similar to those used previous in Figure 9.1 to Figure 9.6.

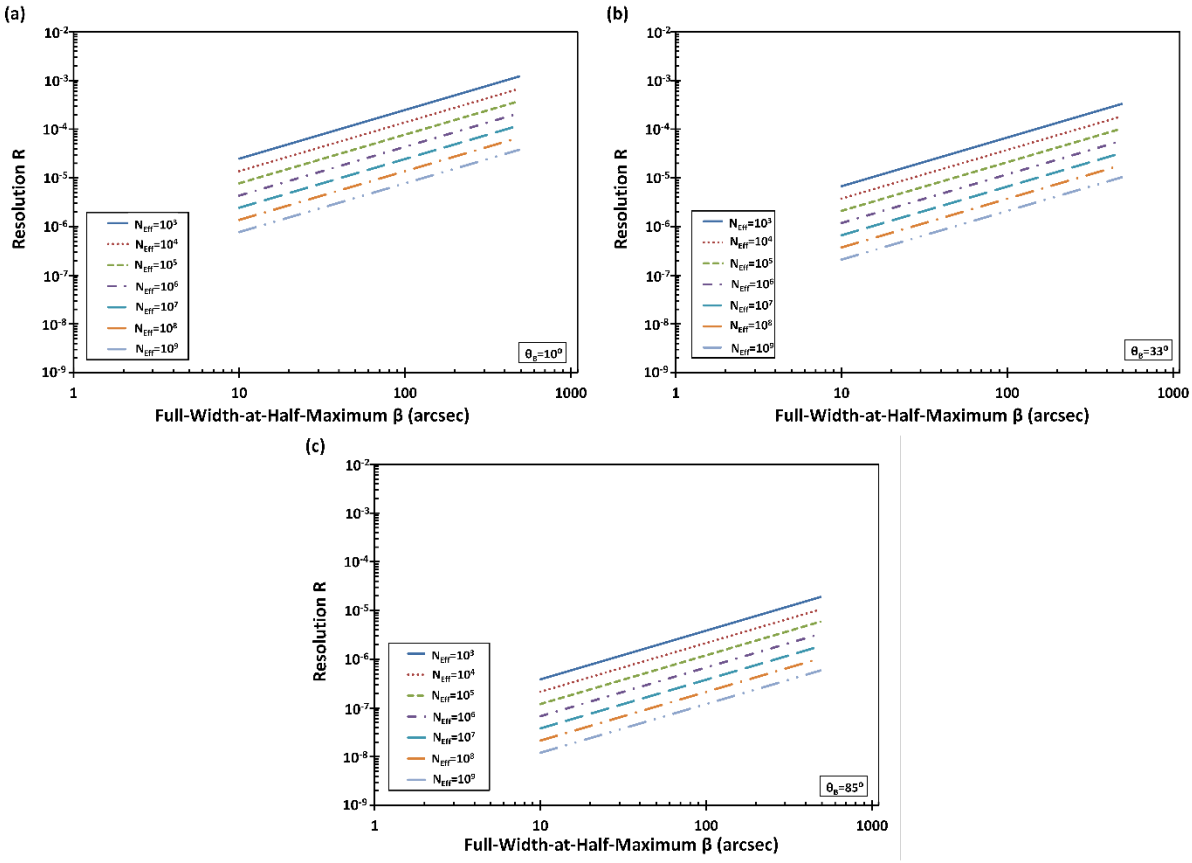

Figure 9.5. Resolution of x-ray diffraction from measurements of a Lorentzian peak position as a function of the full-width-at-half-maximum for various effective counts at Bragg angles of a) 10º, b) 33º and c) 85º.

The results of Figure 9.7 and Figure 9.8 show that the resolution decreases monotonically with the effective number of counts and is directly proportional to the full-width-at-half-maximum similar to measurements involving peak position determination. However, in comparison to peak position measurements, the results of Figure 9.7 and Figure 9.8 indicate that diffraction profiles from peak width measurements yield improved resolution spanning to the 10^{-10} regime. In addition, the dependence of the resolution on the effective count and full-width-at-half-maximum is more

pronounced; there is higher separation between the curves of the resolution as a function of the full-width-at-half- maximum. Also, there is a stronger dependence of the resolution on the effective count where values of 10^{9} yielded resolution in the order of 10^{-10}. Moreover, the results of Figure 9.1 to Figure 9.8 indicate that a Gaussian distribution profile yields higher resolution values in comparison to Lorentzian.

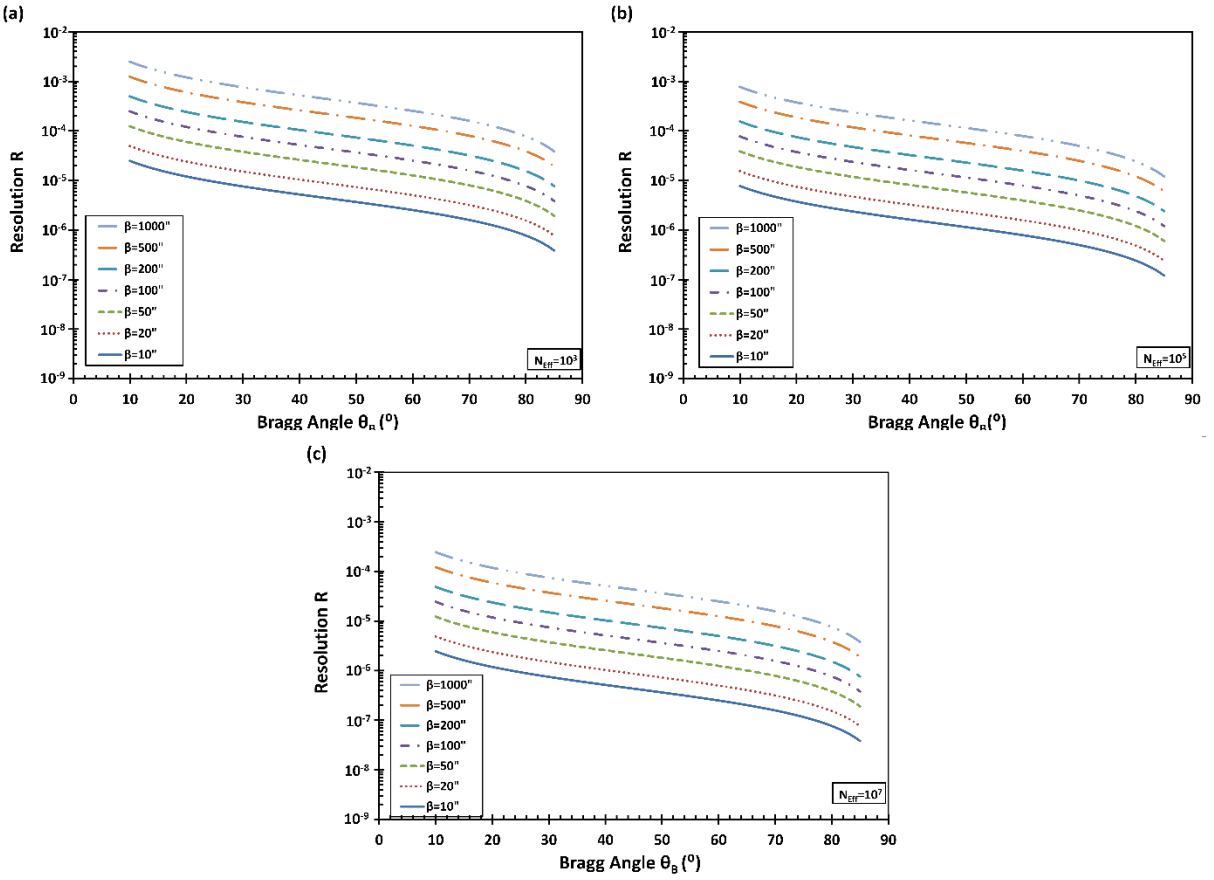

Figure 9.6. Resolution of x-ray diffraction from measurements of a Lorentzian peak position as a function of the Bragg angles for various full-width-at-half maximums at effective counts of a) 10^{3}, b) 10^{5} and 10^{7}.

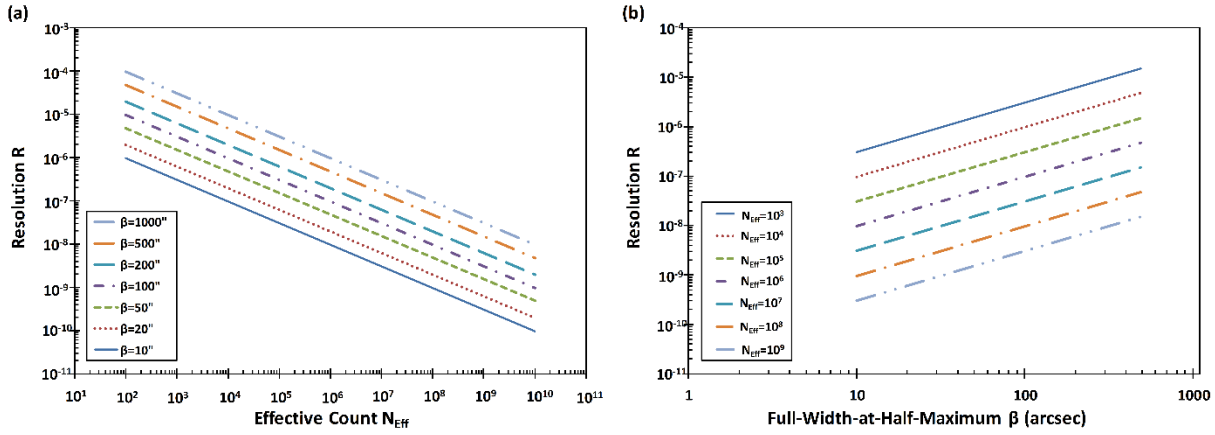

Figure 9.7. Resolution of x-ray diffraction from measurements of a Gaussian peak width as a function of the a) effective count for various full-width-at-half maximum and b) full-width-at-half-maximum for various effective counts.

In general, the sensitivities of the two x-ray methods (peak position and width) may be compared using the ratio

$$P^G = \frac{R_P}{R_W} = \frac{\nu\sqrt{4.36x}\cot(\theta_B)}{(1-\nu)\cos(\alpha)\cos(\phi)}\sqrt{-N_{Eff}\ln(2)\ln\left(1-\frac{1}{\sqrt{N_{Eff}}}\right)}. \quad \textbf{(9.36.)}$$

and

$$P^L = \frac{R_P}{R_W} = \frac{\nu\sqrt{4.36x}\cot(\theta_B)}{(1-\nu)\cos(\alpha)\cos(\phi)}\sqrt{\frac{N_{Eff}}{N_{Eff}-1}}. \quad \textbf{(9.37.)}$$

If P > 1, then the peak width measurement method is preferred, otherwise the peak position measurements yield higher sensitivities (resolution). Therefore, in the most general case, the resolution of x-ray rocking curve measurements for the purpose of determining the residual strain and/or the extent of lattice relaxation depends on multiple factors such as the effective count, FWHM, and Bragg angle. From a practical point of view the above analysis could be easily applied to experimental rocking curves as long as the peak number of counts, FWHM, and the Bragg angles are given. However, depending on the type of measurement, whether one wants to detect

changes in the local strain (shift in the peak position of the x-ray rocking curve) or sense the presence of dislocations (broadening in the x-ray rocking curve) correct application of Equation 9.31 or 9.35 is required to determine the sensitivity of the measurement. For example, the measured x-ray rocking curve for the 004 reflection provided by Healey et al. [288] for a ZnSe epilayer measured with Cu kα_1 radiation exhibited a peak intensity of 1250 counts and a FWHM of 160 arc sec (7.76 x 10^{-4} rad). Points were measured with a spacing of 2 arc sec and the diffraction profile was shown to be Gaussian in character. Solving self-consistently for C_P and N_{eff}, we find C_P = 0.060207 and N_{eff} = 10,000 counts, corresponding to eight measured points. The strain resolution, assuming a Bragg angle of 33° and a Poisson ratio of 0.38, is 8.8 x 10^{-5} as determined on the basis of peak position. Therefore, in this case the attainment of the usually quoted strain resolution of 10^{-5} for high-resolution x-ray measurements would have required an increase of the count time by roughly a factor of 100.

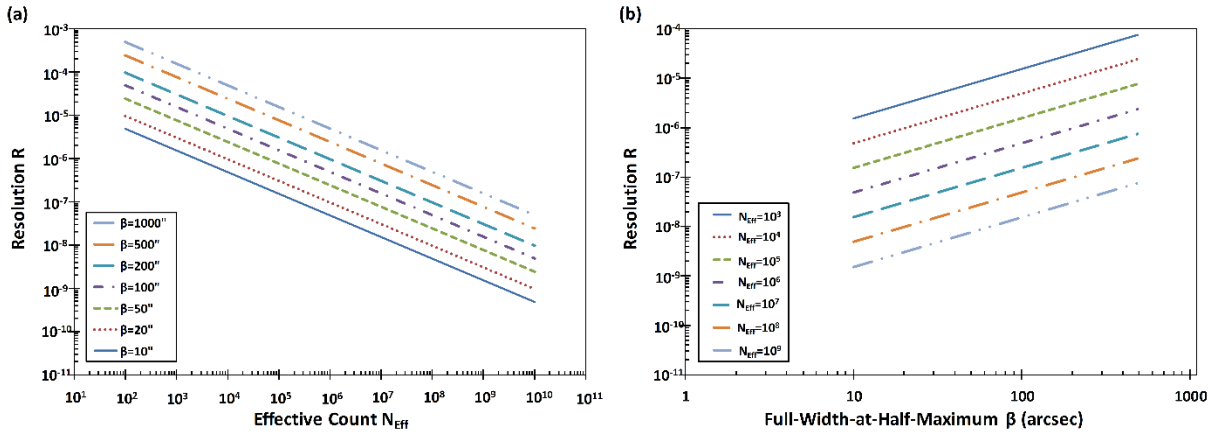

Figure 9.8. Resolution of x-ray diffraction from measurements of a Lorentzian peak width as a function of the a) effective count for various full-width-at-half maximum and b) full-width-at-half-maximum for various effective counts.

In conclusion, the resolution or sensitivity of an x-ray diffraction profile depends on the width and shape of the diffraction peak being measured as well as the counting statistics employed

for its measurement. When analyzing x-ray diffraction profiles from measurements of the peak position and peak width, the resolution (i) decreases monotonically with the effective number of counts, (ii) is directly proportional to the FWHM, and (iii) is dependent on the Bragg angle. It is therefore necessary that the peak number of counts (count rate times count time) should always be provided with any x-ray diffraction method to determine the sensitivity of the measurements. In addition, the choice of x-ray measurement method is essential for accurate determination of diffraction profiles. In the presence of statistical noise, the determination of the extent of relaxation from a change in the local strain requires precise measurement of the change in the peak position. Furthermore, the presence of dislocations within the crystal material produces a broadening in the peak width of the x-ray rocking curve. The sensitivity of detecting a shift in the peak position or a change in the peak width is greatly enhanced with a higher effective count and a lower FWHM.

10. General Conclusion and Future Refinements

In summary, we have developed two of the leading models in the field of heteroepitaxy for understanding the thermal equilibrium and kinetically-limited lattice relaxation of semiconductor heterostructures. An important aspect of this work is that these models are applicable to multilayered and compositionally-graded epitaxial layers. Furthermore, we have also developed an electrical circuit analogy for understanding the equilibrium analysis of strained-layer structures. The development of the circuit model represents a significant breakthrough in the analysis of semiconductor heterostructures, in that it enables equilibrium calculations to be performed by widely-available circuit simulators. More importantly, the circuit model allows intuitive understanding of electric circuits to be readily applied to strained-layer semiconductor structures, promoting innovative design of new multilayered and graded structures. The model enables the development of closed-form solutions for strains and dislocation densities in superlattice and multi quantum well structures, as well as other multilayered structures, which should facilitate improved design of device heterostructures. The circuit model approach therefore represents a transformative innovation in the field of semiconductor strained-layer structures, and an important tool in the development of devices built using these strained-layers, including high-speed transistors, semiconductor lasers, and light emitting diodes.

Though the equilibrium analysis of semiconductor strained-layer heterostructures is important in its own right, for the determination of device stability criteria, it also serves as the starting point for the analysis of kinetically-limited relaxation and non-equilibrium defects such as threading dislocations. From a fabrication point of view, the understanding of the effect of growth kinetics plays an important role in the design of heterostructure devices which exhibits desired strain characteristics and reduced threading defects. Therefore, the developed plastic flow detailed

in this thesis enables crystal growers to understand the relaxation mechanisms associated with various growth process. More specifically we have shown how to design multilayered heterostructures by either tailoring the strain of dislocation profiles. First, we demonstrated that the dislocation compensation mechanism, whereby threading dislocations can be removed by insertion of a mismatched interface in a graded structure, can be explained by the bending over of threading dislocations associated with misfit segments of one sense by misfit dislocations having the opposite sense. For each structure type, we studied the requirements on the thickness and compositional profile in the buffer layer for the elimination of all mobile threading dislocations from the device layer as well as the allowed tolerance in compositional overshoot to achieve structures with low threading dislocation densities. Second, we demonstrated the incorporation of a temperature grading scheme in which we can control the various stages of lattice relaxation by limiting the enhancement of dislocation glide and therefore the lattice relaxation rates.

At the time of the completion of this thesis, Dr. John E. Ayers and I had many works in the process which are unpublished at the time however warrant a quick mention in order to show the future direction of our research. One of our areas of focus include the development of an electrical circuit model applicable to understanding the kinetically-limited lattice relaxation. Though a complex problem to solve, at the current time we have made some progress into developing a simple electrical circuit, however more work is needed to bring this work into fruition. Another key focus includes refinement of the current plastic flow model to account for dislocation pinning but also correctly model the threading dislocation behavior involving thermal annealing processes.

11. Appendix

11.1. Detailed Derivation of z_1 and z_2 for the NLG-MBL

In order to find z_1 and z_2 we differentiate the sum of the strain and dislocation line energy with respect to each, set these partial derivatives to zero, and solve. We assume a diamond or zinc blende crystal structure with (001) orientation and biaxial strain. The strain energy per unit area is

$$E_\varepsilon = \int_0^h Y\varepsilon_{\parallel}^{\,2} dz = \int_0^h Y\left[f(z) + b' \int_0^z \rho(\xi) d\xi \right]^2 dz, \qquad \textbf{(11.1)}$$

where $\rho(z)$ is the misfit dislocation density, b' is the misfit relieving component of the Burgers vector parallel to the interface, $b' = \pm b \sin\alpha \sin\phi$, where b is the length of the Burgers vector, α is the angle between the Burgers vector and the line vector, and λ is the angle between the Burgers vector and the line in the interface plane which is perpendicular to the intersection of the glide plane with the interface, Y is the biaxial modulus, $Y = C_{11} + C_{12} - 2C_{12}^2 / C_{11}$, and C_{11} and C_{12} are the elastic stiffness constants. The line energy of dislocations per unit area, assuming two orthogonal networks with equal cross-sectional density, is

$$E_d = 2\int_0^h F_d(z)\rho_A(z) dz, \qquad \textbf{(11.2)}$$

where

$$F_d(z) \approx \frac{G(z)b^2(z)\left[1-\nu(z)\cos^2\alpha\right]}{4\pi(1-\nu(z))}\left[Ln\left(\frac{h-z}{b(z)}\right) + 1 \right], \qquad \textbf{(11.3)}$$

G is the shear modulus, $G = (C_{11} - C_{12})/2$, and ν is the Poisson ratio, $\nu = C_{12}/(C_{11} + C_{12})$ for the (001) orientation.

To find the equilibrium values z_1 and z_2 we solve the equations

$$0 = \frac{\partial(E_d + E_\varepsilon)}{\partial z_1} = \frac{\partial E_d}{\partial z_1} + \frac{\partial E_\varepsilon}{\partial z_1}, \qquad \textbf{(11.4)}$$

and

$$0 = \frac{\partial\left(E_d + E_\varepsilon\right)}{\partial z_2} = \frac{\partial E_d}{\partial z_2} + \frac{\partial E_\varepsilon}{\partial z_2}, \qquad \textbf{(11.5)}$$

The equilibrium misfit dislocation density profile in the partially-relaxed logarithmically-graded layer is given by

$$\rho = \begin{cases} 0, & z < z_1; \\ \dfrac{m(f_h - f_0)}{b'(h+z)} \dfrac{Ln^{m-1}\left(1+\dfrac{z}{h}\right)}{Ln^m(2)}, & z_1 \le z \le z_2; \text{ and}, \\ 0, & z > z_2. \end{cases} \qquad \textbf{(11.6)}$$

so, the dislocation line energy per unit area is

$$\begin{aligned} E_d &= 2\int_{z_1}^{z_2} F_d(z)\rho(z)dz \\ &= 2\int_{z_1}^{z_2} \left\{ \frac{Gb^2\left(1-\nu\cos^2\alpha\right)}{4\pi(1-\nu)} \left[Ln\left(\frac{h-z}{b}\right)+1 \right] \right\} \left\{ \frac{m(f_h - f_0)}{b'(h+z)} \frac{Ln^{m-1}\left(1+\dfrac{z}{h}\right)}{Ln^m(2)} \right\} dz, \qquad \textbf{(11.7)} \\ &= C\int_{z_1}^{z_2} \left[Ln\left(\frac{h-z}{b}\right)+1 \right] \frac{Ln^{m-1}\left(1+\dfrac{z}{h}\right)}{(h+z)Ln^m(2)} dz \end{aligned}$$

where

$$C = \frac{Gbm(f_h - f_0)\left(1-\nu\cos^2\alpha\right)}{2\pi\sin\alpha\cos\lambda(1-\nu)}, \qquad \textbf{(11.8)}$$

The dislocation energy integral for a sublinearly-graded layer with $m = 1$ is given by

$$E_d = C\left.\frac{Ln(h+z)+Ln\left(\frac{h-z}{b}\right)Ln\left(\frac{h+z}{2h}\right)-Li_2\left(\frac{h-z}{2h}\right)}{Ln(2)}\right|_{z_1}^{z_2}$$

$$= \frac{C}{Ln(2)}\left(\begin{array}{l} Ln(h+z_2)+Ln\left(\frac{h-z_2}{b}\right)Ln\left(\frac{h+z_2}{2h}\right)-Li_2\left(\frac{h-z_2}{2h}\right) \\ -\left(Ln(h+z_1)+Ln\left(\frac{h-z_1}{b}\right)Ln\left(\frac{h+z_1}{2h}\right)-Li_2\left(\frac{h-z_1}{2h}\right)\right)\end{array}\right), \quad \textbf{(11.9)}$$

The dislocation energy integral for a superlinearly-graded layer with $m=2$ is given by

$$E_d = \frac{C}{2Ln^2(2)}\left[\begin{array}{l} Ln^2\left(1+\frac{z}{h}\right)\left(1+Ln\left(\frac{2(h-z)}{b}\right)-Ln\left(1-\frac{z}{h}\right)\right) \\ -2Ln\left(1+\frac{z}{h}\right)Li_2\left(\frac{h+z}{2h}\right)+2Li_3\left(\frac{h+z}{2h}\right)\end{array}\right]_{z_1}^{z_2}$$

$$= \frac{C}{2Ln^2(2)}\left(\begin{array}{l}\left[\begin{array}{l} Ln^2\left(1+\frac{z_2}{h}\right)\left(1+Ln\left(\frac{2(h-z_2)}{b}\right)-Ln\left(1-\frac{z_2}{h}\right)\right) \\ -2Ln\left(1+\frac{z_2}{h}\right)Li_2\left(\frac{h+z_2}{2h}\right)+2Li_3\left(\frac{h+z_2}{2h}\right)\end{array}\right] \\ -\left[\begin{array}{l} Ln^2\left(1+\frac{z_1}{h}\right)\left(1+Ln\left(\frac{2(h-z_1)}{b}\right)-Ln\left(1-\frac{z_1}{h}\right)\right) \\ -2Ln\left(1+\frac{z_1}{h}\right)Li_2\left(\frac{h+z_1}{2h}\right)+2Li_3\left(\frac{h+z_1}{2h}\right)\end{array}\right]\end{array}\right). \quad \textbf{(11.10)}$$

The dislocation energy integral for superlinearly-graded layer with $m=3$ is given by

$$E_d = \frac{C}{3Ln^3(2)}\left[\begin{array}{l} Ln^3\left(1+\frac{z}{h}\right)\left(1+Ln\left(\frac{2(h-z)}{b}\right)-Ln\left(1-\frac{z}{h}\right)\right) \\ -3Ln^2\left(1+\frac{z}{h}\right)Li_2\left(\frac{h+z}{2h}\right)+6Ln\left(1+\frac{z}{h}\right)Li_3\left(\frac{h+z}{2h}\right)-6Li_4\left(\frac{h+z}{2h}\right)\end{array}\right]\Bigg|_{z_1}^{z_2}$$

$$= \frac{C}{3Ln^3(2)}\left[\begin{array}{l} Ln^3\left(1+\frac{z_2}{h}\right)\left(1+Ln\left(\frac{2(h-z_2)}{b}\right)-Ln\left(1-\frac{z_2}{h}\right)\right) \\ -3Ln^2\left(1+\frac{z_2}{h}\right)Li_2\left(\frac{h+z_2}{2h}\right)+6Ln\left(1+\frac{z_2}{h}\right)Li_3\left(\frac{h+z_2}{2h}\right)-6Li_4\left(\frac{h+z_2}{2h}\right) \\ -\left(\begin{array}{l} Ln^3\left(1+\frac{z_1}{h}\right)\left(1+Ln\left(\frac{2(h-z_1)}{b}\right)-Ln\left(1-\frac{z_1}{h}\right)\right) \\ -3Ln^2\left(1+\frac{z_1}{h}\right)Li_2\left(\frac{h+z_1}{2h}\right)+6Ln\left(1+\frac{z_1}{h}\right)Li_3\left(\frac{h+z_1}{2h}\right)-6Li_4\left(\frac{h+z_1}{2h}\right)\end{array}\right)\end{array}\right], \quad \textbf{(11.11)}$$

The partial derivatives of the strain energy per unit area with respect to z_1 and z_2 for power grading coefficient m are given by:

$$\frac{\partial E_d}{\partial z_1} = -C\left[Ln\left(\frac{h-z_1}{b}\right)+1\right]\frac{Ln^{m-1}\left(1+\frac{z_1}{h}\right)}{(h+z_1)Ln^m(2)}, \quad \textbf{(11.12)}$$

and

$$\frac{\partial E_d}{\partial z_2} = C\left[Ln\left(\frac{h-z_2}{b}\right)+1\right]\frac{Ln^{m-1}\left(1+\frac{z_2}{h}\right)}{(h+z_2)Ln^m(2)}, \quad \textbf{(11.13)}$$

The equilibrium in-plane strain profile is given by

$$\varepsilon_{\|} = \begin{cases} f_0 + (f_h - f_0)\dfrac{Ln^m\left(1+\dfrac{z}{h}\right)}{Ln^m(2)}, & z < z_1; \\ f_0 + (f_h - f_0)\dfrac{Ln^m\left(1+\dfrac{z_1}{h}\right)}{Ln^m(2)}, & z_1 \le z \le z_2; \text{ and} \\ f_0 + (f_h - f_0)\left[\dfrac{Ln^m\left(1+\dfrac{z}{h}\right)}{Ln^m(2)} + \dfrac{Ln^m\left(1+\dfrac{z_1}{h}\right)}{Ln^m(2)} - \dfrac{Ln^m\left(1+\dfrac{z_2}{h}\right)}{Ln^m(2)}\right], & z > z_2. \end{cases} \quad \textbf{(11.14)}$$

The strain energy per unit area is

$$E_\varepsilon = Y\int_0^{z_1}\left[f_0 + (f_h - f_0)\frac{Ln^m\left(1+\frac{z}{h}\right)}{Ln^m(2)}\right]dz$$
$$+ Y\int_{z_1}^{z_2}\left[f_0 + (f_h - f_0)\frac{Ln^m\left(1+\frac{z_1}{h}\right)}{Ln^m(2)}\right]dz \quad , \quad \textbf{(11.15)}$$
$$+ Y\int_{z_2}^{h}\left[f_0 + (f_h - f_0)\left(\frac{Ln^m\left(1+\frac{z}{h}\right)}{Ln^m(2)} + \frac{Ln^m\left(1+\frac{z_1}{h}\right)}{Ln^m(2)^m} - \frac{Ln^m\left(1+\frac{z_2}{h}\right)}{Ln^m(2)}\right)\right]dz$$

This can be written as

$$E_\varepsilon = I_1 + I_2 + I_3, \quad \textbf{(11.16)}$$

where

$$I_1 = Y\int_0^{z_1}\left[f_0 + (f_h - f_0)\frac{Ln^m\left(1+\frac{z}{h}\right)}{Ln^m(2)}\right]dz, \quad \textbf{(11.17)}$$

$$I_2 = Y\int_{z_1}^{z_2}\left[f_0 + (f_h - f_0)\frac{Ln^m\left(1+\frac{z_1}{h}\right)}{Ln^m(2)}\right]dz\,, \qquad \textbf{(11.18)}$$

and

$$I_3 = Y\int_{z_2}^{h}\left[f_0 + (f_h - f_0)\left(\frac{Ln^m\left(1+\frac{z}{h}\right)}{Ln^m(2)} + \frac{Ln^m\left(1+\frac{z_1}{h}\right)}{Ln^m(2)} - \frac{Ln^m\left(1+\frac{z_2}{h}\right)}{Ln^m(2)}\right)\right]dz\,, \qquad \textbf{(11.19)}$$

The general form for the strain energy integral I_1 is given by

$$I_1 = Y\left[f_0 z_1 + \frac{(f_h - f_0)h}{Ln^m(2)}\left(-\frac{1}{h}\right)^{-m} m\left(\frac{1}{h}\right)^m Ln^{1+m}\left(1+\frac{z_1}{h}\right)\int_0^\infty t^{m-1}e^{-t}dt\int_1^\infty \frac{e^{Ln\left(1+\frac{z_1}{h}\right)t}}{t^{-m}}dt\right], \qquad \textbf{(11.20)}$$

For sublinearly-graded layer with $m=1$, I_1 is given by

$$I_1 = Y\left[f_0 z_1 - \frac{(f_h - f_0)}{Ln(2)}\left(-y_1 + (h+z_1)Ln\left(1+\frac{z_1}{h}\right)\right)\right], \qquad \textbf{(11.21)}$$

For superlinearly-graded layer with $m=2$, I_1 is given by

$$I_1 = Y\left[f_0 z_1 - \frac{(f_h - f_0)}{Ln^2(2)}\left(2z_1 + (h+z_1)\left(-2 + Ln\left(1+\frac{z_1}{h}\right)\right)Ln\left(1+\frac{z_1}{h}\right)\right)\right], \qquad \textbf{(11.22)}$$

For superlinearly-graded layer with $m=3$, I_1 is given by

$$I_1 = Y\left[f_0(z_1) + \frac{f_h - f_0}{Ln^2(2)}\left(-6z_1 + (h+z_1)Ln\left(1+\frac{z_1}{h}\right)\left(6 + \left(-3 + Ln\left(1+\frac{z_1}{h}\right)\right)Ln\left(1+\frac{z_1}{h}\right)\right)\right)\right], \qquad \textbf{(11.23)}$$

The strain energy integral I_2 is given by

$$I_2 = Y\left[f_0 + (f_h - f_0)\left(\frac{Ln\left(1+\frac{z_1}{h}\right)}{Ln(2)} \right)^m \right] z\Big|_{z_1}^{z_2} = Y(z_2 - z_1)\left[f_0 + (f_h - f_0)\left(\frac{Ln\left(1+\frac{z_1}{h}\right)}{Ln(2)} \right)^m \right], \qquad \textbf{(11.24)}$$

The strain energy integral I_3 is given by

$$I_3 = Y\left[f_0 + (z_2 - z_1)(f_h - f_0)\left(\left(\frac{Ln\left(1+\frac{z_1}{h}\right)}{Ln(2)} \right)^m - \left(\frac{Ln\left(1+\frac{z_2}{h}\right)}{Ln(2)} \right)^m \right) \right]$$
$$+ Y\left[\begin{array}{l} \frac{(f_h - f_0)h}{Ln^m(2)}\left(-\frac{1}{h}\right)^{-m} m\left(\frac{1}{h}\right)^m \int_0^\infty t^{m-1}e^{-t}dt \\ Ln^{1+m}(2)\int_1^\infty \frac{2^t}{t^{-m}}dt - Ln^{1+m}\left(1+\frac{z_1}{h}\right)\int_1^\infty \frac{e^{Ln\left(1+\frac{z_1}{h}\right)t}}{t^{-m}}dt \end{array} \right], \qquad \textbf{(11.25)}$$

For sublinearly-graded layer with $m = 1$, I_3 is given by

$$I_3 = Y\left[\begin{array}{l} (z_2 - z_1)\left[f_0 + (f_h - f_0)\left(\left(\frac{Ln\left(1+\frac{z_1}{h}\right)}{Ln(2)} \right) - \left(\frac{Ln\left(1+\frac{z_2}{h}\right)}{Ln(2)} \right) \right) \right] \\ \frac{(f_h - f_0)}{Ln(2)}\left(y_2 + h\left(Ln(4) - 1\right) - (h + z_2)Ln\left(1+\frac{z_2}{h}\right) \right) \end{array} \right], \qquad \textbf{(11.26)}$$

For superlinearly-graded layer with $m = 2$, I_3 is given by

$$I_3 = Y\left[\begin{array}{l} (z_2 - z_1)\left[f_0 + (f_h - f_0)\left(\left(\frac{Ln\left(1+\frac{z_1}{h}\right)}{Ln(2)} \right)^2 - \left(\frac{Ln\left(1+\frac{z_2}{h}\right)}{Ln(2)} \right)^2 \right) \right] \\ + \frac{(f_h - f_0)}{Ln^2(2)}\left(\begin{array}{l} 2h\left(2 + Ln^2(2) - Ln(4)\right) - \\ (h + z_2)\left(2 - 2Ln\left(1+\frac{z_2}{h}\right) + Ln^2\left(1+\frac{z_2}{h}\right) \right) \end{array} \right) \end{array} \right], \qquad \textbf{(11.27)}$$

For superlinearly-graded layer with $m=3$, I_3 is given by

$$I_3 = Y\left[\begin{array}{l}(z_2-z_1)\left[f_0+(f_h-f_0)\left(\left(\frac{Ln\left(1+\frac{z_1}{h}\right)}{Ln(2)}\right)^3-\left(\frac{Ln\left(1+\frac{z_2}{h}\right)}{Ln(2)}\right)^3\right)\right] \\ \frac{(f_h-f_0)}{Ln^3(2)}\left(\begin{array}{l}2h\left(-6+\left(Ln(2)-3\right)Ln^2(2)+Ln(64)\right) \\ -(h+z_2)\left(-6+Ln\left(1+\frac{z_2}{h}\right)\left(6+\left(Ln\left(1+\frac{z_2}{h}\right)-3\right)Ln\left(1+\frac{z_2}{h}\right)\right)\right)\end{array}\right)\end{array}\right], \quad \textbf{(11.28)}$$

The partial derivatives of I_1 are given by: for sublinearly-graded layer with

$m=1$,

$$\frac{\partial I_1}{\partial z_1} = Y\left[f_0+(f_h-f_0)Ln\left(1+\frac{z_1}{h}\right)\right], \quad \textbf{(11.29)}$$

superlinearly-graded layer with $m=2$,

$$\frac{\partial I_1}{\partial z_1} = Y\left[f_0+\frac{(f_h-f_0)}{Ln^2(2)}\left(2Ln\left(1+\frac{z_1}{h}\right)+\left(-2+Ln\left(1+\frac{z_1}{h}\right)\right)Ln\left(1+\frac{z_1}{h}\right)\right)\right], \quad \textbf{(11.30)}$$

superlinearly-graded layer with $m=3$,

$$\frac{\partial I_1}{\partial z_1} = Y\left[f_0+\frac{(f_h-f_0)}{Ln^3(2)}\left(\begin{array}{l}\left(-3+Ln\left(1+\frac{z_1}{h}\right)\right)Ln\left(1+\frac{z_1}{h}\right) \\ +Ln\left(1+\frac{z_1}{h}\right)\left(-3+Ln\left(1+\frac{z_1}{h}\right)+Ln\left(1+\frac{z_1}{h}\right)\right) \\ +Ln\left(1+\frac{z_1}{h}\right)\left(6+\left(-3+Ln\left(1+\frac{z_1}{h}\right)\right)Ln\left(1+\frac{z_1}{h}\right)\right)\end{array}\right)\right], \quad \textbf{(11.31)}$$

and for all nonlinearly-logarithmically-graded layers $m=1,\ 2$ and 3,

$$\frac{\partial I_1}{\partial z_2} = 0, \quad \textbf{(11.32)}$$

The partial derivatives of I_2 for $m=1,\ 2$ and 3 are given by

$$\frac{\partial I_2}{\partial z_1} = Y\left[\frac{(f_h - f_0)m(z_2 - z_1)}{(h + z_1)Ln^m(2)} Ln^{m-1}\left(1 + \frac{z_1}{h}\right) - \left[f_0 + (f_h - f_0)\left(\frac{Ln^m\left(1 + \frac{z_1}{h}\right)}{Ln^m(2)}\right)\right]\right], \quad \textbf{(11.33)}$$

and

$$\frac{\partial I_2}{\partial z_2} = Y\left[f_0 + (f_h - f_0)\frac{Ln^m\left(1 + \frac{z_1}{h}\right)}{Ln^m(2)}\right], \quad \textbf{(11.34)}$$

The partial derivatives of I_3 for $m = 1,\ 2$ and 3 are given by

$$\frac{\partial I_3}{\partial z_1} = Y\left[\begin{array}{l}\frac{(f_h - f_0)m(z_2 - z_1)}{(h + z_1)Ln^m(2)} Ln^{m-1}\left(1 + \frac{z_1}{h}\right) \\ -\left[f_0 + (f_h - f_0)\left(\frac{Ln^m\left(1 + \frac{z_1}{h}\right)}{Ln^m(2)} - \frac{Ln^m\left(1 + \frac{z_2}{h}\right)}{Ln^m(2)}\right)\right]\end{array}\right], \quad \textbf{(11.35)}$$

and

$$\frac{\partial I_3}{\partial z_2} = Y\left[\begin{array}{l}-\frac{(f_h - f_0)m(z_2 - z_1)}{(h + z_2)Ln^m(2)} Ln^{m-1}\left(1 + \frac{z_2}{h}\right) \\ +\left[f_0 + (f_h - f_0)\left(\frac{Ln^m\left(1 + \frac{z_1}{h}\right)}{Ln^m(2)} - \frac{Ln^m\left(1 + \frac{z_2}{h}\right)}{Ln^m(2)}\right)\right] \\ -\frac{(f_h - f_0)}{Ln^m(2)} Ln^m\left(1 + \frac{z_2}{h}\right)\end{array}\right], \quad \textbf{(11.36)}$$

The equilibrium values of z_1 and z_2 for a given power grading coefficient m are the solutions of

$$0 = \frac{\partial E_d}{\partial z_1} + \frac{\partial I_1}{\partial z_1} + \frac{\partial I_2}{\partial z_1} + \frac{\partial I_3}{\partial z_1}, \quad \textbf{(11.37)}$$

and

$$0 = \frac{\partial E_d}{\partial z_2} + \frac{\partial I_1}{\partial z_2} + \frac{\partial I_2}{\partial z_2} + \frac{\partial I_3}{\partial z_2}, \tag{11.38}$$

z_1 and z_2 can therefore be found from the simultaneous solution of the equations above. Numerical solution of the two preceding equations yields the values of z_1 and z_2 for given values of f_0, f_h, m, and h in a given material system.

11.2. Determination of z_1 and z_2 for the SG-SAL

In order to find z_1 and z_2 we differentiate the sum of the strain energy and dislocation line energy with respect to each, set these partial derivatives to zero, and solve. We assume a diamond or zinc blende crystal structure with (001) orientation and biaxial strain. The strain energy per unit area is

$$E_\varepsilon = \int_0^h Y\varepsilon_{\|}^{\,2} dz = \int_0^h Y\left[f(z) + b' \int_0^z \rho(\xi) d\xi \right]^2 dz, \tag{11.39}$$

where $\rho(z)$ is the misfit dislocation density, b' is the misfit relieving component of the Burgers vector parallel to the interface, $b' = \pm b \sin\alpha \sin\phi$, where b is the length of the Burgers vector, α is the angle between the Burgers vector and the line vector, and λ is the angle between the Burgers vector and the line in the interface plane which is perpendicular to the intersection of the glide plane with the interface, Y is the biaxial modulus, $Y = C_{11} + C_{12} - 2C_{12}^2 / C_{11}$, and C_{11} and C_{12} are the elastic stiffness constants. The line energy of dislocations per unit area, assuming two orthogonal networks with equal cross-sectional density, is

$$E_d = 2\int_0^h F_d(z)\rho(z)dz, \tag{11.40}$$

where

$$F_d(z) \approx \frac{G(z)b^2(z)\left[1 - \nu(z)\cos^2\alpha\right]}{4\pi(1-\nu(z))}\left[\ln\left(\frac{h-z}{b(z)}\right) + 1\right], \tag{11.41}$$

G is the shear modulus, $G=(C_{11}-C_{12})/2$, and ν is the Poisson ratio, $\nu=C_{12}/(C_{11}+C_{12})$ for the (001) orientation.

To find the equilibrium values z_1 and z_2 we solve the equations

$$0=\frac{\partial(E_d+E_\varepsilon)}{\partial z_1}=\frac{\partial E_d}{\partial z_1}+\frac{\partial E_\varepsilon}{\partial z_1}, \tag{11.42}$$

and

$$0=\frac{\partial(E_d+E_\varepsilon)}{\partial z_2}=\frac{\partial E_d}{\partial z_2}+\frac{\partial E_\varepsilon}{\partial z_2}. \tag{11.43}$$

The equilibrium misfit dislocation density profile in the partially-relaxed S-graded layer is given by

$$\rho=\begin{cases}0, & z<z_1;\\ \dfrac{f_h}{b'\sigma\sqrt{2\pi}}\exp\left[\dfrac{-(z-\mu)^2}{2\sigma^2}\right], & z_1\le z\le z_2;\text{ and}\\ 0, & z>z_2.\end{cases} \tag{11.44}$$

so, the dislocation line energy per unit area is

$$\begin{aligned}E_d&=2\int_{z_1}^{z_2}F_d(z)\rho(z)dz\\ &=2\int_{z_1}^{z_2}\left\{\frac{Gb^2(1-\nu\cos^2\alpha)}{4\pi(1-\nu)}\left[\ln\left(\frac{h-z}{b}\right)+1\right]\right\}\left\{\frac{f_h}{b'\sigma\sqrt{2\pi}}\exp\left[-\frac{(z-\mu)^2}{2\sigma^2}\right]\right\}dz,\\ &=C\int_{z_1}^{z_2}\left[\ln\left(\frac{h-z}{b}\right)+1\right]\exp\left[-\frac{(z-\mu)^2}{2\sigma^2}\right]dz\end{aligned} \tag{11.45}$$

where

$$C=\frac{Gbf_h(1-\nu\cos^2\alpha)}{\sigma\sin\alpha\cos\lambda(1-\nu)(2\pi)^{3/2}} \tag{11.46}$$

Applying the fundamental theorem of calculus, we obtain the partial derivatives of the strain energy per unit area with respect to z_1 and z_2 which are

$$\frac{\partial E_d}{\partial z_1} = -C\left[\ln\left(\frac{h-z_1}{b}\right)+1\right]\exp\left[-\frac{(z_1-\mu)^2}{2\sigma^2}\right], \tag{11.47}$$

and

$$\frac{\partial E_d}{\partial z_2} = C\left[\ln\left(\frac{h-z_2}{b}\right)+1\right]\exp\left[-\frac{(z_2-\mu)^2}{\sigma^2/2}\right]. \tag{11.48}$$

The equilibrium in-plane strain profile is given approximately by

$$\varepsilon_{\|} = \begin{cases} \left(\frac{f_h}{2}\right)\left[-erf\left(\frac{\mu-z}{\sigma\sqrt{2}}\right)+erf\left(\frac{\mu}{\sigma\sqrt{2}}\right)\right], & z < z_1; \\ \left(\frac{f_h}{2}\right)\left[-\frac{z}{z_1}erf\left(\frac{\mu-z_1}{\sigma\sqrt{2}}\right)+\frac{z}{z_1}erf\left(\frac{\mu}{\sigma\sqrt{2}}\right)\right], & z_1 \le z \le z_2; \text{ and .} \\ \left(\frac{f_h}{2}\right)\left[\begin{array}{l} erf\left(\frac{z-\mu}{\sigma\sqrt{2}}\right)-erf\left(\frac{z_2-\mu}{\sigma\sqrt{2}}\right)- \\ \frac{z_2}{z_1}erf\left(\frac{\mu-z_1}{\sigma\sqrt{2}}\right)+\frac{z_2}{z_1}erf\left(\frac{\mu}{\sigma\sqrt{2}}\right) \end{array}\right]. & z > z_2. \end{cases} \tag{11.49}$$

The strain energy per unit area is

$$\begin{aligned} E_\varepsilon &= \frac{Yf_h^2}{4}\int_0^{z_1}\left[-erf\left(\frac{\mu-z}{\sigma\sqrt{2}}\right)+erf\left(\frac{\mu}{\sigma\sqrt{2}}\right)\right]^2 dz \\ &+ \frac{Yf_h^2}{4}\int_{z_1}^{z_2}\left[-\frac{z}{z_1}erf\left(\frac{\mu-z_1}{\sigma\sqrt{2}}\right)+\frac{z}{z_1}erf\left(\frac{\mu}{\sigma\sqrt{2}}\right)\right]^2 dy. \\ &+ \frac{Yf_h^2}{4}\int_{z_2}^{h}\left[\begin{array}{l} erf\left(\frac{z-\mu}{\sigma\sqrt{2}}\right)-erf\left(\frac{z_2-\mu}{\sigma\sqrt{2}}\right)- \\ \frac{z_2}{z_1}erf\left(\frac{\mu-z_1}{\sigma\sqrt{2}}\right)+\frac{z_2}{z_1}erf\left(\frac{\mu}{\sigma\sqrt{2}}\right) \end{array}\right]^2 dz \end{aligned} \tag{11.50}$$

This can be written as

$$E_\varepsilon = I_1 + I_2 + I_3, \tag{11.51}$$

where

$$I_1 = \frac{Yf_h^2}{4}\int_0^{z_1}\left[-erf\left(\frac{\mu - z}{\sigma\sqrt{2}}\right)+erf\left(\frac{\mu}{\sigma\sqrt{2}}\right)\right]^2 dz, \tag{11.52}$$

$$I_2 = \frac{Yf_h^2}{4}\int_{y_1}^{y_2}\left[-\frac{z}{z_1}erf\left(\frac{\mu - z_1}{\sigma\sqrt{2}}\right)+\frac{z}{z_1}erf\left(\frac{\mu}{\sigma\sqrt{2}}\right)\right]^2 dz, \tag{11.53}$$

and

$$I_3 = \frac{Yf_h^2}{4}\int_{y_2}^{h}\left[erf\left(\frac{z-\mu}{\sigma\sqrt{2}}\right)-erf\left(\frac{z_2-\mu}{\sigma\sqrt{2}}\right)-\frac{z_2}{z_1}erf\left(\frac{\mu - z_1}{\sigma\sqrt{2}}\right)+\frac{z_2}{z_1}erf\left(\frac{\mu}{\sigma\sqrt{2}}\right)\right]^2 dz. \tag{11.54}$$

Expanding the integrands, we obtain

$$I_1 = \frac{Yf_h^2}{4}\int_0^{z_1}\left[erf^2\left(\frac{\mu - z}{\sigma\sqrt{2}}\right)-2erf\left(\frac{\mu}{\sigma\sqrt{2}}\right)erf\left(\frac{\mu - z}{\sigma\sqrt{2}}\right)+erf^2\left(\frac{\mu}{\sigma\sqrt{2}}\right)\right]dz, \tag{11.55}$$

$$I_2 = \frac{Yf_h^2}{4}\int_{z_1}^{z_2}\left[\begin{array}{l} erf^2\left(\frac{\mu - z_1}{\sigma\sqrt{2}}\right)-2\left(\frac{z}{z_1}\right)^2 erf\left(\frac{\mu}{\sigma\sqrt{2}}\right)erf\left(\frac{\mu - z_1}{\sigma\sqrt{2}}\right) \\ +\left(\frac{z}{z_1}\right)^2 erf^2\left(\frac{\mu}{\sigma\sqrt{2}}\right)\end{array}\right]dz, \tag{11.56}$$

and

$$I_3 = \frac{Yf_h^2}{4}\int_{z_2}^{h}\left[\begin{array}{l} erf^2\left(\frac{z-\mu}{\sigma\sqrt{2}}\right)+erf^2\left(\frac{z_2-\mu}{\sigma\sqrt{2}}\right)+\left(\frac{z_2}{z_1}\right)^2 erf^2\left(\frac{\mu - z_1}{\sigma\sqrt{2}}\right)+\left(\frac{z_2}{z_1}\right)^2 erf^2\left(\frac{\mu}{\sigma\sqrt{2}}\right) \\ -2\left(\frac{z_2}{z_1}\right)erf\left(\frac{z-\mu}{\sigma\sqrt{2}}\right)erf\left(\frac{z_2-\mu}{\sigma\sqrt{2}}\right)-2\left(\frac{z_2}{z_1}\right)erf\left(\frac{z-\mu}{\sigma\sqrt{2}}\right)erf\left(\frac{\mu - z_1}{\sigma\sqrt{2}}\right) \\ +2\left(\frac{z_2}{z_1}\right)erf\left(\frac{z-\mu}{\sigma\sqrt{2}}\right)erf\left(\frac{\mu}{\sigma\sqrt{2}}\right)+2\left(\frac{z_2}{z_1}\right)erf\left(\frac{z_2-\mu}{\sigma\sqrt{2}}\right)erf\left(\frac{\mu - z_1}{\sigma\sqrt{2}}\right) \\ -2\left(\frac{z_2}{z_1}\right)erf\left(\frac{z_2-\mu}{\sigma\sqrt{2}}\right)erf\left(\frac{\mu}{\sigma\sqrt{2}}\right)-2\left(\frac{z_2}{z_1}\right)^2 erf\left(\frac{\mu - z_1}{\sigma\sqrt{2}}\right)erf\left(\frac{\mu}{\sigma\sqrt{2}}\right)\end{array}\right]dz. \tag{11.57}$$

The partial derivatives of I_1 are given by

$$\frac{\partial I_1}{\partial z_1} = \frac{Yf_h^2}{4}\left\{\left[erf\left(\frac{\mu - z_1}{\sigma\sqrt{2}}\right)+erf\left(\frac{\mu}{\sigma\sqrt{2}}\right)\right]^2\right\}, \tag{11.58}$$

and

$$\frac{\partial I_1}{\partial z_2} = 0. \tag{11.59}$$

The partial derivatives of I_2 are given by

$$\frac{\partial I_2}{\partial z_1} = \frac{Y f_h^{\,2}}{12 z_1^3}\left\{\begin{array}{l}\left[-erf\left(\frac{\mu - z_1}{\sigma\sqrt{2}}\right) + erf\left(\frac{\mu}{\sigma\sqrt{2}}\right)\right]\times \\ \left(\frac{2}{\sigma} z_1 (z_2^2 - z_1^2)\sqrt{\frac{2}{\pi}} \exp\left[-\frac{(z_1 - \mu)}{2\sigma^2}\right]\right. \\ \left. + (2z_2^2 + z_1^2)\left[erf\left(\frac{\mu - z_1}{\sigma\sqrt{2}}\right) - erf\left(\frac{\mu}{\sigma\sqrt{2}}\right)\right]\right)\end{array}\right\}, \tag{11.60}$$

and

$$\frac{\partial I_2}{\partial z_2} = \frac{Y f_h^{\,2} z_2^2}{4 z_1^2}\left\{\left[-erf\left(\frac{\mu - z_1}{\sigma\sqrt{2}}\right) + erf\left(\frac{\mu}{\sigma\sqrt{2}}\right)\right]^2\right\}, \tag{11.61}$$

The partial derivatives of I_3 are

$$\frac{\partial I_3}{\partial z_1} = \frac{Yf_h^2}{2}\frac{z_2}{z_1^3\pi\sigma}\exp\left[-\frac{z_2^2+h^2+z_1^2+2\mu^2}{2\sigma^2}\right]$$

$$\left\{-2z_1^2\sigma\left(\exp\left[\frac{h^2+2(z_1+z_2)\mu}{2\sigma^2}\right]-\exp\left[\frac{z_2^2+2(z_1+h)\mu}{2\sigma^2}\right]\right)\right.$$

$$+\exp\left[\frac{\mu^2}{2\sigma^2}\right]\left[\begin{array}{l} z_1(h-\mu)erf\left(\frac{h-\mu}{\sigma\sqrt{2}}\right)\exp\left[\frac{z_2^2+h^2}{2\sigma^2}\right]\left(\begin{array}{l} z_1\sqrt{2\pi}\exp\left[\frac{z_1\mu}{2\sigma^2}\right] \\ -\pi\sigma\exp\left[\frac{z_1^2+\mu^2}{2\sigma^2}\right]erf\left(\frac{\mu}{\sigma\sqrt{2}}\right)\end{array}\right) \\ +z_2(z_2-h)\pi\sigma\exp\left[\frac{z_2^2+h^2+z_1^2+\mu^2}{2\sigma^2}\right]erf\left(\frac{z_1-\mu}{\sigma\sqrt{2}}\right) \\ -z_1(h-\mu)erf\left(\frac{z_2-\mu}{\sigma\sqrt{2}}\right)\exp\left[\frac{z_2^2+h^2}{2\sigma^2}\right]\left(\begin{array}{l} z_1\sqrt{2\pi}\exp\left[\frac{z_1\mu}{\sigma^2}\right] \\ -\pi\sigma\exp\left[\frac{z_1^2+\mu^2}{2\sigma^2}\right]erf\left(\frac{\mu}{\sigma\sqrt{2}}\right)\end{array}\right)+erf\left(\frac{\mu}{\sigma\sqrt{2}}\right)\left[\begin{array}{l} -z_1\sqrt{2\pi}\left(\begin{array}{l} z_2^2\exp\left[\frac{z_2^2+h^2+2z_1\mu}{2\sigma^2}\right] \\ -z_2h\exp\left[\frac{z_2^2+h^2+2z_1\mu}{2\sigma^2}\right] \\ -\sigma^2\exp\left[\frac{z_1^2+h^2+2z_2\mu}{2\sigma^2}\right] \\ +\sigma^2\exp\left[\frac{z_1^2+z_2^2+2h\mu}{2\sigma^2}\right]\end{array}\right) \\ +z_2(z_2-h)\pi\sigma\exp\left[\frac{z_2^2+h^2+z_1^2+\mu^2}{2\sigma^2}\right]\end{array}\right] \\ +erf\left(\frac{z1-\mu}{\sigma\sqrt{2}}\right)\left[\begin{array}{l} -z_1\sqrt{2\pi}\left(\begin{array}{l} z_2^2\exp\left[\frac{z_2^2+h^2+2z_1\mu}{2\sigma^2}\right] \\ -y_2h\exp\left[\frac{z_2^2+h^2+2z_1\mu}{2\sigma^2}\right]- \\ \sigma^2\exp\left[\frac{z_1^2+h^2+2z_2\mu}{2\sigma^2}\right] \\ +\sigma^2\exp\left[\frac{z_1^2+z_2^2+2h\mu}{2\sigma^2}\right]\end{array}\right)+\pi\sigma\exp\left[\frac{z_1^2+z_2^2+h^2+\mu^2}{2\sigma^2}\right]\left(\begin{array}{l} z_1(h-\mu)\left[erf\left(\frac{z_2-\mu}{\sigma\sqrt{2}}\right)-erf\left(\frac{h-\mu}{\sigma\sqrt{2}}\right)\right] \\ +2z_2(z_2-h)erf\left(\frac{\mu}{\sigma\sqrt{2}}\right)\end{array}\right)\end{array}\right]\end{array}\right]\left.\right\}$$

(11.62)

and

$$\frac{\partial I_3}{\partial z_2} = \frac{Yf_h^2}{4}\frac{1}{z_1^2\pi\sigma}\exp\left[-\frac{2(z_2-\mu)^2+(h-\mu)^2}{2\sigma^2}\right]$$

$$\left\{4z_1^2\sigma\exp\left[\frac{\mu(-2(h+z_2)+\mu)}{2\sigma^2}\right]\left(\exp\left[\frac{h^2+2z_2\mu}{2\sigma^2}\right]-\exp\left[\frac{z_2^2+2h\mu}{2\sigma^2}\right]\right)\right.$$

$$+\exp\left[\frac{z_2^2-4z_2\mu+2\mu(\mu-h)}{2\sigma^2}\right]\left[-z_2(3z_2-2h)\pi\sigma\exp\left[\frac{z_2^2+h^2+\mu^2}{2\sigma^2}\right]erf^2\left(\frac{z_1-\mu}{\sigma\sqrt{2}}\right)\right.$$

$$+2z_1(h-\mu)erf\left(\frac{z_2-\mu}{\sigma\sqrt{2}}\right)\exp\left[\frac{h^2}{2\sigma^2}\right]\left(\begin{array}{l} z_1\sqrt{2\pi}\exp\left[\frac{z_2\mu}{\sigma^2}\right] \\ -\pi\sigma\exp\left[\frac{z_2^2+\mu^2}{2\sigma^2}\right]erf\left(\frac{\mu}{\sigma\sqrt{2}}\right)\end{array}\right)$$

$$+erf\left(\frac{\mu}{\sigma\sqrt{2}}\right)\left[\begin{array}{l} -2z_1(h-\mu)\exp\left[\frac{h^2}{2\sigma^2}\right]erf\left(\frac{h-\mu}{\sigma\sqrt{2}}\right)\left(\begin{array}{l} z_1 erf^{-1}\left(\frac{\mu}{\sigma\sqrt{2}}\right)\exp\left[\frac{z_2\mu}{\sigma^2}\right] \\ -\pi\sigma\exp\left[\frac{z_2^2+\mu^2}{2\sigma^2}\right]\end{array}\right) \\ +2z_1\sqrt{2\pi}\left(\begin{array}{l}\sigma^2\exp\left[\frac{z_2^2+2h\mu}{2\sigma^2}\right] \\ -(z_2(h-z_2)+\sigma^2)\exp\left[\frac{z_1^2+z_2^2+2h\mu}{2\sigma^2}\right]\end{array}\right) \\ +z_2(3z_2-2h)\pi\sigma\exp\left[\frac{z_2^2+h^2+z_1^2+\mu^2}{2\sigma^2}\right]\end{array}\right]$$

$$\left.\left.+2erf\left(\frac{z_1-\mu}{\sigma\sqrt{2}}\right)\left[\begin{array}{l} z_1\sqrt{2\pi}\left(\begin{array}{l}\sigma^2\exp\left[\frac{z_2^2+2h\mu}{2\sigma^2}\right] \\ -\exp\left[\frac{z_2^2+h^2+2z_1\mu}{2\sigma^2}\right](y_2(h-z_2)+\sigma^2)\end{array}\right) \\ -\pi\sigma\exp\left[\frac{z_2^2+h^2+\mu^2}{2\sigma^2}\right]\left(\begin{array}{l} z_1(h-\mu)\left[erf\left(\frac{z_2-\mu}{\sigma\sqrt{2}}\right)-erf\left(\frac{h-\mu}{\sigma\sqrt{2}}\right)\right] \\ +2z_2(3z_2-2h)erf\left(\frac{\mu}{\sigma\sqrt{2}}\right)\end{array}\right)\end{array}\right]\right]\right\}$$

(11.63)

The equilibrium values of z_1 and z_2 are the solutions of

$$0 = \frac{\partial E_d}{\partial z_1}+\frac{\partial I_1}{\partial z_1}+\frac{\partial I_2}{\partial z_1}+\frac{\partial I_3}{\partial z_1}, \qquad \textbf{(11.64)}$$

and

$$0 = \frac{\partial E_d}{\partial z_2} + \frac{\partial I_1}{\partial z_2} + \frac{\partial I_2}{\partial z_2} + \frac{\partial I_3}{\partial z_2}. \quad \textbf{(11.65)}$$

z_1 and z_2 can therefore be found from the simultaneous solution of the equations above. Numerical solution of the two preceding equations yields the values of z_1 and z_2 for given values of μ, σ, and h in a given material system.

11.3. Copyright Permissions

Due to the number of publications summarized in this thesis, I have chosen to include only the license number from the copyright clearance center given that the actual permissions are of considerable length. However, the actual contract may be available anytime upon request.

Semiconductor Science and Technology:

License #: 4074830415040, 4074830354054

Journal of Vacuum Science & Technology B:

License #: 4074780829194, 4074801160795, 4074800878649

Journal of Applied Physics:

License #: 4074780711526, 4074780363431.

Journal of Electronic Materials:

License #: 4074780651478, 4074780586438, 4074780527996, 4074780471509, 4074800003932, 4074791459451, 4074791061193, 4074780989406, 4074780939929, 4074780887290.

International Journal of High Speed Electronic and Systems:

License #: 4078821487634.

12. References

[1] E. R. Cohen and B. N. Taylor, "The 1986 Adjustment of the Fundamental Physical Constants," report of the Committee on Data for Science and Technology of the International Council of Scientific Unions (CODATA) Task Group on Fundamental Constants, CODATA Bulletin 63 (Elmsford, NY: Pergamon, 1986).
[2] J. Donahue, The Structure of the Elements (New York: J. Wiley and Sons, 1974).
[3] W. B. Pearson, A Handbook of Lattice Spacings and Structure of Metals and Alloys (Oxford-London: Pergamon Press, 1967).
[4] H. C. Casey, Jr., and F. A. Trumbore, Mater. Sci. Eng., 6, 69 (1970).
[5] E. M. H. Driscoll, A. F. W. Willoughby, J. B. Mullin, and B. W. Straughan, in *Gallium Arsenide and Related Compounds* (Institute of Physics, London). Volumes in Inst. of Physics Conference Series, 24, 275 (1975).
[6] J. V. Ozolin'sh, G. K. Averkieva, A. F. Ilvin'sh, and N. A. Goryunova, Sov. Phys. Cryst. (English Transl.), 7, 691 (1963).
[7] M. Neuberger, Handbook of Electronic Materials, Vol. 2: III-V Semiconductor Compunds (new York: Plenum, 1971).
[8] W. L. Roth, in Physics and Chemistry of II-VI Compounds, eds. M. Aven and J. S. Prener (Amsterdam: North-Holland Publishing Co., 1975).
[9] B. Greenberg, private communication.
[10] V. Grossman, M. Behringer, H. Heinke, and D. Hommel, J. Cryst. Growth, 184/185, 100 (1998).
[11] M. Leszczynski and J. F. Walker, Appl. Phys. Lett., 62, 1484 (1993).
[12] R. Feder and I. Light, J. Appl. Phys., 39, 4870 (1968).
[13] E. D. Pierron, D. L. Parker, and J. B. McNeely, J. Appl. Phys., 38, 4669 (1967).
[14] S. I. Novikova, Sov. Phys. Sol. State, 3, 129 (1961).
[15] C. Giannini, L. Tapfer, T. Peluso, N. Lovergine, and L. Vasanelli, J. Phys. D, 28, A125 (1995).
[16] J. S. Browder and S. S. Ballard, Appl. Optics, 8, 793 (1969).
[17] R. B. Roberts, G. K. White, and T. M. Sabine, Australian J. Phys., 34, 701 (1981).
[18] S. S. Ballard, S. E. Brown, and J. S. Browder, Appl. Optics, 17, 1152 (1978).
[19] H. P. Singh and B. Dayal, Phys. Stat. Solidi (b), 23, K93 (1967).
[20] L. S. Ladd, R. Clark, and D. Roy, U. S. Air Force Technical Report AL-TDR-64-9 (1964).
[21] L. Vegard, Z. Phys., 5, 17 (1921).
[22] S. P. Nikanorov, Yu. A. Burenkov, and A. V. Stepanov, Sov. Phys. Solid State (English transl.), 13, 2516 (1972).
[23] Yu. A. Burenkov, S. P. Nikanorov, and A. V. Stepanov, Sov. Phys. Sol. State (Engl. Transl.), 12, 1940 (1971).
[24] Y. K. Yogurtcu, A. J. Miller, and G. A. Saunders, J. Phys. Chem. Sol., 42, 49 (1981).
[25] R. I. Cottam and G. A. Saunders, J. Phys., C6, 2105 (1973).
[26] D. Gerlich, J. Appl. Phys., 34, 2915 (1963).
[27] I. M. Sil'vestrova, I. B. Kobyakov, and A. A. Shternberg, Sov. Phys. Techn. Phys. (Engl. Transl.), 25, 1433 (1980).
[28] C. G. Hodgins and J. C. Irwin, Phys. Status Solidi, A28, 647 (1975).
[29] E. Peissker, P. Haasen, and H. Alexander, Phil. Mag., 7, 1279 (1962).
[30] R. L. Bell and A. F. W. Willoughby, J. Mat. Sci., 1, 219 (1966).
[31] K. R. Breen, P. N. Uppal, and J. S. Ahearn, J. Vac. Sci. Technol. B, 7, 758 (1989).

[32] M. J. Matragrano, D. G. Ast, J. R. Shealy, and V. Krishnamoorthy, J. Appl. Phys., 79, 8371 (1996).
[33] F. R. N. Nabarro, Theory of Crystal Dislocations (New York: Dover, 1987) p. 201.
[34] J. W. Matthews and A. E. Blakeslee, J. Cryst. Growth, 27, 118 (1974).
[35] D. Hull and D. J. Bacon, Introduction to Dislocations, 4th Edition (Oxford: Butterworth Heinemann, 2001), p. 72.
[36] M. Peach and J. S. Koehler, Phys. Rev., 80, 436 (1950).
[37] D. Hull and D. J. Bacon, Introduction to Dislocations, 4th Edition (Oxford: Butterworth Heinemann, 2001) pp. 42-43.
[38] A. George and J. Rabier, Revue Phys. Appl., 22, 941 (1987).
[39] B. W. Dodson, "Stress dependence of dislocation glide activation energy in single-crystal silicon-germanium alloys up to 2.6 GPa," Phys. Rev. B, 38, 12383 (1988).
[40] J. P. Hirth and J. Lothe, Theory of Crystal Dislocations (New York: McGraw Hill, 1968).
[41] R. Hull, J. C. Bean, D. Bahnk, L. J. Peticolas, Jr., K. T. Short, and F. C. Unterwald, "Interpretation of dislocation propagation velocities in strained Ge_xSi_{1-x}/Si(100) heterostructures by the diffusive kink model," J. Appl. Phys., 70, 2052 (1991).
[42] W. A Jesser and J. W. Matthews, "Evidence for pseudomorphic growth of iron on copper," Phil. Mag., 15, 1097 (1967).
[43] B. Bertoli, E. N. Suarez, J. E. Ayers, and F. C. Jain, J. Appl. Phys., 106, 073519 (2009).
[44] J. Tersoff, Appl. Phys. Lett., 62, 693 (1993) Appl. Phys. Lett., 64, 2748 (1994).
[45] K. Streubel, N. Linder, R. Wirth, and A. Jaeger, IEEE J. Sel. Top. Quant. Electron., 8, 321 (2002).
[46] O. Kwon, J. Boeckl, M. L. Lee, A. J. Pitera, E. A Fitzgerald, and S. A. Ringel, J. Appl. Phys., 97, 034504 (2005).
[47] P. Lever, H. H. Tan, and C. Jagadish, J. Appl. Phys., 95, 5710 (2004).
[48] D. Bimberga, M. Grundmanna, F. Heinrichsdorff, N. N. Ledentsov, V. M. Ustinov, A. E. Zhukov, A. R. Kovsh, M. V. Maximov, Y. M. Shernyakov, B.V. Volovik, A. F. Tsatsul'nikov, P.S. Kop'ev, Zh. I. Alferov, Thin Solid Films, 367, 235 (2000).
[49] D. E. Grider, S. E. Swirhun, D. H. Narum, A. I. Akinwande, T. E. Nohava, W. R. Stuart, P. Joslyn, and K. C. Hsieh, J. Vac. Sci. Technol. B, 8, 301 (1990).
[50] S. Mendach, C. M. Hu, Ch. Heyn, S. Schnull, H. P. Oepen, R. Anton, and W. Hansen, Physica E, 13, 1204 (2002).
[51] T. Kujofsa and J. E. Ayers, J. Vac. Sci. Technol. B, (32), 031205 (2014).
[52] T. Kujofsa, A. Antony, S. Xhurxhi, F. Obst, D. Sidoti, B. Bertoli, S. Cheruku, J. P. Correa, P. B. Rago, E. N. Suarez, F. C. Jain, and J. E. Ayers, J. Electron. Mat., 42, 3408 (2013).
[53] T. Kujofsa and J. E. Ayers, J. Electron. Mat., 45, 2831 (2016).
[54] T. Kujofsa and J. E. Ayers, J. Electron. Mat., 43, 2993 (2014).
[55] J. W. Matthews and A. E. Blakeslee, J. Cryst. Growth 27, 118 (1974).
[56] J. W. Matthews, *Epitaxial Growth, Part B*, Academic Press, New York, 1975.
[57] V. Bush, J. Franklin. Inst., 217, 289 (1934).
[58] S. Whitehead, J. Sci. Instrum., 21, 73 (1944).
[59] R. B. Stambaugh, Ind. Eng. Chem., 44, 1590 (1952).
[60] S. Frieberg, Expe. Mech., 2, 24 (1962).
[61] R. Olsson and M. Bath, Phys. Earth Planet In., 10, 1 (1975).
[62] T. Kujofsa and J. E. Ayers, Semicond. Sci. Technol., 31, 115014 (2016).
[63] J. E. Ayers, Semicond. Sci. Technol., 23, 045018 (2008).

[64] D. Sidoti, S. Xhurxhi, T. Kujofsa, S. Cheruku, J. P. Correa, B. Bertoli, P. B. Rago, E. N. Suarez, F. C. Jain, J. E. Ayers, J. Appl. Phys., 109, 023510 (2011).
[65] S. Xhurxhi, F. Obst, D. Sidoti, B. Bertoli, T. Kujofsa, S. Cheruku, J. P. Correa, P. B. Rago, E. N. Suarez, F. C. Jain, and J. E. Ayers, J. Electron. Mat., 40, 2348 (2011).
[66] T. Kujofsa, W.Yu, S. Cheruku, B. Outlaw, F. Obst, D. Sidoti, B. Bertoli, P. B. Rago, E. N. Suarez, F. C. Jain and J. E. Ayers, J. Electron. Mater. 41, 2993 (2012).
[67] J. W. Matthews, S. Mader, and T. B. Light, J. Appl. Phys., 41, 3800 (1970).
[68] B. W. Dodson and J. Y. Tsao, Appl. Phys. Lett., 51, 1325 (1987); Appl. Phys. Lett., 52, 852 (1988).
[69] D. C. Houghton, J. Appl. Phys., 70, 2136 (1991).
[70] T. Sasaki, H. Suzuki, A. Sai, M. Takahasi, S. Fujikawa, I. Kamiya, Y. Ohshita, and M. Yamaguchi, J. Cryst. Growth, 323, 13 (2011).
[71] M. Horbaschk, A. Benkert, C. Schumacher, K. Brunner, and R. B. Neder, Appl. Phys. Lett., 94, 211905 (2009).
[72] E. A. Fitzgerald, Y.-H. Xie, D. Monroe, P. J. Silverman, J. M. Kuo, A. R. Kortan, F. A. Thiel, and B. E. Weir, J. Vac. Sci. Technol., B10, 1807 (1992).
[73] E. A. Fitzgerald, A. Y. Kim, M. T. Currie, T. A. Langdo, G. Taraschi, and M. T. Bulsara, Mater. Sci. Engr., B67, 53 (1999).
[74] T. Kujofsa, W. Yu, S. Cheruku, B. Outlaw, F. Obst, D. Sidoti, B. Bertoli, P. B. Rago, E. N. Suarez, F. C. Jain and J. E. Ayers, J. Electron. Mater. 41, 2993 (2012).
[75] J. E. Ayers, Heteroepitaxy of Semiconductors: Theory, Growth, and Characterization (Boca Raton, FL: CRC Press, 2007).
[76] J. W. Matthews, J. Vac. Sci. technol., 12, 126 (1975).
[77] J. W. Matthews and A. E. Blakeslee, J. Cryst. Growth 27, 118 (1974).
[78] M. Tachikawa and M. Yamaguchi, Appl. Phys. Lett., 56, 484 (1990).
[79] A. E. Romanov, W. Pompe, G. E. Beltz, and J. S. Speck, Appl. Phys. Lett., 69, 3342 (1996).
[80] S. K. Ghandhi, "VLSI Fabrication Principles: Silicon and Gallium Arsenide, 2nd Edition" (New York: John Wiley and Sons, 1994).
[81] D. J. Dunstan, Phil. Mag. A73, 1323 (1996).
[82] F. Romanato, E. Napolitani, A. Carnera, A. V. Drigo, L. Lazzarini, G. Salviati, C. Ferrari, A. Bosacchi, and S. Franchi, J. Appl. Phys., 86, 4748 (1999).
[83] D. Richman and J. J. Tietjen, Trans. AIME, 239, 418 (1967).
[84] J. J. Tietjen, J. I. Pankove, I. J. Hegyi, and H. Nelson, Trans. AIME, 239, 385 (1968).
[85] C. J. Nuese, J. J. Tietjen, J. J. Gannon, and H. F. Gossenberger, Trans. AIME, 242, 400 (1968).
[86] M. S. Abrahams, L. R. Weisberg, C. J. Buiocchi, and J. Blanc, J. Mater. Sci., 4, 223 (1969).
[87] R. M. Biefeld, C. R. Hills, and S. R. Lee, J. Cryst. Growth, 91, 515 (1988).
[88] F. K. LeGoues, B. S. Meyerson, and J. F. Morar, Phys. Rev. Lett., 66, 2903 (1991).
[89] E. A. Fitzgerald, Y.-H. Xie, D. Monroe, P. J. Silverman, J. M. Kuo, A. R. Kortan, F. A. Thiel, and B. W. Weir, J. Vac. Sci. Technol. B, 10, 1807 (1992).
[90]K. L. Kavanagh, J. C. Chang, J. Chen, J. M. Fernandez, and H. H. Wieder, J. Vac. Sci. Technol. B, 10, 1820 (1992).
[91] F. Schaffler, D. Tobben, H.-J. Herzog, G. Abstreiter, and B. Hollander, Semicond. Sci. Technol., 7, 260 (1992).
[92] A. Sacedon, F. Gonzalez-Sanz, E. Calleja, E. Munoz, S. I. Molina, F. J. Pacheco, D. Araujo, R. Garcia, M. Lourenco, Z. Yang, P. Kidd, and D. Dunstan, Appl. Phys. Lett., 66, 3334 (1995).

[93] A. Bosacchi, A. C. De Riccardis, P. Frigeri, S. Franchi, C. Ferrari, S. Gennari, L. Lazzarini, L. Nasi, G. Salviati, A. V. Drigo, and F. Romanato, J. Cryst. Growth, 175/176, 1009 (1997).
[94] S. P. Ahrenkiel, M. W. Wanlass, J. J. Carapella, R. K. Ahrenkiel, S. W. Johnston, and L. M. Gedvilas, Sol. Energy Mater. Sol. Cells, 91, 908 (2007).
[95] L. H. Wong, J. P. Liu, F. Romanato, C. C. Wong, and Y. L. Foo, Appl. Phys. Lett., 90, 061913 (2007).
[96] S. Nakamura, P. Jayavel, T. Koyama, and Y. Hayakawa, J. Cryst. Growth, 300, 497 (2007).
[97] J. F. Ocampo, E. Suarez, F. C. Jain, and J. E. Ayers, J. Electron. Mater., 37, 1035 (2008).
[98] H. Choi, Y. Jeong, J. Cho, and M. H. Jeon, J. Cryst. Growth, 311, 1091 (2009).
[99] D. Sidoti, S. Xhurxhi, T. Kujofsa, S. Cheruku, J. Reed, B. Bertoli, P. B. Rago, E. N. Suarez, F. C. Jain and J. E. Ayers, J. Electron. Mater., in press (2010).
[100] [1] C.-S. Lee and W.-T. Chien, J. Electrochem. Soc., 158, H452 (2011).
[101] H. Yang, H. Wang, and C. L. Tan, IEEE Trans. Electron Dev., 51, 1221 (2004).
[102] J.-H. Tsai, J. Electrochem. Soc., 158, H889 (2011).
[103] L. J. Mawst, J. D. Kirch, C.-C. Chang, T. Kim, T. Garrod, D. Botez, S. Ruder, T. F. Kuech, T. Earles, R. Tatavari, N. Pan, and A. Wibowo, J. Cryst. Growth, 370, 230 (2013).
[104] I. Mathews, D. O'Mahoney, A. Gocalinska, M. Manganaro, E. Pelucchi, H. Schmidt, A. P. Morrison, and B. Corbett, Appl. Phys. Lett., 102, 033906 (2013).
[105] J. Tersoff J, Appl. Phys. Lett. 62, 693 (1993); Appl. Phys. Lett., 64, 2748 (1994).
[106] E. A. Fitzgerald, Y.-H. Xie, D. Monroe, P. J. Silverman, J. M. Kuo, A. R. Kortan, F. A. Thiel, and B. W. Weir, J. Vac. Sci. Technol. B, 10, 1807 (1992).
[107] M. K. Hudait, Y. Lin, M. N. Palmisiano and S. A. Ringel, IEEE Electron Dev. Lett. 24, 538 (2003).
[108] T. Jian, W. Xiaoliang and X. Hongling, J. Semicond., 35, 113006 (2014).
[109] R. Suzuki, N. Taoka, M. Yokoyama, S. Lee, S. H. Kim, T. Hoshii, T. Yasuda, W. Jevasuwan, T. Maeda, O. Ichikawa, N. Fukuhara, M. Hata, M. Takenaka and S. Takagi, Appl. Phys. Lett. 100, 132906 (2012).
[110] S. Kim, M. Yokoyama, N. Taoka, R. Iida, S. Lee, R. Nakane, Y. Urabe, N. Miyata, T. Yasuda, H. Yamada, N. Fukuhara, M. Hata, M. Takenaka and S. Takagi, Appl. Phys. Express 4 02420 (2011).
[111] M. S. Leite, R. L. Woo, J. N. Munday, W. D. Hong, S. Mesropian, D. C. Law and H. A. Atwater, Appl. Phys. Lett. 102, 033901 (2013).
[112] H. Roehle, R. J. B. Dietz, H. J. Hensel, J. Böttcher, H. Künzel, D. Stanze, M. Schell, and B. Sartorius, Opt. Express, 18, 2296 (2010).
[113] G. Salviati, C. Ferrari, L. Lazzarini, S. Franchi, A. Bosacchi, F. Taiariol, M. Mazzer, C. Zanotti-Fregonara, F. Romanato, and A. V. Drigo, Inst. Phys. Conf. Ser., 146, 337 (1995).
[114] D. Lee, M. S. Park, Z. Tang, H. Luo, R. Beresford, and C. R. Wie, J. Appl. Phys., 101, 063523 (2007).
[115] F. Capotondi, G. Biasiol, D. Ercolani, V. Grillo, E. Carlino, F. Romanato, and L. Sorba, Thin Sol. Films, 484, 400 (2005).
[116] C. Lynch, R. Beresford, and E. Chason, J. Vac. Sci. Technol. B, 22, 1539 (2004).
[117] Z. Jiang, W. Wang, H.Gao, L. Liu, H. Chen, J. Zhou. Appl. Surf. Sci., 254, 5241 (2008).
[118] X. Z. Shang, S. D. Wu, C. Liu, W. X. Wang, L. W. Guo, Q. Huang, J. Phys. D, 39, 1800 (2006).
[119] J. Chen, J. M. Fernandez, J. C. P. Chang, K. L. Kavanagh, and H. H. Wieder, Semicond. Sci. Technol., 7, 601(1992).

[120] J. Chen, J. M. Fernandez, J. C. P. Chang, K. L. Kavanagh, and H. H. Wieder, Semicond. Sci. Technol., 7, 601(1992).
[121] M. S. Abrahams, L. R. Weisberg, C. J. Buiocchi, and J. Blanc, J. Mater. Sci., 4, 223 (1969).
[122] C.-S. Lee and W.-T. Chien, J. Electrochem. Soc., 158, H452 (2011).
[123] H. Yang, H. Wang, and C. L. Tan, IEEE Trans. Electron Dev., 51, 1221 (2004).
[124] J.-H. Tsai, J. Electrochem. Soc., 158, H889 (2011).
[125] W. E. Hoke, T. D. Kennedy, A. Torabi, C. S. Whelan, P. F. Marsh, R. E. Leoni, S. M. Lardizabel, Y. Yang, J. H. Jang, I. Adesida, C. Xu, and K. C. Hsieh, J. Cryst. Growth, 251, 804 (2003).
[126] G. Belenky, D. Wang, Y. Lin, D. Donetsky, G. Kipshidze, L. Shterengas, D. Westerfeld, W. L. Sarney, and S. Svensson, Appl. Phys. Lett., 102, 111108 (2013).
[127] T. Hosoda, D. Wang, G. Kipshidze, W. L. Sarney, L. Shterengas, and G. Belenky, Semicond. Sci. Technol., 27, 055011 (2012).
[128] M. Arai, Y. Kondo, S. Kanazawa, T. Tadokoro, and M. Kohtoku, 2012 Conference on Lasers and Electro-Optics (CLEO), p. 2 (2012).
[129] L. J. Mawst, J. D. Kirch, C.-C. Chang, T. Kim, T. Garrod, D. Botez, S. Ruder, T. F. Kuech, T. Earles, R. Tatavari, N. Pan, and A. Wibowo, J. Cryst. Growth, 370, 230 (2013).
[130] I. Mathews, D. O'Mahoney, A. Gocalinska, M. Manganaro, E. Pelucchi, H. Schmidt, A. P. Morrison, and B. Corbett, Appl. Phys. Lett., 102, 033906 (2013).
[131] K. L. Kavanagh, J. C. Chang, J. Chen, J. M. Fernandez, and H. H. Wieder, J. Vac. Sci. Technol. B, 10, 1820 (1992).
[132] F. Schaffler, D. Tobben, H.-J. Herzog, G. Abstreiter, and B. Hollander, Semicond. Sci. Technol., 7, 260 (1992).
[133] A. Sacedon, F. Gonzalez-Sanz, E. Calleja, E. Munoz, S. I. Molina, F. J. Pacheco, D. Araujo, R. Garcia, M. Lourenco, Z. Yang, P. Kidd, and D. Dunstan, Appl. Phys. Lett. 66, 3334 (1995).
[134] P. M. Mooney, J. L. Jordan-Sweet, J. O. Chu and F.K. LeGoues, Appl. Phys. Lett. 66, 3642 (1995).
[135] M. K. Hudait, Y. Lin, D. M. Wilt, J. S. Speck, C. A. Tivarus, E. R. Heller, J. P. Pelz and S. A. Ringel, Appl. Phys. Lett. 82, 3212 (2003).
[136] L. J. Mawst, P. Dudley, J. Kirch, T. Kim, S. Ruder, T. F. Kuech, and R. Tatavarti. Photovoltaic Specialists Conference (PVSC), 2011 37th IEEE, 517 (2011).
[137] S. M. Vernon, S. P. Tobin, V. E. Haven, K. G. Wolfson, M. W. Wanlass, and R. J. Matson, Proc. 19th IEEE Photovoltaics Spec. Conf., 1987, pp. 108–112.
[138] K. Hayashi, T. Soga, H. Nishikawa, T. Jimbo, and M. Umeno, Proc. 1st World Conf. Photovoltaic Energy Convers., 1994, pp. 1890–1893.
[139] J. F. Geisz, J. M. Olson, M. J. Romero, C. S. Jiang, and A. G. Norman, Proc. 4th World Conf. Photovoltaic Energy Convers., 2006, pp. 772–775.
[140] J. R. Lang et al., Appl. Phys. Lett., 103, 092102 (2013).
[141]J. Tersoff, Appl. Phys. Lett. 62, 693 (1993).
[142] J. Tersoff, Appl. Phys. Lett., 64, 2748 (1994).
[143] E. A. Fitzgerald, Y.-H. Xie, D. Monroe, P. J. Silverman, J. M. Kuo, A. R. Kortan, F. A. Thiel, and B. W. Weir, J. Vac. Sci. Technol. B, 10, 1807 (1992).
[144] D. Richman D and J. J. Tietjen, Trans. AIME, 239, 418 (1967).
[145] J. J. Tietjen, J. I. Pankove, I. J. Hegyi, and H. Nelson, Trans. AIME, 239, 385 (1968).
[146] C. J. Nuese, J. J. Tietjen, J. J. Gannon, and H. F. Gossenberger, Trans. AIME, 242, 400 (1968).

[147] M. S. Abrahams, L. R. Weisberg, C. J. Buiocchi, and J. Blanc, J. Mater. Sci., 4, 223 (1969).
[148] R. M. Biefeld, C. R. Hills, and S. R. Lee, J. Cryst. Growth, 91, 515 (1988).
[149] F. K. LeGoues, B. S. Meyerson, and J. F. Morar, Phys. Rev. Lett., 66, 2903 (1991).
[150] K. L. Kavanagh, J. C. Chang, J. Chen, J. M. Fernandez, and H. H. Wieder, J. Vac. Sci. Technol. B, 10, 1820 (1992).
[151] F. Schaffler, D. Tobben, H.-J. Herzog, G. Abstreiter, and B. Hollander, Semicond. Sci. Technol., 7, 260 (1992).
[152] A. Sacedon, F. Gonzalez-Sanz, E. Calleja, E. Munoz, S. I. Molina, F. J. Pacheco, D. Araujo, R. Garcia, M. Lourenco, Z. Yang, P. Kidd, and D. Dunstan, Appl. Phys. Lett. 66, 3334 (1995).
[153] A. Bosacchi, A. C. De Riccardis, P. Frigeri, S. Franchi, C. Ferrari, S. Gennari, L. Lazzarini, L. Nasi, G. Salviati, A. V. Drigo, and F. Romanato, J. Cryst. Growth, 175/176, 1009 (1997).
[154] H. Choi, Y. Jeong, J. Cho, and M. H. Jeon, J. Cryst. Growth, 311, 1091 (2009).
[155] J. E. Ayers, Heteroepitaxy of Semiconductors: Theory, Growth, and Characterization (Boca Raton, FL: CRC Press, 2007) p. 180.
[156] B. Bertoli, D. Sidoti, S. Xhurxhi, T. Kujofsa, S. Cheruku, J. P. Correa, P. B. Rago, E. N. Suarez, J. E. Ayers, and F. C. Jain, J. Appl. Phys., 108, 113525 (2010).
[157] S. Xhurxhi, F. Obst, D. Sidoti, B. Bertoli, T. Kujofsa, S. Cheruku, J. P. Correa, P. B. Rago, E. N. Suarez, F. C. Jain, and J. E. Ayers, J. Electron. Mater., 40, 2348 (2011).
[158] T. Kujofsa, A. Antony, S. Xhurxhi, F. Obst, D. Sidoti, B. Bertoli, S. Cheruku, J. P. Correa, P. B. Rago, E. N. Suarez, F. C. Jain, and J. E. Ayers, J. Electron. Mater., (In press).
[159]C.-S. Lee and W.-T. Chien, J. Electrochem. Soc., 158, H452 (2011).
[160] H. Yang, H. Wang, and C. L. Tan, IEEE Trans. Electron Dev., 51, 1221 (2004).
[161]J.-H. Tsai, J. Electrochem. Soc., 158, H889 (2011).
[162] W. E. Hoke, T. D. Kennedy, A. Torabi, C. S. Whelan, P. F. Marsh, R. E. Leoni, S. M. Lardizabel, Y. Yang, J. H. Jang, I. Adesida, C. Xu, and K. C. Hsieh, J. Cryst. Growth, 251, 804 (2003).
[163] G. Belenky, D. Wang, Y. Lin, D. Donetsky, G. Kipshidze, L. Shterengas, D. Westerfeld, W. L. Sarney, and S. Svensson, Appl. Phys. Lett., 102, 111108 (2013)
[164] T. Hosoda, D. Wang, G. Kipshidze, W. L. Sarney, L. Shterengas, and G. Belenky, Semicond. Sci. Technol., 27, 055011 (2012).
[165] M. Arai, Y. Kondo, S. Kanazawa, T. Tadokoro, and M. Kohtoku, 2012 Conference on Lasers and Electro-Optics (CLEO), p. 2 (2012).
[166] L. J. Mawst, J. D. Kirch, C.-C. Chang, T. Kim, T. Garrod, D. Botez, S. Ruder, T. F. Kuech, T. Earles, R. Tatavari, N. Pan, and A. Wibowo, J. Cryst. Growth, 370, 230 (2013).
[167] I. Mathews, D. O'Mahoney, A. Gocalinska, M. Manganaro, E. Pelucchi, H. Schmidt, A. P. Morrison, and B. Corbett, Appl. Phys. Lett., 102, 033906 (2013).
[168] D. J. Dunstan and A.J. Bushby, Proc. R. Soc. Lond. A, 460, 2781 (2004).
[169] Sudip Saha, Daniel T. Cassidy and D. A. Thompson, J. Cryst. Growth, 386, 183 (2014).
[170] B. Paszkiewics et al., Vacuum, 82, 389 (2008).
[171] J. W. Mathews, Epitaxial Growth, Part B, Academic Press, New York, 1975.
[172] T. Kujofsa and J. E. Ayers, J. Electron. Mat., 42, 3034 (2013).
[173] T. Kujofsa, S. Cheruku, B. Outlaw, S. Xhurxhi, F. Obst, D. Sidoti, B. Bertoli, P. B. Rago, E. N. Suarez, F. C. Jain, and J. E. Ayers, J. Electron. Mat., 41, 2993 (2012).
[174] J. F. Ocampo, E. Suarez, F. C. Jain, and J. E. Ayers, J. Electron. Mater., 37, 1035 (2008).
[175] S. M. Hubbard, C. D. Cress, C. G. Bailey, R. P. Raffaelle, S. G. Bailey and D. M. Wilt, Appl. Phys. Lett., 92, 123512 (2008).

[176] D. Bimberga, M. Grundmanna, F. Heinrichsdorff, N. N. Ledentsov, V. M. Ustinov, A. E. Zhukov, A. R. Kovsh, M. V. Maximov, Y. M. Shernyakov, B.V. Volovik, A. F. Tsatsul'nikov, P.S. Kop'ev, Zh. I. Alferov, Thin Solid Films, 367, 235 (2000).
[177] A. Stiff-Roberts, S. Krishna, P. Bhattacharya, and S. Kennerly, J. Vac. Sci. Technol. B, 20, 1185 (2002).
[178] N. Nuntawong, S. Birudavolu, C. P. Hains, S. Huang, H. Xu, and D. L. Huffaker, Appl. Phys. Lett., 85, 3050 (2004).
[179] X. Q. Zhang, S. Ganapathy, H. Kumano, K. Uesugi, and I. Suemune, J. Appl. Phys., 92, 6813 (2002).
[180] X. Q. Zhang, S. Ganapathy, I. Suemune, H. Kumano, K. Uesugi, Y. Nabetani and T. Matsumoto, Appl. Phys. Lett., **83**, 4524 (2003).
[181] B. I. Miller, U. Koren, M. G. Young, and M. D. Chien, Appl. Phys. Lett., **58**, 1952 (1991).
[182] G. Zhang and A. Ovtchinnikov, Appl. Phys. Lett., 62, 1644 (1993).
[183] B. Tillack, P. Zaumseil, G. Morgenstern, D. Kruger, and G. Ritter, Appl. Phys. Lett., 67, 1143 (1995).
[184] P. Lever, H. H. Tan, and C. Jagadish, J. Appl. Phys., 95, 5710 (2004).
[185] A. M. Gocalinska, M. Manganaro and E. Pelucchi, Cryst. Growth Des., 16, 2363 (2016).
[186] J. W. Matthews, *Epitaxial Growth, Part B,* (Academic Press, New York, NY, 1975.)
[187] J. Tersoff, Appl. Phys. Lett. 62, 693 (1993).
[188] D. J. Dunstan, Phil. Mag. A73, 1323 (1996)
[189] L. M. Brown, Phil Mag 96, 2696 (2016).
[190] J. E. Ayers, Appl. Phys. Lett., 92, 102104 (2008).
[191] K. Streubel, N. Linder, R. Wirth, and A. Jaeger, IEEE J. Sel. Top. Quant. Electron., 8, 321 (2002).
[192] O. Kwon, J. Boeckl, M. L. Lee, A. J. Pitera, E. A Fitzgerald, and S. A. Ringel, J. Appl. Phys., 97, 034504 (2005).
[193] P. Lever, H. H. Tan, and C. Jagadish, J. Appl. Phys., 95, 5710 (2004).
[194] D. Bimberga, M. Grundmanna, F. Heinrichsdorff, N. N. Ledentsov, V. M. Ustinov, A. E. Zhukov, A. R. Kovsh, M. V. Maximov, Y. M. Shernyakov, B.V. Volovik, A. F. Tsatsul'nikov, P.S. Kop'ev, Zh. I. Alferov, Thin Solid Films, 367, 235 (2000).
[195] D. E. Grider, S. E. Swirhun, D. H. Narum, A. I. Akinwande, T. E. Nohava, W. R. Stuart, P. Joslyn, and K. C. Hsieh, J. Vac. Sci. Technol. B, 8, 301 (1990).
[196] S. Mendach, C. M. Hu, Ch. Heyn, S. Schnull, H. P. Oepen, R. Anton, and W. Hansen, Physica E, 13, 1204 (2002).
[197] T. Kujofsa and J. E. Ayers, J. Vac. Sci. Technol. B, (32), 031205 (2014).
[198] T. Kujofsa, A. Antony, S. Xhurxhi, F. Obst, D. Sidoti, B. Bertoli, S. Cheruku, J. P. Correa, P. B. Rago, E. N. Suarez, F. C. Jain, and J. E. Ayers, J. Electron. Mat., 42, 3408 (2013).
[199] T. Kujofsa and J. E. Ayers, J. Electron. Mat., 45, 2831 (2016).
[200] T. Kujofsa and J. E. Ayers, J. Electron. Mat., 43, 2993 (2014).
[201] J. E. Ayers, Semicond. Sci. Technol., 23, 045018 (2008).
[202] D. Sidoti, S. Xhurxhi, T. Kujofsa, S. Cheruku, J. P. Correa, B. Bertoli, P. B. Rago, E. N. Suarez, F. C. Jain, J. E. Ayers, J. Appl. Phys., 109, 023510 (2011).
[203] S. Xhurxhi, F. Obst, D. Sidoti, B. Bertoli, T. Kujofsa, S. Cheruku, J. P. Correa, P. B. Rago, E. N. Suarez, F. C. Jain, and J. E. Ayers, J. Electron. Mat., 40, 2348 (2011).
[204] J. E. Ayers, T. Kujofsa, P. B. Rago and J. E. Raphael, *Heteroepitaxy of Semiconductors: Theory, Growth and Characterization, Second Edition,* CRC Press, Boca Raton, FL, 2016.

[205] D. J. Dunstan, Phil. Mag. A73, 1323 (1996).
[206] F. Romanato, E. Napolitani, A. Carnera, A. V. Drigo, L. Lazzarini, G. Salviati, C. Ferrari, A. Bosacchi, and S. Franchi, J. Appl. Phys., 86, 4748 (1999).
[207] K. Streubel, N. Linder, R. Wirth, and A. Jaeger, IEEE J. Sel. Top. Quant. Electron., 8, 321 (2002).
[208] P. Lever, H. H. Tan, and C. Jagadish, J. Appl. Phys., 95, 5710 (2004).
[209] S. Mendach, C. M. Hu, Ch. Heyn, S. Schnull, H. P. Oepen, R. Anton, and W. Hansen, Physica E, 13, 1204 (2002).
[210] G. K. Veerabathrana), S. Sprengel, A. Andrejew, and M.-C. Amann, Appl. Phys. Lett. 110, 071104 (2017).
[211] L. Shen, R. Coffie, D. Buttari, S. Heikman, A. Chakraborty, A. Chini, S. Keller, S. P. DenBaars, and U. K. Mishra, IEEE Electron Dev. Lett., 25, 7 (2004).
[212] H. Yang, H. Wang, K. Radhakrishnan, and C. L. Tan, IEEE Trans. Electron Dev., 51, 1221 (2004).
[213] D. Kohen, X. S. Nguyen, S. Yadav, A. Kumar, R. I. Made, C. Heidelberger, X. Gong, K. H. Lee, K. Eng, K. Lee, Y. C. Yeo, S. F. Yoon and E. A. Fitzgerald, AIP Adv., 6, 085106 (2016).
[214] T. Kujofsa, S. Cheruku, W. Yu, B. Outlaw, S. Xhurxhi, F. Obst, D. Sidoti, B. Bertoli, P. B. Rago, E. N. Suarez, F. C. Jain, and J. E. Ayers, J. Electron. Mat., 42, 2764 (2013).
[215] T. Kujofsa, S. Cheruku, B. Outlaw, S. Xhurxhi, F. Obst, D. Sidoti, B. Bertoli, P. B. Rago, E. N. Suarez, F. C. Jain, and J. E. Ayers, J. Electron. Mat., 41, 2993 (2012).
[216] B. W. Dodson, and J. Y. Tsao, Appl. Phys. Lett., 51, 1325 (1987).
[217] D. Andersen and R. Hull, J. Appl. Phys., 121, 075302 (2017).
[218] S. M. Hubbard, C. D. Cress, C. G. Bailey, R. P. Raffaelle, S. G. Bailey and D. M. Wilt, Appl. Phys. Lett., 92, 123512 (2008).
[219] A. Stiff-Roberts, S. Krishna, P. Bhattacharya, and S. Kennerly, J. Vac. Sci. Technol. B, 20, 1185 (2002).
[220] X. Q. Zhang, S. Ganapathy, H. Kumano, K. Uesugi, and I. Suemune, J. Appl. Phys., 92, 6813 (2002).
[221] B. I. Miller, U. Koren, M. G. Young, and M. D. Chien, Appl. Phys. Lett., **58**, 1952 (1991).
[222] N. Nuntawong, S. Birudavolu, C. P. Hains, S. Huang, H. Xu, and D. L. Huffaker, Appl. Phys. Lett., 85, 3050 (2004).
[223] T. Kujofsa and J. E. Ayers, Semicond. Sci. Technol., 31, 125005 (2016).
[224] T. Kujofsa and J. E. Ayers, Semicond. Sci. Technol., 31, 115014 (2016).
[225] J. W. Matthews, *Epitaxial Growth, Part B*, (Academic Press, New York, NY, 1975.)
[226] S. Akram, H. Ehsani, and I. B. Bhat, J. Cryst. Growth, 124, 628 (1992).
[227] S. Kalisetty, M. Gokhale, K. Bao, J. E. Ayers, and F. C. Jain, Appl. Phys. Lett., 68, 1693 (1996).
[228] P. Sheldon, K. M. Jones, M. M. Al-Jassim, and B. G. Yacobi, J. Appl. Phys., 63, 5609 (1988).
[229] J. E. Ayers, L. J. Schowalter, and S. K. Ghandhi, J. Cryst. Growth, 125, 329 (1992).
[230] I. Yonenaga, K. Watanabe, S. Itoh, and S. Fujiwara, J. Mater. Sci., 41, 2601 (2006).
[231] X. G. Zhang, D. W. Parent, P. Li, A. Rodriguez, G. Zhao, J. E. Ayers, and F. C. Jain, J. Vac. Sci. Technol. B, (2000).
[232] W. L. Roth, in Physics and Chemistry of II-VI Compounds, eds. M. Aven and J. S. Prener (Amsterdam: North-Holland Publishing Co., 1967).
[233] C. G. Hodgins and J. C. Irwin, Phys. Stat. Sol., A28, 647 (1975).
[234] J. E. Ayers, J. Cryst. Growth, 135, 71 (1994).

[235] Y. S. Touloukian, R. K. Kirby, R. E. Taylor, and T. Y. R. Lee, eds., Thermophysical Properties of Matter, Vol. 13: Thermal Expansion, Nonmetallic Solids (New York: Plenum, 1977).
[236] SS. Ballard, S. E. Brown, and J. S. Browder, Appl. Optics, 17, 1152 (1978).
[237] C. Giannini, L. Tapfer, T. Peluso, N. Lovergine, and L. Vasanelli, J. Phys. D, 28, A125 (1995).
[238] O. Madelung, Ed., Landolt-Bornstein: Numerical Data and Functional Relationships in Science and Technology – New Series, Vol. 17b (Berlin: Springer, 1982).
[239] S. S. Ballard and J. S. Browder, Appl. Optics, 12, 1873 (1966).
[240] R. B. Roberts, G. K. White, and T. M. Sabine, Aust. J. Phys., 34, 701 (1981).
[241] J. W. Matthews and A. E. Blakeslee, J. Cryst. Growth, 27, 118 (1974).
[242] J. H. van der Merwe, J. Appl. Phys., 34, 123 (1962).
[243] R. People and J. C. Bean, Appl. Phys. Lett., 49, 229 (1986).
[244] A. Fischer, H. Kühne and H. Richter, Phys. Rev. Lett., 73, 2712 (1994).
[245] L. B. Freund, J. Appl. Mech., 54, 553 (1987)
[246] X. G. Zhang, P. Li, D. W. Parent, P. Li, G. Zhao, J. E. Ayers, and F. C. Jain, J. Electron. Mater., 28, 553 (1999).
[247] T. Reisinger, M. J. Kastner, K. Wolf, E. Steinkirchner, W. Hackl, H. Stanzl, and W. Gebhardt, Mater. Sci. Forum, 182-184, 147 (1995).
[248] J. Petruzzello, B. L. Greenberg, D. A. Cammack, and R. Dalby, J. Appl. Phys., 63, 2299 (1988).
[249] C. B. O'Donnell, G. Lacey, G. Horsburgh, A. G. Cullis, C. R. Whitehouse, P. J. Parbrook, W. Meredith, I. Galbraith, P. Mock, K. A. Prior, and B. C. Cavanett, J. Cryst. Growth, 184/185, 95 (1988).
[250] C. D. Lee, B. K. Kim, J. W. Kim, S. K. Chang, and S. H. Suh, J. Appl. Phys., 76, 928 (1994).
[251] A. G. Kontos, E. Anastassakis, N. Chrysanthakopoulos, M. Calamiotou, and U. W. Pohl, J. Appl. Phys., 86, 412 (1999).
[252] D. J. Olego, J. Vac. Sci. Technol. B, 6, 1193 (1988).
[253] S. Ruvimov, E. D. Bourret, J. Washburn, and Z. Liliental-Weber, Appl. Phys. Lett., 68, 346 (1996).
[254] Y. S. Touloukian, R. K. Kirby, R. E. Taylor, and T. Y. R. Lee, eds., Thermophysical Properties of Matter, Vol. 13: Thermal Expansion, Nometallic Solids (New York: Plenum, 1977).
[255] K. Morimoto, *J. Appl. Phys. 66, 4206 (1989)*
[256] I. J. Fritz, Appl. Phys. Lett., 51, 1080 (1987).
[257] X. G. Zhang, S. Kalisetty, J. Robinson, G. Zhao, D. W. Parent, J. E. Ayers, and F. C. Jain, J. Electron. Mater., 26, 697 (1997).
[258] G. Alexe, H. Heinke, L. Haase, D. Hommel, J. Schreiber, M. Albrecht and H. P. Strunk. J. Appl. Phys., 97, 103506 (2005).
[259] P. Haasen, Acta. Met., 5, 598 (1957).
[260] T. Kujofsa, W.Yu, S. Cheruku, B. Outlaw, F. Obst, D. Sidoti, B. Bertoli, P. B. Rago, E. N. Suarez, F. C. Jain and J. E. Ayers, J. Electron. Mater. 41, 2993 (2012).
[261] T. Kujofsa S. Cheruku, D. Sidoti, S. Xhurxhi, F. Obst, J. P. Correa, B. Bertoli, P. B. Rago, E. N. Suarez, F. C. Jain, and J. E. Ayers, J. Vac. Sci. Technol. B, 34, 051201 (2016).
[262] T. Kujofsa and J. E. Ayers, J. Electron. Mater. 44, 3030 (2015).
[263] T. Kujofsa and J. E. Ayers, J. Electron. Mater. 45, 4580 (2016).
[264] X. G. Zhang, A. Rodriguez, X. Wang, P. Li, F. C. Jain, and J. E. Ayers, Appl. Phys. Lett., 77, 2524 (2000).
[265] J. F. Ocampo, E. Suarez, D. Shah, P. B. Rago, F. C. Jain, and J. E. Ayers, J. Electron. Mat., 37, 1035 (2008).

[266] S. I. Molina, F. J. Pacheco, D. Araujo, R. Garcia and A. Sacedon, J. Appl. Phys., 65, 2460, (1994).
[267] A. Sacedon, F.GonzalesSanz, E. Calleja, E. Munoz and S. I. Molina, J. Appl. Phys., 66, 3334, (1995).
[268] K. Arimoto, M. Watanabe, J. Yamanaka, K. Nakagawa, K. Sawano, Y. Shiraki, N. Usami and K.Nakajima, J. Solid State Elec., 53, 1135, (2009).
[269] D. E. Grider, S. E. Swirhun, D. H. Narum, A. I. Akinwande, T. E. Nohava, W. R. Stuart, and P. Joslyn, J. Vac. Sci. Technol. B, 8 (1990) 301-304.
[270] L. Shen, H. H. Wieder, and W. S. C. Chang, Mater. Res. Soc. Symp., 379 (1997) 297-301.
[271] A. Wakita, H. Rohden, V. Robbins, N. Mll, Chung-Yi Su, A. Nagy, and D. Basile, Jpn. J. Appl. Phys., 38 (1999) 1186-1189.
[272] X. Z. Shang, S. D. Wu, C. Liu, W. X. Wang, L. W. Guo, Q. Huang, J. Phys. D, 39 (2006) 1800-1804.
[273] B. Lee, J. H. Baek, J. H. Lee, S. W. Choi, S. D. Jung, W. S. Han, and E. H. Lee, Appl. Phys. Lett., 68 (1996) 2973-2975.
[274] I. Tangring, H. Q. Ni, B. P. Wu, D. H. Wu, Y. H. Xiong, S. S. Huang, Z. C. Niu, S. M. Wang, Z. H. Lai, and A. Larsson, Appl. Phys. Lett., 91 (2007) 221101.
[275] J.-F. He, H.-L. Wang, X.-J. Shang, M.-F. Li, Y. Zhu, L.-J. Wang, Y. Yu, H.-Q. Ni, Y.-Q. Xu, and Z.-C. Niu, J. Phys. D, 44 (2011) 335102.
[276] M. Stoehr, F. Hamdani, J. P. Lascaray, and M. Maurin, Phys. Rev. B., 44, 8912 (1991).
[277] Chyi, J. I., Shieh, J. L., Pan, J. W., & Lin, R. M, J. Appl. Phys. 79, 8367 (1996).
[278] E. F. Chor, C.J. Peng, Electron. Lett. 32, 1409 (1996).
[279] H. Choi, Y. Jeong, J. Cho, and M. H. Jeon, J. Cryst. Growth 311, 1091 (2009).
[280] B. Bertoli, D. Sidoti, S. Xhurxhi, T. Kujofsa, S. Cheruku, J. P. Correa, P. B. Rago, E. N. Suarez, J. E. Ayers, and F. C. Jain, J. Appl. Phys. 108, 113525 (2010).
[281] S. Xhurxhi, F. Obst, D. Sidoti, B. Bertoli, T. Kujofsa, S. Cheruku, J. P. Correa, P. B. Rago, E. N. Suarez, F. C. Jain, and J. E. Ayers, J. Electron. Mater. 40, 2348 (2011).
[282] T. Kujofsa, A. Antony, S. Xhurxhi, F. Obst, D. Sidoti, B. Bertoli, S. Cheruku, J. P. Correa, P. B. Rago, E. N. Suarez, F. C. Jain, and J. E. Ayers, J. Electron. Mater. 42, 3408 (2013).
[283] T. Kujofsa and J. E. Ayers, J. Electron. Mat. 44, 3030 (2015).
[284] T. Kujofsa, S. Cheruku, W. Yu, B. Outlaw, S. Xhurxhi, F. Obst, D. Sidoti, B. Bertoli, P. B. Rago, E. N. Suarez, F. C. Jain, and J. E. Ayers, J. Electron. Mat. 42, 2764 (2013).
[285] P. F. Fewster, Prog. Cryst. Growth Charact. Mater, 48/49, 245-273 (2004).
[286] X. G. Zhang et al., J. Vac. Sci. Technol. B. 18, 1375 (2000).
[287] X. G. Zhang et al., J. Electron. Mater., 26, 697 (1997).
[288] P. D. Healey et al., Acta. Cryst., A51, 498 (1995).
[289] A. R. Lang, *Ch. 12: X-Ray Detectors (pg. 320-332)* in B. K. Tanner and D. K. Bowen, Characterization of Crystal Growth Defects by X-Ray Methods on "Nato Advanced Study Institute Series B: Physics," Plenum Press, New York, NY, 1980.
[290] B. D. Cullity, Elements of X-Ray Diffraction, 2nd edition, Reading, MA: Addison-Wesley Publishing Company, 1978.
[291] P. Gay, P.B. Hirsch, and A. Kelly, Acta Met. 1, 315 (1953).
[292] J.E. Ayers, J. Cryst. Growth 135, 71 (1994).